Lecture Notes on Mathematical Modelling
in the Life Sciences

Paul C. Bressloff

Waves in Neural Media

From Single Neurons to Neural Fields

Springer

Lecture Notes on Mathematical Modelling in the Life Sciences

For further volumes:
http://www.springer.com/series/10049

Paul C. Bressloff

Waves in Neural Media

From Single Neurons to Neural Fields

Springer

Paul C. Bressloff
University of Utah
Department of Mathematics
Salt Lake City, UT, USA

ISSN 2193-4789 ISSN 2193-4797 (electronic)
ISBN 978-1-4614-8865-1 ISBN 978-1-4614-8866-8 (eBook)
DOI 10.1007/978-1-4614-8866-8
Springer New York Heidelberg Dordrecht London

Library of Congress Control Number: 2013948234

Mathematics Subject Classification (2010): 35C07, 82C31, 92C20, 92C30, 92C37, 82C31

Printed on acid-free paper

Springer is part of Springer Science+Business Media (www.springer.com)

To the Shmu

Preface

This is a book on mathematical neuroscience, in which the unifying theme is wavelike phenomena at multiple spatial and temporal scales. There are already several excellent books on applications of dynamical systems theory and bifurcation theory to neuroscience, but these are mainly concerned with mathematical models of neurons and networks that take the form of systems of ordinary differential equations (ODEs). Spatial aspects are usually restricted to standard partial differential equation (PDE) models of action potential propagation along axons and the spatial spread of voltage along dendrites (the cable equation). However, there are many other interesting spatiotemporal phenomena that are not usually addressed in any detail, at least within a single book. These include electrical and chemical waves along spiny dendrites, calcium waves in astrocytes, excitable and oscillatory waves in cortical and subcortical structures, binocular rivalry waves and ambiguous perception, oscillatory waves and swimming locomotion, cytoskeletal waves and neuritogenesis, spreading depression and migraine auras, the spread of prions and other neurodegenerative diseases within the brain, and epileptic waves in complex neural networks. All of these phenomena are linked by the notion of the time-dependent propagation or spread of some quantity in space, whether it is chemical concentration, a protein aggregate, voltage, or spiking activity of a population of neurons. They should be distinguished from another important class of spatial phenomena, namely, pattern-forming instabilities, which could be the subject of a future book!

In order to develop the themes of this book, I have endeavored to give a pedagogical introduction to the mathematical modeling of biological neurons and networks, as well as a toolbox of analytical techniques used to study wavelike phenomena, including the construction of traveling wave solutions of PDES and nonlocal equations, stability analysis, phase-plane analysis, singular perturbation theory, phase-reduction and averaging methods, and homogenization theory. A common thread throughout the book is an emphasis on stochasticity. In recent years, there has been an explosion of interest in the role of noise in biological systems, partly driven by the presence of low copy numbers in gene and biochemical networks. Noise is also ubiquitous in the brain, ranging from fluctuations in gene expression and the opening of ion-channel proteins to the Poisson-like spiking activity of individual

cortical neurons, the presence of fluctuations during perceptual decision making and bistable perception, and the generation of spontaneous activity during resting brain states. Hence, the book contains an introduction to the theory of stochastic processes and how it can be used to study the effects of noise on wave propagation and wave initiation. In the latter case, one typically has to solve an escape problem, in which noise drives some quantity such as voltage, calcium concentration, or population spiking activity above a threshold. This results, for example, in the generation of a spontaneous action potential, a calcium spark, or a transition between cortical up and down states, respectively.

Before giving a more detailed description of the contents of this book, I thought that I would elaborate a little on my own approach to neuroscience. This is not to favor one approach over another—a diversity of methodological and conceptual frameworks is crucial in trying to understand such a complex system as the brain—but rather to highlight my own tastes and biases. Let me begin with a story (perhaps apocryphal). Several years ago a well-known mathematical biology journal was relaunched with a new editorial board. At the final organizational meeting of the editors in chief, after some good food and wine, a satisfied glow spread around the room as the list of associate editors was drawn up, covering the major areas of biology. However, someone then sheepishly pointed out that one area was missing—neuroscience! I suspect that neuroscience has a slightly complicated relationship with the rest of theoretical biology due to the ambiguous notion of "computation." One sense of the word, which applies to all areas of biology, refers to the high level of biological detail and computational complexity in a model, which means that it is usually less amenable to mathematical analysis than simpler reduced models. The focus tends to be on issues such as parameter searches and data fitting, sensitivity analysis, numerical convergence, and computational efficiency. It follows that one way to characterize a modeling approach is where it lies on the mathematical–computational biology axis. Within this context, the present book is on mathematical rather than computational neuroscience, since I consider reduced, mathematically tractable models of wavelike phenomena.

The other sense of the word "computation" refers to a functional interpretation of the brain as a biological computer that processes sensory inputs via a sequence of internal brain states to produce a motor output or a change in cognitive state. A common assumption is that if we had a complete understanding of the physiology of the heart at the molecular, cellular, and systems levels, then we would understand the function of the heart, whereas the same is not true of the brain. That is, what makes neuroscience so challenging, beyond the incredible complexity of the brain as a biological organ, is how one links physiological brain states to behavior and cognition. Consequently, a major drive in computational neuroscience (in the second sense) is to link physiological descriptions of neurons and networks with computation and information processing. Popular themes are spike trains and neural coding, statistical correlations, the role of feedback in predictive coding, learning algorithms, Bayesian statistics, and maximum entropy. The current book is not concerned with this form of computational neuroscience either, since I do not really discuss the possible functional role of wavelike neural phenomena, although the role of waves

in development and disease is discussed at length. There have been some attempts to interpret the computational role of waves, based on the observation that cortical waves often occur between sensory processing events. However, such an observation is correlative at best and provides very little insight into the causal mechanisms of perception. Unfortunately, the same could be said of many of the overhyped results coming from functional magnetic resonance imaging (fMRI), where parts of the brain light up when someone is telling a joke or planning to commit a crime.

In the media lately, a number of distinguished physicists have had some harsh words to say about philosophy and its relevance to scientific questions. I personally disagree with such attitudes, partly due to my own interests in philosophy and also because I have found it useful to stand back occasionally in order to place my own work in a broader context. I think that this is particularly important in a field such as neuroscience, with all of its potential clinical, psychological, ethical, sociological, and cultural ramifications. Of course, reading philosophy does not make me a philosopher, so I proceed with caution. Nevertheless, I am a naturalist, in the sense that I do not believe the brain is made of different "stuff" or obeys different physical laws from planets, sushi, and hot tubs. On the other hand, I tend not to view the brain in functionalist terms, that is, as the hardware to the mind's software. I favor a more direct biological interpretation in terms of an evolved and adaptive system that enables an organism to carry out goal-directed behavior in a changing physical and social environment (although many people believe that this can be reformulated in terms of algorithms and computation). A related idea is that meaning or semantics cannot be generated from a purely syntactic process, since one needs to take into account the evolutionary and biographical history of an embodied mind acting within a societal and cultural context. Another reason I tend to steer clear of computational approaches is that I fear that using such a paradigm is in danger of imposing order, rationality, and engineering design principles on a rather messy and haphazard system. I tend to agree with the idea that the brain is a "kludge," in which modules that evolved to solve simpler problems have been thrown together suboptimally as the complexity of an organism has increased. I also feel that randomness plays a significant role in how we "think," which counters the idea of following a computer program or algorithm. I do not mean randomness in the sense of exploiting stochasticity to enhance performance (e.g., simulated annealing or random search), which itself could be algorithmic, but randomness as irrationality. People commit suicide, skateboard down Everest on a piano, and drink root beer (an alien concept to an Englishman).

The "elephant in the room" is the so-called hard problem of consciousness, that is, of explaining how and why we have qualia or phenomenal experiences. (This is a controversial issue, since some view qualia as an illusion based on misguided folk psychology or poor intuition pumps.) A related question is how one goes from objective brain states to subjective mental states. I would describe myself as a nonreductionist, in the sense that I believe mental properties supervene on (but are distinct from) physical properties and are an emergent feature of the physical brain. However, a systematic framework for understanding this emergence is currently beyond our grasp. An analogy is how one goes from microscopic descriptions of

molecules to macroscopic descriptions of states of matter. The latter also supervene on the former, but in this case we do have a framework for crossing the divide, namely, statistical mechanics. Hence, I do not believe we will discover a "statistical mechanics" of the brain, at least not during the funding periods of the European "Human Brain Project" and the USA's "BRAIN Initiative!" An interesting alternative to emergentism is neutral monism, which posits that protean versions of mental properties inhere in all physical objects—a form of panpsychism.

Having elucidated what this book is not about and why, let me now turn to its contents. The book is divided into three parts: Neurons (Chaps. 1–4), Networks (Chaps. 5–8), and Development and disease (Chap. 9). Chapter 1 provides a detailed introduction to the working parts of a neuron, including conductance-based models of action potential generation, synaptic and dendritic processing, and ion channels. Two important mathematical topics are also introduced. First, the dynamics of a periodically forced neural oscillator is used to introduce phase-reduction and averaging methods, phase-resetting curves, and synchronization. These are later applied to the study of waves in oscillatory neural media (Chap. 5). Second, a detailed account of stochastic ion channels and membrane voltage fluctuations is given, which also provides background material on stochastic processes. A major theme is how to model and analyze stochastic hybrid systems, in which a continuous variable (e.g., voltage) couples to a discrete jump Markov process (e.g., number of open ion channels). Spontaneous action potential generation is formulated as a first passage time problem, which is solved using perturbation methods such as WKB and matched asymptotics. These methods are later used to analyze related problems such as the generation of calcium sparks (Chap. 4) and bistability in populations of spiking neurons (Chap. 6). Chapter 2 covers the classical problem of waves in one-dimensional excitable media, as exemplified by the FitzHugh–Nagumo model of action potential propagation along an axon. Standard methods for analyzing front and pulse solutions of PDEs are described, including phase-plane analysis, singular perturbation methods and slow–fast analysis, and Evans functions for wave stability. In addition, the problem of wave propagation failure in myelinated axons is considered, where an averaging method is used to determine the effects of spatial discreteness on wave speed. This method is later used to analyze wave propagation failure in inhomogeneous neural fields (Chap. 7). Finally, stochastic traveling waves are considered, where formal perturbation methods are used to show how to separate out fast fluctuations of the wave profile from the slow diffusive-like wandering of the wave.

Chapter 3 presents two different models of traveling waves along spiny dendrites: a spike–diffuse–spike model of propagating voltage spikes mediated by active dendritic spines and a reaction–diffusion model of Ca^{2+}/calmodulin-dependent protein kinase II (CaMKII) translocation waves. The former model introduces methods that are also used to analyze solitary waves propagating in spiking neural networks (Chap. 5). The latter model turns out to be identical in form to the diffusive susceptible-infected (SI) model of the spread of epidemics, which is a generalization of the scalar Fisher–KPP equation of population genetics. One characteristic feature of such equations is that they support traveling fronts propagating into an unstable steady state, in which the wave speed and longtime asymptotics are determined by

the dynamics in the leading edge of the wave—the so-called pulled fronts. In particular, a sufficiently localized initial perturbation will asymptotically approach the traveling front solution that has the minimum possible wave speed. Hence, pulled fronts have very different properties from those considered in Chap. 2. Homogenization methods are also presented, which allow one to approximate the discrete distribution of spines by a smooth distribution. Chapter 4 gives a comprehensive review of calcium wave modeling, with an emphasis on their role in neuronal calcium signaling. Two models of intracellular waves are considered in some detail: a reaction–diffusion model of calcium dynamics and the fire–diffuse–fire model of calcium release. The latter is formally very similar to the spike–diffuse–spike model of spiny dendrites and is analyzed accordingly. Stochastic models of spontaneous calcium release (calcium puffs and sparks) are then analyzed using the stochastic methods introduced in Chap. 1. Finally, several models of intercellular calcium waves in astrocytes are presented. Traditionally, astrocytes were thought to be physiologically passive cells that only play a supporting role in the central nervous system by regulating and optimizing the environment within which neurons operate. However, there is an increasing amount of empirical data indicating that astrocytes play a more active role in modulating synaptic transmission and neuronal signal processing.

In the second part of the book, we consider a variety of neural network models that have been used to investigate the mechanisms and properties of wave propagation in cortex and other parts of the nervous system. There has been a rapid increase in the number of computational studies of network dynamics, which are based on biophysically detailed conductance-based models of synaptically (and possibly electrically) coupled neurons. These models provide considerable insights into the role of ionic currents, synaptic processing, and network structure on spatiotemporal dynamics, but they tend to be analytically intractable. This has motivated an alternative approach to network dynamics, involving simplified neuron models that hopefully capture important aspects of wave phenomena, while allowing a more concise mathematical treatment. In the case of oscillatory networks, such a simplification can be achieved by reducing a conductance-based neuron model to a phase model along the lines of Chap. 1. Alternatively, one can use a simplified spiking neuron model such as integrate-and-fire in order to investigate waves in excitable and oscillatory neural media. Both of these approaches are considered in Chap. 5, which also provides a summary of various wave phenomena in cortical and subcortical structures. Chapter 6 describes the construction of population-based rate models under the assumption that the spiking of individual neurons is unimportant. The issue of how stochasticity at the single-cell level manifests itself at the population level is discussed, introducing topics such as balanced networks, Poisson statistics, and asynchronous states. Stochastic methods are then used to analyze bistability in a stochastic population model. Finally, the transition from spatially structured neural networks to continuum neural fields is highlighted. The latter take the form of nonlocal integrodifferential equations, in which the integral kernel represents the distribution of synaptic connections.

Chapter 7 develops the theory of waves in excitable neural fields, where the fundamental network element is a local population of cells rather than a single neuron. It is shown how many of the PDE methods and results from the analysis of waves in reaction–diffusion equations considered in Part I can be extended to the nonlocal equations of neural field theory. First, the existence and stability of solitary traveling fronts and pulses in one-dimensional excitatory neural fields are considered. In the case of traveling pulses, it is necessary to include some form of local negative feedback mechanism such as synaptic depression or spike frequency adaptation. Two approaches to analyzing wave propagation failure in inhomogeneous neural media are then presented: one based on averaging methods and the other on interfacial dynamics. Finally, wave propagation in stochastic neural fields is analyzed and oscillatory waves in two-dimensional neural media are briefly discussed. In Chap. 8, neural field theory is used to model binocular rivalry waves. During binocular rivalry, visual perception switches back and forth between different images presented to the two eyes. The resulting fluctuations in perceptual dominance and suppression provide a basis for noninvasive studies of the human visual system and the identification of possible neural mechanisms underlying conscious visual awareness. Various psychophysical experiments have demonstrated that the switch between a dominant and suppressed visual percept propagates as a traveling front for each eye. In addition to considering the particular problem of binocular rivalry waves, the more general issue of how to develop neural field models of the functional architecture of primary visual cortex (V1) is discussed.

In the final part of the book, Chap. 9, a variety of topics regarding wavelike phenomena in the developing and diseased brain are presented. First, the possible role of calcium and retinal waves in early development is summarized. There is then a detailed description and analysis of cytoskeletal waves involved in neurite growth and cell polarization. This introduces another interesting phenomenon, namely, wave pinning. Three distinct examples of waves in the diseased brain are considered: spreading depression and migraine auras, epileptic waves, and the spread of neurodegenerative waves due to protein aggregation. In order to tackle the latter two phenomena, a review of complex network theory is included, covering topics such as small-world networks, scale-free networks, neuronal avalanches, branching processes, and epidemics on networks.

I end this introduction by noting that I sometimes have to deal with comments such as “neuroscience is pre-Newtonian” or “systems neuroscience lacks a Navier–Stokes equation.” My reaction to such comments is that it is for these very reasons that neuroscience is so exciting. One does not have to be as smart as Isaac Newton to work at the frontiers of a twenty-first-century science and have the chance to make a significant contribution. Of course, it also means that the contents of this book could one day be irrelevant and pass into dust the way of my flesh. If this does happen dear reader, please do not ask for your money back!

Salt Lake City, UT, USA Paul C. Bressloff

Acknowledgements

I would first like to thank my past graduate students: Pete Roper, Stefan Folias, Andy Oster, Berton Earnshaw, Will Nesse, Zack Kilpatrick, Jay Newby, Yi-Ming Lai, and Matt Webber. I have really enjoyed mentoring all of my students and collaborating on so many fun projects. There are a number of people who have inspired my own work in spatiotemporal aspects of mathematical neuroscience, either independently or in collaboration: Shun-Ichi Amari, Carson Chow, Jack Cowan, Steve Coombes, Bard Ermentrout, Olivier Faugeras, Marty Golubitsky, David Holcman, Jim Keener, Carlo Laing, John Rinzel, Jon Rubin, Dave Terman, Bill Troy, and Hugh Wilson. I would like to give a particular thanks to Jack Cowan, for his encouragement and guidance, and Steve Coombes for keeping the fire burning in the UK. I thank my parents Andy and Jackie for their unstinting love and support, Neil and his family for putting up with the crazy brother, and, last but not least, my wife Alessandra, who gave me the greatest gift of all, our son Luca. Ti amo e grazie mille per tutto.

Contents

Part I
Neurons

Chapter 1
Single Neuron Modeling

In this introductory chapter we describe conductance-based models of single neurons, which take into account action potential generation, the effects of external stimuli, synaptic and dendritic processing, and ion channel fluctuations. In the appendix we provide an informal introduction to stochastic calculus. In Chap. 2 we turn to the classical theory of waves in one-dimensional neural media, as exemplified by action potential propagation along axons. This will introduce some of the techniques used throughout the book, including phase-plane analysis, slow–fast systems, stability theory and Evans functions, averaging theory, and stochastic wave propagation. We then consider two examples of intracellular waves propagating along spiny dendrites (Chap. 3): the spike–diffuse–spike model of calcium-mediated spikes and a reaction–diffusion model of CaMKII translocation waves. A number of additional methods will be presented, including the analysis of waves in spiking models, homogenization theory, and the theory of pulled fronts. Finally, in Chap. 4 we consider both intracellular and intercellular calcium waves, emphasizing aspects that are specific to neurons. In particular, we highlight the important role of calcium signaling in astrocytes.

1.1 Conductance-Based Model of a Neuron

Cortical neurons typically consist of a cell body (or soma) where the nucleus containing DNA is located, a branching output structure known as the *axon* and a branching input structure known as the *dendritic tree*; see Fig. 1.1. Neurons mainly communicate with each other by sending electrical impulses or spikes (action potentials) along their axons. (Some neurons are also coupled diffusively via gap junctions [126].) These axons make contacts on the dendrites of other neurons via microscopic junctions known as *synapses*. The arrival of an electrical spike at a synaptic junction leads to the flow of electrical current along the dendritic tree of the stimulated neuron. If the total synaptic current from all of the activated synapses forces the electrical potential within the cell body to cross some threshold, then the neuron

P.C. Bressloff, *Waves in Neural Media: From Single Neurons to Neural Fields*,
Lecture Notes on Mathematical Modelling in the Life Sciences,
DOI 10.1007/978-1-4614-8866-8_1,

fires a spike. The standard biophysical model for describing the dynamics of a single neuron with somatic membrane potential v is based upon conservation of electric charge:

$$C\frac{dv}{dt} = -I_{\text{con}} + u + I_{\text{ext}}, \tag{1.1}$$

where C is the cell capacitance, I_{con} is the membrane current, u denotes the sum of synaptic currents entering the cell body, and I_{ext} describes any externally injected currents. Ions can diffuse in and out of the cell through ion specific channels embedded in the cell membrane. Ion pumps within the cell membrane maintain concentration gradients, such that there is a higher concentration of Na^+ and Ca^{2+} outside the cell and a higher concentration of K^+ inside the cell. The membrane current through a specific channel varies approximately linearly with changes in the potential v relative to some equilibrium or reversal potential, which is the potential at which there is a balance between the opposing effects of diffusion and electrical forces. Summing over all channel types, the total membrane current (flow of positive ions) leaving the cell through the cell membrane is

$$I_{\text{con}} = \sum_s g_s(v - V_s), \tag{1.2}$$

where g_s is the conductance due to channels of type s and V_s is the corresponding reversal potential. In the case of a channel selective to a single ion, V_s satisfies the Nernst equation

$$V_s = \frac{k_B T}{q} \ln\left(\frac{[outside]_s}{[inside]_s}\right), \tag{1.3}$$

where q is the charge of the ion, k_B is the Boltzmann constant, T is temperature (in degrees Kelvin), and $[outside]_s, [inside]_s$ denote the extracellular and intracellular concentrations of the given ion. Typical values for the common ion species are $V_{\text{K}} \approx -75\,\text{mV}$, $V_{\text{Na}} \approx 50\,\text{mV}$, $V_{\text{Ca}} \approx 150\,\text{mV}$, and $V_{\text{Cl}} \approx -60\,\text{mV}$ (which is close to the resting potential of the cell).

The generation and propagation of an action potential arises from nonlinearities associated with active membrane conductances. Recordings of the current flowing through single channels indicate that channels fluctuate rapidly between open and closed states in a stochastic fashion. Nevertheless, most models of a neuron use deterministic descriptions of conductance changes, under the assumption that there are a large number of approximately independent channels of each type. It then follows from the law of large numbers that the fraction of channels open at any given time is approximately equal to the probability that any one channel is in an open state. The conductance g_s for ion channels of type s is thus taken to be the product $g_s = \bar{g}_s P_s$ where $\bar{g}_s$ is equal to the density of channels in the membrane multiplied by the conductance of a single channel and P_s is the fraction of open channels. The voltage dependence of the probabilities P_s in the case of a delayed-rectifier K^+ current and a fast Na^+ current was originally obtained by Hodgkin and Huxley [279] as part of their Nobel Prize winning work on the generation of action potentials in the squid giant axon. The delayed-rectifier K^+ current is responsible for

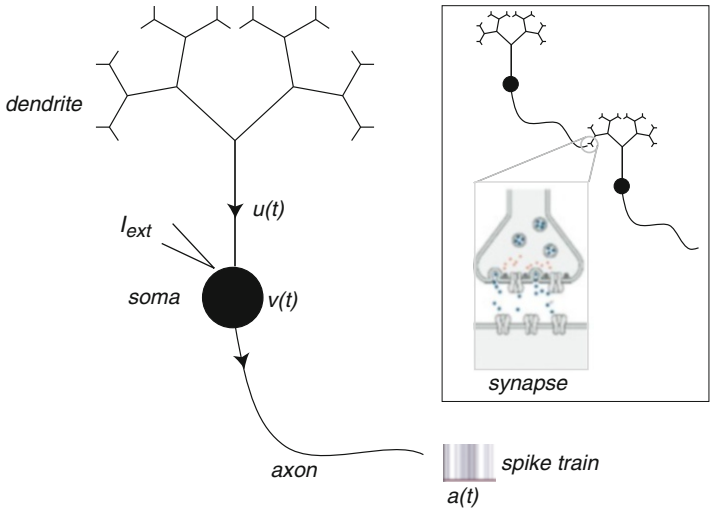

Fig. 1.1 Basic structure of a neuron. (Inset shows a synaptic connection from an upstream or presynaptic neuron and a downstream or postsynaptic neuron.) See text for details

terminating an action potential by repolarizing a neuron. One finds that opening of the K^+ channel requires structural changes in 4 identical and independent subunits so that $P_K = n^4$ where n is the probability that any one gate subunit has opened. In the case of the fast Na^+ current, which is responsible for the rapid depolarization of a cell leading to action potential generation, the probability of an open channel takes the form $P_{\rm Na} = m^3 h$ where m^3 is the probability that an activating gate is open and h is the probability that an inactivating gate is open. Depolarization causes m to increase and h to decrease, whereas hyperpolarization has the opposite effect.

The dynamics of the gating variables m, n, h are usually formulated in terms of a simple kinetic scheme that describes voltage-dependent transitions of each gating subunit between open and closed states. More specifically, for each $X \in \{m, n, h\}$

$$\frac{dX}{dt} = \alpha_X(v)(1 - X) - \beta_X(v)X, \tag{1.4}$$

where $\alpha_X(v)$ is the rate of the transition $closed \to open$ and $\beta_X(v)$ is the rate of the reverse transition $open \to closed$. Equation (1.4) can be rewritten in the alternative form

$$\tau_X(v)\frac{{\rm d}X}{{\rm d}t} = X_\infty(v) - X, \qquad \text{with } X \in \{m, n, h\}, \tag{1.5}$$

where

$$\tau_X(v) = \frac{1}{\alpha_X(v) + \beta_X(v)}, \qquad X_\infty(v) = \alpha_X(v)\tau_X(v).$$

It follows that the conductance variables m, n, and h approach the asymptotic values $m_\infty(v)$, $n_\infty(v)$, and $h_\infty(v)$ exponentially with time constants $\tau_m(v)$, $\tau_n(v)$, and $\tau_h(v)$,

respectively. From basic thermodynamic arguments, the opening and closing rates are expected to be exponential functions of the voltage. Hodgkin and Huxley [279] fitted exponential-like functions to the experimental data obtained from the squid axon:

$$\alpha_m = \frac{0.1(v+40)}{1-\exp[-0.1(v+40)]} \qquad \alpha_h = 0.07\exp[-0.05(v+65)],$$
$$\alpha_n = \frac{0.01(v+55)}{1-\exp[-0.1(v+55)]} \qquad \beta_m = 4.0\exp[-0.556(v+65)],$$
$$\beta_h = \frac{1}{1+\exp[-0.1(v+35)]} \qquad \beta_n = 0.125\exp[-0.125(v+65)].$$

All potentials are measured in mV, all times in ms, and all currents in $\mu A/cm^2$. The corresponding asymptotic functions $X_\infty(v)$ and time constants $\tau_X(v)$ are plotted in Fig. 1.2.

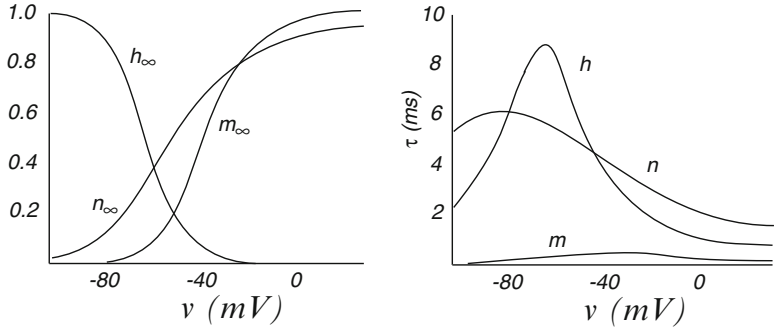

Fig. 1.2 Voltage-dependent steady-state levels of activation and inactivation (*left panel*) and voltage-dependent time constants (*right panel*) for the Hodgkin–Huxley model

We can now write down the Hodgkin–Huxley model for the generation of an action potential, which takes the membrane current to be the sum of a leakage current, a delayed-rectifier K^+ current, and a fast Na^+ current,

$$C\frac{dv}{dt} = f(v,m,n,h) + I_{\text{ext}}, \tag{1.6}$$

with

$$f(v,m,n,h) = -\bar{g}_{\text{Na}}m^3h(v-V_{\text{Na}}) - \bar{g}_{\text{K}}n^4(v-V_{\text{K}}) - \bar{g}_{\text{L}}(v-V_{\text{L}}). \tag{1.7}$$

The maximal conductances and reversal potentials used in the original model are $\bar{g}_{\text{L}} = 0.003\,\text{ms/mm}^2$, $\bar{g}_{\text{K}} = 0.36\,\text{mS/mm}^2$, $\bar{g}_{\text{Na}} = 1.2\,\text{mS/mm}^2$, $V_{\text{L}} = -54.387\,\text{mV}$, $V_{\text{K}} = -77\,\text{mV}$, and $V_{\text{Na}} = 50\,\text{mV}$. Note that the leakage current groups together various voltage-independent processes such as the currents carried by ion pumps that maintain the concentration gradients. The variables m,n,h evolve according to (1.4). The temporal evolution of the variables v,f,m,n,h during a single action potential is

shown in Fig. 1.3. Injection of a depolarizing current induces a rapid increase in the m variable describing activation of the Na^+ current. Since the slower h variable is initially around 0.6, there is a large influx of Na^+ ions, producing a sharp downward spike in the membrane current and a rapid depolarization through positive feedback. However, the rise in the membrane potential causes the Na^+ conductance to inactivate by driving h towards zero. In addition, the depolarization activates the K^+ conductance, resulting in a subsequent hyperpolarization.

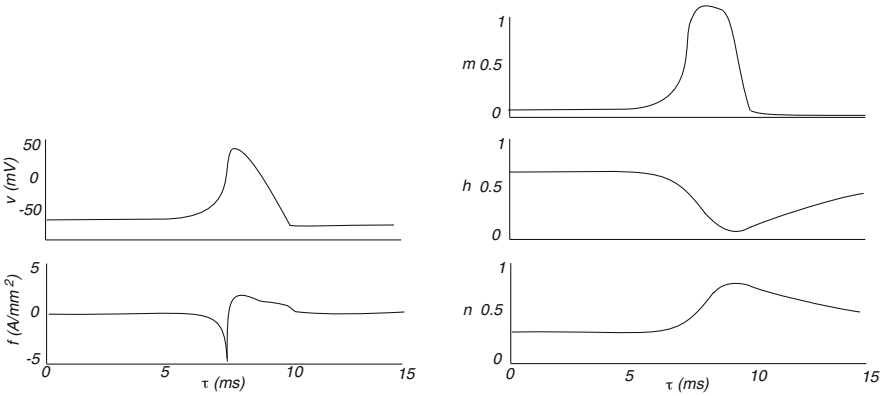

Fig. 1.3 The dynamics of v, f, n, m, h in the Hodgkin–Huxley model during the firing of an action potential induced by a current injection at $t = 5$ ms

Once a neuron has generated an action potential, it propagates as a traveling pulse along the axon of the neuron. In order to model a propagating action potential, it is necessary to combine the Hodgkin–Huxley conductance-based model given by (1.4) and (1.6) with a one-dimensional cable equation describing passive voltage changes along an axon or dendrite. The result is a partial differential equation of the form

$$C\frac{\partial v}{\partial t} = K\frac{\partial^2 v}{\partial x^2} + f(v,m,n,h), \tag{1.8}$$

where K is related to the membrane space constant of the cable; see Sect. 1.4, and $X = m,n,h$ evolve according to (1.4). Equation (1.8) is an example of a nonlinear reaction–diffusion equation used to model wave propagation in an excitable medium; one characteristic of an excitable medium is that it cannot support the passing of another wave until a certain amount of time has passed (known as the refractory period). A rigorous proof of the existence of traveling wave solutions of the spatially extended Hodgkin–Huxley equations has been developed [104, 267]. However, following standard treatments of waves in excitable media [242, 322, 444], we will develop the theory by considering the simpler FitzHugh–Nagumo model [192, 446]; see Chap. 2.

There is an ongoing debate about how best to characterize the output of a neuron, from either a dynamical systems or an information processing perspective. It is generally agreed that the detailed shape of an action potential is usually unimportant, so, at the fine temporal scale of a few milliseconds, the output of a neuron can be

represented in terms of the times at which the neuron fires an action potential (or spike). Given the conductance-based model (1.1), one typically identifies a firing threshold κ such that if $v(t)$ crosses the threshold from below at time $t = T$, then the neuron fires an action potential. If T^m denotes the mth firing time of the neuron since $t = 0$, say, then we have the threshold condition

$$T^m = \inf\{t, t > T^{m-1} | v(t) = \kappa, \dot{v}(t) > 0\}. \tag{1.9}$$

As an alternative to a spike timing representation of neuronal output, one can consider a rate-based representation that is obtained by filtering the spike train with some causal integral kernel $\Gamma(t)$, $\Gamma(t) = 0$ for $t < 0$:

$$z(t) = \sum_m \Gamma(t - T^m) = \int_{-\infty}^{\infty} \Gamma(t - \tau) a(\tau) d\tau, \tag{1.10}$$

where

$$a(t) = \sum_m \delta(t - T^m). \tag{1.11}$$

For example, if $\Gamma(t) = T^{-1}$ for $0 \le t < T$ and is zero otherwise, then $z(t)$ simply counts the number of spikes within the time interval $[t - T, t]$. In the special case of a regular spike train with $T^{m+1} - T^m = \Delta_0$ for all m, $z(t) = 1/\Delta_0$ in the limit $T \to \infty$.

Suppose, for the moment, that we ignore synaptic currents and consider what happens as the external input I_{ext} to a neuron is increased. Experimentally it is found that most cortical neurons switch from a resting state characterized by a low rate of (noise-driven) spontaneous firing to an active state characterized by either tonic (regular, repetitive) firing or bursting [131]. There has been considerable theoretical work on the transitions from resting to active states in conductance-based models based on bifurcation theory; see [173, 301] for excellent reviews. We will focus on tonic firing neurons, since these comprise the majority of cells in cortical networks. In the case of constant input $I_{\text{ext}} = I$, the firing rate $\bar{z}$ (mean number of spikes per second) of the neuron is typically found to be a nonlinear function of the input:

$$\bar{z} = F(I) \tag{1.12}$$

with the form of F depending on the nature of the bifurcation from the stable resting state to repetitive firing. A common bifurcation scenario in conductance-based models of cortical neurons is a saddle–node on an invariant circle [173, 301], which is classified as type I excitability. Close to the bifurcation point (see Fig. 1.4), we have

$$F(I) = F_0 \sqrt{I - I_c}, \tag{1.13}$$

where I_c is the critical current for onset of regular spiking. (Another common form of excitability is type II, in which the loss of stability of the resting state and the transition to repetitive firing occur via a Hopf bifurcation. There are also more exotic

forms of excitability as detailed elsewhere [201, 423].) If one includes stochastic effects arising from synaptic and membrane noise, for example, then the effective mean firing rate becomes a smooth sigmoid-like function of injected current,

$$F(I) = \frac{F_0}{1 + \mathrm{e}^{-\eta(I-\kappa)}}, \tag{1.14}$$

where η is the gain and κ is the firing threshold. In the high-gain limit $\eta \to \infty$, this reduces to a Heaviside firing rate function

$$F(I) = F_0 H(I-\kappa) = \begin{cases} F_0 & \text{if } I > \kappa \\ 0 & \text{if } I < \kappa. \end{cases} \tag{1.15}$$

Yet another commonly used firing rate function is the piecewise linear function

$$F(I) = \begin{cases} 0, & I < \kappa, \\ \eta(u-\kappa), & \kappa < I < \kappa + \eta^{-1}, \\ 1, & I > \kappa + \eta^{-1}. \end{cases} \tag{1.16}$$

This preserves the hard threshold of the saddle–node on a limit cycle bifurcation but ensures that the firing rate saturates at high input currents.

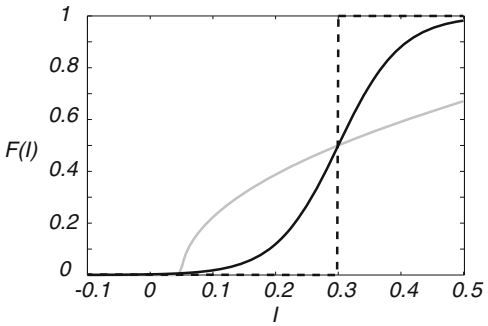

Fig. 1.4 Various forms of the nonlinear firing rate function $F(I)$. Sigmoid function (*black curve*) and Heaviside function (*dashed curve*) have a threshold $\kappa = 0.3$, whereas the square root function (*gray curve*) has a critical current $I_c = 0.05$

The issue of how to represent a single neuron becomes even more salient when considering synaptically coupled spiking networks (Chap. 5) and neural fields (Chap. 6). In order to make analytical progress, it is necessary either to consider a very simple model of a spiking neuron such as integrate-and-fire [323] (Sect. 5.3) or to carry out some form of reduction of a conductance-based model. In the case of weakly coupled neural oscillators, one can reduce the dynamics to a network of coupled phase oscillators; see Chap. 5. The basic ideas underlying so-called phase reduction methods can be understood by considering the simpler case of a single, periodically forced neural oscillator.

1.2 Periodically Forced Neural Oscillator

A conductance-based model of a neuron with constant input current can be formulated as an M-dimensional ($M \geq 2$) system of ODEs

$$\frac{d\mathbf{x}}{dt} = \mathbf{f}(\mathbf{x}), \qquad \mathbf{x} = (x_1, \ldots x_M). \tag{1.17}$$

Here x_1, say, represents the membrane potential of the neuron (treated as a point processor) and x_m, $m > 1$, represent various ionic channel gating variables. Suppose that the neuron has a stable periodic solution $\mathbf{x}(t) = \mathbf{x}(t + \Delta_0)$ where $\omega_0 = 2\pi/\Delta_0$ is the *natural frequency* of the oscillator. In *phase space* the solution is an isolated attractive trajectory called a *limit cycle*. The dynamics on the limit cycle can be described by a uniformly rotating phase such that

$$\frac{d\theta}{dt} = \omega_0, \tag{1.18}$$

and $\mathbf{x}(t) = \mathbf{g}(\theta(t))$ with $\mathbf{g}$ a 2π-periodic function. Note that the phase is *neutrally stable* with respect to perturbations along the limit cycle—this reflects invariance of an autonomous dynamical system with respect to time shifts. Now suppose that a small external periodic input is applied to the oscillator such that

$$\frac{d\mathbf{x}}{dt} = \mathbf{f}(\mathbf{x}) + \varepsilon \mathbf{p}(\mathbf{x}, t), \tag{1.19}$$

where $\mathbf{p}(\mathbf{x}, t) = \mathbf{p}(\mathbf{x}, t + \Delta)$ and $\omega = 2\pi/\Delta$ is the forcing frequency. If the amplitude ε is sufficiently small and the cycle is stable, then deviations transverse to the limit cycle are small so that the main effect of the perturbation is to induce shifts in the phase. Therefore, we need to extend the definition of phase to a neighborhood of the limit cycle. This leads to the notion of an *isochrone* [221, 350, 679].

1.2.1 Isochrones and Phase-Resetting Curves

Suppose that we observe the unperturbed system stroboscopically at time intervals of length Δ_0. This leads to a Poincare mapping

$$\mathbf{x}(t) \to \mathbf{x}(t + \Delta_0) \equiv \mathscr{P}(\mathbf{x}(t)).$$

This mapping has all points on the limit cycle as fixed points. Choose a point $\mathbf{x}^*$ on the cycle and consider all points in the vicinity of $\mathbf{x}^*$ that are attracted to it under the action of $\mathscr{P}$. They form an $(M-1)$-dimensional hypersurface $\mathscr{I}$, called an isochrone, crossing the limit cycle at $\mathbf{x}^*$ (see Fig. 1.5). A unique isochrone can be drawn through each point on the limit cycle so we can parameterize the isochrones by the phase, $\mathscr{I} = \mathscr{I}(\theta)$. Finally, we extend the definition of phase by taking all

points $\mathbf{x} \in \mathscr{I}(\theta)$ to have the same phase, $\Theta(\mathbf{x}) = \theta$, which then rotates at the natural frequency ω_0 (in the unperturbed case). Hence, for an unperturbed oscillator in the vicinity of the limit cycle, we have

$$\omega_0 = \frac{d\Theta(\mathbf{x})}{dt} = \sum_k \frac{\partial \Theta}{\partial x_k} \frac{dx_k}{dt} = \sum_k \frac{\partial \Theta}{\partial x_k} f_k(\mathbf{x}).$$

Now consider the perturbed system but with the unperturbed definition of the phase:

$$\frac{d\Theta(\mathbf{x})}{dt} = \sum_k \frac{\partial \Theta}{\partial x_k} (f_k(\mathbf{x}) + \varepsilon p_k(\mathbf{x},t)) = \omega_0 + \varepsilon \sum_k \frac{\partial \Theta}{\partial x_k} p_k(\mathbf{x},t).$$

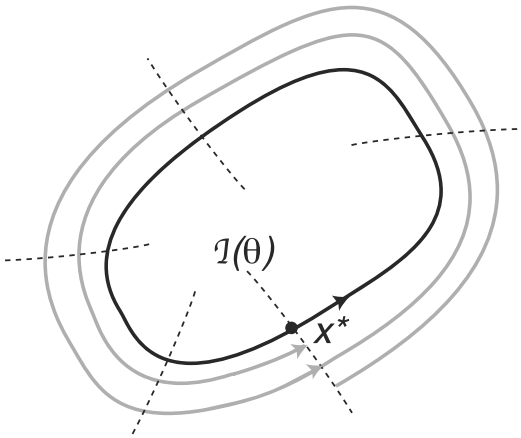

Fig. 1.5 Isochrones in the neighborhood of a stable limit cycle

To a first approximation we can neglect deviations of $\mathbf{x}$ from the limit cycle which we denote by $\mathbf{x}^*$:

$$\frac{d\Theta(\mathbf{x})}{dt} = \omega_0 + \varepsilon \sum_k \frac{\partial \Theta(\mathbf{x}^*)}{\partial x_k} p_k(\mathbf{x}^*,t).$$

Finally, since points on the limit cycle are in 1:1 correspondence with the phase θ, we obtain the closed phase equation

$$\frac{d\theta}{dt} = \omega_0 + \varepsilon Q(\theta,t), \tag{1.20}$$

where

$$Q(\theta,t) = \sum_k \frac{\partial \Theta(\mathbf{x}^*(\theta))}{\partial x_k} p_k(\mathbf{x}^*(\theta),t) \tag{1.21}$$

is a 2π-periodic function of θ and a Δ-periodic function of t.

Consider, as an example, the complex amplitude equation that arises for a limit cycle oscillator close to a Hopf bifurcation [248]:

$$\frac{dA}{dt} = (1+i\eta)A - (1+i\alpha)|A|^2 A, \quad A \in \mathbb{C}. \tag{1.22}$$

In polar coordinates $A = Re^{i\phi}$,

$$\frac{dR}{dt} = R(1-R^2), \quad \frac{d\phi}{dt} = \eta - \alpha R^2.$$

The solution for arbitrary initial data $R(0) = R_0$, $\theta(0) = \theta_0$ is

$$\begin{aligned} R(t) &= \left[1 + \frac{1-R_0^2}{R_0^2} e^{-2t}\right]^{-1/2}, \\ \phi(t) &= \phi_0 + \omega_0 t - \frac{\alpha}{2}\log(R_0^2 + (1-R_0^2)e^{-2t}), \end{aligned} \tag{1.23}$$

where $\omega_0 = \eta - \alpha$ is the natural frequency of the stable limit cycle at $R = 1$. Strobing the solution at times $t = n\Delta_0$, we see that

$$\lim_{n\to\infty} \phi(n\Delta_0) = \phi_0 - \alpha \ln R_0.$$

Hence, we can define a phase on the whole plane

$$\Theta(R,\phi) = \phi - \alpha \ln R. \tag{1.24}$$

It follows that the isochrones are logarithmic spirals with $\phi - \alpha \ln R =$ constant. Now rewrite (1.22) in Cartesian coordinates

$$\begin{aligned} \frac{dx}{dt} &= x - \eta y - (x^2+y^2)(x-\alpha y) + \varepsilon \cos \omega t, \\ \frac{dy}{dt} &= y + \eta y - (x^2+y^2)(y+\alpha x), \end{aligned}$$

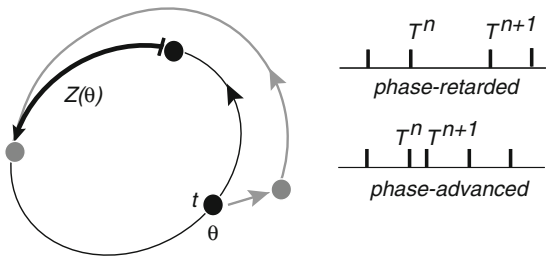

Fig. 1.6 Phase shift $Z(\theta)$ induced by a small perturbation of the membrane potential applied at time $t = 0$ when the phase of the limit cycle is θ. *Black* (*gray*) *dots* represent points on the unperturbed (perturbed) trajectory. The phase shift induces a corresponding shift in successive firing times

where we have added a periodic modulation in the x-direction. Rewrite the phase (1.24) as

$$\Theta = \tan^{-1}\frac{y}{x} - \frac{\alpha}{2}\log(x^2+y^2),$$

so that

$$\frac{\partial\Theta}{\partial x} = -\frac{y}{x^2+y^2} - \alpha\frac{x}{x^2+y^2}.$$

On the limit cycle $\mathbf{x}_0(\theta) = (\cos\theta, \sin\theta)$, we have

$$\frac{\partial\Theta(\mathbf{x}_0)}{\partial x} = -\sin\theta - \alpha\cos\theta.$$

It follows that the corresponding phase equation is

$$\frac{d\theta}{dt} = \omega_0 - \varepsilon(\alpha\cos\theta + \sin\theta)\cos\omega t.$$

The phase reduction method is particularly useful because the function $Q(\theta,t)$ can be related to an easily measurable property of a neural oscillator, namely, its *phase-resetting curve* (PRC), which we denote by the 2π-periodic function $Z(\theta)$. The PRC is found experimentally (or numerically) by perturbing the oscillator with a brief depolarizing voltage stimulus of size $\varepsilon\Delta V$ at different times in its cycle and measuring the resulting phase shift from the unperturbed system [221, 679]; see Fig. 1.6. Taking the coordinate x_1 as the membrane potential, it follows from (1.20) that

$$\frac{d\theta}{dt} = \omega_0 + \varepsilon\Delta x_1\frac{\partial\Theta(\mathbf{x}^*(\theta))}{\partial x_1}\delta(t-t_0). \tag{1.25}$$

Integrating this equation over a small interval around t_0, we see that the impulse induces a phase shift $\Delta\theta = (\varepsilon\Delta x_1)Z(\theta_0)$ where $Z(\theta) = \partial\Theta(\mathbf{x}^*(\theta))/\partial x_1$ and $\theta_0 = \theta(t_0)$. Thus comparing the phase at large times for the unperturbed and perturbed cases generates the PRC. Given the PRC $Z(\theta)$, the response of the neuron to a more general time-dependent voltage perturbation $\varepsilon P(t)$ is determined by the phase equation

$$\frac{d\theta}{dt} = \omega_0 + \varepsilon Z(\theta)P(t). \tag{1.26}$$

We can also express the PRC in terms of the firing times of a neuron (assuming fast reconvergence to the limit cycle). Suppose that there exists a well-defined threshold κ signaling the onset of fast somatic membrane depolarization and the subsequent firing of an action potential spike. Let T^n denote the nth firing time of the neuron as defined by (1.9). Since the membrane voltage $v(t) = x_1(\theta(t))$, the threshold corresponds to a particular phase of the limit cycle, which we choose to be $\theta = 0$. In the absence of perturbations, we have $\theta(t) = 2\pi t/\Delta_0$, so that the firing times are $T^n = n\Delta_0$ where Δ_0 is the natural period of oscillation. On the other hand, a small perturbation applied at the point θ on the limit cycle at time $t, T^n < t < T^{n+1}$, induces a phase shift that changes the next time of firing according to (see Fig. 1.6)

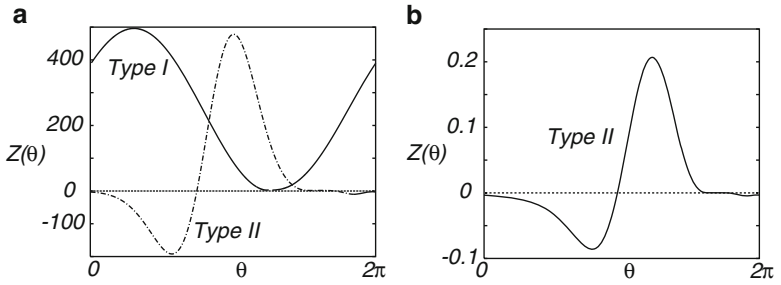

Fig. 1.7 (**a**) Morris–Lecar model showing two different response types. In both cases $v_k = -0.7$, $u_L = -0.5$, $u_{Ca} = 1$, $g_K = 2$, $g_L = 0.5$, $v_1 = -0.01$, $v_2 = 0.15$. For a type I response, $g_{Ca} = 1.33$, $v_3 = 0.1$, $v_4 = 0.145$, $\phi = 1/3$, and $I = 0.0695$. For a type II response, $g_{Ca} = 1.1$, $v_3 = 0$, $v_4 = 0.3$, $\phi = 0.2$, and $I = 0.25$. Responses have been scaled to the same ranges. (**b**) Hodgkin–Huxley model with external drive $I = 10$ showing type II phase-resetting curve

$$\frac{T^{n+1} - T^n}{\Delta_0} = 1 - \frac{(\varepsilon \Delta V) Z(\theta)}{2\pi}. \tag{1.27}$$

For certain types of neuron a depolarizing stimulus always advances the onset of the next spike, that is, the PRC is always positive, whereas for others the stimulus may also delay the next spike. Oscillators with a strictly positive PRC are called type I whereas those for which the PRC has a negative regime are called type II. A numerical example illustrating both types of PRC is shown in Fig. 1.7a for the Morris–Lecar model of a neuron, which was originally introduced to describe how under constant current injection barnacle muscle fibers respond with a host of oscillatory voltage waveforms [440]. It takes the form

$$\begin{aligned} \frac{dv}{dt} &= I - g_L(v - v_L) - g_K w(v - v_K) - g_{Ca} m_\infty(v)(v - v_{Ca}), \\ \frac{dw}{dt} &= \lambda(v)(w_\infty(v) - w), \end{aligned} \tag{1.28}$$

with

$$\begin{aligned} m_\infty(v) &= 0.5(1 + \tanh[(v - v_1)/v_2]), \\ w_\infty(v) &= 0.5(1 + \tanh[(v - v_3)/v_4]), \\ \lambda(v) &= \phi \cosh[(v - v_3)/(2v_4)]. \end{aligned}$$

Here, g_L is the leakage conductance, g_K, g_{Ca} are potassium and calcium conductances, v_L, v_K, v_{Ca} are corresponding reversal potentials, $m_\infty(v)$, $w_\infty(v)$ are voltage-dependent gating functions, and $\lambda(v)$ is a voltage-dependent rate. The type II PRC for the Hodgkin–Huxley model is shown in Fig. 1.7b.

1.2.2 Phase-Locking and Synchronization

Now suppose that $Q(\theta, t)$ in (1.20) is expanded as a double Fourier series

$$Q(\theta,t) = \sum_{l,k} a_{l,k} e^{ik\theta + il\omega t}.$$

Substitute for θ using the zero-order approximation $\theta = \omega_0 t + \theta_0$:

$$Q(\theta,t) = \sum_{l,k} a_{l,k} e^{ik\theta_0 + i(k\omega_0 + l\omega)t}.$$

It follows that Q contains fast oscillating terms (compared to the time scale Δ_0/ε) together with slowly varying terms that satisfy the *resonance condition*

$$k\omega_0 + l\omega \approx 0. \tag{1.29}$$

Only the latter will lead to large variations in the phase, so we can average the forcing term Q keeping only the resonant terms. The simplest case is $\omega \approx \omega_0$ for which the resonant terms satisfy $l = -k$ and

$$Q(\theta,t) \to \sum_k a_{-k,k} e^{ik(\theta - \omega t)} = q(\theta - \omega t). \tag{1.30}$$

The phase equation then becomes

$$\frac{d\theta}{dt} = \omega_0 + \varepsilon q(\theta - \omega t).$$

The phase difference between the oscillator and external drive, $\psi = \theta - \omega t$, then satisfies the equation

$$\frac{d\psi}{dt} = -\Delta\omega + \varepsilon q(\psi), \tag{1.31}$$

where $\Delta\omega = \omega - \omega_0$ is the degree of *frequency detuning*. Similarly, if $\omega \approx m\omega_0/n$, then

$$Q(\theta,t) \to \sum_k a_{-nj,mj} e^{ij(m\theta - n\omega t)} = \hat{q}(m\theta - n\omega t), \tag{1.32}$$

and

$$\frac{d\psi}{dt} = m\omega_0 - n\omega + \varepsilon m\hat{q}(\psi), \tag{1.33}$$

where $\psi = m\theta - n\omega t$.

The above is an example of an application of the averaging theorem [248]. Assuming that $\Delta\omega = \omega - \omega_0 = \mathcal{O}(\varepsilon)$ and defining $\psi = \theta - \omega t$, we have

$$\frac{d\psi}{dt} = -\Delta\omega + \varepsilon Q(\psi + \omega t, t) = \mathcal{O}(\varepsilon). \tag{1.34}$$

Define

$$q(\psi) = \lim_{T\to\infty} \frac{1}{T} \int_0^T Q(\psi + \omega t, t) dt, \tag{1.35}$$

and consider the averaged equation

$$\frac{d\psi}{dt} = -\Delta\omega + \varepsilon q(\psi). \tag{1.36}$$

It is easy to establish that q only contains the resonant terms of Q as above. The averaging theorem ensures that there exists a change of variables that maps solutions of the full equation to those of the averaged equation to leading order in ε. The question then remains as to what extent solutions of the averaged equations are a good approximation to the solutions of the full equation. In general, one can only establish that a solution of the full equation is ε-close to a corresponding solution of the averaged system for times of $\mathcal{O}(\varepsilon^{-1})$. No such problem occurs however for hyperbolic fixed points corresponding to phase-locked states.

Suppose that the 2π-periodic function $q(\psi)$ has a unique maximum q_{max} and a unique minimum q_{min} in the interval $[0, 2\pi)$. We can then distinguish between two regimes [502]:

Synchronization regime: If the degree of detuning for a given drive amplitude is sufficiently small,

$$\varepsilon q_{min} < \Delta\omega < \varepsilon q_{\max},$$

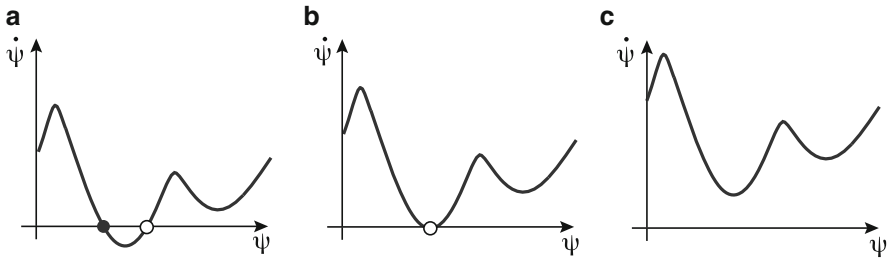

Fig. 1.8 Saddle–node bifurcation signaling a transition from a synchronized to a drifting state as the size of frequency detuning $|\Delta\omega|$ increases (**a**) Synchronization regime. (**b**) Saddle–node bifurcation. (**c**) Drift regime

then there exists at least one pair of stable/unstable fixed points (ψ_s, ψ_u). (This follows from the fact that $q(\psi)$ is 2π-periodic and continuous so it has to cross any horizontal line an even number of times.) The system evolves to the synchronized state

$$\theta(t) = \omega t + \psi_s,$$

in which the oscillator is *phase-locked* to the external drive and is *frequency entrained*. Note that the stability of a phase-locked state is determined by the sign of $q'(\psi)$ with $q'(\psi_s) < 0$ and $q'(\psi_u) > 0$ (see Fig. 1.8a).

Drift regime: As $|\Delta\omega|$ increases, it approaches one of the critical values $\varepsilon q_{min,max}$ where the two fixed points coalesce in a saddle–node bifurcation and phase-locking disappears; see Fig. 1.8b, c. Hence, if the degree of tuning is large, then $d\psi/dt$ never changes sign and the oscillation frequency differs from the drive frequency ω. The phase $\psi(t)$ rotates through 2π with period

$$T_\psi = \left| \int_0^{2\pi} \frac{d\psi}{\varepsilon q(\psi) - \Delta\omega} \right|. \tag{1.37}$$

The mean frequency of rotation is thus $\Omega = \omega + \Omega_\psi$ where $\Omega_\psi = 2\pi/T_\psi$ is known as the *beat frequency*. One is often interested in how the behavior varies in the $(\Delta\omega, \varepsilon)$-plane (see Fig. 1.9). First the boundary between the two regimes consists of the two straight lines $\Delta\omega = \varepsilon q_{max,min}$. Second, close to the boundary Ω_ψ has a characteristic form. Suppose, for example, that $\Delta\omega - \Delta\omega_{max}$ is small for fixed ε with $\Delta\omega_{max} = \varepsilon q_{max}$. The integral in (1.37) is then dominated by a small region around ψ_{max}. Expanding $q(\psi)$ as a Taylor series,

$$\begin{aligned} \Omega_\psi = \frac{2\pi}{T_\psi} &\approx 2\pi \left| \int_{-\infty}^{\infty} \frac{d\psi}{\varepsilon q''(\psi_{max})\psi^2 - (\Delta\omega - \Delta\omega_{max})} \right|^{-1} \\ &= \sqrt{\varepsilon |q''(\psi_{max})| (\Delta\omega - \Delta\omega_{max})}. \end{aligned} \tag{1.38}$$

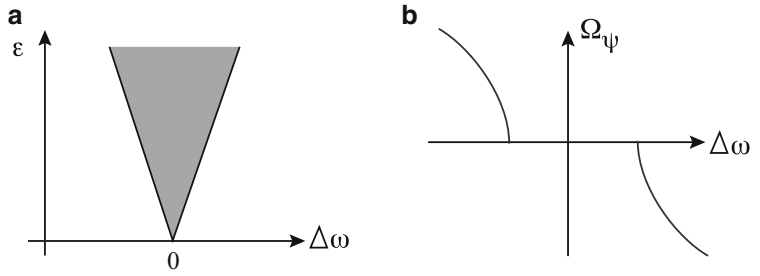

Fig. 1.9 (**a**) Synchronization regime (*shaded*) in $(\Delta\omega, \varepsilon)$-plane. (**b**) Variation of beat frequency with $\Delta\omega$ for fixed ε

1.3 Synaptic Processing

In the conductance-based model given by (1.6), we decomposed the total input current to the soma into an external part $I_{\text{ext}}(t)$ and a synaptic part $u(t)$. In this section, we consider the current generated at a single synapse and the sequence of events underlying conductance changes in the postsynaptic membrane due to the arrival of an action potential at the presynaptic terminal. We then show how these conductance changes can be modeled in terms of a kinetic scheme describing the opening and closing of ion channels in the postsynaptic membrane.

1.3.1 Excitatory and Inhibitory Synapses

The basic stages of synaptic processing induced by the arrival of an action potential at an axon terminal are shown in Fig. 1.10. (See [99] for a more detailed description.) An action potential arriving at the terminal of a presynaptic axon causes voltage-gated Ca^{2+} channels within an active zone to open. The influx of Ca^{2+} produces a high concentration of Ca^{2+} near the active zone [45, 195], which in turn causes vesicles containing neurotransmitter to fuse with the presynaptic cell membrane and release their contents into the synaptic cleft (a process known as exocytosis). The released neurotransmitter molecules then diffuse across the synaptic cleft and bind to specific receptors on the postsynaptic membrane. These receptors cause ion channels to open, thereby changing the membrane conductance and membrane potential of the postsynaptic cell. A single synaptic event due to the arrival of an action potential at time T induces a synaptic current of the form

$$I_{\text{syn}}(t) = g_{\text{syn}}(t-T)(V_{\text{syn}} - v(t)), \tag{1.39}$$

where v is the voltage of the postsynaptic neuron, V_{syn} is the synaptic reversal potential, and $g_{\text{syn}}(t)$ is the change in synaptic conductance with $g_{\text{syn}}(t) = 0$ for $t < 0$. The sign of V_{syn} relative to the resting potential V_{rest} (typically $V_{\text{rest}} \approx -65\,\text{mV}$) determines whether the synapse is excitatory ($V_{\text{syn}} > V_{\text{rest}}$) or inhibitory ($V_{\text{syn}} < V_{\text{rest}}$). For simplicity, it is often assumed that a neuron spends most of its time close to rest such that $V_{\text{syn}} - v \approx V_{\text{syn}} - V_{\text{rest}}$, with the factor $V_{\text{syn}} - V_{\text{rest}}$ absorbed into g_{syn}. One is then effectively taking the arrival of a spike as generating a synaptic current rather than a change in conductance.

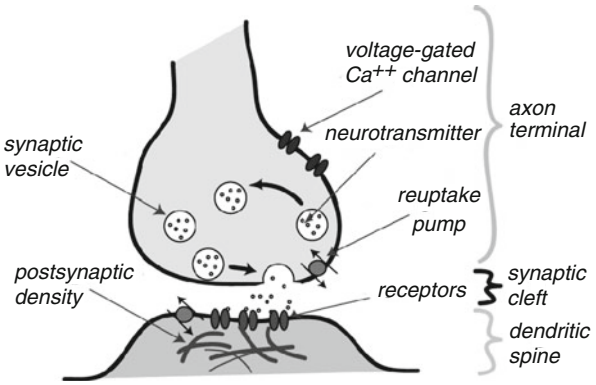

Fig. 1.10 Basic stages of synaptic processing shown for an excitatory synapse. See text for details

The predominant fast, excitatory neurotransmitter of the vertebrate central nervous system is the amino acid *glutamate*, whereas in the peripheral nervous system, it is *acetylcholine*. Glutamate-sensitive receptors in the postsynaptic membrane can be subdivided into two major types, namely, NMDA and AMPA [99].

At an AMPA receptor the postsynaptic channels open very rapidly. The resulting increase in conductance peaks within a few hundred microseconds, with an exponential decay of around 1 ms. The time course of the synaptic conductance change can be modeled in terms of an nth state Markov process [154] (see Sect. 1.3.3). Usually a simplified representation of $g_{\text{syn}}(t)$ is used that is given by the difference of exponentials

$$g_{\text{syn}}(t) = \bar{g}\left(\frac{1}{\tau_2} - \frac{1}{\tau_1}\right)(\mathrm{e}^{-t/\tau_1} - \mathrm{e}^{-t/\tau_2})H(t), \tag{1.40}$$

with $H(t)$ the Heaviside function. In many cases, the rise time is much shorter than the fall time ($\tau_1 \ll \tau_2$) so that we have an exponential synapse with $g_{\text{syn}}(t) = \bar{g}\mathrm{e}^{-t/\tau_d}$. In the limit $\tau_2 \to \tau_1 = \alpha^{-1}$, (1.40) reduces to the well-known α function

$$g_{\text{syn}}(t) = \bar{g}\alpha^2 t\mathrm{e}^{-\alpha t}H(t). \tag{1.41}$$

These expressions for the conductance are also used for GABA inhibitory synapses (see below). In contrast to an AMPA receptor, the NMDA receptor operates about ten times slower and the amplitude of the conductance change depends on the postsynaptic membrane potential. If the postsynaptic potential is at rest and glutamate is bound to the NMDA receptor, then the channel opens, but it is physically obstructed by Mg^{2+} ions. As the membrane is depolarized, the Mg^{2+} ions move out and the channel becomes permeable to Na^+ and Ca^{2+} ions. The NMDA conductance can be derived from a model in which the binding rate constant of Mg^{2+} varies as an exponential function of the local voltage v [304]:

$$g_{\text{syn}}(t) = g\frac{\mathrm{e}^{-t/\tau_1} - \mathrm{e}^{-t/\tau_2}}{1 + \eta[Mg^{2+}]\mathrm{e}^{-\gamma v(t)}}, \quad t > 0, \tag{1.42}$$

where $[X]$ denotes concentration of X and η is a rate constant. The rapid influx of calcium ions due to the opening of NMDA channels is thought to be the critical trigger for the onset of *long-term potentiation* or LTP, a major component of synaptic plasticity (see also Sect. 4.1).

The most common inhibitory neurotransmitter in the central nervous system of both vertebrates and invertebrates appears to be GABA. There are two major forms of postsynaptic receptors termed A and B. The GABA_A receptors open channels selective to chloride ions, whose reversal potential $V_{\text{syn}} = -70\,\text{mV}$ is close to that of the resting potential. The postsynaptic conductance change is quite fast, rising within 1 ms and decaying within 10–20 ms. GABA_B receptors are at least 10 times slower and open ion channels selective for K^+ ions. Thus they tend to be considerably more hyperpolarizing with $V_{\text{syn}} \approx -100\,\text{mV}$. The two receptor classes tend to be segregated with GABA_A occurring at or close to the soma and GABA_B further out on the dendrites. Another way to distinguish between GABA_A and GABA_B receptors is that the former are *ionotropic* (as are NMDA and AMPA) while the latter are *metabotropic* [99]. Neurotransmitter binding to an ionotropic receptor directly opens an ion channel through a series of conformational changes of the receptor. On

the other hand, neurotransmitter binding to a metabotropic receptor indirectly opens an ion channel elsewhere in the membrane through a sequence of biochemical steps mediated by G proteins.

1.3.2 Synaptic Depression

A single synaptic event due to the arrival of an action potential at time T induces a synaptic current of the form (1.39). As a crude approximation we might try summing individual responses to model the synaptic current arising from a train of action potentials arriving at times T^m, integer m:

$$I_{\rm syn}(t) = \sum_m g_{\rm syn}(t - T^m)(V_{\rm syn} - v(t)). \tag{1.43}$$

Note that this sum only includes spikes for which $T^m < t$ since $g_{\rm syn}(t) = 0$ for $t < 0$ (causality condition). For many synapses such a simple ansatz does not hold, since some form of short-term synaptic depression causes the amplitude of the response to depend on the previous history of presynaptic firing [4, 405]. One way to incorporate this history-dependent effect is to take [1]

$$I_{\rm syn}(t) = \left[\sum_m q(T^m) g_{\rm syn}(t - T^m)\right](V_{\rm syn} - v(t)), \tag{1.44}$$

where the factor $q(T^m)$ reduces the response evoked by an action potential by an amount that depends upon the details of the previous spike train data. One interpretation of the factor q is that it represents a short-term (reversible) reduction in the release probability for synaptic transmission due to a depletion in the number of vesicles that can readily fuse with the cell membrane [700]. In certain cases, it is also possible for a synapse to undergo a temporary facilitation in response to activation, which may be due to the presence of residual calcium in the axonal terminal [700].

A common phenomenological model of synaptic depression is to assume that between spikes $q(t)$ relaxes at a rate τ_q to its steady-state value of one, but that directly after the arrival of a spike it changes discontinuously, that is, $q \to \gamma q$ with $\gamma < 1$. The depression time constant τ_q can vary between around 100 ms and a few seconds [4]. The model for synaptic depression may be written succinctly as

$$\frac{dq}{dt} = \frac{(1-q)}{\tau_q} - (1-\gamma)\sum_n q(T^n)\delta(t - T^n), \quad q(0) = 1, \tag{1.45}$$

which has the solution of the form

$$q(T^m) = 1 - (1-\gamma)\sum_{n<m} \gamma^{[m-n-1]\beta} {\rm e}^{-(T^m - T^n)/\tau_q}.$$

Assuming a regular sequence of incoming spikes $T^n - T^{n-1} = \Delta$ for all n we find that the asymptotic amplitude $q_\infty(\Delta) \equiv \lim_{m\to\infty} q(T^m)$ is given by

$$q_\infty(\Delta) = \frac{1 - \mathrm{e}^{-\Delta/\tau_q}}{1 - \gamma \mathrm{e}^{-\Delta/\tau_q}}. \tag{1.46}$$

One possible computational role for synaptic depression is as a mechanism for cortical gain control [4]. The basic idea can be understood from the dependence of the asymptotic amplitude $q_\infty(\Delta)$ on the stimulus frequency $f = \Delta^{-1}$. Assuming that $\tau_q \gg \Delta$, we can Taylor expand q_∞ in (1.46) to find that $q_\infty(f) \approx \Gamma/f$, where $\Gamma = \tau_q/(1-\gamma)$. The main point to note is that the postsynaptic response per unit time is approximately independent of f (assuming that each spike elicits the same response in the steady state). This means that the synapse is very sensitive to changes in the stimulus frequency. The instantaneous response to a rapid increase Δf in the stimulus rate is given by $\Gamma \Delta f/f$. In other words, the synapse responds to relative rather than absolute changes in the rate of input stimulation.

1.3.3 Kinetic Model of a Synapse

Let $g_{\mathrm{syn}}(t) \sim s(t)$ where $s(t)$ is the fraction of synaptic receptor channels that are in an open conducting state. The probability of being in an open state depends on the presence and concentration $\mathscr{T}$ of neurotransmitter released by the presynaptic neuron. Assuming a first-order kinetic scheme, in which a closed receptor in the presence of a concentration of neurotransmitter $\mathscr{T}$ equilibrates with the open receptor state, we have

$$C \underset{r_2(v)}{\overset{r_1(v,\mathscr{T})}{\rightleftharpoons}} O,$$

where C and O represent the closed and open states of the channel and $r_1(v,\mathscr{T})$ and $r_2(v)$ are the associated rate constants. However, in many cases synaptic channels are found to have time-dependent properties that are more accurately modeled with a second-order kinetic scheme. In fact the presence of one or more receptor sites on a channel allows the possibility of transitions to *desensitized states*. Such states are equivalent to the inactivated states of voltage-dependent ion channels. The addition of such a desensitized state to the first-order process generates a second-order scheme:

$$\begin{aligned} \frac{\mathrm{d}s}{\mathrm{d}t} &= r_1(v,\mathscr{T})(1-s-z) - [r_2(v) + r_3(v)]s + r_4(v)z, \\ \frac{\mathrm{d}z}{\mathrm{d}t} &= r_6(v,\mathscr{T})(1-s-z) - [r_4(v) + r_5(v)]z + r_3(v)s, \end{aligned} \tag{1.47}$$

where z is the fraction of channels in the desensitized state. All neurotransmitter-dependent rate constants have the form $r_i(v,\mathscr{T}) = r_i(v)\mathscr{T}$. It is common for detailed Markov models of voltage-gated channels to assume that the voltage dependence

of all rates takes a simple exponential form. However, it has been shown that the number of states needed by a model to more accurately reproduce the behavior of a channel may be reduced by adopting sigmoidal functions for the voltage-dependent transition rates (see Destexhe et al. [154] for a discussion), so that we write

$$r_i(v) = \frac{a_i}{1+\exp[-(v-c_i)/b_i]}. \tag{1.48}$$

The a_i set the maximum transition rate, b_i the steepness of the voltage dependence, and c_i the voltage at which the half-maximal rate is reached. Furthermore, the concentration of neurotransmitter can often be successfully approximated by a sigmoidal function of the presynaptic potential v_{pre}:

$$\mathscr{T}(v_{\text{pre}}) = \frac{\mathscr{T}_{\max}}{1+\exp[-(v_{\text{pre}}-v_\Delta)/\Delta]}. \tag{1.49}$$

Here, $\mathscr{T}_{\max}$ is the maximal concentration of transmitter in the synaptic cleft, v_{pre} is the presynaptic voltage, Δ gives the steepness, and v_Δ sets the value at which the function is half activated. It is common to take $\Delta = 5\,\text{mV}$ and $v_\Delta = 2\,\text{mV}$. One of the main advantages of using an expression such as (1.49) is that it provides a smooth transformation between presynaptic voltage and transmitter concentration from which postsynaptic currents can easily be calculated from (1.39), (1.47), (1.48), and (1.49).

Now consider the following second-order gating scheme

$$\begin{array}{ccc} C & \overset{r_1(\mathscr{T})}{\underset{r_2}{\rightleftharpoons}} & C_1 \\ & {\scriptstyle r_4}\nwarrow \quad \swarrow{\scriptstyle r_3} & \\ & O & \end{array}$$

where C and C_1 are the closed forms of the receptor, O is the open (conducting) form, and the r_i are voltage-independent transition rates. Under certain assumptions it may be shown that this particular second-order scheme describes the so-called alpha function response commonly used in synaptic modeling. The following approximations are required: (i) The transmitter concentration $\mathscr{T}$ occurs as a pulse $\delta(t-t_0)$ for a release event occurring at time $t = t_0$, that is, $r_1(\mathscr{T}) = r_1\delta(t-t_0)$; (ii) The fraction of channels in C is considered constant and ~ 1. The kinetic equation (1.47) then reduce to

$$\frac{\mathrm{d}\mathbf{c}(t)}{\mathrm{d}t} = \mathbf{Q}\mathbf{c}(t) + \mathbf{I}(t),$$

(assuming $\mathbf{c}(0) = \mathbf{0}$), where

$$\mathbf{Q} = \begin{pmatrix} -\frac{1}{\tau_1} & 0 \\ r_3 & -\frac{1}{\tau_2} \end{pmatrix}, \quad \mathbf{I}(t) = \begin{pmatrix} r_1\delta(t-t_0) \\ 0 \end{pmatrix}, \quad \mathbf{c} = \begin{pmatrix} z \\ s \end{pmatrix},$$

and $\tau_1 = 1/(r_2 + r_3)$, $\tau_2 = 1/r_4$. Here z and s represent the fraction of receptors in the forms C_1 and O, respectively. This Markov chain system has a solution of the form

$$\mathbf{c}(t) = \int_0^t \mathbf{G}(t-s)\mathbf{I}(s)\mathrm{d}s, \quad \mathbf{G}(t) = \mathrm{e}^{t\mathbf{Q}}.$$

The eigenvectors of $\mathbf{Q}$ are $(1, r_3/(\tau_2^{-1} - \tau_1^{-1}))$ and $(0,1)$ with associated eigenvalues $-1/\tau_1$ and $-1/\tau_2$, respectively. Hence, one finds that

$$s(t) = r_1 r_3 \left(\frac{1}{\tau_2} - \frac{1}{\tau_1}\right)^{-1} (\mathrm{e}^{-(t-t_0)/\tau_1} - \mathrm{e}^{-(t-t_0)/\tau_2}), \quad t > t_0.$$

In the limit $\tau_2 \to \tau_1 \to \tau_s$ this reduces to an alpha function

$$s(t) = r_1 r_3 (t - t_0)\mathrm{e}^{-(t-t_0)/\tau_s}, \quad t > t_0.$$

This kinetic derivation of the alpha function only holds for $s \ll 1$ in order to remain consistent with condition (ii).

The time course of some ion-channel open and closed states seems to follow a power law rather than multiexponential law at large times [429]. In order to understand such power-law behavior, consider an ion channel with N closed states such that the transition to an open state can only take place from state 1 at one end of a chain

$$0 \overset{\alpha}{\leftarrow} 1 \underset{\beta_1}{\overset{\gamma_1}{\rightleftharpoons}} 2 \ldots \underset{\beta_{N-1}}{\overset{\gamma_{N-1}}{\rightleftharpoons}} N.$$

The corresponding kinetic equations are

$$\begin{aligned}
\frac{dc_1}{dt} &= \beta_1 c_2 - (\gamma_1 + \alpha)c_1, \\
\frac{dc_n}{dt} &= \gamma_{n-1}c_{n-1} + \beta_n c_{n+1} - (\gamma_n + \beta_{n-1})c_n, \quad 1 < n < N, \\
\frac{dc_N}{dt} &= \gamma_{N-1}c_{N-1} - \beta_{N-1}c_N.
\end{aligned}$$

In the following we take $\gamma_n = \beta_n = 1$ for all n and $\alpha = 1$, so that the system of equations describes a discrete diffusion process along a chain with a reflecting boundary at $n = N$ and an absorbing boundary at $n = 0$. In the large N limit, it can be shown that given the initial condition $p_n(0) = \delta_{n,1}$, the exact solution is

$$c_n(t) = \mathrm{e}^{-2t}[I_{n-1}(t) - I_{n+1}(t)], \tag{1.50}$$

where $I_n(t)$ is the modified Bessel function of integer order:

$$I_n(t) = \int_{-\pi}^{\pi} \mathrm{e}^{ink}\mathrm{e}^{2t\cos(k)}\frac{dk}{2\pi}.$$

By carrying out an asymptotic expansion for large t, it can be shown that

$$c_n(t) \approx \frac{n}{2\pi^{1/2}t^{3/2}}.$$

Define $F(t)$ to be the total probability of finding the system in a closed state:

$$F(t) = \sum_{n=1}^{N} c_n(t).$$

It follows that $dF/dt = -\alpha c_1$ and, hence, $F(t) \approx (\pi t)^{-1/2}$ for large N, t and $\alpha = 1$. More recently, it has been suggested that synapses with multiple states, which exhibit dynamics over a wide range of time scales and show power-law-like behavior, could have some interesting computational properties [208, 219]. For example, it has been suggested that such synapses could provide a way of combining high levels of memory storage with long retention times [208].

1.4 Dendritic Processing

Typically, a single neuron in cerebral cortex has up to 10,000 synapses, which are spatially distributed along the dendritic tree (and perhaps on the cell body and proximal part of the axon). In order to find the total synaptic current $u(t)$ entering the cell body, it is necessary to determine how the various local currents flow along the dendritic tree and combine at the soma. We will show that if the dendrites are modeled as passive electrical cables, then the dendritic tree acts as a linear spatiotemporal filter of synaptic currents.

1.4.1 The Cable Equation

Neurons display a wide range of dendritic morphologies, ranging from compact arborizations to elaborate branching patterns. At the simplest level, the dendritic tree can be treated as a passive electrical medium that filters incoming synaptic stimuli in a diffusive manner. The current flow and potential changes along a branch of the tree may be described with a second-order, linear partial differential equation commonly known as the *cable equation*. (The application of cable theory to the study of passive, spatially extended dendrites was pioneered by Wilfrid Rall in the 1960s and 1970s. For more recent accounts of this work see [515] and the annotated collection of papers edited by Segev, Rinzel, and Shepherd [299].) The cable equation is based on a number of approximations: (1) magnetic fields due to the movement of electric charge can be neglected, (2) changes in ionic concentrations are sufficiently small so that Ohm's law holds, (3) radial and angular components of voltage can be ignored so that the cable can be treated as one-dimensional medium, and (4) dendritic membrane properties are voltage-independent, that is, there are no active elements.

A nerve cable consists of a long thin, electrically conducting core surrounded by a thin membrane whose resistance to transmembrane current flow is much greater than that of either the internal core or the surrounding medium. Injected current can travel long distances along the dendritic core before a significant fraction leaks out across the highly resistive cell membrane. Linear cable theory expresses conservation of electric current in infinitesimal cylindrical elements of nerve fiber modeled using the equivalent circuit shown in Fig. 1.11. Define $v(x,t)$ as the membrane potential at position x along a cable at time t (measured relative to the resting potential of the membrane). Let C_m be the capacitance per unit area of the cell membrane, R the resistivity of the intracellular fluid (in units of resistance $\times$ length), R_m the cell membrane resistance (in units of resistance $\times$ area), and a the cable radius. Note that C_m, R_m, R are independent of cable radius—the corresponding quantities expressed per unit length of cable are

$$r = \frac{R}{\pi a^2}, \quad \frac{1}{r_m} = \frac{2\pi a}{R_m}, \quad c_m = 2C_m \pi a. \tag{1.51}$$

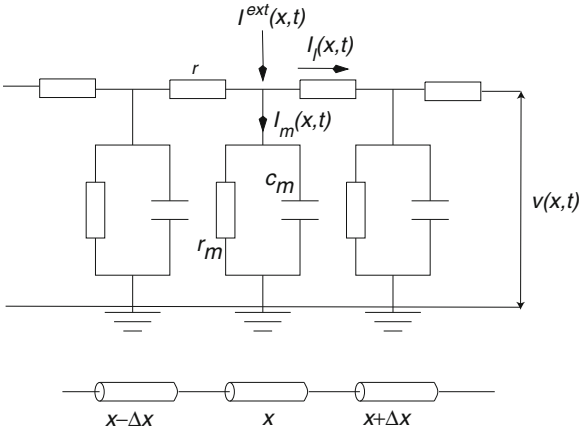

Fig. 1.11 Equivalent circuit for successive cylindrical segments of passive dendritic membrane

Current conservation implies that (see Fig. 1.11)

$$I^{ext}(x,t) - I_m(x,t) = \frac{I_l(x,t) - I_l(x-\Delta x,t)}{\Delta x} \approx \frac{\partial I_l(x,t)}{\partial x}, \tag{1.52}$$

where $I^{ext}(x,t)$ is an external injected current density. From Ohm's law we also have

$$I_l(x,t)r = \frac{v(x,t) - v(x+\Delta x,t)}{\Delta x} \approx -\frac{\partial v(x,t)}{\partial x}, \tag{1.53}$$

and

$$I_m(x,t) = c_m \frac{\partial v(x,t)}{\partial t} + \frac{v(x,t)}{r_m}. \tag{1.54}$$

Combining these three equations yields the uniform cable equation

$$\tau_m \frac{\partial v(x,t)}{\partial t} = -v(x,t) + \lambda_m^2 \frac{\partial^2 v(x,t)}{\partial x^2} + r_m I_{ext}(x,t), \qquad t \geq 0, \tag{1.55}$$

where $\tau_m = R_m C_m$ is the membrane time constant and $\lambda_m = (R_m a/2R)^{1/2}$ is the membrane space constant. (It follows that the coupling constant appearing in the Hodgkin–Huxley equation (1.8) is $K = \lambda_m^2/R_m$.)

Infinite Cable. In the case of an infinite uniform cable, $x \in \mathbb{R}$, we can solve (1.55) by Fourier transforming with respect to x. That is, define the Fourier transform of v (and other quantities) as

$$\tilde{v}(k,t) = \int_{-\infty}^{\infty} \mathrm{e}^{-ikx} v(x,t)dx,$$

with inverse transform

$$v(x,t) = \int_{-\infty}^{\infty} \mathrm{e}^{ikx} \tilde{v}(k,t) \frac{dk}{2\pi}.$$

Then

$$\tau_m \frac{\partial \tilde{v}(k,t)}{\partial t} = -\tilde{v}(k,t) - \lambda_m^2 k^2 \tilde{v}(k,t) + r_m \tilde{I}_{ext}(k,t), \quad x \in \mathbb{R}, \quad t \geq 0. \tag{1.56}$$

This first-order ODE can now be solved straightforwardly as

$$\tilde{v}(k,t) = \frac{r_m}{\tau_m} \int_{-\infty}^{t} \tilde{G}_0(k,t-t') \tilde{I}^{ext}(k,t')dt', \tag{1.57}$$

where $\tilde{G}_0(k,t) = \mathrm{e}^{-(1+\lambda_m^2 k^2)t/\tau_m}$. Taking the inverse Fourier transform and using the convolution theorem shows that

$$v(x,t) = r_m \int_{-\infty}^{t} \left[\int_{-\infty}^{\infty} G_0(x-x',t-t') I^{ext}(x',t')dx' \right] dt', \tag{1.58}$$

where we have absorbed τ_m into r_m and

$$\begin{aligned} G_0(x,t) &= \int_{-\infty}^{\infty} \frac{\mathrm{d}k}{2\pi} \mathrm{e}^{ikx} \mathrm{e}^{-(1+\lambda_m^2 k^2)t/\tau_m} \\ &= \frac{1}{2\lambda_m \sqrt{\pi t/\tau_m}} \mathrm{e}^{-t/\tau_m} \mathrm{e}^{-\tau_m x^2/4\lambda_m^2 t}. \end{aligned} \tag{1.59}$$

The function $G_0(x,t)$ is the fundamental solution or Green's function for the cable equation with unbounded domain. It is positive and symmetric and satisfies the homogeneous cable equation

$$\left(\tau_m \frac{\partial}{\partial t} + 1 - \lambda_m^2 \frac{\partial^2}{\partial x^2}\right) G_0(x,t) = 0, \tag{1.60}$$

with initial condition

$$G_0(x,0) = \delta(x). \tag{1.61}$$

Moreover, for any $0 < s < t$, it satisfies the Markovian property

$$G_0(x-y,t) = \int_{-\infty}^{\infty} G_0(x-z,s) G_0(z-y,t-s) \mathrm{d}z. \tag{1.62}$$

The Green's function is plotted as a function of time in Fig. 1.12a for a range of separations x.

Semi-infinite Cable. Using Fourier cosine or sine transforms with respect to x it is straightforward to determine the Green's function for a semi-infinite cable $x \in [0,\infty)$ with either an open-end boundary condition

$$v(0,t) = 0 \tag{1.63}$$

or a closed-end boundary condition (zero current flow)

$$\left.\frac{\partial v(x,t)}{\partial x}\right|_{x=0} = 0 \tag{1.64}$$

One finds that

$$v(x,t) = r_m \int_{-\infty}^{t} \left[\int_0^{\infty} G_{\pm}(x,x',t-t') I^{ext}(x',t') dx'\right] dt' \tag{1.65}$$

where

$$G_{\pm}(x,y,t) = G_0(x-y,t) \pm G_0(x+y,t) \tag{1.66}$$

for the open $(-)$ and closed $(+)$ cases. For a discussion of finite-length cables see [342].

Single Branching Node. Let us now consider a single branching node and label each semi-infinite segment by the index $i = 1,\ldots,N$. (Typically $N = 3$.) We shall assume that the cables only differ in their radius a_i. In order to simplify the analysis we will measure the distance along the ith cable from the branch point at $x = 0$ in units of $\lambda_{m,i} = \sqrt{R_m a_i / 2R}$ such that the cable equation on each branch can be written as

$$\tau_m \frac{\partial v_i(X,t)}{\partial t} = -v_i(x,t) + \frac{\partial^2 v_i(x,t)}{\partial x^2} + I_i(x,t). \tag{1.67}$$

The boundary conditions are continuity of the potential at the node

$$v_i(0,t) = v_j(0,t), \tag{1.68}$$

and conservation of current

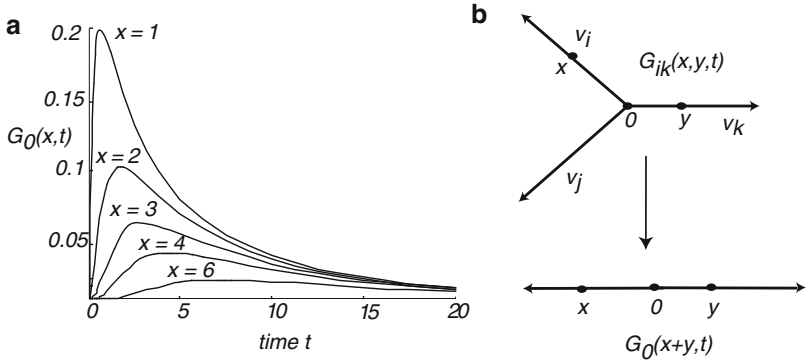

Fig. 1.12 (**a**) Green's function of an infinite cable as a function of time t (in units of τ_m) for various values of distance x (in units of λ). (**b**) Branching dendritic tree of an idealized single neuron and an equivalent cylinder representation

$$\sum_{j=1}^{N} a_j^{3/2} \left. \frac{\partial v_j(x,t)}{\partial x} \right|_{x=0} = 0. \tag{1.69}$$

The factor $a_i^{3/2}$ arises from the fact that we have rescaled length and that the longitudinal resistance varies as the cross-sectional area of the cable. The solution of these equations is

$$v_i(x,t) = \sum_{j=1}^{N} \int_{-\infty}^{t} \left[\int_0^{\infty} G_{ij}(x,x',t-t') I_j(x',t') dx' \right] dt', \tag{1.70}$$

where

$$G_{ij}(x,y,t) = \delta_{i,j} G_0(x-y,t) + (2p_j - \delta_{i,j}) G_o(x+y,t), \tag{1.71}$$

and

$$p_k = \frac{a_k^{3/2}}{\sum_m a_m^{3/2}}. \tag{1.72}$$

It is interesting to note that if $p_k = 1/2$ for a certain segment, then the response to current injected into that segment can be represented by a single equivalent cylinder; see Fig. 1.12b. That is, if $i \neq j$, then $G_{ij}(x,y,t) = G_0(x+y)$, where $x+y$ is the distance of the direct path between x and y on the tree. Hence, the node in some sense acts no differently than an ordinary point on a single cable. This is the basis of Rall's equivalent cylinder concept [515].

Dendritic Tree. An arbitrary dendritic tree Γ may be considered as a set of branching nodes linked by finite pieces of uniform cable. Given an external current density $I^{ext}(x,t)$ the voltage response has the formal solution (absorbing r_m into the definition of G)

$$v(x,t) = \int_{-\infty}^{t} \left[\int_{\Gamma} G(x,y,t-s) I_{\text{ext}}(y,s) dy \right] ds. \tag{1.73}$$

The associated Green's function $G(x,y,t-s)$ satisfies the homogeneous cable equation on each segment together with boundary conditions at the branching and terminal nodes of the tree. Rules for constructing such a Green's function have been developed by Butz and Cowan [95] using a graphical calculus and by Abbott et al. [3] using path-summing methods. The latter approach can be understood in terms of a compartmental model obtained by spatially discretizing the cable equation. The construction of the discretized Green's function involves summing over paths of a random walk on the tree with the corresponding Green's function for the cable equation recovered in the continuum limit [77].

1.4.2 Dendritic Filtering of Synaptic Inputs

So far we have considered the linear response of a dendritic cable to external current injection as determined by the Green's function or transfer function. Suppose that we replace the external current by a synaptic current of the form discussed in Sect. 1.3. That is, $I_{\text{ext}}(x,t) \to I(x,t)$, where $I(x,t)$ is the synaptic current density at location x at time t:

$$I(x,t) = \rho(x) \sum_m g_{\text{syn}}(t - T^m(x))[V_{\text{syn}} - v(x,t)] \equiv g(x,t)[V_{\text{syn}} - v(x,t)], \tag{1.74}$$

where $g(x,t) = \rho(x) \sum_m g_{\text{syn}}(t - T^m(x))$. Here $\rho(x)$ is the density of synapses (assuming that they have identical properties) and $\{T^m(x)\}$ is the sequence of spikes arriving into the synapses located at x. In the case of a discrete set of identical synapses at dendritic locations $\{x_j, j = 1,\ldots,M\}$, we have $\rho(x) = \sum_j \delta(x - x_j)$ and $T^m(x_j) = T_j^m$. The formal solution for the membrane potential is now [see (1.73)]

$$v(x,t) = \int_{-\infty}^{t} \left[\int_{\Gamma} G(x,x',t-t') g(x',t') [V_{\text{syn}} - v(x',t')]] dx' \right] dt' \tag{1.75}$$

which is a Volterra integral equation of the second kind. In order to solve this integral equation, we introduce the convolution operator $*$,

$$[G * f](x,t) := \int_{-\infty}^{t} \left[\int_{\Gamma} G(x,x',t-t') f(x',t') dx' \right] dt' \tag{1.76}$$

for any function $f(x,t)$. We can then iterate (1.75) to obtain a series solution for v:

$$\begin{aligned} v &= V_{\text{syn}} G * g - G * (gv) \\ &= V_{\text{syn}} G * g - V_{\text{syn}} G * (g[V_{\text{syn}} G * g - G * (gv)]) \\ &= V_{\text{syn}} G * g - V_{\text{syn}}^2 G * [gG * g] + G * [gG * (gv)] \end{aligned}$$

$$
\begin{aligned}
&= V_{\rm syn} G * g - V_{\rm syn}^2 G * (gG * g) + V_{\rm syn}^3 G * (gG * [gG * g]) - \ldots \\
&= V_{\rm syn} (G - V_{\rm syn} G * gG + V_{\rm syn}^2 G * gG * gG - \ldots) * g \\
&= V_{\rm syn} \hat{G} * g, \qquad (1.77)
\end{aligned}
$$

where

$$
\hat{G} := G - V_{\rm syn} G * gG + V_{\rm syn}^2 G * gG * gG - \ldots \qquad (1.78)
$$

is a Neumann series expansion for the effective Green's function $\hat{G}$, which is convergent for a passive cable [344]. More explicitly, we can write the solution as

$$
v(x,t) = V_{\rm syn} \int_{-\infty}^{t} \left[\int_{\Gamma} \hat{G}(x,t;x',t') g(x',t') dx' \right] dt', \qquad (1.79)
$$

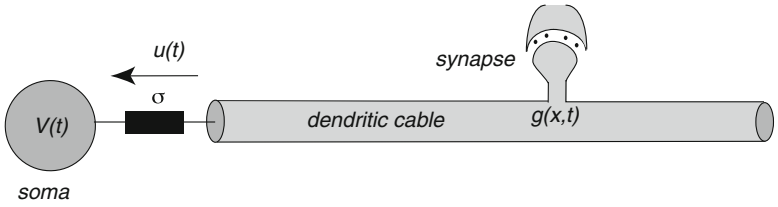

Fig. 1.13 Schematic diagram of a neuron consisting of a soma resistively coupled to one end of a dendritic cable. A synaptic conductance change $g(x,t)$ at position x on the cable induces a synaptic current into the soma at $x = 0$

with $\hat{G}$ satisfying the Volterra integral equation

$$
\begin{aligned}
\hat{G}(x,t;x',t') &= G(x,x',t-t') \qquad (1.80) \\
&\quad - V_{\rm syn} \int_{t'}^{t} \left[\int_{0}^{\infty} G(x,x'',t-t'') g(x'',t'') \hat{G}(x'',t'';x',t') dx'' \right] dt''.
\end{aligned}
$$

One can check that iteration of this equation recovers the series expansion for $\hat{G}$. The major point to note is that the resulting series involves interactions between synaptic conductances at different points on the dendritic cable. For simplicity, however, we shall assume that $V_{\rm syn} \gg v(x,t)$ so that $\hat{G} \to G$ and synaptic interactions become negligible.

Given a distribution of synaptic inputs innervating the dendritic tree, what is the net synaptic current $u(t)$ entering the soma? In order to address this problem, consider a semi-infinite uniform dendritic cable, $0 \le x < \infty$, with the soma located at the end $x = 0$. The soma is modeled as a conductance-based point process that is passively coupled to the dendritic cable as illustrated in Fig. 1.13:

$$
C \frac{{\rm d}v}{{\rm d}t} = -I_{\rm con} + \sigma [v(0,t) - v(t)], \qquad (1.81)
$$

and

$$\tau_m \frac{\partial v(x,t)}{\partial t} = -v(x,t) + \lambda_m^2 \frac{\partial^2 v(x,t)}{\partial x^2} + r_m V_{\rm syn} g(x,t). \tag{1.82}$$

Here $u(t) = \sigma[v(0,t) - v(t)]$ is the net current density flowing into the soma from the dendritic cable at $x = 0$. (We are neglecting direct synaptic inputs into the soma.) Current conservation implies the boundary condition

$$-\frac{1}{r}\frac{\partial v}{\partial x}(0,t) = \sigma[v(0,t) - v(t)]. \tag{1.83}$$

Since we can eliminate the term $-\sigma v(t)$ in (1.81) by shifting the linear term in v, it follows that the total synaptic current into the soma is $u(t) = \sigma v(0,t)$.

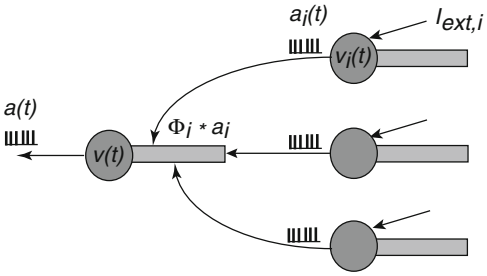

Fig. 1.14 Schematic diagram of a feedforward network showing a set of afferent neurons labeled by i synaptically driving another neuron

The inhomogeneous boundary problem for $v(0,t)$ can be solved formally using the Green's function G_+ for the semi-infinite cable with a closed boundary:

$$\begin{aligned} v(0,t) = {} & r_m V_{\rm syn} \int_{-\infty}^{t} \left[\int_0^{\infty} G_+(0,x',t-t') g(x',t') dx' \right] dt' \\ & -\sigma r \int_{-\infty}^{t} G_+(0,0,t-t')[v(0,t') - v(t')] dt' \end{aligned} \tag{1.84}$$

This shows that the effective synaptic current $u(t)$ flowing into the soma will itself be affected by the cell firing an action potential, due to the dependence of $v(0,t)$ on the somatic potential $v(t)$. However, suppose that the second term on the r.h.s. is negligible compared to the first term arising from synaptic inputs. This approximation corresponds to imposing the homogeneous boundary condition $\partial v/\partial x(0,t) = 0$. It then follows that the total synaptic input into the soma is

$$u(t) = \sigma r_m V_{\rm syn} \int_{-\infty}^{t} \left[\int_0^{\infty} G_+(0,x',t-t') g(x',t') dx' \right] dt' \tag{1.85}$$

A similar analysis can also be carried out for more general dendritic topologies with the soma coupled to one of the terminals of the tree. We conclude that under the

given approximations, the passive dendritic tree acts like a spatiotemporal linear filter on incoming spike trains, whose properties are determined by the underlying Green's function on the tree.

Recall from (1.74) that $g(x,t) = \rho(x)\sum_m g_{\text{syn}}(t - T^m(x))$. Suppose that there exists a discrete set of synapses along the dendrite so that $\rho(x) = \sum_j \delta(x - x_j)$ and $T^m(x_j) = T_j^m$. Substituting into (1.85) then gives

$$u(t) = \sum_j \sum_m \Phi_j(t - T_j^m) = \sum_j \int_{-\infty}^{t} \Phi_j(t - t')a_j(t')dt', \tag{1.86}$$

where

$$\Phi_j(t) = \sigma r_m V_{\text{syn}} \int_0^t G_+(0, x_j, t - \tau) g_{\text{syn}}(\tau) d\tau, \tag{1.87}$$

and

$$a_j(t) = \sum_m \delta(t - T_j^m). \tag{1.88}$$

Note that $a_j(t)$ represents the spike train arriving into the jth synapse in terms of a sum of Dirac delta functions. Hence, under our various approximations, we can view the total synaptic input $u(t)$ as the sum of linearly filtered spike trains, with the kernel of each filter determined by synaptic and dendritic processing. Now suppose that each incoming spike train is associated with a distinct afferent neuron, so that there is a one-to-one correspondence between synaptic and afferent neuron labels; see Fig. 1.14. Then $T_j^m = \hat{T}_j^m + \Delta\tau_j$, where $\hat{T}_j^m$ is the mth firing time of the jth afferent neuron and $\Delta\tau_j$ is an axonal propagation time delay. Unless stated otherwise, we will ignore axonal propagation delays and set $T_j^m = \hat{T}_j^m$. Let us also assume that each afferent neuron is described by a conductance-based model of the form

$$C_i \frac{dv_i}{dt} = -I_{\text{con},i} + I_{\text{ext},i} \tag{1.89}$$

where v_i is the somatic membrane potential of the ith afferent neuron, each of which is driven by an external input $I_{\text{ext},i}$. If we associate with each neuron a firing threshold κ, then the spike times T_i^m are determined according to

$$T_i^m = \inf\{t, t > T_i^{m-1} | v_i(t) = \kappa, \dot{v}_i(t) > 0\}. \tag{1.90}$$

Finally, given $u(t)$, the spike train $a(t)$ of the output neuron is determined by (1.1) and (1.9). In summary, the feedforward network involves a mapping $\{I_{\text{ext},i}(t)\} \to \{T_i^m\} \to \{T^m\}$.

1.4.3 Active Dendrites

It has been known for more than twenty years that the dendrites of cortical neurons do not simply act as passive electrical cables but also exhibit a variety of

active physiological processes [608]. For example, thick apical dendrites of pyramidal neurons express voltage-gated Na^+, K^+, and Ca^{2+} channels, which support the back propagation of action potentials (APs) from the soma into the dendritic tree [397, 606]; back-propagating APs are thought to play an important role in spike-timing-dependent synaptic plasticity (STDP) [585]. In addition, sufficient local stimulation of active apical dendrites can initiate regenerative membrane depolarizations known as *dendritic spikes* [333, 555]. Some dendritic spikes are restricted to the local initiation zone rather than invading the cell body and are thus well placed to mediate the long-term potentiation of synaptic inputs in the absence of output spiking of the neuron [226]. On the other hand, Ca^{2+} action potentials initiated in apical dendrites can propagate towards the soma, which provides a mechanism for actively amplifying the effects of distal synapses on AP generation in the cell body [361]. Following advances in imaging techniques and methods of dendritic stimulation, Schiller et al. [556] established in vitro that active processes can also occur in thin basal and apical dendritic branches of pyramidal neurons, where the majority of synapses occur; see Fig. 1.15a. In particular, they found stimulus-evoked dendritic spikes whose major ionic component involved ligand-gated and voltage-gated N-methyl-D-aspartate receptor (NMDAR) channels; see also [362, 400, 520] and the review [12]. When glutamate binds to an NMDAR, it modifies the voltage sensitivity of the corresponding ion-channel current, which develops a negative slope conductance due to removal of a magnesium block [414, 466]. This means that in the presence of high levels of glutamate, the current–voltage (I–V) characteristics of an NMDAR channel are very similar to the voltage-gated Na channel. Hence, during

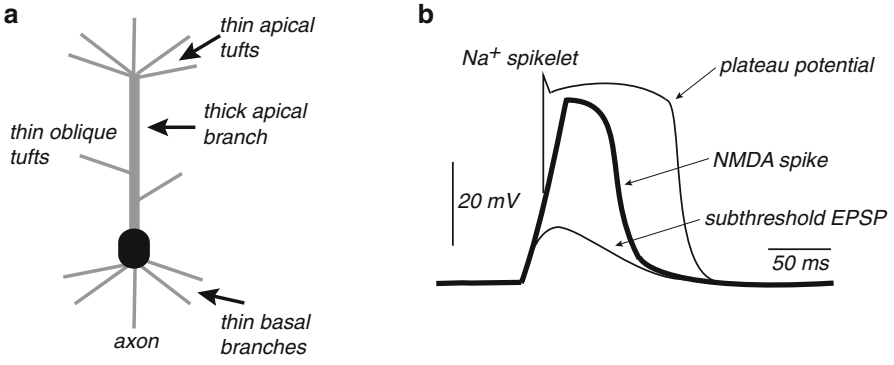

Fig. 1.15 (**a**) Schematic illustration of a pyramidal neuron showing the thick apical dendrite and various thin dendrites. The latter support the initiation of dendritic NMDA spikes. (**b**) Typical waveform of a dendritic NMDA spike. Weak glutamatergic inputs generate EPSP-like (subthreshold) depolarizations. A stronger input can trigger a dendritic plateau potential, consisting of a rapid onset that is often associated with a Na spikelet, a long-lasting plateau phase that can have a duration of several hundred ms, and a sudden collapse at the end of the plateau phase. The plateau potential consists of several dendritic conductances, the most predominant being due to NDMAR channels. Pharmacologically blocking Na and Ca^{2+} channels reveals the pure dendritic NMDA spike [556]

strong stimulation of a thin dendrite due to the local uncaging of glutamate or high frequency stimulation of a cluster of synapses, the NMDARs can fire a regenerative dendritic spike, just as Na channels support the initiation of an action potential following membrane depolarization. However, the duration of the dendritic spike is of the order 100 ms rather than 1 ms; see Fig. 1.15b. Finally, active processes can also be found in dendritic spines, which can support the propagation of saltatory waves; see Sect. 3.1

For relatively small deviations of the membrane potential from some constant value, a linearization of the channel kinetics can be performed. The resulting system has a membrane impedance that displays resonant-like behavior due to the additional presence of effective inductances [61, 141, 341, 342]. We sketch how inductance-like behavior can arise from active neural membrane by considering a generic ion current of the form $I(v,x_1,\ldots,x_M)$, where v is membrane voltage and x_k are gating variables that satisfy

$$\tau_k(v)\frac{dx_k}{dt} = x_{k,\infty}(v) - x_k, \quad k = 1,\ldots,M. \tag{1.91}$$

It is convenient to set $\tau_k(v) = (\alpha_k(v)+\beta_k(v))^{-1}$ and $x_{k,\infty}(v) = \alpha_k(v)\tau_k(v)$. Linearizing around a fixed point $\mathbf{z} = \mathbf{z}^*$ with vectors defined by $\mathbf{z} = (v,x_1,\ldots,x_M)^T$ and $\mathbf{z}^* = (v^*,x_{1,\infty}(v^*),\ldots,x_{M,\infty}(v^*))$, we have

$$\delta I = \frac{\delta v}{R} + \sum_{k=1}^{M} \left.\frac{\partial I}{\partial x_k}\right|_{\mathbf{z}=\mathbf{z}^*} \delta x_k, \tag{1.92}$$

where R is an effective resistance such that $R^{-1} = \partial I/\partial V|_{\mathbf{z}=\mathbf{z}^*}$. From (1.91) it follows that

$$\left(\frac{d}{dt} + \alpha_k + \beta_k\right)\delta x_k = \left(\frac{d\alpha_k}{dV} - x_{k,\infty}\frac{d[\alpha_k+\beta_k]}{dV}\right)\delta V_k. \tag{1.93}$$

Combining (1.92) and (1.93) we arrive at the following equation for the first-order variation of the current:

$$\delta I = \frac{\delta V}{R} + \sum_{k=1}^{M} \delta I_k, \tag{1.94}$$

where

$$\left(r_k + L_k\frac{d}{dt}\right)\delta I_k = \delta V, \tag{1.95}$$

and

$$r_k^{-1} = \tau_k\frac{\partial I}{\partial x_k}\left(\frac{d\alpha_k}{dV} - x_{k,\infty}\frac{d[\alpha_k+\beta_k]}{dV}\right)\Bigg|_{\mathbf{z}=\mathbf{z}^*} \tag{1.96}$$

$$L_k = \tau_k r_k \tag{1.97}$$

Hence, for a small perturbation around the steady state, the current I responds as though the resistance R is in parallel with M impedance lines, each of which is a resistance r_k that is itself in series with an inductance L_k (see Fig. 1.16). Such inductive terms account for the oscillatory *overshoot* commonly seen in response to depolarising current steps or even after the firing of an action potential. This form of equivalent linear membrane circuit is typically called *quasi-active* in order to distinguish it from a truly *active* (i.e. nonlinear) membrane [341].

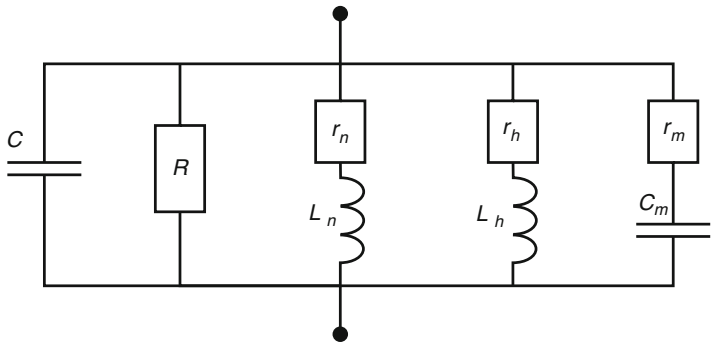

Fig. 1.16 Electrical LRC circuit representing the linearized response of the Hodgkin–Huxley equations

Quasilinear membrane can be incorporated into the cable equation (1.55) by introducing the space-dependent voltage $v(x,t)$ and currents $I_k(x,t)$, $x \in \mathbb{R}$, such that

$$\frac{\partial V}{\partial t} = -\frac{V}{\tau_m} + D_m \frac{\partial^2 V}{\partial x^2} - \frac{1}{C_m}\left[\sum_k I_k - I_{\text{ext}}\right] \tag{1.98a}$$

$$L_k \frac{dI_k}{dt} = -r_k I_k + V. \tag{1.98b}$$

Here $D_m = \lambda_m^2/\tau_m$. Laplace transforming (1.98) with $v(x,0) = 0, I_k(x,0) = 0$ yields the ODE

$$-\frac{d\tilde{V}^2}{dx^2} + \gamma^2(\omega)\tilde{V} = \tilde{I}, \tag{1.99}$$

with $\tilde{V} = \tilde{V}(x,\omega)$, $\tilde{I} = \tilde{I}(x,\omega) = \tilde{I}_{\text{ext}}(x,\omega)/C_m$, and

$$\gamma^2(\omega) = \frac{1}{D_m}\left[\frac{1}{\tau_m} + \omega + \frac{1}{C_m}\sum_k \frac{1}{r_k + \omega L_k}\right]. \tag{1.100}$$

It follows that in Laplace space,

$$\tilde{V}(x,\omega) = \int_0^\infty \tilde{G}(x-y,\omega)\tilde{I}(y,\omega)dy, \quad \tilde{G}(x,\omega) = \frac{\mathrm{e}^{-\gamma(\omega)|x|}}{2D_m\gamma(\omega)}, \tag{1.101}$$

where $\tilde{G}$ is the Laplace transform of the Green's function on an infinite quasi-active cable. Having obtained G, it is then possible to extend Green's function methods outlined for passive branching cables to the quasi-active case [141].

1.5 Stochastic Ion Channels

In the standard conductance-based model of a neuron (1.6), it is assumed that the number of voltage-gated ion channels is sufficiently large so that one can represent the opening and closing of the channels in terms of deterministic kinetic equations. These keep track of the fraction of open and closed channels as a function of time. However, the opening and closing of a single channel is a stochastic process. This then raises the important issue of how such stochasticity manifests itself when there are relatively few ion channels. (A similar issue applies to synapses with a small number of receptor-mediated ion channels.) In this section, we develop the theory of stochastic ion channels in some detail, since it provides an excellent platform for introducing various methods and ideas in stochastic processes that will be used throughout the book. For reviews on noise in ion channels see [227, 588, 670].

1.5.1 Ensemble of Two-State Ion Channels

First, consider a single ion channel that can exist either in a closed state (C) or an open state (O). Transitions between the two states are governed by a continuous-time jump Markov process

$$C(\text{closed}) \underset{\beta(v)}{\overset{\alpha(v)}{\rightleftharpoons}} O(\text{open}). \tag{1.102}$$

with voltage-dependent transition rates $\alpha(v), \beta(v)$. For the moment, we assume that v is fixed. In order to understand what such a process means, let $Z(t)$ be a discrete random variable taking values $Z \in \{C, O\}$ and set $P_z(t) = \text{Prob}[Z(t) = z]$. From conservation of probability,

$$P_C(t) + P_O(t) = 1.$$

The transition rates then determine the probability of jumping from one state to the other in a small interval Δt:

$$\alpha \Delta t = \text{Prob}[Z(t+\Delta t) = O | Z(t) = C], \quad \beta \Delta t = \text{Prob}[Z(t+\Delta t) = C | Z(t) = O].$$

It follows that there are two possible ways for the ion channel to enter or leave the closed state:

$$P_C(t+\Delta t) = P_C(t) - \alpha P_C(t)\Delta t + \beta P_O(t)\Delta t.$$

Writing down a similar equation for the open state, dividing by Δt, and taking the limit $\Delta t \to 0$ leads to the pair of equations

$$\frac{dP_C}{dt} = -\alpha P_C + \beta P_O \tag{1.103a}$$

$$\frac{dP_O}{dt} = \alpha P_C - \beta P_O. \tag{1.103b}$$

Now suppose that there are N identical, independent two-state ion channels. In the limit $N \to \infty$ we can reinterpret P_C and P_O as the mean fraction of closed and open ion channels within the population, and fluctuations can be neglected. After setting $P_O = X$ and $P_C = 1 - X$, we recover the kinetic equation (1.4). (An identical argument can be applied to the kinetic model of a synapse considered in Sect. 1.3.)

In order to take into account fluctuations in the case of finite N, it is necessary to keep track of the probability $P(n,t)$ that there are n open channels at time t, $0 \leq n \leq N$. (If there are n open channels, then it immediately follows that there are $N-n$ closed channels, so we do not need to keep track of the latter as well.) Consider a time interval $[t, t+\Delta t]$ with Δt sufficiently small so that only one channel has a significant probability of making a $C \to O$ or $O \to C$ transition. There are four possible events that can influence $P(n,t)$ during this interval, two of which involve transitions into the state of n open ion channels, and two of which involve transitions out of the state. Collecting these terms and taking the limit $\Delta t \to 0$ leads to the *master equation*

$$\frac{d}{dt}P(n,t) = \alpha(N-n+1)P(n-1,t) + \beta(n+1)P(n+1,t) - [\alpha(N-n) + \beta n]P(n,t). \tag{1.104}$$

The first term on the right-hand side represents the probability flux that one of $N-(n-1)$ closed channels undergoes the transition $C \to O$, whereas the second term represents the probability flux that one of $n+1$ open channels undergoes the transition $O \to C$. The last two terms represent transitions $n \to n \pm 1$. Define the mean number of open channels at time t by

$$\overline{n}(t) = \sum_{n=0}^{N} nP(n,t).$$

By differentiating both sides of this equation with respect to t and using the master equation (1.104), it can be shown that in the limit of large N (where the upper limit in the sum can be taken to be ∞) we recover the kinetic equation (1.4) with $X = \overline{n}/N$.

The steady-state solution $P_s(n)$ of the master equation (1.104) satisfies $J(n) = J(n+1)$ with

$$J(n) = \omega_-(n)P_s(n) - \omega_+(n-1)P_s(n-1),$$

and

$$\omega_+(n) = (N-n)\alpha, \quad \omega_-(n) = n\beta.$$

Using the fact that n is a nonnegative integer, that is, $P_s(n) = 0$ for $n < 0$, it follows that $J(n) = 0$ for all n. Hence, by iteration,

$$P_s(n) = P_s(0) \prod_{m=1}^{n} \frac{\omega_+(m-1)}{\omega_-(m)} = P_s(0) \left[\frac{\alpha}{\beta}\right]^n \frac{N!}{n!(N-n)!}. \tag{1.105}$$

Taking logs of both sides of this equation and using Stirling's formula $\log(n!) \approx n\log n - n$ it can be shown that for large n, N, $P_s(n) \approx p_s(x)$ where $x = n/N$,

$$p_s(x) = \mathcal{N} \mathrm{e}^{-N\Phi(x)} \tag{1.106}$$

with normalization factor $\mathcal{N}$ and $\Phi(x)$ is the effective potential

$$\Phi(x) = -x\log(\alpha/\beta) + x\log(x) + (1-x)\log(1-x). \tag{1.107}$$

Let x^* be the unique critical point of the effective potential $\Phi(x)$, that is, $\Phi'(x^*) = 0$. Note that x^* coincides with the fixed point of the corresponding deterministic kinetic equations,

$$x^* = \frac{\alpha}{\alpha+\beta}. \tag{1.108}$$

Since N is large, we can make the Gaussian approximation

$$p_s(x) \approx p(0) \exp\left[-N\Phi(x^*) - N\Phi''(x^*)(x-x^*)^2/2\right]. \tag{1.109}$$

Under this approximation, the mean and variance of the fraction of open channels are given by

$$\frac{\bar{n}}{N} = x^* = \frac{\alpha}{\alpha+\beta}, \quad \frac{\langle (n-\bar{n})^2 \rangle}{N^2} = \frac{x^*(1-x^*)}{N}. \tag{1.110}$$

It is clear that fluctuations become negligible in the large-N limit.

1.5.2 Diffusion Approximation

A useful diffusion approximation of the master equation (1.104) for large but finite N can be obtained by carrying out a Kramers–Moyal or system-size expansion to second order in N^{-1} [210, 309], which was originally applied to ion-channel models by Fox and Lu [200]. This yields a *Fokker–Planck* (FP) equation describing the evolution of the probability density of a corresponding continuous stochastic process that is the solution to a *stochastic differential equation* (SDE), which in the physics literature is often called a *Langevin equation*; we will take these terms to be interchangeable. Further details concerning SDEs can be found in appendix section 1.7 and in various references [210, 476]. Moreover, a rigorous analysis of the diffusion approximation and its relationship to the system-size expansion has been carried out by Kurtz [352].

First, introduce the rescaled variable $x = n/N$ and transition rates $N\Omega_{\pm}(x) = \omega_{\pm}(Nx)$. Equation (1.104) can then be rewritten in the form

$$\frac{dp(x,t)}{dt} = N[\Omega_+(x-1/N)p(x-1/N,t) + \Omega_-(x+1/N)p(x+1/N,t) - (\Omega_+(x)+\Omega_-(x))p(x,t)].$$

Treating $x, 0 \leq x \leq 1$, as a continuous variable and Taylor expanding terms on the right-hand side to second order in N^{-1} leads to the FP equation

$$\frac{\partial p(x,t)}{\partial t} = -\frac{\partial}{\partial x}[A(x)p(x,t)] + \frac{1}{2N}\frac{\partial^2}{\partial x^2}[B(x)p(x,t)] \tag{1.111}$$

with

$$A(x) = \Omega_+(x) - \Omega_-(x) \equiv \alpha - (\alpha+\beta)x, \tag{1.112a}$$

$$B(x) = \Omega_+(x) + \Omega_-(x) \equiv \alpha + (\beta-\alpha)x. \tag{1.112b}$$

The FP equation takes the form of a conservation equation

$$\frac{\partial p}{\partial t} = -\frac{\partial J}{\partial x}, \tag{1.113}$$

where $J(x,t)$ is the probability flux,

$$J(x,t) = -\frac{1}{2N}\frac{\partial}{\partial x}[B(x)p(x,t)] + A(x)p(x,t). \tag{1.114}$$

The FP equation is supplemented by the no-flux or reflecting boundary conditions at the ends $x = 0, 1$ and a normalization condition,

$$J(0,t) = J(1,t) = 0, \quad \int_0^1 p(x,t)dx = 1. \tag{1.115}$$

The FP equation has a unique steady-state solution obtained by setting $J(x,t) = 0$ for all $0 \leq x \leq 1$. The resulting first-order ODE can be solved to give a steady-state probability density of the form (1.107), with corresponding potential

$$\Phi_{\rm FP}(x) = -2\int^x \frac{A(x')}{B(x')}dx' = -2\int^x \frac{\Omega_+(x') - \Omega_-(x')}{\Omega_+(x') + \Omega_-(x')}dx'. \tag{1.116}$$

The mean and variance of the fraction of open channels close to the fixed point x^* can again be determined by carrying out a Gaussian approximation, and the results agree with those obtained from the steady-state solution of the master equation. An alternative way of calculating the mean and variance is to note that the solution to the FP equation (1.111) determines the probability density function for a corresponding stochastic process $X(t)$, which evolves according to the SDE or Langevin equation [210]

$$dX = A(X)dt + \frac{1}{\sqrt{N}} b(X) dW(t). \tag{1.117}$$

with $b(x)^2 = B(x)$. Here $W(t)$ denotes a Wiener process with $dW(t)$ distributed according to a Gaussian process with mean and covariance

$$\langle dW(t) \rangle = 0, \quad \langle dW(t) dW(s) \rangle = \delta(t-s) dt ds. \tag{1.118}$$

Note that the noise term in (1.117) is multiplicative, since it depends on the current state $X(t)$. It is well known that there is an ambiguity in how one integrates multiplicative noise terms, which relates to the issue of Ito versus Stratonovich versions of stochastic calculus [210]; see appendix section1.7. However, for this particular example, based on the reduction of a master equation, the explicit form of the corresponding FP equation (1.111) ensures that the noise should be interpreted in the sense of Ito.

Thus, one can view the SDE as describing a stochastic path in phase space that involves a deterministic trajectory converging to the unique stable fixed point x^* that is perturbed by Gaussian-like fluctuations of order $1/\sqrt{N}$. Substituting $X - x^* = Y/\sqrt{N}$ into the SDE equation (1.117) and formally Taylor expanding to lowest order in $1/\sqrt{N}$ yields the so-called linear noise approximation

$$dY = -kY dt + b(x^*) dW(t), \tag{1.119}$$

with

$$k \equiv -A'(x^*) = \alpha + \beta, \quad b(x^*) = \sqrt{B(x^*)} = \sqrt{\frac{2\alpha\beta}{\alpha+\beta}}.$$

This takes the form of an Ornstein–Uhlenbeck equation [210], which can be solved as

$$Y(t) = \mathrm{e}^{-kt} Y_0 + b(x^*) \int_0^t \mathrm{e}^{-k(t-t')} dW(t'), \tag{1.120}$$

given the initial condition $Y(0) = Y_0$. It follows that the mean and covariance of $Y(t)$ are

$$\langle Y(t) \rangle = \mathrm{e}^{-kt} Y_0, \tag{1.121}$$

and

$$\begin{aligned} \mathrm{cov}(Y(t), Y(s)) &\equiv \langle [Y(t) - \langle Y(t) \rangle][Y(s) - \langle Y(s) \rangle] \rangle \\ &= \left\langle b(x^*)^2 \left[\int_0^t \mathrm{e}^{-k(t-t')} dW(t') \right] \left[\int_0^t \mathrm{e}^{-k(s-t'')} dW(t'') \right] \right\rangle \\ &= b(x^*)^2 \mathrm{e}^{-k(t+s)} \int_0^s \mathrm{e}^{2kt'} dt' = \frac{b(x^*)^2}{2k} \mathrm{e}^{-k(t-s)} \left[1 - \mathrm{e}^{-2ks} \right]. \end{aligned} \tag{1.122}$$

Here

$$\frac{b(x^*)^2}{2k} = \frac{\alpha\beta}{(\alpha+\beta)^2} = x^*(1-x^*),$$

and, without loss of generality, we have assumed that $t \geq s$. Thus, in the stationary limit $t \to \infty$,

$$\langle Y(t) \rangle \to 0, \quad \text{cov}(Y(t), Y(s)) \to \frac{b(x^*)^2}{2k} \mathrm{e}^{-k|t-s|}.$$

Since $Y(t)/\sqrt{N} = X(t) - x^*$, we recover the results of (1.110).

Note that (1.116) differs from the effective potential (1.107) obtained directly from the master equation for large N, given that the latter can be rewritten in the form

$$\Phi(x) = \int^x \ln \frac{\Omega_-(x')}{\Omega_+(x')} dx'. \tag{1.123}$$

Although, this discrepancy is not much of an issue when the underlying kinetic equations have a unique fixed point, it can lead to exponentially large errors when there are multiple stable fixed points. The Langevin or diffusion approximation still accounts for the effects of fluctuations well within the basin of attraction of a locally stable fixed point. However, there is now a small probability that there is a noise-induced transition to the basin of attraction of another fixed point. Since the probability of such a transition is usually of order $\mathrm{e}^{-\tau N}$ with $\tau = \mathcal{O}(1)$, except close to the boundary of the basin of attraction, such a contribution cannot be analyzed accurately using standard Fokker–Planck methods [309]. These exponentially small transitions play a crucial role in allowing the network to approach the unique stationary state (if it exists) in the asymptotic limit $t \to \infty$. In other words, for multistable systems, the limits $t \to \infty$ and $N \to \infty$ do not commute [24, 256, 641]. One example where multistability is important is when considering the effects of stochastic ion channels on membrane voltage fluctuations (see below).

1.5.3 Membrane Voltage Fluctuations

Let us now return to a conductance-based model of a neuron, in which the stochastic opening of ion channels generates a stochastic ionic current that drives the membrane voltage. We are particularly interested in how fluctuations affect the initiation of an action potential due to the opening of a finite number of Na^+ channels. Therefore, we imagine freezing the slow K^+ channels, so that they effectively act as a leak current and simplify the sodium channels by treating each as a single activating subunit. The stochastic membrane voltage then evolves according to the piecewise deterministic equation

$$\frac{dV}{dt} = F(V,n) \equiv \frac{1}{N} f(V) n(t) - g(V), \tag{1.124}$$

where $f(v) = g_{\text{Na}}(V_{\text{Na}} - v)$ represents the gated sodium currents, $g(v) = -g_{\text{eff}}[V_{\text{eff}} - v] - I$ represents the sum of effective leakage currents and external inputs I, and $n(t)$ is the number of open sodium channels. Note that (1.124) only holds between jumps in the number of open ion channels, with the latter described by the

master equation (1.104). The stochastic process defined by (1.104) and (1.124) is an example of a so-called stochastic hybrid system with piecewise deterministic dynamics. There has been a lot of recent interest in such systems, particularly within the context of conductance-based models [88, 321, 484, 654]. The associated probability density $p(v,n,t)$, which is defined according to

$$p(v,n,t)dv = \text{Prob}[n(t) = n, v \le V(t) \le v + dv],$$

given an initial condition $V(0) = V_0, n(0) = n_0$, satisfies the differential Chapman–Kolmogorov (CK) equation

$$\begin{aligned}\frac{\partial p}{\partial t} = &-\frac{\partial}{\partial v}\left[\left(\frac{n}{N}f(v) - g(v)\right)p\right] + \omega_+(v,n-1)p(v,n-1,t) \\ &+\omega_-(v,n+1)p(v,n+1,t) - [\omega_+(v,n) + \omega_-(v,n)]p(v,n,t),\end{aligned} \tag{1.125}$$

with

$$\omega_+(v,n) = \alpha(v)(N-n), \quad \omega_-(v,n) = \beta(v)n. \tag{1.126}$$

Note that the right-hand side of (1.124) is negative for large V and positive for small V, which implies that the voltage V is confined to some bounded domain $[V_1, V_2]$.

In order to investigate action potential initiation, we will assume that N is sufficiently large so that we can approximate the jump Markov process for the ion channels by a continuous Markov process using a diffusion approximation, and (ii) we assume that the transitions between different discrete states is much faster than the voltage dynamics so we can assume that, for fixed v, the number of open ion channels is close to the quasi-equilibrium $x^*(v) = \alpha(v)/(\alpha(v)+\beta(v))$. This limiting case was originally considered by Chow and White [116]. Under these approximations, the voltage dynamics is described by an SDE of the form [see (1.119)]

$$dV = \left[f(V)(x^* + Y(t)/\sqrt{N}) - g(V)\right]dt, \quad dY = -kY\,dt + b(x^*)dW(t). \tag{1.127}$$

Thus the stochastic voltage is coupled to a fast Ornstein–Uhlenbeck or colored noise process $Y(t)$. If we make the further assumption that the latter is in quasi-equilibrium for a given V (fast ion channels), $Y(t)dt \approx k^{-1}b(x^*)dW(t)$, then we obtain a scalar SDE for the voltage:

$$dV = [f(V)x^*(V) - g(V)]\,dt + \frac{1}{\sqrt{N}}\sigma(V)f(V)dW(t), \tag{1.128}$$

where

$$\sigma(V) = \frac{b(x^*(V))}{k(V)} = \frac{1}{\alpha(V)+\beta(V)}\sqrt{\frac{2\alpha(V)\beta(V)}{\alpha(V)+\beta(V)}}. \tag{1.129}$$

Taking $\alpha, \beta = \mathcal{O}(1/\varepsilon)$ for some dimensionless parameter $0 < \varepsilon \ll 1$, we see that $\sigma(V) = \mathcal{O}(\varepsilon^{1/2})$. In deriving (1.128), we have effectively taken a zero correlation limit of a colored noise process. It can be shown that the multiplicative noise term should be interpreted in the sense of Stratonovich, and the associated FP equation is given by [210, 321]

$$\frac{\partial p(v,t)}{\partial t} = -\frac{\partial}{\partial v}\left[\mathscr{A}(v)p(v,t)\right] + \frac{1}{N}\frac{\partial}{\partial v}\left[\mathscr{B}(v)\frac{\partial}{\partial v}p(v,t)\right], \tag{1.130}$$

with

$$\mathscr{A}(v) = f(v)x^*(v) - g(v), \quad \mathscr{B}(v) = [\sigma(v)f(v)]^2/2.$$

We have ignored an $\mathscr{O}(\varepsilon)$ contribution to the drift term of the form $\mathscr{B}'(v)/N$. The FP equation is supplemented by reflecting boundary conditions at $v = V_1, V_2$:

$$J(V_1,t) = J(V_2,t) = 0, \tag{1.131}$$

with

$$J(v,t) = \mathscr{A}(v)p(v,t) - \frac{\mathscr{B}(v)}{N}\frac{\partial}{\partial v}p(v,t). \tag{1.132}$$

1.5.4 First Passage Time Problem

A key property that one would like to calculate is the mean time to fire an action potential (MFPT) as a function of the stimulus current I. In the absence of noise, the system evolves according to the deterministic equation

$$\frac{dv}{dt} = \mathscr{A}(v) = \frac{\alpha(v)}{\alpha(v)+\beta(v)}f(v) - g(v) \equiv -\frac{d\Phi_0(v)}{dv}, \tag{1.133}$$

where $\Phi_0(v)$ is a deterministic potential. In Fig. 1.17, we plot $\Phi_0(v)$ as a function of v for various values of the external input current and the particular transition rates

$$\alpha(v) = \beta \exp\left(\frac{2(v-v_1)}{v_2}\right), \quad \beta = \text{constant}.$$

The minima and maxima of the potential correspond to stable and unstable fixed points of the deterministic dynamics, respectively. It can be seen that below a threshold current I_*, $I < I_*$, there exist two stable fixed points $v_\pm$ (minima) separated by an unstable fixed point at v_0 (maximum), that is, the system exhibits bistability. The left-hand fixed point represents the resting state, whereas the right-hand fixed point corresponds to an excited state. Thus, in the bistable regime the deterministic system requires an external perturbation in order to generate an action potential starting from the resting state. On the other hand, for the stochastic system it is possible that fluctuations in the opening and closing of Na^+ ion channels induce a transition from the resting state to the excited state by crossing over the potential hill at v_0. This is directly analogous to a diffusing particle escaping from the left to the right well in a double well potential, which is a classical example of a first passage time (FPT) problem in physics [210, 257]. (Of course, once such an event occurs, one has to take into account the K^+ dynamics in order to incorporate the effects of repolarization

that return the system to the resting state. If one includes the slow opening and closing of these channels, then the underlying deterministic system becomes excitable rather than bistable; see Sect. 2.1. For the moment, we will assume that this does not significantly affect the noise-induced initiation of an action potential. It turns out that such an assumption breaks down if fluctuations in the opening and closing of K^+ channels become significant [456].)

We now outline the basic calculation of the mean time to escape from the resting state using the diffusion approximation. Since the voltage will rapidly approach the excited state v_+ once it has passed the maximum at v_0, the major contribution to the escape time will be due to the fluctuation-driven transition from v_- to v_0. We can model this process by replacing the reflecting boundary condition at $v = V_2$ with an absorbing boundary condition at $v = v_0 < V_2$:

$$p(v_0, t) = 0.$$

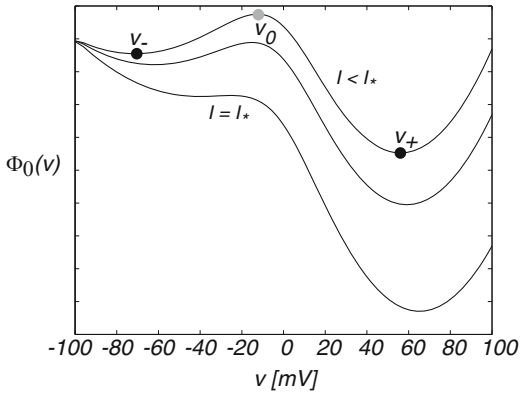

Fig. 1.17 Plot of deterministic potential $\Phi_0(v)$ as a function of voltage v for different values of the external stimulus current I. Parameter values are $N = 10$, $v_{\rm Na} = 120\,{\rm mV}$, $v_{\rm eff} = -62.3\,{\rm mV}$, $g_{\rm Na} = 4.4\,{\rm mS/cm^2}$, $g_{\rm eff} = 2.2\,{\rm mS/cm^2}$, $\beta = 0.8\ {\rm s}^{-1}$, and $\alpha(v) = \beta \exp[(v+1.2)/9]$

We also shift the voltage v so that the left-hand boundary is at $V_1 = 0$. Let $T(v)$ denote the stochastic time for the particle to exit the right-hand boundary at v_0, given that it starts at location $v \in [0, v_0]$ at time $t = 0$. As a first step, we introduce the survival probability $\mathbb{P}(v,t)$ that the particle has not yet exited at time t:

$$\mathbb{P}(v,t) = \int_0^{v_0} p(x,t|v,0)dx. \tag{1.134}$$

It follows that ${\rm Prob}[T(v) \le t] = 1 - \mathbb{P}(v,t)$ and we can define the FPT density according to

$$f(v,t) = -\frac{\partial \mathbb{P}(v,t)}{\partial t}. \tag{1.135}$$

It can be shown from (1.130) and the Markovian nature of the stochastic process that the FPT density satisfies a backward FP equation of the form [210]

$$\frac{\partial \mathbb{P}(v,t)}{\partial t} = \mathscr{A}(v)\frac{\partial \mathbb{P}(v,t)}{\partial v} + \frac{\partial}{\partial v}\left(\mathscr{B}(v)\frac{\partial}{\partial v}\mathbb{P}(v,t)\right), \tag{1.136}$$

where we have absorbed the factor of $1/N$ into $\mathscr{B}$.

A quantity of particular interest is the mean first passage time (MFPT) $\tau(v)$ defined according to

$$\begin{aligned}\tau(v) = \langle T(v)\rangle &\equiv \int_0^\infty f(v,t)t\,dt \\ &= -\int_0^\infty t\frac{\partial \mathbb{P}(v,t)}{\partial t}dt = \int_0^\infty \mathbb{P}(v,t)dt,\end{aligned} \tag{1.137}$$

after integration by parts. Hence, integrating both sides of (1.136) shows that the MFPT satisfies the ODE

$$[\mathscr{A}(v)+\mathscr{B}'(v)]\frac{d\tau(v)}{dv} + \left(\mathscr{B}(v)\frac{d^2}{dv^2}\tau(v)\right) = -1. \tag{1.138}$$

Equation (1.138) is supplemented by reflecting and absorbing boundary conditions for the backward FP equation:

$$\tau'(0) = 0, \quad \tau(v_0) = 0. \tag{1.139}$$

It is straightforward to solve (1.138) by direct integration [210]. First, introducing an integration factor and integrating once gives

$$\mathrm{e}^{\Psi(v)}\tau'(v) = -\int_0^v \frac{\mathrm{e}^{\Psi(v')}}{\mathscr{B}(v')}dv',$$

where

$$\Psi(v) = \int_0^v \frac{\mathscr{A}(v')+\mathscr{B}'(v')}{\mathscr{B}(v')}dv'. \tag{1.140}$$

and we have used the boundary condition $\tau'(0) = 0$. Integrating once more with respect to v and using $\tau(v_0) = 0$ then gives

$$\tau(v) = \int_v^{v_0} \mathrm{e}^{-\Psi(v')}dv' \int_0^{v'} \frac{\mathrm{e}^{\Psi(v'')}}{\mathscr{B}(v'')}dv''. \tag{1.141}$$

There is now a standard procedure for approximating this double integral based on Kramers reaction rate theory [210, 257]. We simply quote the result here: $\tau(v_-) = 1/\lambda$ where

$$\lambda \approx \frac{\mathscr{B}(v_0)}{\pi}\sqrt{\left|\frac{\mathscr{A}'(v_-)}{\mathscr{B}(v_-)}\right|\frac{\mathscr{A}'(v_0)}{\mathscr{B}(v_0)}}\exp\left[\int_{v_-}^{v_0}\frac{\mathscr{A}(v)}{\mathscr{B}(v)}dv.\right]. \tag{1.142}$$

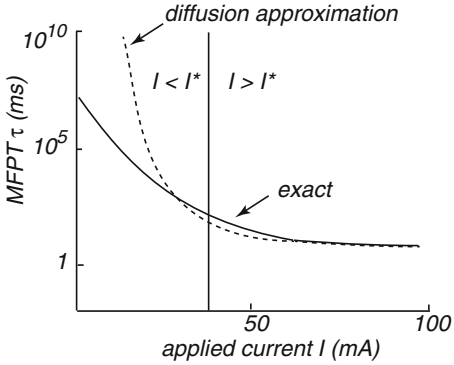

Fig. 1.18 Schematic diagram comparing MFPT calculated using the diffusion approximation with the MFPT of the full system. The scales of the axes are based on numerical results carried out in [321] for $N = 10$. Other parameter values as in Fig. 1.17

Keener and Newby [321] calculated the MFPT using the diffusion approximation and compared it with Monte Carlo simulations of the full stochastic model whose probability density evolves according to the CK equation (1.126). A summary of their findings is shown schematically in Fig. 1.18. The main observation is that although the Gaussian-like diffusion approximation does well in the superthreshold regime ($I > I_*$), it deviates significantly from the full model results in the subthreshold regime ($I < I_*$), where it overestimates the mean time to spike. This is related to the fact that the effective potential of the steady-state density under the diffusion approximation generates exponentially large errors in the MFPT, as discussed at the end of Sect. 1.5.2. Finally, note that the model of stochastic ion channels and membrane voltage fluctuations presented above is based on a number of simplifications. First, only the initiation of an action potential was considered, which involved the opening of sodium channels, while the termination of the action potential due to Na^+ inactivation and K^+ activation was ignored. Indeed, in stochastic versions of the Hodgkin–Huxley equations spontaneous activity can be observed due to fluctuations in K^+ ion channels [116, 456]. That is, if some K^+ channels spontaneously close, then a regenerative Na^+ current can induce an action potential. The second simplification was to treat each ion channel as a single unit rather than as a cluster of subunits. In other words, the Markov chain of events associated with opening and closing of an ion channel involves transitions between more than two internal states.

1.6 Stochastic Hybrid System with Fast Kinetics

As shown by Keener and Newby [321], it is possible to obtain a much more accurate analytical expression for the MFPT in the subthreshold regime by analyzing the CK equation (1.126) in the limit of fast sodium channels. This analysis applies equally

well to small and large N. First, it is convenient to rewrite the CK equation in a more compact and general form:

$$\frac{\partial p}{\partial t} = -\frac{\partial [F(v,n)p(v,n,t)]}{\partial v} + \frac{1}{\varepsilon}\sum_{m=0}^{N} A(n,m;v)p(v,m,t) \tag{1.143}$$

with F given by (1.124) and A a tridiagonal matrix (for fixed v): $A(n,n-1;v) = \omega_+(v,n-1)$, $A(n,n;v) = -\omega_+(v,n) - \omega_-(n)$, $A(n,n+1;v) = \omega_-(n+1)$. We are now making explicit the condition that the open and closing of Na^+ channels occurs on a much faster time scale than the voltage dynamics by scaling the transition rates according to the small parameter $\varepsilon \ll 1$. In the limit $\varepsilon \to 0$, (1.124) reduces to the deterministic or mean field (1.133) with $\mathscr{A}(v) = \sum_n F(v,n)\rho(v,n)$, where $\rho(v,n)$ is the unique steady-state density satisfying $\sum_m A(n,m;v)\rho(v,m) = 0$ (see (1.105)):

$$\rho(v,n) = \frac{N!}{(N-n)!n!}a(v)^n b(v)^{N-n}, \quad a(v) = \frac{\alpha(v)}{\alpha(v)+\beta}, b(v) = \frac{\beta}{\alpha(v)+\beta}. \tag{1.144}$$

The mean number of open channels is $\langle n \rangle = \sum_{n=1}^{N} n\rho(v,n) = Na(v)$. In the regime $0 < \varepsilon \ll 1$, for which there are typically a large number of transitions between different channel states n while the voltage v hardly changes at all. This suggests that the system rapidly converges to the (quasi-)steady-state $\rho(v,n)$, which will then be perturbed as v slowly evolves. The resulting perturbations can be analyzed using a quasi-steady-state (QSS) diffusion or adiabatic approximation [210, 454, 487], in which the CK equation (1.143) is approximated by a Fokker–Planck (FP) equation; see also Sect. 6.4

The QSS approximation was first developed from a probabilistic perspective by Papanicolaou [487]; see also [210]. It has subsequently been applied to a wide range of problems in biology, including cell movement [274, 481], wavelike behavior in models of slow axonal transport [206, 207, 518], and molecular motor-based models of random intermittent search [453, 454]. The basic idea of the QSS reduction is to decompose the probability density as

$$p(v,n,t) = C(v,t)\rho(v,n) + \varepsilon w(v,n,t), \tag{1.145}$$

where $\sum_n p(v,n,t) = C(v,t)$ and $\sum_n w(v,n,t) = 0$. Carrying out an asymptotic expansion in ε, it can be shown that C evolves according to the FP equation [81, 453, 454]

$$\frac{\partial C}{\partial t} = -\frac{\partial}{\partial v}(\mathscr{A}C) + \varepsilon \frac{\partial}{\partial v}\left(\mathscr{D}\frac{\partial C}{\partial v}\right), \tag{1.146}$$

with the drift term given by (1.133), and diffusion coefficient

$$\mathscr{D}(v) = \sum_{n=0}^{N} Z(v,n)F(v,n), \tag{1.147}$$

where $Z(v,n)$ is the unique solution to

$$\sum_m A(n,m;v)Z(v,m) = [\mathscr{A}(v) - F(v,n)]\rho(v,n) \tag{1.148}$$

with $\sum_m Z(v,m) = 0$. As in the case of the diffusion approximation for large N, the FP equation (1.146) captures the Gaussian-like fluctuations within the basin of attraction of a fixed point of the mean field (1.133), but breaks down when considering rare event transitions between metastable states since it yields exponentially large errors in the escape rates. Therefore, one has to deal with the full CK equation (1.143).

1.6.1 First Passage Time Problem and the Projection Method

In order to revisit the FPT problem considered in Sect. 1.5.4, we supplement (1.143) with the following absorbing boundary conditions at v_0:

$$p(v_0,n,t) = 0, \text{ for all } n \in \Sigma = \{0,\ldots,k-1\}. \tag{1.149}$$

Here, Σ denotes the set of integers for which $F(v_0,n) < 0$. The initial condition is taken to be

$$p(v,n,0) = \delta(v - v_-)\delta_{n,n_0}. \tag{1.150}$$

Let T denote the (stochastic) FPT for which the system first reaches v_0, given that it started at v_-. The distribution of FPTs is related to the survival probability that the system has not yet reached v_0:

$$S(t) \equiv \int_0^{v_0} \sum_{n=0}^{N} p(v,n,t)dv. \tag{1.151}$$

That is, Prob$\{t > T\} = S(t)$ and the FPT density is

$$f(t) = -\frac{dS}{dt} = -\int_0^{v_0} \sum_{n=0}^{N} \frac{\partial p}{\partial t}(v,n,t)dv. \tag{1.152}$$

Substituting for $\partial p/\partial t$ using the CK equation (1.143) shows that

$$f(t) = \int_0^{v_0} \left[\sum_{n=0}^{N} \frac{\partial[F(v,n)p(v,n,t)]}{\partial v}\right] dv = \sum_{n=0}^{N} p(v_0,n,t)F(v_0,n). \tag{1.153}$$

We have used $\sum_n A(n,m;v) = 0$ and $\lim_{v\to-\infty} F(v,n)p(v,n,t) = 0$. The FPT density can thus be interpreted as the probability flux $J(v,t)$ at the absorbing boundary, since we have the conservation law

$$\sum_{n=0}^{N} \frac{\partial p(v,n,t)}{\partial t} = -\frac{\partial J(v,t)}{\partial v}, \quad J(v,t) = \sum_{n=0}^{N} F(v,n)p(v,n,t). \tag{1.154}$$

We wish to solve the FPT problem in the weak noise limit $\varepsilon \ll 1$. One of the characteristic features of the weak noise limit is that the flux through the absorbing boundary and the inverse of the MFPT $\langle T \rangle$ are exponentially small, that is, $\langle T \rangle \sim \mathrm{e}^{-C/\varepsilon}$ for some constant C. This means that standard singular perturbation theory cannot be used to solve the resulting boundary value problem, in which one matches inner and outer solutions of a boundary layer around the point $v = v_0$. Instead, one proceeds by finding a quasistationary solution using a Wentzel–Kramers–Brillouin (WKB) approximation. Recently, this approach has been extended by Keener and Newby [321] to a CK equation of the form (1.143), using a so-called projection method [660].

In order to apply the projection method, it is necessary to assume certain properties of the non-self-adjoint linear operator $-\hat{L}$ on the right-hand side of (1.143) with respect to the Hilbert space of functions $h : [0, v_0] \times \{0, \ldots, N\} \to \mathbb{R}$ with inner product defined according to

$$\langle h, g \rangle = \int_0^{v_0} \sum_{n=0}^{N} h(v,n) g(v,n) dv. \tag{1.155}$$

1. $\hat{L}$ has a complete set of eigenfunctions ϕ_r with

$$\hat{L}\phi_r(v,n) \equiv \frac{d}{dv}(F(v,n)\phi_r(v,n)) - \frac{1}{\varepsilon}\sum_{m=0}^{N} A(n,m;v)\phi_r(v,m) = \lambda_r \phi_r(v,n), \tag{1.156}$$

   together with the boundary conditions

$$\phi_r(v_0,n) = 0, \text{ for } n = 0, \ldots, k-1. \tag{1.157}$$

2. The real part of each eigenvalue λ_r is positive definite and the smallest eigenvalue λ_0 is real and simple. Thus we can introduce the ordering $0 < \lambda_0 < \mathrm{Re}[\lambda_1] \leq \mathrm{Re}[\lambda_2] \leq \ldots$.
3. λ_0 is exponentially small, $\lambda_0 \sim \mathrm{e}^{-C/\varepsilon}$, whereas $\mathrm{Re}[\lambda_r] = \mathscr{O}(1)$ for $r \geq 1$. In particular, $\lim_{\varepsilon \to 0} \lambda_0 = 0$ and $\lim_{\varepsilon \to 0} \phi_0(v,n) = \rho(v,n)$.

Under the above assumptions, we can introduce the eigenfunction expansion

$$p(v,n,t) = \sum_{r=0}^{N} C_r \mathrm{e}^{-\lambda_r t}\phi_r(v,n),. \tag{1.158}$$

with $\lambda_0 \ll \mathrm{Re}[\lambda_r]$ for all $r \geq 1$. Thus, at large times we have the quasistationary approximation

$$p(v,n,t) \sim C_0 \mathrm{e}^{-\lambda_0 t}\phi_0(v,n). \tag{1.159}$$

Substituting such an approximation into (1.153) implies that

$$f(t) \sim \mathrm{e}^{-\lambda_0 t} \sum_{n=0}^{N} \phi_0(v_0,n) F(v_0,n), \quad \lambda_1 t \gg 1. \tag{1.160}$$

Equation (1.156) implies that

$$\sum_{n=0}^{N}\int_0^{v_0}\widehat{L}\phi_0(v,n)dv \equiv \sum_{n=0}^{N}F(v_0,n)\phi_0(v_0,n)$$
$$= \lambda_0\sum_{n=0}^{N}\int_0^{v_0}\phi_0(v,n)dv.$$

In other words,

$$\lambda_0 = \frac{\sum_{n=0}^{N}F(v_0,n)\phi_0(v_0,n)}{\langle 1,\phi_0\rangle}. \tag{1.161}$$

Combining (1.161) and the quasistationary approximation (1.160) shows that the (normalized) FPT density reduces to

$$f(t) \sim \lambda_0 \mathrm{e}^{-\lambda_0 t} \tag{1.162}$$

and, hence, $\langle T\rangle = \int_0^\infty t f(t)dt \sim 1/\lambda_0$.

It remains to obtain an approximation ϕ_ε of the principal eigenfunction ϕ_0, which can be achieved using the WKB method as described in Sect. 1.6.2. This yields a quasistationary density that approximates ϕ_0 up to exponentially small terms at the boundary, that is,

$$\hat{L}\phi_\varepsilon = 0, \quad \phi_\varepsilon(u_*,n) = \mathscr{O}(\mathrm{e}^{-C/\varepsilon}). \tag{1.163}$$

In order to express λ_0 in terms of the quasistationary density ϕ_ε, we consider the eigenfunctions of the adjoint operator, which satisfy the equation

$$\hat{L}^\dagger\xi_r(v,n) \equiv -F(v,n)\frac{d\xi_r(v,n)}{dv} - \frac{1}{\varepsilon}\sum_m A(m,n;v)\xi_r(v,m) = \lambda_r\xi_r(v,n), \tag{1.164}$$

and the boundary conditions

$$\xi_r(v_0,n) = 0, \quad n \geq k. \tag{1.165}$$

The two sets of eigenfunctions $\{\phi_r\}$ and $\{\xi_r\}$ form a biorthogonal set with respect to the underlying inner product,

$$\langle\phi_r,\xi_s\rangle = \delta_{r,s}. \tag{1.166}$$

Now consider the identity

$$\langle\phi_\varepsilon,\hat{L}^\dagger\xi_0\rangle = \lambda_0\langle\phi_\varepsilon,\xi_0\rangle. \tag{1.167}$$

Integrating by parts the left-hand side of (1.164) picks up a boundary term so that

$$\lambda_0 = -\frac{\sum_{n=0}^{N}\phi_\varepsilon(v_0,n)\xi_0(v_0,n)F(v_0,n)}{\langle\phi_\varepsilon,\xi_0\rangle}. \tag{1.168}$$

The calculation of the principal eigenvalue λ_0 thus reduces to the problem of determining the quasistationary density ϕ_ε and the adjoint eigenfunction ξ_0.

1.6.2 The WKB Method and the Quasistationary Density

We now show how the WKB method [160, 256, 398, 445, 559] can be used to compute the quasistationary density ϕ_ε. We seek a solution of the form

$$\phi_\varepsilon(v,n) \sim R(v,n)\exp\left(-\frac{\Phi(v)}{\varepsilon}\right), \tag{1.169}$$

where $\Phi(v)$ is a scalar potential. Substituting into $\hat{L}\phi_\varepsilon = 0$ gives

$$\sum_{m=0}^{N}\left(A(n,m;v)+\Phi'(v)\delta_{n,m}F(v,m)\right)R(v,m) = \varepsilon\frac{dF(v,n)R(v,n)}{dx}, \tag{1.170}$$

where $\Phi' = d\Phi/dx$. Introducing the asymptotic expansions $R \sim R^{(0)} + \varepsilon R^{(1)}$ and $\Phi \sim \Phi_0 + \varepsilon\Phi_1$, the leading-order equation is

$$\sum_{m=0}^{N} A(n,m;v)R^{(0)}(v,m) = -\Phi_0'(v)F(v,n)R^{(0)}(v,n). \tag{1.171}$$

(Note that since $F(v,n)$ is nonzero almost everywhere for $v < v_0$, we can identify $-\Phi_0'$ and $R^{(0)}$ as an eigenpair of the matrix operator $\hat{A}(n,m;v) = A(n,m;v)/F(v,n)$ for fixed v.) Positivity of the probability density ϕ_ε requires positivity of the corresponding solution $R^{(0)}$. One positive solution is $R^{(0)} = \rho$, for which $\Phi_0' = 0$. However, such a solution is not admissible since $\Phi_0 =$ constant. It can be proven using linear algebra that if $F(v,n)$ for fixed $v < v_0$ changes sign as n increases from zero, then there exists one other positive solution, which also has the appropriate functional form to describe the potential well. That is, $\Phi_0'(x)$ has the correct sign and vanishes at the fixed points. Hence, it can be identified as the appropriate WKB solution.

Proceeding to the next order in the asymptotic expansion of (1.170), we have

$$\begin{aligned}\sum_{m=0}^{N}&\left(A(n,m;v)+\Phi_0'(v)\delta_{n,m}F(v,m)\right)R^{(1)}(v,m)\\ &= \frac{dF(v,n)R^{(0)}(v,n)}{dx} - \Phi_1'(v)F(v,n)R^{(0)}(v,n).\end{aligned} \tag{1.172}$$

For fixed v and WKB potential Φ_0, the matrix operator $\bar{A}(n,m;v) = A(n,m;v) + \Phi_0'(v)\delta_{n,m}F(v,m)$ on the left-hand side of this equation has a one-dimensional null

space spanned by the positive WKB solution $R^{(0)}$. The Fredholm alternative theorem[1] then implies that the right-hand side of (1.172) is orthogonal to the left null vector S of $\bar{A}$. That is, we have the solvability condition

$$\sum_{n=0}^{N} S(v,n)\left[\frac{dF(v,n)R^{(0)}(v,n)}{dv} - \Phi_1'(v)F(v,n)R^{(0)}(v,n)\right] = 0, \tag{1.173}$$

with S satisfying

$$\sum_{n=0}^{N} S(v,n)\left(A(n,m;v) + \Phi_0'(v)\delta_{n,m}F(v,m)\right) = 0. \tag{1.174}$$

Given $R^{(0)}, S$ and Φ_0, the solvability condition yields the following equation for Φ_1:

$$\Phi_1'(x) = \frac{\sum_{n=0}^{N} S(v,n)[F(v,n)R^{(0)}(v,n)]'}{\sum_{n=0}^{N} S(v,n)F(v,n)R^{(0)}(v,n)}. \tag{1.175}$$

Combining the various results, and defining

$$k(v) = \exp\left(-\int_{v_-}^{v} \Phi_1'(y)dy\right), \tag{1.176}$$

gives to leading order in ε,

$$\phi_\varepsilon(v,n) \sim \mathcal{N}k(v)\exp\left(-\frac{\Phi_0(v)}{\varepsilon}\right)R^{(0)}(v,n), \tag{1.177}$$

where we choose $\sum_n R^{(0)}(v,n) = 1$ for all v and $\mathcal{N}$ is the normalization factor,

$$\mathcal{N} = \left[\int_0^{v_0} k(v)\exp\left(-\frac{\Phi_0(v)}{\varepsilon}\right)\right]^{-1}. \tag{1.178}$$

The latter can be approximated using Laplace's method to give

$$\mathcal{N} \sim \frac{1}{k(v_-)}\sqrt{\frac{|\Phi_0''(v_-)|}{2\pi\varepsilon}}\exp\left(\frac{\Phi_0(v_-)}{\varepsilon}\right). \tag{1.179}$$

[1] Consider an M-dimensional linear inhomogeneous system $\mathbf{Ax} = \mathbf{b}$ with $\mathbf{x}, \mathbf{b} \in \mathbb{R}^M$. Suppose that the $M \times M$ matrix $\mathbf{A}$ has a nontrivial null space and let $\mathbf{v}$ be a null vector of the adjoint matrix $\mathbf{A}^\dagger$, that is, $\mathbf{A}^\dagger\mathbf{v} = 0$. The Fredholm alternative theorem states that the inhomogeneous equation has a (nonunique) solution if and only if $\mathbf{v}\cdot\mathbf{b} = 0$ for all null vectors $\mathbf{v}$.

1.6.3 Calculation of the Principal Eigenvalue

In order to evaluate the principal eigenvalue λ_0 satisfying (1.168), it is necessary to determine the adjoint eigenfunction ξ_0. Following [321, 455], this can be achieved using singular perturbation methods. Since λ_0 is exponentially small in ε, (1.164) yields the leading-order equation

$$\varepsilon F(v,n)\frac{d\xi_0(v,n)}{dx}+\sum_{m=0}^{N}A(m,n;v)\xi_0(v,m)=0, \tag{1.180}$$

supplemented by the absorbing boundary condition

$$\xi_0(v_0,n)=0, \quad n\geq k. \tag{1.181}$$

A first attempt at obtaining an approximate solution that also satisfies the boundary conditions is to construct a boundary layer in a neighborhood of the unstable fixed point v_0 by performing the change of variables $v=v_0-\varepsilon z$ and setting $Q(z,n)=\xi_0(v_0-\varepsilon z)$. Equation (1.180) then becomes

$$F(v_0,n)\frac{dQ(z,n)}{dz}+\sum_{m=0}^{N}A(m,n;v_0)Q(z,m)=0. \tag{1.182}$$

This inner solution has to be matched with the outer solution $\boldsymbol{\xi}_0=\mathbf{1}$, which means that

$$\lim_{z\to\infty}Q(z,n)=1 \tag{1.183}$$

for all n. Consider the eigenvalue equation

$$\sum_{n=0}^{N}\left(A(n,m;v)-\mu_r(v)\delta_{n,m}F(v,m)\right)S_r(v,n)=0, \tag{1.184}$$

with $r=0,\ldots,N$. We take $S_0(v,n)=1$ so that $\mu_0=0$ and set $S_1(v,n)=S(v,n),\mu_1(v)=-\Phi_0'(v)$, where S satisfies (1.174). We then introduce the eigenfunction expansion

$$Q(z,n)=c_0+\sum_{r=1}^{N}c_rS_r(v_0,n)\mathrm{e}^{-\mu_r(v_0)z}. \tag{1.185}$$

In order that the solution remains bounded as $z\to\infty$ we require that $c_r=0$ if $\mathrm{Re}[\mu_r(v_0)]<0$. The boundary conditions (1.181) generate a system of linear equations for the coefficients c_r with codimension k. One of the unknowns is determined by matching the outer solution, which suggests that there are $k-1$ eigenvalues with negative real part. The eigenvalues are ordered so that $\mathrm{Re}[\mu_r(v_0)]<0$ for $r>N+1-k$.

There is, however, one problem with the above eigenfunction expansion, namely, that $\mu_1(v_0)\equiv-\Phi_0'(v_0)=0$ so that the zero eigenvalue is degenerated at $v=v_0$. Hence, the solution needs to include a secular term involving the generalized eigen-

vector $\hat{S}$,

$$\sum_{n=0}^{N} A(n,m;v_0)\hat{S}(v_0,n) = -F(v_0,m). \tag{1.186}$$

The Fredholm alternative theorem ensures that $\hat{S}$ exists and is unique, since the stationary density $\rho(v_0,m)$ is the right null vector of $A(n,m;v_0)$ and $\sum_n \rho(v_0,n)F(v_0,n) \equiv \mathscr{A}(v_0) = 0$; see (1.133). The solution for $\mathbf{Q}(z)$ is now

$$Q(z,n) = c_0 + c_1(\hat{S}(v_0,n) - z) + \sum_{r=2}^{N+1-k} c_r S_r(v_0,n)\mathrm{e}^{-\mu_r(v_0)z}. \tag{1.187}$$

The presence of the secular term means that the solution is unbounded in the limit $z \to \infty$, which means that the inner solution cannot be matched with the outer solution. One way to remedy this situation is to introduce an alternative scaling in the boundary layer of the form $v = v_0 + \varepsilon^{1/2}z$, as detailed in [455]. One can then eliminate the secular term $-c_1 z$ and show that

$$c_1 \sim \sqrt{\frac{2|\Phi_0''(v_0)|}{\pi}} + \mathscr{O}(\varepsilon^{1/2}), \quad c_r = \mathscr{O}(\varepsilon^{1/2}) \text{ for } r \geq 2 \tag{1.188}$$

It turns out that we only require the first coefficient c_1 in order to evaluate the principal eigenvalue λ_0 using (1.168). This follows from (1.171) and (1.184) and the observation that the left and right eigenvectors of the matrix $\hat{A}(n,m;v) = A(n,m;v)/F(v,n)$ are biorthogonal. In particular, since the quasistationary approximation ϕ_ε is proportional to $R^{(0)}$ (see (1.177)), it follows that ϕ_ε is orthogonal to all eigenvectors S_r, $r \neq 1$. Simplifying the denominator of (1.168) by using the outer solution $\xi_0 \sim 1$, we obtain

$$\begin{aligned}\lambda_0 &\sim -\frac{\sum_n \xi_0(v_0,n)F(v_0,n)\phi_\varepsilon(v_0,n)}{\langle \phi_\varepsilon, \mathbf{1}\rangle} \\ &\sim c_1 \frac{k(v_0)B(v_0)}{k(v_-)}\sqrt{\frac{|\Phi''(v_-)|}{2\pi}}\exp\left(-\frac{\Phi_0(v_0)-\Phi_0(v_-)}{\varepsilon}\right),\end{aligned} \tag{1.189}$$

with

$$B(v_0) = -\sum_{n=0}^{\infty} \hat{S}(v_0,n)F(v_0,n)\rho(v_0,n). \tag{1.190}$$

Substituting for c_1

$$\lambda_0 \sim \frac{1}{\pi}\frac{k(v_0)B(v_0)}{k(v_-)}\sqrt{\Phi_0''(v_-)|\Phi_0''(v_0)|}\exp\left(-\frac{\Phi_0(v_0)-\Phi_0(v_-)}{\varepsilon}\right). \tag{1.191}$$

Finally, comparison of (1.186) and (1.190) with (1.148) and (1.147) establishes that $B(v_0) \equiv \mathscr{D}(v_0)$.

The above analysis holds for any CK equation of the form (1.143). There are essentially three basic steps needed in order to evaluate the escape rate formula (1.191), which we now apply to the specific model of membrane voltage fluctuations.

1. Find the unique nontrivial positive eigenfunction $\psi_n(v) = R^{(0)}(v,n)$ and associated eigenvalue $\mu(v) = -\Phi_0'(v)$. In the case of the stochastic ion-channel model, (1.171) takes the explicit form

$$\begin{aligned}&(N-n+1)\alpha\psi_{n-1} - [n\beta + (N-n)\alpha]\psi_n + (n+1)\beta\psi_{n+1}\\ &\quad = \mu\left(\frac{n}{N}f(v) - g(v)\right)\psi_n\end{aligned} \tag{1.192}$$

Motivated by the form of the stationary density $\rho(v,n)$, we try the solution

$$\psi_n(v) = \frac{\Lambda(v)^n}{(N-n)!n!}, \tag{1.193}$$

which yields the following equation relating Λ and μ:

$$\frac{n\alpha}{\Lambda} + \Lambda\beta(N-n) - n\beta - (N-n)\alpha = \mu\left(\frac{n}{N}f(v) - g(v)\right).$$

We now fix μ in terms of Λ so that the terms linear in n vanish:

$$\mu = \frac{N}{f}\left[\alpha\left(\frac{1}{\Lambda}+1\right) - \beta(\Lambda+1)\right].$$

Eliminating μ then shows that

$$\Lambda(v) = \frac{g(v)}{f(v)-g(v)}.$$

We deduce that

$$\mu(v) = N\frac{\alpha(v)f(v) - (\alpha(v)+\beta)g(v)}{g(v)(f(v)-g(v))}, \tag{1.194}$$

and the normalized eigenvector is

$$\psi_n(v) = \frac{N!}{(N-n)!n!}\frac{(f(v)-g(v))^{N-n}g(v)^n}{f(v)^N}. \tag{1.195}$$

Note that $\mu(v)$ vanishes at the fixed points v_-, v_0 of the mean field (1.133) with $\mu(v) > 0$ for $0 < v < v_-$ and $\mu(v) > 0$ for $v_- < v < v_0$. Moreover, $\psi_n(v) = \rho(v,n)$ at the fixed points $v_0, v_\pm$. In conclusion $R^{(0)}(v,n) = \psi_n(v)$ and the effective potential Φ_0 is given by

$$\Phi_0(v) = -\int_{v_-}^{v}\mu(y)dy. \tag{1.196}$$

The effective potential is defined up to an arbitrary constant, which has been fixed by setting $\Phi_0(v_-) = 0$.

2. Determine the null eigenfunction $\eta_n(v) = S(v,n)$ of (1.174), which becomes

$$\begin{aligned}&(N-m)\alpha\eta_{m+1} - [(N-m)\alpha + m\beta]\eta_m + m\beta\eta_{m-1}\\ &= \mu\left(\frac{m}{N}f(v) - g(v)\right)\eta_m.\end{aligned} \tag{1.197}$$

Trying a solution of the form $\eta_m(v) = \Gamma(v)^m$ yields

$$(N-m)\alpha\Gamma - ((N-m)\alpha + m\beta) + m\beta\Gamma^{-1} = \mu\left(\frac{m}{N}f(v) - g(v)\right). \tag{1.198}$$

Γ is then determined by canceling terms independent of m, which gives

$$\eta_n(v) = \left(\frac{b(v)g(v)}{a(v)(f(v)-g(v))}\right)^n. \tag{1.199}$$

The prefactor $k(v)$ may now be determined using (1.175) and (1.176).

3. Calculate the generalized eigenvector $\zeta_n = \hat{S}(v_0,n)$ of (1.186), which reduces to

$$(N-n)\alpha(v_0)\zeta_{n+1} + n\beta\zeta_{n-1} - ((N-n)\alpha(v_0) + n\beta)\zeta_n = g(v_0) - \frac{n}{N}f(v_0). \tag{1.200}$$

It is straightforward to show that this has the solution

$$\zeta_n = \frac{f(v_0)}{N(\alpha(v_0)+\beta)}n. \tag{1.201}$$

It follows that the factor $B(v_0)$ defined by (1.190) is

$$\begin{aligned}B(v_0) &= -\frac{f(v_0)}{N(\alpha(v_0)+\beta)}\sum_{n=0}^{N}\rho(v_0,n)\left[-g(v_0)n + \frac{f(v_0)}{N}n^2\right]\\ &= -\frac{f(v_0)}{N(\alpha(v_0)+\beta)}\left[-g(v_0)\langle n\rangle + \frac{f(v_0)}{N}\langle n^2\rangle\right]\\ &= \frac{f(v_0)^2\alpha(v_0)\beta}{N(\alpha(v_0)+\beta)^3},\end{aligned} \tag{1.202}$$

where have used the fixed point condition $g(v_0) = f(v_0)a(v_0)$.

Keener and Newby [321] showed that the WKB and asymptotic methods outlined above yield a MFPT that was in excellent agreement with numerical simulations in both the superthreshold and subthreshold regimes.

1.7 Appendix: Stochastic Calculus

In this appendix we give an informal introduction to stochastic calculus, following along the lines of Jacobs [302]. A more detailed treatment can be found in Gardiner [210], and a rigorous mathematical account can be found in [476]. The basic approach is to treat a continuous-time stochastic process as the limit of a discrete time process. That is, an SDE prescribes how a stochastic variable $X(t)$ changes in each infinitesimal time step dt. Determining changes over finite times then requires evaluating an associated stochastic integral. In order to make sense of this, we discretize time into small, but finite, intervals of duration Δt and consider a corresponding stochastic difference equation for $X_n = X(n\Delta t)$.

1.7.1 Ito Calculus

Suppose that we divide the time interval $[0,T]$ into N increments of size $\Delta t = T/N$ and set $t_n = n\Delta t$. Consider the stochastic difference equation

$$\Delta X(t_n) \equiv X(t_{n+1}) - X(t_n) = \Delta W_n,$$

where each ΔW_n, $n = 0,\ldots,N-1$, is an independent, identically distributed (i.i.d) Gaussian variable with zero mean and variance $\sigma^2 = \Delta t$:

$$P(\Delta W) = \frac{1}{\sqrt{2\pi\Delta t}} \mathrm{e}^{-(\Delta W)^2/2\Delta t}. \tag{1.203}$$

Iterating the difference equation starting from $X(0) = 0$ yields

$$X_n \equiv X(n\Delta t) = \sum_{j=0}^{n-1} \Delta W_j.$$

Using the fact that the sum of Gaussian random variables is also a Gaussian, it follows that the probability density for X_n is a Gaussian. Thus, we only need to determine its mean and variance. Since the ΔW_j are all independent, we have

$$\langle X_n \rangle = \sum_{j=0}^{n-1} \langle \Delta W_j \rangle = 0, \quad \mathrm{Var}(X_n) = \sum_{j=0}^{n-1} \mathrm{Var}(\Delta W_j) = N\Delta t,$$

and

$$P(X_n) = \frac{1}{\sqrt{2\pi n\Delta t}} \mathrm{e}^{-X_n^2/(2n\Delta t)}.$$

We can now construct a corresponding continuous-time process by taking the limit $N \to \infty$ such that $\Delta t \to 0$ with $N\Delta T = T$ fixed. In particular,

$$X(T) = \lim_{N\to\infty} \sum_{j=0}^{N-1} \Delta W_j \equiv \int_0^T dW(t) \equiv W(T),$$

where $W(T)$ is identified as a Wiener process. (A rigorous treatment would be more precise with regard to what is meant by the convergence of random variables.) It is still a Gaussian, whose mean and variance are obtained by taking the limit $N \to \infty$ of the results for X_n. We deduce that $W(t)$ has the Gaussian probability density

$$P(w(t)) = \frac{1}{\sqrt{2\pi t}} \mathrm{e}^{-w(t)^2/2t}.$$

Now consider the modified stochastic difference equation

$$X_{n+1} - X_n = f(t_n)\Delta W_n,$$

where $f(t)$ is a deterministic function of time. Once again X_n is a Gaussian random variable, with

$$\langle X_n \rangle = \sum_{j=0}^{n-1} \langle f(t_j)\Delta W_j \rangle = 0, \quad \mathrm{Var}(X_n) = \sum_{j=0}^{n-1} \mathrm{Var}(f(t_j)\Delta W_j) = \sum_{j=0}^{n-1} f(t_j)^2 \Delta t.$$

Taking the continuum limit along identical lines to the previous case yields the continuous-time Gaussian variable

$$X(T) = \lim_{N\to\infty} \sum_{j=0}^{N-1} f(t_j)\Delta W_j \equiv \int_0^T f(t)dW(t), \tag{1.204}$$

with zero mean and variance

$$\mathrm{Var}(X(T)) = \int_0^T f(s)^2 ds. \tag{1.205}$$

Substituting for $X(T)$ into this equation gives

$$\left\langle \int_0^T f(t)dW(t) \int_0^T f(s)dW(s) \right\rangle = \int_0^T f(s)^2 ds,$$

which can be captured by the rule

$$\langle dW(t)dW(s) \rangle = \delta(t-s)dt\,ds. \tag{1.206}$$

However, care must be taken with this rule when $\delta(t-s)$ appears inside an integral having t or s as one of its limits. For example, consider the double stochastic integral

$$\int_0^T \left[\int_0^t f(s)dW(s) \right] g(t)dW(t) \equiv \lim_{N\to\infty} \sum_{n=0}^{N-1} \left[\sum_{m=0}^{n-1} f(t_m)dW_m \right] g(t_n)dW_n.$$

We see that there are no terms in the double sum on the right-hand side that have a product of Wiener increments in the same time interval. Thus, taking the expectation of both sides,

$$\left\langle \int_0^T \left[\int_0^t f(s)dW(s) \right] g(t)dW(t) \right\rangle = 0.$$

Hence, we require

$$\int_0^t f(s)\delta(t-s)ds = 0, \quad \int_0^t f(s)\delta(s)ds = f(0). \tag{1.207}$$

Following the previous examples, let us turn to a discretized version of the general SDE for $X(t)$,

$$dX = a(X,t)dt + b(X,t)dW(t), \tag{1.208}$$

which takes the form

$$X_{n+1} - X_n = a(X_n,t_n)\Delta t + b(X_n,t_n)\Delta W_n. \tag{1.209}$$

Iterating this equation starting from a fixed $X(0) = x_0$ yields

$$X_N = x_0 + \sum_{n=0}^{N-1} a(X_n,t_n)\Delta t + \sum_{n=0}^{N-1} b(X_n,t_n)\Delta W_n.$$

The continuum limit then gives the stochastic integral equation

$$X(T) = x_0 + \int_0^T a(X(t),t)dt + \int_0^T b(X(t),t)dW(t), \tag{1.210}$$

with the final term defined as the Ito stochastic integral

$$\int_0^T b(X(t),t)dW(t) = \lim_{N\to\infty} \sum_{n=0}^{N-1} b(X_n,t_n)\Delta W_n. \tag{1.211}$$

The integral equation is not very useful for generating an explicit solution for $X(t)$. However, from the definition of the Ito stochastic integral, it immediately follows that

$$\left\langle \int_0^T b(X(t),t)dW(t) \right\rangle = 0, \tag{1.212}$$

since X_n is a function of previous Wiener increments $\Delta W_{n-1}, \ldots, \Delta W_0$ so it is uncorrelated with ΔW_n. The stochastic difference equation (1.209) is the starting point for developing numerical schemes for solving an SDE. However, if one is interested in carrying out explicit calculations, it is usually more useful to go to the associated Fokker–Planck equation for the probability density. In order to derive the FP equation from the corresponding SDE, we first need to consider the object $(dW)^2$.

In terms of Wiener increments,

$$\int_0^T (dW(t))^2 = \lim_{N\to\infty} \sum_{n=0}^{N-1} (\Delta W_n)^2.$$

Taking the expectation of both sides and using the fact that each ΔW_n is an i.i.d., gives

$$\left\langle \int_0^T (dW(t))^2 \right\rangle = \int_0^T \langle (dW(t))^2 \rangle = \int_0^T dt = T. \tag{1.213}$$

What about the variance? Using the Gaussian probability density (1.203), it is simple to show that

$$\mathrm{Var}[(\Delta W)^2] = 2(\Delta t)^2 = 2T^2/N^2.$$

Hence,

$$\begin{aligned}\mathrm{Var}\left[\int_0^T (dW(t))^2\right] &= \lim_{N\to\infty} \mathrm{Var}\left[\sum_{n=0}^{N-1} (\Delta W_n)^2\right] = \lim_{N\to\infty} \sum_{n=0}^{N-1} \mathrm{Var}\left[(\Delta W_n)^2\right] \\ &= \lim_{N\to\infty} \frac{2T^2}{N} = 0.\end{aligned}$$

We thus obtain the surprising result that the integral of $(dW)^2$ is deterministic and thus equal to its mean:

$$\int_0^T (dW(t))^2 = T = \int_0^T dt. \tag{1.214}$$

In other words, we can set $(dW)^2 = dt$, a result known as Ito's rule. Using similar arguments, it can also be shown that $dW^m = 0$ for $m > 2$.

1.7.2 Ito's Formula and the Fokker–Planck Equation

The result $dW(t)^2 = dt$ has important implications for how one carries out a change of variables in stochastic calculus. This is most directly established by considering the SDE for an arbitrary function $f(X(t))$ with $X(t)$ evolving according to (1.208):

$$\begin{aligned}df(X(t)) &= f(X(t) + dX(t)) - f(X(t)) \\ &= f'(X(t))dX(t) + \frac{1}{2} f''(X(t))dX(t)^2 + \ldots \\ &= f'(X(t))[a(X,t)dt + b(X,t)dW(t)] + \frac{1}{2} f''(X(t))b(X,t)^2 dW(t)^2,\end{aligned}$$

where all terms of higher order than dt have been dropped. Now using $dW(t)^2 = dt$, we obtain the following SDE for f, which is known as Ito's formula:

$$df(X(t)) = \left[a(X(t),t)f'(X(t)) + \frac{1}{2} b(X,t)^2 f''(X(t))\right] dt + b(X,t)f'(X(t))dW(t). \tag{1.215}$$

Hence, changing variables in Ito calculus is not given by ordinary calculus unless f is a constant or a linear function.

We can now use Ito's formula to derive the FP equation for an Ito SDE. First,

$$\begin{aligned}\frac{\langle df(X(t))\rangle}{dt} &= \left\langle a(X(t),t)f'(X(t)) + \frac{1}{2}b(X(t),t)^2 f''(X(t)) \right\rangle \\ &= \int \left[a(x,t)f'(x) + \frac{1}{2}b(x,t)^2 f''(x) \right] p(x,t)dx, \\ &= \int f(x) \left[-\frac{\partial}{\partial x}(a(x,t)p(x,t)) + \frac{1}{2}\frac{\partial^2}{\partial x^2}(b(x,t)^2 p(x,t)) \right] dx. \quad (1.216)\end{aligned}$$

after integration by parts, where $p(x,t)$ is the probability density of the stochastic process $X(t)$ under the initial condition $X(t_0) = x_0$. However, we also have

$$\begin{aligned}\frac{\langle df(X(t))\rangle}{dt} &= \left\langle \frac{df(X(t))}{dt} \right\rangle \\ &= \frac{d}{dt}\langle f(X(t),t)\rangle \\ &= \int f(x)\frac{\partial}{\partial t}p(x,t)dx. \quad (1.217)\end{aligned}$$

Comparing (1.216) and (1.217) and using the fact that $f(x)$ is arbitrary, we obtain the Ito version of the FP equation

$$\frac{\partial}{\partial t}p(x,t) = -\frac{\partial}{\partial x}(a(x,t)p(x,t)) + \frac{1}{2}\frac{\partial^2}{\partial x^2}(b(x,t)^2 p(x,t)). \quad (1.218)$$

1.7.3 Multiplicative Noise and Stratonovich Integrals

It turns out that there is more than one way to define a stochastic difference equation driven by an incremental Wiener process and thus more than one way to obtain an SDE in the continuum limit. This issue only arises in the case of multiplicative noise, that is, when the term multiplying $dW(t)$ depends on the state variable $X(t)$. Recall that in the Ito integral (1.211), it is the value of $b(x,t)$ at the start of the nth time step that multiplies ΔW_n, so that there are no contributions of the form $(\Delta W_n)^2$. An alternative definition of a stochastic integral is the Stratonovich integral

$$\oint_0^T b(X(t),t)dW(t) = \lim_{N\to\infty} \sum_{n=0}^{N-1} b\left(\frac{X_{n+1}+X_n}{2}, t_n \right) \Delta W_n, \quad (1.219)$$

where we have used $\oint$ to distinguish it from the Ito integral. Now b depends on the value X_{n+1} at the end of the nth time step, which means there will be an extra term involving $(\Delta W_n)^2$. In order to compare the Ito and Stratonovich integrals, suppose that X_n evolves according to the stochastic difference equation (1.209). Thus, in the

continuum limit $X(t)$ is the solution to an Ito SDE. Suppose that we Taylor expand the nth term in the sum defining the Stratonovich integral about the point X_n and set $b_n = b(X_n, t_n)$:

$$b\left(\frac{X_{n+1}+X_n}{2}, t_n\right) = b_n + \frac{\Delta X_n}{2}\frac{\partial b_n}{\partial x} + \frac{1}{2}\left(\frac{\Delta X_n}{2}\right)^2 \frac{\partial^2 b_n}{\partial x^2} + \ldots$$

Substituting for ΔX_n using (1.209) and dropping terms that are higher order than Δt shows that

$$b\left(\frac{X_{n+1}+X_n}{2}, t_n\right) = b_n + \left(\frac{a_n}{2}\frac{\partial b_n}{\partial x} + \frac{b_n^2}{8}\frac{\partial^2 b_n}{\partial x^2}\right)\Delta t + \left(\frac{b_n}{2}\frac{\partial b_n}{\partial x}\right)\Delta W_n.$$

Applying this result to the sum appearing in the definition of the Stratonovich integral, (1.219), and again dropping higher-order terms in Δt, yields the result

$$\sum_{n=0}^{N-1} b\left(\frac{X_{n+1}+X_n}{2}, t_n\right)\Delta W_n = \sum_{n=0}^{N-1} b_n \Delta W_n + \sum_{n=0}^{N-1}\frac{b_n}{2}\frac{\partial b_n}{\partial x}(\Delta W_n)^2.$$

Finally, taking the continuum limit with $dW(t)^2 = dt$, we have

$$\oint_0^T b(X(t),t)dW(t) = \int_0^T b(X(t),t)dW(t) + \frac{1}{2}\int_0^T \frac{\partial b(X(t),t)}{\partial x} b(X(t),t)dt. \tag{1.220}$$

Now suppose that $Y(t)$ is a stochastic process evolving according to the Stratonovich SDE

$$dY = a(Y,t) + b(Y,t)dW(t). \tag{1.221}$$

This means that the integral equation satisfied by $Y(t)$ is based on the Stratonovich integral, that is,

$$Y(t) = y_0 + \int_0^t a(Y(s),s)ds + \oint_0^t b(Y(t),t)dW(t). \tag{1.222}$$

Using (1.220), we can rewrite the solution in terms of an Ito integral according to

$$Y(t) = y_0 + \int_0^t \left[a(Y(s),s) + \frac{1}{2}\frac{\partial b(Y(s),s)}{\partial y} g(Y(s),s)\right] ds + \int_0^t b(Y(s),s)dW(s). \tag{1.223}$$

The latter is the solution to an equivalent Ito SDE of the form

$$dY = \left[a(Y(t),t) + \frac{b(Y(t),t)}{2}\frac{\partial b(Y(t),t)}{\partial y}\right] dt + b(Y(t),t)dW(t). \tag{1.224}$$

Finally, given that we know the FP equation corresponding to an Ito SDE, we can immediately write down the FP equation corresponding to the Stratonovich SDE equation (1.221):

$$\frac{\partial}{\partial t}p(y,t) = -\frac{\partial}{\partial y}(a(y,t)p(y,t)) + \frac{1}{2}\frac{\partial}{\partial y}\left(b(y,t)\frac{\partial}{\partial y}[b(y,t)p(y,t)]\right). \tag{1.225}$$

Chapter 2
Traveling Waves in One-Dimensional Excitable Media

We now consider our first example of wave propagation in neural media, namely, the propagation of an action potential along the axon of a neuron. Such a phenomenon can be formulated mathematically in terms of finding a traveling pulse solution of the spatially extended Hodgkin–Huxley equations (1.8) and (1.4). Formally speaking, a traveling wave is a solution of a PDE on an infinite domain that travels at constant velocity and fixed shape. For one-dimensional systems, one can distinguish two types of solitary traveling wave: a traveling front linking a stable resting state to a stable excited state and a traveling pulse that begins and ends at the resting state; see Fig. 2.1. For the Hodgkin–Huxley model, a traveling front would occur if the recovery variable n associated with K^+ channels were frozen; otherwise repolarization ensures that the trailing edge of the wave returns to the resting state. In order to develop the basic theory of wave propagation in one-dimensional excitable media, we will consider a simplified version of the Hodgkin–Huxley equations given by the FitzHugh–Nagumo (FN) equations [192, 446]:

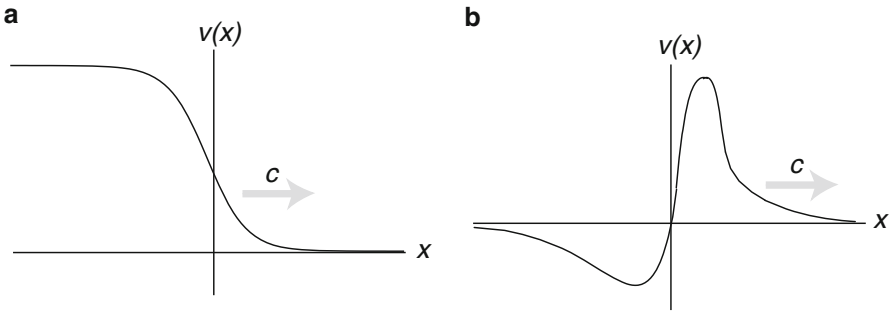

Fig. 2.1 Schematic illustration of (**a**) a traveling front, and (**b**) a traveling pulse

P.C. Bressloff, *Waves in Neural Media: From Single Neurons to Neural Fields*,
Lecture Notes on Mathematical Modelling in the Life Sciences,
DOI 10.1007/978-1-4614-8866-8_2, © Springer Science+Business Media New York 2014

$$\frac{\partial v}{\partial t} = \frac{\partial^2 v}{\partial x^2} + f(v) - w \equiv f(v,w), \tag{2.1a}$$

$$\frac{\partial w}{\partial t} = \varepsilon(v - w) \equiv \varepsilon g(v,w). \tag{2.1b}$$

with $0 < \varepsilon \ll 1$ and

$$f(v) = v(v-a)(1-v). \tag{2.2}$$

Here v represents a fast voltage variable and w is a slow recovery variable. The time and space scales have been non-dimensionalized so that the effective diffusivity of the cable is unity. A number of excellent reviews of waves in excitable systems can be found elsewhere [242, 316, 322, 444].

2.1 Excitable Systems

Before consider traveling wave solutions, it is instructive to consider the excitable behavior of the space-clamped (x-independent) FN model. The space-clamped FN model takes the form of a planar dynamical system

$$\frac{dv}{dt} = f(v,w), \tag{2.3a}$$

$$\frac{dw}{dt} = \varepsilon g(v,w). \tag{2.3b}$$

The fast variable has a cubic nullcline (along which $\dot{v} = 0$) and the slow variable has a monotonically increasing nullcline (along which $\dot{w} = 0$). It is assumed that the nullclines have a single intersection point at (v^*, w^*). This corresponds to a fixed point of the system, which we identify with the resting state. A schematic diagram of the phase plane is shown in Fig. 2.2. For a finite range of values of w, there exist three solutions $v = v(w)$ of the equation $f(v,w) = 0$, which we denote by $V_-(w), V_0(w)$, and $V_+(w)$. Whenever these solutions coexist, we have the ordering $V_-(w) \le V_0(w) \le V_+(w)$. Let W_* denote the minimal value of w for which $V_-(w)$ exists, and let W^* denote the maximal value of w for which $V_+(w)$ exists.

First, suppose that the fixed point is located on the left-hand branch close to the minimum of the cubic. It is straightforward to show that the fixed point is linearly stable by evaluating the eigenvalues of the corresponding Jacobian. Moreover, the system is excitable in the sense that sufficiently large perturbations of the resting state result in a time-dependent trajectory taking a prolonged excursion through state space before returning to the resting state; see Fig. 2.3. Such a trajectory rapidly transitions to the right branch V_+, after which it slowly moves upward in a neighborhood of the branch before reaching the maximum. It then rapidly transitions back to the left branch V_- followed by a slow returns to the resting state along this branch. The time-dependent plot of the variable v can be interpreted as an action potential. Since the resting state is linearly stable, small perturbations simply result in small

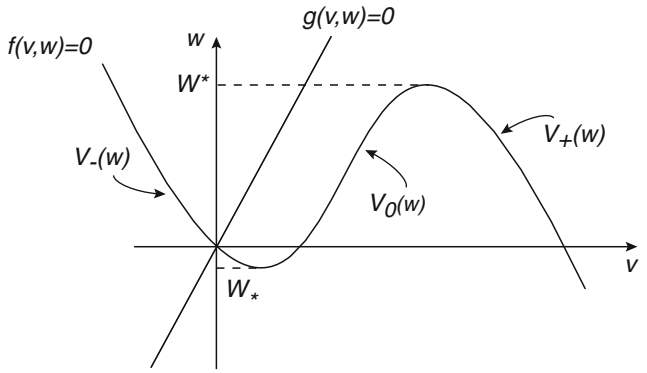

Fig. 2.2 Schematic diagram of the phase plane for the FitzHugh–Nagumo equations

excursions that decay exponentially in time. Hence, there is effectively a threshold phenomenon in which subthreshold perturbations result in a simple return to the resting state, whereas superthreshold perturbations generate an action potential.

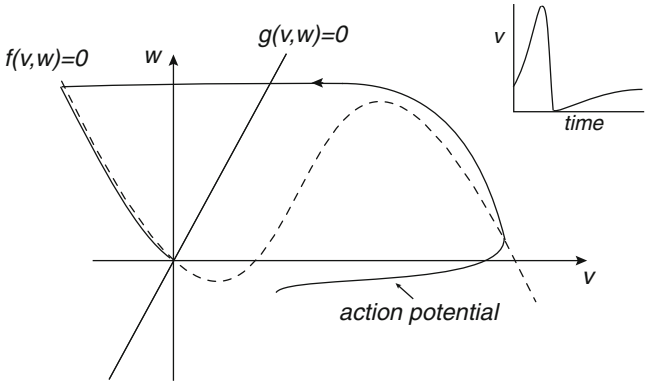

Fig. 2.3 Schematic diagram illustrating the trajectory of a single action potential in the phase plane for the FitzHugh–Nagumo equations. The unique rest point is stable. Inset shows the action potential as a function of time

A more mathematical description of the above events can be developed in terms of singular perturbation theory [242, 322]. Due to the separation of time scales with $\varepsilon \ll 1$, the fast variable v rapidly adjusts whenever it can to maintain the quasi-equilibrium $f(v,w) = 0$. This can be captured by introducing the slow time scale $\tau = \varepsilon t$ such that (2.3) become

$$\varepsilon \frac{dv}{d\tau} = f(v,w), \quad \frac{dw}{d\tau} = g(v,w). \tag{2.4}$$

Now setting $\varepsilon = 0$ and assuming that v is moving along the stable branches $V_{\pm}(w)$ of $f(v,w) = 0$, the dynamics of the recovery variable reduces to

$$\frac{dw}{d\tau} = g(V_{\pm}(w), w) \equiv G_{\pm}(w). \tag{2.5}$$

In the case of rapid transitions between the left and right branches, the dynamics with respect to the fast time scale can be approximated by setting $\varepsilon = 0$ in (2.3),

$$\frac{dv}{dt} = f(v,w), \quad \frac{dw}{dt} = 0. \tag{2.6}$$

Thus, on this time scale, w is constant and v converges to a stable solution of $f(v,w) = 0$. Suppose that the system starts from a superthreshold initial condition (v_0, w_0) such that $v_0 > V_0(w_0)$. After rapidly reaching the right branch, it takes a finite time to reach the upper "knee" of the nullcline $f(v,w)$ and is obtained by integrating (2.5):

$$T_e = \int_{w_0}^{W^*} \frac{dw}{G_+(w)}. \tag{2.7}$$

On the other hand, the time taken to return to the resting state along the left branch is infinite, since $G_-(w)$ vanishes at the fixed point.

It is possible to convert the FN equations from an excitable to an oscillatory regime by adding a constant external current I_{ext} to the right-hand side of the voltage equation in (2.3). For an intermediate range of values of I_{ext} one finds that the fixed point shifts to the middle branch $V_0(w)$ where it is unstable. The fixed point now coexists with a limit cycle, along which the trajectory alternates periodically between the left and right branches, while w varies between W_* and W^*; see Fig. 2.4. The resulting limit cycle behavior with fast jumps alternating with slow dynamics is known as a *relaxation oscillator*. For small ε, the period T of the oscillator is dominated by the times to move along the left and right branches. Hence

$$T = \int_{W_*}^{W^*} \left(\frac{1}{G_+(w)} - \frac{1}{G_-(w)} \right) dw, \tag{2.8}$$

with $G_+ > 0$ and $G_- < 0$.

Another well-known planar model of an excitable neuron is the Morris–Lecar (ML) model [440] (see Eq. (1.28)) which we write in the form

$$\frac{dv}{dt} = a(v) f_{\text{Na}}(v) + w f_{\text{K}}(v) - g(v) \tag{2.9a}$$

$$\frac{dw}{dt} = \frac{w_\infty(v) - w}{\tau_w(v)}, \tag{2.9b}$$

where $f_i(v) = g_i(v_i - v)$ and w represents the fraction of open K^+ channels. The fraction of Na^+ channels (or Ca^{2+} channels in the original formulation of the model) is assumed to be in quasi steady state. Again we can analyze the generation of action

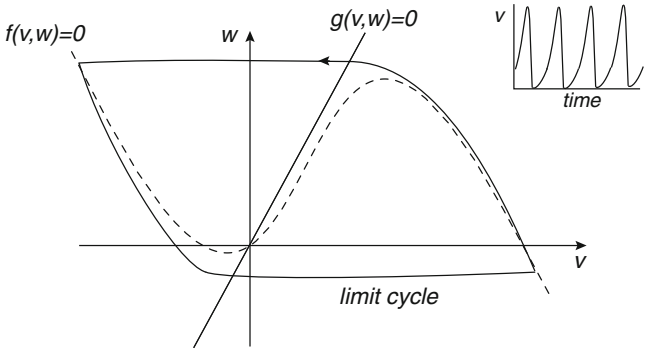

Fig. 2.4 Schematic diagram illustrating the trajectory of a globally stable periodic orbit in the phase plane for the FitzHugh–Nagumo equations. The unique rest point is unstable. Inset shows the periodic orbit as a function of time

potentials using a slow/fast analysis of the deterministic system. However, it turns out that this adiabatic approximation breaks down when stochastic fluctuations in the opening and closing of K^+ channels are taken into account. This can be established by considering a stochastic version of the ML model [456] consisting of N sodium and M potassium channels (see also Sect. 1.5):

$$\frac{dv}{dt} = F(v,m,n) \equiv \frac{n}{N} f_{\rm Na}(v) + \frac{m}{M} f_{\rm K}(v) - g(v). \tag{2.10}$$

We assume that each channel can either be open or closed and can switch between each state according to the kinetic scheme

$$C \underset{\beta_i(v)}{\overset{\alpha_i(v)}{\rightleftarrows}} O, \quad i = \text{Na, K}, \tag{2.11}$$

The Na^+ channels open and close rapidly relative to the voltage and K^+ dynamics. The probability density function $p(v,m,n,t)$ of the resulting stochastic hybrid system (see Sect. 1.6) evolves according to the differential Chapman–Kolmogorov (CK) equation,

$$\frac{\partial p}{\partial t} = -\frac{\partial (Fp)}{\partial v} + \mathbb{L}_{\rm K} p + \mathbb{L}_{\rm Na} p. \tag{2.12}$$

The jump operators $\mathbb{L}_j$, $j = \text{Na}, \text{K}$, are defined according to

$$\mathbb{L}_j = (\mathbb{E}_n^- - 1)\omega_j^+(n,v) + (\mathbb{E}_n^+ - 1)\omega_j^-(n,v), \tag{2.13}$$

with $\mathbb{E}_n^{\pm} f(n) = f(n \pm 1)$, $\omega_j^-(n,v) = n\beta_j(v)$ and $\omega_j^+(n,v) = (N-n)\alpha_j(v)$.

Introducing the small parameter ε with $\alpha_{\rm Na}, \beta_{\rm Na}, M = \mathcal{O}(1/\varepsilon)$, one can extend the WKB approximation method of Sect. 1.6 to analyze noise-induced transitions in the phase plane [456]. The WKB potential Φ can be interpreted as the action of an effective Hamiltonian dynamical system whose solutions determine charac-

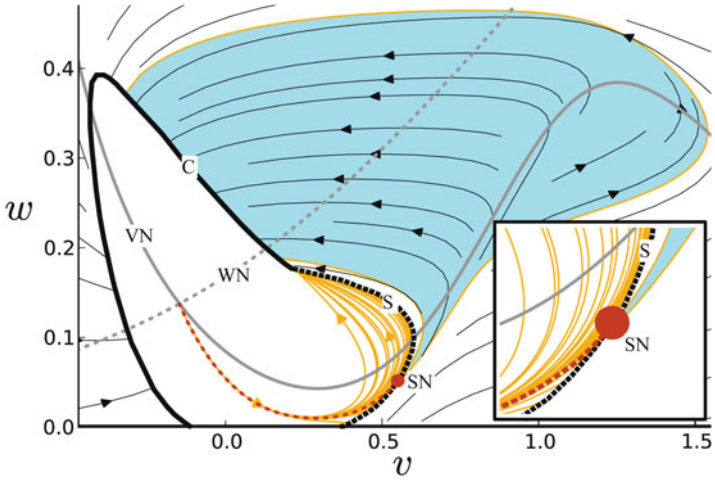

Fig. 2.5 Illustration of spontaneous action potentials (SAPs) for the stochastic ML model (2.10) with a finite number of sodium and potassium ion channels [456]. Orange curves are SAP trajectories, shown until they reach the effective metastable separatrix (S). The dashed red curve is a SAP that reaches S near the metastable saddle (SN). All of the SAP trajectories in the shaded region—containing the most probable, observable SAP trajectories—are visually indistinguishable from the dashed red line before crossing S. Deterministic trajectories are shown as black streamlines. Also shown are a caustic (C), caustic formation point (CP), v nullcline (VN), and w nullcline (WN). Parameter values are $N = M = 10$ and $\varepsilon = 0.1$

teristic paths in the phase plane (see also Sect. 4.4). The latter correspond to the paths a stochastic trajectory is most likely to follow during a metastable transition (i.e., a path of maximum likelihood [160]). Based on the fast/slow analysis of the deterministic system (2.9), one might expect w to be approximately constant along a stochastic trajectory that jumps between the left and right branches of the voltage nullcline, since the K^+ channels open and close slowly. In fact this does not hold for spontaneous action potentials arising from K^+ channel fluctuations [456] (see Fig. 2.5), which is in contrast to the effects of noise in the voltage or fast sodium channels. In general, it is difficult to solve FPT problems in more than one dimension. In the case of a metastable state with a well-defined basin of attraction, one has to calculate the MFPT to cross the separatrices forming the boundary of the basin of attraction. There is an additional level of complexity for an excitable system, due to the fact that there is no well-defined deterministic separatrix. Interestingly, as illustrated in Fig. 2.5, the stochastic ML model has an effective separatrix that any stochastic trajectory has to cross in order to generate a stochastic action potential [456]; see also [327]. Another commonly observed feature of the WKB approximation in two or more dimensions is the formation of caustics, where characteristic projections of the Hamiltonian intersect. There is now quite an extensive literature on the effects of noise in excitable systems, as reviewed in [383]. Most of these studies consider extrinsic Gaussian noise in the voltage dynamics and phenomena such as stochastic and coherence resonance. In Sect. 2.6 we will consider the effects of

Gaussian noise on wave propagation in a spatially extended excitable system. One can motivate this form of noise by considering diffusion approximations of models of stochastic ion channels. However, as the above example shows, certain caution must be exercised when considering such approximations.

Finally, we note that fast/slow decomposition has been applied extensively in recent years to the study of rhythmic activity patterns in single neurons and in synaptically coupled relaxation oscillators (see also Sect. 5). In the latter case, if synapses turn on and off on the fast time scale, then geometric singular perturbation theory can be used to investigate how synaptic inputs modify geometric structures such as null surfaces in the phase spaces of individual neurons, as reviewed by Rubin and Terman [537]; see also Chap. 9 of [173]. Moreover, such methods have been used to study a three-dimensional version of the Hodgkin–Huxley model, in which there is one fast variable and two slow variables [539, 540]. In addition to the transition from excitable to regular oscillatory behavior, as observed in classical relaxation oscillators, the model neuron also exhibits more complex dynamics such as mixed-mode oscillations that are associated with slow action potentials.

2.2 Traveling Fronts in a Scalar Bistable Equation

In the absence of a recovery variable, the FN equations reduce to the so-called scalar bistable equation

$$\frac{\partial v}{\partial t} = \frac{\partial^2 v}{\partial x^2} + f(v), \quad -\infty < x < \infty \tag{2.14}$$

with $f(v)$ given by the cubic (2.2). For such a choice of nonlinearity, the corresponding ODE, $dv/dt = f(v)$, has stable equilibria at $v = 0, 1$ separated by an unstable equilibrium at $x = a$. We define a traveling front solution according to

$$v(x,t) = v(x - ct) = V(\xi), \quad \xi = x - ct \tag{2.15}$$

for some yet to be determined wave speed c, supplemented by asymptotic boundary conditions ensuring that the front links the two stable fixed points of the x-independent system. For concreteness, we take

$$V(\xi) \to 1 \text{ as } \xi \to -\infty, \quad V(\xi) \to 0 \text{ as } \xi \to \infty. \tag{2.16}$$

Substituting the traveling front solution into the bistable Eq. (2.14) yields the ODE

$$V_{\xi\xi} + cV_\xi + f(V) = 0, \tag{2.17}$$

where $V_\xi = dV/d\xi$.

Classical phase-plane analysis can be used to find a traveling front solution by rewriting the second-order equation in the form

$$V_\xi = Z, \quad Z_\xi = -cZ - f(V). \tag{2.18}$$

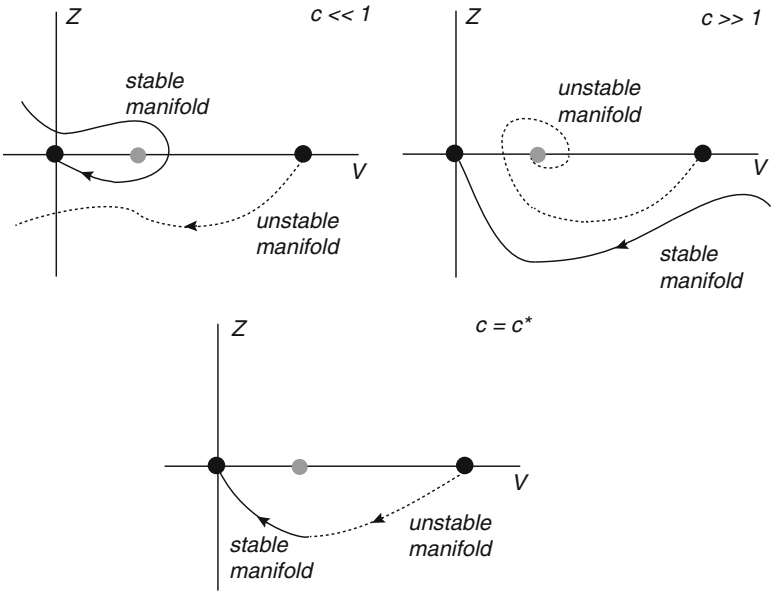

Fig. 2.6 Shooting method for constructing a front solution in the (V,Z) phase plane with $Z = V_\xi$. See text for details

One now has to look for a heteroclinic connection that links the excited state $(V,Z) = (1,0)$ at $\xi \to -\infty$ to the resting state at $\xi \to \infty$. This can be achieved using a geometric argument based on a shooting method, as illustrated in Fig. 2.6. For the sake of illustration, suppose that $0 < a < 1/2$ so that $c > 0$ (see below). First note that irrespective of the speed c, the fixed points $(1,0)$ and $(0,0)$ are saddles, each with one-dimensional stable and unstable manifolds. By looking at trajectories in the phase plane, it is straightforward to see that when $c \ll 1$, the unstable manifold of $(1,0)$ lies below the stable manifold of $(0,0)$ when $0 < V < 1$, whereas the opposite holds when c is very large. Since these manifolds depend continuously on c, it follows that there must exist at least one value of c for which the manifolds cross, and this corresponds to the heteroclinic connection that represents the traveling front solution. It can also be established that this front is unique. A useful formula for determining the sign of the wave speed can be obtained by multiplying both sides of (2.17) by V_ξ and integrating with respect to ξ:

$$\begin{aligned} c\int_{-\infty}^{\infty}(V_\xi)^2 d\xi &= -\int_{-\infty}^{\infty} V_\xi f(V(\xi))d\xi - \int_{-\infty}^{\infty} V_\xi V_{\xi\xi} d\xi, \\ &= \int_0^1 f(V)dV, \end{aligned} \tag{2.19}$$

since $V(\xi)$ is monotone, and $\int_{-\infty}^{\infty} V_\xi V_{\xi\xi} d\xi = \int_{-\infty}^{\infty} \frac{d[V_\xi^2/2]}{d\xi} d\xi = 0$. As the integral on the left-hand side is positive, it follows that the sign of c is determined by the

sign of the area of f between the two stable equilibria. If $0 < a < 1/2$, then the latter is positive and the wave moves to the right, converting the medium from the resting state to the excited state. On the other hand, a left-moving front occurs when $1/2 < a < 1$, converting the medium from the excited state to the resting state. If the negative and positive areas exactly cancel, then the front is stationary.

The numerical construction of the traveling front using a shooting method does not depend on the precise form of f. However, if f is given by the cubic (2.2), then it is possible to construct the front explicitly. That is, we substitute the ansatz $Z = -AV(1-V)$ into (2.17) to obtain the condition $A^2(2V-1) + cA - (V-a) = 0$. Collecting terms linear in V and terms independent of V requires $A = 1/\sqrt{2}$ and $c = (1-2a)/\sqrt{2}$. This immediately establishes that c switches sign at $a = 1/2$. Since $W = V_\xi$, it follows that the corresponding wave profile is

$$V(\xi) = \frac{1}{2}\left[1 - \tanh(\xi/2\sqrt{2})\right].$$

Finally, recall that we have non-dimensionalized the units of space and time in the bistable equation by setting the membrane time and space constants of the cable to unity ($\tau_m = 1, \lambda_m = 1$); see (1.55). Hence, in physical units, the speed of the wave is

$$\hat{c} = \frac{c\lambda_m}{\tau_m} = \frac{c}{2C_m}\sqrt{\frac{d}{R_m R}}, \tag{2.20}$$

where d is the cable diameter. Based on empirical estimates, one finds that $\hat{c} \sim \sqrt{d}\,\mathrm{mm/sec}$. In the case of a squid axon of diameter $d = 500\,\mu\mathrm{m}$, the estimated propagation speed is of around $20\,\mathrm{mm/ms}$.

Another choice of nonlinearity for which an explicit front can be calculated is the piecewise linear function

$$f(v) = -v + H(v-a). \tag{2.21}$$

Substituting into Eq. (2.17) gives

$$V_{\xi\xi} + cV_\xi - V + H(V-a) = 0. \tag{2.22}$$

Translation symmetry of the system means that we are free to choose V to cross the threshold a at $\xi = 0$ so that $V(\xi) > a$ for $\xi < 0$ and $V(\xi) < a$ for $\xi > 0$. Solving the resulting linear equation on either side of the threshold point $\xi = 0$ and imposing the threshold condition $V(0) = a$ yields the explicit solution

$$V(\xi) = \begin{cases} a\mathrm{e}^{\lambda_- \xi}, & \xi > 0 \\ 1 + (a-1)\mathrm{e}^{\lambda_+ \xi}, & \xi < 0, \end{cases} \tag{2.23}$$

where $\lambda_\pm$ are the roots of the characteristic equation $\lambda^2 + c\lambda - 1 = 0$. The wave speed is then obtained by imposing continuity of V_ξ at $\xi = 0$, $(a-1)\lambda_+ = a\lambda_-$, which after rearranging gives

$$c = \frac{1-2a}{\sqrt{a-a^2}}. \tag{2.24}$$

2.3 Traveling Pulses in the FitzHugh–Nagumo Equations

The bistable equation cannot support a traveling pulse solution because there is no recovery variable, that is, it does describe an excitable system. In order to obtain traveling pulse solutions, it is necessary to consider the full FitzHugh–Nagumo equations (2.1). Suppose that the unique fixed point (v^*, w^*) lies on the left-hand branch as in Fig. 2.2. Assume a traveling wave solution of the form $(v(x,t), w(x,t)) = (V(\xi), W(\xi))$ with $\xi = x - ct$ so that (2.1) reduce to the system of ODEs

$$V_{\xi\xi} + cV_\xi + f(V,W) = 0, \tag{2.25a}$$

$$cW_\xi + \varepsilon g(V,W) = 0. \tag{2.25b}$$

These are supplemented by the asymptotic boundary conditions

$$\lim_{\xi \to \pm\infty} (V(\xi), W(\xi)) = (v^*, w^*). \tag{2.26}$$

Mathematically speaking, one needs to find a trajectory in the phase space (V,Z,W) with $Z = V_\xi$ that is homoclinic to the resting state $(v^*, 0, w^*)$. (Although the resting state is stable in the space-clamped system, it is a saddle in the phase plane (V,Z,W) of the spatially extended system.) The existence of such an orbit can be demonstrated using geometric singular perturbation theory [104, 267]. The basic idea is to formally set $\varepsilon = 0$ and construct a singular homoclinic orbit. This will consist of four parts: the jump-up from the resting state to the right branch $V_+(w)$, an active phase along $V_+(w)$, the jump-down to the left branch $V_-(w)$, and a quiescent phase as it returns to the resting state along $V_-(w)$; see Fig. 2.7. Given the existence of a singular homoclinic orbit, one can then prove that such an orbit persists for $\varepsilon > 0$ provided that ε is sufficiently small. In this section we will focus on the construction of the singular solution, exploiting the fact that the jumps take place on a fast spatial scale ξ, whereas the active and quiescent phases occur on a slow spatial scale $z = \varepsilon\xi$.x

In order to analyze the jump-up from the resting state to the active phase, we set $\varepsilon = 0$ in (2.25) to obtain the reduced system

$$V_{\xi\xi} + cV_\xi + f(V,W) = 0, \tag{2.27a}$$

$$W_\xi = 0. \tag{2.27b}$$

Thus the recovery variable is a constant w and V evolves according to the bistable equation

$$V_{\xi\xi} + cV_\xi + f(V,w) = 0, \tag{2.28}$$

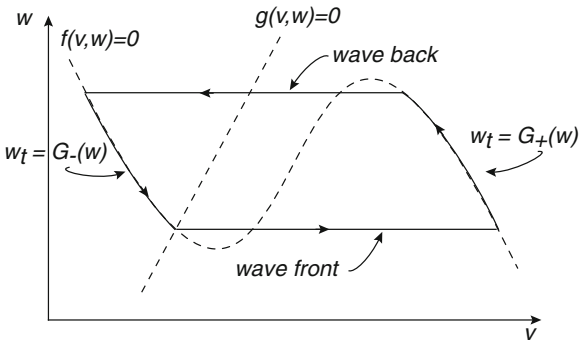

Fig. 2.7 Phase portrait of the fast traveling solitary pulse for the FN equations in the singular limit $\varepsilon \to 0$. The arrow directions are for increasing time (decreasing ξ)

for $f(V,w) = v(v-a)(1-v) - w$. Following Sect. 2.2, we know that for fixed w there exists a unique traveling front solution of (2.28) with associated wave speed $c = c(w)$ that is a heteroclinic connection with $V \to V_L(w)$ as $\xi \to \infty$ and $v \to V_R(w)$ as $\xi \to -\infty$. Moreover,

$$c(w) = \frac{\int_{V_-(w)}^{V_+(w)} f(V,w)dV}{\int_{-\infty}^{\infty} V_\xi^2 d\xi}. \tag{2.29}$$

Setting $w = w^*$ with $V_L(w^*) = v^*$ we obtain the wave speed $c^* = c(w^*)$. Next consider the slow active phase with $c = c^*$. Introducing the slow time scale $z = \varepsilon\xi$ we have

$$\varepsilon^2 V_{zz} + c\varepsilon V_z + f(V,W) = 0, \tag{2.30a}$$
$$cW_z + g(V,W) = 0. \tag{2.30b}$$

Setting $\varepsilon = 0$ then leads to the reduced system

$$f(V,W) = 0, \tag{2.31a}$$
$$W_z = \frac{1}{c^*} g(V,W). \tag{2.31b}$$

Taking the solution $V = V_R(W)$ of $f(V,W) = 0$, it follows that the trajectory moves along the right branch at a rate determined by $G_+(W) = g(V_R(W),W)$.

Now suppose that the trajectory leaves the branch at some value $W = W_d < W^*$ (where W^* is at the maximum of the cubic $f(V,W) = 0$) and jumps back down to the left branch. Similar to the jump-up phase, the recovery variable is constant, and V evolves according to the bistable Eq. (2.28) with $w = W_d$. Again using Sect. 2.2, we can construct a unique traveling wave solution with associated wave speed $c(W_d) < 0$ that is a heteroclinic connection from $V_R(W_d)$ to $V_L(W_d)$. The wave speed is negative, since the jump-down starts from an active state rather than a quiescent

state; it is thus referred to as a wave back. The requirement that the solution be a steadily propagating pulse means that the speeds of the jump-up and jump-down solutions must be the same, which implies that

$$c(w^*) = -c(W_d). \tag{2.32}$$

This condition uniquely determines the transition point W_d. Finally, the trajectory returns to the resting state by moving along the left branch at a rate determined by $G_-(W)/c^*$.

A number of comments are in order. First, from the perspective of matched asymptotics in the slow variable z, the active and quiescent phases correspond to outer solutions that are slowly varying, whereas the jump-up and jump-down phases correspond to transition layers or inner solutions. Denote the wave-front and wave-back solutions by $V_\pm(\xi)$. Matching the inner and outer solutions then leads to the following asymptotic conditions:

$$\begin{aligned}
\lim_{\xi\to-\infty} V_+(\xi) &= V_R(W(0)), \quad W(0) = w^* \\
\lim_{\xi\to\infty} V_+(\xi) &= \lim_{z\to\infty} V_L(W(z)) = v^* \\
\lim_{\xi\to-\infty} V_-(\xi) &= V_L(W(z_T)), \quad W(z_T) = W_d \\
\lim_{\xi\to\infty} V_-(\xi) &= V_R(W(z_T))
\end{aligned}$$

The location z_T where the jump-down occurs is determined from the slow dynamics according to

$$z_T = c^* \int_{w^*}^{W_d} \frac{dW}{G_+(W)} dW. \tag{2.33}$$

One can interpret z_T as the width of the pulse. Second, it may be the case that there is no solution of $c(w^*) = -c(W_d)$ such that $W_d < W^*$. The jump-down transition then occurs at the upper knee, and the solution is referred to as a phase wave, that is, the jump occurs at a time or phase determined solely by the outer dynamics. The wave behavior is then qualitatively different, since the wave can travel at any speed above some minimum, analogous to the well-known Fisher–KPP equation of population genetics [191, 345]; see Sect. 3.3.

2.3.1 Periodic Wave Trains

One of the characteristic features of excitable systems is that they exhibit refractoriness. That is, once the system has responded to a superthreshold stimulus by generating an action potential, there is a refractory period during which no subsequent stimuli can be evoked. From the singular construction of a traveling pulse, the refractory period can be estimated as follows: after the jump-down there is a range of values of the recovery variable, $W_0 \le w \le W_d$ for which the front solution to the

bistable Eq. (2.2) has negative wave speed, $c(w) \leq 0$, with $c(W_0) = 0$. The time taken to reach W_0 from W_d along the left branch is (for fixed x and rescaled time)

$$T_{\text{ref}} = \int_{W_0}^{W_d} \frac{dW}{|G_-(W)|}. \tag{2.34}$$

We can identify T_{ref} as the refractory period. Once excitability has been restored, it is possible to evoke another wave of excitation. However, the speed of the subsequent pulse is expected to be slower due to the residual refractoriness of the system. Now suppose that we periodically initiate action potentials at one end of a semi-infinite cable. This will asymptotically produce a periodic wave train with the time between successive pulses equal to the forcing period T. Assuming that the wave train travels at a speed c, the spatial separation or wavelength of the pulses will be $\lambda = cT$. The speed of the wave train is expected to be smaller than the speed of an isolated pulse due to refractoriness, although this effect should decrease as T increases. In other words, there exists a dispersion curve $c = c(T)$ with $c(T)$, a monotonically increasing function of T.

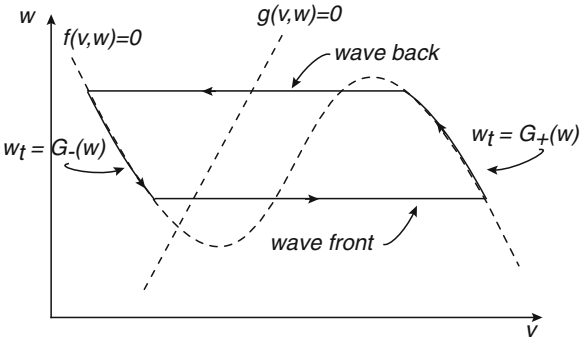

Fig. 2.8 Phase portrait for the fast periodic wave train for the FN equations in the singular limit $\varepsilon \to 0$

It is possible to estimate the dispersion curve for the FitzHugh–Nagumo equations using the previous singular construction. A periodic wave train consists of an alternating sequence of jump-ups and jump-downs, separated by regions of slow dynamics. A phase portrait for such a solution is shown in Fig. 2.8. The major difference from an isolated pulse (see Fig. 2.7) is that the jump-up occurs before reaching the resting state, with $W = W_P > w_*$. Denoting the corresponding value at the jump-down by W_Q, we require that the speeds of the corresponding wave front and wave back are the same, that is, $c(W_P) = -c(W_Q)$. Since the time taken for the jumps is negligible, the major contributions to the period T come from the time spent traversing the right and left branches:

$$T = \int_{W_P}^{W_Q} \frac{dW}{G_+(W)} + \int_{W_Q}^{W_P} \frac{dW}{G_-(W)}. \tag{2.35}$$

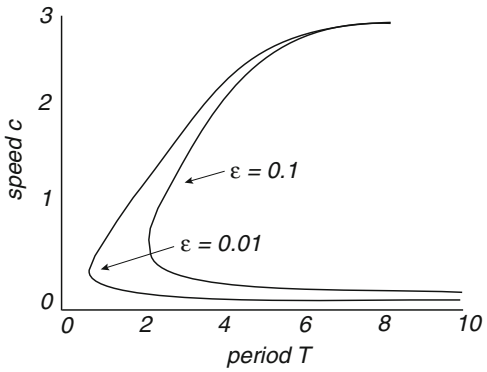

Fig. 2.9 Illustration of typical dispersion curves $c = c(T)$ for T-periodic wave-train solutions of the FN equations. A stable fast branch coexists with an unstable slow branch. They annihilate in a saddle–node bifurcation

Solving for W_Q in terms of W_P using the matching of speeds and inverting the relation $c = c(W_P)$ then generate the dispersion curve $c(T)$. It turns out that the dispersion curve breaks down when the wavelength $\lambda \equiv cT = \mathcal{O}(\varepsilon)$, because the transitional fronts and backs become arbitrarily close together so that it is no longer possible to carry out matched asymptotics. In order to construct the true dispersion curve, it is necessary to carry out a regular perturbation analysis in ε with $c = \mathcal{O}(\varepsilon)$ [156]. One then finds that the dispersion curve consists of two branches that annihilate in a saddle–node bifurcation at $T = T_c$; see Fig 2.9. Hence there are no traveling pulses for $T < T_c$. It can be shown that the upper branch of fast traveling pulses is stable, whereas the lower branch of slow pulses is unstable. (The issue of wave stability will be addressed in Sect. 2.4.) Note that as $T \to \infty$, $c \to c_\infty$ on the upper branch, where c_∞ is the speed of an isolated pulse. Interestingly, c also approaches a finite limit as $T \to \infty$ on the lower branch, suggesting that there also exists a slow unstable isolated pulse; this is indeed found to be the case.

2.3.2 Kinematics

It is also possible to have wave trains consisting of action potentials that are irregularly spaced and move at different speeds. Rinzel and Maginu [523] developed a kinematic theory of wave propagation that uses the dispersion relation to determine the instantaneous speed of a pulse. That is, suppose an initial pulse is generated at $x = 0$ at time t_1. The time at which the pulse reaches a given point x will be $T_1(x) = t_1 + x/c_\infty$, where c_∞ is the speed of a solitary pulse. Suppose that a second spike is initiated at $x = 0$ at time t_2. The instantaneous speed of the new pulse at x will depend on the time difference $T_2(x) - T_1(x)$ due to refractoriness. The Rinzel and Maginu approximation is to take the instantaneous speed to be $c(T_2(x) - T_1(x))$, where $c(T)$ is the dispersion curve for a periodic wave train. It then follows that

$$\frac{dT_2(x)}{dx} = \frac{1}{c(T_2(x) - T_1(x))}, \tag{2.36}$$

and the time interval $\phi = T_2(x) - T_1(x)$ between two action potentials initiated at $x = 0$ will evolve in space according to

$$\frac{d\phi}{dx} = \frac{1}{c(\phi)} - \frac{1}{c_\infty} \equiv \Gamma(\phi). \tag{2.37}$$

If the function $\Gamma(\phi)$ has one or more zeroes $\bar{\phi}$, then the phase difference between the two action potentials will lock at $\bar{\phi}$; the phase-locked state will be stable if $\Gamma'(\phi) < 0$. Note the kinematic approximation can be extended to multiple action potentials under the assumption that the instantaneous speed only depends on the relative phase of the preceding action potential. If $T_{n+1}(x)$ is the arrival time of the $n+1$th action potential, then

$$\frac{dT_{n+1}(x)}{dx} = \frac{1}{c(T_{n+1}(x) - T_n(x))}. \tag{2.38}$$

Note that an explicit version of kinematic theory can be derived using the singular solution of the FN equations [322], assuming that recovery always occurs via a phase wave at the value W^*. Suppose that $w_n(x)$ is the value of the recovery variable along the wave front of the nth pulse when it is located at x. The instantaneous speed of the front is thus $c(w_n)$. The time between fronts of successive action potentials is then given by

$$T_{n+1}(x) - T_n(x) = \int_{w_n}^{w^*} \frac{dw}{G_+(w)} + \int_{w_*}^{w_{n+1}} \frac{dw}{G_-(w)}. \tag{2.39}$$

Differentiating both sides with respect to x and using $dT_n/dx = 1/c(w_n)$ yields

$$\frac{1}{G_-(w_{n+1})}\frac{dw_{n+1}}{dx} = \frac{1}{G_-(w_n)}\frac{dw_n}{dx} + \frac{1}{c(w_{n+1})} - \frac{1}{c(w_n)}. \tag{2.40}$$

This generates an iterative equation for $w_n(x)$, which can be solved to determine the speed and arrival time of each successive action potential.

2.4 Wave Stability and Evans Functions

This section requires some basic definitions and results in functional analysis, in particular, with regard to Banach spaces and the spectrum of linear differential operators; see appendix section 2.7.

2.4.1 Stability of Fronts in the Bistable Equation

In order to introduce some of the basic principles of wave stability, let us return to the simple case of the scalar bistable Eq. (2.14). Let $V(\xi)$, $\xi = x - ct$, denote the unique traveling front solution with speed c such that $V(\xi) \to 1$ as $\xi \to -\infty$ and $V(\xi) \to 0$ as $\xi \to \infty$. In order to investigate the linear stability of such a solution, we set

$$v(x,t) = V(\xi) + \phi(\xi,t), \tag{2.41}$$

where ϕ is some small perturbation belonging to an appropriately defined Banach space $\mathscr{B}$ (complete, normed vector space). It is convenient to use the moving coordinate ξ so that we may see how the perturbation evolves in the moving frame of the front. Substituting for v in (2.14) and keeping only terms linear in ϕ gives

$$\frac{\partial \phi}{\partial t} = \mathbb{L}\phi \equiv \frac{\partial^2 \phi}{\partial \xi^2} + c\frac{\partial \phi}{\partial \xi} + f'(V)\phi, \quad \xi \in \mathbb{R}, \quad t > 0. \tag{2.42}$$

Equation (2.42) takes the form of a linear equation with associated linear differential operator $\mathbb{L} : \mathscr{D}(\mathbb{L}) \to \mathscr{B}$ with domain $\mathscr{D}(\mathbb{L}) \subseteq \mathscr{B}$. Determining the linear stability of the front thus reduces to the problem of calculating the spectrum $\sigma(\mathbb{L})$ of $\mathbb{L}$. That is, the front will be asymptotically stable if $\|\phi\| \to 0$ as $t \to \infty$ for all $\phi \in \mathscr{B}$, with $\|\cdot\|$ the norm on $\mathscr{B}$. This is guaranteed if $\sigma(\mathbb{L})$ lies strictly in the left-hand side of the complex plane, that is, there exists $\beta > 0$ such that $Re(\lambda) \leq -\beta$ for all $\lambda \in \sigma(\mathbb{L})$. The longtime asymptotics is then $\|\phi\| \sim \mathrm{e}^{-\beta t}$. However, differentiating both sides of (2.17) with respect to ξ gives

$$V_{\xi\xi\xi} + cV_{\xi\xi} + f'(V)V_\xi \equiv \mathbb{L}V_\xi = 0,$$

which implies that zero is an eigenvalue of $\mathbb{L}$ with associated eigenfunction V_ξ. This is not a major issue, once one notices that V_ξ is the generator of infinitesimal translations of the front solution:

$$V(\xi + h) = V(\xi) + hV_\xi(\xi) + \mathscr{O}(h^2).$$

Hence, such perturbations only cause a phase shift of the original front and can thus be discounted. This motivates defining stability of the solution V in terms of the stability of the family of waves obtained by rigid translations of V. In other words, V is said to be stable if and only if $v(x,t) = V(\xi) + \phi(\xi,t)$ converges to $V(\xi + h)$ for some constant, finite h as $t \to \infty$. This will hold provided that zero is a simple eigenvalue of $\mathbb{L}$ and the remainder of the spectrum lies in a half-space $\{\lambda, Re(\lambda) \leq -\beta\}$ for some real $\beta > 0$. It is important to note that the spectrum of $\mathbb{L}$ will depend on the choice of Banach space $\mathscr{B}$. Restricting the class of admissible functions can push the spectrum to the left-half complex plane. However, this may exclude classes of perturbations that are physically relevant. A common choice is thus $L^2(\mathbb{R})$, which includes all normalizable, continuous functions on $\mathbb{R}$ with respect to the L_2 norm:

$$\|\phi\| = \int_{-\infty}^{\infty} |\phi(\xi)|^2 d\xi < \infty.$$

We now turn to the spectrum of the differential operator appearing in (2.42). As explained in appendix section 2.7, $\sigma(\mathbb{L})$ consists of isolated eigenvalues of finite multiplicity combined with the essential spectrum, which includes any continuous and residual spectrum. $\mathbb{L}$ is of the general form of the second-order operator considered in appendix section 2.7 (see (2.106)) with constant coefficient $p = c$ and x-dependent coefficient $q(x) = f'(V(x))$. Moreover, $q(x) \to q_\pm$ as $x \to \pm\infty$ with $q_+ = f'(0) = -a$ and $q_- = f'(1) = -1 + a$. Since the essential spectrum is located to the left of the parabolas defined by (2.108), and $q_\pm < 0$, we deduce that the essential spectrum is bounded to the left of $Re(\lambda) = \min\{-a, a-1\}$ and thus does not contribute to any instabilities. The stability of the front thus depends on the eigenvalues λ of $\mathbb{L}$, where

$$\mathbb{L}\phi \equiv \phi_{\xi\xi} + c\phi_\xi + f'(V)\phi = \lambda\phi, \tag{2.43}$$

with $\phi \in L^2(\mathbb{R})$. Suppose that $Re(\lambda) \geq 0$ so $\phi(\xi) \sim \mathrm{e}^{-\beta\xi}$ as $\xi \to \infty$ with $\beta \geq c$. (This follows from noting $f'(V) \to -a$ as $\xi \to \infty$ and analyzing the resulting constant-coefficient characteristic equation.) Performing the change of variables $\psi(\xi) = \phi(\xi)\mathrm{e}^{c\xi/2}$ yields the modified eigenvalue problem

$$\mathbb{L}_1\psi \equiv \psi_{\xi\xi} + \left(f'(V) - \frac{c^2}{4}\right)\psi = \lambda\psi, \tag{2.44}$$

with $\psi \in L^2(\mathbb{R})$, since it also decays exponentially as $|\xi| \to \infty$. The useful feature of the modified operator is that it is self-adjoint, implying that any eigenvalues in the right-half complex plane are real. Multiplying both sides of the self-adjoint eigenvalue Eq. (2.44) by ψ and integrating over $\mathbb{R}$, we have

$$\lambda \int_{-\infty}^{\infty} \psi^2 d\xi = -\int_{-\infty}^{\infty} \left[\psi_\xi^2 - \left(f'(V) - \frac{c^2}{4}\right)\psi^2\right] d\xi. \tag{2.45}$$

Recall that V_ξ is an eigenfunction of $\mathbb{L}$ with $\lambda = 0$, so that if $\Phi(\xi) = V_\xi(\xi)e^{c\xi/2}$, then $\Phi_{\xi\xi} + (f'(\psi) - c^2/4)\Phi = 0$. Hence, (2.45) can be rewritten as

$$\begin{aligned}
\lambda \int_{-\infty}^{\infty} \psi^2 d\xi &= -\int_{-\infty}^{\infty} \left[\psi_\xi^2 + \frac{\Phi_{\xi\xi}\psi^2}{\Phi}\right] d\xi \\
&= -\int_{-\infty}^{\infty} \left[\psi_\xi^2 - \frac{2\psi\psi_\xi\Phi_\xi}{\Phi} + \frac{\Phi_\xi^2\psi^2}{\Phi^2}\right] d\xi \\
&= -\int_{-\infty}^{\infty} \Phi^2 \left(\frac{d}{d\xi}(\psi/\Phi)\right)^2 d\xi.
\end{aligned}$$

This last result implies that $\lambda \leq 0$, and if $\lambda = 0$, then $\psi \sim \Phi = V_\xi$. We conclude that there are no eigenvalues in the right-half complex plane and $\lambda = 0$ is a simple eigenvalue. Thus the traveling front of the scalar bistable equation is stable.

2.4.2 The Evans Function

Determining the stability of traveling pulse solutions of the FN equations (2.1) or the Hodgkin–Huxley equations (1.8) is much more complicated. One general result, however, is that the discrete spectrum of the differential operator obtained by linearizing about a traveling wave solution may be associated with the zeros of a complex analytic function known as the Evans function. Indeed, Evans [177] originally developed the formalism within the context of the stability of solitary pulses in Hodgkin–Huxley-type equations for action potential propagation. Since then, the Evans function construction has been extended to a wide range of PDEs; see the review [551]. The basic construction of the Evans function can be illustrated relatively easily by considering a higher-dimensional version of the bistable equation [173].

Consider a general class of reaction–diffusion equations of the form

$$\frac{\partial u}{\partial t} = D\frac{\partial^2 u}{\partial x^2} + F(u), \tag{2.46}$$

where $u(x,t) \in \mathbb{R}^N$ and $F : \mathbb{R}^N \to \mathbb{R}^N$. Moreover, D is assumed to be a diagonal matrix with positive definite entries corresponding to the diffusion coefficients of the various component fields. Suppose that the system exhibits bistability, that is, there are two stable fixed points $u = u_j$, $j = 1,2$, with $F(u_j) = 0$. We will assume that there exists a traveling front solution $U(\xi)$ with speed c that connects u_1 and u_2. Linearizing about the wave solution along identical lines to the scalar case by setting $u(x,t) = U(\xi) + p(\xi)e^{\lambda t}$ leads to the eigenvalue problem

$$\mathbb{L}p \equiv Dp_{\xi\xi} + cp_\xi + \partial F(U)p = \lambda p, \tag{2.47}$$

where $\partial F(U)$ denotes the matrix with components $\partial F_i/\partial U_j$. It is convenient to rewrite this as a system of $2N$ first-order equations

$$\begin{pmatrix} p_\xi \\ q_\xi \end{pmatrix} = \begin{pmatrix} 0 & I_n \\ D^{-1}(\lambda - \partial F(U)) & -cD^{-1} \end{pmatrix} \begin{pmatrix} p \\ q \end{pmatrix}. \tag{2.48}$$

Any eigensolution of this equation must satisfy the asymptotic conditions

$$\lim_{\xi \to \pm\infty} (p(\xi), q(\xi)) = (0,0).$$

Setting $z = (p,q)^T \in \mathbb{R}^n$, $n = 2N$, the associated ODE takes the general form

$$\mathscr{T}(\lambda)z(\xi) \equiv \frac{dz}{d\xi} - A(\xi;\lambda)z = 0, \tag{2.49}$$

with $A(\xi;\lambda) = A(\xi) + \lambda B(\xi)$. Thus we have a family of linear operators $\mathscr{T}(\lambda) : \mathscr{D} \to \mathscr{B}$ parameterized by λ. We take $\mathscr{B} = L^2(\mathbb{R}, \mathbb{R}^n)$ and $\mathscr{D}$ to be the space of admissible functions such that $z \in \mathscr{B}, \mathscr{T}(\lambda)z \in \mathscr{B}$. The basic form of the linear Eq. (2.49) holds for a wide range of PDEs supporting solitary traveling waves [551]. The discrete spectrum of the operator $\mathbb{L}$ thus corresponds to the values of λ for which $\mathscr{T}(\lambda)$ is not invertible.

An important concept for analyzing (2.49) is that of *exponential dichotomies*. First, consider the linear constant-coefficient equation

$$\frac{dz}{d\xi} = A(\lambda)z, \tag{2.50}$$

for which $A(\lambda)$ is independent of ξ. Suppose that the matrix $A(\lambda)$ is hyperbolic, that is, all its eigenvalues have nonzero real part. We can then decompose $\mathbb{R}^n$ (or its complexification) as

$$\mathbb{R}^n = E_s(\lambda) \oplus E_u(\lambda),$$

where $E_{s,u}(\lambda)$ are the generalized stable and unstable eigenspaces of the matrix $A(\lambda)$. Thus E_s is spanned by $n_+(\lambda)$ eigenfunctions that decay exponentially as $\xi \to \infty$ and E_u is spanned by $n_-(\lambda)$ eigenfunctions that decay exponentially as $\xi \to -\infty$ with $n_+(\lambda) + n_-(\lambda) = n$. The notion of exponential dichotomies can now be extended to (2.49) by noting that

$$\lim_{\xi \to \pm\infty} A(\xi;\lambda) \to A_\pm(\lambda) \tag{2.51}$$

where $A_\pm$ correspond to the matrix appearing in (2.48) in the limits $U(\xi) \to u_1$ and $U(\xi) \to u_2$, respectively. Moreover, the spectral properties of $\mathscr{T}(\lambda)$ can be expressed in terms of these exponential dichotomies. We summarize the main results below:

- Equation (2.49) is said to have an exponential dichotomy on $\mathbb{R}^+$ if and only if the matrix $A_+(\lambda)$ is hyperbolic. Let $\mathscr{V}_+(\lambda)$ denote the linear subspace spanned by solutions of (2.49) that decay as $\xi \to \infty$. The codimension of $\mathscr{V}_+(\lambda)$ is defined to be the Morse index $i_+(\lambda)$ of the exponential dichotomy on $\mathbb{R}^+$, and $i_+(\lambda) = \dim E_u^+(\lambda)$.
- Equation (2.49) is said to have an exponential dichotomy on $\mathbb{R}^-$ if and only if the matrix $A_-(\lambda)$ is hyperbolic. Let $\mathscr{V}_-(\lambda)$ denote the linear subspace spanned by solutions of (2.49) that decay as $\xi \to -\infty$. The dimension of $\mathscr{V}_-(\lambda)$ is defined to be the Morse index $i_-(\lambda)$ of the exponential dichotomy on $\mathbb{R}^-$, and $i_-(\lambda) = \dim E_u^-(\lambda)$.
- λ is in the discrete spectrum if and only if $A_\pm(\lambda)$ are both hyperbolic with the same Morse index $i_+(\lambda) = i_-(\lambda)$ such that $\mathscr{V}_+(\lambda) \cap \mathscr{V}_-(\lambda) \neq \{0\}$.
- λ is in the essential spectrum if either at least one of the two asymptotic matrices $A_\pm(\lambda)$ is not hyperbolic or else if both are hyperbolic but their Morse indices differ.

In most applications the essential spectrum Σ_{ess} lies in the left-half complex plane and thus does not contribute to instabilities of a wave solution. Therefore, suppose that $\lambda \notin \Sigma_{\text{ess}}$. It then follows that $i_+(\lambda) = i_-(\lambda) = k$, say. (For the multicomponent bistable equation $k = N = n/2$.) In order to construct the Evans function, introduce a basis for the subspaces $\mathscr{V}_\pm(\lambda)$ according to

$$\mathscr{V}_-(\lambda) = \text{span}\{Q_1^-, Q_2^-, \ldots, Q_k^-\}, \quad \mathscr{V}_+(\lambda) = \text{span}\{Q_1^+, Q_2^+, \ldots, Q_{n-k}^+\}$$

where each $Q_j^\pm(\xi)$ is an n-dimensional basis vector. Now form the $n \times n$ matrix $\mathscr{M}(\xi)$, in which the first k columns are given by the vectors $Q_j^-(\xi)$, $j = 1, \ldots, k$, and the next $n-k$ columns are given by Q_j^+, $j = 1, \ldots, n-k$. The Evans function is then defined according to

$$\mathscr{E}(\lambda) = \det \mathscr{M}(\xi_0), \tag{2.52}$$

for an arbitrary point ξ_0 which can be taken to be zero. The Evans function has a number of important properties. First, λ is an eigenvalue if and only if $\mathscr{E}(\lambda) = 0$. Second, if λ is a zero of $\mathscr{E}(\lambda)$, then the order of this zero is equal to the algebraic multiplicity of λ viewed as an eigenvalue. Third, the Evans function is analytic. The first property is simple to establish. For $\mathscr{E}(\lambda) = 0$ if and only if $\det \mathscr{M}(\xi_0) = 0$, and the latter holds if and only if there exist constant coefficients c_i^+, c_j^- such that

$$\sum_{j=1}^{k} c_j^- Q_j^-(\xi_0) + \sum_{i=1}^{n-k} c_i^+ Q_i^+(\xi_0) = 0,$$

that is,

$$\sum_{j=1}^{k} c_j^- Q_j^-(\xi_0) = -\sum_{i=1}^{n-k} c_i^+ Q_i^+(\xi_0).$$

Hence, λ is a zero of $\mathscr{E}(\lambda)$ if and only if $\mathscr{V}_+(\lambda)$ and $\mathscr{V}_-(\lambda)$ have a nonzero intersection, which means that λ is an eigenvalue, since the corresponding eigensolution decays at both $\xi = \infty$ and $\xi = -\infty$. Finally, note that one of the powerful features of the Evans function construction is that it can be applied to a wide variety of wave phenomena beyond fronts, including pulses, periodic wave trains, and multi-bump pulses [551]. In a sense, a single pulse is a special case of a front, since the exponential dichotomies on $\mathbb{R}^+$ and R^- are the same, that is,

$$\lim_{\xi \to \pm\infty} A(\xi; \lambda) \to A_0(\lambda),$$

with $A_0(\lambda)$ evaluated at the same resting state.

Finally, a word of caution: linear stability does not necessarily imply nonlinear stability. When considering perturbations about a traveling wave solution of a nonlinear PDE, $p(x,t) = u(x,t) - U(\xi)$, one can decompose the PDE as

$$\frac{\partial p}{\partial t} = \mathbb{L}p + \mathscr{N}(p), \tag{2.53}$$

where $\mathscr{N}(p) = \mathscr{O}(|p|^2)$. Determining linear stability of the traveling wave in terms of the spectrum $\sigma(\mathbb{L})$ assumes that the perturbation p remains small with respect to the given norm. A challenging mathematical problem is determining whether or not this is true. In the simpler case of ODEs one can use the stable manifold the-

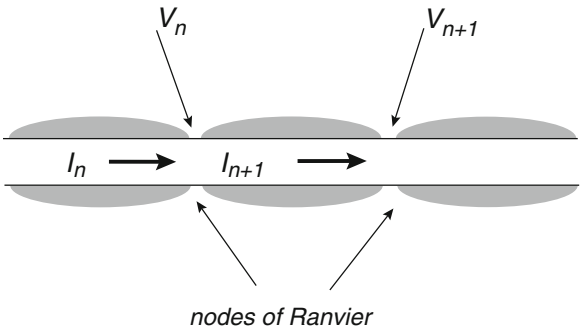

Fig. 2.10 Schematic diagram of a myelinated axon. Currents in myelinated region are confined to the axial direction. Potentials at the nodes are governed by active currents

orem to show that linear (in)stability implies nonlinear (in)stability in the case of hyperbolic fixed points. In the case of non-hyperbolic fixed points one has to use the center manifold theorem and bifurcation theory. A number of techniques have been used to study nonlinear stability of traveling waves, including center manifold reductions, Lyapunov functionals, and energy methods [551]. For example, the nonlinear stability of traveling wave solutions of the reaction–diffusion system (2.46) can be proven using a center manifold reduction. Nonlinear stability theory is also important if one wishes to determine what happens when a traveling wave becomes unstable, since perturbations grow and the linear approximation breaks down.

2.5 Myelinated Axons and Discrete Diffusion

Many vertebrate axons are coated with a lipid material called *myelin*, which is made up of the membranes of *glial cells* (see Sect. 4.5) that wrap around the axon many times to form a thick insulating layer. This wrapping increases the effective membrane resistance and decreases the membrane capacitance by a factor of around 100. At regularly spaced intervals the axon is exposed to the extracellular medium at the so-called nodes of Ranvier, where there is a high density of sodium channels; see Fig. 2.10. The length L of myelin sheath between successive nodes is typically 1–2 mm, and the width l of a single node of Ranvier is around 1 µm. Propagation of an action potential along a myelinated axon is considerably faster than along a nonmyelinated axon. In terms of the cable equation, this can be understood as consequence of the fact that the transmembrane currents in the myelinated sections are

negligible so that the myelinated sheath acts like a simple resistor. In effect, the action potential does not propagate continuously along the axon but rather jumps from node to node as a saltatory (leaping) wave.

Wave propagation along a myelinated axon can be modeled by spatially discretizing the diffusion term in the spatially extended Hodgkin–Huxley model (1.8). Suppose that the membrane voltage does not vary within each node of Ranvier, that is, the nodes are isopotential and denote the voltage of the nth node by V_n. Treating each myelin sheath as a pure Ohmic resistor with resistance rL, where r is the intracellular resistance per unit length, the axial current between nodes n and $n+1$ is

$$I_{n+1} = -\frac{1}{rL}(V_{n+1} - V_n). \tag{2.54}$$

Conservation of current at the nth node of Ranvier then implies that the total transmembrane current into the node is

$$2\pi al\left(C_m \frac{\partial V_n}{\partial t} + I_{\text{ion}}\right) = I_n - I_{n+1} = \frac{1}{rL}(V_{n+1} - 2V_n + V_{n-1}), \tag{2.55}$$

where a is the radius of the cable. It follows that

$$\frac{\partial V_n}{\partial t} = -\hat{I}_{\text{ion}} + D(V_{n+1} - 2V_n + V_{n-1}), \tag{2.56}$$

with coupling coefficient

$$D = \frac{R_m}{(2\pi ar)lL\tau_m} = \frac{\lambda_m^2}{lL\tau_m}.$$

We have used $R = \pi a^2 r$, $\tau_m = R_m C_m$ and $\lambda_m = (R_m a/2R)^{1/2}$; see Sect. 1.4.1.

2.5.1 The Discrete Bistable Equation

In order to investigate the effects of myelination on propagation speed, let us consider the simpler case of the spatially discrete bistable equation

$$\frac{\partial V_n}{\partial t} = f(V_n) + D(V_{n+1} - 2V_n + V_{n-1}), \tag{2.57}$$

where $f(V) = V(V-a)(1-V)$. Proving the existence of traveling wave solutions of (2.57) is nontrivial [699]. However, assuming that such a solution does exist, one can use perturbation methods to estimate the wave speed [317, 321]. A traveling wave solution is defined according to the iterative relationship $V_{n+1}(t) = V_n(t+\tau_d)$ where τ_d represents the time delay for the wave to jump between successive nodes. The corresponding invariant wave profile $\Phi(t)$ satisfies a delay differential equation that is obtained by substituting $V_n(t) = \Phi(t)$ into (2.57):

$$\frac{d\Phi}{dt} = D(\Phi(t-\tau_d) - 2\Phi(t) + \Phi(t+\tau_d)) + f(\Phi(t)). \tag{2.58}$$

Suppose that we fix the time units by setting $\tau_m = 1$. If the function $\Phi(t)$ is sufficiently smooth and τ_d is sufficiently small, then we can expand $\Phi(t \pm \tau_d)$ as a Taylor series in τ_d. Keeping only terms up to τ_d^2 yields the leading-order equation

$$D\tau_d^2 \Phi_{tt} - \Phi_t + f(\Phi) = 0. \tag{2.59}$$

This is identical in form to the bistable Eq. (2.17) for a traveling front of (dimensionless) wave speed c, provided that we set $\xi = -ct$ and $D\tau_d^2 = c^{-2}$. It follows that $\Phi(-\xi/c)$ is the traveling front solution of the continuous bistable equation and $c = (1-2a)/\sqrt{2}$. The wave speed of the saltatory wave (in physical time units) is then

$$\hat{c} = \frac{L+l}{\tau_d} = (L+l)c\sqrt{\frac{D}{\tau_m}} = \frac{L+l}{\sqrt{lL}}\left(\frac{c\lambda_m}{\tau_m}\right). \tag{2.60}$$

Comparison with (2.20) shows that myelination increases wave speed by a factor $(L+l)/\sqrt{lL} \approx 10$ assuming that $L \approx 100l$.

Higher-order corrections to the wave speed can be determined using regular perturbation theory [317, 321]. Thus, in terms of the small parameter $\varepsilon = D^{-1}$, we introduce the series expansions (with $\tau_m = 1$)

$$\Phi(t) = \Phi_0(t) + \varepsilon\Phi_1(t) + \ldots, \quad {\tau_d}^2 = \frac{\varepsilon}{c^2} + \varepsilon^2\tau_1 + \ldots \tag{2.61}$$

Substituting into the discrete bistable Eq. (2.58) and collecting terms of equal powers in ε yields a hierarchy of equations for Φ_n, with Φ_0 satisfying (2.59) for $D\tau_d^2 = c^{-2}$, and

$$\mathbb{L}\Phi_1 \equiv \frac{1}{c^2}\Phi_1'' - \Phi_1' + f'(\Phi_0)\Phi_1 = -\frac{\Phi_0^{(4)}}{12c^4} - \tau_1\Phi_0''. \tag{2.62}$$

Here $\mathbb{L}$ denotes a linear differential operator acting on the space $L^2(\mathbb{R})$ of square-integrable function on $\mathbb{R}$. The operator $\mathbb{L}$ is not invertible, since $\mathbb{L}\Phi_0' = 0$, which follows from differentiating (2.58) with respect to t. (A similar operator arose in our discussion of wave stability in Sect. 2.4.) It follows from the Fredholm alternative (see appendix section 2.7) that a solution for Φ_1 exists if and only if the right-hand side of (2.62) is orthogonal to the null-space of the adjoint operator $\mathbb{L}^\dagger$. The latter is

$$\mathbb{L}^\dagger\Psi = \frac{1}{c^2}\Psi'' + \Psi' + f'(\Phi_0)\Psi, \tag{2.63}$$

which has a one-dimensional null-space spanned by $\Psi(t) = \mathrm{e}^{-c^2t}\Phi_0'(t)$. We thus have a solvability condition for the leading-order correction τ_1 to the delay:

$$\int_{-\infty}^{\infty} \mathrm{e}^{-c^2t}\Phi_0'(t)\left[\frac{\Phi_0^{(4)}}{12c^4} + \tau_1\Phi_0''\right]dt = 0.$$

Once τ_1 has been determined, the propagation speed is (in physical time units)

$$\hat{c} = c(L+l)\sqrt{\frac{D}{\tau_m}}\left(1 - \frac{\tau_1 c^2}{2D\tau_m} + \mathcal{O}([c^2/D\tau_m]^2)\right). \tag{2.64}$$

2.5.2 Propagation Failure

The above perturbation analysis establishes that for sufficiently large coupling D, there are traveling front solutions that approach the speed of the appropriately scaled continuous model. Another important property of the discrete bistable equation is that if D is sufficiently small, then wave propagation failure occurs, reflecting the fact that there are nontrivial standing front solutions even when $\int_0^1 f(v)dv > 0$ [165, 183, 317, 318]. Here we describe one method for estimating the critical value of coupling D_c below which propagation fail, which has been developed by Keener [318] using averaging theory. The first step is to rewrite the discrete bistable equation in the form

$$(1+g'(x))[v_t - f(v)] = Dv_{xx}, \tag{2.65}$$

where $g(x)$ is the periodic sawtooth function

$$g(x) = \frac{L}{2} - x, \quad 0 < x < L, \quad g(x+nL) = g(x), \tag{2.66}$$

and

$$1 + g'(x) = L\sum_n \delta(x - nL). \tag{2.67}$$

Equation (2.65) implies that $v_{xx} = 0$ between nodes, that is, $v(x,t) = A_n x + B_n$ for $nL < x < (n+1)L$. Matching $v(x,t)$ with $V_n(t)$ and $V_{n+1}(t)$ at both ends shows that $A_n = L^{-1}[V_{n+1} - V_n]$ and hence $v_x((n+1)L,t) = L^{-1}(V_{n+1} - V_n)$. If we now integrate (2.65) over the interval $[nL,(n+1)L)$, then we recover the discrete bistable equation

$$\partial_t V_n - f(V_n) = \frac{D}{L}[v_x((n+1)L,t) - v_x(nL,t)] = D[V_{n+1} - 2V_n + V_{n-1}]. \tag{2.68}$$

In order to proceed, we will smooth out the function $g(x)$ by taking

$$1 + g'(x) = \frac{L}{\sqrt{2\pi\sigma^2}}\sum_n \exp\left(-\frac{(x-nL)^2}{2\sigma^2}\right), \tag{2.69}$$

so that $1 + g'(x) > 0$ for all x. At the end of the calculation we will take the limit $\sigma \to 0$ to recover the sawtooth function. We then have the scalar bistable equation with an inhomogeneous diffusion coefficient,

$$v_t = f(v) + \frac{D}{1+g'(x)}v_{xx}.$$

Following Keener [318], it is convenient to carry out the coordinate transformation $y = y(x) \equiv x + g(x) - L/2$ so that

$$v_t = f(v) + \partial_y \left([1 + g'(x)] \partial_y v \right).$$

If $g(x)$ is a sawtooth-like function, then y is a steplike function with $y = nL$ for $nL < x < (n+1)L$ in the limit $\sigma \to 0$. Hence $1 + g'(y(x)) = \sum_n \delta(y(x) - nL)$ blows up for all $nL < x < (n+1)L$, whereas $1 + g'(y(x)) = 0$ when $x = nL$. That is, $1 + g'(x) = 1/(1 + g'(y(x)))$, so that (after rewriting y as x),

$$v_t = f(v) + \partial_x \left(\frac{D}{1 + g'(x)} v_x \right).$$

Fixing the spatial units by setting $L = 1$ (having already non-dimensionalized time), and using the fact that waves exist for sufficiently large D, we introduce the small dimensionless parameter $\varepsilon = 1/\sqrt{D}$. Rescaling space according to $x \to x/\sqrt{D}$, we finally obtain the modified bistable equation

$$v_t = f(v) + \partial_x \left(\frac{1}{1 + g'(x/\varepsilon)} v_x \right). \tag{2.70}$$

Thus the problem of wave propagation failure for the discrete bistable equation has been reduced to the problem of calculating the mean wave speed $\bar{c}(\varepsilon)$ of a wavelike solution of an inhomogeneous continuous bistable equation and determining how $\bar{c}(\varepsilon)$ vanishes as ε increases (the coupling D decreases).

Equation (2.70) is now in a suitable form to apply the averaging method of Keener [318]; see below. The basic result is that the wavelike solution takes the form

$$v(x,t) = V(x - \phi(t)) + \mathcal{O}(\varepsilon), \tag{2.71}$$

where $V(x)$ is the wave solution in the homogeneous case ($g = 0$). The phase $\phi(t)$ evolves according to

$$\frac{d\phi}{dt} = c - \Phi(\phi/\varepsilon) \tag{2.72}$$

with c the speed of the unmodulated wave,

$$\Phi(\phi/\varepsilon) = \frac{1}{\Lambda} \int_{-\infty}^{\infty} g'([\xi + \phi]/\varepsilon) V''(\xi) V'(\xi) e^{c\xi} d\xi, \tag{2.73}$$

and

$$\Lambda = \int_{-\infty}^{\infty} e^{c\xi} V'(\xi)^2 d\xi. \tag{2.74}$$

Equation (2.72) implies that the solution is not translationally invariant; rather, it moves with a time-dependent velocity ϕ'. If $c - \Phi(\phi/\varepsilon)$ is strictly positive, then $\phi'(t)$ is a positive, periodic function of t with period

$$T = \int_0^{\varepsilon} \frac{d\phi}{c - \Phi(\phi/\varepsilon)}. \tag{2.75}$$

The mean speed of the wave is $\bar{c} = \varepsilon/T$. On the other hand, if $c - \Phi(\phi/\varepsilon)$ vanishes for some ϕ, then propagation failure is expected to occur:

Averaging method for discrete bistable equation. Standard applications of the averaging theorem in dynamical systems theory [248] only apply to structurally stable solutions, whereas traveling wave solutions are not structurally stable. Therefore, it is necessary to consider a modified averaging procedure as outlined by Keener [318, 319]. The first step is to rewrite (2.70) as the second-order system

$$v_x = (1 + g'(x/\varepsilon))u, \quad u_x = v_t - f(v). \tag{2.76}$$

Introducing the exact change of variables $v = w + \varepsilon u g(x/\varepsilon)$ yields the new system

$$w_x = u - \varepsilon u_x g(x/\varepsilon), \quad u_x = w_t + \varepsilon u_t g(x/\varepsilon) - f(w + \varepsilon u g(x/\varepsilon)). \tag{2.77}$$

It can be seen that if we ignore terms of order ε, then the system of equations is independent of x/ε. This lowest-order averaged system reduces to the standard bistable equation, which we know supports a traveling front solution $V(x - ct)$. Including the inhomogeneous factors $g(x/\varepsilon)$ means that the system is no longer translationally invariant. However, we can look for solutions that are in some sense close to a traveling front by going to a traveling coordinate system by setting $\xi = x - \phi(t)$, with

$$w_\xi = u - \varepsilon u_\xi g([\xi + \phi]/\varepsilon) \tag{2.78a}$$

$$u_\xi = -\phi' w_\xi - \varepsilon \phi' u_\xi g([\xi + \phi]/\varepsilon) - f(w + \varepsilon u g([\xi + \phi]/\varepsilon). \tag{2.78b}$$

We now seek a perturbative solution of the form

$$w = w_0(\xi) + \varepsilon w_1(\xi) + \ldots, \quad v(\xi) = v_0(\xi) + \varepsilon v_1(\xi) + \ldots, \quad \phi'(t) = c + \varepsilon \phi_1'(t) + \ldots$$

Substituting into (2.78) and collecting terms of equal powers in ε yields a hierarchy of equations, the first two of which are

$$\partial_\xi w_0 = u_0, \quad \partial_\xi u_0 = -c u_0 - f(w_0), \tag{2.79}$$

which recovers the homogeneous bistable equation for w_0, and

$$\partial_\xi w_1 - u_1 = -(\partial_\xi u_0) g([\xi + \phi]/\varepsilon), \tag{2.80a}$$

$$\partial_\xi u_1 + f'(w_0) w_1 + c u_1 = -\phi_1' u_0 - f'(w_0) u_0 g([\xi + \phi]/\varepsilon). \tag{2.80b}$$

Let us take the solution of the lowest-order equation to be the traveling front solution $V(\xi)$ constructed in Sect. 2.2: $w_0 = V, u_0 = V'$. The next-order system of Eq. (2.80) can be rewritten in the vector form

$$\mathbb{L}\begin{pmatrix} w_1 \\ u_1 \end{pmatrix} = \begin{pmatrix} h_w \\ -\phi_1' V' + h_u \end{pmatrix}, \quad \mathbb{L} = \begin{pmatrix} \partial_\xi & -1 \\ f'(V) & \partial_\xi + c \end{pmatrix}, \tag{2.81}$$

with h_w and h_u determined by inhomogeneous terms on the right-hand side of (2.80a) and (2.80b), respectively. Following our analysis of the linear operator (2.62), we know that the matrix operator appearing in (2.81) has a null-space spanned by (V', V''). Similarly, the adjoint operator

$$\mathbb{L}^\dagger = \begin{pmatrix} -\partial_\xi & f'(w_0) \\ -1 & -\partial_\xi + c \end{pmatrix}$$

has the null vector $e^{c\xi}(-V'',V')$. Hence, applying the Fredholm alternative, we see that $\phi'(t)$ must satisfy

$$\begin{aligned}\phi_1'(t)\int_{-\infty}^{\infty} e^{c\xi}V'(\xi)^2 d\xi &= \int_{-\infty}^{\infty} e^{c\xi}[-V''(\xi)h_w(\xi)+V'(\xi)h_u(\xi)d\xi \\ &= \int_{-\infty}^{\infty} e^{c\xi}[V''(\xi)^2 - f'(V)V'(\xi)^2]g([\xi+\phi]/\varepsilon)d\xi \\ &= \int_{-\infty}^{\infty} g([\xi+\phi]/\varepsilon)\frac{d}{d\xi}\left[V''(\xi)V'(\xi)e^{c\xi}\right]d\xi, \\ &= -\frac{1}{\varepsilon}\int_{-\infty}^{\infty} g'([\xi+\phi]/\varepsilon)V''(\xi)V'(\xi)e^{c\xi}d\xi,\end{aligned}$$

after using $V'''+cV''+f'(V)V'=0$ and performing integration by parts. We thus obtain the phase Eq. (2.72) with $\phi(t)=c+\varepsilon\phi_1(t)$.

It turns out that solving the phase equation in the case of a cubic nonlinearity is rather involved [318]. Therefore, for the sake of illustration, we will consider the simpler case of the piecewise linear function (2.21). There then exists a unique traveling front solution of the homogeneous bistable equation given by (2.23) with corresponding wave speed (2.24). Substituting (2.23) into (2.74) gives

$$\begin{aligned}\Lambda &= (a\lambda_-)^2\int_0^{\infty} e^{c\xi}e^{2\lambda_-\xi}d\xi + ([a-1]\lambda_+)^2\int_{-\infty}^{0} e^{c\xi}e^{2\lambda_+\xi}d\xi \\ &= (a\lambda_-)^2\left[\frac{1}{c+2\lambda_+}-\frac{1}{c+2\lambda_-}\right] \\ &= 2\sqrt{a-a^2}(a-a^2),\end{aligned}$$

where we have used the results $a\lambda_- = (a-1)\lambda_+$,

$$c+2\lambda_\pm = \pm\sqrt{c^2+4} = \frac{\pm 1}{\sqrt{a-a^2}}, \quad \lambda_- = -\frac{1}{2}\left[c+\sqrt{c^2+4}\right] = \frac{a-1}{\sqrt{a-a^2}}.$$

Similarly, substituting (2.23) into (2.73) gives, to leading order in ε,

$$\begin{aligned}\Phi(\phi/\varepsilon) &= \frac{1}{\Lambda}a^2\lambda_-^3\int_0^{\infty} g'([\xi+\phi]/\varepsilon)e^{c\xi}e^{2\lambda_-\xi}d\xi \\ &\quad + \frac{1}{\Lambda}[a-1]^2\lambda_+^3\int_{-\infty}^{0} g'([\xi+\phi]/\varepsilon)e^{c\xi}e^{2\lambda_+\xi}d\xi \\ &\approx \frac{1}{\Lambda}\left[a^2\lambda_-^3\int_0^{\infty} g'([\xi+\phi]/\varepsilon)d\xi + [a-1]^2\lambda_+^3\int_{-\infty}^{0} g'([\xi+\phi]/\varepsilon)d\xi\right] \\ &= \frac{\varepsilon}{\Lambda}(a\lambda_-)^2[\lambda_+-\lambda_-]g(\phi/\varepsilon)+\mathcal{O}(\varepsilon^2) \\ &= \frac{\varepsilon}{2[a-a^2]}g(\phi/\varepsilon)+\mathcal{O}(\varepsilon^2).\end{aligned}$$

Applying this to the sawtooth function (2.66), the phase Eq. (2.72) reduces to

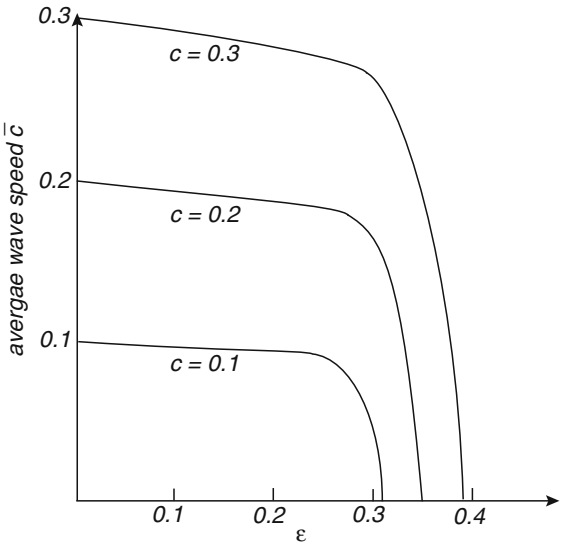

Fig. 2.11 Illustrative sketch of mean wave speed as a function of ε for the discrete bistable Eq. (2.65) with $L = 2\pi$

$$\frac{d\phi}{dt} = c - \frac{\varepsilon}{2[a-a^2]}\left[\frac{1}{2} - \frac{\phi}{\varepsilon}\right],$$

and

$$T = 2\ln\left(\frac{c+\varepsilon/\chi}{c-\varepsilon/\chi}\right), \quad \chi = 4[a-a^2].$$

We deduce that the mean wave speed is

$$\bar{c} = \frac{\varepsilon}{2}\frac{1}{\ln\left(\frac{c+\varepsilon/\chi}{c-\varepsilon/\chi}\right)}. \tag{2.82}$$

This predicts propagation failure when $\varepsilon \geq \chi c$. In particular, propagation failure is more likely to occur as ε increases, which is equivalent to reducing the coupling strength D. Finally, note that the cubic nonlinearity yields different behavior, both qualitatively and quantitatively. The main reason for this is that the above averaging procedure results in an expression for the mean wave speed that involves exponentially small terms of the form $e^{-\pi/\varepsilon}$ [318]. This has two major implications. First, it is necessary to include higher-order terms in the perturbation analysis in order to obtain sufficient accuracy. Second, the rapid increase in $e^{-\pi/\varepsilon}$ as ε increases can result in a sharp transition to propagation failure at relatively small values of ε, as illustrated in Fig. 2.11.

2.6 Stochastic Traveling Waves

In Sect. 1.5 we showed how the stochastic opening and closing of a finite number of ion channels can generate a multiplicative noise term in a space-clamped, conductance-based model of a neuron. The membrane voltage then evolves according to a stochastic differential equation (SDE) such as (1.128). This suggests that ion channel fluctuations could also affect the propagation of action potentials in a spatially extended model. Such an observation motivates the more general issue of how to analyze traveling wave solutions of stochastic partial differential equations (SPDEs). In this section we review a formal perturbation method for analyzing traveling front solutions in the case of weak noise [14, 494, 546, 557], which we apply to a stochastic version of the bistable equation. (The rigorous treatment of SPDEs is much more complicated than SDEs because one has to keep track of the regularity of solutions with respect to both time and space. Nevertheless, there have been some recent mathematical studies of a stochastic version of spatially extended excitable membranes based on the Hodgkin–Huxley equations [17, 88].)

Consider a scalar SPDE of the form

$$\frac{\partial}{\partial t}V(x,t)=\frac{\partial^2}{\partial x^2}V(x,t)+f(V(x,t))+\sqrt{\varepsilon}g(V(x,t))\eta(x,t), \tag{2.83}$$

Here $\eta(x,t)$ is a Gaussian random function with zero mean and correlation

$$\langle\eta(x,t)\eta(x',t')\rangle=2C([x-x']/\lambda)\delta(t-t') \tag{2.84}$$

The parameter λ is the spatial correlation length of the noise such that $C(x/\lambda)\to\delta(x)$ in the limit $\lambda\to 0$, and ε determines the strength of the noise, which is assumed to be weak. Note that we can formally set $\eta(x,t)dt=dW(x,t)$, where $W(x,t)$ is a space-dependent Wiener process with zero mean and $\langle dW(x,t)dW(x',t)\rangle=2C([x-x']/\lambda)$. We have also included a multiplicative noise factor $g(V)$, and based on our analysis of channel fluctuations, we treat the multiplicative noise in the sense of Stratonovich (see Sect. 1.7). The starting point of the perturbation method is the observation that multiplicative noise in the Stratonovich sense leads to a systematic shift in the speed of the front (assuming a front of speed c exists when $\varepsilon=0$) [14]. This is a consequence of the fact that $\langle g(V)\eta\rangle\neq 0$ even though $\langle\eta\rangle=0$. The former average can be calculated using Novikov's theorem [465, 486]:

$$\varepsilon^{1/2}\langle g(U)\eta\rangle=\varepsilon C(0)\langle g'(U)g(U)\rangle dt, \tag{2.85}$$

Note that in the limit $\lambda\to 0$, $C(0)\to 1/\Delta x$ where Δx is a lattice cutoff, which can be identified with the step size of the spatial discretization scheme used in numerical simulations.

Novikov's theorem. Suppose that $X(s)$ is a Gaussian random function with zero mean and correlation

$$\langle X(s)X(s')\rangle=C(s,s'),$$

then for any functional $\mathscr{L}[h]$,

$$\langle X(s)\mathscr{L}[X]\rangle = \int_{-\infty}^{\infty} C(s,s')\left\langle \frac{\delta \mathscr{L}[X]}{\delta X(s')}\right\rangle ds'.$$

Applying this theorem to $\langle g(U)\eta\rangle$, we have

$$\langle g(V)\eta\rangle = 2\int_{-\infty}^{\infty} C([x-x']/\lambda)\left\langle g'(V(x,t))\frac{\delta V(x,t)}{\delta \eta(x',t)}\right\rangle dx'.$$

The stochastic voltage is a functional of the noise term $\eta(x,t)$, as can be seen by formally integrating Eq. (2.83) with respect to time:

$$V(x,t) = \int_{-\infty}^{\infty}\left[\frac{\partial^2}{\partial x^2}V(x,t'') + f(V(x,t'')) + \sqrt{\varepsilon}g(V(x,t''))\eta(x,t'')\right]H(t-t'')dt''.$$

It follows that

$$\frac{\delta V(x,t)}{\delta \eta(x',t')} = \sqrt{\varepsilon}g(V(x,t'))H(t-t')\delta(x-x'),$$

which yields (2.85) after using $H(0) = 1/2$.

An alternative derivation of (2.85) is based on Fourier transforming (2.83) [546]. It is convenient to restrict x to a bounded domain, $-L/2 \le x \le L/2$, and to impose periodic boundary conditions. We can then introduce the discrete Fourier series

$$V(x,t) = \frac{1}{L}\sum_n \mathrm{e}^{ik_n x}V_n(t), \quad W(x,t) = \frac{1}{L}\sum_n \mathrm{e}^{ik_n x}W_n(t) \tag{2.86}$$

with $k_n = 2\pi n/L$ and $W_n(t)$, an independent Wiener process, such that

$$\langle dW_n(t)\rangle = 0, \quad \langle dW_n(t)dW_m(t)\rangle = 2L\delta_{m+n,0}dt. \tag{2.87}$$

Fourier transforming (2.83) gives in differential form

$$dU_n(t) = [-k_n^2 V_n(t) + F_n(t)]dt + \frac{\varepsilon^{1/2}}{L}\sum_m g_{n-m}(t)dW_m(t), \tag{2.88}$$

where F_n, g_n are the Fourier coefficients of the time-dependent functions $F\circ U(t)$ and $g\circ U(t)$, respectively. The associated Stratonovich Fokker–Planck equation takes the form [209] (see also Sect. 1.7)

$$\frac{\partial P}{\partial t} = -\sum_l \frac{\partial}{\partial u_l}[(-k_l^2 V_n(t) + F_l(t))P] + \frac{\varepsilon}{L}\sum_{l,m,q}\frac{\partial}{\partial V_l}g_{l-q}\frac{\partial}{\partial V_m}g_{m+q}P. \tag{2.89}$$

Multiplying both sides of this equation by V_n and integrating with respect to V_m, integer m, leads to the following evolution equation for the mean:

$$\frac{d\langle V_n\rangle}{dt} = -k_n^2\langle V_n\rangle + \langle F_n\rangle + \frac{\varepsilon}{L}\sum_{m,q}\left\langle \frac{\partial g_{n-q}}{\partial V_m}g_{m+q}\right\rangle. \tag{2.90}$$

Finally, taking the inverse transform of (2.90) gives

$$\frac{d\langle U(x,t)\rangle}{dt} = \frac{\partial^2}{\partial x^2}\langle V(x,t)\rangle + \langle F(V(x,t))\rangle + \frac{\varepsilon}{\Delta x}\left\langle g(U(x,t))g'(U(x,t))\right\rangle, \tag{2.91}$$

where we have used the result $\partial g_n/\partial U_m = [g'(U)]_{n-m}$. Note that it is necessary to introduce a cutoff in the frequencies, which is equivalent to introducing a fundamental lattice spacing of Δx. Alternatively, the multiplicative noise can be taken to have a small but finite corre-

lation length in space so that $C(0) = 1/\Delta x$. Comparison of (2.90) with the mean of (2.83) yields the desired result.

Following [14], it is convenient to rewrite (2.83) so that the fluctuating term has zero mean:

$$\frac{\partial}{\partial t}V(x,t) = \frac{\partial^2}{\partial x^2}V(x,t) + h(V(x,t)) + \sqrt{\varepsilon}R(V,x,t), \tag{2.92}$$

where

$$h(V) = f(V) + \varepsilon C(0)g'(V)g(V) \tag{2.93}$$

and

$$R(V,x,t) = g(V)\eta(x,t) - \varepsilon^{1/2}C(0)g'(U)g(U). \tag{2.94}$$

The stochastic process R has zero mean (so does not contribute to the effective wave speed) and correlation:

$$\langle R(V,x,t)R(V,x',t')\rangle = \langle g(V(x,t))\eta(x,t)g(V(x',t')\eta(x',t')\rangle + \mathscr{O}(\varepsilon^{1/2}). \tag{2.95}$$

The next step in the analysis is to assume that the fluctuating term in (2.92) generates two distinct phenomena that occur on different time scales: a diffusive-like displacement of the front from its uniformly translating position at long time scales and fluctuations in the front profile around its instantaneous position at short time scales [14, 494, 546, 557]. In particular, following [14], we express the solution V of (2.92) as a combination of a fixed wave profile V_0 that is displaced by an amount $\Delta(t)$ from its uniformly translating position $\xi = x - \bar{c}t$ and a time-dependent fluctuation Φ in the front shape about the instantaneous position of the front:

$$V(x,t) = V_0(\xi - \Delta(t)) + \varepsilon^{1/2}\Phi(\xi - \Delta(t),t). \tag{2.96}$$

The wave profile V_0 and associated wave speed $\bar{c}$ are obtained by solving the modified deterministic equation

$$\bar{c}\frac{dV_0}{d\xi} + \frac{d^2V_0^2}{d\xi^2} + h(V_0(\xi)) = 0. \tag{2.97}$$

Both $\bar{c}$ and V_0 depend nontrivially on the noise strength ε due to the ε dependence of the function h; see (2.93). As an example, suppose that $f(V) = V(V-a)(1-V)$ and $g(V) = V(1-V)$ [14]. The form of multiplicative noise is chosen so that it preserves the stationary states $V = 0, 1$. Hence, the noise is most important in regions close to the front but vanishes asymptotically at $\xi \pm \infty$. The effective nonlinearity h is also a cubic with

$$h(V) = V(1-V)(a' - k'V), \quad a' = a - \varepsilon C(0), \quad k' = 1 - 2\varepsilon C(0).$$

Thus, from the analysis of the bistable equation in Sect. 2.2, we find that $\bar{c} = (k' - 2a')/\sqrt{2k'}$.

It turns out that if V_0 is chosen to satisfy (2.97) then to leading order, the stochastic variable $\Delta(t)$ undergoes unbiased Brownian motion (a Wiener process):

$$\langle \Delta(t) \rangle = 0, \quad \langle \Delta(t)^2 \rangle = 2D(\varepsilon)t \tag{2.98}$$

with a diffusion coefficient $D(\varepsilon) = \mathscr{O}(\varepsilon)$ (see below). Thus $\Delta(t)$ represents the effects of slow fluctuations, whereas Φ represents the effects of fast fluctuations. Note that since $\Delta(t) = \mathscr{O}(\varepsilon^{1/2})$, (2.96) implies that $V(x,t) = V_0(x-\bar{c}t) + \mathscr{O}(\varepsilon^{1/2})$. Hence, averaging with respect to the noise shows that $\langle V(x,t) \rangle = V_0(x-\bar{c}t) + \mathscr{O}(\varepsilon^{1/2})$. Thus, in the case of weak noise, averaging over many realizations of the stochastic wave front generates a mean front whose speed is approximately equal to $\bar{c}$.

Calculation of diffusion coefficient. Substitute the decomposition (2.96) into (2.92) and expand to first order in $\mathscr{O}(\varepsilon^{1/2})$ (exploiting the fact that the usual rules of calculus apply in the case of Stratonovich noise, see Sect. 1.7):

$$\begin{aligned} &-[\bar{c}+\dot{\Delta}(t)]V_0'(\xi_t) + \varepsilon^{1/2}\left[\partial_t \Phi(\xi_t,t) - [\bar{c}+\dot{\Delta}(t)]\partial_\xi \Phi(\xi_t,t)\right] \\ &\quad = h(V_0(\xi_t) + \varepsilon^{1/2} h'(V_0(\xi_t))\Phi(\xi_t,t) \\ &\quad +\partial_\xi^2 \left[V_0(\xi_t) + \varepsilon^{1/2}\Phi(\xi_t,t)\right] + \varepsilon^{1/2} R(V_0(\xi_t),x,t) + \mathscr{O}(\varepsilon), \end{aligned}$$

where $\xi_t \equiv \xi - \Delta(t)$. Imposing (2.97) and dividing through by $\varepsilon^{1/2}$ then gives

$$\frac{\partial \Phi(\xi,t)}{\partial t} + \mathbb{L}_\xi \Phi(\xi,t) = \varepsilon^{-1/2} V_0'(\xi)\dot{\Delta}(t) + R(V_0(\xi),\xi,t) + \mathscr{O}(\varepsilon^{1/2}), \tag{2.99}$$

where $\mathbb{L}_\xi$ is the non-self-adjoint linear operator

$$\mathbb{L}_\xi A(\xi) = A''(\xi) + \bar{c}A'(\xi) + h'(V_0(\xi))A(\xi) \tag{2.100}$$

for any function $A(\xi) \in L^2(\mathbb{R})$. We have also made the approximation $\xi_t \approx \xi$, since $\Delta(t) = \mathscr{O}(\varepsilon^{1/2})$. The linear differential operator $\mathbb{L}_\xi$ has a zero eigenvalue with associated eigenfunction $V_0'(\xi)$, which can be seen by differentiating (2.97) with respect to ξ, and reflects the fact that the underlying system is equivariant with respect to uniform translations. We then have the solvability condition for the existence of a bounded solution of (2.99), namely, that the inhomogeneous part on the right-hand side is orthogonal to all elements of the null-space of the adjoint operator $\mathbb{L}_\xi^\dagger$. The latter is defined with respect to the inner product

$$\int_{-\infty}^{\infty} B(\xi)\mathbb{L}_\xi A(\xi) d\xi = \int_{-\infty}^{\infty} \left[\mathbb{L}_\xi^\dagger B(\xi)\right] A(\xi) d\xi \tag{2.101}$$

where $A(\xi)$ and $B(\xi)$ are arbitrary integrable functions. Hence,

$$\mathbb{L}_\xi^\dagger B(\xi) = B''(\xi') - \bar{c}B'(\xi) + h'(V_0(\xi))B(\xi). \tag{2.102}$$

The linear operator $\mathbb{L}^\dagger$ also has a zero eigenvalue, with corresponding eigenfunction $\mathscr{V}(\xi) = \mathrm{e}^{\bar{c}\xi}V_0'(\xi)$. Thus taking the inner product of both sides of (2.99) with respect to $\mathscr{V}(\xi)$ leads to the solvability condition

$$\int_{-\infty}^{\infty} \mathscr{V}(\xi)\left[V_0'(\xi)\dot{\Delta}(t) + \varepsilon^{1/2} R(V_0,\xi,t)\right] d\xi = 0, \tag{2.103}$$

which implies that $\Delta(t)$ satisfies the stochastic differential equation (SDE)

$$d\Delta(t) = -\varepsilon^{1/2} \frac{\int_{-\infty}^{\infty} \mathscr{V}(\xi) dR(V_0, \xi, t) d\xi}{\int_{-\infty}^{\infty} \mathscr{V}(\xi) V_0'(\xi) d\xi}. \tag{2.104}$$

Using the lowest-order approximation $dR(V_0, \xi, t) = g(V_0(\xi))dW(\xi, t)$, we deduce that (for $\Delta(0) = 0$) $\Delta(t)$ is a Wiener process with diffusion coefficient

$$D(\varepsilon) = \varepsilon \frac{\int_{-\infty}^{\infty} \int_{-\infty}^{\infty} \mathscr{V}(\xi) \mathscr{V}(\xi') g(V_0(\xi)) g(V_0(\xi')) C([\xi - \xi']/\lambda) d\xi d\xi'}{\left[\int_{-\infty}^{\infty} \mathscr{V}(\xi) V_0'(\xi) d\xi \right]^2}. \tag{2.105}$$

Although the above analysis is based on a formal perturbation calculation, rather than rigorous analysis, it does appear to capture well the effects of weak external noise on front propagation in a variety of reaction–diffusion models [486, 546]. In Sect. 7.4, we will show how the method can be extended to study stochastic traveling waves in nonlocal neural field equations, which represent large-scale continuum models of spatially structured neural networks. Note, however, that one class of front solution where the method breaks down is a so-called pulled front, which propagates into an unstable rather than a metastable state and whose dynamics is dominated by the linear spreading of small perturbations within the leading edge of the front [544]. One well-known reaction–diffusion model that supports pulled fronts is the Fisher–KPP equation [191, 345]. As we will describe later, pulled fronts also arise in a PDE model of CaMKII translocation waves along spiny dendrites [72, 161] (Sect. 3.2), in certain neural field models (Sect. 7.4), and in a model of protein aggregation (Sect. 9.6).

2.7 Appendix: Linear Differential Operators

Throughout this book, we will encounter linear operators acting on some function space. As already demonstrated in this chapter, linear differential operators arise when analyzing the stability of a traveling wave solution of some PDE, or when carrying out a formal perturbation expansion. In this appendix, we summarize some of the basic results regarding linear differential operators acting on a function space, viewed from the perspective of a linear map acting on an infinite-dimensional vector space. For simplicity, we will restrict ourselves to real-valued functions $f : \mathbb{R} \to \mathbb{R}$, although it is straightforward to generalize the results to complex-valued functions.

2.7.1 Function Spaces

Consider the set of all real functions $f(x)$ on the interval $[a, b]$. This is a vector space over the set of real numbers: given two functions $f_1(x), f_2(x)$ and two real

numbers a_1, a_2, we can form the sum $f(x) = a_1 f_1(x) + a_2 f_2(x)$ such that $f(x)$ is also a function on $[a,b]$. Either on physical grounds or for mathematical convenience, we usually restrict ourselves to a subspace of functions that are differentiable to some given order. For example, the space of functions on $[a,b]$ with n continuous derivatives is denoted by $C^n[a,b]$, and the space of analytic functions (those whose Taylor expansion converges to the given function) is denoted by $C^\omega[a,b]$.

In order to describe the convergence of a sequence of functions $f_n, n = 1,2,\ldots$ to a limit function f, we need to introduce the concept of a *norm*, which is a generalization of the usual measure of the length of a finite-dimensional vector. The norm $\|f\|$ of a function f is a real number with the following properties:

(i) Positivity: $\|f\| \geq 0$, and $\|f\| = 0$ if and only if $f = 0$
(ii) The triangle inequality: $\|f+g\| \leq \|f\| + \|g\|$
(iii) Linearity: $\|\lambda f\| = |\lambda| \|f\|$ for $\lambda \in \mathbb{R}$

Common examples of norms are the "sup" norm

$$\|f\|_\infty = \sup_{x\in[a,b]} |f(x)|,$$

and the L^p norm

$$\|f\|_p = \left(\int_a^b |f(x)|^p dx \right)^{1/p}.$$

Given the L^p norm, we can introduce another important function space $L^p[a,b]$, which is the space of real-valued functions on $[a,b]$ for which $\|f\|_p < \infty$. However, there is one subtlety here, namely, that it is possible for $\|f\| = 0$ without f being identically zero. For example, f may vanish at all but a finite set of points (set of measure zero). This violates the positivity property of a norm. Therefore, one should really treat elements of $L^p[a,b]$ as equivalence classes of functions, where functions differing on a set of measure zero are identified.

Given a normed function space, convergence of a sequence $f_n \to f$ can be expressed as

$$\lim_{n\to\infty} \|f_n - f\| = 0.$$

In the case of the "sup" norm, f_n is said to converge *uniformly* to f, whereas for the L^1 norm, it is said to converge *in the mean*. An important property of a function space is that of being *complete*. First, consider the following definition of a *Cauchy sequence*: A sequence f_n in a normed vector space is Cauchy if for any $\varepsilon > 0$, we can find an integer N such that $n, m > N$ implies that $\|f_m - f_n\| < \varepsilon$. In other words, elements of the sequence become arbitrarily close together as $n \to \infty$. A normed vector space is then *complete* with respect to its norm if every Cauchy sequence converges to some element in the space. A complete normed vector space is called a Banach space $\mathscr{B}$. In many applications, the norm of the function space is taken to be the so-called natural norm obtained from an underlying *inner product*. For example, if we define an inner product for $L^2[a,b]$ according to

$$\langle f,g\rangle = \int_a^b f(x)g(x)dx,$$

then the $L^2[a,b]$ norm can be written as

$$\|f\|_2 = \sqrt{\langle f,f\rangle}.$$

A Banach space with an inner product is called a *Hilbert space* $\mathscr{H}$.

2.7.2 Fredholm Alternative Theorem

In the case of one-dimensional traveling wave solutions, it is more natural to consider functions on the real line $\mathbb{R}$ rather than a finite interval. Suppose that $\mathbb{L}$ is a linear differential operator acting on a subspace of $L^2(\mathbb{R})$, which we denote by the domain $\mathscr{D}(\mathbb{L})$. Linearity of the operator means that for $f_1, f_2 \in \mathscr{D}(\mathbb{L})$ and $a_1, a_2 \in \mathbb{R}$,

$$\mathbb{L}(a_1 f_1 + a_2 f_2) = a_1 \mathbb{L} f_1 + a_2 \mathbb{L} f_2.$$

Given the standard inner product on $L^2(\mathbb{R})$, we define the adjoint linear operator $\mathbb{L}^\dagger$ according to

$$\langle f, \mathbb{L} g\rangle = \langle \mathbb{L}^\dagger f, g\rangle, \quad f,g \in \mathscr{D}(L).$$

The operator is said to be self-adjoint if $\mathbb{L}^\dagger = \mathbb{L}$. Note that, in practice, one determines $\mathbb{L}^\dagger$ using integration by parts. For functions defined on finite intervals, this generates boundary terms that only vanish if appropriate boundary conditions are imposed. In general, this can result in different domains for $\mathbb{L}$ and $\mathbb{L}^\dagger$. Therefore, the condition for self-adjointness becomes $\mathbb{L} = \mathbb{L}^\dagger$ and $\mathscr{D}(\mathbb{L}) = \mathscr{D}(\mathbb{L}^\dagger)$. Given a differential operator $\mathbb{L}$ on $L^2(\mathbb{R})$, we can now state the *Fredholm alternative theorem*: The inhomogeneous equation

$$\mathbb{L} f = h$$

has a solution if and only if

$$\langle h, v\rangle = 0 \quad \text{for all v satisfying} \quad \mathbb{L}^\dagger v = 0.$$

2.7.3 Spectrum of a Linear Differential Operator

Let $\mathscr{B}$ be a Banach space and $\mathbb{L} : \mathscr{D}(\mathbb{L}) \to \mathscr{B}$ be a linear operator with domain $\mathscr{D}(\mathbb{L}) \subseteq \mathscr{B}$. For any complex number λ, introduce the new operator

$$\mathbb{L}_\lambda = \mathbb{L} - \lambda \mathbb{I},$$

where $\mathbb{I}$ is the identity operator on $\mathscr{B}$. If $\mathbb{L}_\lambda$ has an inverse, then $R_\lambda(\mathbb{L}) = \mathbb{L}_\lambda^{-1}$ is called the resolvent of $\mathbb{L}$. Given these definitions, λ is said to be a regular point for $\mathbb{L}$ if the following hold:

(i) R_λ exists.
(ii) R_λ is bounded.
(iii) R_λ is defined on a dense subset of $\mathscr{B}$.

The spectrum $\sigma(\mathbb{L})$ is then the set of points that are not regular, which generally consists of three disjoint parts:

(a) The *point spectrum* of eigenvalues is the set of values of λ for which R_λ does not exist.
(b) The *continuous spectrum* is the set of values of λ for which R_λ exists but is unbounded.
(c) The *residual spectrum* is the set of values of λ for which R_λ exists, is bounded, but is not defined on a dense subset of $\mathscr{B}$.

The continuous spectrum and residual spectrum are contained in the essential spectrum, which is any point in $\sigma(\mathbb{L})$ that is not an isolated eigenvalue of finite multiplicity.

We will illustrate how to calculate the essential spectrum of a simple linear operator acting on $\mathscr{B} = L^2(\mathbb{R})$ [242]:

$$\mathbb{L}u = u_{xx} + pu_x - qu \tag{2.106}$$

for constant positive coefficients p, q and $\mathscr{D}(\mathbb{L}) = \{u : u \in L^2(\mathbb{R}), \mathbb{L}u \in L^2(\mathbb{R})\}$. Firstly, suppose that $\mathbb{L}_\lambda$ is not invertible for some λ. This means that there exists $\phi \in \mathscr{B}$ such that $\mathbb{L}_\lambda \phi = 0$. The latter equation is a linear second-order ODE with constant coefficients and thus has solutions of the form $e^{\nu_\pm x}$ with $\nu_\pm$, the roots of the characteristic polynomial $\nu^2 + p\nu - (q+\lambda) = 0$. Such a solution cannot decay at both $x = \pm\infty$ and so does not belong to $\mathscr{B}$. It follows that $\mathbb{L}$ has no eigenvalues and the resolvent R_λ exists. We can then represent R_λ in terms of the Green's function G defined according to $\mathbb{L}_\lambda^\dagger G(x-x') = \delta(x-x')$, where $\mathbb{L}^\dagger$ is the adjoint of $\mathbb{L}$ with respect to the standard inner product on $L^2(\mathbb{R})$:

$$\mathbb{L}_\lambda^\dagger u = u_{xx} - pu_x - (q+\lambda)u.$$

For any $h \in \mathscr{D}(R_\lambda) \subseteq \mathscr{B}$ we can express the solution $u = R_\lambda h$ to the inhomogeneous equation $\mathbb{L}_\lambda u = h$ as

$$u(x) = \int_{-\infty}^{\infty} h(y)G(y-x)dy.$$

For constant coefficients, the Green's function can be solved explicitly according to

$$G(y) = \begin{cases} \alpha e^{\mu_+ y} & y \le 0 \\ \alpha e^{\mu_- y} & y \ge 0, \end{cases}$$

where $\mu_\pm$ are the roots of the characteristic polynomial

$$P(\mu) = \mu^2 - p\mu - (\lambda + q),$$

and α is chosen such that $-1 = \alpha(\mu_+ - \mu_-)$.

If $P(\mu)$ has one root μ_+ with positive real part and one root μ_- with negative real part, then clearly $G \in L_1(\mathbb{R})$ so that R_λ is bounded with dense domain equal to $\mathscr{B}$. This situation holds, for example, when λ is real and $\lambda > -p$. The roots of $P(\mu)$ vary continuously with λ in the complex plane. Hence, the boundedness of R_λ will break down when one of the roots crosses the imaginary axis at ik, say, with $\lambda = -q - k^2 - ika$. This is a parabola in the complex λ plane (λ_r, λ_i) given by $\lambda_r = -q - \lambda_i^2/p^2$. If λ_r is to the right of this parabola,

$$\lambda_r > -q - \frac{\lambda_i^2}{p^2},$$

then $P(\mu)$ has a root on either side of the imaginary axis and R_λ is bounded. We conclude that the essential spectrum lies to the left of the parabola,

$$\sigma(\mathbb{L}) \subseteq \{\lambda : \mathrm{Re}(\lambda) \leq -q - \mathrm{Im}(\lambda)^2/p^2\}. \tag{2.107}$$

It can be shown that the essential spectrum includes the parabola itself. It immediately follows that the essential spectrum lies in the left-half complex plane if $q > 0$.

In Sect. 2.4, we considered the linear stability of a traveling front, which required finding the spectrum of a second-order linear operator with nonconstant coefficients; see (2.42). It turns out that one can generalize the above analysis to an operator with x-dependent coefficients $p(x), q(x)$. Suppose that $p(x), q(x) \to p_\pm, q_\pm$ as $x \to \pm\infty$. Introduce the parabolas

$$S_\pm = \{\lambda : \lambda = -q_\pm - k^2 - ikp_\pm\}. \tag{2.108}$$

Let A denote the union of the regions to the left of the curves $S_\pm$ that includes the curves themselves. Then the essential spectrum of $\mathbb{L}$ lies in A and includes $S_\pm$.

Chapter 3
Wave Propagation Along Spiny Dendrites

The majority of excitatory synapses that occur in the cerebral cortex are located on tiny specialized protoplasmic protuberances called dendritic *spines* [607]; see Fig. 3.1. They typically occupy 20–70 % of the total dendritic membrane. Since the input impedance of a spine head is typically large, a small excitatory synaptic current can produce a large local depolarization. Moreover, the thin stem neck connecting the spine to the main body of the dendrite provides an axial resistance that partially decouples the spine-head dynamics from the dendritic tree. Hence, it has long been theorized that the dendritic spine is a favorable site for the initiation of an action potential [427, 572] and is thus a possible substrate for local computations [571]. Modeling studies also suggest that if the heads of dendritic spines have excitable membrane properties, then the spread of current from one spine along the dendrites could bring adjacent spines to their thresholds for impulse generation. The result would be a sequence of spine-head action potentials, representing a saltatory propagating wave in the distal dendritic branches [19, 129]. Calcium-imaging experiments provide strong evidence that the spine heads are endowed with voltage-dependent Na^+ and Ca^{2+} channels that can indeed support an all-or-nothing response to an excitatory synaptic input [694].

Early theoretical studies of spines also considered their potential role in synaptic plasticity and Hebbian learning. This was motivated by the idea that small changes in spine morphology, such as changes in the width of the spine neck, could lead to large changes in the amplitude of response to excitatory synaptic inputs on to the spine. It is now known that spines are rich in actin filaments, which have the capacity to drive such changes in spine shape [413]. Moreover, there is increasing experimental evidence that the growth and removal of spines provides an important substrate for structural changes during brain development [410, 480, 693]. It is less clear whether changes in spine morphology play a significant role in adult plasticity. Nevertheless, the basic geometry of a spine does provide an isolated biochemical microenvironment for Ca^{2+} to accumulate, and Ca^{2+} is thought to be a major chemical signal for the induction of synaptic plasticity [343, 462]. The dynamics of calcium diffusion in dendritic spines has been explored in a number of computational models [202, 283].

P.C. Bressloff, *Waves in Neural Media: From Single Neurons to Neural Fields*,
Lecture Notes on Mathematical Modelling in the Life Sciences,
DOI 10.1007/978-1-4614-8866-8_3,

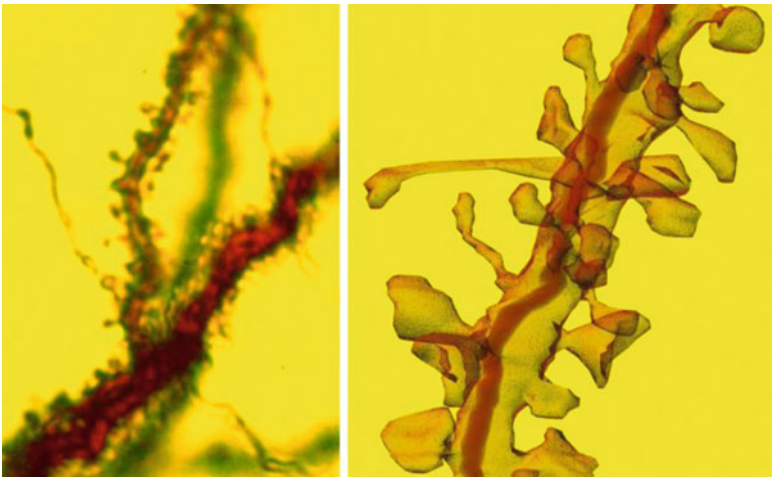

Fig. 3.1 An example of a piece of spine-studded dendritic tissue (from rat hippocampal region CA1 stratum radiatum). Magnified view on right-hand side shows a dendrite $\sim 5\,\mu$m in length. Taken with permission from SynapseWeb, Kristen M. Harris, PI, http://synapses.clm.utexas.edu/

Another important signaling molecule involved in the induction of synaptic plasticity is Ca^{2+}–calmodulin-dependent protein kinase II (CaMKII) [295, 386]. CaMKII is also found to be abundant within dendritic spines, where it can detect changes in the local levels of Ca^{2+} entering the synapse following plasticity-inducing stimuli, via binding of CaMKII to Ca^{2+}/CaM. Confinement of CaMKII within spines arises from the geometry of the spine and through interactions with protein receptors and cytoskeletal elements within the postsynaptic density (PSD), which is the protein-rich region at the tip of the spine head. Activated CaMKII phosphorylates substrates responsible for the expression of synaptic plasticity, namely, the number and the conductivity of synaptic AMPA receptors [151, 370]. Moreover, once activated, CaMKII can transition into a Ca^{2+}/CaM-independent, hyperactivated state via the autophosphorylation of neighboring enzymatic subunits and thus continue to phosphorylate its substrates even after the plasticity-inducing Ca^{2+} signal has ended [261, 427, 547, 689]. Experimentally, translocation of CaMKII into spines can be induced in a local region of dendrite by exposing it to a puff of glutamate, and this can initiate a wave of CaMKII translocation that spreads towards the distal end of the dendrite with an average speed of $\sim 1\,\mu$m/s [532]. It is found that the wave is preceded by a much faster Ca^{2+}-mediated spike that propagates along the dendrite (see above), which could provide a mechanism for priming CaMKII outside the stimulus region for diffusion-based activation. Moreover, the CaMKII translocation wave is associated with an increase in AMPA receptor numbers at both stimulated and nonstimulated synapses [532]. This suggests that it could provide a possible molecular substrate for heterosynaptic plasticity.

In this chapter we consider two mathematical models of wave propagation along spiny dendrites: (I) a spike–diffuse–spike model of spine-mediated spikes [129, 139] and (II) a reaction–diffusion model of CaMKII translocation waves [72, 161]. The former model introduces methods for analyzing solitary waves propagating in spiking networks; see also Sect. 5.4. The latter model turns out to be identical in form to the diffusive SI model introduced by Noble [464] to explain the spread of bubonic plague through Europe in the fourteenth century. This, in turn, is a generalization of the scalar Fisher–KPP equation [191, 345] which was originally introduced to model the invasion of a gene into a population. One characteristic feature of such equations is that they support traveling fronts propagating into an unstable steady state, in which the wave speed and longtime asymptotics are determined by the dynamics in the leading edge of the wave—so-called pulled fronts [544]. In particular, a sufficiently localized initial perturbation will asymptotically approach the traveling front solution that has the minimum possible wave speed. Hence, pulled fronts have very different properties from those found for the bistable equation in Sect. 2.2. Another important topic raised by these models is how to use homogenization methods to approximate the discrete distribution of spines by a smooth distribution.

3.1 Solitary Waves in a Spike–Diffuse–Spike Model of Active Spines

The first theoretical study of active wave propagation along a dendritic cable that is mediated by dendritic spines was carried out by Baer and Rinzel [19]. They considered a continuum model of a dendritic tree coupled to a distribution of excitable dendritic spines. The active spine-head dynamics is modeled with Hodgkin–Huxley kinetics, while the (distal) dendritic tissue is modeled with the cable equation. The spine head is coupled to the cable via a spine-stem resistance that delivers a current proportional to the number of spines at the contact point. There is no direct coupling between neighboring spines; voltage spread along the cable is the only way for spines to interact. Numerical studies of the Baer–Rinzel model [19] show both smooth and saltatory traveling wave solutions, the former arising in the case of uniform spine distributions and the latter when spines are clustered in groups. The saltatory nature of a propagating wave may be directly attributed to the fact that active spine clusters are physically separated. In this section we describe an alternative, analytically tractable treatment of saltatory waves based on the so-called spike–diffuse–spike (SDS) model of active dendritic spines [129, 138, 624, 625], which reduces the spine-head dynamics to an all-or-nothing action potential response.

In order to formulate the model, we first consider a continuum of spines with $\rho(x)$ representing the spine density per unit length along a uniform, passive dendritic cable. Denoting the voltage at position x on the cable at time t by $V = V(x,t)$, the associated cable equation is given by (see Sect. 1.4)

$$\frac{\partial V}{\partial t} = -\frac{V}{\tau_m} + D_m \frac{\partial^2 V}{\partial x^2} + \rho(x)\frac{a-V}{C_m r_s}, \tag{3.1}$$

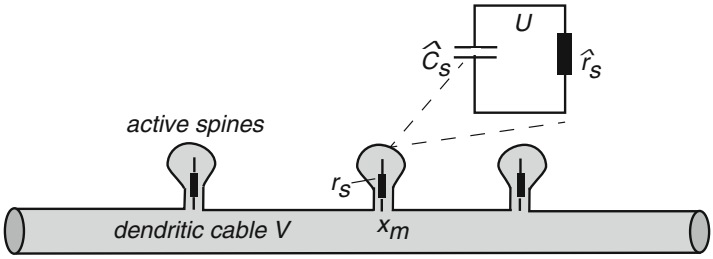

Fig. 3.2 Schematic diagram of a dendritic cable with active spines

where $D_m = \lambda_m^2/\tau_m$ with τ_m and λ_m the membrane time and space constants of the cable, C_m is the membrane capacitance per unit length, and r_s is the spine-stem resistance of an individual spine. In the SDS model, the function $a(x,t)$ represents the sequence of action potentials generated in the spine head at x whenever the associated subthreshold spine-head potential $U(x,t)$, driven by current from the shaft, crosses some threshold h. Given the high resistance of the spine stem, we neglect subthreshold currents into the cable. The voltage U evolves according to the integrate-and-fire (IF) equation (see Sect. 5.3)

$$\hat{C}_s \frac{\partial U}{\partial t} = -\frac{U}{\hat{r}_s} + \frac{V-U}{r_s}, \tag{3.2}$$

such that whenever U crosses the threshold h it is immediately reset to zero. Here $\hat{C}_s$ and $\hat{r}_s$ are the membrane capacitance and resistance of the spine head; see Fig. 3.2. Let $T^j(x)$ denote the jth firing time of the spine head at position x such that $U(x,T^j(x)) = h$. Then

$$a(x,t) = \sum_j \eta(t - T^j(x)), \tag{3.3}$$

with $\eta(t) = 0$ for all $t < 0$. The shape of the action potential is specified by the function $\eta(t)$, which can be fitted to the universal shape of an action potential.

3.1.1 Existence of a Solitary Wave for a Uniform Density

Let us begin by considering the simplest case of a uniform spine density $\rho(x) = \rho_0$ and a rectangular pulse shape of height η_0 and duration τ_d. We define a solitary wave as one that causes the spine head at x to reach threshold only once at the time $t = T(x) \equiv x/c$. We recognize c as the speed of the wave so that $a(x,t) = \eta(t - x/c)$, which suggests adopting a moving coordinate frame $\xi = ct - x$. Equation (3.1) becomes

$$D_m V_{\xi\xi}(\xi) - cV_\xi(\xi) - (\tau_m^{-1} + \beta)V(\xi) = -\beta a(\xi/c), \tag{3.4}$$

where $\beta = \rho_0/(C_m r_s)$, and

$$a(\xi) = \begin{cases} 0 & -\infty < \xi < 0 \\ \eta_0 & 0 < \xi < c\tau_d \\ 0 & \xi > c\tau_d. \end{cases} \tag{3.5}$$

If one is looking for traveling pulses which satisfy $\lim_{\xi\to\pm\infty} V(\xi) = 0$, then the solution to (3.4) takes the form

$$V(\xi) = \begin{cases} \alpha_1 \exp(m_+\xi), & -\infty < \xi < 0 \\ \alpha_2 \exp(m_+\xi) + \alpha_3 \exp(m_-\xi) + \frac{\beta\eta_0}{\tau_m^{-1}+\beta}, & 0 < \xi < c\tau_d \\ \alpha_4 \exp(m_-\xi), & \xi > c\tau_d \end{cases} \tag{3.6}$$

with

$$m_\pm = \frac{c \pm \sqrt{c^2 + 4D_m(\tau_m^{-1}+\beta)}}{2D_m}. \tag{3.7}$$

By ensuring the continuity of the solution and its first derivative at $\xi = 0$ and $\xi = c\tau_d$ one may solve for the unknowns $\alpha_1 \ldots \alpha_4$ as

$$\alpha_1 = \alpha_3 \frac{m_-}{m_+}[1 - \exp(-m_+ c\tau_d)], \tag{3.8}$$

$$\alpha_2 = -\alpha_3 \frac{m_-}{m_+} \exp(-m_+ c\tau_d), \tag{3.9}$$

$$\alpha_3 = \frac{\beta\eta_0}{\tau_m^{-1}+\beta} \frac{m_+}{(m_- - m_+)}, \tag{3.10}$$

$$\alpha_4 = \alpha_3[1 - \exp(-m_- c\tau_d)]. \tag{3.11}$$

As yet the speed of the pulse is undetermined. However, by demanding that the IF process in the spine head reaches threshold at $\xi = 0$ and that $\lim_{\xi\to\pm\infty} U(\xi) = 0$, one can determine a self-consistent value for the speed of the traveling wave along similar lines to the analysis of solitary waves in one-dimensional networks of IF neurons [62, 63, 167]; see Sect. 5.4. In the traveling coordinate frame, (3.2) becomes

$$c\hat{C}_s U_\xi = -g_s U + \frac{V}{r_s} \tag{3.12}$$

with $U(0) = h$ and $g_s = r_s^{-1} + \hat{r}_s^{-1}$. This first-order system may be solved as

$$U(\xi) = \exp(-\xi/[c\hat{\tau}]) \left[h - \frac{1}{c\hat{C}_s r_s} \int_\xi^0 V(\xi') \exp(\xi'/[c\hat{\tau}]) d\xi' \right], \tag{3.13}$$

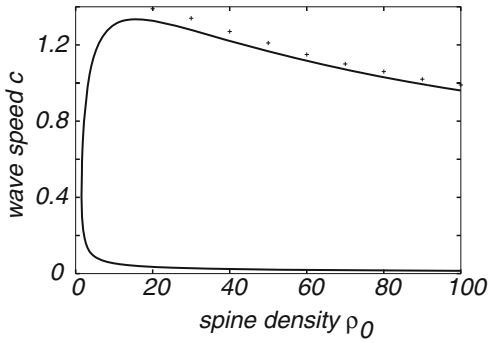

Fig. 3.3 Speed of a traveling pulse as a function of uniform spine density ρ_0 for $\tau_m = D_m = 1$, $h = 2.5$, $r_s = 2$, $\widehat{r_s} = 0.8$, $\hat{C}_s = 1$, $C_m = 1$, $\tau_d = 2$, $\eta_0 = 100$. The crosses show the results of a direct numerical simulation of the SDS model with $N = 200$ discrete spines uniformly distributed along a cable of length $L = 10$

where $\hat{\tau} = \hat{C}_s/g_s$. In order for this to be bounded as $\xi \to -\infty$, the term inside the large parentheses must vanish as $\xi \to -\infty$. This yields the dispersion relationship for the speed of the pulse as a function of system parameters:

$$h = \frac{1}{\hat{C}_s r_s} \frac{\alpha_1}{\hat{\tau}^{-1} + cm_+} \tag{3.14}$$

In Fig. 3.3 we plot dispersion curves for the speed c of a traveling pulse as a function of the spine density ρ_0, which are obtained by numerically solving (3.14). Note that there are two solution branches for a given density ρ_0. Direct simulations suggest that it is the upper (faster) branch that is stable, which can be confirmed analytically using linear stability analysis (see below). Figure 3.3 also shows that for a wide range of ρ_0 the speed of the stable wave is approximately λ_m/τ_m in physical units, in agreement with the original observations of Baer and Rinzel [19].

One useful feature of the SDS model is that it yields an exact expression for the speed of the wave that can easily be solved to obtain the dependence in terms of other system parameters such as the spine-stem resistance. Hence, one can find the minimum spine density capable of supporting a traveling pulse as well as extract information about how the speed decays as a function of spine density. In Fig. 3.4(a) we plot the speed of a traveling pulse as a function of the spine-stem resistance r_s. It is clear that for realistic choices of the biophysical parameters in the model, that propagation failure can occur for too large a choice of the spine-stem resistance. Moreover, for small r_s, the speed of a stable pulse is very sensitive to r_s, demonstrating that a modifiable value of the spine-stem resistance could have important ramifications for neural processing. Finally in Fig. 3.4(b) we show the dependence of the wave speed on the width, τ_d, of a rectangular pulse generated in the spine head. Interestingly, for a fixed pulse height, there is a minimum duration time below which propagation cannot occur. This highlights the fact that it is crucial to model the shape of an action potential in the reduced IF model with biologically realistic

choices for the amplitude and duration of the spine-head pulse. For large values of τ_d the speed of the wave approaches a constant value (i.e., the speed of the wave becomes insensitive to the precise choice of τ_d).

3.1.2 Linear Stability Analysis

For the purposes of linear stability analysis it is more convenient to work in terms of the original variables (x,t) rather than in the moving frame. Since the shape of the traveling pulse is fixed by the function $\eta(t)$, it is natural to consider local perturbations of the firing times given by $T(x) = x/c + \Delta(x)$. A similar approach is used to analyze the stability of traveling waves in IF networks with synaptic and passive dendritic interactions [62, 63]; see Sect. 5.4. The membrane potential $V(x,t)$ satisfying (3.1) with $a(t) = \eta(t - T(x))$ can be evaluated in terms of the Green's function G_0 for the infinite cable equation. That is, setting $C_m = 1$ and taking $\tau_m \gg \rho_0/r_s$,

$$V(x,t) = \frac{\rho_0}{r_s} \int_{-\infty}^{t} \left[\int_{-\infty}^{\infty} G_0(x-y, t-s)\eta(s - T(y))dy \right] ds \tag{3.15}$$

with G_0 given by (1.59). If we now demand that the IF process (3.2) driven by the potential $V(x,t)$ reaches threshold at time $T(x)$, then we obtain the following self-consistency condition for a traveling pulse (with $\hat{C}_s = 1$):

$$h = U(x, T(x)) = \frac{1}{r_s} \int_{-\infty}^{0} \mathrm{e}^{t/\hat{\tau}} V(x, t + T(x))dt. \tag{3.16}$$

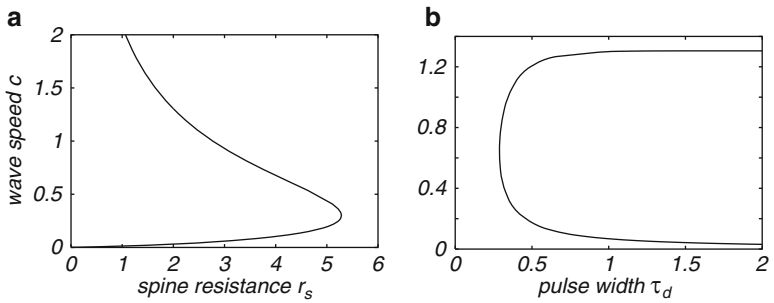

Fig. 3.4 (**a**) Speed of a traveling pulse as a function of spine-stem resistance r_s with $\rho_0 = 25$ and $\tau_d = 2$. (**b**) Speed of a traveling pulse as a function of pulse width τ_d with $\rho_0 = 25$ and $r_s = 2$. All other parameters are as Fig. 3.3. Note that for sufficiently large r_s or small τ_d solitary waves cannot propagate

We now expand (3.15) and (3.16) in powers of the perturbation $\Delta(x)$. The zeroth-order term generates the self-consistency condition for the speed c of the unperturbed traveling pulse:

$$h = \frac{1}{r_s}\int_{-\infty}^{0} e^{t/\hat{\tau}}\,\overline{V}(x,t+x/c)dt, \tag{3.17}$$

where

$$\overline{V}(x,t) = \frac{\rho_0}{r_s}\int_{-\infty}^{t}\left[\int_{-\infty}^{\infty} G_0(x-y,t-s)\eta(s-y/c)dy\right]ds. \tag{3.18}$$

We can evaluate (3.18) using Fourier transforms without needing to restrict η to be a rectangular pulse. That is, expand $\eta(s)$ as

$$\eta(t) = \int_{-\infty}^{\infty} e^{i\omega t}\tilde{\eta}(\omega)\frac{d\omega}{2\pi}, \tag{3.19}$$

and then perform the integrations over y and s with

$$\int_{-\infty}^{\infty} e^{-ikx}G_0(x,t)dx = e^{-\varepsilon(k)t}, \quad \varepsilon(k) = \tau_m^{-1} + D_m k^2, \tag{3.20}$$

to obtain

$$\overline{V}(x,t) = \frac{\rho_0}{r_s}\int_{-\infty}^{\infty} e^{i\omega(t-x/c)}\frac{\tilde{\eta}(\omega)}{\varepsilon(\omega/c)+i\omega}\frac{d\omega}{2\pi}. \tag{3.21}$$

Substitution of (3.21) into (3.17) finally gives

$$h = \frac{\rho_0}{r_s^2}\int_{-\infty}^{\infty}\frac{\tilde{\eta}(\omega)}{[\varepsilon(\omega/c)+i\omega][\hat{\tau}^{-1}+i\omega]}\frac{d\omega}{2\pi}. \tag{3.22}$$

When one considers a rectangular pulse shape for the action potential waveform of height η_0 and duration τ_d such that

$$\tilde{\eta}(\omega) = \eta_0\frac{1-e^{-i\omega\tau_d}}{i\omega}, \tag{3.23}$$

then it is a simple matter to check that the dispersion relationship (3.22) reduces to (3.14).

The first-order term in the expansion of (3.16) yields a linear equation for the perturbations $\Delta(x)$ from which the linear stability of the traveling pulse can be deduced. This linear equation takes the form

$$0 = \frac{1}{r_s}\int_{-\infty}^{0} e^{t/\hat{\tau}}\delta_\Delta V(x,t+x/c)dt, \tag{3.24}$$

where (after integration by parts)

$$\delta_\Delta V(x,t) = \frac{\rho_0}{r_s}\int_{-\infty}^{t}\left[\int_{-\infty}^{\infty} G_0(x-y,t-s)\eta'(s-y/c)[\Delta(x)-\Delta(y)]dy\right]ds. \tag{3.25}$$

Equations (3.24) and (3.25) have solutions of the form $\Delta(x) = e^{\lambda x}$ with λ satisfying the characteristic equation

$$I(\lambda) \equiv \int_{-\infty}^{\infty} \frac{ik\tilde{\eta}(\omega)}{[\varepsilon(\omega/c + i\lambda) + i\omega][\hat{\tau}^{-1} + i\omega]} \frac{d\omega}{2\pi} - I(0) = 0. \tag{3.26}$$

Asymptotic stability holds if all nonzero solutions of the characteristic equation have negative real part. (The existence of a solution $\lambda = 0$ reflects the translation invariance of the underlying system; see Sect. 2.4.) Equation (3.26) can be evaluated by closing the contour in the lower-half complex ω-plane. Since $\eta(s) = 0$ for $s < 0$ it follows that any poles of $\tilde{\eta}(\omega)$ lie in the upper-half complex plane so that we only have to consider poles arising from the zeros of the function $\varepsilon(\omega/c + i\lambda) + i\omega$. The latter are given explicitly by $\omega = i\omega_{\pm}(\lambda)$ where

$$\frac{\omega_{\pm}(\lambda)}{c} = -\left(\lambda + \frac{c}{2D_m}\right) \pm \sqrt{R(\lambda)}, \tag{3.27}$$

where

$$R(\lambda) = \frac{c^2}{4D_m^2} + c\lambda/D_m + 1/(D_m\tau_m). \tag{3.28}$$

Let us decompose λ into real and imaginary parts according to $\lambda = \alpha + i\beta$. Then

$$\omega_{\pm}(\lambda) = -u_{\pm}(\alpha,\beta) - iv_{\pm}(\alpha,\beta), \tag{3.29}$$

with

$$\frac{u_{\pm}(\alpha,\beta)}{c} = \alpha + \frac{c}{2D_m} \mp A(\alpha,\beta), \quad \frac{v_{\pm}(\alpha,\beta)}{c} = \beta \mp B(\alpha,\beta), \tag{3.30}$$

and (for $\beta > 0$)

$$A(\alpha,\beta) = \sqrt{\frac{1}{2}\left[R(\alpha) + \sqrt{R(\alpha)^2 + c^2\beta^2/D_m^2}\right]},$$

$$B(\alpha,\beta) = \sqrt{\frac{1}{2}\left[-R(\alpha) + \sqrt{R(\alpha)^2 + c^2\beta^2/D_m^2}\right]}. \tag{3.31}$$

One may now determine the linear stability of a solitary pulse by simultaneously solving $\mathrm{Re}[I(\lambda)] = \mathrm{Re}[I(0)] = 0$ and $\mathrm{Im}[I(\lambda)] = \mathrm{Im}[I(0)] = 0$ for α and β, with c determined by (3.22) (or equivalently (3.14) for the specific case of a rectangular pulse shape). This is illustrated in Fig. 3.5 for a rectangular pulse, which shows solutions with $\beta = 0$ and $\alpha < 0$ along the upper branch of Fig. 3.3. Moreover, α changes sign as it passes through the point where $d\rho_0/dc = 0$ in the (c, ρ_0) plane while moving from the upper solution branch to the lower. Hence, of the two possible traveling

wave solutions, the faster one is stable. Other solutions with $\alpha < 0$ and $\beta > 0$ are also found for both the fast and slow branches but do not affect the above stability argument.

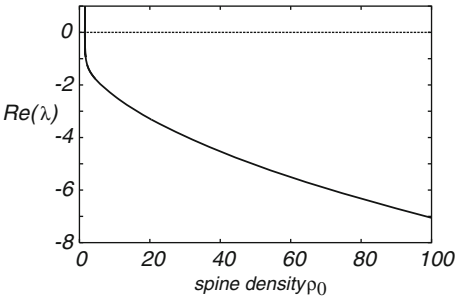

Fig. 3.5 A plot of the eigenvalues arising in the linearization of the SDS model shows that solutions with $\alpha < 0$ and $\beta = 0$ can be found for the branch of solutions with greatest speed. The graph above shows the behavior of $\alpha = \mathrm{Re}(\lambda)$ with $\beta = 0$ for the upper solution branch of Fig. 3.3. Note that $\alpha = 0$ at the point in the (c, ρ) plane at which the speed of the two possible traveling waves becomes equal. For the slower branch one finds that there exists solutions in the (α, β) plane with $\alpha > 0$ indicating that the slower branch is unstable

3.1.3 Discrete Distribution of Spines

So far we have assumed that the spine density is uniform. Although wave propagation failure is known to occur if the spine density is below some critical level, the numerical studies of Baer and Rinzel [19] suggest that propagation may be recovered by redistributing the spines into equally spaced dense clusters. Since interspine distances are of the order of μm and electronic length λ_m is typically measured in mm, we shall consider spine-head voltage at a cluster site to be the local spatial average of membrane potential in adjacent spines. Hence, we consider a discrete distribution of spines for which

$$\rho(x) = \bar{n} \sum_m \delta(x - x_m), \tag{3.32}$$

where x_m is the location of the mth spine cluster and $\bar{n}$ is the number of spines in a cluster. Such a distribution breaks continuous translation symmetry so that saltatory or lurching waves are expected rather than traveling waves of constant profile. (Saltatory waves are also found in myelinated axons; see Sect. 2.5.) We define a saltatory wave as an ordered sequence of firing times $\ldots T_{m-1} < T_m < T_{m+1}$ in which each spine cluster only fires once. Substituting the discrete density (3.32) into (3.1) with

$$\rho(x) a(x,t) = \bar{n} \sum_m \eta(t - T_m) \delta(x - x_m),$$

and making the approximation $\bar{n} \ll r_s$ so that the term $\rho(x)V/r_s$ can be neglected, we obtain the equation (using physical units)

$$\frac{\partial V}{\partial t} = -\frac{V}{\tau_m} + D_m \frac{\partial^2 V}{\partial x^2} + \frac{\bar{n}}{r_s} \sum_n \delta(x - x_n)\eta(t - T_n), \tag{3.33}$$

where we have absorbed a factor of r_m/τ_m into η and $D_m = \lambda_m^2/\tau_m$. This can be solved using the Green's functions G_0 of the cable equation:

$$V(x,t) = \frac{\bar{n}}{r_s} \sum_{m=0}^{\infty} H(x - x_m, t - T_m), \tag{3.34}$$

where we assumed the initial condition $V(x,0) = 0$ for all x.

$$H(x,t) = \int_0^t G_0(x,t-s)\eta(s)ds, \quad G_0(x,t) = \frac{1}{\sqrt{4\pi D_m t}} \mathrm{e}^{-t/\tau_m - x^2/4D_m t}. \tag{3.35}$$

Suppose that the spine clusters are uniformly distributed along the cable such that $x_m = md$, where d is the spacing between clusters. We will derive a condition for the existence of a saltatory wave solution given by $T_m = m\Delta$ for large m. The parameter Δ measures the time between successive threshold crossings at adjacent spine-head clusters such that the speed $c = d/\Delta$. First, using the causality condition $H(x,t) = 0$ for $t < 0$, it follows from (3.34) that

$$V(Nd, N\Delta) = \frac{\bar{n}}{r_s} \sum_{n=1}^{N} H(nd, n\Delta), \tag{3.36}$$

The wave speed of a saltatory wave (if it exists) is then determined self-consistently from the threshold condition

$$h = \lim_{N\to\infty} V(Nd, N\Delta) = \frac{\bar{n}}{r_s} \sum_{n=1}^{\infty} H(nd, n\Delta). \tag{3.37}$$

In order to calculate the wave speed, it is useful to rewrite (3.35) in the form

$$H(x,t) = \int_{-\infty}^{\infty} \frac{dk}{2\pi} \mathrm{e}^{ikx} \mathrm{e}^{-\varepsilon(k)t} \eta(k,t), \tag{3.38}$$

where $\eta(k,t) = \int_0^t \eta(s)\mathrm{e}^{\varepsilon(k)s}ds$. One may then exploit the convolution structure of (3.38) to evaluate it in closed form for a given $\eta(t)$. For the sake of illustration, consider again the rectangular pulse shape η, for which

$$\eta(k,t) = \eta_0(\mathrm{e}^{\varepsilon(k)\min(t,\tau_d)} - 1)/\varepsilon(k),$$

so that $H(x,t) = \eta_0[A(x,t - \min(t,\tau_d)) - A(x,t)]$, with

$$A(x,t) = \int_{-\infty}^{\infty} \frac{dk}{2\pi} \frac{\mathrm{e}^{ikx - \varepsilon(k)t}}{\varepsilon(k)}. \tag{3.39}$$

This is a standard integral given explicitly by

$$A(x,t) = \frac{1}{4}\sqrt{\frac{\tau_m}{D_m}}\left\{ e^{-|x|/\sqrt{\tau_m D_m}} \operatorname{erfc}\left(-\frac{|x|}{\sqrt{4D_m t}} + \sqrt{\frac{t}{\tau_m}} \right) + e^{|x|/\sqrt{\tau_m D_m}} \operatorname{erfc}\left(\frac{|x|}{\sqrt{4D_m t}} + \sqrt{\frac{t}{\tau_m}} \right) \right\}. \tag{3.40}$$

Finally, we may write the threshold condition in the form

$$h = \frac{\overline{n}}{r_s^2} \sum_{m=1}^{\infty} \hat{H}(md, m\Delta), \tag{3.41}$$

where $\hat{H}(x,t) = \eta_0[\hat{A}(x,t-\tau_d) - \hat{A}(x,t)]$, and

$$\hat{A}(x,t) = \int_{-\infty}^{0} e^{s/\hat{\tau}} A(x,t-s)ds. \tag{3.42}$$

The sum in (3.41) can then be performed numerically to obtain the speed of a saltatory wave $c = c(d,h)$.

In Fig. 3.6(a) we plot the speed c as a function of cluster spacing d for fixed threshold h, which shows that if the spine clusters are separated beyond some critical spacing, on the order of the electronic length $\lambda_m = 1$, a saltatory pulse will fail to propagate. Again linear stability analysis establishes that, as in the continuum model, it is the faster of the two branches that is stable. It is also instructive to consider the region in the (d,h) parameter plane where saltatory pulses exist. This may be obtained by continuing the limit point defining propagation failure of a saltatory pulse in the (d,c) plane as a function of h. The resulting phase diagram is shown in Fig. 3.6(b) and establishes that with increasing d the critical threshold for propagation failure decreases. Interestingly, the minimum wave speed of a stable saltatory pulse is found to be relatively insensitive to variation in cluster spacing d and threshold h. Now that the speed of a saltatory pulse has been determined as a function of system parameters it is possible to close the expression for the shape of a solitary pulse given by $V(x,t) = (\overline{n}/r_s)\sum_m H(x-md, t-md/v)$. A plot of this analytical expression is shown in Fig. 3.7, which clearly demonstrates that the saltatory pulse has a nonconstant profile.

Finally, note that there have been a number of recent extensions of the spike–diffuse–spike model. These include taking into account the branching structure of the dendritic tree [625], in which the Green's function G_0 is replaced by the Green's function of the tree, and incorporating active processes within the dendritic cable. In the latter case, each infinitesimal cable compartment is modeled as a quasi-linear LRC circuit, where the membrane resistance r_m is in series with an inductance L [624]; see Fig. 1.11. It should also be pointed out that from a mathematical perspective, the spike–diffuse–spike model is very similar in structure to the fire–diffuse–fire model of calcium puffs; see Sect. 4.3.

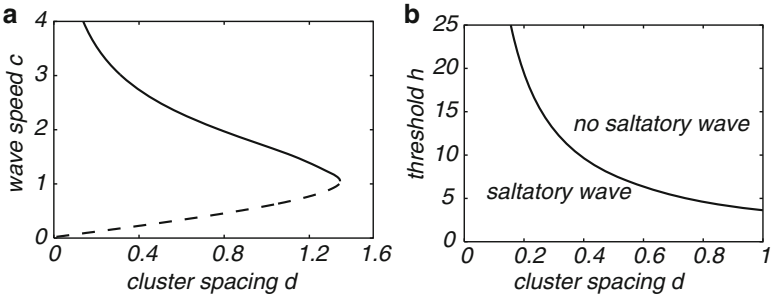

Fig. 3.6 (**a**) Plot of wave speed c for a saltatory pulse as a function of cluster spacing d. Here, $\hat{\tau} = \tau_d = 1$, $h = 2.5$, $r_s = 2$, $\eta_0 = 100$, and $\bar{n} = 2$. The upper (lower) branch is stable (unstable). (**b**) Continuation of the limit point in (**a**) showing the region in the (d,h)-plane where stable saltatory traveling waves exist

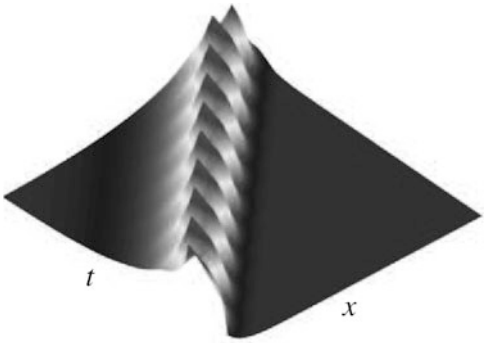

Fig. 3.7 Plot of the analytically obtained saltatory solution $V(x,t)$ in the dendritic cable with parameters as in Fig. 3.6 and $d = 1$. The x axis covers 10 lattice sites and the t axis $10d/c$

3.2 Reaction–Diffusion Model of CaMKII Translocation Waves

As we indicated at the beginning of this chapter, CaMKII (Ca^{2+}–calmodulin-dependent protein kinase II) is a key regulator of glutamatergic synapses and plays an essential role in many forms of synaptic plasticity. It has recently been observed experimentally that chemically stimulating a local region of dendrite not only induces the local translocation of CaMKII from the dendritic shaft to synaptic targets within spines, but also initiates a wave of CaMKII translocation that spreads distally through the dendrite with an average speed of order 1 μm/s [532]. In Fig. 3.8, we provide a cartoon of the mechanism for translocation waves hypothesized by Rose et al. [532]. Before local stimulation using a glutamate/glycine puff, the majority of CaMKII is in an inactive state and distributed uniformly throughout the dendrite. Upon stimulation, all CaMKII in the region of the puff (∼30 μm of dendrite) is converted to an active state, probably the autonomous state of CaMKII (see Fig. 3.8a), and begins translocating into spines. Simultaneously, a Ca^{2+} spike is

initiated and rapidly travels the length of the dendrite (as modeled in Sect. 3.1), causing CaMKII to bind Ca^{2+}/CaM along the way. In this primed or partially phosphorylated state, CaMKII does not yet translocate into spines. In the meantime, a portion of the activated CaMKII from the stimulated region diffuses into the region of primed CaMKII and the two types interact, with the result that primed CaMKII is activated. Some of these newly activated holoenzymes translocate into spines while others diffuse into more distal regions of the dendrite containing primed CaMKII, and the wave proceeds in this fashion. In certain cases one also finds a second wave propagating proximally from the stimulated site to the soma [532]. A schematic diagram illustrating the progression of a translocation wave along a dendrite following the rapid priming phase is shown in Fig. 3.8b.

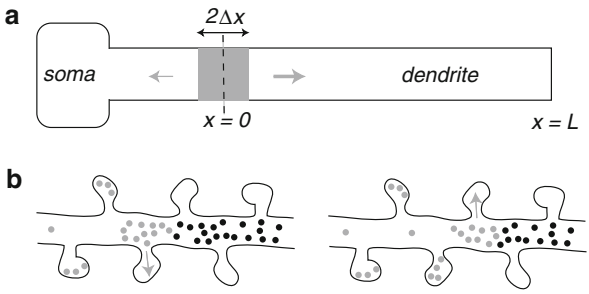

Fig. 3.8 Proposed mechanism of CaMKII translocation waves. (**a**) A glutamate/glycine puff activates CaMKII locally and initiates a fast Ca^{2+} spike that propagates distally (*indicated by larger horizontal arrow*) and primes CaMKII in the remainder of the dendrite. In certain cases one also finds a second wave propagating proximally from the stimulated site to the soma (*indicated by smaller horizontal arrow*). (**b**) Activated CaMKII (*gray dots*) both translocates into spines and diffuses into distal regions of the dendrite where it activates primed CaMKII (*black dots*). The net effect is a wave of translocated CaMKII propagating along the dendrite

A simple mathematical model of the above mechanism can be constructed using a system of reaction–diffusion equations for the concentrations of activated and primed CaMKII in the dendrite and spines [72, 161]. These equations incorporate three major components of the dynamics: *diffusion* of CaMKII along the dendrite, *activation* of primed CaMKII, and *translocation* of activated CaMKII from the dendrite to spines. For simplicity, consider a uniform one-dimensional, nonbranching dendritic cable as shown in Fig. 3.8a. Suppose that a region of width 30 μm is stimulated with a glutamate/glycine puff at time $t = 0$. The center of the stimulated region is taken to be at $x = 0$ and the distal end of the dendrite is at $x = L = 150\,\mu\text{m}$. The diffusion, activation, and translocation of CaMKII along the dendrite following stimulation are modeled according to the following system of equations:

$$\frac{\partial P}{\partial t} = D\frac{\partial^2 P}{\partial x^2} - k_0 AP \tag{3.43a}$$

$$\frac{\partial A}{\partial t} = D\frac{\partial^2 A}{\partial x^2} + k_0 AP - hA \tag{3.43b}$$

$$\frac{\partial S}{\partial t} = hA, \tag{3.43c}$$

where D is the diffusivity of CaMKII within the cytosol. Here $P(x,t)$ and $A(x,t)$ denote the concentration of primed and activated CaMKII at time $t > 0$ and location x along the dendrite. $S(x,t)$ denotes the corresponding concentration of CaMKII in the population of spines at the same time and distance. For simplicity, all parameters are constant in space and time. The reaction term kAP represents the conversion of CaMKII from its primed to active state based on the irreversible first-order reaction scheme

$$A + P \to 2A$$

with mass action kinetics, where k_0 is the rate at which primed CaMKII is activated per unit concentration of activated CaMKII. The decay term hA represents the loss of activated CaMKII from the dendrite due to translocation into a uniform distribution of spines at a rate h. The model assumes that translocation is irreversible over the time scale of simulations, which is reasonable given that activated CaMKII accumulation at synapses can persist for several minutes [569].

As a further simplification we will only consider the distal transport of CaMKII from the stimulated region by taking $0 \le x \le L$ and imposing closed or reflecting boundary conditions at the ends $x = 0, L$. Hence, no CaMKII can escape from the ends. In reality activated CaMKII could also diffuse in the proximal direction and trigger a second proximal translocation wave. However, the choice of boundary condition has little effect on the properties of the wave. Taking the distal half of the stimulated region to be $0 \le x \le 15\,\mu$m, consider the following initial conditions: $P(x,0) = 0$ and $A(x,0) = P_0$ for $0 \le x \le 15\,\mu$m, whereas $P(x,0) = P_0$ and $A(x,0) = 0$ for $x \ge 15\,\mu$m, where P_0 is the uniform resting concentration of CaMKII in the dendrite. Typical values of C range from 0.1 to 30μM [605], covering two orders of magnitude. We also set $S(x,0) = 0$ everywhere. In other words, we assume that all the CaMKII is activated within the stimulated region at $t = 0$, but none has yet translocated into spines nor diffused into the nonstimulated region. We also neglect any delays associated with priming CaMKII along the dendrite. This is a reasonable approximation, since the Ca^{2+} spike travels much faster than the CaMKII translocation wave [532]; see Sect. 3.1. Thus by the time a significant amount of activated CaMKII has diffused into nonstimulated regions of the dendrite, any CaMKII encountered there will already be primed. The benefit of this assumption is that it eliminates the need to model the Ca^{2+} spike. However, a more detailed model that takes into account the initial transient associated with the priming phase could be constructed by coupling the reaction–diffusion equations with the spike–diffuse–spike model of Sect. 3.1.

Note that the system of equations (3.43) is identical in form to the diffusive SI model introduced by Noble [464] to explain the spread of bubonic plague through Europe in the fourteenth century. In the latter model, $P(x,t)$ and $A(x,t)$ would rep-

resent the densities of susceptible and infective people at spatial location x at time t, respectively; k_0 would be the transmission rate and h the death rate. In the absence of translocation into spines ($h = 0$), the total amount of CaMKII is conserved so that $A(x,t) + P(x,t) = P_0$ for all x and $t \geq 0$. Equations (3.43) then reduce to the scalar Fisher–KPP equation

$$\frac{\partial A}{\partial t} = D\frac{\partial^2 A}{\partial x^2} + k_0 A(P_0 - A), \tag{3.44}$$

which was originally introduced to model the invasion of a gene into a population. The Fisher–KPP equation and its generalizations have been widely used to describe the spatial spread of invading species including plants, insects, genes, and diseases; see, for example, [285, 444, 575, 648] and references therein. One characteristic feature of such equations is that they support traveling fronts propagating into an unstable steady state, in which the wave speed and longtime asymptotics are determined by the dynamics in the leading edge of the wave—so-called pulled fronts [544]. In particular, a sufficiently localized initial perturbation (such as the stimulus used to generate CaMKII waves) will asymptotically approach the traveling front solution that has the minimum possible wave speed. (If we perform the change of variables $Q = P_0 - P$ in the CaMKII model, then the traveling wave solution constructed below propagates into the unstable state $A = 0, Q = 0$.) An overview of the theory of pulled fronts is presented in appendix section 3.3.

3.2.1 Translocation Waves for a Uniform Distribution of Spines

A traveling wave solution of (3.43a) and (3.43b) is $P(x,t) = P(\xi)$ and $A(x,t) = A(\xi)$, $\xi = x - ct$, where $c, c > 0$, is the wave speed, such that

$$P(\xi) \to P_0, \quad A(\xi) \to 0 \quad \text{as}\, \xi \to \infty$$

and

$$P(\xi) \to P_1 < P_0, \quad A(\xi) \to 0 \quad \text{as}\, \xi \to -\infty.$$

Here P_1 is the residual concentration of primed CaMKII following translocation of activated CaMKII into spines. The minimum wave speed can be calculated by substituting the traveling wave solution into (3.43a) and (3.43b) and linearizing near the leading edge of the wave where $P \to P_0$ and $A \to 0$. In the traveling wave coordinate frame (3.43a) and (3.43b) are transformed to

$$-c\frac{dP}{d\xi} = D\frac{d^2P}{d\xi^2} - k_0 AP \tag{3.45a}$$

$$-c\frac{dA}{d\xi} = D\frac{d^2A}{d\xi^2} + k_0 AP - hA \tag{3.45b}$$

This is a system of two second-order ordinary differential equations in the variable ξ. A global view of the nature of traveling wave solutions can be ob-

tained by identifying (3.45a) and (3.45b) with the equation of motion of a classical particle in two spatial dimensions undergoing damping due to "friction" and subject to an "external force." Thus we identify A and P with the "spatial" coordinates of the particle, ξ with the corresponding "time" coordinate, and the speed c as a "friction coefficient." If we ignore boundary effects by taking $-\infty < \xi < \infty$, then we can view a traveling wave solution as a particle trajectory that connects the point $(P,A) = (0,0)$ at $\xi = -\infty$ to the point $(P,A) = (P_0,0)$ at $\xi = \infty$. A restriction on the allowed values of c can now be obtained by investigating how the point $(1,0)$ is approached in the large-ξ limit.

Linearizing Eqs. (3.45a) and (3.45b) about the point $(P,A) = (P_0,0)$ we obtain a pair of second-order linear equations, which have solutions of the form $(P-P_0,A) = \mathbf{V}e^{-\lambda\xi}$ where λ and $\mathbf{V}$ satisfy the matrix equation

$$c\lambda\mathbf{V} = \begin{pmatrix} D\lambda^2 & -k \\ 0 & D\lambda^2 + k - h \end{pmatrix}\mathbf{V}, \tag{3.46}$$

where $k = k_0P_0$. Solving for the eigenvalue λ leads to the four solutions

$$\lambda = 0, \quad \frac{c}{D}, \quad \frac{c \pm \sqrt{c^2 - 4D(k-h)}}{2D} \tag{3.47}$$

and these, along with their corresponding eigenvectors $\mathbf{V}$, determine the shape of the wave as it approaches the point $(1,0)$. Note that the last two eigenvalues have a nonzero imaginary part when $c^2 < 4D(k-h)$, implying that as ξ becomes large the wave oscillates about the point $(1,0)$. This cannot be allowed since it would imply that the activated CaMKII concentration A takes on negative values (inspection of the corresponding eigenvectors shows that their components in the A-direction are nonzero and so A would indeed oscillate). Therefore, we must have

$$c \geq c_{\min} = 2\sqrt{D(k-h)}, \tag{3.48}$$

which implies that $k > h$. Note that the minimum wave speed can be identified with the linear spreading velocity of a pulled front; see appendix section 3.3. This then yields a more direct method for obtaining the minimum wave speed. That is, the characteristic equation obtained from (3.46) yields the dispersion relation

$$c(\lambda) = D\lambda + \frac{k-h}{\lambda}. \tag{3.49}$$

The theory of pulled fronts shows that the minimum wave speed is obtained by minimizing $c(\lambda)$. The equation $c'(\lambda) = 0$ gives $D\lambda = (k-h)/\lambda$, which has the solution $\lambda_0 = \sqrt{(k-h)/D}$, so that $c_{\min} = c(\lambda_0) = 2D\lambda_0 = 2\sqrt{D(k-h)}$.

An example of a numerically determined traveling wave solution with minimal speed $c_{\min}$ is shown in Fig. 3.9 for parameter values consistent with experimental studies of CaMKIIα, which is one of the two main isoforms of CaMKII. In its inactive state CaMKIIα tends to be located in the cytosol, whereas the other isoform, CaMKIIβ, is weakly actin bound [570]. One finds empirically that $D \sim 1\,\mu\text{m}^2/\text{s}$, $h \sim 0.05\,\text{s}^{-1}$ and $c \sim 1\,\mu\text{m/s}$ [532, 569, 570] for CaMKIIα. (CaMKIIβ has a diffusivity and translocation rate an order of magnitude smaller but exhibits compa-

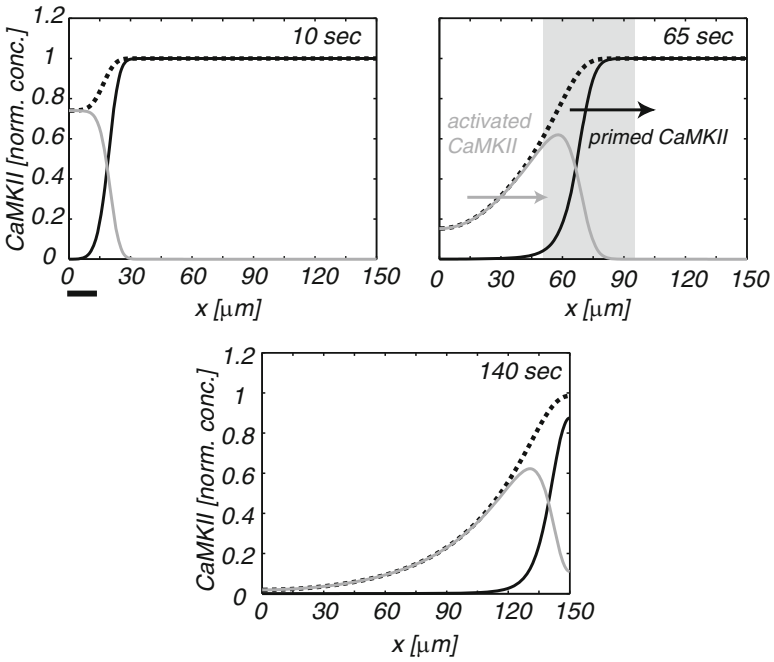

Fig. 3.9 Three successive snapshots of a numerically simulated translocation wave propagating along a homogeneous dendrite. Solutions of (3.43a) and (3.43b) are plotted for parameter values consistent with experimental data on CaMKII [532, 569, 570]. The translocation rate $h = 0.05\,\mathrm{s}$, diffusivity $D = 1\,\mu\mathrm{m}^2/\mathrm{s}$ and the activation rate $k_0 P_0 = 0.21\,\mathrm{s}$. At time $t = 0$ all of the CaMKII within the stimulated region (*indicated by thick bar*) is in the activated state, whereas all of the CaMKII within the nonstimulated region is in the primed state. Concentrations are normalized with respect to the initial concentration of primed CaMKII. Composite wave consists of a pulse of activated CaMKII (*gray curve*) moving at the same speed as a front of primed CaMKII (*black curve*). Also shown is the total CaMKII concentration along the dendrite (*dashed black curve*), which decreases with time due to translocation into spines. As indicated in the center plot, the front forms an interface between a quiescent region containing a uniform concentration of primed CaMKII and a region dominated by translocation of activated CaMKII into spines. The dynamics in the interfacial (*shaded*) region is dominated by diffusion–activation of primed CaMKII

rable wave speeds.) The formula for the wave speed then gives an estimate for the unknown activation rate, $k \sim 0.2\,\mathrm{s}^{-1}$. It can be seen in Fig. 3.9 that the wave profile of primed CaMKII is in the form of a front, whereas the co-moving wave profile of activated CaMKII is a localized pulse.

The above analysis predicts wave propagation failure when the translocation rate h is greater than the effective activation rate k. Experimentally, h is determined by globally activating CaMKII along a dendrite and determining the rate at which the level of CaMKII decays [569, 570]. The detailed microscopic mechanism whereby CaMKII is translocated into spines is currently not known, so it is difficult to relate h to individual spine properties. A simple hypothesis is that the translocation rate depends on the spine density according to $h = \rho_0 v_0$, where v_0 is an effective "velocity" associated with translocation into an individual spine. Since the activa-

tion rate $k = k_0 P_0$, where P_0 is the initial concentration of primed CaMKII in the nonstimulated region of the dendrite, the model predicts that CaMKII translocation waves will fail to propagate when

$$\rho_0 v_0 > k_0 P_0. \tag{3.50}$$

For example, this inequality predicts that dendrites with a high density of spines are less likely to exhibit translocation waves than those with a low spine density. It also predicts that dendrites with a larger initial concentration of primed CaMKII in the shaft are more likely to exhibit translocation waves than those with a smaller initial concentration. Since the initial concentration P_0 of primed CaMKII depends on the effectiveness of the Ca^{2+} spike in both propagating along the dendrite and priming the inactive state, the model agrees with the experimental finding that translocation waves fail to propagate when L-type Ca^{2+} channels are blocked [532]. One also finds that Ca^{2+} spikes are less likely to propagate towards the soma, which could explain why translocation waves are more often observed propagating towards the distal end of a dendrite.

3.2.2 *Pulsating Waves in the Presence of Discretely Distributed Spines*

One of the major simplifications of the above model is that the discrete nature of dendritic spines is ignored by treating the spine density ρ and, hence, the translocation rate h as uniform. Given the fact that the radius of the spine neck is typically at the submicron level, which is much smaller than any other length scale of the system, one can take into account the discreteness of spines by representing the spine density as the sum of Dirac delta functions (3.32), which represents clusters of $\bar{n}$ spines at discrete locations x_n; see Sect. 3.1. It immediately follows that the translocation rate h is itself space-dependent and (3.43a) and (3.43b) become heterogeneous. For the sake of illustration, consider the case of a set of spine clusters that are uniformly spaced with $x_n = n\Delta$ where Δ is the spine cluster spacing. In order to separate the effects of discreteness from the effects of spine density, we will assume that the size of a cluster scales with Δ so that $\overline{n} = \rho_0 \Delta$ with ρ_0 fixed. Thus, setting $\overline{h} = \rho_0 v_0$, we have the space-dependent translocation rate

$$h(x) = \overline{h}\Delta \sum_{n\in\mathbb{Z}} \delta(x - n\Delta), \tag{3.51}$$

such that $L^{-1}\int_0^L h(x)dx = \overline{h}$ for $L \gg \Delta$.

In recent years, there has been an increasing interest in studying biological invasion in heterogeneous environments using reaction–diffusion equations [40, 102, 212, 335, 574, 575, 587, 664, 687]. Heterogeneity is often incorporated by assuming that the diffusion coefficient and the growth rate of a population are periodically varying functions of space. One of the simplest examples of a single population model in a periodic environment was proposed by Shigesada et al.

[574, 575], in which two different homogeneous patches are arranged alternately in one-dimensional space so that the diffusion coefficient and the growth rate are given by periodic step functions. The authors showed numerically that an invading population starting from a localized perturbation evolves to a traveling periodic wave in the form of a pulsating front. The population density $u(x,t)$ of such a wave is defined by the condition $u(x,t) = u(x+\sigma, t+T)$ such that $\lim_{x\to\infty} u(x,t) = 0$ and $\lim_{x\to-\infty} u(x,t) = p(x)$, where $p(x)$ is a spatially periodic stationary solution of the corresponding reaction–diffusion equation. This form of solution repeats itself in a time interval T if it is observed at two successive points separated by a distance σ. The speed of the wave is then taken to be $c = \sigma/T$. Shigesada et al. [574] also used linearized information within the leading edge of the pulsating front to derive wave speed estimates, generalizing the analysis of pulled fronts in homogeneous media [544]. An interesting recent extension of this approach has been used to study pulsating fronts in periodically modulated nonlocal neural field equations [132]. The theory of pulsating fronts has also been developed in a more general and rigorous setting [40, 212, 587, 664, 687].

The analysis of CaMKII translocation waves developed in [72] follows the basic formulation of Shigesada et. al. [574] by linearizing (3.43b) at the leading edge of the wave where $A(x,t) \to 0$ and $\mathscr{P}(x,t) \to P_0$:

$$\frac{\partial A}{\partial t} = D\frac{\partial^2 A}{\partial x^2} + kA - h(x)A, \tag{3.52}$$

with $h(x)$ given by the Δ-periodic function (3.51). Assume a solution of the form $A(x,t) = a(\xi)\mathscr{P}(x)$, $\xi = x - ct$, and set

$$\frac{\partial}{\partial t} \to -c\frac{\partial}{\partial \xi}, \quad \frac{\partial}{\partial x} \to \frac{\partial}{\partial x} + \frac{\partial}{\partial \xi}.$$

Substitution into (3.52) then gives

$$-c\mathscr{P}(x)a'(\xi) = D\left[a''(\xi)\mathscr{P}(x) + 2a'(\xi)\mathscr{P}'(x) + a(\xi)\mathscr{P}''(x)\right] + [k - h(x)]a(\xi)\mathscr{P}(x).$$

Dividing through by $a(\xi)\mathscr{P}(x)$ and rearranging yields

$$D\frac{a''(\xi)}{a(\xi)} + \left[2D\frac{\mathscr{P}'(x)}{\mathscr{P}(x)} + c\right]\frac{a'(\xi)}{a(\xi)} = -D\frac{\mathscr{P}''(x)}{\mathscr{P}(x)} - k + h(x). \tag{3.53}$$

Applying the operator $\partial_x\partial_\xi$ to both sides of (3.53) implies that either $\mathscr{P}'(x)/\mathscr{P}(x)$ is a constant or $a'(\xi)/a(\xi)$ is a constant. Only the latter condition is consistent with $P(x)$ being a periodic function. Thus, $a(\xi) = A_0 e^{-\lambda\xi}$ with λ determined by solutions to the damped Hill equation

$$\mathscr{P}''(x) - 2\lambda\mathscr{P}'(x) + \left[\lambda^2 + \frac{k - h(x) - c\lambda}{D}\right]\mathscr{P}(x) = 0. \tag{3.54}$$

Note that if $\mathscr{P}(x) = e^{\lambda x}U(x)$ then $U(x)$ satisfies the undamped Hill equation

$$DU''(x) + [k - h(x) - c\lambda]\, U(x) = 0. \tag{3.55}$$

In order to determine the minimal wave speed $c_{\min}$, it is necessary to find a bounded periodic solution $P(x)$ of (3.54), which yields a corresponding dispersion relation $c = c(\lambda)$, whose minimum with respect to λ can then be determined (assuming it exists). Unfortunately, for general periodic functions $h(x)$, it is not possible to solve (3.54) explicitly, and some form of approximation scheme is required as described in the next section.

3.2.3 *Homogenization of Pulsating Waves for a Fast Periodic Modulation of Spine Density*

Since the spine cluster spacing Δ is at least an order of magnitude smaller than the width of the traveling wave of the homogeneous system, one can use homogenization theory to approximate the discrete effects of spines by a corresponding continuum model [72]. Such a method has also been applied to studying variations in electrical voltage/conductance [424] and the distribution of protein receptors [68] along spiny dendrites. Interestingly, Smaily et al. [587] independently applied the same homogenization procedure to analyze wave speed in the population model of Shigesada et. al. [574]. A more general discussion of homogenization techniques applied to traveling fronts can be found in the review by Xin [687].

As a first step, we introduce a macroscopic length scale σ and set $\Delta = \varepsilon\sigma$ with $\varepsilon \ll 1$. We identify σ with the effective width of the primed CaMKII front, which turns out to be around 20–30 µm in the given parameter regimes. Equation (3.55) can then be rewritten in the form

$$\frac{d^2U}{dx^2} + \left[\overline{\Gamma} - \Delta\Gamma\left(\frac{x}{\varepsilon}\right)\right] U(x) = 0, \tag{3.56}$$

where

$$\overline{\Gamma} = [k - c\lambda - \overline{h}]/D \tag{3.57}$$

and

$$\Delta\Gamma(y) = \frac{\overline{h}}{D}\left(\sigma \sum_{n\in\mathbb{Z}} \delta(y - n\sigma) - 1\right) \tag{3.58}$$

such that $\Delta\Gamma(y)$ is a σ-periodic function of y. Applying the homogenization procedure outlined below leads to the result

$$U(x) = \langle U(x)\rangle \left[1 + \varepsilon^2 \Delta U(x/\varepsilon)\right] + \mathcal{O}(\varepsilon^3), \tag{3.59}$$

where $\langle U \rangle$ satisfies the averaged equation

$$\frac{d^2\langle U\rangle}{dx^2} + \Gamma_\varepsilon \langle U\rangle = 0, \tag{3.60}$$

and

$$\Gamma_\varepsilon = \overline{\Gamma} - \varepsilon^2 \Gamma_2 + \mathscr{O}(\varepsilon^3), \quad \Gamma_2 = \frac{1}{12}\left(\frac{\overline{h}\sigma}{D}\right)^2, \tag{3.61}$$

$$\Delta U(y) = \frac{\overline{h}\sigma^2}{D}\left[\frac{y}{2\sigma} - \frac{y^2}{2\sigma^2} - \frac{1}{12}\right]. \tag{3.62}$$

Homogenization method for discrete spines. The basic idea of multi-scale homogenization is to expand the solution of Eq. (3.56) as a power series in ε, with each term in the expansion depending explicitly on the "slow" (macroscopic) variable x and the "fast" (microscopic) variable $y = x/\varepsilon$ [68, 424, 587]:

$$U(x,y) = U_0(x) + \varepsilon U_1(x,y) + \varepsilon^2 U_2(x,y) + \ldots, \tag{3.63}$$

where $U_j(x,y), j = 1,\ldots$ are σ-periodic in y. The perturbation series expansion is then substituted into Eq. (3.56) with x, y treated as independent variables so that derivatives with respect to x are modified according to $\partial_x \to \partial_x + \varepsilon^{-1}\partial_y$. This generates a hierarchy of equations corresponding to successive powers of ε:

$$\frac{\partial^2 U_1}{\partial y^2} = 0 \tag{3.64}$$

$$\frac{d^2 U_0}{dx^2} + 2\frac{\partial^2 U_1}{\partial x \partial y} + \frac{\partial^2 U_2}{\partial y^2} + \left[\overline{\Gamma} - \Delta\Gamma(y)\right] U_0 = 0 \tag{3.65}$$

at powers $\varepsilon^{-1}, 1$ and

$$\frac{\partial^2 U_n}{\partial x^2} + 2\frac{\partial^2 U_{n+1}}{\partial x \partial y} + \frac{\partial^2 U_{n+2}}{\partial y^2} + \left[\overline{\Gamma} - \Delta\Gamma(y)\right] U_n = 0 \tag{3.66}$$

at $\mathscr{O}(\varepsilon^n), n \geq 1$.

Equation (3.64) and boundedness of U_1 imply that U_1 is independent of y and can thus be absorbed into $U_0(x)$. Thus the leading-order corrections arising from small-scale fluctuations in the spine density occur at $\mathscr{O}(\varepsilon^2)$. Define the spatial average of a periodic function $F(y)$, denoted by $\langle F \rangle$, according to

$$\langle F \rangle = \frac{1}{\sigma}\int_0^\sigma F(y)dy. \tag{3.67}$$

Taking the spatial average of (3.65) with $U_0 = \langle U_0 \rangle$ then gives

$$\frac{d^2 U_0}{dx^2} + \overline{\Gamma} U_0 = 0. \tag{3.68}$$

We have exploited the fact that U_2 is periodic in y so $\langle \partial^2 U_2/\partial y^2 \rangle = 0$. In order to calculate U_2, we first subtract the averaged Eq. (3.68) from (3.65) to obtain

$$\frac{\partial^2 U_2}{\partial y^2} = \Delta\Gamma(y) U_0(x). \tag{3.69}$$

It follows that $U_2(x,y) = U_0(x)\chi(y)$ with $\chi''(y) = \Delta\Gamma(y)$ and χ a σ-periodic function of y. Integrating once with respect to y gives $\chi'(y) = \chi'(0) + \int_0^y \Delta\Gamma(z)dz$. We can eliminate the unknown $\chi'(0)$ by spatially averaging with respect to y and using $\langle\chi'\rangle = 0$. This gives $\chi'(y) = \oint_0^y \Delta\Gamma(z)dz$ with

$$\oint_0^y f(z)dz \equiv \int_0^y f(z)dz - \left\langle \int_0^y f(z)dz \right\rangle \tag{3.70}$$

for any integrable function f. Another integration with respect to y shows that

$$\chi(y) = \chi(0) + \int_0^y \oint_0^{y'} \Delta\Gamma(z)dzdy'.$$

Spatially averaging this equation with respect to y in order to express $\chi(0)$ in terms of $\langle\chi\rangle$ and multiplying through by $U_0(x)$ finally gives

$$\begin{aligned} \Delta U_2(x,y) &\equiv U_2(x,y) - \langle U_2\rangle(x) \\ &= U_0(x) \oint_0^y \oint_0^{y'} \Delta\Gamma(z)dzdy'. \end{aligned} \tag{3.71}$$

It remains to determine the equation satisfied by $\langle U_2\rangle$. Spatially averaging Eq. 3.66) for $n = 2$ gives

$$\frac{d^2\langle U_2\rangle}{dx^2} + \overline{\Gamma}\langle U_2\rangle = \langle \Delta\Gamma(y)U_2(x,y)\rangle. \tag{3.72}$$

Substituting (3.71) into (3.72) and reordering the resulting multiple integral yields the result

$$\frac{d^2\langle U_2\rangle}{dx^2} + \overline{\Gamma}\langle U_2\rangle = -\left\langle \left(\oint_0^y \Delta\Gamma(z)dz \right)^2 \right\rangle U_0(x). \tag{3.73}$$

Finally, writing $\langle U\rangle = U_0 + \varepsilon^2\langle U_2\rangle + \ldots$ we obtain the homogenized version of the Hill equation (3.55):

$$\frac{d^2\langle U\rangle}{dx^2} + \Gamma_\varepsilon\langle U\rangle = 0, \tag{3.74}$$

where

$$\Gamma_\varepsilon = \overline{\Gamma} + \varepsilon^2\Gamma_2 + \mathscr{O}(\varepsilon^3), \quad \Gamma_2 = \left\langle \left(\oint_0^y \Delta\Gamma(z)dz \right)^2 \right\rangle. \tag{3.75}$$

It is straightforward to calculate the integrals in (3.71) and (3.75) for a periodic spine density with $\Delta\Gamma(y)$ given by (3.58) [424]:

$$\Gamma_2 = \left\langle \left(\oint_0^y \Delta\Gamma(z)dz \right)^2 \right\rangle = \frac{1}{12}\left(\frac{\overline{h}\sigma}{D}\right)^2, \tag{3.76}$$

$$\oint_0^y \oint_0^{y'} \Delta\Gamma(z)dzdy' = \frac{\overline{h}\sigma^2}{D}\left[\frac{y}{2\sigma} - \frac{y^2}{2\sigma^2} - \frac{1}{12}\right]. \tag{3.77}$$

We thus obtain (3.59) and (3.60).

Note that it is possible to extend the above homogenization scheme to the case of randomly rather than periodically distributed spines, provided that the resulting heterogeneous medium is *ergodic*. That is, the result of averaging over all realizations of the ensemble of spine distributions is equivalent to averaging over the length L of the dendrite in the infinite-

L limit. If such an ergodic hypothesis holds and L is sufficiently large so that boundary terms can be neglected, then the above analysis carries over with $\langle\cdot\rangle$ now denoting ensemble averaging [424].

Recall from our discussion of (3.54) that the solution $\mathscr{P}(x) = e^{\lambda x}U(x)$ has to be a bounded Δ-periodic function of x. It follows from (3.59) and (3.60) that $e^{\lambda x}\langle U(x)\rangle$ should be a finite constant. Writing the solution of (3.60) as $\langle U(x)\rangle \sim e^{-\sqrt{-\Gamma_2}\varepsilon x}$, yields the characteristic equation

$$\lambda = \sqrt{\frac{c\lambda - k + \overline{h}}{D} - \varepsilon^2\Gamma_2}, \tag{3.78}$$

where we have substituted for $\overline{\Gamma}$ using (3.57). Squaring both sides and rearranging thus leads to the following dispersion relation for the wave speed c:

$$c = c(\lambda) \equiv D\lambda + \frac{k - \overline{h} + \varepsilon^2 D\Gamma_2}{\lambda}. \tag{3.79}$$

Minimizing with respect λ then shows that

$$c_{\min} = 2\sqrt{D(k-\overline{h}) + \varepsilon^2 D^2\Gamma_2}, \tag{3.80}$$

For sufficiently small ε, we can Taylor expand (3.80) to obtain

$$c_{\min} \approx \overline{c} + \frac{2D^2\Gamma_2}{\overline{c}}\varepsilon^2, \tag{3.81}$$

with $\overline{c} = 2\sqrt{D(k-\overline{h})}$ the wave speed of the corresponding homogeneous distribution of spines. Hence, a periodic variation in the spine density due to clustering leads to an $\mathscr{O}(\varepsilon^2)$ increase in the wave speed. An analogous result was obtained by Smaily et. al. [587] for the Shigesada et. al. model [574]. Note that (3.59) also implies that there are small-scale fluctuations of the wave profile in the leading edge of the wave

$$\frac{\Delta P(x/\varepsilon)}{\langle P\rangle} = \varepsilon^2 \Delta U(x/\varepsilon) + \mathscr{O}(\varepsilon^3). \tag{3.82}$$

Since $\varepsilon = \Delta/\sigma$, it follows from (3.62) that fluctuations in the wave profile vary between $-\overline{h}\Delta^2/(12D)$ at spine clusters and $\overline{h}\Delta^2/(24D)$ between spine clusters. In terms of physical parameters, the minimum wave speed is

$$c_{\min} = 2\sqrt{D(k-\overline{h}) + \Delta^2\overline{h}^2/12}. \tag{3.83}$$

It immediately follows that for fixed $\overline{h}, k, D$ (and hence $\overline{c}$), spine clustering increases the speed of a translocation wave. This is illustrated in Fig. 3.10, where we plot the minimal wave speed $c_{\min}$ given by (3.83) as a function of the activation rate k for various values of the cluster spacing Δ. An additional important consequence of clustering is that it reduces the threshold for the existence of a translocation wave.

That is, there exists a critical value of the activation rate, $k = \kappa(\Delta)$, below which translocation waves do not exist and $\kappa(\Delta)$ is a decreasing function of Δ. In the homogenization limit $\Delta \to 0$, we recover the result $\kappa = \bar{h}$.

The existence of a pulsating wave due to spine clustering and the associated increase (decrease) in the minimal speed (threshold) of the wave can also be confirmed numerically. For the sake of illustration, consider a dendrite of length $L = 300\,\mu\text{m}$ with reflecting boundary conditions at both ends $x = 0, L$. The initial conditions are taken to be

$$\begin{aligned} P(x,0) &= P_0, A(x,0) = 0 \text{ for all} x \notin [0, \delta L] \\ P(x,0) &= 0, A(x,0) = P_0 \text{ for all} x \in [0, \delta L], \end{aligned}$$

with $\delta L = 15\,\mu\text{m}$. We discretize space by setting $x = m\delta x$, where δx is the step length and $m = 0, 1, \ldots, M$ with $M = L/\delta x$. In discrete spatial units the spine cluster spacing is taken to be $\Delta = P\delta x$. The spine cluster distribution is then represented numerically by the discrete sum

$$\rho(m\delta x) = \frac{1}{\delta x} \sum_{j=0}^{M/P} \delta_{m,jP},$$

where $\delta_{m,j}$ is the Kronecker delta and δx is chosen so that M, P and M/P are integers. An example of a pulsating wave is shown in Fig. 3.11. Comparison between waves for a spatially uniform distribution of spines and a spatially discrete distribution of spine clusters shows that the wave is periodically modulated and faster in the latter case. This is a consequence of the fact that translocation is less effective

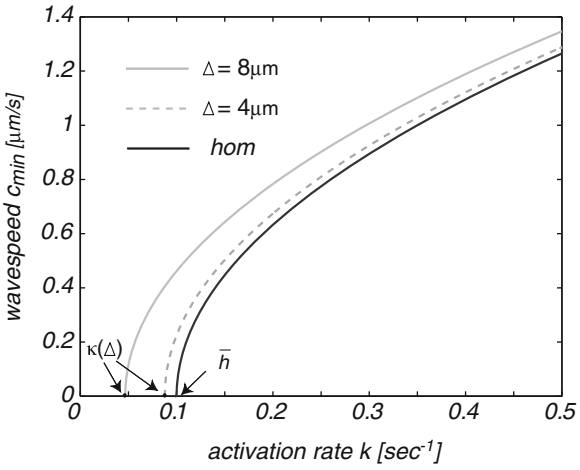

Fig. 3.10 Plot of minimal wave speed $c_{\min}$ as a function of activation rate $k = k_0 P_0$ for various values of the spine cluster spacing Δ. Also shown is the corresponding wave speed for a homogeneous spine distribution (*black curve*). Other parameters are $\bar{h} = 0.1\,\text{s}^{-1}$ and $D = 1\,\mu\text{m}^2/\text{s}$. Note that wave propagation failure occurs as $k \to \kappa(\Delta)$ from above where $\kappa(\Delta)$ is the propagation threshold

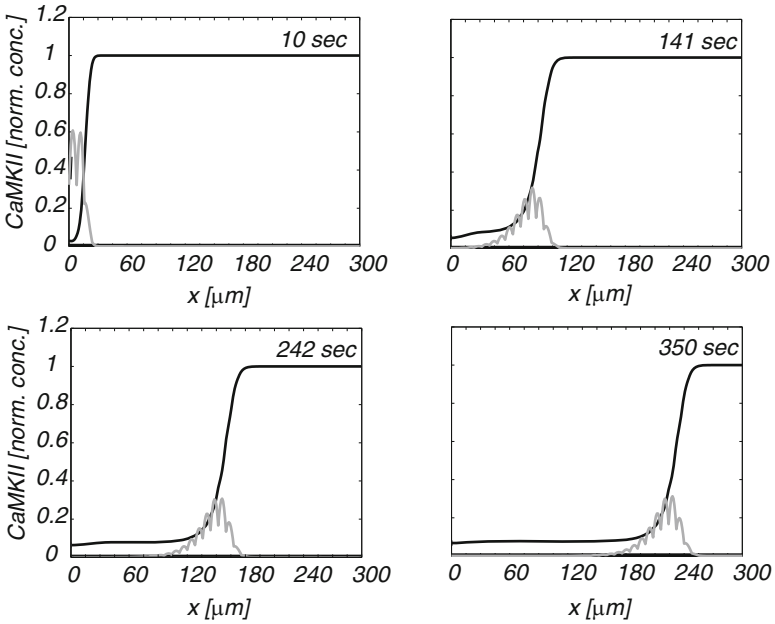

Fig. 3.11 Numerical traveling wave solution of (3.43a) and (3.43b) for an inhomogeneous distribution of spine clusters with $\Delta = 8\,\mu$m. The translocation rate $\overline{h} = 0.1$ s, diffusivity $D = 1\,\mu\text{m}^2/\text{s}$ and the activation rate $k = 0.19$ s. At time $t = 0$ all of the CaMKII within the stimulated region (*indicated by thick bar*) is in the activated state, whereas all of the CaMKII within the nonstimulated region is in the primed state. Concentrations are normalized with respect to the initial concentration of primed CaMKII. The resulting wave profiles for activated (*gray curve*) and primed (*black curve*) CaMKII along the dendrite are shown at four successive snapshots in time. The numerically estimated wave speed $c_{\min} \approx 0.66\,\mu$m/s, which is faster than the wave speed $\overline{c} = 0.6\,\mu$m/s of the corresponding uniform spine distribution

in the presence of spine clusters. Although doubling the degree of clustering only leads to a change in wave speed of order 0.05μm/s (consistent with the analytical calculations), it leads to a significant difference in propagation times along a 300 μm dendrite.

3.2.4 Wave Speed for a Slowly Modulated Spine Density

So far we have considered the effects of heterogeneity at a microscopic length scale comparable to the spacing of individual spines. In particular, we took the homogenized translocation rate $\overline{h}$ to be constant over the length of a dendrite. However, it is found experimentally that there is a slow proximal to distal variation in the density of spines [22, 346]. An illustration of a typical spine density found in pyramidal neurons of mouse cortex [22] is shown in Fig. 3.12. Such a variation in spine

density can be incorporated into (3.43a) and (3.43b) by setting $h = \overline{h} + \Delta h(\varepsilon x)$, where $\overline{h}$ denotes the translocation rate at the initiation point x_0 of the wave and $\Delta h(\varepsilon x)$ represents the slow modulation of the (homogenized) translocation rate over the length of a dendrite with $\varepsilon \ll 1$. The general problem of biological invasion in slowly modulated heterogeneous environments can be analyzed using a Hamilton–Jacobi method for front velocity selection [421, 687]; see Sect. 3.3. This method was originally applied to homogeneous media by Freidlin using large deviation theory [203, 204, 212] and was subsequently formulated in terms of PDEs by Evans and Sougandis [178]. We will illustrate the method by applying it to the reaction–diffusion model of CaMKII translocation waves with slow periodic modulation; see also [72]

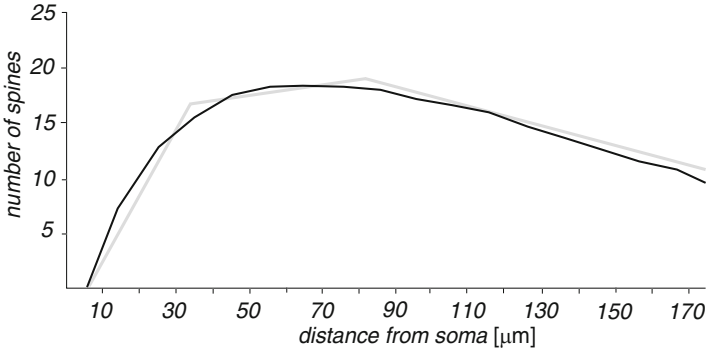

Fig. 3.12 Illustrative example of the spine density variation along the basal dendrite of a pyramidal cell in mouse cortex (*black curve*). Density is calculated as the number of spines per 10 μm segment of the dendrite from the soma to the tip of the dendrite. Abstracted from experimental data in [22]. Also shown is a simplified piecewise linear approximation of the spine density variation (*gray curve*)

The first step in the analysis is to rescale space and time in (3.43a) and (3.43b) according to $t \to t/\varepsilon$ and $x \to x/\varepsilon$; see [178, 204, 421]:

$$\varepsilon \frac{\partial P}{\partial t} = D\varepsilon^2 \frac{\partial^2 P}{\partial x^2} - k_0 AP \tag{3.84a}$$

$$\varepsilon \frac{\partial A}{\partial t} = D\varepsilon^2 \frac{\partial^2 A}{\partial x^2} + k_0 AP - [\overline{h} + \Delta h(x)]A. \tag{3.84b}$$

Under the spatial rescaling the front region where A (P) rapidly increases (decreases) as x decreases from infinity becomes a step as $\varepsilon \to 0$. This motivates the introduction of solutions of the form

$$P(x,t) \sim P_0 \left[1 - \mathrm{e}^{-G_\varepsilon(x,t)/\varepsilon}\right], \quad A(x,t) \sim A_0(x)\mathrm{e}^{-G_\varepsilon(x,t)/\varepsilon} \tag{3.85}$$

with $G_\varepsilon(x,t) > 0$ for all $x > x(t)$ and $G_\varepsilon(x(t),t) = 0$. The point $x(t)$ determines the location of the front and $c = \dot{x}$. Substituting (3.85) into (3.84a) and (3.84b) gives

$$-\frac{\partial G_\varepsilon}{\partial t} = D\left[\frac{\partial G_\varepsilon}{\partial x}\right]^2 - D\varepsilon\frac{\partial^2 G_\varepsilon}{\partial x^2} - k_0 A_0(x)\left[1-\mathrm{e}^{-G_\varepsilon(x,t)/\varepsilon}\right]$$

$$-A_0(x)\frac{\partial G_\varepsilon}{\partial t} = A_0(x)\left[D\left[\frac{\partial G_\varepsilon}{\partial x}\right]^2 - D\varepsilon\frac{\partial^2 G_\varepsilon}{\partial x^2} + k_0 P_0\left[1-\mathrm{e}^{-G_\varepsilon(x,t)/\varepsilon}\right] - [\overline{h}+\Delta h(x)]\right]$$

$$+\varepsilon^2 A_0''(x)G_\varepsilon - 2\varepsilon A_0'(x)\frac{\partial G_\varepsilon}{\partial x}.$$

Since $\mathrm{e}^{-G_\varepsilon(x,t)/\varepsilon} \to 0$ as $\varepsilon \to 0$ for $G_\varepsilon > 0$, it follows that the limiting function $G(x,t) = \lim_{\varepsilon\to 0} G_\varepsilon(x,t)$ satisfies

$$-\frac{\partial G}{\partial t} = D\left[\frac{\partial G}{\partial x}\right]^2 - k_0 A_0(x) \tag{3.86a}$$

$$-\frac{\partial G}{\partial t} = D\left[\frac{\partial G}{\partial x}\right]^2 + k - [\overline{h}+\Delta h(x)], \tag{3.86b}$$

where $k = k_o P_0$ as before. It immediately follows that

$$A_0(x) = \left[\frac{k-\overline{h}-\Delta h(x)}{k}\right] P_0. \tag{3.87}$$

The remaining equation (3.86b) can be analyzed along identical lines to a previous study of the heterogeneous Fisher–KPP equation [421]. Formally comparing (3.86b) with the Hamilton–Jacobi equation $\partial_t G + H(\partial_x G, x) = 0$, we define the Hamiltonian

$$H = Dp^2 + k - [\overline{h}+\Delta h(x)], \tag{3.88}$$

where $p = \partial_x G$ is interpreted as the conjugate momentum of x. It now follows that (3.86b) can be solved in terms of the Hamilton equations

$$\frac{dx}{ds} = 2Dp, \quad \frac{dp}{ds} = \frac{d\Delta h}{dx}. \tag{3.89}$$

Combining these equations yields the second-order ODE

$$\ddot{x} - 2D\Delta h(x)' = 0. \tag{3.90}$$

This takes the form of a Newtonian particle moving in a "potential" $V(x) = -2D\Delta h(x)$. Given the solution $x(s) = \phi(s;x,t)$ with $\phi(0;x,t) = x_0$ and $\phi(t;x,t) = x$, we can then determine $G(x,t)$ according to

$$G(x,t) = -E(x,t)t + \frac{1}{2D}\int_0^t \dot{\phi}(s;x,t)^2 ds. \tag{3.91}$$

Here

$$E(x,t) = H(\dot{\phi}(s;x,t)/2D, \phi(s;x,t)), \tag{3.92}$$

which is independent of s due to conservation of energy.

For certain choices of the modulation function $\Delta h(x)$, (3.90) can be solved explicitly [421]. In particular, suppose that the spine density curve in Fig. 3.3 is approximated by a piecewise linear function, in which the density increases linearly with distance from the soma to some intermediate location κ along the dendrite and then decreases linearly towards the distal end. Assuming that the right-moving wave is initiated beyond the point κ, $x_0 > \kappa$, then we can simply take $\Delta h(x) = -\beta(x - x_0)$ for $\beta > 0$. Substituting into (3.90) and integrating twice with respect to s using the Cauchy conditions gives

$$\phi(s;x,t) = x_0 + (x - x_0)s/t + D\beta ts - D\beta s^2. \tag{3.93}$$

The corresponding "energy" function is then

$$E(x,t) = \frac{(x - x_0)^2}{4Dt^2} + k - \overline{h} + \frac{\beta}{2}(x - x_0) + \frac{\beta^2}{4}Dt^2 \tag{3.94}$$

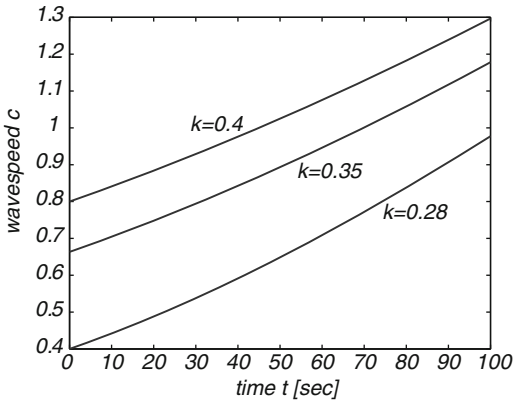

Fig. 3.13 Plot of time-dependent variation in wave speed c given by (3.96) for various values of the activation rate k. Other parameters are $\overline{h} = 0.24\,\mathrm{s}^{-1}$ and $D = 1\,\mu\mathrm{m}^2/\mathrm{s}$. At $t = 0$, $c(0) = 2\sqrt{D(k - \overline{h})}$

and (3.91) shows that

$$G(x,t) = \frac{(x - x_0)^2}{4Dt} - [k - \overline{h}]t - \frac{\beta}{2}(x - x_0)t - \frac{\beta^2}{12}Dt^3. \tag{3.95}$$

We can now determine the wave speed c by imposing the condition $G(x(t),t) = 0$. This leads to a quadratic equation with positive solution

$$x(t) = x_0 + D\beta t^2 + 2Dt\sqrt{\frac{k-\overline{h}}{D} + \frac{\beta^2}{3}t^2}$$
$$= x_0 + \overline{c}t\sqrt{1 + \frac{4\beta^2 D^2 t^2}{3\overline{c}^2}} + D\beta t^2$$

with $\overline{c} = 2\sqrt{D(k-\overline{h})}$. Finally, differentiating both sides with respect to t yields

$$c \equiv \dot{x}(t) = \overline{c}\sqrt{1+\Gamma_0\beta^2 t^2} + \frac{\overline{c}\Gamma_0\beta^2 t^2}{\sqrt{1+\Gamma_0\beta^2 t^2}} + 2D\beta t, \tag{3.96}$$

where $\Gamma_0 = 4D^2/(3\overline{c}^2)$. For sufficiently small times such that $D\beta t \ll 1$, we have the approximation

$$c \approx \overline{c} + 2D\beta t + \frac{2(D\beta t)^2}{\overline{c}}. \tag{3.97}$$

Figure 3.13 shows example plots of the time-dependent wave speed for various choices of the activation rate k. It can be seen that there are significant changes in speed over a time course of 100 s, which is comparable to the time a wave would travel along a dendrite of a few hundred microns. In principle, it should be possible to test experimentally the predictions of the above analysis by initiating a translocation wave at different points along a dendrite and determining the corresponding wave speed.

3.3 Appendix: Pulled and Pushed Fronts

In this appendix, we review some of the basic properties of fronts propagating into unstable states. For a much more detailed account, see the review by van Saarloos [544] and Chap. 4 of [422]. For concreteness, we focus on a slight generalization of the Fisher–KPP equation

$$\frac{\partial u}{\partial t} = \frac{\partial^2 u}{\partial x^2} + f(u), \quad f \in C^1[0,1], \quad f(0) = f(1) = 0, \tag{3.98}$$

for which the homogeneous fixed point $u = 0$ is unstable ($f'(0) > 0$) and $u = 1$ is stable ($f'(1) < 0$). We also assume that $f(u) > 0$ for all $u \in (0,1)$. We are interested in determining the longtime asymptotics of a front propagating to the right into the unstable state $u = 0$, given initial conditions for which $u(x,0) = 0$ for sufficiently large x. It is not possible to carry out an asymptotic analysis by simply moving to a traveling coordinate frame, since there is a continuous family of front solutions. However, considerable insight into the evolution of a localized initial condition can be obtained by linearizing about the unstable state.

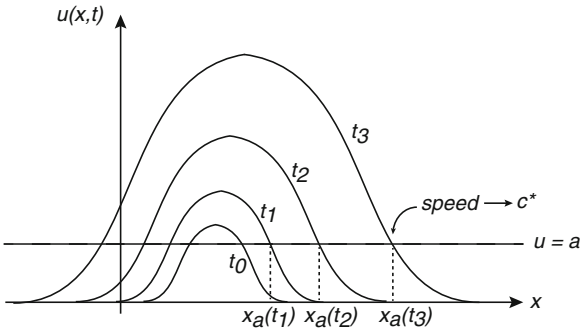

Fig. 3.14 Illustrative sketch of the growth and spreading of a solution $u(x,t)$ of the Fisher equation linearized about the unstable state $u = 0$, given a localized initial condition $u(x,t_0)$

3.3.1 The Linear Spreading Velocity

Linearizing (3.98) about $u = 0$,

$$\frac{\partial u}{\partial t} = \frac{\partial^2 u}{\partial x^2} + f'(0)u. \tag{3.99}$$

Substitution of the Fourier mode $e^{-i\omega t+ikx}$ gives the dispersion relation

$$\omega(k) = i(f'(0) - k^2). \tag{3.100}$$

The state $u = 0$ is then said to be linearly unstable if $\mathrm{Im}[\omega(k)] > 0$ for some range of k-values. In the case of the Fisher–KPP equation, after writing $k = k_r + ik_i$, this will occur when $f'(0) + k_i^2 > k_r^2$. Consider some generic initial condition $u(x,0)$ that is sufficiently localized in space (to be made precise later). Since there exists a range of unstable linear eigenmodes, we expect the localized initial condition to grow and spread out within the linear regime, as illustrated in Fig. 3.14. Tracking the evolution of a level curve $x_a(t)$ with $u(x_a(t),t) = a$, the *linear spreading velocity* c^* is defined to be the asymptotic speed of the point $x_a(t)$ in the rightward moving edge (assuming it exists):

$$c^* = \lim_{t\to\infty} \frac{dx_a(t)}{dt}. \tag{3.101}$$

The linearity of the underlying evolution equation (3.99) means that c^* is independent of the value a. (Note that for an isotropic medium, the leftward moving edge moves with the same asymptotic speed but in the opposite direction.) Suppose that c^* is finite. If we were to move in the traveling coordinate frame $\xi = x - c^*t$, then the leading rightward edge would neither grow nor decay exponentially. Imposing this condition on the Fourier expansion of the solution $u(x,t)$ then determines c^* in terms of the dispersion curve $\omega(k)$. More specifically, denoting the Fourier transform of the initial condition $u_0(x) = u(x,0)$ by $\tilde{u}_0(k)$, we have

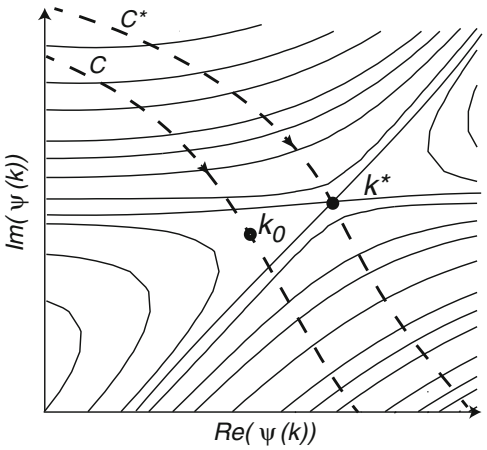

Fig. 3.15 Method of steepest descents. Sketch of $\mathrm{Re}(\psi)$ contours in the complex k-plane for an analytic function in the region of a saddle point at k^*. The integration contour C is deformed so that it passes through the saddle point

$$\begin{aligned} u(x,t) &= \int_{-\infty}^{\infty} \tilde{u}_0(k) \mathrm{e}^{i[kx-\omega(k)t])} \frac{dk}{2\pi} \\ &= \int_{-\infty}^{\infty} \tilde{u}_0(k) \mathrm{e}^{ik\xi} \mathrm{e}^{-i[\omega(k)-c^*k]t)} \frac{dk}{2\pi} \\ &= \int_{-\infty}^{\infty} \tilde{u}_0(k) \mathrm{e}^{ik\xi} \mathrm{e}^{\psi(k)t} \frac{dk}{2\pi}, \end{aligned} \tag{3.102}$$

where

$$\psi(k) = -i[\omega(k) - c^*k] = \omega_i(k) - c^*k_i - i[\omega_r(k) - c^*k_r] \tag{3.103}$$

In the limit $t \to \infty$ with ξ finite, we can approximate this integral using steepest descents. For the moment, we assume that $\tilde{u}(k)$ is an entire function (analytic in every finite region of the complex plane) so that we can deform the contour in the complex k-plane, that is, $(-\infty,\infty) \to C$, with C linking points at infinity in the complex plane where $\mathrm{Re}(\psi) < 0$.

Method of steepest descents. We briefly describe the method of steepest descents for a general analytic function $\psi(k)$; see also Fig. 3.15 and [275]. First, one would like to choose C so that the maximum of $\psi_r \equiv \mathrm{Re}(\psi)$ along the contour at k_0, say, is as large as possible, since this point will dominate the integral. Recall, however, that one of the Cauchy–Riemann conditions on an analytic function is that $\nabla^2(\mathrm{Re}(\psi)) = 0$, which means that $\mathrm{Re}(\psi)$ cannot have any maxima or minima (except at singularities or branch points where ψ would be nonanalytic). Therefore $\nabla(\mathrm{Re}(\psi)) = 0$ only at saddle points. Second, for a general integration contour, evaluating the integral in a neighborhood of the point k_0 will overestimate the value of the integral, since it does not take into account cancellations due to the rapidly oscillating function $\mathrm{e}^{i\mathrm{Im}(\psi(k))}$. The latter issue can be eliminated by choosing the contour that is the path of steepest ascent to a saddle point and the steepest descent away from the saddle. (If there exists more than one saddle, then one chooses the "highest" one). By construction, the path is parallel to $\mathrm{Re}(\psi)$. Hence, from the Cauchy–Riemann conditions, $\nabla(\mathrm{Im}(\psi)) = 0$

so that $\psi_i \equiv \mathrm{Im}(\psi)$ is constant along the contour. In other words, there are no fast oscillations along the path of steepest ascent and descent and one can obtain a good estimate of the integral by Taylor expanding about the saddle point. Thus, taking $\psi_i(k) = \psi_i(k^*)$ along C^*, we have

$$\begin{aligned} I &\equiv \int_{-\infty}^{\infty} \tilde{u}_0(k) \mathrm{e}^{ik\xi} \mathrm{e}^{\psi(k)t} \frac{dk}{2\pi} \\ &= \int_{C^*} \tilde{u}_0(k) \mathrm{e}^{ik\xi} \mathrm{e}^{\psi(k)t} \frac{dk}{2\pi} \\ &\approx \tilde{u}_0(k^*) \mathrm{e}^{i\psi_i(k^*)t} \int_{C^*} \mathrm{e}^{ik\xi} \mathrm{e}^{\psi_r(k)t} \frac{dk}{2\pi}. \end{aligned}$$

Finally, we Taylor expand $\psi_r(k)$ to second order in $\Delta k = k - k^*$, noting that $\psi'(k^*) = 0$ and $\psi_r''(k^*) < 0$ at the saddle,

$$\psi_r(k) = \psi_r(k^*) + \frac{(\Delta k)^2}{2} \psi_r''(k^*),$$

and approximate the remaining contour integral by a Gaussian. This then gives

$$I \approx \frac{1}{\sqrt{4\pi D t}} \tilde{u}_0(k^*) \mathrm{e}^{i[k^*\xi + \psi_i(k^*)t]} \mathrm{e}^{-\xi^2/4Dt} \mathrm{e}^{\psi_r(k^*)t}, \tag{3.104}$$

where $D = -\psi_r''(k^*)/2$.

Let us now apply steepest descent to the integral (3.102) for $\psi(k)$ given by (3.103) such that $\psi_r(k) = \omega_i(k) - c^* k_i$ and $\psi_i(k) = -[\omega_r(k) - c^* k_r]$. At the (unique) saddle point k^* at which $\psi'(k^*) = 0$, we have

$$c^* = \left. \frac{d\omega(k)}{dk} \right|_{k=k^*}. \tag{3.105}$$

Moreover, equation (3.104) becomes

$$I \approx \frac{1}{\sqrt{4\pi D t}} \tilde{u}_0(k^*) \mathrm{e}^{i[k^*\xi - [\omega_r(k^*) - c^* k_r^*]t]} \mathrm{e}^{-\xi^2/4Dt}, \tag{3.106}$$

where

$$D = -\frac{1}{2} \omega_i''(k^*). \tag{3.107}$$

Finally, we can determine the linear spreading velocity c^* by requiring that the asymptotic solution neither grows nor decays with time, $\psi_r(k^*) = 0$, which implies

$$c^* = \frac{\omega_i(k^*)}{k_i^*}. \tag{3.108}$$

Note that equating real and imaginary parts in (3.105) and combining with (3.108) means that we have three equations in the three unknowns c^*, k_r^*, k_i^*. In the particular case of the Fisher–KPP equation (3.98),

$$k_r^* = 0, \quad k_i^* = \sqrt{f'(0)}, \quad c^* = 2\sqrt{f'(0)}, \quad D = 1. \tag{3.109}$$

Since $k_r^* = 0$, we can combine (3.105) and (3.108) into the single condition $c^* = c(\lambda^*)$, $\lambda^* = k_i^*$, where

$$c(\lambda) = \frac{\omega_i(i\lambda)}{\lambda}, \quad \left.\frac{dc(\lambda)}{d\lambda}\right|_{\lambda=\lambda^*} = 0. \tag{3.110}$$

It can also be seen that the modulus of u falls off as

$$|u(x,t)| \sim \frac{1}{\sqrt{t}} \mathrm{e}^{-\lambda^* \xi} \mathrm{e}^{-\xi^2/4t}. \tag{3.111}$$

A more direct way to derive the function $c(\lambda)$ is to consider the linearized PDE in the moving frame $\xi = x - ct$,

$$-c\frac{dU}{d\xi} = \frac{d^2U}{d\xi^2} + f'(0)U,$$

and to assume the leading-edge solution $U(\xi) \sim \mathrm{e}^{-\lambda\xi}$.

In the above analysis, it was assumed that the Fourier transform of the initial condition $u_0(x)$ was an entire function. This would apply to cases for which $u_0(x)$ is a Dirac delta function, has compact support, or decays faster than any exponential for large enough x (e.g., a Gaussian). Now suppose that $u_0(x)$ falls off exponentially for large x, $u_0(x) \sim \mathrm{e}^{-\lambda x}$ for some λ. Then $\tilde{u}_0(k)$ has a pole in the upper-half complex plane at $k = k'$ with $\mathrm{Im}(k') = \lambda$. It follows that when deforming the contour C in the complex k-plane in order to perform steepest descents, we pick up a contribution from the pole. Taking this into account, it can be shown that, within the linear regime, initial conditions whose exponential decay rate $\lambda > \lambda^*$ lead to profiles that asymptotically spread with the linear spreading velocity v^*. On the other hand, if $\lambda < \lambda^*$ then the profile advances at a speed faster than c^* [544].

So far we have investigated the evolution of a localized initial condition in the linear regime. It still remains to determine whether or not there are classes of initial conditions under which the full nonlinear system converges to a unique asymptotic front solution and how the speed of the front c is related to the linear spreading velocity c^*. It turns out that for front propagation into a linearly unstable state, there are only two possibilities when starting from sufficiently steep initial conditions, that is, initial conditions that fall off faster than $\mathrm{e}^{-\lambda^* x}$ [544]:

Pulled front: $c = c^*$ so that the front dynamics is determined by the behavior in the leading edge of the front where $u(x,t) \approx 0$, that is, the front is pulled along by the linear spreading of small perturbations into the linearly unstable state.

Pushed front: $c > c^*$ so that nonlinearities play an important role in determining the velocity of the front, pushing it into the unstable state.

In the special case of initial conditions with compact support, it can be proven that the solution evolves into a front that propagates at the minimal possible wave speed $c_{\min}$, which is bounded above and below [15]:

$$c^* = 2\sqrt{f'(0)} \leq c_{\min} < 2\sqrt{\sup_u \left[\frac{f(u)}{u}\right]}. \tag{3.112}$$

For any concave function, $f(u) \leq uf'(0)$, the lower and upper bounds coincide and we have a pulled front; this applies to the standard Fisher–KPP equation where $f(u) = u(1-u)$. On the other, the upper and lower bounds do not coincide for concave $f(u)$. The minimal front velocity can then be larger than the linear velocity indicative of a pushed front. An example of the latter is the Ginzburg–Landau term $f(u) = u(1-u)(1+\alpha u)$ with $\alpha > 0$. One finds that for compact initial conditions, a pulled front is selected when $\alpha \leq 2$, whereas a pushed front is selected when $\alpha > 2$ [33].

3.3.2 Variational Method for Front Velocity Selection

Over recent years a number of methods have been developed to tackle the general problem of front velocity selection, that is, which of the infinity of possible wave speeds is selected by a given initial condition. One method analyzes the dynamics of the front position using Hamilton–Jacobi theory. Although it is only applicable to pulled fronts, it has the advantage of being able to tackle the effects of heterogeneities, as illustrated in Sect. 3.2.4 for CaMKII translocation waves. Here we briefly describe another method due to Benguria and Depassier [36], which is based on a variational principle. The latter can be applied to both pulled and pushed fronts, although in many cases it only provides lower and upper bounds for the front velocity. Consider a front solution of the reaction–diffusion Eq. (3.98) in traveling wave coordinates,

$$u_{\xi\xi} + cu_\xi + f(u) = 0, \tag{3.113}$$

with $\lim_{\xi\to-\infty} u(\xi) = 1$ and $\lim_{\xi\to\infty} u(\xi) = 0$, $\xi = x - ct$. Set $q(u) = -u_\xi > 0$ for $u \in (0,1)$, so that (3.113) becomes

$$q(u)\frac{dq}{du} - cq(u) + f(u) = 0, \quad q(0) = 0, \quad q(1) = 0. \tag{3.114}$$

Let $g \in C^1[0,1]$ be a positive, monotonically decreasing function with $\int_0^1 g(u)du < \infty$, and set $h = -g' > 0$. We denote the space of admissible functions g by the domain $\mathscr{D}$. Multiplying (3.114) by g/q and integrating with respect to u gives (after integration by parts)

$$\int_0^1 \left(h(u)q(u) + \frac{f(u)}{u}g(u)\right)du = c\int_0^1 g(u)du. \tag{3.115}$$

For fixed u, the functional

$$\Phi[q] = qh + \frac{f}{q}g$$

has a minimum at $q_0 = \sqrt{fg/h}$ with $\Phi[q_0] = 2\sqrt{fgh}$. It follows that

$$c\int_0^1 g(u)du = \int_0^1 \Phi[q(u)]du \geq 2\int_0^1 \sqrt{f(u)g(u)h(u)}du,$$

that is,

$$c \geq 2\frac{\int_0^1 \sqrt{f(u)g(u)h(u)}du}{\int_0^1 g(u)du} \equiv I[g]. \tag{3.116}$$

As we show below, there exists a function $\hat{g} \in \mathscr{D}$ that maximizes the lower bound for c in such a way that the equality holds. Hence, we have the variational principle

$$c = \max_{g\in\mathscr{D}} \left(2\frac{\int_0^1 \sqrt{f(u)g(u)h(u)}du}{\int_0^1 g(u)du} \right), \tag{3.117}$$

which can be used to estimate c using a parameterized set of trial functions. This result can also be used to derive the upper bound of (3.112) [36].

In order to establish the existence of the function $\hat{g}$, we first require $\Phi[q] = \Phi[q_0]$ for all u, that is, $hq = f\hat{g}/q$. Combined with (3.114) this gives

$$-\frac{\hat{g}'}{\hat{g}} = \frac{c}{q} - \frac{q'}{q},$$

which can be integrated to yield

$$\hat{g}(u) = q(u)\exp\left(\int_u^{u_0} \frac{c}{q(u')}du' \right) \tag{3.118}$$

for some u_0, $0 < u_0 < 1$. Since $\hat{g} > 0$ on $(0,1)$ and $h = \hat{g}f/q^2 > 0$ we deduce that $\hat{g} \in C^1[0,1]$ and is a positive, decreasing function. It remains to check that $\int_0^1 \hat{g}(u)du < \infty$, which requires determining the behavior near $u = 0$. Linearizing (3.113) around $u = 0$ shows that if $u \sim \mathrm{e}^{-\lambda\xi}$ for $\xi \to \infty$ with $\lambda = (c + \sqrt{c^2 - 4f'(0)})/2$, then $q \sim \lambda u$ for $u \sim 0$. The integral solution for $\hat{g}$ then implies that

$$\hat{g} \sim \lambda \frac{1}{u^{c/\lambda - 1}}, \quad u \sim 0.$$

Therefore, if $c < 2\lambda$, that is, $c > 2\sqrt{f'(0)}$, then $\int_0^1 \hat{g}(u)du < \infty$ and $\hat{g} \in \mathscr{D}$. Finally, in the special case $c = 2\sqrt{f'(0)}$, one can take the set of trial functions $g_\alpha(u) = \alpha u^{\alpha-1}$ with $g_\alpha \in \mathscr{D}$ for $0 < \alpha < 1$ and show that $I[g_\alpha] \to 2\sqrt{f'(0)}$ as $\alpha \to 0$. This means $c = 2\sqrt{f'(0)} \geq \max_g I[g] \geq 2\sqrt{f'(0)}$, that is, $c = \max_g I[g]$.

Chapter 4
Calcium Waves and Sparks

Calcium (Ca^{2+}) is one of the most important and well-studied cellular signaling molecules. From a modeling perspective, it attracts a great deal of interest due to the fact that calcium signaling often involves complex spatiotemporal dynamics, including oscillations and waves. There are a number of excellent general reviews on the modeling of calcium dynamics within cells, including Chap. 7 of Keener and Sneyd [322] and Falcke [181]. In this chapter, we focus on the mathematical modeling and analysis of calcium waves and their potential significance in neuronal calcium signaling; see also the reviews by Berridge [43] and Ross [534]. Although there are a number of very detailed whole-cell models of calcium signaling, we will focus on simplified models that are analytically tractable. In particular, we will highlight some of the mathematical methods used to characterize calcium waves.

4.1 Calcium Signaling in Neurons

In vertebrates, most of the Ca^{2+} is stored in bones, from where it can be released by hormonal stimulation to maintain a high extracellular Ca^{2+} concentration (around 1 mM). On the other hand, active ion pumps and exchangers maintain the cytoplasmic Ca^{2+} concentration at relatively low levels (around 10–100 nM). The resulting steep concentration gradient across the plasma membrane means that cells are able to increase their cytoplasmic Ca^{2+} concentration rapidly by opening either voltage-gated or ligand-gated Ca^{2+} ion channels. Within the context of neuronal processing, the activation of voltage-gated calcium channels (VGCCs) at axon terminals triggers the release of synaptic neurotransmitter (see Sect. 1.3); VGCCs also contribute to the generation of dendritic action potentials (see Sects. 1.4.3 and 3.1). A classical example of ligand gating in neurons is the entry of Ca^{2+} through NMDA receptors on postsynaptic dendritic spines. The resulting transient Ca^{2+} signal is thought to play a major role in the induction of changes in synaptic strength; see below.

Another major mechanism whereby cells, including neurons, regulate their cytoplasmic Ca^{2+} concentration is via the intracellular supply of Ca^{2+} from internal

P.C. Bressloff, *Waves in Neural Media: From Single Neurons to Neural Fields*,
Lecture Notes on Mathematical Modelling in the Life Sciences,
DOI 10.1007/978-1-4614-8866-8_4,

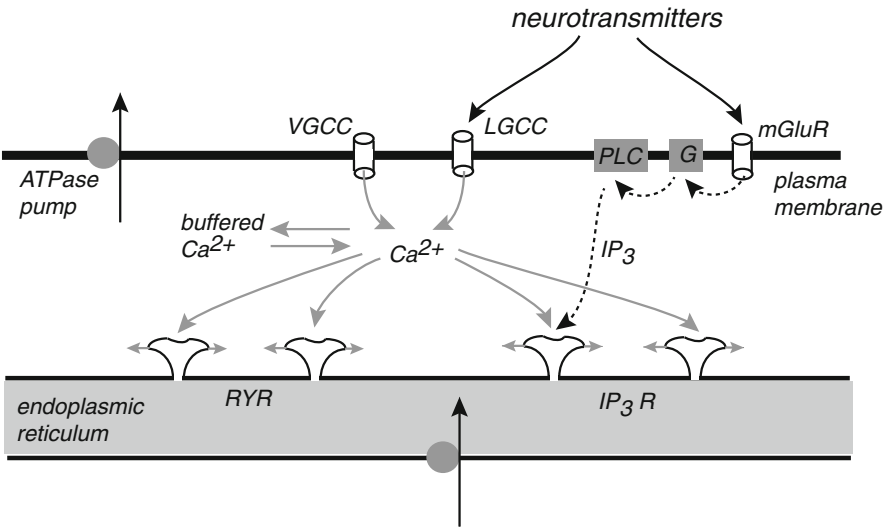

Fig. 4.1 Neural calcium signaling. The entry of Ca^{2+} from outside the cell is mediated by voltage-gated (VGCC) and ligand-gated (LGCC) calcium channels. Stimulation of metabotropic glutamate receptors (mGluRs) produces IP_3 second messengers that bind to IP_3 receptors (IP_3Rs), which subsequently release Ca^{2+} from the endoplasmic reticulum. Both IP_3Rs and Ryanodine receptors (RyRs) are sensitive to Ca^{2+}, resulting in Ca^{2+}-induced Ca^{2+}-release (CICR). The latter can sometimes result in the propagation of a Ca^{2+} wave along the dendrites

stores such as the *endoplasmic reticulum* (ER) and *mitochondria*. *Inositol (1,4,5)-trisphosphate* (IP_3) receptors and *Ryanodine* (Ry) receptors distributed throughout the ER, for example, mediate the release of Ca^{2+} into the cytoplasm, whereas Ca^{2+} ion pumps maintain the relatively high Ca^{2+} concentration within the ER. The Ry receptor plays a critical role in excitation–contraction coupling in skeletal and cardiac muscle cells, but is also found in nonmuscle cells such as neurons. One important feature of Ry receptors is that they can undergo Ca^{2+}-induced Ca^{2+}-release (CICR), in which elevated cytoplasmic Ca^{2+} activates Ry receptors that release further Ca^{2+}, which then activates other Ry receptors, resulting in a nonlinear regenerative feedback mechanism. The IP_3 receptor is similar in structure to the Ry receptor, but is found predominantly in nonmuscle cells and is sensitive to the second messenger IP_3. The binding of an extracellular ligand such as a hormone or a neurotransmitter to a metabotropic receptor results in the activation of a G-protein and the subsequent activation of phospholipase C (PLC). This then cleaves phosphatidylinositol bisphosphate (PIP_2) into diacylglycerol (DAG) and IP_3. The water soluble IP_3 is free to diffuse throughout the cell cytoplasm and bind to IP_3 receptors located on the ER membrane, which then open and release Ca^{2+} from the ER. The opening and closing of an IP_3 receptor is also modulated by the concentration of cytoplasmic Ca^{2+}, so it too can undergo CICR. Yet another mechanism for controlling cytoplasmic Ca^{2+} is through buffering (binding) to large proteins. Indeed, it is estimated that

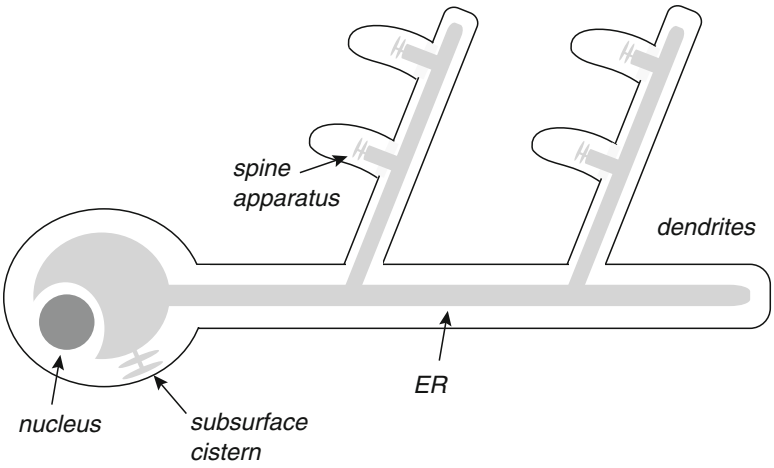

Fig. 4.2 The endoplasmic reticulum (ER) is a single and continuous membrane-bound organelle that is distributed throughout the dendrites and axon (not shown) of a neuron [516]. It is responsible for the synthesis and posttranslational modification of most secretory and membrane proteins, as well as the regulation of Ca^{2+} levels. The shape of the ER is heterogeneous, but can be divided into three domains: the nuclear envelope, the ribosome-bound rough ER (RER), and the ribosome-free smooth ER (SER). The RER is constituted primarily by sheets or cisternae, whereas the SER is predominantly composed of 60–100 nm diameter tubules that form irregular polygons with a common luminal space connected via three-way junctions. The ER present in the soma and proximal dendritic compartment is rich in ribosomes, corresponding to the RER, whereas the ER distributed in distal dendrites and axons corresponds mostly to SER and contains only a few sparse ribosomes. The ER comes into close proximity with the plasma membrane at various locations, forming subsurface cisternae within the soma and axon initial segment, and the spine apparatus within dendritic spines

at least 99 % of the total cytoplasmic Ca^{2+} is bound to buffers. A summary of the basic extracellular and intracellular mechanisms for controlling the concentration of cytoplasmic Ca^{2+} is shown in Fig. 4.1.

The signaling mechanisms and dynamics of Ca^{2+} release from the ER in neurons have been much less well studied than extracellular sources of Ca^{2+}. However, the ER is a continuous network that is distributed throughout a neuron, extending all the way into the dendrites and axon and coming into close contact with the plasma membrane and synapses at many locations; see Fig. 4.2. Hence, as suggested by Berridge [43], it is likely that the integrative and regenerative properties of the ER and plasma membrane provide a binary membrane system that regulates a variety of neuronal process via Ca^{2+} signaling, including excitability, neurotransmitter release, synaptic plasticity, and gene transcription.

(a) Within the soma and initial axonal segment, the ER forms flattened sheets known as *subsurface cisternae* that come into close contact with the plasma membrane. These internal structures are thought to play an important role in regulating neuronal excitability. For example, many neurons exhibit significant after-hyperpolarizations (AHPs) following either a single action potential or a

burst of action potentials, which suppress subsequent firing of the cell (spike frequency adaptation). Often AHPs have both a fast component and a slow component, which arise from the opening of two separate Ca^{2+}-activated K^+ channels (gK_{Ca1} and gK_{Ca2}). The fast activation of gK_{Ca1} is due to the entry of extracellular Ca^{2+} via VCCNs during the course of an action potential, whereas the slow activation of gK_{Ca2} is probably due to CICR from Ry receptors located in the subsurface cisternae.

(b) Within the axon, the ER consists of connecting tubules that run parallel along the axon. The axonal ER network extends into a synapse, coming into close contact with the plasma membrane and associated neurotransmitter secretory vesicles. It is thought that calcium release from Ry and IP_3 receptors contributes to the formation of localized high-concentration bursts of Ca^{2+} necessary for the exocytosis (transport and fusion) of vesicles to the plasma membrane.

(c) The ER network is also distributed throughout the dendritic tree and into spines, where it terminates at the so-called spine apparatus. The latter consists of closely packed plates of ER that are located within the middle of the spine and is thus well placed to contribute to Ca^{2+} signaling during synaptic plasticity. The latter refers to the rapid and long-lasting changes in synaptic strength that are thought to provide the subcellular substrate for learning and memory. Much of the information regarding synaptic plasticity in mammalian neurons has been obtained from studies of hippocampal and cerebellar neurons [120, 123, 385, 402]. In particular, it has been found that the same synapses can be switched rapidly and reversibly from an enhanced state of *long-term potentiation* (LTP) to a reduced state of *long-term depression* (LTD). Interestingly, both LTP and LTD are induced by a transient increase in the local Ca^{2+} concentration within a spine. It was originally thought that the bidirectional switch only depended on the amplitude of the Ca^{2+} signal, with a stronger stimulus inducing LTP and a weaker one LTD. Now, however, it appears likely that the detailed spatial and temporal structure of the calcium signal may be important. Although the influx of extracellular Ca^{2+} through NMDA receptors or voltage-gated channels is still the major contributor to the induction of LTP and LTD, there is increasing evidence that there is also a component arising from intracellular stores [428, 447, 534]. Activation of the ER could be mediated either by Ca^{2+} itself via CICR or by stimulation of metabotropic glutamate (mGlu) receptors in the plasma membrane, resulting in the production of IP_3. The fact that CICR requires both cytoplasmic IP_3 and Ca^{2+} suggests that IP_3 receptors could act as *coincidence detectors* for mGluR activation and postsynaptic Ca^{2+} signaling arising from back-propagating action potentials or dendritic Ca^{2+} spikes [658].

(d) One of the most dramatic consequences of CICR is the propagation of intracellular Ca^{2+} waves mediated primarily by the opening of IP_3 receptors. These waves were first observed in nonneuronal cells such as *Xenopus laevis* oocytes [367, 490], where the resulting changes in Ca^{2+} concentration across the whole cell provided a developmental signal. The discovery of Ca^{2+} waves in neurons is more recent [303, 428, 447, 534, 658]. Since these cells have extensive den-

dritic and axonal arborizations, the distribution of the components of the Ca^{2+} signaling apparatus within the cell plays a crucial role in determining whether or not local Ca^{2+} release transforms into a propagating wave, and how far it travels. For example, in pyramidal neurons of the hippocampus and cortex, Ca^{2+} waves are usually observed in the primary apical dendrite and perhaps the soma, rarely reaching beyond the point where thick dendrites begin to branch. Since the ER network is distributed throughout the cell, this suggests that there is a heterogeneous distribution of mGlu receptors and IP_3 receptors along the dendrite. Ca^{2+} waves rarely propagate from the dendrite to the soma, unless there is a sufficiently strong and sustained stimulation of a neuron that results in high levels of cytoplasmic IP_3 or higher concentrations of internally stored Ca^{2+}. If a Ca^{2+} wave did reach the soma, then it would generate a strong Ca^{2+} signal in the soma and nucleus due to the high concentration of IP_3 receptors in these regions. It has been suggested that a Ca^{2+} wave could allow a strongly stimulated synapse in the dendrites to signal to the nucleus, where the large increase in Ca^{2+} concentration could activate gene transcription, which is a necessary step in more persistent forms of synaptic plasticity such as late long-term potentiation (L-LTP). However, the role of Ca^{2+} waves in initiating gene transcription is still controversial. On the other hand, the likely contribution of IP_3 receptor-mediated Ca^{2+} release during normal LTP and LTD indicates that Ca^{2+} waves could be important in determining the spatiotemporal pattern of synaptic changes.

(e) Many nonneuronal cell types exhibit spontaneous localized Ca^{2+} release events known as *sparks* [110]. Calcium sparks, which are thought to be the building blocks of the large regenerative Ca^{2+} signal that controls contraction in cardiac and skeletal muscle cells, arise from the opening of clusters of RyRs by local CICR. The frequency of calcium spark events is sensitive to changes in membrane potential, although they rarely induce calcium waves [111]. Similar events known as calcium *puffs* have been found in *Xenopus laevis* oocytes [489, 490, 690]. They are also spatially and temporally localized, are fast, and occur stochastically. However, in contrast to sparks, they are mediated by IP_3Rs and coalesce more easily to form calcium waves. Localized events in neurons with spark-like and puff-like properties have recently been observed in slice preparations, and their frequency can be modulated by synaptic activity and changes in membrane potential [389, 403]. Although it is likely that they also occur in vivo, it is not yet clear whether or not they have a specific function.

4.2 Reaction–Diffusion Models of Ca^{2+} Dynamics

One of the major challenges in modeling calcium waves is that the ER and cytoplasm comprise two highly interconnected three-dimensional domains (ignoring, for simplicity, other intracellular compartments such as the mitochondria). Assuming

that Ca^{2+} undergoes normal diffusion within each compartment, together with buffering, we can write down the following pair of diffusion equations for the Ca^{2+} concentrations c, c_e in the cytoplasm and ER [322]:

$$\frac{\partial c}{\partial t} = \nabla \cdot (D_c \nabla c) - J_{\text{on}} + J_{\text{off}}, \quad \mathbf{r} \in \Omega_c \tag{4.1}$$

and

$$\frac{\partial c_e}{\partial t} = \nabla \cdot (D_e \nabla c_e) - \hat{J}_{\text{on}} + \hat{J}_{\text{off}}, \quad \mathbf{r} \in \Omega_e, \tag{4.2}$$

where Ω_c and Ω_e denote the cytoplasmic and ER domains, respectively, D_c and D_e are the corresponding diffusivities in the two domains, and the on/off fluxes take into account the binding/unbinding of Ca^{2+} to buffering proteins. These equations are supplemented by various boundary conditions that take into account the exchange of Ca^{2+} between the cytoplasm and the plasma membrane or ER. Let J_{in} denote the total inward flux of Ca^{2+} from the plasma membrane to the cytoplasm via voltage-gated and ligand-gated ion channels, and let J_{p1} be the outward flux due to ATPase ion pumps in the plasma membrane. Then

$$D_c \nabla c \cdot \mathbf{n} = J_{\text{in}} - J_{\text{p1}}, \quad \mathbf{r} \in \partial\Omega_{c,m}, \tag{4.3}$$

where $\partial\Omega_{c,m}$ is the surface of the plasma membrane with unit normal $\mathbf{n}$. Similarly, let J_{IP} and J_{Ry} denote the inward fluxes from the ER to the cytoplasm via IP_3Rs and RyRs, respectively, and let J_{p2} denote the outward flux due to ion pumps in the ER. This yields

$$D_c \nabla c \cdot \hat{\mathbf{n}} = -D_e \nabla c_e \cdot \hat{\mathbf{n}} = J_{\text{IP}} + J_{\text{Ry}} - J_{\text{p2}}, \quad \mathbf{r} \in \partial\Omega_e, \tag{4.4}$$

where $\partial\Omega_e$ is the boundary of the ER with unit normal $\hat{\mathbf{n}}$. A schematic diagram of all the fluxes is shown in Fig. 4.3.

Let us first consider a space-clamped version of this model, in which one treats the cytoplasm and ER as two well-mixed homogeneous compartments. In that case, the various surface and volume fluxes are combined as follows:

$$\frac{dc}{dt} = -J_{\text{on}} + J_{\text{off}} + \frac{|\partial\Omega_{c,m}|}{|\Omega_c|}[J_{\text{in}} - J_{\text{p1}}] + \frac{|\partial\Omega_e|}{|\Omega_c|}[J_{\text{IP}} + J_{\text{Ry}} - J_{\text{p2}}] \tag{4.5}$$

and

$$\frac{dc_e}{dt} = -\hat{J}_{\text{on}} + \hat{J}_{\text{off}} - \frac{|\partial\Omega_e|}{|\Omega_e|}[J_{\text{IP}} + J_{\text{Ry}} - J_{\text{p2}}]. \tag{4.6}$$

Each of the fluxes in these equations corresponds to a component of the so-called Ca^{2+}-signaling toolkit [44]. Thus, the equations for Ca^{2+} dynamics have to be coupled to additional biochemical equations describing the dynamics of ion pumps, the Ca^{2+}-dependent gating of the Ry and IP_3 receptors, and how the latter are regulated by the second messenger IP_3. Often the external flux J_{in} is simply taken to be a linear increasing function of the IP_3 concentration. There have been many studies of space-clamped Ca^{2+} models with particular focus on calcium oscillations

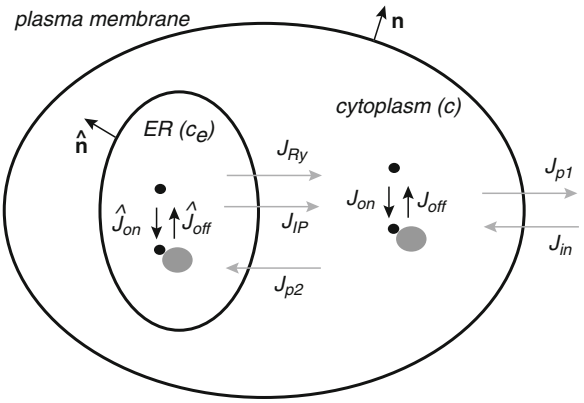

Fig. 4.3 Schematic diagram showing various fluxes in reaction–diffusion model of Ca^{2+} dynamics

[181, 322]. Although the models differ in their degree of complexity with regards the component fluxes, they can often be reduced to simpler models that have similar structure to the FitzHugh–Nagumo (FN) model of excitability. For example, suppose that we ignore fluxes through the plasma membrane so that the total intracellular Ca^{2+} is conserved, that is, $|\Omega_c|c + |\Omega_e|c_e$ is a constant. Furthermore, suppose that there are only two intracellular fluxes, $J_{\rm IP}$ and $J_{\rm p2}$, and the IP_3 concentration is fixed. Ignoring the effects of buffering, one can write down an analogous equation to (2.3) of the form

$$\frac{dc}{dt} = f(c,h), \quad \tau(c)\frac{dh}{dt} = h_\infty(c) - h, \tag{4.7}$$

where c is the concentration of free cytosolic Ca^{2+}, $f(c,h)$ represents the net flux into the cytoplasm from the ER, and h is an inactivation variable that plays a similar role to the recovery variable w of the original FN equations. One interpretation of h is the fraction of IP_3 receptors that are not inactivated by bound Ca^{2+}. Li and Rinzel [381] derived such a two-variable model by reducing the classical kinetic model of Ca^{2+}-gated IP_3 receptors due to De Young and Keizer [692]; see Sect. 4.4.1.

Unfortunately, the complex geometry and heterogeneity of the ER means that the spatially distributed model given by (4.1)–(4.4) is far too complicated to analyze, even when simplified models of the various fluxes are considered. A common strategy is to ignore the detailed structure of the ER by assuming that the concentrations c and c_e coexist at every point in space. This is motivated by the idea that since diffusion is fast over short distances, local variations due to heterogeneities are smoothed out. Phenomenologically speaking, this leads to the *calcium bidomain equations*

$$\frac{\partial c}{\partial t} = \nabla\cdot(\overline{D}_c\nabla c) - J_{\rm on} + J_{\rm off} + \chi_c[J_{\rm IP} + J_{\rm Ry} - J_{\rm p2}] \tag{4.8}$$

and

$$\frac{\partial c_e}{\partial t} = \nabla \cdot (\overline{D}_e \nabla c_e) - \hat{J}_{\rm on} + \hat{J}_{\rm off} - \chi_e [J_{\rm IP} + J_{\rm Ry} - J_{\rm p2}]. \tag{4.9}$$

Here $\chi_c = |\partial\Omega_e|/|\Omega_c|, \chi_e = |\partial\Omega_e|/|\Omega_e|$ are surface to volume ratios, and $\overline{D}_c, \overline{D}_e$ are effective diffusion coefficients. Note, however, that in order to determine the effective diffusion coefficients, which will depend on the geometry of the ER, and justify the precise form of the factors χ_c, χ_e, it is necessary to derive these equations from first principles using homogenization theory [224, 322]. Elements of the theory are described in appendix section 4.6. Now suppose that only the fluxes $J_{\rm IP}$ and $J_{\rm p2}$ are included along the lines of the space-clamped model. However, in contrast to the latter, it is now necessary to keep track of both the cytoplasmic and ER Ca^{2+} concentrations, since they are spatially varying. A one-dimensional bidomain model with constant diffusion coefficients then takes the form

$$\frac{\partial c}{\partial t} = D_c \frac{\partial^2 c}{\partial x^2} + f(c, c_e, h) \tag{4.10a}$$

$$\frac{\partial c_e}{\partial t} = D_e \frac{\partial^2 c}{\partial x^2} - \chi_e f(c, c_e, h) \tag{4.10b}$$

$$\tau(c) \frac{\partial h}{\partial t} = h_\infty(c) - h, \tag{4.10c}$$

where $f(c, c_e, h)$ represents the net Ca^{2+} flux from the ER to the cytoplasm the spatial dimensions have been fixed such that $\chi_c = 1$. Analysis of traveling wave solutions of (4.10) proceeds along very similar lines to that of the Hodgkin–Huxley equations for membrane voltage excitability; see Chap. 2. Depending on parameter values, the model system can support solitary waves when the physiological state of the cytoplasm is excitable, periodic waves when it is oscillatory, and traveling fronts when it is bistable [322].

However, one important feature that needs to be taken into account in the case of calcium excitability is buffering. Insights into the effects of buffering can be obtained by looking at reduced models of excitability such as the bistable equation or the FN equations [592, 635, 636, 653]. Following [592, 653], consider a simple extension of the bistable equation (Sect. 2.2). First, note that the basic chemical reaction for Ca^{2+} buffering takes the form

$$P + Ca^{2+} \underset{k_-}{\overset{k_+}{\rightleftharpoons}} B,$$

where P is the buffering protein and B is the protein/Ca^{2+} complex. Let c and b denote, respectively, the concentration of free cytosolic Ca^{2+} and buffered Ca^{2+}. The extended bistable equation is then (in one spatial dimension)

$$\frac{\partial c}{\partial t} = D_c \frac{\partial^2 c}{\partial x^2} + f(c) + k_- b - k_+ c(b_t - b), \tag{4.11a}$$

$$\frac{\partial b}{\partial t} = D_b \frac{\partial^2 b}{\partial x^2} - k_- b + k_+ c(b_t - b). \tag{4.11b}$$

Here b_t is the total buffer concentration, $f(c)$ takes into account all Ca^{2+} fluxes, and the diffusion coefficients of free and buffered Ca^{2+} are assumed to be constants. Suppose that the buffer reaction rates $k_\pm$ are faster than the time constants of Ca^{2+} dynamics. The buffer concentration b can be taken to be in the quasi steady state $k_- b - k_+ c(b_t - b) = 0$, that is,

$$b = \frac{b_t c}{K + c}, \quad K = \frac{k_-}{k_+}. \tag{4.12}$$

Adding (4.11a) and (4.11b) and eliminating b using (4.12) gives [653]

$$\begin{aligned}\frac{\partial c}{\partial t} &= \frac{1}{1+\theta(c)}\left(\frac{\partial^2 w(c)}{\partial x^2} + f(c)\right) \\ &= \frac{D_c + D_b\theta(c)}{1+\theta(c)}\frac{\partial^2 c}{\partial x^2} - \frac{2D_b\theta(c)}{(K+c)(1+\theta(c))}\left(\frac{\partial c}{\partial x}\right)^2 + \frac{f(c)}{1+\theta(c)},\end{aligned}$$

where

$$w(c) = D_c c + D_b b_t \frac{c}{K+c}, \quad \theta(c) = \frac{b_t K}{(K+c)^2}. \tag{4.13}$$

It is clear that a mobile buffer ($D_b > 0$) generates a nonlinear advection–diffusion equation for c; the advection term vanishes if the buffer is immobile ($D_b = 0$).

The form of the effective reaction–diffusion equation for c suggests making then change of variables $w = w(c)$, with w, a monotone increasing function of c since $w'(c) = D_c + D_b\theta(c) > 0$. Denoting the unique inverse of the function $w(c)$ by $c = \phi(w)$, we can write

$$\frac{\partial w}{\partial t} = \frac{D_c + D_b\Theta(w)}{1+\Theta(w)}\left(\frac{\partial^2 w}{\partial x^2} + f(\phi(w))\right), \tag{4.14}$$

where $\Theta(w) = b_t K/(K+\phi(w))^2$. Now suppose that $f(c)$ has two stable zeros $c_\pm$ separated by an unstable zero c_0 with $c_- < c_0 < c_+$. It immediately follows that $f(\Theta(w))$ has three corresponding zeros $w_\pm, w_0$ with $w_- < w_0 < w_+$ and $w_\pm$ stable. A traveling front solution of wave speed v, $w(x,t) = W(x - vt)$, satisfies the ODE

$$V_{\xi\xi} + \frac{v}{D_{eff}(W)}W_\xi + f(\phi(W)). \tag{4.15}$$

Proceeding as in Sect. 2.2, multiply both sides of this equation by W_ξ and integrate to show that

$$v\int_{-\infty}^{\infty} \frac{W_\xi^2}{D_{\text{eff}}(W(\xi))}d\xi = \int_{w_-}^{w_+} f(\phi(w))dw.$$

Since the integral on the left-hand side is positive definite, the sign of v is determined by the sign of the integral on right-hand side. In particular, a right-moving wave ($v > 0$) exists provided that

$$\int_{c_-}^{c_+} (D_c + D_b\theta(c))\, f(c)dc > 0, \tag{4.16}$$

where we have converted back to the original variable c. It can be seen that immobile buffers ($D_b = 0$) have no effect on the existence of a traveling wave; this result also holds true for wave stability and uniqueness. On the other hand, mobile buffers can eliminate a traveling wave when they are of high affinity (small K) or have a large diffusion coefficient (large D_b).

4.3 Discrete Calcium Sources and the Fire–Diffuse–Fire Model

4.3.1 Discrete Calcium Sources and Averaging

The above reaction–diffusion models assumed that Ca^{2+} release from the ER is homogeneous in space. This neglects the fact that IP_3 receptors (as well as Ry receptors) tend to be arranged in clusters. For example, in *Xenopus* oocytes, the density of clusters is around 1 per $30\,\mu m^2$, with each cluster containing about 25 IP_3 receptors [322]. Consequently, the propagation of Ca^{2+} waves tends to be saltatory, jumping from one cluster to the next. (Clustering of IP_3 receptors is also thought to occur along dendrites [534]). We have previously encountered saltatory waves due to discreteness effects, namely, action potential propagation along myelinated axons (Sect. 2.5) and solitary Ca^{2+} spikes propagating along spiny dendrites (Sect. 3.1). The latter waves depend on the action of VGCCs and other voltage-gated ion channels and are thus distinct from the Ca^{2+} waves considered in this chapter, which depend on Ca^{2+} release from internal pools. Nevertheless, the analytical techniques used to study these other examples can be adapted to the present case. First, we will discuss how the averaging method of Sect. 2.5 can be used to study wave propagation failure in the presence of discrete release sites, following [318]. We will then describe an alternative, *fire–diffuse–fire* (FDF) model of saltatory Ca^{2+} waves, which is identical in structure to the spike–diffuse–spike (SDS) model of Sect. 3.1. (In contrast to other chapters, we will use c to denote cytosolic Ca^{2+} concentration and v to denote wave speed.)

Consider a one-dimensional model of Ca^{2+} diffusion and release of the form [318]

$$\frac{\partial c}{\partial t} = -k_c c + D_c \frac{\partial^2 c}{\partial x^2} + L \sum_n \delta(x - nL) f(c), \tag{4.17}$$

where $f(c)$ represents the Ca^{2+}-dependent rate of release from each cluster (taken to be identical), and the decay term represents the effects of ion pumps. The clusters are assumed to be evenly spaced with spatial separation L. For simplicity, the ER concentration c_e and IP_3 concentration p are taken to be fixed. It is tempting to apply homogenization theory to this problem (see appendix section 4.6), assuming diffusion is fast on the length scale L, that is, $L^2 k_c / D_c \ll 1$. Intuitively, one would expect the L-periodic function $g(x) = L \sum_n \delta(x - nL)$ to be replaced by its spatial average $\int_0^L g(x)dx/L = 1$. However, as highlighted by Keener [318, 319] and discussed in Sect. 2.5, the homogenized system cannot account for the fact that discreteness

effects can lead to wave propagation failure in regimes that the continuous model would predict traveling waves exist. This reflects the fact that wave solutions are not structurally stable. The occurrence of propagation failure can be established by constructing standing wave-front solutions [318, 322]. The latter are stationary solutions of (4.17). On the intervals $nL < x < (n+1)L$, this gives

$$0 = -k_c c + D_c \frac{\partial^2 c}{\partial x^2}, \tag{4.18}$$

which is supplemented by jump conditions at $x = nL$,

$$D_c \frac{\partial c}{\partial x}\Big|_{nL_-}^{nL_+} + Lf(c_n) = 0. \tag{4.19}$$

The latter is obtained by integrating the stationary equation on either side of $x = nL$. The general solution of (4.18) is

$$c(x) = c_n \cosh(\beta(x-nL)/L) + \hat{c}_n \sinh(\beta(x-nL)/L), \quad nL < x < (n+1)L,$$

where $\beta^2 = k_c L^2/D_c$, $c_n = c(nL)$ and $\beta \hat{c}_n/L = c'(nL_+)$. Continuity of the solution at $x = (n+1)L$ shows that

$$c_n \cosh(\beta) + \hat{c}_n \sinh(\beta) = c_{n+1},$$

that is,

$$\hat{c}_n = \frac{c_{n+1} - c_n \cosh(\beta)}{\sinh(\beta)}.$$

It follows that

$$c'(nL_+) = (c_{n+1} - c_n \cosh(\beta)) \frac{\beta}{L \sinh(\beta)}$$

and

$$c'(nL_-) = -(c_{n-1} - c_n \cosh(\beta)) \frac{\beta}{L \sinh(\beta)}.$$

Substituting these results into the jump condition yields the difference equation

$$\frac{k_s}{\beta \sinh(\beta)} (c_{n+1} - 2c_n \cosh(\beta) + c_{n-1}) + f(c_n) = 0. \tag{4.20}$$

It is usually not possible to obtain an explicit solution of a nonlinear difference equation. One exception is if $f(c)$ is piecewise linear,

$$f(c) = f_0 H(c - c^*), \tag{4.21}$$

where c^* is a release threshold. Without loss of generality, suppose that the standing wave solution crosses threshold from below in the interval $0 < x < L$. Try a solution of the form $c_n = A_- \mu^{-n}$ for $n \le 0$ and $c_n = C - A_+ \mu^n$ for $n \ge 0$ with $0 < \mu < 1$. The constant C is determined by taking the limit $n \to \infty$ in (4.20) with $c_n \to C > c^*$:

$$\frac{k_s}{\beta \sinh(\beta)}(C - 2C\cosh(\beta) + C) + f_0 = 0,$$

so that

$$C = \frac{\beta \sinh(\beta)}{2\cosh(\beta) - 2}\frac{f_0}{k_c} = \frac{\beta \cosh(\beta/2)}{2\sinh(\beta/2)}\frac{f_0}{k_c}.$$

The constant μ then satisfies the quadratic equation $\mu - 2\lambda + \mu^{-1} = 0$ with $\lambda = \cosh(\beta)$. Choosing the root that is less than one, we have $\mu = \lambda - \sqrt{\lambda^2 - 1} = \mathrm{e}^{-\beta}$. Finally, the factors $A_\pm$ can be determined by considering the difference equation for $n = 0, 1$, which gives [322]

$$A_-(\beta) = \frac{\mu(\beta)C(\beta)}{1 + \mu(\beta)}, \quad A_+(\beta) = \mathrm{e}^{\beta} A_-(\beta).$$

Given that $C, A_\pm$ and $\mu_\pm$ are all functions of β (assuming that f_0/k_c is fixed), the conditions for the existence of a standing wave-front solution are

$$A_-(\beta) < c^*, \quad C(\beta) - A_+(\beta)\mu(\beta) = \mathrm{e}^{\beta} A_-(\beta) \geq c^*. \tag{4.22}$$

For a given β, a traveling wave exists if the threshold c^* lies beneath the curve $A_-(\beta)$, whereas a standing wave exists if c^* lies between $A_-(\beta)$ and $\mathrm{e}^{\beta} A_-(\beta)$; in the latter case propagation failure occurs. Note, in particular, that increasing the threshold c^* or increasing β makes propagation failure more likely. Moreover, increasing β corresponds to increasing the cluster spacing L or decreasing the Ca^{2+} diffusion coefficient D_c.

Having established that wave propagation failure can occur, we now describe how to calculate the wave speed as a function of "discreteness" using the averaging method of Keener [318, 319]. The analysis proceeds along identical lines to the study of inhomogeneous diffusivity in the discrete bistable equation; see Sect. 2.5. First, rewrite (4.17) in the dimensionless form

$$\frac{\partial c}{\partial t} = -c + \frac{\partial^2 c}{\partial x^2} + (1 + g'(x/\varepsilon))f(c), \tag{4.23}$$

where $\varepsilon = \sqrt{L^2 k_c / D} \ll 1$, a factor of k_c^{-1} has been absorbed into f, and $g(x)$ is the periodic sawtooth function, $g(x) = 1/2 - x$ for $0 < x < 1$ and $g(x+n) = g(x)$. (More precisely, $g(x)$ is assumed to be the sum of Gaussians (2.69) of width σ, with the limit $\sigma \to 0$ taken at the end of the calculation.) Suppose that the nonlinear function $f(c)$ is one for which there exists a traveling front solution $c(x,t) = C(x - vt)$ of the homogeneous equation ($g \equiv 0$). The main result of the averaging method is that for ε sufficiently small, there exists a wavelike solution or pulsating wave of the form [318]

$$c(x,t) = C(x - \phi(t)) + \mathcal{O}(\varepsilon), \tag{4.24}$$

where the phase $\phi(t)$ evolves according to [see also (2.72)]

$$\frac{d\phi}{dt} = v - \Phi(\phi/\varepsilon) \tag{4.25}$$

with

$$\Phi(\phi/\varepsilon) = \frac{1}{\Lambda}\int_{-\infty}^{\infty} g'([\xi+\phi]/\varepsilon) f(C(\xi)) C'(\xi) \mathrm{e}^{\nu\xi} d\xi, \tag{4.26}$$

and

$$\Lambda = \int_{-\infty}^{\infty} \mathrm{e}^{\nu\xi} C'(\xi)^2 d\xi. \tag{4.27}$$

Equation (4.25) implies that the solution is not translationally invariant, rather it moves with a time-dependent velocity ϕ'. If $v - \Phi(\phi/\varepsilon)$ is strictly positive then $\phi'(t)$ is a positive, periodic function of t with period

$$T = \int_0^{\varepsilon} \frac{d\phi}{v - \Phi(\phi/\varepsilon)}. \tag{4.28}$$

The mean speed of the wave is $\bar{v} = \varepsilon/T$. On the other hand. if $v - \Phi(\phi/\varepsilon)$ vanishes for some ϕ, then propagation failure is expected to occur.

Averaging method for discrete Ca^{2+} release sites. The first step is to rewrite (4.23) as the first-order system

$$c_x = u, \quad u_x = c_t - (1 + g'(x/\varepsilon)) f(c) + c. \tag{4.29}$$

Introducing the exact change of variables $u = w - \varepsilon g(x/\varepsilon) f(u)$ yields the new system

$$c_x = w - \varepsilon g(x/\varepsilon) f(c), \quad w_x = c_t - f(c) + c + \varepsilon g(x/\varepsilon) f'(c) c_x. \tag{4.30}$$

It can be seen that if the $\mathcal{O}(1)$ system of equations is independent of x/ε, then the lowest-order averaged system reduces to the homogeneous equation, which we are assuming supports a traveling front solution $C(x - vt)$. Including the inhomogeneous factors $g(x/\varepsilon)$ means that the system is no longer translationally invariant. However, we can look for solutions that are close to a traveling front by going to a traveling coordinate system with $\xi = x - \phi(t)$ to give [318]

$$c_\xi - w = -\varepsilon g([\xi+\phi]/\varepsilon) f(c) \tag{4.31a}$$

$$-c_t + w_\xi + \phi' c_\xi + f(c) - c = \varepsilon g([\xi+\phi]/\varepsilon) f'(c) c_\xi. \tag{4.31b}$$

We now seek a perturbative solution of the form

$$c = C(\xi) + \varepsilon c_1(\xi,t) + \ldots, \quad w(\xi) = C'(\xi) + \varepsilon w_1(\xi,t) + \ldots, \quad \phi'(t) = v + \varepsilon \phi_1'(t) + \ldots$$

Substituting into equations (4.31) and collecting terms of equal powers in ε yields a hierarchy of equations, the first of which is

$$\partial_\xi c_1 - w_1 = -g([\xi+\phi]/\varepsilon) f(C) \tag{4.32a}$$

$$-\partial_t c_1 + \partial_\xi w_1 + v w_1 + f'(C) c_1 - c_1 = v g([\xi+\phi]/\varepsilon) f(C) - \phi_1'(t) C' + g([\xi+\phi]/\varepsilon) f'(C) C'. \tag{4.32b}$$

Equations (4.32) can be rewritten as

$$-\begin{pmatrix} 0 \\ \partial_t c_1 \end{pmatrix} + \mathbb{L}\begin{pmatrix} c_1 \\ w_1 \end{pmatrix} = \begin{pmatrix} h_c \\ -\phi_1' C' + h_w \end{pmatrix}, \quad \mathbb{L} = \begin{pmatrix} \partial_\xi & -1 \\ f'(C) - c & \partial_\xi + c \end{pmatrix}, \tag{4.33}$$

with h_c and h_w determined by inhomogeneous terms on the right-hand side of equations (4.32a) and (4.32b), respectively. Following our analysis of the linear operator (2.62), we know that the matrix operator appearing in equation (4.33) has a null space spanned by (C', C''). Similarly, the adjoint operator

$$\mathbb{L}^\dagger = \begin{pmatrix} -\partial_\xi & f'(C)-C \\ -1 & -\partial_\xi + c \end{pmatrix}$$

has the null vector $e^{c\xi}(-C'', C')$. Hence, applying the Fredholm alternative, it follows that $\phi'(t)$ must satisfy the phase equation (4.25) with $\phi(t) = v + \varepsilon\phi_1(t)$.

For the particular choice $f(c) = H(c - c^*)$ used in the analysis of standing waves with $f_0/k_c = 1$, the homogeneous equation is identical to the one analyzed at the end of Sect. 2.2. Thus, there exists a unique traveling front solution of the form (2.23) with corresponding wave speed (2.24). The mean wave speed can then be calculated explicitly along similar lines to Sect. 2.5, so that

$$\bar{v} = \frac{\varepsilon}{2} \frac{1}{\ln\left(\frac{v+\varepsilon/\chi}{v-\varepsilon/\chi}\right)}. \tag{4.34}$$

with $v = (1-2c^*)/\sqrt{c^* - c^{*2}}$ and $\chi = 4[c^* - c^{*2}]$. This would predict propagation failure when $\varepsilon \geq \chi v$, that is,

$$\varepsilon \geq 4(1-2c^*)(\sqrt{c^* - c^{*2}}). \tag{4.35}$$

Since the analysis is based on the assumption that ε is small, we expect this condition to be reasonable when $c^* \approx 0.5$. Taylor expanding about this point the condition for propagation failure is approximately $\varepsilon > 2(1-2c^*)$. Similarly, the condition (4.22) based on the standing wave analysis predicts propagation failure when $\varepsilon/(2(e^\varepsilon - 1)) < c^*$, which reduces to $\varepsilon > 2(1-2c^*)$ when $c^* \approx 1/2$. Thus the two approaches agree for small ε and yield qualitatively similar results for large ε. Finally, as in the analysis of myelinated axons, a cubic nonlinearity for the release function $f(c)$ yields an expression for the mean wave speed that involves exponentially small terms so it is necessary to include higher-order terms in the perturbation analysis in order to obtain sufficient accuracy [318].

4.3.2 The Fire–Diffuse–Fire Model of Ca^{2+} Release

An alternative approach to studying the effects of discrete Ca^{2+} release sites is to consider the so-called *FDF* model [127, 137, 140, 325, 497, 511]. The basic idea of the model is that once the Ca^{2+} concentration reaches a threshold value c^* at a given release site, that site fires and instantaneously releases a fixed amount σ of Ca^{2+} into the cytoplasm [325, 497, 511]. It is also straightforward to take into account the effects of ion pumps by including a decay term and replacing instantaneous release by a fixed pulse of finite width [127]. The FDF model is then almost identical to the SDS model of Ca^{2+} spikes propagating along spiny dendrites [129, 130]. Since the latter model was analyzed in detail in Sect. 3.1, we can carry over the previous results after minor modifications. Therefore, consider the following version of the FDF model [127]:

$$\frac{\partial c}{\partial t} = -\frac{c}{\tau_c} + D_c \frac{\partial^2 c}{\partial x^2} + \sum_n \delta(x - x_n)\eta(t - T_n), \tag{4.36}$$

where T_n is the firing time of the site x_n, which only fires once:

$$T_n = \inf\{t \,|\, c(x_n, t) \geq c^*\}. \tag{4.37}$$

For concreteness, let

$$\eta(t) = (\sigma/\tau_d)H(t)H(\tau_d - t),$$

so that each Ca^{2+} puff or spark is of size σ and duration τ_d. Suppose that the Ca^{2+} release sites are regularly spaced, $x_m = mL$, and consider a saltatory wave solution $T_m = m\Delta$ with speed $v = L/\Delta$. The existence of such a wave can be determined straightforwardly by noting that (4.36) is identical to (3.33) under the mapping

$$V \to c, \quad \frac{\bar{n}}{r_s}\eta_0 \to \frac{\sigma}{\tau_d}.$$

The one major difference between the two models is that thresholding in the SDS model is mediated by an IF process (3.2), which introduces an additional time constant $\hat{\tau}$. Therefore, in order to apply the analysis of saltatory waves along a spiny dendrite to the FDF model (see in Sect. 3.1.3), we need to take the limit $\hat{\tau} \to 0$. This then gives the following threshold condition for the existence of a saltatory wave:

$$c^* = \sum_{n=1}^{\infty} H(nL, n\Delta), \tag{4.38}$$

with

$$H(x,t) = \frac{\sigma}{\tau_d}\int_0^{\tau_d} G_0(x, t-s)\mathrm{d}s, \quad G_0(x,t) = \frac{1}{\sqrt{4\pi D_c t}}\mathrm{e}^{-t/\tau_c - x^2/4D_c t}. \tag{4.39}$$

In the limit $\tau_d \to 0$, $H(x,t) \to \sigma G_0(x,t)$ and the threshold condition becomes

$$\begin{aligned} c^* &= \sigma \sum_{n=1}^{\infty} G_0(nL, n\Delta) \\ &= \sigma \sum_{n=1}^{\infty} \frac{1}{\sqrt{4\pi D_c n\Delta}} \exp\left(-n\left[\frac{L^2 t}{4D_c\Delta} + \frac{\Delta}{\tau_c}\right]\right) \equiv g(\Delta). \end{aligned} \tag{4.40}$$

In the additional limit $\tau_c \to \infty$ (i.e., neglecting the flux due to ion pumps), the results of [497] are recovered. In particular, $g(\Delta)$ becomes a monotone function of Δ, and the speed of the traveling waves scales linearly as D_c/L. The latter follows after introducing the dimensionless threshold $\tilde{c}^* = c^* L/\sigma$ and noting that Lg/σ is then only a function of the dimensionless quantity $\Delta D_c/L^2$. However, this result is inconsistent with the analysis of standing waves, which showed that propagation failure can occur by decreasing the diffusion coefficient. The discrepancy is resolved by taking into account the effects of ion pumps, that is, taking τ_c to be finite. Moreover, $g(\Delta)$

is now non-monotone and consequently one finds two solution branches with the faster one corresponding to stable waves [127]. This result also holds in the case of finite pulse width τ_d, for which

$$H(x,t)=\frac{\sigma}{\tau_d}\left[A(x,t-\min(t,\tau_d))-A(x,t)\right], \tag{4.41}$$

with $A(x,t)$ given by (3.40). In summary, the main qualitative results of the SDS model carry over to the FDF model, for example, one finds that propagation failure occurs if the spacing between release sites becomes too large.

One of the limitations of the above FDF model is that it neglects variations in the Ca^{2+} concentration within the ER. However, in many cells, Ca^{2+} release can result in a significant local depletion of ER Ca^{2+}. In order to take this into account, the FDF model has been extended in the form of a bidomain threshold-release model [621, 622]:

$$\frac{\partial c}{\partial t}=D_c\frac{\partial^2 c}{\partial x^2}+J_{rel}(c,c_e)-J_2(c,c_e) \tag{4.42a}$$

$$\frac{\partial c_e}{\partial t}=D_e\frac{\partial^2 c}{\partial x^2}-\chi_e\left[J_{IP}(c,c_e)-J_2(c,c_e)\right], \tag{4.42b}$$

where the release and uptake fluxes, $J_{rel}(c,c_e)-J_2(c,c_e)$, are functions of the cytosolic and ER Ca^{2+} concentrations. For simplicity, assume that there is a continuous and uniform distribution of Ca^{2+} release sites and that the release flux depends on the difference in the cytosolic and ER Ca^{2+} concentrations:

$$J_{rel}(x,t)\equiv J_{rel}(c(x,t),c_e(x,t))=(c_e(x,t)-c(x,t))\eta(t-T(x)), \tag{4.43}$$

with

$$T(x)=\inf\{t\,|\,c(x,t)\geq c^*\}. \tag{4.44}$$

The release sites could be either RyRs or IP_3Rs; in the latter case the IP_3 concentration p is held fixed. Finally, the reuptake flux due to the action of ion pumps is taken to have the linear form

$$J_2(c,c_e)=\frac{c}{\tau_c}-\frac{c_e}{\tau_e}. \tag{4.45}$$

The existence and stability of a solitary pulse solution of (4.42) can be investigated along similar lines to Sect. 3.1.1.

4.4 Stochastic Models of Ca^{2+} Release

The fluorescent imaging of localized Ca^{2+} puffs and sparks has established that Ca^{2+} release is a stochastic process that occurs at spatially discrete sites consisting of clusters of IP_3Rs and RyRs, respectively. In *Xenopus* oocytes, Ca^{2+} puffs have an amplitude ranging from around 50 to 600 nM, a spatial spread of approximately

6 μm and a typical duration of 1 s [489, 490, 690]. For sufficiently high levels of IP_3 concentration, the amplification of Ca^{2+} puffs by CICR can lead to the formation of Ca^{2+} waves. Ca^{2+} sparks in heart and skeletal muscle tend to be of shorter duration and less spatial spread and are less likely to result in wave propagation [110, 111]. As we have already mentioned Ca^{2+} puffs and sparks have also been observed in neurons [534], suggesting that one needs to take into account stochastic release events when modeling Ca^{2+} waves. Typically, one combines a stochastic model of localized release through RyRs or IP_3Rs with a deterministic reaction–diffusion model of Ca^{2+} waves such as the FDF model [137, 320]. The stochastic modeling of the Ca^{2+}-dependent opening and closing of these receptors proceeds along analogous lines to the modeling of voltage-gated ion channels considered in Sect. 1.5.

4.4.1 Stochastic Model of Ca^{2+} Puffs in a Cluster of IP_3Rs

Stochastic models of Ca^{2+} puffs typically treat a cluster of IP_3Rs as a set of N channels that open and close independently, but are indirectly coupled by the common cytoplasmic Ca^{2+} concentration [180, 182, 579, 612]. Models differ in the level of detail regarding individual receptors. The first deterministic kinetic model of Ca^{2+}-gated IP_3Rs was proposed by De Young and Keizer, in their study of agonist-induced Ca^{2+} oscillations. This model assumes that the IP_3 receptor consists of three equivalent receptor subunits, all of which have to be in a conducting state in order to generate a Ca^{2+} flux. Each subunit is taken to have an IP_3-binding site, an activating Ca^{2+}-binding site, and an inactivating Ca^{2+}-binding site; the conducting state corresponds to the state in which all subunits have the first two binding sites occupied but the third unoccupied. Although the De Young–Keizer model is simple to describe, it involves a relatively large number of variables that have to be coupled to the Ca^{2+} and IP_3 concentrations. A simplified version of the model was subsequently developed by Li and Rinzel [381]. They exploited the fact that the binding of IP_3 and activating Ca^{2+} are fast relative to inactivating Ca^{2+} and used a quasi-steady-state argument to reduce the eight-state subunit model to a model that simply keeps track of whether or not the inactivating Ca^{2+}-binding site of a subunit is occupied. More specifically, the Li–Rinzel model is a two-variable model given by

$$\frac{dc}{dt} = J_{\mathrm{IP}} + J_{\mathrm{leak}} - J_{\mathrm{p2}} \tag{4.46a}$$

$$\frac{dh}{dt} = \alpha_h(1-h) - \beta_h h, \tag{4.46b}$$

where c is the cytoplasmic Ca^{2+} concentration, h is the fraction of receptors in a cluster not inactivated by Ca^{2+}, and p is the IP_3 concentration, which is assumed fixed. The three Ca^{2+} fluxes included in the model are the channel flux J_{IP} and

leakage flux $J_{\rm leak}$ from the ER to the cytoplasm, and the flux $J_{\rm p2}$ pumped back into the ER; see also Fig. 4.2. The expressions for the various fluxes are

$$J_{\rm IP} = f(c,p)h^3[c_e - c], \quad J_{\rm leak} = \nu_0[c_e - c], \quad J_{\rm P2} = \frac{\nu_1 c^2}{k_3^2 + c^2}, \tag{4.47}$$

with

$$f(c,p) = \left(\frac{p}{p+k_4}\right)^3 \cdot \left(\frac{c}{c+k_5}\right)^3, \quad \alpha_h = \nu_2 \frac{p+k_4}{p+k_6}, \quad \beta_h = \nu_3 c. \tag{4.48}$$

The various cubic terms reflect the existence of three subunits. Parameter values of the model can be found in [381]. We see that the simplified model resembles the Hodgkin–Huxley model (see Sect. 1.1), after replacing Ca^{2+} concentration c by membrane voltage v and c_e by a reversal potential.

We now describe a stochastic version of the Li–Rinzel model for a cluster of IP_3Rs due to Shuai and Jung [579]. For stochastic versions of the full De Young–Keizer model, see, for example, [180, 182, 244, 612]. The deterministic equations (4.46) describe the mean behavior of a large cluster of Ca^{2+} channels, just as the Hodgkin–Huxley equations for membrane voltage apply to a large number of voltage-gated ion channels. As we discussed in Sect. 1.5, if the number of channels is relatively small, then it is necessary to take into account thermally driven fluctuations in the opening and closing of individual channels. In the case of the Li–Rinzel model, one only needs to consider the opening and closing process for the gating variable h of each subunit. The latter is modeled as the two-state Markov process

$$C(\text{closed}) \underset{\beta_h(c)}{\overset{\alpha_h}{\rightleftharpoons}} O(\text{open}). \tag{4.49}$$

Suppose that there are N independent IP_3Rs, each with three independent subunits labeled $i = 1,2,3$ that are described by the above two-state Markov process. Let $N_i(t)$ $(i = 1,2,3)$ denote the number of receptors at time t that have the ith subunit open. Under the adiabatic assumption that the Ca^{2+} concentration c evolves much more slowly than the state transitions of the channels, we can write down a master equation for the probability $P(n_i,t) = \text{Prob}[N_i(t) = n_i | N_i(0) = n_0]$ according to

$$\begin{aligned} \frac{dP(n_i,t)}{dt} &= (N - n_i + 1)\alpha_h P(n_i - 1,t) + (n_i + 1)\beta_h P(n_i + 1,t) \\ &\quad - (n_i\beta_h + (N - n_i)\alpha_h)P(n_i,t), \quad i = 1,2,3. \end{aligned} \tag{4.50}$$

As with voltage-gated ion channels, we have a stochastic hybrid system, since the transition rate β_h depends on the Ca^{2+} concentration $c(t)$, which evolves according to a piecewise deterministic equation of the form (4.46a). The latter, in turn, couples to the discrete stochastic variables $N_i(t)$ through the flux

$$J_{\rm IP} = f(c(t),p)[c_e - c(t)] \prod_{i=1}^{3} \frac{N_i(t)}{N}. \tag{4.51}$$

[Note that one should really write down a differential Chapman–Kolmogorov equation for the joint probability density $p(n_1,n_2,n_3,c,t)$ along the lines of (1.126)]. Finally, for large N, one can obtain a further simplification by carrying out a Kramers–Moyal expansion of the master equation (4.50) along the lines of Sect. 1.5.2. This yields the following SDE for $H_i(t) = N_i(t)/N$ with H_i treated as a continuous stochastic variable:

$$dH_i = \alpha_h(1-H_i) - \beta_h H_i + \frac{1}{\sqrt{N}} b(H_i) dW_i, \tag{4.52}$$

where

$$b(H_i) = \sqrt{\alpha_h(1-H_i) + \beta_h H_i},$$

and $W_i(t)$ is an independent Wiener process with

$$\langle dW_i(t) \rangle = 0, \quad \langle dW_i(t) dW_j(t') \rangle = \delta(t-t') dt\, dt' \delta_{i,j}.$$

Shuai and Jung [579] simulated the stochastic Li–Rinzel model in order to investigate the effects of noise on Ca^{2+} oscillations in a space-clamped model. They assumed that the deterministic system (4.46) was monostable at low and high IP_3 concentrations and exhibited limit cycle oscillations (occurring via a Hopf bifurcation) at intermediate concentrations. They showed that noise can enlarge the range of IP_3 concentrations over which oscillations occur—an effect known as *coherence resonance*. They also found a broad distribution of puff amplitudes, lifetimes, and interpuff intervals. In particular, at low IP_3 concentrations, the amplitude distribution is a monotonically decaying function, whereas at higher concentrations, it is unimodal. This suggests that Ca^{2+} puffs become more significant as IP_3 concentration is increased and hence could impact the spontaneous generation of Ca^{2+} waves. This issue was investigated numerically by Falcke [180] using a stochastic version of the De Young–Keizer model that was incorporated into a reaction–diffusion model of spatially distributed channel clusters. He showed that there is indeed a transition from Ca^{2+} puffs to waves as the IP_3 concentration is increased. At low concentrations, only puffs occur, since there is not enough Ca^{2+} released to stimulate neighboring clusters, which means that the response is purely local. However, as IP_3 concentration increases, global Ca^{2+} waves can emerge from local nucleation sites of high Ca^{2+} concentration. At intermediate levels of IP_3, global events are rare and waves only progress a short distance before dying out. On the other hand, for higher IP_3 concentrations, global waves occur regularly with a well-defined period. Again this oscillatory-like behavior can occur in parameter regimes for which the deterministic model is non-oscillatory.

4.4.2 Stochastic Model of Ca^{2+} Sparks in a Cluster of RyRs

We now turn to a stochastic model of Ca^{2+} sparks due to Hinch [276]; see also [241]. This model was originally developed for *cardiac myocytes* (heart muscle cells) and

includes details of the geometry of Ca^{2+} release units, in particular, the narrow junctional gap known as the diadic space that separates the sarcoplasmic reticulum (SR) from the plasma membrane; see Fig. 4.4. (In smooth muscle cells the smooth ER is referred to as the sarcoplasmic reticulum.) However, it is possible that a similar mechanism occurs in neurons at the specialized subsurface cisternae of the ER, which also form narrow junctions with the plasma membrane; see Fig. 4.2. In a typical myocyte, there could be up to 10,000 Ca^{2+} release units, each one containing a cluster of around $N = 50$ RyRs on the surface of the SR. The cluster of RyRs is apposed to L-type Ca^{2+} channels located on so-called t-tubules, which are invaginations of the plasma membrane into the myocyte. (The Ca^{2+} channels are not involved in the spontaneous generation of Ca^{2+} sparks so are ignored in the model.) The diadic space separating the SR from the t-tubules is a region of the mytoplasm (intracellular fluid of myocytes), which is approximately cylindrical in shape with width 10 nm and radius 100 nm. Since the diadic space is a small enclosed volume, it supports an elevation in Ca^{2+} concentration relative to the bulk mytoplasm following the release of Ca^{2+} from an RyR. Such a local elevation plays a crucial role in the Ca^{2+}-induced Ca^{2+}-release (CICR) that results in a Ca^{2+} spark. The SR in a neighborhood of the RyRs is known as the junctional SR (JSR), which may have a different Ca^{2+} concentration from the bulk or network SR (NSR).

We now briefly introduce the model of Hinch in nondimensional form; details of model approximations and estimates of experimentally based model parameters can be found in [276]. First, the diadic space is modeled as a single compartment with Ca^{2+} concentration c satisfying the current conservation equation

$$\tau_D \frac{dc}{dt} = J_{\mathrm{RyR}} - J_{\mathrm{D}}. \tag{4.53}$$

Here τ_D is a time constant, J_{RyR} is the total Ca^{2+} current through the RyRs, and J_{D} is the diffusive current from the diadic space to the bulk mytoplasm. The latter is modeled as the Fickian current

$$J_{\mathrm{D}} = c - c_m, \tag{4.54}$$

where c_m is the bulk mytoplasm Ca^{2+} concentration. The total current through the RyRs is taken to be proportional to the number n of open RyRs times the Ca^{2+} concentration c_{sr} in the JSR:

$$J_{\mathrm{RyR}} = c_{\mathrm{sr}} x, \quad x = \frac{n}{N}, \tag{4.55}$$

with N the total number of RyRs in the cluster. Each RyR has Ca^{2+}-binding sites, which can be activating or deactivating. When an RyR is in an activated state it is promoted to a mode where it continuously opens and closes according to a Markov process (see Sect. 1.5), with a mean open time of 1 ms [695]. The opening of an RyR channel results in an extra Ca^{2+} current flowing into the diadic space, which increases the rate at which Ca^{2+} binds to the other RyRs via CICR, thus creating a positive feedback loop. This feedback loop provides a mechanism for bistability.

Note that the RyRs also contain inactivating Ca^{2+}-binding sites, but these do not play a role in initiating a Ca^{2+} spark so are not included in the model. For simplicity, the RyRs are modeled using a two-state Markov process involving a single closed state and a single open state (see also [324]):

$$C(\text{closed}) \underset{k_-}{\overset{k_+(c)}{\rightleftharpoons}} O(\text{open}), \tag{4.56}$$

with transition rates

$$k_+(c) = \frac{1}{k\tau_o}\frac{c^\alpha}{c^\alpha + 1}, \quad k_- = \frac{1}{\tau_o}. \tag{4.57}$$

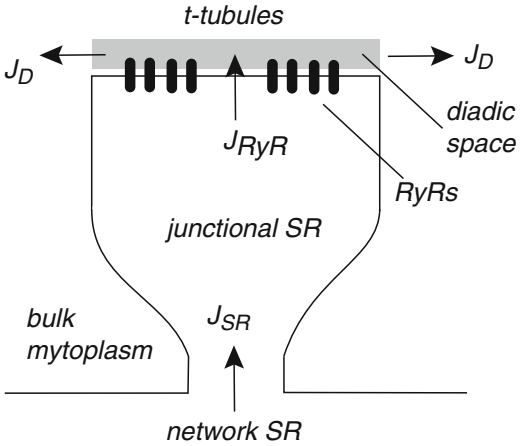

Fig. 4.4 Schematic diagram of a Ca^{2+} release unit in a cardiac myocyte. It is divided into four compartments: the network SR, the junctional SR, the diadic space, and the bulk mytoplasm. See text for details

Here τ_o is the mean open time of an RyR, α is the number of Ca^{2+} ions that are needed to open an RyR, and k determines the proportion of time the RyRs are open. It is assumed that the RyRs are gated independently of each other. They are, however, indirectly coupled via the Ca^{2+} concentration in the diadic space. The time constant τ_D of diffusive flux from the diadic space is several orders of magnitude smaller than the mean open time τ_o of an RyR, that is, $\tau_D \sim 3\,\mu s$ whereas $\tau_o \sim 1\,ms$. Therefore, the Ca^{2+} concentration in the diadic space can be taken to be in quasi-equilibrium, $\tau_D \to 0$, so that

$$c = c_m + c_{sr}x. \tag{4.58}$$

It follows that the transition rate can be reexpressed as a function of the fraction of open channels and the Ca^{2+} concentration in the SR, $k_+ = k_+(c_m + c_{sr}x)$.

Now consider N independent RyRs within a Ca^{2+} release unit, each described by the above two-state Markov process. Let $N(t)$ be the number of open channels at

time t and set $p_n(t) = \text{Prob}[N(t) = n|N(0) = n_0]$. Following along similar lines to Sect. 1.5.1, it can be shown that $p_n(t)$ evolves according to a master equation with transitions rates $\omega_\pm(n/N) : n \to n \pm 1$:

$$\omega_+(x) = N(1-x)\frac{(c_m + c_{\rm sr}x)^\alpha}{k((c_m + c_{\rm sr}x)^\alpha + 1)}, \quad \omega_-(x) = Nx. \tag{4.59}$$

For the moment, it is assumed that c_m and $c_{\rm sr}$ are fixed so that ω_+ can be treated as a function of x alone. (In Sect. 4.4.4, the dynamics of c_{sr} following initiation of a Ca^{2+} spark will also be taken into account.) The units of time are fixed by setting $\tau_{\rm o} = 1$. The master equation for the RyR cluster is then

$$\frac{dp_n}{dt} = \omega_+((n-1)/N)p_{n-1} + \omega_-((n+1)/N)p_{n+1} - (\omega_+(n/N) + \omega_-(n/N))p_n, \tag{4.60}$$

with boundary conditions $p_{N+1} = p_{-1} \equiv 0$. Multiplying both sides of the master equation (4.60) by n/N and summing over n gives

$$\frac{d\langle n/N\rangle}{dt} = \langle \Omega_+(n/N)\rangle - \langle \Omega_-(n/N)\rangle, \tag{4.61}$$

where $\omega_\pm = N\Omega_\pm$, and the brackets $\langle \ldots \rangle$ denote a time-dependent ensemble averaging over realizations of the stochastic dynamics, that is, $\langle A(n/N)\rangle = \sum_n p_n A(n/N)$ for any function of state $A(n/N)$. In the thermodynamic limit $N \to \infty$ (infinite cluster size), statistical correlations can be ignored so that one can take the mean-field limit $\langle \Omega_\pm(n/N)\rangle \to \Omega_\pm(\langle n/N\rangle)$. This then yields a deterministic equation for the fraction x of open RyRs:

$$\frac{dx}{dt} = \Omega_+(x) - \Omega_-(x) = (1-x)\frac{(c_m + c_{\rm sr}x)^\alpha}{k((c_m + c_{\rm sr}x)^\alpha + 1)} - x. \tag{4.62}$$

It can be shown that, for physiologically reasonable parameter values, this equation exhibits bistability [276], that is, there exists a pair of stable fixed points $x_\pm$ separated by an unstable fixed point x_0. The fixed point $x_- \approx 0$ represents a quiescent state, whereas the other fixed point x_+ represents a Ca^{2+} spark in which a significant fraction of RyRs are in the active mode and can be interpreted as a burst phase. Hence, this model operates in a completely different regime to the model considered by Shuai and Jung [579], which was in a monostable state (a fixed point or limit cycle) in the deterministic limit. Bistability of the Hinch model means that a Ca^{2+} spark is a distinct event rather than a broad distribution of events.

Noise-induced transitions from x_- to x_+ determine the distribution of inter-spark intervals, just as noise-induced transitions from x_+ to x_- determine the distribution of spark lifetimes. Hence, estimating the mean time for the occurrence of a spark event reduces to the problem of calculating the MFPT to reach x_+, starting from a neighborhood of x_-, by crossing x_0. (The dominant contribution to this MFPT is the time to reach x_0, since the system then quickly relaxes to x_+.) We encountered an analogous problem in Sect. 1.5, where we considered the mean time

for spontaneous action potential initiation due to ion-channel fluctuations. We first estimated the MFPT by carrying out a diffusion approximation of the underlying master equation (1.104), and calculating the MFPT of the corresponding Fokker–Planck equation. However, the diffusion approximation resulted in exponentially large errors. Therefore, we considered an alternative approach in Sect. 1.6, which was based on WKB methods and asymptotic analysis. Here we consider a corresponding WKB approximation of the master equation (4.60). Such an approach has been used increasingly to analyze escape problems in chemical and biological systems [160, 164, 175, 176, 256, 339, 340], including the Ca^{2+} release model of Hinch [277]. Note, however, that in contrast to the analysis of membrane voltage fluctuations in Sect. 1.6, the analysis of calcium sparks is performed with respect to the small parameter $1/N$ rather than ε. That is, we carry out a system-size expansion rather than assuming fast kinetics. For the moment, we simply state the results and leave the details to Sect. 4.4.3.

If x_- is not on the boundary $x = 0$ then a standard analysis shows that the mean time τ_i to initiate a Ca^{2+} spark starting from the quiescent state x_- is

$$\tau_i = \frac{2\pi}{\Omega_+(x_-)\sqrt{|\gamma(x_0)|\gamma(x_-)}} e^{N[\Phi(x_0)-\Phi(x_-)]}. \tag{4.63}$$

with

$$\gamma(x) = \frac{\Omega_-'(x)}{\Omega_-(x)} - \frac{\Omega_+'(x)}{\Omega_+(x)}, \quad \Phi(x) = \int^x \ln\left(\frac{\Omega_-(y)}{\Omega_+(y)}\right) dy.$$

Similarly, the mean duration τ_f of a spark, which corresponds to the mean time to transition back from x_+ to x_-, is given by

$$\tau_f = \frac{2\pi}{\Omega_+(x_+)\sqrt{|\gamma(x_0)|\gamma(x_+)}} e^{N[\Phi(x_0)-\Phi(x_+)]}. \tag{4.64}$$

Note that at a fixed point x_j, $\Omega_+(x_j) = \Omega_-(x_j)$ so that $\text{sign}(\gamma(x_j)) = \text{sign}(\Omega_-'(x_j) - \Omega_+'(x_j))$. Thus, $\gamma(x_0) < 0$ (unstable) and $\gamma(x_\pm) > 0$ (stable). One also finds that $\Phi(x_0) > \Phi(x_\pm)$ so that τ_i, τ_f are exponentially large. It turns out that in the case of Ca^{2+} release, the quiescent state x_- is in an $\mathcal{O}(1/N)$ neighborhood of the boundary $x = 0$, so that the prefactor of the MFPT has to be modified accordingly; see [276, 277] for details. Nevertheless, the leading order exponential is unchanged. From the perspective of modeling stochastic Ca^{2+} waves using the FDF model of Sect. 4.3.2, the main result that emerges from the analysis of Ca^{2+} sparks is that the deterministic threshold mechanism needs to be replaced by a probabilistic mechanism. In the deterministic case, a cluster of receptors fires whenever the intracellular Ca^{2+} crosses a fixed threshold. On the other hand, in a stochastic FDF model, Ca^{2+} release is a probabilistic process. Given the MFPT τ_i, the probability of a spark event in a time interval t is given by

$$P_i(t) = 1 - e^{-t/\tau_i}. \tag{4.65}$$

Recall that the transition rates $\Omega_\pm$, and thus τ_i, are functions of the Ca^{2+} concentration c_m of the mytoplasm, which has so far been assumed fixed. Indeed, one finds that the probability of release in a given time interval t is a sigmoidal function of c_m [276]. This stochastic release process can now be incorporated into a stochastic version of the FDF model by taking the sequence of release times T_n in (4.36) to be generated according to a sigmoidal probability distribution that is parameterized by the Ca^{2+} concentration in the mytoplasm, which itself evolves according to (4.36); see [137, 320] for details. The resulting model can be used to simulate the spontaneous occurrence of Ca^{2+} waves.

4.4.3 WKB Method and Quasistationary Approximation

We now present the details of how to calculate the rate of escape from a metastable state. Although, we focus here on the particular problem of Ca^{2+} release, the basic approach applies to the master equation of any bistable system in the large N (weak noise) limit. Throughout the analysis we will switch between n/N and x, with x treated as a continuous variable; this is a reasonable approximation when N is large. First, note that the master equation (4.60) with the given reflecting boundary conditions at $x = 0, 1$ has a unique stationary state given by (see also Sect. 1.5.1)

$$p_n^* = p_k^* \prod_{m=k+1}^{n} \frac{\Omega_+((m-1)/N)}{\Omega_-(m/N)} = p_k^* \exp\left(\sum_{m=1}^{n} \ln\left(\frac{\Omega_+((m-1)/N)}{\Omega_-(m/N)} \right) \right). \quad (4.66)$$

The functions $\Omega_\pm(x)$ are smooth and the second derivatives of $\ln \Omega_\pm(x)$ are bounded (except in the limits $x \to 0$ and $x \to 1$). Therefore, away from the boundaries, the sums can be approximated by the trapezium rule [276]

$$\sum_{m=k}^{n} \ln(f(m/N)) = \frac{\ln(f(k/N) + \ln f(n/N)}{2} + N \int_{k/N}^{n/N} \ln(f(y)) dy + \mathcal{O}(1/N),$$

so that

$$p_n^* = \frac{\mathcal{N}}{\sqrt{\Omega_+(x)\Omega_-(x)}} e^{-N\Phi(x)}, \quad x = n/N, \quad (4.67)$$

where $\Phi(x)$ is the effective potential

$$\Phi(x) = \int^x \ln\left(\frac{\Omega_-(y)}{\Omega_+(y)} \right) dy, \quad (4.68)$$

and $\mathcal{N}$ is a normalization factor such that $\sum_{n=0}^{N} p_n^* = 1$.

Now suppose that we place an absorbing boundary at the unstable fixed point $x_0 = n_0/N$. Although there no longer exists a stationary solution, the flux through the absorbing boundary is exponentially small for large N, so that we can use a

spectral projection method analogous to Sect. 1.6. First, rewrite the master equation (4.60) for $n = 0, \ldots, n_0$ as the linear system

$$\frac{d\mathbf{p}}{dt} = \mathbf{Q}\mathbf{p}, \tag{4.69}$$

where $\mathbf{p} = (p_0(t), p_1(t), \ldots, p_{n_0}(t))^T$, $\mathbf{Q}$ is the matrix of transition rates, and $p_{n_0}(t) = 0$ (absorbing boundary condition). Suppose that the eigenvalues of $\mathbf{Q}$ are ordered according to $0 > \lambda_0 \geq \mathrm{Re}[\lambda_1] \geq \mathrm{Re}[\lambda_2] \geq \ldots$ with corresponding eigenfunctions $\phi_n^{(j)}$, and consider the eigenfunction expansion

$$p_n(t) = \sum_{r=0}^{n_0} C_r \mathrm{e}^{-\lambda_r t} \phi_n^{(r)}. \tag{4.70}$$

We assume that $|\lambda_0| \sim \mathrm{e}^{-\eta N}$ for $\eta = \mathscr{O}(1)$, whereas λ_r for $r > 0$ are only weakly dependent on N. It follows that all other eigenmodes decay to zero much faster than the perturbed stationary density. Thus at large times, we have the quasistationary approximation

$$p_n(t) \sim C_0 \mathrm{e}^{-\lambda_0 t} \phi_n^{(0)}. \tag{4.71}$$

One can now use a WKB ansatz (see below) to generate a quasistationary solution ϕ_n^ε for which $\mathbf{Q}\phi^\varepsilon = 0$ and $\phi_{n_0}^\varepsilon \sim \mathscr{O}(\mathrm{e}^{-\eta N})$. Since the WKB solution does not satisfy the absorbing boundary condition, it is necessary to perform an asymptotic expansion in order to match the quasistationary solution with the solution in a neighborhood of x_0. In the process this determines λ_0, whose inverse can be identified as the MFPT to escape from the basin of attraction of the metastable state x_-.

Dropping exponentially small terms and writing $\phi_n^\varepsilon = \phi^\varepsilon(x)$ with x treated as a continuous variable, we have

$$\begin{aligned} 0 = {} & \Omega_+(x-1/N)\phi^\varepsilon(x-1/N) \\ & +\Omega_-(x+1/N)\phi^\varepsilon(x+1/N) - (\Omega_+(x)+\Omega_-(x))\phi^\varepsilon(x). \end{aligned} \tag{4.72}$$

We seek a WKB solution of the form

$$\phi^\varepsilon(x) \sim K(x;\varepsilon)\mathrm{e}^{-\Phi(x)/\varepsilon}, \tag{4.73}$$

with $K(x;\varepsilon) \sim \sum_{m=0}^\infty \varepsilon^m K_m(x)$. Substituting (4.73) into (4.72), Taylor expanding with respect to ε, and collecting the $\mathscr{O}(1)$ terms gives

$$\Omega_+(x)(\mathrm{e}^{\Phi'(x)} - 1) + \Omega_-(x)(\mathrm{e}^{-\Phi'(x)} - 1) = 0, \tag{4.74}$$

where $\Phi' = d\Phi/dx$. Solving this quadratic equation in $\mathrm{e}^{\Phi'}$ shows that

$$\Phi = \int^x \ln \frac{\Omega_-(y)}{\Omega_+(y)} dy \quad \text{or} \quad \Phi = \text{constant}. \tag{4.75}$$

Proceeding to the next level, equating terms at $\mathcal{O}(\varepsilon)$ gives

$$\Omega_+ e^{\Phi'}\left(-\frac{K_0'}{K_0}+\frac{\phi''}{2}\right)+\Omega_- e^{-\Phi'}\left(\frac{K_0'}{K_0}+\frac{\phi''}{2}\right)-\Omega_+' e^{\Phi'}+\Omega_- e^{-\Phi'}=0.$$

Substituting for Φ using (4.74) and solving for K_0 yields the following leading order forms for ϕ^ε:

$$\phi^\varepsilon(x)=\frac{A}{\sqrt{\Omega_+(x)\Omega_-(x)}}e^{-N\Phi(x)}. \tag{4.76}$$

with Φ given by (4.75), which is sometimes called the activation solution, and

$$\phi^\varepsilon(x)=\frac{B}{\Omega_+(x)-\Omega_-(x)}, \tag{4.77}$$

which is sometimes called the relaxation solution. The constants A, B are determined by matching solutions around x_0. Clearly, (4.77) is singular at any fixed point x_j, where $\Omega_+(x_j)=\Omega_-(x_j)$, so is not a valid solution for the required quasistationary density. On the other hand, it does have an interpretation in terms of a corresponding Hamiltonian–Jacobi formulation of the WKB ansatz.

The WKB ansatz was also used in the analysis of metastability in stochastic ion-channel models in Sect. 1.6 and in the analysis of sharp interfaces for slowly modulated pulled fronts; see Sect. 3.2.4. Following along similar lines to the latter example, we can formally interpret (4.74) as a stationary Hamilton–Jacobi equation $H(x,\Phi'(x))=0$ for Φ, with Hamiltonian

$$H(x,p)=\sum_{r=\pm}\Omega_r(x)\left[e^{rp}-1\right]. \tag{4.78}$$

This suggests a corresponding classical mechanical interpretation, in which H determines the motion of a particle with position x and conjugate momentum p. A trajectory of the particle is given by the solution of Hamilton's equations

$$\dot{x}=\frac{\partial H}{\partial p}=\sum_{r=\pm1}r\Omega_r(x)e^{rp} \tag{4.79}$$

$$\dot{p}=-\frac{\partial H}{\partial x}=\sum_{r=\pm1}\frac{\partial\Omega_r}{\partial x}(x)\left[e^{rp}-1\right]. \tag{4.80}$$

Here the time t should be viewed as a parameterization of paths rather than as a real time variable. Introducing the Lagrangian

$$L(x,\dot{x})=p\cdot\dot{x}-H(x,p), \tag{4.81}$$

it follows that $\Phi(x)$ with $\Phi(\bar{x})=0$ corresponds to the classical action evaluated along the least-action trajectory from $\bar{x}$ to x:

$$\Phi(x)=\inf_{x(t_0)=\bar{x},x(T)=x}\int_0^T L(x,\dot{x})dt. \tag{4.82}$$

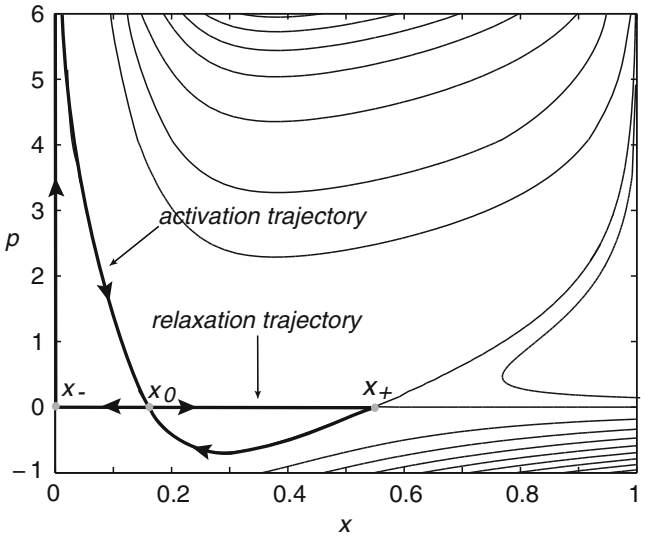

Fig. 4.5 Phase portrait of Hamiltonian equations of motion for $\Omega_\pm = \omega_\pm/N$ given by equation (4.59) with $c_m = 0.01, c_e = 4, \alpha = 4$ and $k = 0.8$. The zero-energy solutions are shown as *thicker curves*

In terms of the underlying stochastic process $X(t)$, the least-action path can be interpreted as the most probable fluctuational path from $\bar{x}$ to x (in the large-N limit) [205, 398]. Since $p = S'$ everywhere along this path, we have

$$\Phi(x) = \int_{\bar{x}}^{x} p(x')dx', \tag{4.83}$$

with the integral taken along the trajectory. It follows that the leading order term in the WKB approximation is determined by finding zero-energy solutions $p = p(x)$ such that $H(x, p(x)) = 0$. One solution is $p = 0$ or $\Phi =$ constant, which represents the classical action along a deterministic (or relaxation) trajectory. For example, once the system escapes from the metastable state x_-, it tends to rapidly converge to the other metastable state x_+ along such a deterministic path. (The contribution of relaxation trajectory to the mean escape time is usually neglected.) Another solution for Φ is (4.75), which can be interpreted as the action along a non-deterministic path that represents the most probable path of escape from x_- to x_0 [160, 164, 175, 176]. In Fig. 4.5 we illustrate the Hamiltonian phase space for the model showing the constant energy solutions of the Hamiltonian given by (4.78); the zero-energy activation and relaxation trajectories through the fixed points of the deterministic system are highlighted as thicker curves

Given the quasistationary approximation, the rate of escape from the metastable state centered about $x = x_-$ can be calculated by matching it with an appropriate inner solution in a neighborhood of the point $x = x_0$ [160, 164, 175, 256, 277]. This is necessary since the quasistationary solution (4.76) does not satisfy the absorbing

boundary condition at the point x_0 separating the two metastable states. There are a number of different ways of carrying out the matched asymptotics; see, for example, [277]. Here we will follow an approach based on fixing the probability flux J_0 through x_0 and then matching the activation solution for $x < x_0$ with the relaxation solution for $x > x_0$ using a diffusion approximation of the full master equation (4.60) in the vicinity of x_0 [164, 175, 256]. The latter yields the Fokker–Planck equation (1.111), which can be rewritten in the form of a conservation equation

$$\frac{\partial}{\partial t}P(x,t) = -\frac{\partial}{\partial x}J(x,t) \tag{4.84}$$

with

$$J(x,t) = (\Omega_+(x) - \Omega_-(x))P(x,t) - \frac{1}{2N}\frac{\partial}{\partial x}\left[(\Omega_+(x) + \Omega_-(x))P(x,t)\right].$$

Substituting the quasistationary solution $p(x,t) = C_0 e^{-\lambda_0 t}\Pi(x)$ into (4.84) and using the fact that λ_0 is exponentially small give

$$J_0 = (\Omega_+(x) - \Omega_-(x))\Pi(x) - \frac{1}{2N}\frac{\partial}{\partial x}\left[(\Omega_+(x) + \Omega_-(x))\Pi(x)\right],$$

where J_0 is the constant flux through x_0. In a neighborhood of x_0, this equation can be Taylor expanded to leading order in $x - x_0$ and integrated to obtain the solution

$$\Pi(x) = \frac{J_0 N}{\Omega_+(x_0)} \mathrm{e}^{(x-x_0)^2/\sigma^2} \int_x^\infty \mathrm{e}^{-(y-x_0)^2/\sigma^2} dy, \tag{4.85}$$

where

$$\sigma = \sqrt{\frac{2\Omega_+(x_0)}{N[\Omega_+'(x_0) - \Omega_-'(x_0)]}} \tag{4.86}$$

determines the size of the boundary layer around x_0.

In order to match the activation and relaxation solutions, the following asymptotic behavior of the inner solution (4.85) is used:

$$\Pi(x) = \begin{cases} \dfrac{NJ_0\sigma^2}{(x-x_0)\Omega_+(x_0)}, & x - x_0 \gg \sigma \\ \dfrac{NJ_0\sigma\sqrt{\pi}}{\Omega_+(x_0)} \mathrm{e}^{(x-x_0)^2/\sigma^2}, & x_0 - x \gg \sigma. \end{cases} \tag{4.87}$$

The solution to the right of the saddle matches the relaxation solution (4.77) since $\Omega_+(x) - \Omega_-(x) \approx (x - x_0)[\Omega_+'(x_0) - \Omega_-'(x_0)]$ for $x \approx x_0$ such that $B = J_0$. In order to match the solution on the left-hand side of x_0 with the activation solution (4.76), Taylor expand $\Phi(x)$ about x_0 using $\Phi'(x_0) = 0$ and $\Phi''(x_0) = 2/N\sigma^2$. It follows that

$$J_0 = \frac{A\Omega_+(x_0)}{\sqrt{\Omega_+(x_0)\Omega_-(x_0)}} \sqrt{\frac{|\Phi''(x_0)|}{2\pi N}} \mathrm{e}^{-N\Phi(x_0)}. \tag{4.88}$$

The final step in the analysis is to link the flux J_0 with the escape rate λ_0. This is achieved by substituting the quasistationary solution into the continuity equation (4.84) and integrating over the interval $x \in [0, x_0]$ with a reflecting boundary condition at $x = 0$:

$$\frac{1}{\lambda_0} = \frac{1}{J_0} \int_0^{x_0} \phi^{\varepsilon}(y) dy. \tag{4.89}$$

Since the activation solution is strongly peaked around the fixed point x_-, a Gaussian approximation of $\phi^{\varepsilon}(x)$ around x_- yields the final result

$$\lambda_0 = \frac{\Omega_+(x_-)}{2\pi} \sqrt{|\Phi''(x_0)|\Phi''(x_-)} \mathrm{e}^{-N[\Phi(x_0)-\Phi(x_-)]}. \tag{4.90}$$

Hence, we obtain (4.63) with $\tau_i = \lambda_0^{-1}$ and

$$\Phi''(x) = \frac{d}{dx} \ln \left(\frac{\Omega_-(x)}{\Omega_+(x)} \right) = \frac{\Omega_-'(x)}{\Omega_-(x)} - \frac{\Omega_+'(x)}{\Omega_+(x)} = \gamma(x).$$

Similarly, we can obtain (4.64) for the mean time τ_f to terminate a spark.

4.4.4 Stochastic Phase-Plane Analysis

In the above analysis of Ca^{2+} sparks, the concentration c_{sr} in the JSR was held fixed. This is a reasonable approximation when considering the initiation of a Ca^{2+} spark. However, following Ca^{2+} release from the RyRs, the Ca^{2+} concentration c_{sr} slowly changes according to

$$\tau_{sr} \frac{dc_{\mathrm{sr}}}{dt} = -c_{sr}x + k_{sr}[c_0 - c_{\mathrm{sr}}]. \tag{4.91}$$

where $\tau_{sr} \gg \tau_{\mathrm{o}} \gg \tau_D$. The first term on the right-hand side is the loss of Ca^{2+} through the RyRs, whereas the second terms are the influx J_{SR} of Ca^{2+} from the NSR with fixed Ca^{2+} concentration c_0; see Fig. 4.4. The variation of c_{sr} means that one has to modify the analysis of the time to terminate the Ca^{2+} spark. Following Hinch [276], this can be achieved by combining the theory of stochastic transitions outlined in Sect. 4.4.2 with the classical phase-plane analysis of slow–fast excitable systems such as the FitzHugh–Nagumo equations (see Sect. 2.1). That is, (4.62) and (4.91) form an excitable system with the fraction x of open RyRs acting as the fast variable and c_{sr} acting as the slow variable. In Fig. 4.6 we sketch the nullclines of the deterministic system in a parameter regime where there is a single, stable fixed point (x^*, c_{sr}^*). In the full stochastic model, the initiation of a Ca^{2+} spark induces a transition to the right-hand x-nullcline according to $x_-(c_{sr}^*) \to x_+(c_{sr}^*)$ as outlined in Sect. 4.4.2. The slow variable then moves down the right-hand nullcline $x_+(c_{sr})$ according to the equation

$$\tau_{sr} \frac{dc_{\mathrm{sr}}}{dt} = -c_{sr}x_+(c_{\mathrm{sr}}) + k_{sr}[c_0 - c_{\mathrm{sr}}]. \tag{4.92}$$

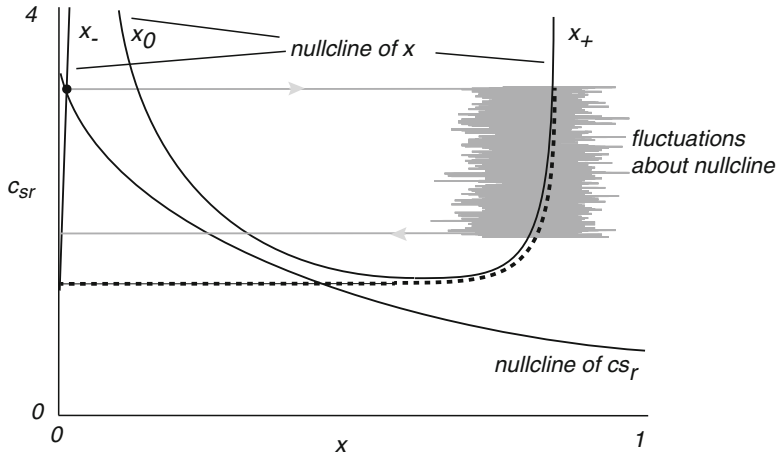

Fig. 4.6 Sketch of nullclines in the deterministic planar Ca^{2+} spark model with x denoting the fraction of open RyRs and c_{SR} the Ca^{2+} concentration in the junctional SR. The c_{sr} nullcline is a monotonically decreasing function $x(c_{sr})$, whereas the x nullcline is cubic-like with three branches $x_{\pm}(c_{sr})$ and $x_0(c_{sr})$. (Note that the branch $x_-(c_{sr}) \approx 0$; we have moved it away from the vertical axis for the sake of illustration.) In the given diagram there is a single, stable fixed point on the left-hand branch. In the stochastic version of the model a Ca^{2+} spark initiates a jump to the right-hand branch $x_+(c_{sr})$ along the lines outlined in Sect. 4.4.2. This is followed by a stochastic trajectory in which the slow variable $c_{sr}(t)$ moves down the nullcline until it undergoes a noise-induced transition back to the left-hand branch before the knee at $x = x_c$. In the deterministic case, the return transition occurs at the knee (*dashed curve*)

That is, although x is a stochastic variable, it fluctuates much faster than the dynamics of c_{sr} so one can substitute a time-averaged value of x in (4.91).

Suppose that $c_{sr}(t)$ is the solution of (4.92) with $c_{sr}(0) = c_{sr}^*$, that is, the Ca^{2+} spark occurs at $t = 0$. In principle, the spark can terminate at any time $t > 0$ due to fluctuations in the number of open RyRs. Again using a separation of time scales, we can estimate the rate of transition back to the left-hand branch at time t using

$$\lambda(t) = \frac{\Omega_+(x_+(t))\sqrt{|\gamma(x_0(t))|\gamma(x_+(t))}}{2\pi} e^{N[\Phi(x_+(t))-\Phi(x_0(t))]}, \tag{4.93}$$

where $x_+(t) = x_+(c_{sr}(t))$, etc. One can now calculate the distribution of spark durations T. Let $P(\tau) = \mathbb{P}(T > \tau)$ and introduce the spark duration probability density

$$p(\tau) = -\frac{dP}{d\tau}.$$

The probability that a spark terminates in an infinitesimal time interval $\delta\tau$ is $\lambda(\tau)\delta\tau$, so that

$$P(\tau + \delta\tau) = P(\tau)(1 - \lambda(\tau)\delta\tau).$$

Taking the limit $\delta\tau \to 0$ and integrating gives $P(\tau) = \exp\left(-\int_0^\tau \lambda(t)dt\right)$, and hence

$$p(\tau) = \lambda(\tau)\exp\left(-\int_0^\tau \lambda(t)dt\right). \tag{4.94}$$

4.4.5 Whole-Cell Model of Ca^{2+} Sparks

One of the major simplifications of the Hinch model [276] is that the background Ca^{2+} concentrations in the mytoplasm (c_m) and the NSR ($c_{\rm nsr}$) are held fixed. It thus fails to capture the collective behavior of a large population of Ca^{2+} release units (CaRUs) that are coupled via global changes in these background concentrations (assuming diffusion can be neglected on the relevant time scales). This has motivated the development of a whole-cell model of calcium-induced calcium release in cardiac myocytes, based on a system of $\mathcal{N}$ globally coupled CaRUs [672, 673]. We will describe a simplified version of the model in which Ca^{2+} pumps, leakage currents, and voltage-gated Ca^{2+} channels are not modeled explicitly. Let c_j and $\hat{c}_j$ denote the Ca^{2+} concentration in the dyadic space and JSR of the jth CaRU, $j = 1,\ldots,\mathcal{N}$. Then

$$\tau_D \frac{dc_j}{dt} = J^j_{\rm RyR} - J^j_{\rm D}, \qquad \tau_{sr}\frac{d\hat{c}_j}{dt} = J^j_{sr} - J^j_{\rm RyR}, \tag{4.95}$$

where $J^j_{\rm RyR}$ is the total Ca^{2+} current through the RyRs, $J^j_{\rm D}$ is the diffusive current from the diadic space of the jth CaRU to the bulk mytoplasm, and $J^j_{\rm sr}$ is the current from the NSR to the JSR of the jth CaRU. The various fluxes are given by

$$J^j_{\rm D} = c_j - c_m, \quad J^j_{\rm RyR} = x_j\hat{c}_j, \quad J^j_{sr} = k_{sr}[c_{\rm nsr} - \hat{c}_j], \tag{4.96}$$

where x_j is the fraction of open RyRs in the jth CaRU. Finally, from conservation of Ca^{2+} ions, the bulk concentrations c_m and $c_{\rm nsr}$ evolve according to

$$\tau_{\rm m}\frac{dc_m}{dt} = -\sum_{j=1}^{\mathcal{N}} J^j_D + J_m, \qquad \tau_{sr}\frac{dc_{\rm nsr}}{dt} = J_{\rm nsr} - \sum_{j=1}^{\mathcal{N}} J^j_{sr}. \tag{4.97}$$

Here J_m and $J_{\rm nsr}$ are the total external currents into the mytoplasm and NSR, respectively, arising from Ca^{2+} pumps and other factors.

When the number $\mathcal{N}$ of CaRUs is large, one can develop a probability density version of the above model, which takes the form of a differential Chapman–Kolmogorov (CK) equation describing the evolution of a single equivalent stochastic CaRU [672]. The basic idea is to introduce a probability density $p(c,\hat{c},n,t)$, with $p(c,\hat{c},n,t)dcd\hat{c}$ interpreted as the fraction of CaRUs at time t that have Ca^{2+} concentrations in the range $c \le c(t) \le c+dc, \hat{c} \le \hat{c}(t) \le \hat{c}+d\hat{c}$ and are in the internal state n, with the latter determined by the number of open RyRs, for example. Introduce the single CaRU equations

$$\tau_D \frac{dc}{dt} \equiv F(c,\hat{c},n) = \frac{n}{N}\hat{c} + c_m - c$$
$$\tau_{sr} \frac{d\hat{c}}{dt} \equiv \hat{F}(\hat{c},n) = k_{sr}[c_{\rm nsr} - \hat{c}] - \frac{n}{N}\hat{c}. \tag{4.98}$$

The probability density p then evolves as

$$\frac{\partial p}{\partial t} = -\frac{\partial (Fp)}{\partial c} - \frac{\partial (\hat{F}p)}{\partial \hat{c}} + \sum_{n'} A(n,n';c,\hat{c}) p(c,\hat{c},n',t), \tag{4.99}$$

with $A(n,n',c,\hat{c})$ constructed from the transition rates of the master equation describing the opening and closing of RyRs within each CaRU. Note that the CK equation (4.99) is formally similar to the CK equation (1.143) for membrane voltage fluctuations considered; see Sects. 1.5 and 1.6. However, the solution of (1.126) represents the distribution of state trajectories with respect to repeated trails of a single neuron, whereas the solution of (4.99) represents the distribution of state trajectories with respect to a large ensemble of identical CaRUs. Moreover, the latter are globally coupled due to the dependence of $F, \hat{F}$ and A on the Ca^{2+} concentrations $c_m, c_{\rm nsr}$. Within the probabilistic framework these evolve according to the equations

$$\tau_{\rm m} \frac{dc_m}{dt} = -\int_0^\infty \int_0^\infty \rho(c,\hat{c},t)[c_m - c] dc d\hat{c} + J_m \tag{4.100}$$
$$\tau_{sr} \frac{dc_{\rm nsr}}{dt} = J_{\rm nsr} - k_{sr} \int_0^\infty \int_0^\infty \rho(c,\hat{c},t)[c_{\rm nsr} - \hat{c}] dc d\hat{c}, \tag{4.101}$$

with $\rho(c,\hat{c},t) = \sum_n p(c,\hat{c},n,t)$. The probability density formulation of CaRUs can increase computational efficiency compared to Monte Carlo simulations of the full ODE model [672, 673].

4.5 Intercellular Calcium Waves in Astrocytes

So far we have considered intracellular Ca^{2+} waves that propagate within a single cell. However, one also finds intercellular Ca^{2+} waves (ICWs) consisting of increases in cytoplasmic Ca^{2+} concentration that are communicated between cells and appear as waves that spread out from an initiating or trigger cell. The speed and size of ICWs depend on the initiating stimulus and the particular propagation mechanism. An ICW often propagates at a speed of 10–20 μm/s and lasts for periods of up to tens of seconds, indicating that it can involve the recruitment of hundreds of contiguous cells. ICWs were first observed in cultures of astrocytes (discussed below) in response to extracellular glutamate [143], and in airway epithelial cells following mechanical stimulation [550]. They have subsequently been found in a wide range of cell types and under a variety of stimulus conditions, as reviewed in [380, 554].

4.5.1 Astrocytes and the Tripartite Synapse

Within the context of the central nervous system (CNS), ICWs are emerging as a major long-range signaling mechanism of a particular type of glial (nonneuronal) cell known as an *astrocyte*; see Fig. 4.7. Other types of glial cells include *oligodendrocytes* and *radial glial cells*. The former are responsible for myelination in the CNS just as Schwann cells are responsible for myelination in the peripheral nervous system; see also Sect. 2.5. On the other hand, radial glial cells play a pivotal role during development, with regard to both neuronal migration and neurogenesis [101]; see Sect. 9.1. Radial glial cells usually disappear post-development, but some cells, such as Bergmann glia in the cerebellum and Muller glia in the retina, maintain their radial glia-like properties into adulthood.

Traditionally, astrocytes were thought to be physiologically passive cells that only play a supporting role in the CNS by regulating and optimizing the environment within which neurons operate. Their housekeeping duties include maintaining local ion and pH homeostasis, delivering glucose and providing metabolic support via contacts with the vasculature, and clearing neuronal waste such as metabolic products and excess neurotransmitters in the synaptic cleft. However, over the past 20 years there has been an increasing amount of empirical data indicating that astrocytes play an active role in modulating synaptic transmission [253, 268, 449]. That is, astrocytes respond to synaptic neurotransmitters such as glutamate by elevating their intracellular Ca^{2+} levels. This then results in the release of glutamate and other signaling molecules from the astrocytes (gliotransmission), which in turn influences synaptic activity. Thus, astrocytes could potentially contribute to higher brain function and, consequently, behavior. This is consistent with the fact that the number of astrocytes relative to the number of neurons increases dramatically with

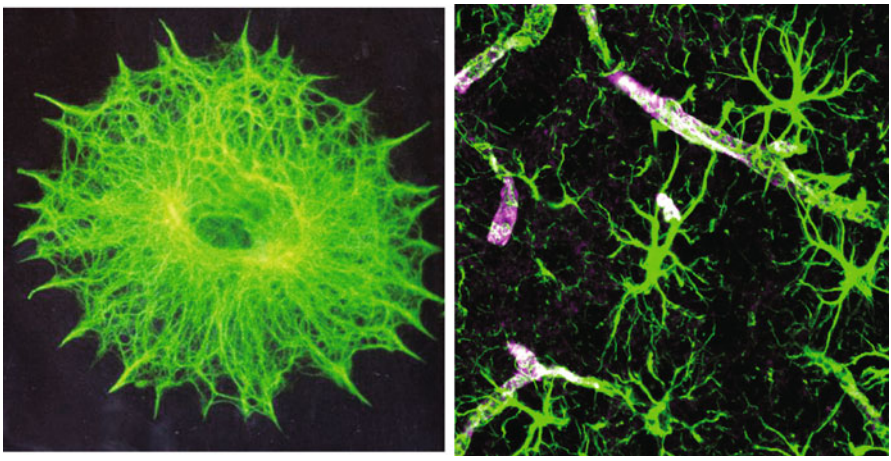

Fig. 4.7 *Left*: Astrocyte in vitro stained with GFAP to show filaments. *Right*: Astrocytes stained for GFAP, with end-feet ensheathing blood vessels [Public domain figure from Wikipedia Commons]

brain complexity, ranging from 1:25 in the leech, 1:6 in *C elegans*, 1:3 in lower mammals, to 1.4:1 in the human cortex. Conversely, it is known that following injury to the nervous system or under pathological conditions such as Alzheimer's disease, epilepsy, and schizophrenia, the structure and protein expression of astrocytes are altered [564]. One interpretation of these structural changes is that they are indicative of the supportive action of astrocytes following injury. On the other hand, given that many CNS disorders are correlated with alterations in synaptic transmission and gliotransmission regulates synaptic processing, it is possible that changes in gliotransmission contribute to these disorders; see Chap. 9.

In many higher organisms, astrocytes establish nonoverlapping anatomical and functional domains of size around 100 µm, and their distribution is highly organized.

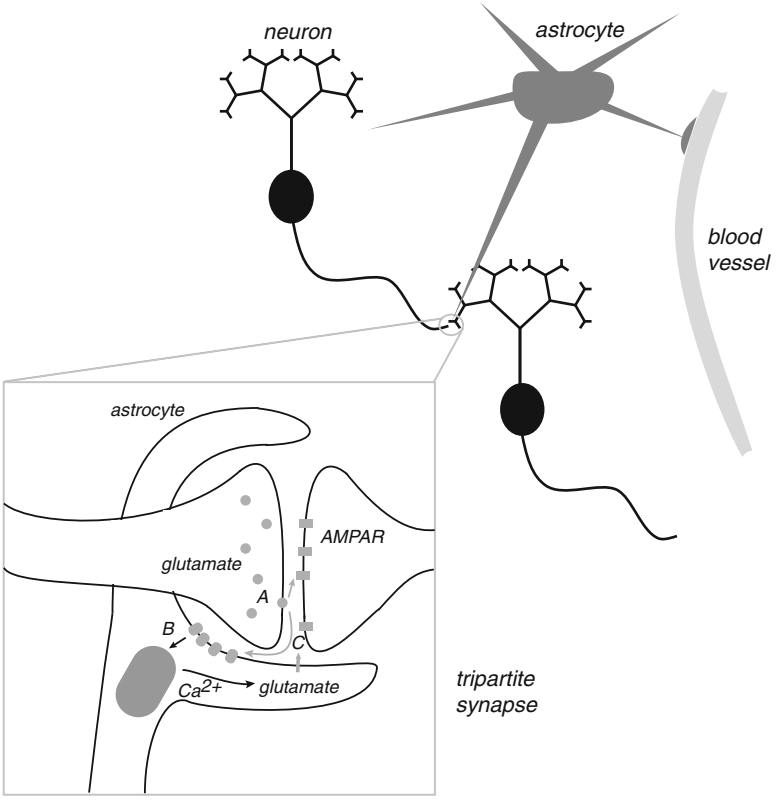

Fig. 4.8 Astrocytes modulate synaptic transmission and blood flow via Ca^{2+} signaling. *Inset*: the tripartite synapse. Synaptic transmission of glutamate (A) activates not only postsynaptic receptors such as AMPA but also astrocytic receptors that elevate astrocytic Ca^{2+} levels (B). This then induces the local release of glutamate from the astrocyte (C), which can modulate the synapse. Astrocytes also form a link between a neuron and the local vasculature. Increases in astrocytic Ca^{2+} concentration propagate via astrocyte end feet to small blood vessels, where they control vessel diameter and blood flow

The resulting astrocytic network parcellates the whole neutrophil such that a single astrocyte can make contact with thousands of synapses. The processes of a single astrocyte make contact with a synapse by wrapping around both the presynaptic and postsynaptic domains to form what is known as a *tripartite synapse* [253, 268, 449]; see Fig. 4.8. Hence, from a geometrical perspective, it is well placed to modulate synaptic transmission. The first component of glial–neuronal interactions at a synapse, namely, the metabotropic glutamate receptor 5 (mGluR5)-dependent elevation in astrocytic Ca^{2+} concentration in response to the release of glutamate neurotransmitters, was discovered in the early 1990s using Ca^{2+} imaging to study cultured glial cells [106, 143]. Both intracellular Ca^{2+} oscillations and ICWs propagating between neighboring astrocytes were observed. Subsequent studies have established that neuroglial signaling also occurs in astrocytes of isolated retina and brain slices [265, 460]. (Note, however, that a recent study of adult rodents has called into question the link between neuroglial Ca^{2+} signaling at the tripartite synapse [610]. It would appear that the astrocytic expression of mGluR5 receptors is developmentally regulated and, in particular, is undetectable in mature rodent brains; almost all previous studies of the tripartite synapse have been in immature animals.) Following the observation that neuronal activity increases Ca^{2+} levels in astrocytes, it was subsequently discovered that the resulting Ca^{2+} elevation induces gliotransmission of glutamate and a variety of other signaling molecules including ATP [249, 491]. Gliotransmission has been demonstrated to modulate synaptic transmission presynaptically and postsynaptically. For example, glutamate can enhance neurotransmitter release presynaptically by binding to metabotropic (mGlu) receptors or kainate receptors [189, 388]. Another example of enhanced synaptic transmission is the binding of ATP to postsynaptic receptors, which induces elevations in Ca^{2+}. This, in turn, can drive the insertion of additional AMPA receptors, thus temporarily increasing synaptic efficacy [236]. (The binding of ATP to postsynaptic receptors also provides a mechanism for the propagation of ICWs via paracrine signaling; see below.) On the other hand, hydrolysis of ATP results in the accumulation of adenosine, causing a reduction of synaptic transmission [493].

In addition to directly modulating synaptic transmission, astrocytes appear to regulate NMDA-receptor function. Recall from Sect. 1.3 that NMDA receptors are crucial for the induction of long-term synaptic plasticity, requiring both glutamate and postsynaptic depolarization in order to activate. The opening of an NMDA channel leads to a temporary increase of intracellular Ca^{2+} within the postsynaptic domain, whose amplitude and temporal profile determine whether the synapse is potentiated or depressed. It turns out that there is an additional glycine-binding site that regulates NMDA-receptor activity, whose co-agonist D-serine is released by astrocytes during gliotransmission. Increases in the level of D-serine appear to shift the balance point of long-term plasticity from depression to potentiation [485], a process known as metaplasticity. Finally, not only does astrocytic Ca^{2+} signaling modulate synaptic transmission and plasticity, it also controls blood flow, since intracellular waves propagate to small blood vessels via astrocyte end feet, where they control vessel diameter; see Fig. 4.8.

Following the original studies of ICWs in astrocyte cultures [106, 143], intracellular Ca^{2+} wave propagation between astrocytes has been observed in vitro in brain slices and whole retina preparations [265, 460, 492]. These empirical findings, combined with the structure of the tripartite synapse, have led to the suggestion that networks of astrocytes could form an extraneuronal pathway for rapid long-distance signaling within the CNS, which interacts reciprocally with neuronal networks. In particular, ICWs could provide a potential mechanism for coordinating and synchronizing the activity of a large group of neuronal and nonneuronal cells. It should be pointed out, however, that the function of ICWs in astrocytes remains controversial, since there have been very few in vivo observations of ICWs in the CNS, excluding the case of spontaneous ICWs during early development where astrocytes play a role in the generation, differentiation, and migration of neurons [666]; see Sect. 9.1. One recent exception is a study demonstrating in vivo spontaneous ICWs (termed glissandi) in mouse hippocampal astrocytes. (ICWs have also been observed in vivo in other glial networks, e.g., Bergmann glia in the cerebellum of rodents [287].) Another concern regarding the functional role of ICWs, either in vitro or in vivo, is whether they require strong inducing stimuli that do not have a normal physiological counterpart. On the other hand, certain pathological conditions such as brain trauma, brain ischemia (oxygen deprivation), and seizures are often associated with strong stimuli. They are all coupled with the release of ATP and glutamate and reductions in the level of extracellular Ca^{2+} that collectively could promote ICW generation. Such ICWs could exacerbate an injury by propagating signals that initiate

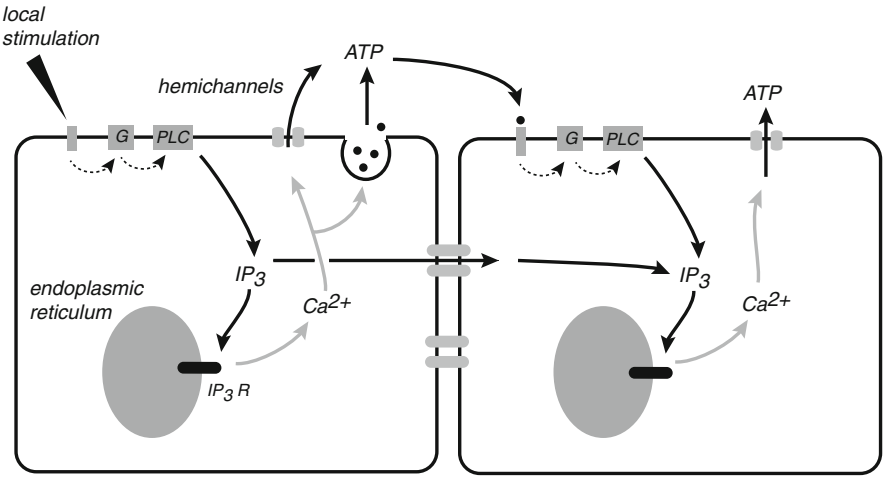

Fig. 4.9 Two mechanisms for the propagation of ICWs. Local stimulation of a single cell induces an elevation in intracellular IP_3 that generates an intracellular Ca^{2+} wave. Diffusion of IP_3 through gap-junction coupling with an adjacent cell initiates a second intracellular Ca^{2+} wave. In addition, or alternatively, stimulation of the first cell releases ATP via hemichannels in the plasma membrane or vesicular release; this could also be dependent on intracellular Ca^{2+}. The extracellular diffusion of ATP to neighboring cells can activate metabotropic receptors that then stimulate the production of IP_3 and the production of downstream intracellular Ca^{2+} waves

cell apoptosis (cell death) in surrounding cells [681]. There is also growing evidence that ICWs provide a source of excitation during epileptic episodes [564, 647, 668]; see Sect. 9.4. For example, studies of a brain slice that exhibits epileptiform activity, showed that there was also a corresponding increase in the frequency of Ca^{2+} oscillations in astrocytes [623]. Moreover, the release of glutamate from astrocytes has been observed to cause synchronous neuronal depolarizations [186].

4.5.2 Mechanisms and Models of Intercellular Calcium Waves

There are thought to be two basic mechanisms for the propagation of ICWs between adjacent cells that occur in astrocytes and other cell types: (a) diffusion of the second messenger IP_3 and, to a lesser extent, Ca^{2+} via gap junctions; (b) paracrine signaling via a diffusing extracellular messenger such as ATP. These mechanisms are illustrated in Fig. 4.9.

Gap-Junction Signaling

Gap junctions are arrays of transmembrane channels that connect the cytoplasm of two neighboring cells and thus provide a direct diffusion pathway between the cells. Cells sharing a gap-junction channel each provides a hemichannel (also known as a connexon) that connect head-to-head [545]. Each hemichannel is composed of proteins called connexins that exist as various isoforms named Cx23 through Cx62, with Cx43 being the most common. The physiological properties of a gap junction, including its permeability and gating characteristics, are determined by the particular connexins forming the channel. Although gap junctions are readily permeable to Ca^{2+} and IP_3, the diffusion of Ca^{2+} through a channel is greatly restricted due to buffering, so that the propagation of ICWs is primarily mediated by the diffusion of IP_3 when gap junctions are the main mechanism. The possible role of gap junctions in the propagation of ICWs was initially suggested by the observation in epithelial cells that waves only spread in adjacent cells from localized membrane sites in direct contact with the initiating cell. Moreover, the ICWs were not influenced by fluid flow over the apical surface of cells, that would have interfered with extracellular signals [259]. Further evidence for the role of gap junctions came from the study of glioma cells that lacked gap junctions [107]. These cells only supported ICWs when they were transfected with connexins; however, the presence of connexins could also enhance ATP and thus contribute to paracrine signaling (see below). Subsequent experimental and modeling studies have established that the diffusion of IP_3 through gap junctions can support the propagation of ICWs [379, 591]. In particular, ICWs could be initiated by an elevation of IP_3 in a single cell followed by diffusion to other cells without any regeneration of IP3. On the other hand, the range of the waves tends to be limited to only a few cells, suggesting that some other mechanism may be needed in order to generate longer-range waves.

The first model of ICWs mediated by gap junctions was based on studies of mechanical stimulation of cultured epithelial cells [590, 591]. It has subsequently been extended to models of ICWs in networks of astrocytes of varying complexity [163, 281, 310]. The models all have the same basic structure, but differ in terms of whether or not regenerative mechanisms or extracellular signaling mechanisms are included. A simple 1D version of an ICW model is shown in Fig. 4.10. Each cell is treated as a square of size L with local coordinates (x,y), $0 \le x,y \le L$. There are N cells labeled $n = 1,\ldots,N$ arranged on a regular lattice with nearest neighbor coupling. The intracellular dynamics within each cell is described by reaction–diffusion equations of the form given in Sect. 4.2. For example, in the original model of Sneyd et al. [591], this included equations for cytoplasmic Ca^{2+} concentration (c_n), IP_3 concentration p_n, and a slow variable h_n representing the fraction of IP3 receptors that have not been inactivated by Ca^{2+}. An example of an intracellular model for the nth cell is (see, e.g., [280])

$$\frac{\partial p_n}{\partial t} = D_p \nabla^2 p_n - k_p p_n, \tag{4.102a}$$

$$\frac{\partial c_n}{\partial t} = D_c \nabla^2 p_n - k_c c_n + f(c_n, h_n, p_n), \tag{4.102b}$$

$$\tau_h \frac{dh_n}{dt} = h_\infty(c_n) - h_n. \tag{4.102c}$$

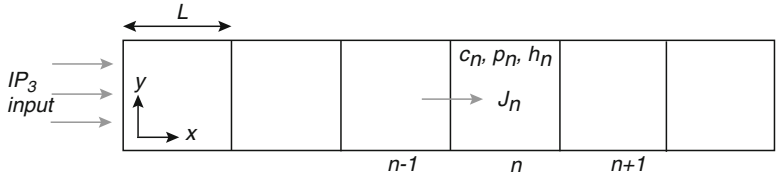

Fig. 4.10 Schematic diagram of a 1D model of intercellular Ca^{2+} waves mediated by gap junctions

Here the nonlinear function f represents the net flux due to Ca^{2+} release from IP_3 receptors. It is usually assumed that $D_p \gg D_c$ due to Ca^{2+} buffering. Coupling between adjacent cells in incorporated into the model using the boundary conditions for IP_3. Thus along the common vertical edge between cells $n-1$ and n, $1 < n < N$, the IP_3 flux J_n is taken to be of the form

$$-D_p \left.\frac{\partial p_{n-1}(x,y)}{\partial x}\right|_{x=L} = D_p \left.\frac{\partial p_n(x,y)}{\partial x}\right|_{x=0} \equiv \mathscr{K}[p_{n-1}(L,y) - p_n(0,y)]. \tag{4.103}$$

These are supplemented by no-flux boundary conditions for IP_3 across all other edges; all cell borders are assumed to be impermeable to Ca^{2+}. In a 2D version of the model arranged on a square grid, IP_3 can also flow across common horizontal

edges of neighboring cells, while no-flux boundary conditions are imposed along the exterior boundary of the grid. A typical simulation of such a model is to inject IP_3 in the cell at one end of the lattice, which is then allowed to diffuse from cell to cell, resulting in the propagation of an intracellular calcium wave. It is important to note that the ICW is not a traveling wave in the mathematical sense used throughout this book. Rather, the spread of Ca^{2+} is mediated by passive diffusion of intracellular Ca^{2+} and intra-/intercellular IP_3. Thus the rate of spread decreases with distance from the stimulated cell, and the arrival time of the wave increases exponentially with distance. In order to create more persistent ICWs, it is necessary to incorporate some regenerative mechanism. One example of such a mechanism is to assume that the rate of production of IP_3 can be amplified by intracellular Ca^{2+} so that (4.102a) becomes [281]

$$\frac{\partial p_n}{\partial t} = D_p \nabla^2 p_n + \frac{\nu c_n^2}{K + c_n^2} - k_p p_n.$$

Hofer et al. [281] showed that for an intermediate range of values of ν, partial regeneration of IP_3 supports ICWs that propagate further than those relying solely on passive diffusion of IP_3. Finally, an alternative mechanism for increasing the range of ICWs, which does not require some form of regeneration or active process, is to combine gap-junction coupling with an extracellular pathway involving ATP [163, 310]; see below.

Paracrine Signaling

Early evidence for the involvement of an extracellular component to ICWs arose from the observation that ICWs can propagate between disconnected groups of astrocytes, provided that the degree of separation does not exceed around 100 µm [266]. More recently, advanced imaging techniques have revealed that ICWs are associated with a cloud of extracellular ATP [249, 457]. There are a variety of pathways that could mediate ATP release, including hemichannels in the plasma membrane and vesicular discharge. Modeling studies suggest that a combination of gap-junction and paracrine signaling can significantly increase the range of ICWs [298]. It is also possible that there is a regenerative mechanism that boosts the propagation of ICWs. One candidate for active rather than passive (diffusive) wave propagation is Ca^{2+}-dependent ATP release via connexin hemichannels [652]. In the case of astrocytes, the dominant propagation mechanism depends on where they are located within the nervous system. For example, ICWs in the neocortex tend to be mediated by gap junctions, whereas in the hippocampus, both gap-junction and paracrine signaling play a role.

Here we will describe a mathematical model of paracrine signaling in astrocyte networks due to Bennett et al. [37]. Suppose that $a(t)$ denotes the extracellular concentration of ATP in the vicinity of a single cell. ATP binds to metabotropic P2Y receptors in the cell membrane according to the first-order kinetic scheme

$$ATP + R \underset{k_-}{\overset{k_+}{\rightleftharpoons}} R.$$

In the case of fast binding kinetics, the fraction of P2Y receptors that are bound by ATP is given by the quasi-equilibrium solution

$$r = \frac{a}{K_R + a}, \quad K_R = \frac{k_-}{k_+}. \tag{4.104}$$

This then drives activation of G-proteins according to the kinetic scheme

$$G_0 \underset{k_d}{\overset{k_a(r+r_0)}{\rightleftharpoons}} G_1,$$

where $G_{0,1}$ represent the inactive and active states of the G-protein. Denoting the amount of activated protein by g and the total G-protein by g_T, we have

$$\frac{dg}{dt} = k_a(r + r_0)(g_T - g) - k_d g. \tag{4.105}$$

Again assuming fast kinetics, the quasi-equilibrium solution is

$$g = g_T \frac{r + r_0}{K_G + r + r_0}, \quad K_G = \frac{k_d}{k_a}. \tag{4.106}$$

A major simplification of the model is to assume that the release of IP_3 within the cell is mainly driven by activation of G-protein so that Ca^{2+} dependence is ignored. If p is the intracellular IP_3 concentration then

$$\frac{dp}{dt} = \kappa g - k_{\text{deg}} p, \tag{4.107}$$

for constants κ, k_{deg}. The next stage of paracrine signaling, namely, the release of ATP by astrocytes is not yet well understood. However, IP_3 as a triggering mechanism, possibly via Ca^{2+} release from intracellular stores, is probably involved. In the model of Bennett et al. [37], IP_3 is assumed to directly cause ATP release from the cell surface into the extracellular space at the rate

$$J_{\text{ATP}}(p,t) = \kappa_{\text{ATP}} \chi(t) \left[\frac{p - p_{\min}}{K_{\text{rel}} + p} \right]_0. \tag{4.108}$$

Here κ_{ATP} and K_{rel} are constants, $[z]_0 = z$ for $z > 0$ and $[z]_0 = 0$ for $z < 0$, and $\chi(t)$ takes into account depletion of ATP stores within the cell. That is $\chi(0) = 1$ and

$$\frac{d\chi}{dt} = -\gamma J_{\text{ATP}}(t). \tag{4.109}$$

The rate of ATP release is thresholded in order to insure that very small levels of ATP are not amplified, and the depletion factor $\chi(t)$ is included in order to terminate

ATP release; the latter is motivated by the observation that ATP release is suppressed by repeated stimulation of a cell.

Finally, coupling between cells is modeled in terms of a diffusion equation for the extracellular ATP concentration that takes into account the IP_3-mediated release of ATP from the astrocytes. One way to proceed would be to use a continuum bidomain model, in which astrocytes and extracellular ATP coexist at every point in space. Taking $a = a(\mathbf{x},t), p = p(\mathbf{x},t)$ and denoting the density of astrocytes by $\rho(\mathbf{x})$, we would then have

$$\frac{\partial a}{\partial t} = D_{\rm ATP}\nabla^2 a + \rho(\mathbf{x})J_{\rm ATP}(p,t) - \frac{a}{K_{\rm deg}+a}. \tag{4.110}$$

Alternatively, one could explicitly distinguish between extracellular space and the intracellular space of astrocytes, in which case the fluxes $J_{\rm ATP}$ only exist at the boundaries of the cells. The latter approach is used in the computer simulations of Bennett et al. [37], who take a simplified cubic geometry for the astrocytes and also allow for intracellular diffusion of IP_3. Note that under a quasi-steady-state approximation, (4.107) and (4.110) form a closed system of differential equations, since (4.104) and (4.107) can be used to express g in terms of a. Hence, one can solve for the ATP and IP_3 concentrations independently of Ca^{2+} and then incorporate ICWs by using the IP_3 to drive a standard model of Ca^{2+} release from intracellular stores such as Li–Rinzel. However, if there is regenerative Ca^{2+}-dependent production of IP_3 or a Ca^{2+}-dependent mechanism for gliotransmission of ATP, then it is necessary to couple the Ca^{2+} dynamics to that of IP_3 and ATP.

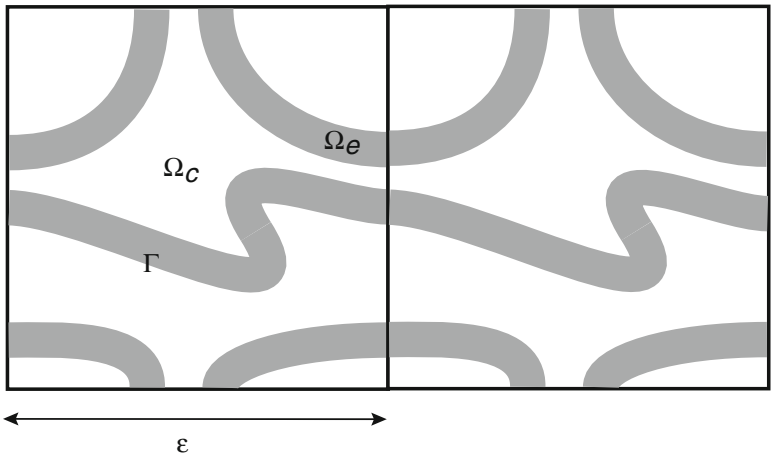

Fig. 4.11 Illustration of a 2D periodic heterogeneous medium consisting of a cytosolic domain Ω_c and an ER domain Ω_e separated by a boundary Γ

4.6 Appendix: Homogenization

As we noted in Sect. 4.2, it is not practical to try modeling the detailed microstructure of the cytoplasmic and ER boundaries, which are highly interleaved. This motivates consideration of a mean-field description of the Ca^{2+} concentrations, in which the concentrations c, c_e are taken to coexist at every point in space with effective diffusion coefficients. As shown by Goel et al. [224], the resulting bidomain model can be derived from first principles using homogenization theory. In this appendix we sketch the basic steps in their derivation. Note that we also encountered a 1D example of homogenization theory in Sect. 3.2.3, where we spatially averaged over a discrete distribution of dendritic spines.

Consider a domain $\Omega \subset \mathbb{R}^3$ in which the ER is treated as a periodic network that occupies a fraction of Ω, as illustrated in Fig. 4.11. For simplicity, assume that the unit cell is a cube of length ε. The ER Ca^{2+} occupies a connected domain Ω_e^ε, and the complementary connected domain $\Omega_c^\varepsilon = \Omega / \Omega_e^\varepsilon$ is occupied by cytosolic Ca^{2+}. The concentrations c^ε and c_e^ε satisfy the 3D diffusion equation in their respective domains:

$$\frac{\partial c}{\partial t} = \nabla \cdot (A_\varepsilon(\mathbf{x}/\varepsilon)\nabla c(\mathbf{x})), \quad \mathbf{x} \in \Omega_c^\varepsilon \tag{4.111a}$$

$$\frac{\partial c_e}{\partial t} = \nabla \cdot (B_\varepsilon(\mathbf{x}/\varepsilon)\nabla c_e(\mathbf{x})), \quad \mathbf{x} \in \Omega_e^\varepsilon, \tag{4.111b}$$

where A_ε and B_ε are the diffusion tensors for Ca^{2+} in the cytosol and ER, respectively. The boundary conditions on the membrane Γ_ε separating the cytosol from the ER take the form

$$A_\varepsilon(\mathbf{x}/\varepsilon)\nabla c(\mathbf{x}) \cdot \mathbf{n}_c^\varepsilon = \varepsilon f(c^\varepsilon, c_e^\varepsilon), \quad \text{on} \, \Gamma_\varepsilon \tag{4.112a}$$

$$-B_\varepsilon(\mathbf{x}/\varepsilon)\nabla c_e(\mathbf{x}) \cdot \mathbf{n}_c^\varepsilon = \varepsilon f(c^\varepsilon, c_e^\varepsilon), \quad \text{on} \, \Gamma_\varepsilon, \tag{4.112b}$$

where $n_c^\varepsilon, n_e^\varepsilon$ denote the unit exterior normals to the boundaries $\partial\Omega_c^\varepsilon$ and $\partial\Omega_e^\varepsilon$, respectively, satisfying $n_c^\varepsilon = -n_e^\varepsilon$ on Γ_ε, and f determines the net flux from the ER to the cytosol.

The basic idea of the homogenization method is to supplement the macroscopic spatial variables $\mathbf{x} = (x_1, x_2, x_3)$ with a set of microscopic variables $\mathbf{y} = (y_1, y_2, y_3), 0 \le y_i \le 1$, that are the coordinates of a unit cube [496, 630]. Denote by Ω_c (Ω_e) the set of points $y = x/\varepsilon$ in the unit cube for which $\mathbf{x} \in \Omega_c^\varepsilon$ ($\mathbf{x} \in \Omega_e^\varepsilon$). The concentrations $c^\varepsilon, c_e^\varepsilon$ are then taken to be functions of x and y with $\mathbf{x} \in \Omega, \mathbf{y} \in \Omega_c$ for c^ε, and $\mathbf{x} \in \Omega, \mathbf{y} \in \Omega_e$ for c_e^ε:

$$c^\varepsilon = c(\mathbf{x}, \mathbf{y}, t), \quad c_e^\varepsilon = c_e(\mathbf{x}, \mathbf{y}, t) \tag{4.113}$$

with $y = x/\varepsilon$. The next step is to introduce formal asymptotic expansion for c^ε and c_e^ε of the form

$$c^\varepsilon = c^0(\mathbf{x}, \mathbf{y}, t) + \varepsilon c^1(x, y, t) + \varepsilon^2 c^2(\mathbf{x}, \mathbf{y}, t) + \ldots \tag{4.114a}$$

$$c_e^\varepsilon = c_e^0(\mathbf{x}, \mathbf{y}, t) + \varepsilon c_e^1(\mathbf{x}, \mathbf{y}, t) + \varepsilon^2 c_e^2(\mathbf{x}, \mathbf{y}, t) + \ldots, \tag{4.114b}$$

where c^k and c_e^k are 1-periodic functions of $\mathbf{y}$. Setting

$$\nabla u = \nabla_{\mathbf{x}} u(\mathbf{x},\mathbf{y}) + \varepsilon^{-1}\nabla_{\mathbf{y}} u(\mathbf{x},\mathbf{y}),$$

it follows that (4.111) becomes

$$\frac{\partial c^\varepsilon}{\partial t} = \left(\varepsilon^{-2}\nabla_{\mathbf{y}}\cdot(A_\varepsilon(\mathbf{y})\nabla_{\mathbf{y}}) + \varepsilon^{-1}[\nabla_{\mathbf{x}}\cdot(A_\varepsilon(\mathbf{y})\nabla_{\mathbf{y}}) + \nabla_{\mathbf{y}}\cdot(A_\varepsilon(\mathbf{y})\nabla_{\mathbf{x}})] + A_\varepsilon(\mathbf{y})\nabla_{\mathbf{x}}^2\right) c^\varepsilon$$
$$\text{for}\,\mathbf{x}\in\Omega,\mathbf{y}\in\Omega_c \tag{4.115a}$$

$$\frac{\partial c_e^\varepsilon}{\partial t} = \left(\varepsilon^{-2}\nabla_{\mathbf{y}}\cdot(B_\varepsilon(\mathbf{y})\nabla_{\mathbf{y}}) + \varepsilon^{-1}[\nabla_{\mathbf{x}}\cdot(B_\varepsilon(\mathbf{y})\nabla_{\mathbf{y}}) + \nabla_{\mathbf{y}}\cdot(B_\varepsilon(\mathbf{y})\nabla_{\mathbf{x}})] + A_\varepsilon(\mathbf{y})\nabla_{\mathbf{x}}^2\right) c_e^\varepsilon$$
$$\text{for}\,\mathbf{x}\in\Omega,\mathbf{y}\in\Omega_e, \tag{4.115b}$$

and the boundary conditions (4.112) become

$$A_\varepsilon(\mathbf{y})\left[\nabla_{\mathbf{x}}+\varepsilon^{-1}\nabla_{\mathbf{y}}\right]c\cdot\mathbf{n}_c^\varepsilon = \varepsilon f(c^\varepsilon,c_e^\varepsilon), \quad \text{for}\,\mathbf{x}\in\Omega,\mathbf{y}\in\Gamma_\varepsilon \tag{4.116a}$$

$$-B_\varepsilon(\mathbf{y})\left[\nabla_{\mathbf{x}}+\varepsilon^{-1}\nabla_{\mathbf{y}}\right]c_e\cdot\mathbf{n}_c^\varepsilon = \varepsilon f(c^\varepsilon,c_e^\varepsilon), \quad \text{for}\,\mathbf{x}\in\Omega,\mathbf{y}\in\Gamma_\varepsilon. \tag{4.116b}$$

Substituting the asymptotic expansions for c^ε and c_e^ε and collecting terms of the same order in ε then yields a hierarchy of equations for c^k, c_e^k. At $\mathcal{O}(\varepsilon^{-2})$, we have

$$\nabla_{\mathbf{y}}\cdot(A_\varepsilon(\mathbf{y})\nabla_{\mathbf{y}})c^0 = 0, \quad \mathbf{y}\in\Omega_c \tag{4.117a}$$

$$\nabla_{\mathbf{y}}\cdot(B_\varepsilon(\mathbf{y})\nabla_{\mathbf{y}})c_e^0 = 0, \quad \mathbf{y}\in\Omega_e. \tag{4.117b}$$

together with the boundary conditions

$$A_\varepsilon(\mathbf{y})\nabla_{\mathbf{y}}c\cdot\mathbf{n} = 0 = B_\varepsilon(\mathbf{y})\nabla_{\mathbf{y}}c_e^0\cdot\mathbf{n}, \quad \mathbf{y}\in\Gamma, \tag{4.118}$$

where $\mathbf{n}$ is a unit normal on Γ. For fixed x, the only periodic solution to these equations is $c^0 = \text{constant}, c_e^0 = \text{constant}$, that is,

$$c^0 = c^0(x,t), \quad c_e^0 = c_e^0(x,t). \tag{4.119}$$

The $\mathcal{O}(\varepsilon^{-1})$ equations are

$$\nabla_{\mathbf{y}}\cdot\left(A_\varepsilon(\mathbf{y})\left[\nabla_{\mathbf{x}}c^0+\nabla_{\mathbf{y}}c^1\right]\right) = 0, \quad \mathbf{y}\in\Omega_c \tag{4.120a}$$

$$\nabla_{\mathbf{y}}\cdot\left(B_\varepsilon(\mathbf{y})\left[\nabla_{\mathbf{x}}c_e^0+\nabla_{\mathbf{y}}c_e^1\right]\right) = 0, \quad \mathbf{y}\in\Omega_e, \tag{4.120b}$$

together with the boundary conditions

$$A_\varepsilon(\mathbf{y})[\nabla_{\mathbf{x}}c^0+\nabla_{\mathbf{y}}c^1]\cdot\mathbf{n} = 0 = B_\varepsilon(\mathbf{y})[\nabla_{\mathbf{x}}c_e^0+\nabla_{\mathbf{y}}c_e^1]\cdot\mathbf{n}, \quad \mathbf{y}\in\Gamma. \tag{4.121}$$

The solutions for c^1 and c_e^1 can be written in the form

$$c^1(x,y,t) = \sum_{i=1}^{3} V_i^c(y)\frac{\partial c^0(x,t)}{\partial x_i} + \bar{c}^1(x,t), \tag{4.122a}$$

$$c_e^1(x,y,t) = \sum_{i=1}^{3} V_i^e(y) \frac{\partial c_e^0(x,t)}{\partial x_i} + \bar{c}_e^1(x,t), \tag{4.122b}$$

with the 1-periodic vectors $\mathbf{V}^c$ and $\mathbf{V}^e$ satisfying the "cell equations"

$$\nabla_{\mathbf{y}} \cdot (A_\varepsilon(\mathbf{y}) [\nabla_{\mathbf{y}} V_k^c(\mathbf{y}) + \mathbf{e}_k]) = 0, \quad \mathbf{y} \in \Omega_c \tag{4.123a}$$
$$\nabla_{\mathbf{y}} \cdot (B_\varepsilon(\mathbf{y}) [\nabla_{\mathbf{y}} V_k^e(\mathbf{y}) + \mathbf{e}_k]) = 0, \quad \mathbf{y} \in \Omega_e, \tag{4.123b}$$

and

$$A_\varepsilon(\mathbf{y})[\nabla_{\mathbf{y}} V_k^c(\mathbf{y}) + \mathbf{e}_k] \cdot \mathbf{n} = 0 = B_\varepsilon(\mathbf{y})[\nabla_{\mathbf{y}} V_k^e(\mathbf{y}) + \mathbf{e}_k] \cdot \mathbf{n}, \quad \mathbf{y} \in \Gamma, \tag{4.124}$$

for $k = 1,2,3$, where $\mathbf{e}_k$ is the vector with components $e_{jk} = \delta_{jk}$.

In order to derive mean-field equations for the homogenized concentrations c^0, c_e^0, it is necessary to proceed to $\mathscr{O}(1)$, for which

$$\nabla_{\mathbf{x}} \cdot \left[A_\varepsilon(\mathbf{y})(\nabla_{\mathbf{x}} c^0 + \nabla_{\mathbf{y}} c^1)\right] + \nabla_{\mathbf{y}} \cdot \left[A_\varepsilon(\mathbf{y})(\nabla_{\mathbf{x}} c^1 + \nabla_{\mathbf{y}} c^2)\right] = \frac{\partial c^0}{\partial t}, \quad \mathbf{y} \in \Omega_c \tag{4.125a}$$

$$\nabla_{\mathbf{x}} \cdot \left[B_\varepsilon(\mathbf{y})(\nabla_{\mathbf{x}} c_e^0 + \nabla_{\mathbf{y}} c_e^1)\right] + \nabla_{\mathbf{y}} \cdot \left[B_\varepsilon(\mathbf{y})(\nabla_{\mathbf{x}} c_e^1 + \nabla_{\mathbf{y}} c_e^2)\right] = \frac{\partial c_e^0}{\partial t}, \quad \mathbf{y} \in \Omega_e \tag{4.125b}$$

with boundary conditions

$$A_\varepsilon(\mathbf{y})[\nabla_{\mathbf{x}} c^1 + \nabla_{\mathbf{y}} c^2] \cdot \mathbf{n} = f(c^0, c_e^0), \quad \mathbf{y} \in \Gamma \tag{4.126a}$$
$$B_\varepsilon(\mathbf{y})[\nabla_{\mathbf{x}} c^1 + \nabla_{\mathbf{y}} c^2] \cdot \mathbf{n} = -f(c^0, c_e^0), \quad \mathbf{y} \in \Gamma. \tag{4.126b}$$

Integrating (4.125a) over Ω_c gives

$$\int_{\Omega_c} \left(\nabla_{\mathbf{x}} \cdot \left[A_\varepsilon(\mathbf{y})(\nabla_{\mathbf{x}} c^0 + \nabla_{\mathbf{y}} c^1)\right] + \nabla_{\mathbf{y}} \cdot \left[A_\varepsilon(\mathbf{y})(\nabla_{\mathbf{x}} c^1 + \nabla_{\mathbf{y}} c^2)\right]\right) d\mathbf{y} = |\Omega_c| \frac{\partial c^0}{\partial t}, \tag{4.127}$$

where $|\Omega_c|$ is the volume fraction of the unit cell occupied by the cytosol. Using (4.122a), the first term on the left-hand side becomes

$$\begin{aligned}
&\int_{\Omega_c} \nabla_{\mathbf{x}} \cdot \left[A_\varepsilon(\mathbf{y})(\nabla_{\mathbf{x}} c^0 + \nabla_{\mathbf{y}} c^1)\right] d\mathbf{y} \\
&= \int_{\Omega_c} \nabla_{\mathbf{x}} \cdot \left[A_\varepsilon(\mathbf{y})(\nabla_{\mathbf{x}} c^0 + \nabla_{\mathbf{y}} \left(\sum_{i=1}^{3} V_i^c(y) \frac{\partial c^0}{\partial x_i}\right)\right] d\mathbf{y} \\
&= \nabla_{\mathbf{x}} \cdot \left(\tilde{A}_\varepsilon \nabla_{\mathbf{x}} c^0\right),
\end{aligned}$$

where

$$[\tilde{A}_\varepsilon]_{ik} = \int_{\Omega_c} \sum_j [A_\varepsilon(\mathbf{y})]_{ij} \left[\frac{\partial V_k^c(\mathbf{y})}{\partial y_j} + \delta_{j,k}\right] d\mathbf{y}. \tag{4.128}$$

Finally, applying the divergence theorem to the second term on the left-hand side of (4.127),

$$\begin{aligned}\int_{\Omega_c} \nabla_{\mathbf{y}} \cdot \left[A_\varepsilon(\mathbf{y})(\nabla_{\mathbf{x}} c^1 + \nabla_{\mathbf{y}} c^2)\right] d\mathbf{y} &= \int_\Gamma A_\varepsilon(\mathbf{y})(\nabla_{\mathbf{x}} c^1 + \nabla_{\mathbf{y}} c^2) \cdot \mathbf{n} d\Gamma(\mathbf{y}) \\ &= \int_\Gamma f(c^0, c_e^0) d\Gamma(y) \\ &= |\Gamma| f(c^0, c_e^0).\end{aligned}$$

Combining all of the results, we obtain a macroscopic equation for c^0 given by

$$|\Omega_c| \frac{\partial c^0}{\partial t} = \nabla_{\mathbf{x}} \cdot \left(\tilde{A}_\varepsilon \nabla_{\mathbf{x}} c^0\right) + |\Gamma| f(c^0, c_e^0). \tag{4.129}$$

Proceeding in an identical fashion, we also obtain a macroscopic equation for c_e^0:

$$|\Omega_e| \frac{\partial c_e^0}{\partial t} = \nabla_{\mathbf{x}} \cdot \left(\tilde{B}_\varepsilon \nabla_{\mathbf{x}} c_e^0\right) - |\Gamma| f(c^0, c_e^0), \tag{4.130}$$

where $\tilde{B}_\varepsilon$ is defined according to (4.128) with A_ε replaced by B_ε on the right-hand side. Equations (4.129) and (4.130) constitute a bidomain model with homogenized diffusion tensors $\tilde{A}_\varepsilon$ and $\tilde{B}_\varepsilon$. The latter can be determined by solving the cell equations (4.123) and (4.124) for $\mathbf{V}^c$ and $\mathbf{V}^e$. Goel et al. [224] calculated effective diffusion tensors for several different ER microstructures. They found that diffusion in the cytoplasm could be halved as the ER volume fraction increased from 0 to 0.9.

Part II
Networks

Chapter 5
Waves in Synaptically Coupled Spiking Networks

In the second part of this book, we consider a variety of neural network models that have been used to investigate the mechanisms and properties of wave propagation in the cortex and other parts of the nervous system. There has been a rapid increase in the number of computational studies of network spatiotemporal dynamics, including oscillations and waves, which are based on biophysically detailed conductance-based models of synaptically (and possibly electrically) coupled neurons; see, for example, [153]. These models provide considerable insights into the role of ionic currents, synaptic processing, and network structure on spatiotemporal dynamics, but they tend to be analytically intractable. This has motivated an alternative approach to network dynamics, involving simplified neuron models that hopefully capture important aspects of wave phenomena, while allowing a more concise mathematical treatment. In the case of oscillatory networks, such a simplification can be achieved by reducing a conductance-based neuron model to a phase model along the lines of Sect. 1.2. Alternatively, one can use a simplified spiking neuron model such as integrate-and-fire (Sect. 3.1) in order to investigate waves in excitable and oscillatory neural media. Both of these approaches are considered in this chapter. (Note that we do not discuss another important method for analyzing the dynamics of synaptically coupled spiking networks, namely, fast/slow decomposition and geometric singular perturbation theory, which is reviewed extensively elsewhere [173, 537, 538].) In Chaps. 6 and 7 we turn to population-based approaches, for which the fundamental active element is taken to be a local population of cells rather than a single neuron, and the cortex is treated as a continuum neural field. The mathematical advantage of neural fields is that many of the PDE methods from Part I can be adapted to study traveling wave solutions. An illustrative application of neural field theory to binocular rivalry waves and models of visual cortex is presented in Chap. 8.

P.C. Bressloff, *Waves in Neural Media: From Single Neurons to Neural Fields*,
Lecture Notes on Mathematical Modelling in the Life Sciences,
DOI 10.1007/978-1-4614-8866-8_5, © Springer Science+Business Media New York 2014

5.1 Waves in Cortical and Subcortical Systems

We begin by summarizing the basic structure of the brain and then describe various experimental studies of waves in different regions of the brain, focusing on cortical and subcortical structures. The brain can be divided into three main parts: the forebrain, midbrain, and hindbrain; see Fig. 5.1. The forebrain consists of the cerebral cortex, thalamus, and limbic system, the midbrain consists of the tectum and tegmentum, and the hindbrain is made of the cerebellum, pons, and medulla. Often the midbrain, pons, and medulla are referred to collectively as the *brainstem*, which is responsible for vital life functions such as breathing, blood pressure, and heart pumping. The *cerebral cortex* is the largest part of the human brain and is responsible for higher brain function. The cortex is subdivided into four main sections or "lobes": (i) the frontal lobe, associated with planning, rational and emotional thinking, and problem solving; (ii) the parietal lobe, associated with motor control and somatosensory processing; (iii) the occipital lobe, associated with visual processing; (iv) the temporal lobe, associated with auditory processing, language, and memory. Cortical folding increases the effective size of the cortex, which when unfolded forms a thin sheet of neural tissue only a few millimeters thick. Neurons are arranged into six distinct layers through the depth of the cortex, each with its own characteristic set of interneurons, input sources (afferents), and output targets (efferents). For example, layer IV is the primary input layer of the sensory cortex, receiving sensory information via the thalamus, superficial layers I–III mediate intracortical connections, while deep layers V and VI send feedback to subcortical regions including the thalamus; see Fig. 5.2. For a more detailed description of the

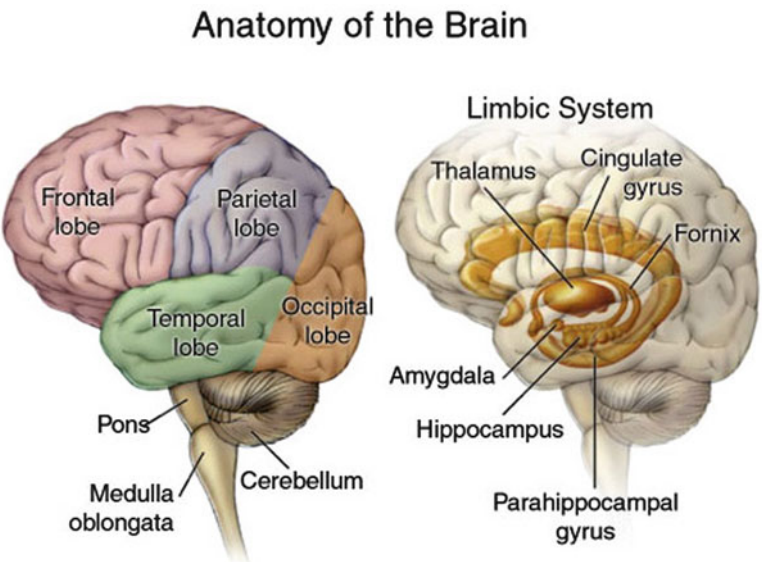

Fig. 5.1 Schematic illustration of the brain, showing cortical, thalamic, and hippocampal regions. See text for details [Public domain figure from Wikipedia Commons]

functional structure of primary visual cortex, see Sect. 8.1. *The limbic system* is a complex set of brain structures, including the hippocampus and amygdala, which is located on either side of the thalamus and adjacent to the inner border of the cortex. The limbic system appears to be primarily involved in memory and emotions. For example, the *hippocampus* is required for converting short-term memories to long-term memories and is also implicated in maintaining cognitive maps for spatial navigation. The *amygdala*, on the other hand, is involved in processing emotionally significant stimuli such as those related to fear and reward. Finally, moving on from the limbic system, the *cerebellum* of the hindbrain is associated with the regulation and coordination of fine movements, as well as posture and balance.

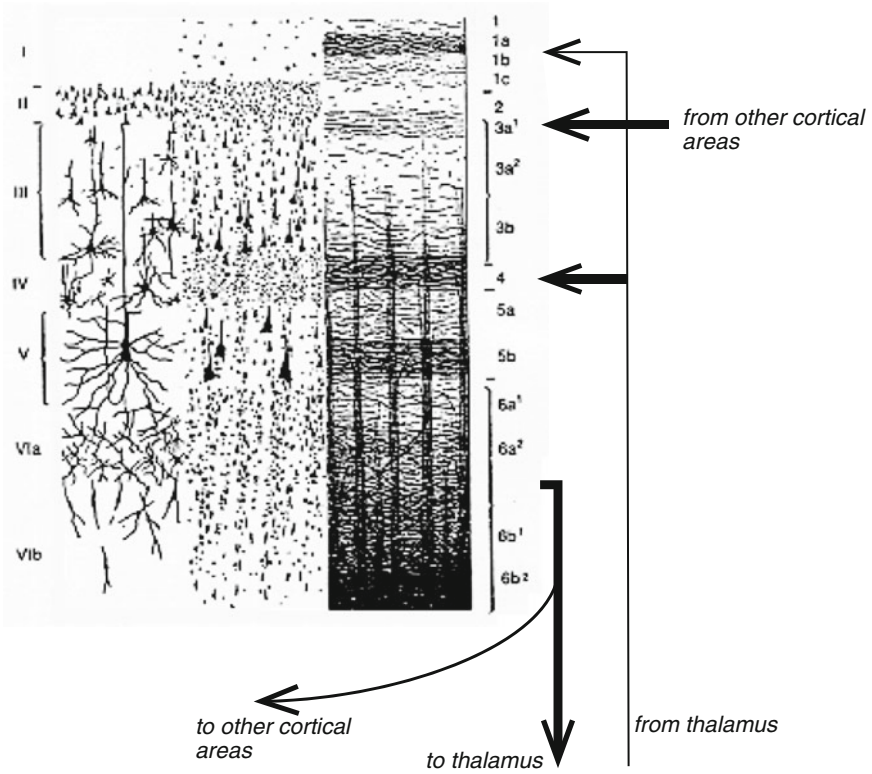

Fig. 5.2 Schematic illustration of the layered structure of primate sensory cortex. See text for details [Public domain figure from Wikipedia Commons]

Cortical Waves

A common in vitro method for studying the propagation of electrical activity in the cortex (or hippocampus) is to remove a vertical brain slice and bathe it in a pharmacological medium that blocks the effects of inhibition. This type of slice preparation

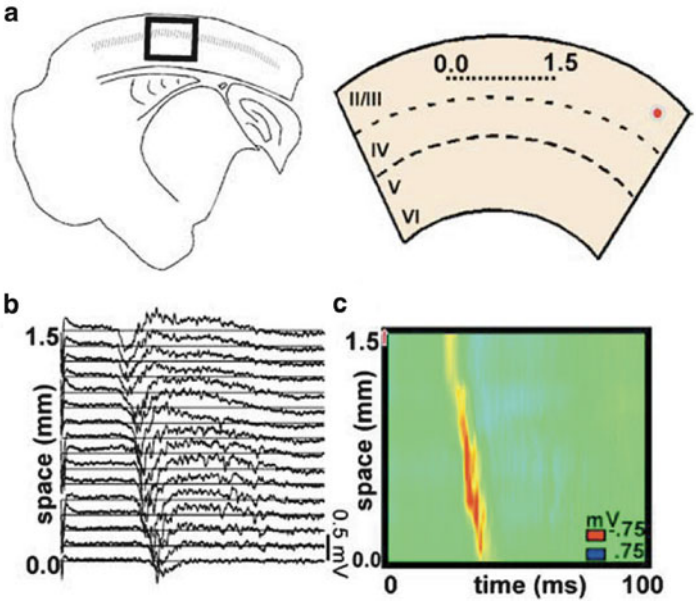

Fig. 5.3 Propagating wave of activity in a brain slice preparation in which inhibition has been blocked. (**a**) Schematic of a slice removed from the somatosensory cortex of the rat. The cortex is a thin (submillimeter) layered sheet of neurons. A slice approximately 500 μm thickness is obtained by cutting vertically through the cortical layers. (**b**) A multielectrode array placed into layers II/III of the slice records extracellularly the propagation of a wave. (**c**) Pseudocolor plot of propagating activity (Adapted from Pinto et al. [507])

was originally developed as an experimental model of epilepsy. Synchronized discharges can be evoked by a weak electrical stimulus to a local site on the slice and each discharge propagates away from the stimulus as a continuous traveling pulse at a characteristic speed of about 10 cm/s [112, 228, 507, 521, 685], as illustrated in Fig. 5.3. The underlying mechanism for the propagation of such waves is synaptic in origin rather than diffusive, in contrast to the much faster propagation of action potentials along the axons of individual neurons; see Chap. 2. The pharmacological dependence of propagating activity in vitro has been well characterized and implicates polysynaptic fast glutamatergic transmission (AMPA) as the major factor in sustaining propagating activity. On the other hand, if a cortical slice is bathed in normal cerebral fluid so that inhibition is present, then the speed of propagating activity is slowed by a factor of 10, and the propagating pulse of ensemble activity has significantly more fluctuations consistent with the complex oscillation profile seen in the corresponding local field potential [124, 549, 685]. This type of oscillatory wave consists of several oscillation cycles embedded in a single propagating wave envelope. The resulting activity is non-epileptic, with individual neurons firing at a relatively low rate of around 10 Hz, and is mediated by slower NMDA-based excitation. It has been suggested that these waves are the in vitro analog of

low-frequency oscillations observed during slow-wave sleep [602]; see below. An alternative type of oscillatory wave, which is often referred to as a "one-cycle-one-wave," has been observed in disinhibited cortical slices or in slices for which NMDA receptor-mediated excitation has been enhanced. In this case, the cortical slice acts like an oscillatory medium with a frequency around 10 Hz, and the traveling pulse takes the form of a phase wave [684]; see Sect. 5.2.2. In two-dimensional (tangential) slices, these oscillations can develop into two-dimensional waves, including spiral waves [292].

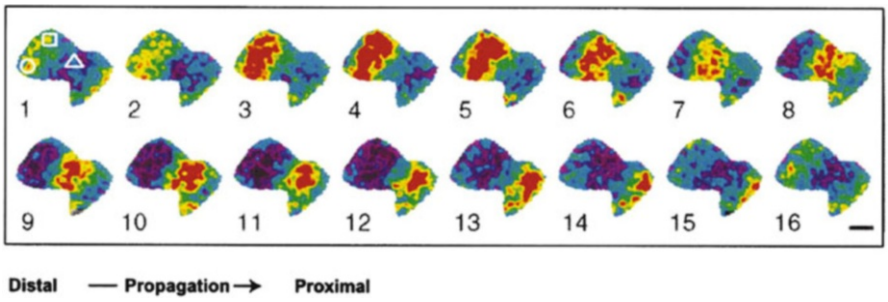

Fig. 5.4 Propagating wave of activity in the central olfactory lobe of the mollusk *Limax*. Successive images of the membrane potential in the olfactory lobe shown for one cycle. A band of depolarization can be seen propagating from the distal to the proximal end of the lobe. The time scale is 112 ms/frame and the length-scale bar is 100 µm (Adapted from Kleinfeld et al. [338])

A variety of sensory stimuli have been linked to propagating waves in vivo [442, 553, 683]. For example, a number of studies of vertebrate and invertebrate olfactory bulbs have shown that they support propagating phase waves [149, 338, 357]; see Fig. 5.4. These waves occur spontaneously, but transiently switch to standing oscillations during the presentation of an odorant stimulus, suggesting that the spatiotemporal patterns may play a role in olfactory processing. Propagating waves consisting of low-frequency oscillations superimposed on a traveling pulse have been observed in the visual cortex of anesthetized rats [255, 688], cats [39], and primates [243]. One feature of these visually evoked waves is that they exhibit anisotropy. For example, Xu et al. [688] found that the stimulus-evoked wave propagated fast in V1 but then slowed down as it approached the V1/V2 border, causing wave compression. This was followed by the initiation of a reflected wave that propagated backward into V1 and a transmitted wave propagating across V2. In addition to these single-cycle events, it is also possible to observe traveling phase waves in the visual cortex [512]. The precise functional role of spontaneous and stimulus-evoked waves in the cortex is not currently known. However, one possible contribution has been proposed in the case of sensory brain regions [170, 683]. More specifically, synchrony could represent a state of perceptual recognition, while waves could correspond to a state of perceptual scanning. In the latter case, a phase wave would provide a background depolarization in successive cortical regions, in which neurons have an increased probability of firing and a higher synaptic transmission ef-

ficacy (enhanced sensitivity). Thus, rotating waves such as spiral waves could act as an organizing center that periodically sensitizes an area without the need for any pacemaker. Interestingly, it has recently been hypothesized that in the motor cortex, synchrony and phase waves switch roles, with synchrony encoding the absence of motor action while waves with different frequencies and directions of propagation encode different motor actions [269].

Sleep–Wake Cycle

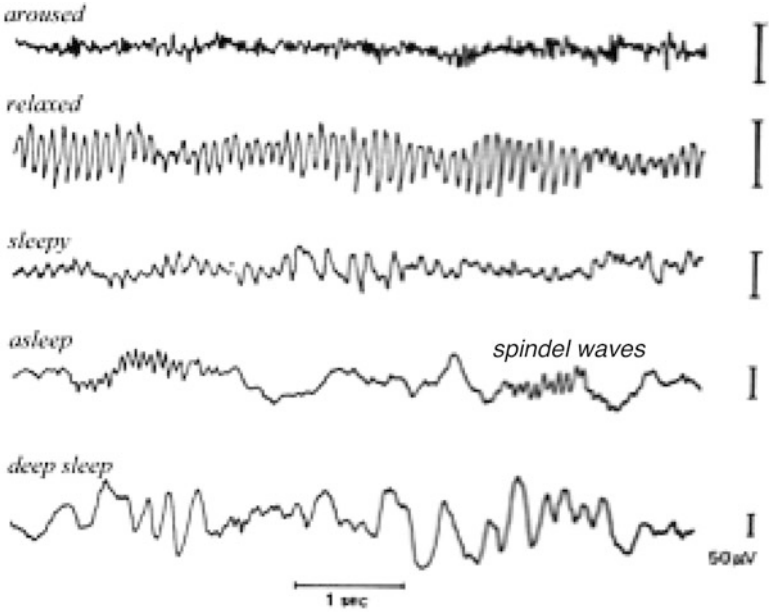

Fig. 5.5 EEG recordings from cortex at different stages of the sleep–wake cycle [Adapted from wiki.brown.edu]

Cortical oscillations and waves as measured using *electroencephalogram* (EEG) and microelectrode recordings have different signatures depending on the general state of the brain [153, 272, 442, 602]; see Fig. 5.5. Such rhythms either are generated directly in cortex or emerge from interactions with the thalamus and with a sheet of inhibitory neurons between the thalamus and cortex known as the thalamic reticular nucleus (TRN); see Fig. 5.6. The waking state and the rapid eye movement (REM) stage of sleep are both characterized by low-amplitude fast oscillations that tend to have a low level of spatiotemporal coherence. On the other hand, during non-REM sleep and anesthesia, the brain exhibits significant oscillatory activity at a variety of frequencies and with striking long-range synchrony. Of

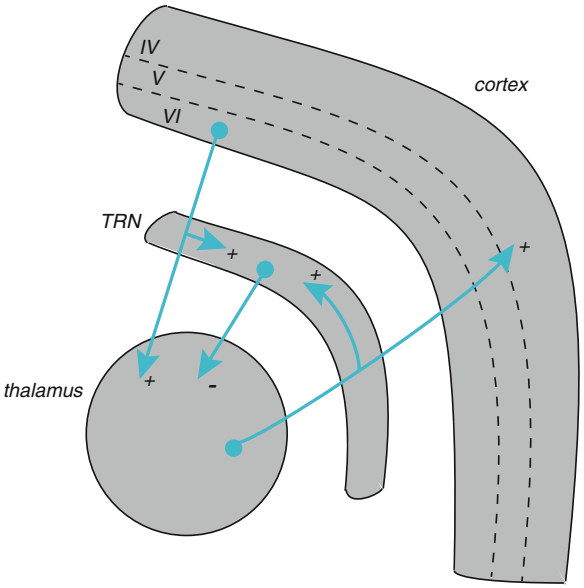

Fig. 5.6 Three principal regions thought to be responsible for the various rhythms and waves observed during the sleep–wake cycle. Surrounding the thalamus and interposed between the thalamus and cortex is a thin layer of GABAergic neurons known as the thalamic reticular nucleus (TRN). These neurons are reciprocally coupled to excitatory neurons in the thalamus, forming the reticulothalamic loop. Thalamic neurons innervate pyramidal cells in input layer IV of cortex, while pyramidal cells in cortical layer VI send feedback connections to thalamus, resulting in the thalamocortical loop. There are also axon collaterals from layer VI neurons to neurons in the TRN

particular significance is a slow oscillation (< 1 Hz) of the membrane potential of cortical neurons, comprising a hyperpolarization phase or *down state*, during which the majority of neurons are silent for several seconds, followed by a depolarization phase or *up state* of smaller duration in which neurons fire at a rate of around 10 Hz. Cortical slice studies [549] combined with computational modeling [27, 122] suggest that the transition to the up state is due to the spontaneous activation of a small subset of kindling neurons in deep cortical layers, followed by propagation of activity vertically through the layers and horizontally across the cortical network. The transition to the down state involves some combination of synaptic depression and the opening of a slow Na^+-dependent K^+ conductance. Superimposed on the slow oscillations is another rhythm known as *spindle waves*, which appear in the EEG during non-REM sleep as 7–14 Hz oscillations that wax and wane over a period of a few seconds. Unlike the slow oscillations, which are cortical in origin, the spindle waves are generated by de-inactivation of a low-threshold Ca^{2+} current in thalamic cells following inhibition from TRN cells, which is sufficient to generate a rebound burst of action potentials that then excites the TRN cells; see Sect. 5.4.3. Propagating spindle waves with speeds of 1 cm/s can be observed in thalamic slices following local current injection [334]. (Note that various EEG rhythms are referred to as "waves" even though this does not necessarily imply that they are actually

propagating as waves—they can be standing oscillations, e.g., spindle waves, sharp waves.) Transitions between non-REM sleep, REM sleep, and arousal are controlled by a variety of neurotransmitters released from brainstem nuclei including acetylcholine, norepinephrine, and serotonin.

Hippocampal Waves

The primary regions of the hippocampus, which is shaped like a ram's horn (*cornu ammonis*), are CA1, CA3, the dentate gyrus, and the subiculum; see Fig. 5.7. The main input pathway (perforant path) to the hippocampus comes from the entorhinal cortex (EC), which is strongly and reciprocally connected to many other parts of the cerebral cortex. Within the hippocampus, the flow of information from the EC is largely unidirectional (see inset of Fig. 5.7), with signals propagating through a series of densely packed cell regions: the dentate gyrus $\rightarrow$ CA3 via the mossy fibers $\rightarrow$ CA1 via the Shaffer collaterals $\rightarrow$ the subiculum $\rightarrow$ EC. Each of these regions also contains complex intrinsic circuitry and extensive lateral connections. In particular, both the dentate gyrus and CA3 have extensive recurrent connections that are thought to be important in the storage of memories within the hippocampus [10]. The hippocampus exhibits two major modes of physiological activity, known as the *theta rhythm* and *large irregular activity* (LIA), each of which corresponds to distinct patterns of population activity and EEG rhythms [98]. The properties of these activity states have been determined primarily from studies of the rat, although analogous states have been found in primates.

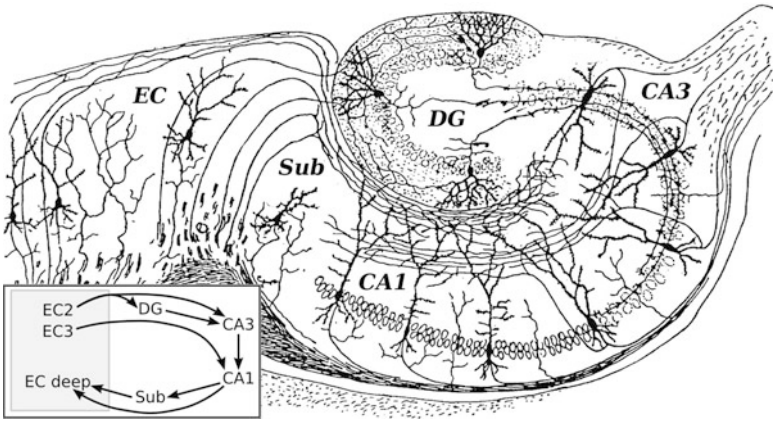

Fig. 5.7 Modified drawing of the neural circuitry of the rodent hippocampus by Santiago Ramn y Cajal. Histologie du Systeme Nerveux de l'Homme et des Vertebretes, Vols. 1 and 2. A. Maloine. Paris. 1911. DG: dentate gyrus. Sub: subiculum. EC: entorhinal cortex [Public domain figure from Wikipedia Commons]

During the theta phase, the EEG is dominated by large regular oscillations with a frequency range of 6–9 Hz [97]. It is associated with sparse population activity, in which the vast majority of neurons are silent within any short time window, with the small remaining fraction of cells firing at relatively high rates (up to 50 Hz) for around a second. Theta rhythms occur during REM sleep and during periods of active, alert behavior (particularly locomotion), where cell activity is primarily determined by the spatial location of the animal, so that the set of active neurons is constantly changing. This is exemplified by the selective activation of CA1 pyramidal cells at particular locations in space called *place fields* [474]. A given configuration of place cells provides an internal representation of the environment that affords an animal knowledge of its position relative to important locations. A key observation is that the spike activity of a hippocampal CA1 cell advances to earlier phases of the theta cycle as the animal passes through the cell's place field [475]. One possible interpretation of this phase advance is that it reflects a prediction of the sequence of upcoming locations based on the rat's current position, that is, it is part of a path integration system [384]. It was originally thought that theta oscillations were synchronized across the hippocampus, but it has subsequently been shown that theta oscillations in freely behaving rats propagate as traveling waves [393].

The LIA mode occurs during non-REM sleep and during periods of waking immobility such as resting or eating. The pattern of irregular activity is occasionally interrupted by large amplitude surges called *sharp waves* [96], which coincide with 50–100 ms bursts of spiking activity in pyramidal cells of CA3 and CA1. Superimposed on the sharp waves are short-lasting high-frequency oscillations called *ripples*, with frequencies in the range 150–200 Hz in rats. An in vitro study indicates that the sharp wave–ripple complexes (SPW-R) propagate from CA3 to CA1 and then to the subiculum with a speed around 5 cm s^{-1} [399]. One of the interesting features of sharp waves is that they have been implicated in memory consolidation during sleep [611]. For example, place cells exhibit experience-dependent reactivation during sleep that is representative of previous behavior [677]. More specifically, neurons with overlapping place fields during spatial exploration within an environment show increased coactivity during subsequent sleep, firing in the same sequence as they fired when the rodent was exploring its surroundings in the awake state.

Pathological States

Propagating waves of activity are also associated with a variety of pathological brain states, including cortical spreading depression and epileptic seizures. Cortical spreading depression is a complex pulse-like wave of transient depolarization of neurons and glial cells that propagates slowly across cortical and subcortical gray matter at speeds of 1–5 mm/min [596]. Spreading depression, which is thought to play a major role in migraine with aura [358, 639], appears to involve the diffusion and active transport of extracellular ions such as K^+ and is thus modeled in terms of reaction–diffusion equations rather than spiking networks or neural field equations;

see Sect. 9.3. On the other hand, the latter models have been used to study the initiation, propagation, and termination of epileptiform activity [158, 507]. Epilepsy is characterized by spontaneously occurring seizures that may involve a significant portion of the brain at onset (primary generalized seizures) or originate from a circumscribed brain region and may or may not spread to other regions (focal seizures) [125, 348, 415, 430]; see Sect. 9.4. In the case of focal seizures, a localized region of pacemaker neurons within deep layers of cortex can drive hypersynchronous activity that rapidly spreads vertically through the layers and then spreads horizontally as a traveling pulse. There is also a relationship between epilepsy and sleep, which is not surprising given that sleep also involves changes in levels of synchrony. For example, the increased synchronization during non-REM sleep might facilitate the abnormal synchronization of the epileptic brain, while the relatively desynchronized state during REM sleep or waking might suppress it. Unfortunately, the relationship between sleep and epilepsy is far more complex and heterogeneous [584].

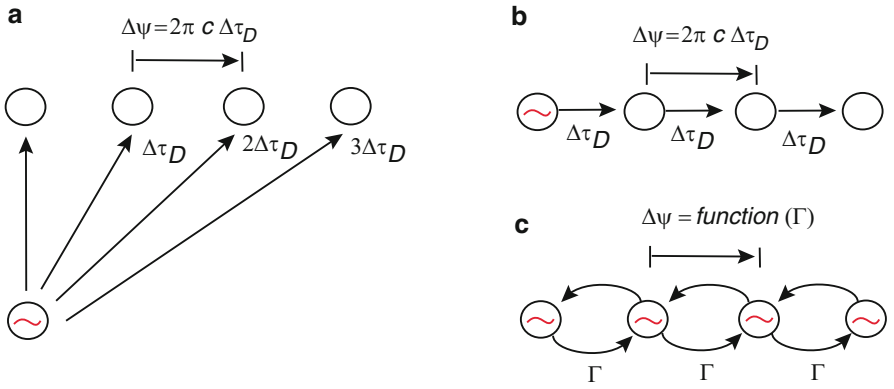

Fig. 5.8 Three mechanisms for generating and sustaining propagating waves. (**a**) Fictive waves due to a local oscillator driving adjacent cortical regions with increasing time delays $\Delta\tau_D$. (**b**) A local oscillator drives a chain of excitable cells. (**c**) Traveling phase wave in a chain of neuronal oscillators with local coupling parameter Γ

Basic Wave Propagation Mechanisms

Ermentrout and Kleinfeld [170] have highlighted three basic mechanisms for wave propagation in the cortex and other neural circuits; see Fig. 5.8:

1. A single oscillator directly excites neighboring areas with increasing time delays that generates a fictive propagating wave. This has been suggested as one mechanism for traveling waves in anesthetized visual cortex, with the spread of the wave determined by axonal propagation delays in long-range horizontal connections [39, 243]. The predominant wave mechanism is monosynaptic.

2. A single pacemaker oscillator (or local group of oscillators) drives an excitable neural medium. Each time the pacemaker fires, it generates a solitary propagating wave of activity. If the pacemaker ceases to be active, then waves no longer occur. This polysynaptic mechanism underlies the propagation of solitary pulses in disinhibited cortical slices and is one framework for understanding the spread of synchronous activity in focal epilepsy or during slow-wave sleep. We will consider traveling waves in excitable spiking networks in Sect. 5.4.
3. The whole medium is in an oscillatory state so that wave propagation represents a spatial gradient in the phase of the oscillators, as has been observed in various sensory cortices as well as central pattern generators (CPGs) for locomotion. In these cases one can interpret the resulting wave as a phase-locked solution of a coupled phase oscillator model; see Sect. 5.2.

One important issue is determining what the fundamental oscillatory unit is in each of these mechanisms—a single neuron as considered here or a local population of neurons (see Chap. 6). A related issue is the time scale over which phase-locking occurs—does it occur at the level of individual spikes, or bursts of action potentials, or population firing rates?

5.2 Phase Reduction of Synaptically Coupled Neural Oscillators

In Sect. 1.4 we considered a feedforward neuronal network in which a single output neuron was synaptically driven by a set of afferent neurons that were themselves driven by external inputs; see Fig. 1.14. However, in order to model the dynamics of neuronal networks in the cerebral cortex, for example, it is necessary to take into account the fact that around 80 % of inputs into a cortical neuron are from other cortical neurons, indicative of a highly recurrent network architecture. This means that the output spike train of one neuron feeds back as input to a subset of other neurons that themselves innervate the given neuron; see Fig. 5.9. Therefore, consider a network of N synaptically coupled cortical neurons labeled $i = 1, \ldots, N$. Let $v_i(t)$ denote the somatic membrane potential of the ith neuron, evolving according to a conductance-based model of the form

$$C\frac{\mathrm{d}v_i}{\mathrm{d}t} = -I_{\mathrm{con,i}}(v_i, \ldots) + u_i(t), \tag{5.1}$$

supplemented by additional equations for the ionic gating variables. (For the moment we are ignoring any external currents.) The total synaptic current $u_i(t)$ entering the soma is generated by the incoming spike trains from other neurons in the network that are filtered by synaptic and dendritic processing. Denote the sequence of firing times of the jth neuron by $\{T_j^m, m \in \mathbf{Z}\}$, with

$$T_j^m = \inf\{t, t > T_j^{m-1} | v_j(t) = \kappa, \dot{v}_j(t) > 0\}, \tag{5.2}$$

where κ is the firing threshold. Following Sect. 1.4, the net synaptic current into postsynaptic neuron i due to innervation by the spike train from presynaptic neuron j is taken to have the general form $\sum_m \Phi_{ij}(t - T_j^m)$, where $\Phi_{ij}(t)$ represents the temporal filtering effects of synaptic and dendritic processing on the spike train from neuron j innervating neuron i. (For the moment we ignore short-term synaptic depression and the effects of axonal propagation delays.) Assuming that all synaptic inputs sum linearly, we find that the total synaptic input to the soma of the ith neuron is

$$u_i(t) = \sum_{j=1}^N \sum_m \Phi_{ij}(t - T_j^m) = \sum_{j=1}^N \int_{-\infty}^t \Phi_{ij}(t - t')a_j(t')dt', \tag{5.3}$$

where we have set

$$a_j(t) = \sum_{m \in \mathbf{Z}} \delta(t - T_j^m). \tag{5.4}$$

That is, $a_j(t)$ represents the output spike train of the jth neuron in terms of a sum of Dirac delta functions. In general, (5.1)–(5.3) are difficult to analyze, particularly when N is large, so that some form of approximation scheme is needed. One approach is to use the phase reduction procedure of Sect. 1.2.

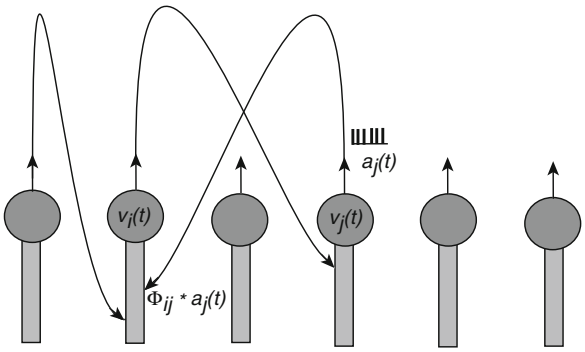

Fig. 5.9 Schematic diagram of a recurrent neuronal network. Not all connections are shown

Consider a network of N identical conductance-based neurons, each of which is acting as a limit cycle oscillator. (It is straightforward to extend the analysis to nonidentical oscillators with different intrinsic frequencies, e.g.) If the synaptic interactions between the neurons are sufficiently weak, then the phase reduction method outlined in Sect. 1.2 can be applied at the network level. This leads to a system of coupled equations for the phases of the neural oscillators in the network, in which the effective phase interaction function H depends on both the nature of the synaptic interactions and the intrinsic properties of each oscillator as expressed through its phase-resetting curve (see Fig. 5.10). Denoting the state of the ith neuron by $\mathbf{x}_i \in \mathbb{R}^k$, with $x_{1,i} = v_i$, and taking $\Phi_{ij}(t) = w_{ij}\Phi(t)$, the network dynamics given by (5.1) and (5.3) can be written as the coupled system of ODEs

$$\frac{dx_{\mu,i}}{dt} = f_\mu(\mathbf{x}_i) + \varepsilon\delta_{\mu,1}\sum_{j=1}^{N} w_{ij}\sum_m \Phi(t - T_j^m) \tag{5.5}$$

for $\mu = 1,\ldots,k$. Suppose that in the absence of interactions each neuron has a stable limit cycle $\mathbf{X}$ with natural frequency ω_0, and introduce the phase variable θ_i such that

$$\frac{d\theta_i}{dt} = \omega_0. \tag{5.6}$$

There is a one-to-one mapping $\theta_i \to \mathbf{X}(\theta_i)$ on the limit cycle. Treating $p_i(t) = \varepsilon\sum_{j=1}^{N} w_{ij}\sum_m \Phi(t - T_j^m)$ as a weak time-dependent perturbation of the voltage of the ith oscillator, we can use the method of isochrones in Sect. 1.2, to obtain the phase equation

$$\frac{d\theta_i}{dt} = \omega_0 + \varepsilon\sum_{j=1}^{N} w_{ij}Z(\theta_i(t))\sum_m \Phi(t - T_j^m), \tag{5.7}$$

where $Z(\theta_i)$ is the phase-resetting curve (PRC)—more precisely, the component of the PRC with respect to voltage perturbations.

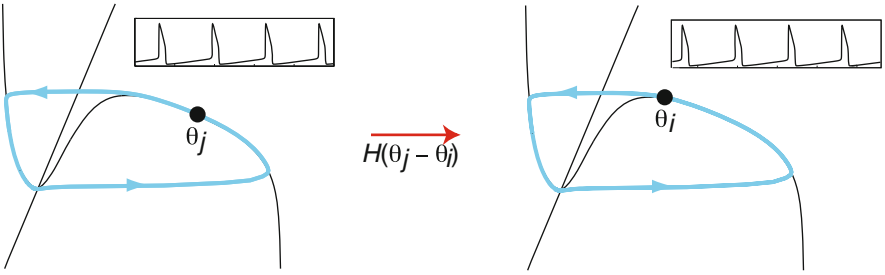

Fig. 5.10 A system of two synaptically coupled limit cycle oscillators can be reduced to a pair of phase equations involving an effective phase interaction function $H(\theta_j - \theta_i)$. See text for details

In order to obtain a closed system of equations, it is necessary to express the firing times T_j^m in terms of the phase $\theta_j(t)$. Assume that the jth neuron fires whenever the phase θ_j crosses zero. The firing times then satisfy the condition

$$\theta_j(T_j^m) = 2\pi m, \quad \dot{\theta}_j(T_j^m) > 0. \tag{5.8}$$

If we now set $\psi_j(t) = \theta_j(t) - \omega_0 t$ then ψ_i is a slowly varying function of time (for small ε) so that to a first approximation

$$T_j^m = (2\pi m - \psi_j(t))/\omega_0 = t + (2\pi m - \theta_j(t))/\omega_0, \tag{5.9}$$

that is, the current phase determines the most recent sequence of firing times. Hence, (5.7) reduces to the closed system of equations

$$\frac{d\theta_i}{dt} = \omega_0 + \varepsilon \sum_{j=1}^{N} w_{ij} Z(\theta_i(t)) P(\theta_j(t)), \tag{5.10}$$

where

$$P(\theta_j(t)) = \sum_m \Phi[(\theta_j(t) - 2\pi m)/\omega_0].$$

The final step of the analysis is to use the method of averaging to obtain effective interactions that depend only on phase differences. Substituting $\psi_i = \theta_i - \omega_0 t$ into the phase equation (5.10) gives

$$\frac{d\psi_i}{dt} = \varepsilon \sum_{j=1}^{N} w_{ij} Z(\psi_i(t) + \omega_0 t) P(\psi_j(t) + \omega_0 t). \tag{5.11}$$

The corresponding averaged equation is then

$$\frac{d\psi_i}{dt} = \varepsilon \sum_{j=1}^{N} w_{ij} H(\psi_j - \psi_i), \tag{5.12}$$

where

$$\begin{aligned} H(\psi_j - \psi_i) &= \frac{1}{\Delta_0} \int_0^{\Delta_0} Z(\psi_i + \omega_0 t) P(\psi_j + \omega_0 t]) dt \\ &= \frac{1}{2\pi} \int_0^{2\pi} Z(\theta + \psi_i - \psi_j) P(\theta) d\theta, \end{aligned} \tag{5.13}$$

with $\Delta_0 = 2\pi/\omega_0$. We have exploited the periodicity of the functions R, P. A useful alternative expression for H is obtained by substituting for P:

$$\begin{aligned} H(\psi) &= \frac{1}{2\pi} \int_0^{2\pi} Z(\theta - \psi) \sum_m \Phi([\theta - 2\pi m]/\omega_0) d\theta \\ &= \frac{1}{2\pi} \int_0^{\infty} Z(\theta - \psi) \Phi(\theta/\omega_0) d\theta. \end{aligned} \tag{5.14}$$

5.2.1 Phase-Locking

We define a 1:1 phase-locked solution of the phase equation (5.12) to be of the form

$$\psi_i(t) = (\omega - \omega_0) t + \overline{\psi}_i, \tag{5.15}$$

where ω is the *collective frequency* of the coupled oscillators and $\Psi = (\bar{\psi}_1, \ldots, \bar{\psi}_n)$ is a set of constant phases. Substitution into (5.12) leads to the fixed-point equations

$$\omega = \omega_0 + \varepsilon \sum_j w_{ij} H(\overline{\psi}_j - \overline{\psi}_i), \quad i = 1, \ldots, N. \tag{5.16}$$

After choosing some reference oscillator, the N phase equations determine the collective period ω and $N-1$ relative phases with the latter independent of ε. The local stability of a phase-locked solution can be analyzed by setting $\psi_i(t) = \overline{\psi}_i + [\omega - \omega_0]t + \delta\psi_i(t)$ and expanding to first order in $\delta\psi_i(t)$:

$$\frac{\mathrm{d}\delta\psi_i}{\mathrm{d}t} = \varepsilon \sum_{j=1}^{N} \mathscr{H}_{ij}(\Phi)\delta\psi_j, \tag{5.17}$$

where

$$\mathscr{H}_{ij}(\Phi) = w_{ij}H'(\overline{\psi}_j - \overline{\psi}_i) - \delta_{i,j}\sum_k w_{ik}H'(\overline{\psi}_k - \overline{\psi}_i), \tag{5.18}$$

and $H'(\psi) = dH(\psi)/\mathrm{d}\psi$. One of the eigenvalues of the Jacobian $\mathscr{H}$ is always zero, and the corresponding eigenvector points in the direction of the flow, that is $(1,1,\ldots,1)$. The phase-locked solution will be stable provided that all other eigenvalues have a negative real part [166].

Consider, for example, two identical oscillators ($N=2$) that are symmetrically coupled, with $w_{12} = w_{21} = 1$ and $w_{11} = w_{22} = 0$. The phase difference $\psi = \psi_2 - \psi_1$ satisfies the simple equation

$$\frac{d\psi}{dt} = \varepsilon H^-(\psi), \tag{5.19}$$

where $H^{\pm}(\psi) = H(-\psi) \pm H(\psi)$. Phase-locked states are then given by the zeros of the odd function H^-:

$$H^-(\overline{\psi}) = 0. \tag{5.20}$$

A given phase-locked state is stable provided that

$$\varepsilon \frac{\mathrm{d}H^-(\psi)}{\mathrm{d}\psi}\bigg|_{\overline{\psi}} < 0. \tag{5.21}$$

Note that by symmetry both the inphase ($\overline{\psi} = 0$) and antiphase ($\overline{\psi} = \pi$) states are guaranteed to exist. However, there may be additional fixed points depending on the parameters. The collective frequency of oscillation is determined by the even part of H:

$$\omega = \omega_0 + \frac{\varepsilon}{2}H^+(\overline{\psi}). \tag{5.22}$$

It turns out that the stability of the inphase state for a pair of neurons depends on a number of factors [258, 651]: whether the synapses are excitatory or inhibitory, whether the kinetics are fast or slow, whether the phase-resetting curve is type I or type II, and the size of any axonal delays. We shall illustrate this by considering a simple example.

Example: Pair of Hodgkin–Huxley neurons. In Fig. 5.11 we show a typical phase-resetting curve $R(\phi)$ for the Hodgkin–Huxley model (1.6) together with the resulting phase interaction function $H(\psi)$ for $\Phi(t)$ given by an α function:

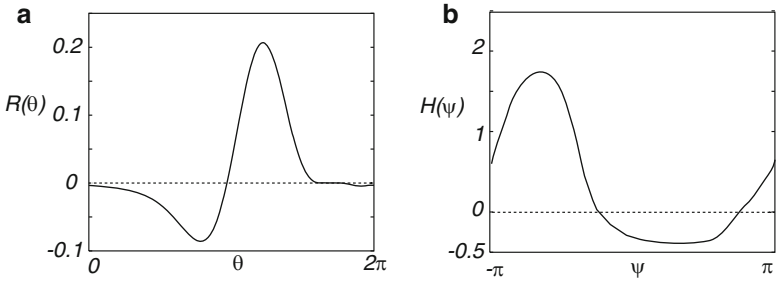

Fig. 5.11 Plot of type II phase-resetting curve $R(\theta)$ for the Hodgkin–Huxley model together with effective phase interaction function $H(\psi)$

$$\Phi(t) = \alpha^2 t \mathrm{e}^{-\alpha t}. \tag{5.23}$$

If we approximate the PRC by $Z(\phi) = -\sin\phi$ then

$$\begin{aligned} H(\psi) &= \frac{1}{2\pi}\int_0^{2\pi} Z(\theta-\psi)P(\theta)d\theta \\ &= \frac{\alpha^2}{2\pi}\frac{d}{d\alpha}\int_0^{\infty} \sin(\theta-\psi)\mathrm{e}^{-\alpha\theta/\omega_0}d\theta \\ &= \frac{\alpha^2}{2\pi}\mathrm{Im}\frac{d}{d\alpha}\int_0^{\infty} \mathrm{e}^{i(\theta-\psi)}\mathrm{e}^{-\alpha\theta/\omega_0}d\theta. \end{aligned}$$

Now

$$\frac{d}{d\alpha}\int_0^{\infty} \mathrm{e}^{i\theta}\mathrm{e}^{-\alpha\theta/\omega_0}d\theta = -\frac{\omega_0}{(\alpha - i\omega_0)^2}$$

and so

$$H(\psi) = A\sin\psi - B\cos\psi, \tag{5.24}$$

where

$$A = [\alpha^2 - \omega_0^2]K, \quad B = 2\alpha\omega_0 K, \quad K = \frac{\alpha^2\omega_0}{2\pi[\alpha^2+\omega_0^2]^2}.$$

The odd part is then $H^-(\psi) = -A\sin\psi$ with $A \neq 0$ provided that $\alpha \neq \omega_0$, and then there are phase-locked states at $\psi = 0, \pi$ as expected. The synchronous solution is stable if $\varepsilon H^{-\prime}(0) < 0$. This implies that synchronization will occur for excitatory coupling if $\alpha > \omega_0$ and for inhibitory coupling if $\alpha < \omega_0$. Thus, *inhibition* rather than excitation synchronizes the neurons when the synapses have sufficiently slow kinetics. The reverse is true for the antiphase solution $\psi = \pi$. If higher-order terms in the Fourier series expansion of H are included, $H(\psi) = \sum_n h_n \mathrm{e}^{in\psi}$, then the transition from synchronous to antisynchronous behavior is smoother, that is, the system no longer makes a sudden jump from one to the other at a critical value of α.

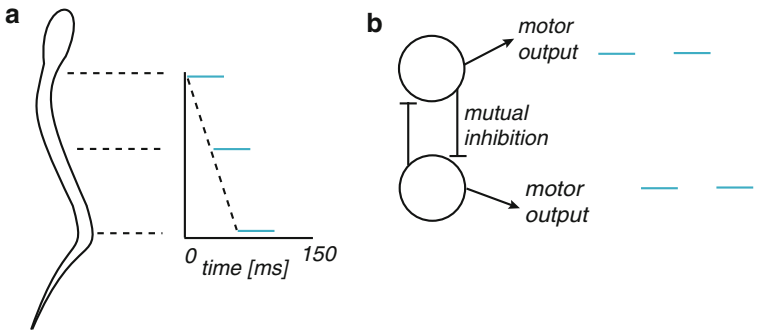

Fig. 5.12 (**a**) Swimming locomotion is associated with a phase gradient along the spinal cord of a lamprey. (Gray bars indicate active phase of a given neuron at different spatial locations or segments along the spinal cord.) (**b**) Half-center oscillator consisting of a pair of neurons that have reciprocal inhibition and fire in antiphase

5.2.2 Traveling Phase Waves on a Chain

The idea that a network of synaptically coupled spiking neurons can be reduced to a corresponding network of coupled phase oscillators is the starting point for considering a different type of wave than previous chapters, which can arise when the network is endowed with spatial structure. That is, suppose that the oscillators are arranged on a regular 1D lattice with sites labeled $n = 1, \ldots N$, and assume that the synaptic weight w_{nm} of the connection from lattice site m to lattice site n depends on the spatial separation of the two sites, $w_{nm} = w(n-m)$. It is then possible for the lattice of oscillators to support a phase-locked solution in which there is an approximately constant phase gradient Γ along the bulk of the lattice. In other words $\theta_n(t) \approx \omega t + n\Delta\theta$. Such a solution is known as a *phase wave*. Considerable insight into the conditions under which spatial phase gradients occur have been obtained in studies of central pattern generators (CPGs) for swimming locomotion in invertebrates such as the leech and primitive vertebrates such as the lamprey [121, 273, 404, 443]; see Fig. 5.12. At the simplest level, this may be modeled in terms of a chain of N phase oscillators θ_n with nearest-neighbor synaptic coupling as shown in Fig. 5.13. Each oscillator represents the CPG of an individual segment of the spinal cord. In the case of the lamprey, each oscillatory unit is a so-called half-center oscillator; see Fig. 5.12b. A half-center oscillator consists of two neurons that are reciprocally coupled by (intrasegmental) inhibition and consequently oscillate in antiphase. The swimming movement is thus produced by alternating neural activity between the left and right side of the body that propagates along the body as a phase wave to produce a side-to-side undulating wave; see Fig. 5.12a. Note that the individual CPG neurons of a half-center oscillator need not be intrinsic oscillators, in which case reciprocal inhibition is required in order to generate the rhythm, for example, via post-inhibitory rebound. In the case of the lamprey, however, it

now appears that excitation from an external drive combined with membrane properties is sufficient for rhythm generation in an individual CPG neuron. In particular, the primary mechanism for terminating a burst is the activation of fast and slow Ca^{2+}-dependent K^+ channels [273, 443]. In the case of the leech, intrasegmental neurons on either side of the body axis fire synchronously, which is consistent with the fact that the undulatory motion during swimming is dorsoventral rather than side-to-side.

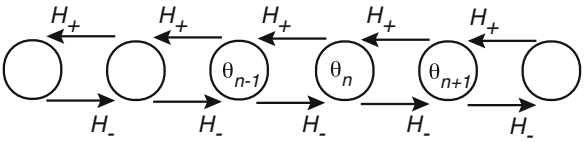

Fig. 5.13 A chain of N phase oscillators

During swimming, approximately one full body-length wave is maintained by period-independent intersegmental phase lags; see Fig. 5.12a. That is, there is a phase wave that propagates along the spinal cord such that the phase lag $\Delta\theta = \theta_{n+1} - \theta_n$ between adjacent segments is a fixed percentage of the cycle period. For example, a lamprey typically has 100 segments so that the phase lag is around 1 %. At least two symmetry-breaking mechanisms have been identified for maintaining a phase gradient along a chain of oscillators [171, 347, 443]:

(a) Asymmetry in the form of a gradient in intrinsic frequencies of the individual neurons, that is, $\omega_n = \omega_0 + n\omega_1$ where $\omega_{0,1}$ are constants, will induce a gradient in the relative phases of the coupled system. The resulting phase wave propagates opposite to the direction of the gradient, that is, from high to low frequencies. Such a frequency gradient has been found in the lamprey CPG for swimming, with frequency decreasing from the head (rostral end) to the tail (caudal end). On the other hand, the distribution of intrinsic frequencies appears to be "U-shaped" in the leech, with the highest frequencies occurring mid-body [443]. Interestingly, a spatial gradient of frequencies has also been observed experimentally in slices of molluscan olfactory lobe, with the wave propagating from high to low frequencies as predicted by theory [167]; see Sect. 7.5.

(b) Asymmetry between the ascending and descending synaptic interactions so that $H_+ \neq H_-$. In this case, a constant phase lag can be obtained in the bulk of the chain provided that $H_+(\theta)$ or $H_-(\theta)$ vanishes at a nonzero value of θ, which is known as the edge condition [171, 347]; see below. Asymmetric coupling has been found in both the leech and the lamprey. In the latter case, the descending interactions have stronger functional coupling than ascending connections, whereas in the leech, the coupling strength is symmetric while the specific pattern of connections is asymmetric. More specifically, leech CPG neurons within a hemi-segment (segment on one side of the body) are active at three different phases separated by 120°, and there are asymmetries between ascending and descending fibers associated with a given phase group.

We will illustrate the above two mechanisms using a simple model of a chain with $H_{\pm}(\theta) = W_{\pm}H(\theta)$. Such a network is described by the following system of coupled phase equations:

$$\begin{aligned}
\dot{\theta}_1 &= \omega_1 + W_+ H(\theta_2 - \theta_1) \\
\dot{\theta}_n &= \omega_n + W_+ H(\theta_{n+1} - \theta_n) + W_- H(\theta_{n-1} - \theta_n), \quad n = 2, \ldots, N-1 \\
\dot{\theta}_N &= \omega_N + W_- H(\theta_{N-1} - \theta_N).
\end{aligned} \tag{5.25}$$

Introducing the intersegmental phase differences $\psi_n = \theta_{n+1} - \theta_n$ leads to the $N-1$-dimensional system of equations

$$\dot{\psi}_n = \Delta\omega_n + W_+[H(\psi_{n+1}) - H(\psi_n)] + W_-[H(-\psi_n) - H(-\psi_{n-1})], \quad n = 1, \ldots, N-1 \tag{5.26}$$

with boundary conditions

$$H(-\psi_0) = 0 = H(\psi_N) \tag{5.27}$$

and $\Delta\omega_n = \omega_{n+1} - \omega_n$. Suppose that there is a gradient of frequencies along the chain, that is, $\Delta\omega_n$ has the same sign for all n. Also take an isotropic, odd interaction function, $W_{\pm} = 1$ and $H(\psi) = -H(-\psi)$. Then

$$\dot{\psi}_n = \Delta\omega_n + H(\psi_{m+1}) + H(\psi_{n-1}) - 2H(\psi_n), \quad n = 1, \ldots, N-1. \tag{5.28}$$

The phase-locked solutions $\Psi = (\psi_1, \ldots, \psi_{N-1})$ then satisfy the matrix equation

$$\mathbf{H}(\Psi) = -\mathbf{A}^{-1}\mathbf{D}, \tag{5.29}$$

where $\mathbf{H}(\Psi) = (H(\psi_1), \ldots, H(\psi_{N-1}))^T$, $\mathbf{D} = (\Delta\omega_1, \ldots \Delta\omega_{N-1})$ and $\mathbf{A}$ is a tridiagonal matrix with elements $A_{nn} = -2, A_{n,n+1} = 1 = A_{n+1,n}$. Suppose, for concreteness, that $H(\psi) = \sin\psi$. Then a solution Θ will exist only if every component of $\mathbf{A}^{-1}\mathbf{D}$ lies between ± 1. Let $a_0 = \max\{|\mathbf{A}^{-1}\mathbf{D}_i|\}$. If $a_0 < 1$, then for each $n = 1, \ldots, N-1$ there are two distinct solutions $\psi_n^{\pm}$ in the interval $[0, 2\pi)$ with $H'(\psi_n^-) > 0$ and $H'(\psi_n^+) < 0$. In other words, there are 2^N phase-locked solutions. Linearizing about each phase-locked solution and exploiting the structure of the matrix $\mathbf{A}$, it can be proven that only the solution $\Psi^- = (\psi_1^-, \ldots \psi_{N-1}^-)$ is stable [171]. Assuming that the frequency gradient is monotonic, this solution corresponds to a stable traveling wave. When the frequency gradient becomes too steep to allow phase-locking, that is, $a_0 > 1$, two or more pools of oscillators (frequency plateaus) tend to form and oscillate at different frequencies. Waves produced by a frequency gradient do not have a constant speed or, equivalently, constant phase lags along the chain.

Constant speed waves can be generated from (5.26) by considering phase-locked solutions defined by $\psi_n = \psi$ for all n with a collective period of oscillation determined using $\dot{\psi}_n = \Omega$ such that

$$\Omega = \omega_1 + W_+ H(\psi). \tag{5.30}$$

The steady-state solutions are then

$$\begin{aligned} \Delta\omega_1 + W_- H(-\psi) &= 0 \\ \Delta\omega_n &= 0, \quad n = 2,\ldots,N-2 \\ \Delta\omega_{N-1} - W_+ H(\psi) &= 0. \end{aligned} \tag{5.31}$$

This implies that all internal oscillators ($i = 2,\ldots,N-2$) have the same intrinsic frequency. If we further assume that $\Delta w_1 = 0 = \Delta\omega_{N-1}$, then a constant speed wave will exist provided that, (i) the interactions are unidirectional with $W_- = 0$ and (ii) H satisfies the edge Property $H(\psi) = 0$ for some $\psi \neq 0$. For example, if $H(\psi) = \sin(\psi + \sigma)$ for a fixed phase shift σ, then the steady-state phase solution is $\psi = -\sigma$. It also follows that although the speed of the wave can change by changing the intrinsic frequency ω_1, the phase lag ψ remains the same. This is consistent with the swimming motion of invertebrates. Finally, note that if coupling is in both directions, as in the lamprey CPG, one finds that for sufficiently long chains and $H^+ \neq H^-$, the system typically behaves like the unidirectional case except that there is a small *boundary layer* close to one end [347].

Although the mathematical analysis of phase waves along a chain of oscillators with nearest-neighbor coupling has provided important insights into CPGs and swimming locomotion, there are still a number of outstanding issues. One of the most important is understanding how the phase lags maintain a one body-length wave irrespective of the cycle period. Is this somehow built into the phase interaction function or the distribution of intrinsic frequencies, or does sensory feedback play an important role? For example, it is known that leeches and lampreys can sense their own body movements via proprioceptors and can adjust their cycle period and phase lags accordingly. Moreover, their swimming behavior is strongly affected by changes in their fluid environment, consistent with the idea that fluid resistance forces provided by water are also sensed by proprioceptors [443]. Yet another factor in determining phase lags is the range of synaptic interactions. The chain model assumed nearest-neighbor coupling, which is consistent with experimental observations that short-range coupling plays an important role in determining the phase. However, longer-range projections do also exist, which in lamprey can extend up to 20 segments.

5.2.3 Ring of Phase Oscillators and the Sync Basin

In the above example, a stable phase wave solution was generated through a combination of network heterogeneities (in natural frequencies or synaptic interactions) and boundary effects. An alternative network architecture that supports traveling phase waves is a ring of identical oscillators [166, 671]. However, in this case, one or more stable phase waves can coexist with a stable synchronous state. This then raises the interesting question as to the size of the basin of attraction of the synchronous state (the sync basin) or a particular phase wave as network parameters change. In other words, what is the set of initial conditions that induces a particular phase-locked state? From a dynamical systems perspective, finding such basins of

attraction is nontrivial. However, Wiley et al. [671] have made some progress by analyzing a ring of N identical phase oscillators, each of which is coupled to its k nearest neighbors on either side using a sinusoidal interaction function:

$$\dot{\theta}_i = \omega + \sum_{j=i-k}^{i+k} \sin(\theta_j - \theta_i), \quad i = 1,\ldots,N, \tag{5.32}$$

where $N \gg 1$ and the index i is taken to be periodic mod N. In the case $k = N/2$ (or its integer part), (5.32) reduces to the Kuramoto model of globally coupled oscillators [350]. It is straightforward to show that the system (5.32) always supports a stable synchronous state $\theta_i(t) = \omega t$ for all $i = 1,\ldots,N$. Moreover, numerically it is found that the synchronous state is a global attractor for sufficiently long-range coupling, that is, for $k > k_c \approx 0.34N$ [671]. However, as k decreases below k_c, other competing attractors emerge, which take the form of traveling phase waves (also known as splay states or uniformly twisted waves):

$$\theta_j = \omega t + \frac{2\pi q j}{N} + C, \quad j = 1,\ldots,N. \tag{5.33}$$

Here C is a constant and the integer q is a winding number that specifies the number of complete rotations or twists in phase that occur as the ring is traversed once. We summarize the analysis of (5.32) carried out by Wiley et al. [671].

Moving to a rotating frame by setting $\theta_i = \phi_i - \omega t$ and allowing for a nonuniform coupling $W(i-j)$ between oscillators i and j that depends on the distance $|i-j|$ gives

$$\dot{\phi}_i = \sum_{j=i-k}^{i+k} W(i-j)\sin(\phi_j - \phi_i), \quad i = 1,\ldots,N. \tag{5.34}$$

It is assumed that $W(s)$ is a positive, even, monotonically decreasing function of $|s|$. Equation (5.34) is an example of a gradient system, since it can be rewritten in the form

$$\dot{\phi}_i = -\frac{\partial V}{\partial \phi_i}, \quad V = -\frac{1}{2}\sum_{i,j=1}^{N} W(i-j)\cos(\phi_j - \phi_i), \tag{5.35}$$

where V is a potential function. It follows that all trajectories of (5.34) flow monotonically downhill on the resulting potential surface $V(\phi_1,\ldots,\phi_N)$, and asymptotically approaches fixed points. In other words the only attractors of the system are phase-locked states. Since N is assumed to be large, it is convenient to consider a spatially continuous version of (5.34), which takes the form (see also Sect. 5.4.1)

$$\frac{\partial \phi}{\partial t} = \int_{-\pi}^{\pi} w(x-y)\sin[\phi(y,t) - \phi(x,t)]dy. \tag{5.36}$$

This can be derived by setting $\Delta = \pi/N$, $x = (i - N/2)\Delta$, $\phi_i = \phi(x)$, $W(i-j) = w(x-y)\Delta$ and taking the limit $N \to \infty$. For convenience, w is normalized to unity. It is simple to show that $\phi(x,t) = qx$, integer q, is a phase-locked solution of (5.36)

by direct substitution:

$$0 = \int_{-\pi}^{\pi} w(x-y)\sin[q(x-y)]dy,$$

which holds since w is an even function while sine is an odd function. The ring topology requires that q is an integer, with $q = 0$ corresponding to a synchronous state and $q \neq 0$ to a phase wave with winding number q.

The linear stability of a phase-locked state is determined by setting $\phi(x,t) = qx + \eta(x,t)$ and keeping only linear terms in η:

$$\frac{\partial \eta}{\partial t} = \int_{-\pi}^{\pi} w(x-y)\cos[q(x-y)][\eta(y,t) - \eta(x,t)]dy. \tag{5.37}$$

The corresponding eigenvalue equation is obtained by setting $\eta(x,t) = e^{\lambda t}e^{imx}$ for integer m:

$$\lambda = \lambda(m,q) = \frac{\hat{w}(q+m) + \hat{w}(q-m) - 2\hat{w}(q)}{2}, \tag{5.38}$$

where $\hat{w}$ is the Fourier transform of the weight distribution:

$$\hat{w}(q) = \int_{-\pi}^{\pi} w(y)e^{iqy}dy. \tag{5.39}$$

From the properties of w, all eigenvalues are real and $\lambda(-m,q) = \lambda(m,q)$ so that the condition for stability of the q-phase wave is

$$\hat{w}(q+m) + \hat{w}(q-m) - 2\hat{w}(q) < 0 \tag{5.40}$$

for all $m = 1,2,\ldots$. Note that the existence of a zero eigenvalue ($\lambda(0,q) = 0$) reflects the fact the system is time-translation invariant, that is, it corresponds to a perturbation consisting of a uniform shift of all phases. In general, it is difficult to establish that (5.40) holds for all positive integers m even when q is fixed. However, for a particular choice of w, which yields the continuum version of (5.32), the countably infinite set of stability conditions reduces to a single condition [671].That is, consider the weight distribution

$$w(x) = \begin{cases} (2\pi r)^{-1}, & |x| \leq \pi r \\ 0, & |x| > \pi r \end{cases} \tag{5.41}$$

for $0 < r < 1$, which means that each oscillator is coupled to all oscillators within a fraction r of the ring with coupling strength $1/(2\pi r)$. The Fourier transform of w is

$$\tilde{w}(q) = f(\pi qr) \equiv \frac{\sin(\pi qr)}{\pi qr}, \tag{5.42}$$

so that (5.40) becomes

$$S_Q(M) \equiv \frac{1}{2}[f(Q+M)+f(Q-M)]-f(Q)<0, \quad M=r,2r,\ldots, \tag{5.43}$$

where $Q=qr, M=mr$. Treating M as a continuous, real variable and plotting the function $S_Q(M)$ for various Q, one finds that $S_Q(M)$ is negative for all $M>0$ when Q is sufficiently small, which ensures that the corresponding phase waves are stable. At a critical value $Q=\mu$, ${S_Q}''(0)$ changes sign from negative to positive; ${S_Q}''(0)=f''(Q)$ so μ is the smallest positive root of $f''(Q)$ and can be obtained by solving the transcendental equation

$$\tan(\pi\mu)=\frac{2\pi\mu}{2-(\pi\mu)^2},$$

which yields $\mu\approx 0.66$. Since $S_Q(0)=0$, it follows that the continuous function $S_Q(M)$ becomes positive in a neighborhood of $M=0$ when $Q>\mu$, and one can no longer guarantee stability.

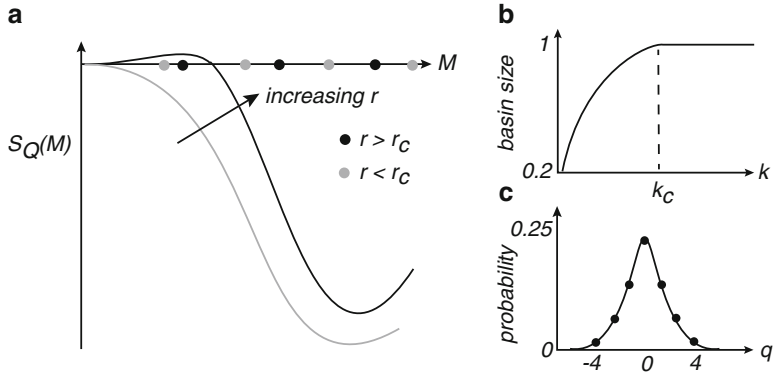

Fig. 5.14 Phase-locked states on a ring of N identical phase oscillators. (**a**) Graphical construction to determine the necessary condition for the stability of a q-phase wave with q fixed. A sketch of the function $S_Q(M)$, $Q=qr$, is shown for $r<r_c$ or $Q<\mu$ (*gray curve*) and $r>r_c$ or $Q>Q_c$ (*black curve*). The points $M=nr$, integer n are also shown for $r<r_c$ (*gray dots*) and $r>r_c$ (*black dots*). (**b**) Variation of the size of the sync basin as a function of k for large N. One way to numerically estimate the basin size is to consider the fraction Γ of uniformly random initial conditions that converge to the synchronous state. For $k>k_c$, the synchronous state becomes a global attractor with $\Gamma=1$. (**c**) For $k=1$, the probability that a uniformly random condition converges to a q-phase wave can be fitted by a Gaussian function of q

The above analysis provides a sufficient condition for stability of a q-phase wave assuming a given range of coupling r [671]: the q-phase wave is stable if $|q|r<\mu$. The stability condition is not necessary, however, because one has to take into account the fact that M is actually discrete. That is, it is possible that the discrete points $M=r,2r,\ldots$, lie outside the interval where $S_Q(M)$ is positive when $Q>\mu$. A simple graphical argument then establishes that for fixed q, increasing r from near zero means that Q crosses μ from below, resulting in an increasing interval over

which $S_Q(M)$ is positive. Even though the points $M = r, 2r, \ldots$, are also moving away from the origin as r increases, the expanding interval eventually encloses the point $M = r$ at a critical value r_c with $Q_c = qr_c(q) > \mu$; see Fig. 5.14a. This argument also establishes that the first eigenmode to become unstable is $M = r$. In summary, given $r > 0$, the q-phase wave is stable if and only if [671]

$$\frac{1}{2}[f(qr+r) + f(qr-r)] < f(qr). \tag{5.44}$$

For a given choice of q, the critical range of coupling $r_c(q)$ where the q-phase wave becomes unstable is the solution to the equation

$$\frac{1}{2}[f(qr_c + r_c) + f(qr_c - r_c)] = f(qr_c). \tag{5.45}$$

Numerically evaluating $r_c(q)$, one finds that $r_c(q)$ is a decreasing function of q. In particular, $r_c(1) \approx 0.68$, which means that all phase waves are unstable for $r > r_c(1)$. In terms of the original discrete network (5.32) with $r = 2k/N$, this means that the synchronous solution is globally stable when $k > k_c(N) \approx 0.34N$; see Fig. 5.14b. (To be more careful, it has not been established that there are no other phase-locked states other than synchrony and phase waves. However, numerical simulations suggest that any additional states are unstable [671].) Finally, one can estimate the relative size of the basin of attraction of a phase-locked state by determining the fraction of uniformly random initial conditions that converge to that particular state; see Fig. 5.14b, c.

Clearly the idealized ring model considered by Wiley et al. [671] is not biologically realistic. However, it provides a useful framework for exploring an issue that has been neglected in almost all studies of oscillations and waves in neural networks. That is, in addition to determining existence and stability, it is also important to consider the types of initial conditions that generate such solutions, particularly when trying to relate models to experiments in which oscillations and waves are initiated by specific environmental conditions or external stimuli such as locally injected currents.

5.2.4 Two-Dimensional Network of Phase Oscillators

Traveling phase waves have recently garnered attention beyond the context of central pattern generators. In particular, Ermentrout and Kleinfeld [170] have argued that the theory of phase waves in spatially structured networks provides a basis for understanding traveling electrical waves that have been observed across a variety of sensory cortices [149, 292, 357, 683, 684]; see Fig. 5.4. The waves are often expressed during periods of rest, whereas synchronous activity tends to dominate during the presentation of a strong stimulus. On the other hand, it has been suggested that in motor cortex it is phase waves that encode motor actions, whereas

synchrony represents an idling state [269]. In contrast to CPGs, the cortex is effectively a two-dimensional oscillatory medium (assuming activity through the cortical layers can be lumped together). There have been relatively few studies of coupled phase oscillators in discrete or continuum two-dimensional arrays [173, 495]. Here we follow Heitmann et al. [269] and consider a two-dimensional sheet of identical, locally coupled Kuramoto oscillators:

$$\frac{\partial \theta}{\partial t} = \Omega + \int_{\mathbb{R}^2} w(|\mathbf{r}-\mathbf{r}'|)\sin[\theta(\mathbf{r}',t)-\theta(\mathbf{r},t)]d\mathbf{r}'. \tag{5.46}$$

For simplicity, the weight kernel is assumed to be isotropic and the domain is taken to be unbounded. Following the analysis of the ring network in Sect. 5.2.3, one expects planar phase wave solutions of the form $\theta(\mathbf{r},t) = \Omega t + \mathbf{k}\cdot\mathbf{r}$. This can be verified by substituting such a solution into (5.46) and using polar coordinates $\mathbf{r} = r(\cos\phi, \sin\phi), \mathbf{k} = k(\cos\phi_k, \sin\phi_k)$ together with the Jacobi–Anger expansion of Bessel functions

$$e^{iz\cos\phi} = \sum_{n=-\infty}^{\infty} i^n J_n(z) e^{in\phi}. \tag{5.47}$$

Thus

$$\begin{aligned} 0 &= \int_{\mathbb{R}^2} w(|\mathbf{r}-\mathbf{r}'|)\sin[\mathbf{k}\cdot(\mathbf{r}'-\mathbf{r})]d\mathbf{r}' \\ &= \mathrm{Im}\int_0^\infty rw(r)\left[\int_0^{2\pi} e^{ikr\cos(\phi-\phi_k)}d\phi\right]dr \\ &= \mathrm{Im}\int_0^\infty rw(r)J_0(kr), \end{aligned}$$

which holds since the right-hand side integral is real.

Since the domain is unbounded we expect the spectrum of the linear operator obtained by linearizing about the phase wave solution to be continuous. That is, writing $\theta(\mathbf{r},t) = \Omega t + \mathbf{k}\cdot\mathbf{r} + \psi(\mathbf{r},t)$ and Taylor expanding (5.46) to first in order in ψ yields the linear equation

$$\frac{\partial \psi}{\partial t} = \int_{\mathbb{R}^2} w(|\mathbf{r}-\mathbf{r}'|)\cos[\mathbf{k}\cdot(\mathbf{r}'-\mathbf{r})](\psi(\mathbf{r}',t)-\psi(\mathbf{r},t))d\mathbf{r}'. \tag{5.48}$$

This has solutions of the form

$$\psi(\mathbf{r},t) = e^{\lambda t}e^{i\mathbf{q}\cdot\mathbf{r}}, \tag{5.49}$$

with $\mathbf{q} = q(\cos\phi_q, \sin\phi_q)$ and λ satisfying

$$\lambda = \int_{\mathbb{R}^2} w(|\mathbf{r}-\mathbf{r}'|)\cos[\mathbf{k}\cdot(\mathbf{r}'-\mathbf{r})]\left(e^{i\mathbf{q}\cdot(\mathbf{r}'-\mathbf{r})}-1\right)d\mathbf{r}'. \tag{5.50}$$

Again using polar coordinates and the Jacobi–Anger expansion, we a obtain a dispersion relation for the continuous spectrum

$$\begin{aligned}\lambda(\mathbf{q}) &= \frac{1}{2}\int_0^\infty rw(r)\int_0^{2\pi}\left[\sum_{n=-\infty}^{\infty}\left(i^n J_n(kr)\mathrm{e}^{in(\phi-\phi_k)}+\text{c.c.}\right)\right]\\ &\quad\times\left[\sum_{m=-\infty}^{\infty} i^m J_m(qr)\mathrm{e}^{im(\phi-\phi_q)}-1\right]d\phi dr\\ &= \frac{1}{2}\int_0^\infty rw(r)\sum_{n=-\infty}^{\infty}\left[J_n(kr)J_{-n}(qr)\mathrm{e}^{in(\phi_q-\phi_k)}+J_n(kr)J_n(qr)\mathrm{e}^{-in(\phi_q-\phi_k)}\right]dr\\ &\quad-\int_0^\infty rw(r)J_0(kr).\end{aligned}$$

Using the identity $J_{-n}(z)=(-1)^n J_n(z)$ then gives

$$\lambda(\mathbf{q})=\int_0^\infty rw(r)\left[\sum_{n=1}^{\infty}(1+(-1)^n)J_n(kr)J_n(qr)\cos(n\Delta\phi)+J_0(kr)(J_0(qr)-1)\right]dr, \tag{5.51}$$

where $\Delta\phi=\phi_q-\phi_k$. It immediately follows that $\lambda(\mathbf{q})$ is real for all $\mathbf{q}$, the spectrum is independent of the direction of $\mathbf{k}$ (reflecting isotropy of the system), and $\lambda(0)=0$ (reflecting time-translation symmetry). The phase wave of wave number k is then stable (modulo uniform phase shifts) if $\lambda(\mathbf{q})<0$ for all $q>0$ and $\Delta\phi\in[0,2\pi]$. Note that it is not sufficient to analyze stability by considering a reduced 1D ring network as was assumed by Heitmann et al. [269], even if one were to consider a bounded 2D domain.

In the case of the synchronous solution $k=0$, (5.51) reduces to

$$\lambda(q)=\int_0^\infty rw(r)(J_0(qr)-1)dr, \tag{5.52}$$

since $J_n(0)=\delta_{n,0}$. Given that $J_0(z)\le 1$ for all z, it follows that $\lambda(q)<0$ for all $q>0$ when the coupling is purely excitatory, that is, $w(r)\ge 0$ for all r. Hence the synchronous state of a 2D network of Kuramoto phase oscillators with excitatory coupling is stable. Heitmann et al. used numerical simulations to explore pattern forming instabilities in the case of center-surround coupling for which (see Fig. 5.15a)

$$w(r)=\mathrm{e}^{-br^2}+4h\mathrm{e}^{-br^2}\left(\frac{1}{3}b^2r^4-br^2\right). \tag{5.53}$$

They found that when $h=0$ (no surround inhibition), the synchronous state is stable, but increasing h destabilizes the synchronous state resulting in regular or irregular phase waves. Performing a numerical continuation of stable solutions as h varied, Heitmann et al. [269] also observed hysteresis in the level of phase coherence R as a function of h, with the latter order parameter defined according to [350]

$$R(t)e^{i\psi(t)} = \int_{\mathbb{R}^2} e^{i\theta(\mathbf{r},t)} d\mathbf{r}. \tag{5.54}$$

A sketch of a numerically determined hysteresis curve is shown in Fig. 5.15b. Synchronous states are identified by high phase coherence ($R \approx 1$), while phase waves are identified by low phase coherence ($R \approx 0$). We summarize the main findings of Heitmann et al. [269]. Starting at low levels of inhibition (small h), the system is in a synchronous state (upper branch of Fig. 5.15b), which then develops small amplitude spatial modulations or ripple patterns as h increases, with intermediate phase coherence, until the ripples destabilize and collapse to a full wave solution (lower branch of Fig. 5.15b). The transition from the lower to upper branch occurs at a smaller value of h then the opposite transition, that is, there is hysteresis. It immediately follows that there exists a range of h values over which there is bistability between the synchronous state and phase waves. Moreover, in the bistable regime, it is found numerically that phase waves tend to develop spatial heterogeneities, which can destabilize the phase waves at lower values of h than regular planar waves.

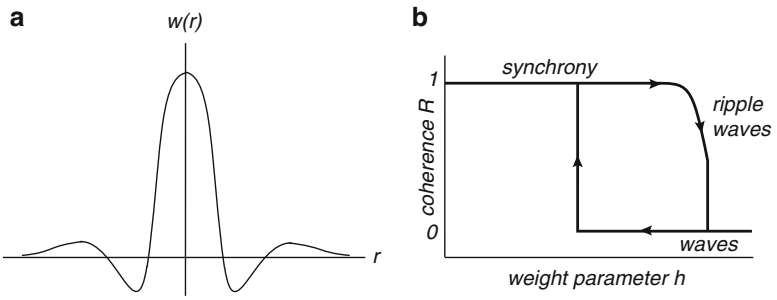

Fig. 5.15 (**a**) Radially symmetric center-surround weight kernel $w(r)$. (**b**) Sketch of hysteresis curve for phase coherence R as a function of weight parameter h, indicating transitions between the synchronous state ($R \approx 1$) and phase waves ($R \approx 0$)

Under the hypothesis that synchrony represents an idling state, whereas a phase wave somehow encodes a voluntary movement, there has to be some mechanism for switching between the two modes. Heitmann et al. [269] exploit the bistability of the model system by proposing that such a switch could be achieved in terms of a state-dependent perturbation that repels each oscillator from the global mean phase ψ (see (5.54)) according to

$$\Delta\theta(x) = k\sin(\theta(x) - \psi). \tag{5.55}$$

One possible physiological implementation of such a perturbation could be a temporary activation of a dense network of inhibitory neurons within the motor cortex by excitatory thalamocortical projections. Interestingly, it is known that voluntary movement is initiated in the cortex when these projections are disinhibited by the basal ganglia [6]. A partial validation of the model was achieved by comparing the output of the network under perturbation-driven transitions with movement-related

modulations of beta oscillations (20–25 Hz), which were obtained from magnetoencephalogram (MEG) recordings of human motor cortex during a repetitive finger-tapping task [54]. The network output was generated by band-pass filtering the real part of the order parameter (5.54). It would be interesting to understand some of these numerical results analytical, using the dispersion relation (5.51), for example, as well as investigating the effects of boundaries (where the spectrum becomes discrete), network heterogeneities such as spatial variations in the natural frequencies of the oscillators, and anistropic weight distributions. As might be expected, the latter tends to select planar waves in particular directions [269]. It would also be interesting to further explore the similarities and differences between phase waves in sensory and motor cortices.

5.3 Synaptically Coupled Integrate-and-Fire (IF) Oscillators

The *integrate-and-fire* (IF) model of a spiking neuron provides a caricature of the capacitative nature of the cell membrane at the expense of a detailed model of the spike generation process [323]. The basic circuit of the IF model consists of a capacitor C in parallel with a resistor R driven by a current $I_i(t)$, where i is a neuron label. The latter is decomposed as $I_i(t) = I_{\text{ext},i}(t) + u_i(t)$ where $I_{\text{ext},i}(t)$ is an external current and $u_i(t)$ is the synaptic current (5.3) generated by the arrival of spikes from other neurons. The voltage $v_i(t)$ of an IF neuron evolves according to the first-order equation

$$C\frac{dv_i}{dt} = -\frac{v_i(t)}{R} + I_i(t). \tag{5.56}$$

The form of the action potential is not described explicitly. Spikes are formal events characterized by the ordered sequence of firing times $\{T_i^m, m \in \mathbf{Z}\}$ determined by the threshold crossing conditions (5.2). However, immediately after firing, the potential is *reset* to a value $v_r < \kappa$,

$$\lim_{t \to [T_i^m]^+} v_i(t) = v_r. \tag{5.57}$$

For simplicity, we set $\kappa = 1$, $v_r = 0$ and $C = R = 1$. We also take $I_{\text{ext},i}(t) = I_0$, where I_0 is a constant background input. A network of synaptically coupled IF neurons is then given by (5.56), (5.2), and (5.3) together with the reset condition (5.57). Taking the synaptic kernel $\Phi_{ij}(t) = w_{ij}\Phi(t)$, $u_i(t)$ satisfies the equation

$$\frac{\mathrm{d}u_i}{\mathrm{d}t} = -u_i + I_0 + \varepsilon \sum_{j=1}^{M} w_{ij} \sum_{m \in \mathbf{Z}} \Phi(t - T_j^m), \tag{5.58}$$

for $T_i^n < t < T_i^{n+1}$. Two network operating regimes can be distinguished according to the value of the background input relative to the threshold $\kappa = 1$. If $I_0 > 1$, then

the network is in an oscillatory regime, since each IF neuron acts as an intrinsic oscillator when $\varepsilon = 0$. On the other hand, if $I_0 < 1$, then the network is in an excitable regime, since synaptic inputs are necessary in order to push a neuron over the threshold. We will consider excitable IF networks in Sect. 5.4

Suppose that $I_0 > 1$. For sufficiently weak coupling ε, the oscillatory IF network can be reduced to a coupled phase model following Sect. 5.2. All that is required is to determine the PRC of a single IF neuron. Therefore, set $I_i(t) = I_0 + \varepsilon I(t)$ in (5.56) and perform the change of variables

$$\theta_i(t) \mod 1 = \frac{1}{\Delta_0}\int_0^{v(t)} \frac{dV}{I_0 - V} = \frac{1}{\Delta_0}\log\frac{I_0}{I_0 - v(t)}, \tag{5.59}$$

where $\Delta_0 = \log(I_0/[I_0 - 1])$ is the natural period of oscillation. [It is convenient to take $\theta \in [0,1)$ rather than $[0, 2\pi)$.] Differentiating both sides with respect to t shows that

$$\frac{d\theta}{dt} = \omega_0 + \varepsilon\frac{I(t)}{I_0 - v(t)} = \omega_0 + \varepsilon I(t)\frac{e^{\theta(t)\Delta_0}}{I_0\Delta_0}, \tag{5.60}$$

where $\omega_0 = 1/\Delta_0$. Thus the phase-resetting curve is the periodic function

$$Z(\theta) = \frac{e^{\theta\Delta_0}}{I_0\Delta_0}, \quad 0 \le \theta < 1. \tag{5.61}$$

The phase interaction function may now be calculated using (5.13), rewritten in the form

$$H(\psi) = \int_0^1 Z(\theta)P(\theta + \psi)d\theta. \tag{5.62}$$

Here $P(\theta) = \sum_m \Phi([\theta - m]\Delta_0)$ is a periodic function of θ that in the case of the alpha function (5.23) can be summed as a geometric series to give

$$P(\theta) = \frac{\alpha^2\Delta_0 e^{-\alpha\theta\Delta_0}}{1 - e^{-\alpha\Delta_0}}\left[\theta\Delta_0 + \Delta_0\frac{e^{-\alpha\Delta_0}}{(1 - e^{-\alpha\Delta_0})}\right], \quad 0 < \theta < 1. \tag{5.63}$$

Using the above phase interaction function, the α-dependence of phase-locked solutions in the case of a symmetric pair of excitatory or inhibitory IF neurons can be determined [651]. The results are summarized in Fig. 5.16a. For excitatory coupling ($\varepsilon > 0$) the synchronous state is unstable for all $0 < \alpha < \infty$. On the other hand, the antisynchronous solution is stable for $\alpha < \alpha_c$ but loses stability when $\alpha > \alpha_c$ with the creation of two stable, partially synchronized or asynchronous states. The emergence of these two additional states can be understood in terms of the behavior of the odd part of the interaction function $H^-(\psi)$ as shown in Fig. 5.16b. In the limit $\alpha \to \infty$ the two asynchronous states asymptotically approach the synchronous state so that the neurons are almost perfectly synchronized. This is consistent with the analysis of Mirollo and Strogatz [431] who proved rigorously that globally coupled IF oscillators almost always synchronize in the presence of instantaneous excita-

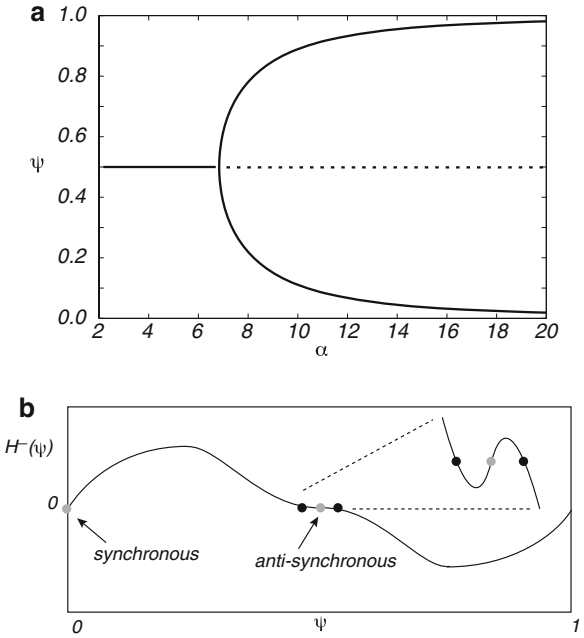

Fig. 5.16 (**a**) Relative phase $\psi = \psi_2 - \psi_1$ for a pair of IF oscillators with symmetric excitatory coupling as a function of α with $I_0 = 2$. In each case the antiphase state undergoes a bifurcation at a critical value of $\alpha = \alpha_c$ where it becomes unstable and two additional stable solutions ψ, $1 - \psi$ are created. The synchronous state remains unstable for all α. (**b**) Odd part of the phase interaction function for α just above the critical value α_c showing two new phase-locked solutions

tory interactions. The stability properties of all solutions are reversed in the case of inhibitory coupling ($\varepsilon < 0$) so that, in particular, the synchronous state is now stable for all α. Introduction of a discrete axonal delay τ_a produces a checkerboard pattern of alternating stable/unstable solution branches that can overlap to produce multistable solutions [133].

One of the useful features of the IF model (5.58) is that it is possible to derive phase-locking equations without the assumption of weak coupling [62, 73, 651]. This can be achieved by solving equation (5.58) directly under the ansatz that the firing times are of the form $T_j^n = (n - \psi_j)\Delta$ for some self-consistent period Δ and constant phases ψ_j. Integrating over the interval $t \in (-\Delta\psi_i, \Delta - \Delta\psi_i)$ and incorporating the reset condition leads to the result

$$1 = (1 - \mathrm{e}^{-\Delta})I_0 + \varepsilon \sum_{j=1}^{N} w_{ij} H(\psi_j - \psi_i), \tag{5.64}$$

with

$$H(\psi) = \mathrm{e}^{-\Delta} \int_0^{\Delta} dt\ \mathrm{e}^t \sum_{k \in \mathbf{Z}} \Phi(t + (k + \psi)\Delta). \tag{5.65}$$

Note that up to a positive constant factor, $H(\psi)$ reduces to the weak coupling phase interaction function of equation (5.62) for $\Delta \to \Delta_0$. It can be seen that (5.64) has an identical structure to that of (5.16). However, the former is exact whereas the latter is only strictly valid to $\mathcal{O}(\varepsilon)$, since it is derived under the assumption of weak coupling. Moreover, the collective period of oscillations Δ must be determined self-consistently in (5.64), since H depends on Δ rather than the natural period Δ_0. It is also possible to study the stability of phase-locked solutions directly in terms of the firing times [73, 215, 649]. In the case of slow synapses, one can carry out a perturbation analysis in terms of the small rate parameter α. One then finds that there are at least two distinct types of local instabilities: (i) instabilities that are independent of the strength of coupling $|\varepsilon|$, which also occur in the corresponding phase reduced mode; (ii) strong coupling instabilities that occur at some critical value of the coupling strength $|\varepsilon|$ [73]. (Note that there could be additional global instabilities arising from discontinuous bifurcations [138].)

Linear stability analysis of phase-locked states. For the sake of illustration, consider the linear stability of the synchronous solution $\psi_i = 0$ for all i. In order to ensure that such a solution exists, we impose the condition $\sum_j w_{ij} = \Gamma$. Defining perturbed firing times according to $T_i^n = n\Delta + \delta_i^n$, we integrate (5.58) from T_i^n to T_i^{n+1} using the reset condition. This leads to a mapping of the firing times that can be expanded to first order in the perturbations δ_i^n [73, 215, 649]:

$$\{I_0 - 1 + \varepsilon\Gamma P(0)\}\left[\delta_i^{n+1} - \delta_i^n\right] = \varepsilon \sum_{j=1}^{N} w_{ij} \sum_{m=-\infty}^{\infty} G_m(0)\left[\delta_j^{n-m} - \delta_i^n\right], \tag{5.66}$$

where $P(\phi) = \sum_m \Phi([\phi - m]\Delta)$ and

$$G_m(\phi) = \mathrm{e}^{-\Delta} \int_0^{\Delta} \mathrm{e}^t \Phi'(t + (m+\phi)\Delta)dt. \tag{5.67}$$

Note that in contrast to the weak coupling regime, P now depends on the collective period Δ rather than the natural period Δ_0 The resulting linear delay-difference equation (5.66) has solutions of the form $\delta_j^n = \mathrm{e}^{n\lambda}\delta_j$ with $0 \le \mathrm{Im}(\lambda) < 2\pi$. Taking $(\delta_1, \ldots \delta_N)$ to be an eigenvector of the weight matrix $\mathbf{w}$ with associated eigenvalue μ_p yields the characteristic equation

$$[I_0 - 1 + \varepsilon\Gamma P(0)]\,(\mathrm{e}^{\lambda} - 1) = \varepsilon[\tilde{G}(\lambda)\mu_p - \Gamma\tilde{G}(0)], \tag{5.68}$$

with

$$\tilde{G}(\lambda) = \sum_{m=-\infty}^{\infty} \mathrm{e}^{-m\lambda} G_m(0, \Delta). \tag{5.69}$$

One solution to (5.68) is $\lambda = 0$ with $\delta_i = \delta$ for all $i = 1, \ldots, N$. This reflects the invariance of the dynamics with respect to uniform phase shifts in the firing times, $T_i^n \to T_i^n + \delta$. Thus the condition for linear stability of a phase-locked state is that all remaining solutions λ of (5.68) have negative real part. This ensures that $\delta_j^n \to 0$ as $n \to \infty$ and, hence, that the synchronous solution is asymptotically stable. [Note that the above analysis does not take into account the possibility of instabilities arising from discontinuous bifurcations. These additional instabilities shift the stability boundaries calculated using linear theory [138].]

It is not possible to obtain exact solutions of (5.68). However, considerable insight into the nature of phase-locking instabilities can be obtained by taking $\Phi(t)$ to be the alpha function (5.23) and performing a perturbation expansion of equation (5.68) with respect to the inverse rise-time α, that is, by working in the regime of slow synapses. First, using the Fourier transform of $\Phi(t)$ gives

$$P(\theta) = \frac{\alpha^2}{\Delta} \sum_{m \in \mathbf{Z}} \frac{e^{i\omega_m \theta \Delta}}{(\alpha + i\omega_m)^2} = \frac{1}{\Delta} + \mathcal{O}(\alpha^2), \tag{5.70}$$

and

$$\tilde{G}(\lambda) = \frac{\alpha^2}{\Delta} e^{-\Delta} \sum_{m \in \mathbf{Z}} \frac{i\omega_m + \lambda/T}{(\alpha + i\omega_m + \lambda/\Delta)^2} \frac{1}{(1 + i\omega_m + \lambda/\Delta)} + \mathcal{O}(\alpha^3), \tag{5.71}$$

with $\omega_m = 2\pi m/\Delta$. Substitute these into the eigenvalue equation (5.68) and expand λ as a power series in α. Interestingly, one finds that there exist two distinct types of solution for λ, one of which is $\mathcal{O}(\alpha)$ and the other is $\mathcal{O}(\alpha^2)$. This is illustrated schematically in Fig. 5.17.

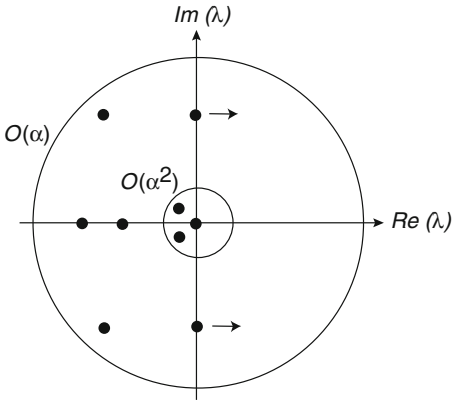

Fig. 5.17 Schematic diagram illustrating the spectrum of the linearized firing time map in the limit of slow synapses. There are N eigenvalues λ^{ω} of $\mathcal{O}(\alpha^2)$, one of which is a zero eigenvalue associated with phase-shift invariance, and $2N$ eigenvalues λ^{s} of $\mathcal{O}(\alpha)$. (The case $N = 3$ is shown.) Destabilization of the synchronous state can occur in the strong coupling regime due to a complex conjugate pair of $\mathcal{O}(\alpha)$ eigenvalues crossing the imaginary axis signaling the onset of a discrete Hopf bifurcation in the firing times

$\lambda = \mathcal{O}(\alpha^2)$ *and weak coupling instabilities*. Performing a perturbation expansion of equation (5.68) under the assumption $\lambda = \mathcal{O}(\alpha^2)$ yields the N eigenvalues

$$\lambda^{w}(\mu_p) \sim \varepsilon[\mu_p - \Gamma]\tilde{G}(0), \tag{5.72}$$

$p = 1, \ldots, N$. Hence, to the lowest order in α, a necessary condition for stability of the synchronous state at a given coupling strength ε is Re $\lambda^{w}(\mu_p) < 0$ for all $p = 1, \ldots, N-1$ (with $\mu_N = \Gamma$). In the weak coupling regime this stability condition is also sufficient, as can be shown by performing a perturbation expansion of equation (5.68) with respect to the coupling strength ε rather than α. Comparison of (5.67) and (5.69) with (5.65) shows that $\tilde{G}(0) \sim H'(0)$). It follows that the $\mathcal{O}(\alpha^2)$ stability condition is equivalent to the one based

on the Jacobian of the phase-averaged model, (5.17). That is, $\varepsilon H'(0)[\mathrm{Re}\,\mu_p - \Gamma] < 0$, $p = 1,\ldots,N-1$ (with $\mu_N = \Gamma$). Such a stability condition only depends on the sign of ε. We wish to determine whether or not this stability condition breaks down as $|\varepsilon|$ is increased (with the sign of ε fixed).

$\lambda = \mathcal{O}(\alpha)$ and strong coupling instabilities. Performing a perturbation expansion of equation (5.68) with $\lambda = \mathcal{O}(\alpha)$ gives the $2N$ eigenvalues

$$\lambda_{\pm}^{s}(\mu_p) = \left[-1 \pm \sqrt{\frac{\varepsilon \mu_p [1 - \mathrm{e}^{-\Delta}]}{(I_0 - 1 + \varepsilon\Gamma/\Delta)\Delta^2}} \right] \alpha\Delta, \tag{5.73}$$

$p = 1,\ldots,N$. In contrast to the previous case, these solutions are guaranteed to lie in the left-half complex plane when ε is sufficiently small so they do not play a role in weak coupling instabilities. However, as ε is increased from zero one or more eigenvalues may cross the imaginary axis from left to right in the complex λ-plane signaling the onset of a discrete Hopf bifurcation in the firing times and the breakdown of 1:1 frequency-locking. The corresponding Hopf frequency is of the form $\omega_H = \omega_1\alpha + \omega_2\alpha^2 + \mathcal{O}(\alpha^3)$ where $w_1 = \mathrm{Im}\lambda_c^s$ at the bifurcation point and ω_2 is determined by higher-order terms in the perturbation expansion. If $\omega_1 \neq 0$, then the instability induces a time periodic variation in the instantaneous firing rates of the neurons, whereas if $\omega_1 = 0$, then the firing rates remain constant but may differ between neurons.

It turns out that the strong coupling instabilities for slow synapses can be understood in terms of a corresponding rate model [73]. First, rewrite (5.58) as

$$\frac{\mathrm{d}v_i}{\mathrm{d}t} = -v_i + I_0 + u_i(t)$$

with

$$u_i(t) = \varepsilon \sum_j w_{ij} \int_0^\infty \Phi(\tau) a_j(t-\tau) d\tau, \quad a_j(t) = \sum_{m \in \mathbf{Z}} \delta(t - T_j^m).$$

If the synapses are sufficiently slow (small α) then $\Phi(t)$ is effectively performing a short-term temporal average over the incoming spike trains, and the synaptic current varies slowly in time. Thus, over time intervals of $\mathcal{O}(\alpha^{-1})$, we can treat the total input to each IF neuron as approximately constant, so that the neuron acts like a regular oscillator with instantaneous firing rate

$$F(u_i) = [\log(I_0 + u_i)/(I_0 + u_i - 1))]^{-1}. \tag{5.74}$$

Hence, under the approximation

$$\int_0^\infty \Phi(\tau) a_j(t-\tau) d\tau \approx \int_0^\infty \Phi(\tau) F(u_j(t-\tau)) d\tau,$$

we obtain the closed set of rate equations

$$u_i(t) = \varepsilon \sum_j w_{ij} \int_0^\infty \Phi(\tau) F(u_j(t-\tau) d\tau. \tag{5.75}$$

Finally, introducing the differential operator $\mathbb{L}$ for which $\mathbb{L}\Phi_i(t) = \delta(t)$, we obtain the second-order equation

$$\frac{1}{\alpha^2}\frac{d^2u_i(t)}{dt^2} + \frac{1}{\alpha}\frac{du_i(t)}{dt} + u_i(t) = \varepsilon\sum_j w_{ij}F(u_j(t)). \tag{5.76}$$

(A related derivation of a rate model based on population averaging will be considered in Sect. 6.1.) Under the condition $\sum_j w_{ij} = \Gamma$ for all i, there exists a homogeneous fixed point $u_i(t) = \bar{u}$ such that $\bar{u} = \varepsilon F(I_0 + \bar{u})\Gamma$. Linearizing (5.76) about the fixed point and substituting a solution of the form $u_i(t) = e^{\lambda t}\delta_i$, where δ is an eigenvector of the weight matrix $\mathbf{w}$, we obtain the set of eigenvalues

$$\frac{\lambda_\pm(\mu_p)}{\alpha} = -1 \pm \sqrt{\varepsilon F'(\bar{u})\mu_p}, \qquad p = 1,\ldots,N. \tag{5.77}$$

The fixed point will be asymptotically stable if and only if $\mathrm{Re}\,\lambda_\pm(\mu_p) < 0$ for all p. It is now straightforward to establish that the $\mathcal{O}(\alpha)$ eigenvalues associated with the linear stability of the synchronous state (see (5.73)) are equivalent to those obtained from the linear stability analysis of the homogeneous state in the firing rate model (5.77). For a direct comparison, take the firing rate to be the same in the two models by setting $F(I_0 + \bar{u}) = 1/\Delta$ so that $\varepsilon\Gamma/\Delta = \bar{u}$ and $1 - e^{-\Delta} = 1/(\bar{u} + I_0)$. Differentiating $F(I_0 + \bar{u})$ with respect to $\bar{u}$ then shows that $F(I_0 + \bar{u})^2/F'(I_0 + \bar{u}) = (\bar{u} + I_0)(\bar{u} + I_0 - 1)$ and the result follows.

The above analysis establishes that, in the limit of slow synapses, a strong coupling instability in the synchronous state of the spiking model is reflected by a corresponding instability in the homogeneous fixed point of the rate model. As $|\varepsilon|$ is increased from zero, a codimension one bifurcation of the rate model occurs in two distinct ways. If a single real eigenvalue crosses the origin in the complex λ-plane ($\omega_1 = 0$) then a static bifurcation can occur, leading to the emergence of additional fixed-point solutions with inhomogeneous firing rates. On the other hand, if a pair of complex conjugate eigenvalues crosses the imaginary axis from left to right in the complex plane ($\omega_1 \neq 0$), then a continuous Hopf bifurcation can occur, leading to the formation of periodic solutions, that is, time-dependent firing rates. This suggests that the spiking model undergoes a corresponding transition to a non-phase-locked state, consisting of spatiotemporal modulations of the interspike intervals that are well described by the firing-rate model, at least in the small α regime. Moreover, the fine temporal structure of these modulations, which are averaged out in the firing-rate model, should become significant with increasing α in the spiking model. This is indeed found to be the case [73].

In Fig. 5.18 we illustrate a strong coupling instability in an excitatory–inhibitory pair of IF neurons. It is straightforward to show that the rate-based version of this network exhibits periodic variations in the mean firing rates in the strong coupling regime. It can be established from (5.72) and (5.73) that the synchronous state of the IF network is stable for sufficiently weak coupling but destabilizes due to a Hopf bifurcation in the firing time map at a critical coupling $\varepsilon_c(\alpha)$. A direct numerical simulation of the system shows that beyond the bifurcation point, the neurons jumps

to a state in which they exhibit periodic bursting patterns. This can be understood in terms of mode-locking associated with periodic variations of the interspike intervals (ISIs) $\Delta_k^n = T_k^{n+1} - T_k^n$, $k = E, I$, on closed attracting orbits. Suppose that the kth oscillator has a periodic solution of length M_k so that $\Delta_k^{n+pM_k} = \Delta_k^n$ for all integers p. If $\Delta_k^1 \gg \Delta_k^n$ for all $n = 2, \ldots, M_k$, say, then the resulting spike train exhibits bursting with the interburst interval equal to Δ_k^1 and the number of spikes per burst equal to M_k. Although both oscillators have different interburst intervals ($\Delta_1^1 \neq \Delta_2^1$) and numbers of spikes per burst ($M_1 \neq M_2$), their spike trains have the same total period, that is, $\sum_{n=1}^{M_1} \Delta_1^n = \sum_{n=1}^{M_2} \Delta_2^n$. Due to the periodicity of the activity, the ISIs only fall on a number of discrete points on the orbit. The variation of the ISIs Δ_i^n with n is compared directly with the corresponding variation of the firing rates of the reduced model in Fig. 5.18b, which shows that the instantaneous firing rate captures the modulation in the ISIs.

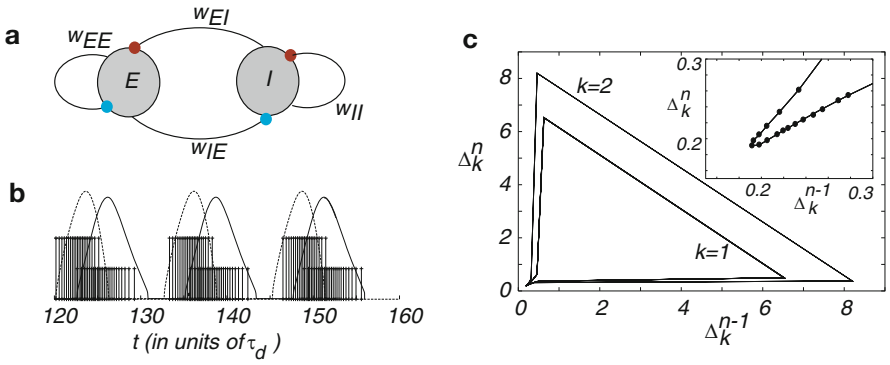

Fig. 5.18 Strong coupling instability in an excitatory–inhibitory pair of IF neurons. (**a**) Basic network. Synaptic weights are $w_{EE} = w_{II} = 0$, $w_{IE} = 1$ and $w_{EI} = -2$. The synaptic rate constant is $\alpha = 1$ and the coupling strength is $\varepsilon = 2$. (**b**) Spike train dynamics of the two neurons. For the sake of illustration the firing times of the two oscillators are represented with lines of different heights (marked with a +). *Smooth curves* represent variations in the firing rates of the corresponding rate model. (**c**) A plot of the interspike intervals (ISIs) $(\Delta_k^{n-1}, \Delta_k^n)$, $k = E, I$, of the spike trains shown in (**b**) showing how they lie on closed periodic orbits. *Points* on an orbit are connected by lines. Each triangular region is associated with only one of the neurons, highlighting the difference in interburst intervals. The inset is a blowup of orbit points for one of the neurons within a burst

5.4 Spiking Network Models of Cortical and Subcortical Waves

5.4.1 Traveling Pulses in an Excitatory Spiking Network

In the previous section we showed how oscillations and phase-locking in a synaptically coupled IF network can be analyzed in terms of an underlying firing time map. It turns out that the firing times can also be used to investigate solitary wave propagation in an excitable IF network, for which $I_0 < 1$ [62, 63, 167]. Consider a

network of IF neurons distributed along an infinite 1D lattice:

$$\frac{dv_j}{dt} = -v_j + I_0 + g\sum_{k\in\mathbf{Z}} W(j-k)\Phi(t-T_k), \tag{5.78}$$

with the threshold condition $v_j(T_j) = 1$ and the reset condition $\lim_{\varepsilon\to 0^+} v_j(T_j+\varepsilon) = 0$. For simplicity, we are assuming that each neuron fires only once during passage of a traveling pulse. (Numerical simulations indicate that wave propagation is not dramatically altered if each neuron fires multiple spikes [167].) We now define a traveling pulse solution as one for which there is a constant time lag between the firing of adjacent neurons, that is, $T_k = k\Delta$ (up to an arbitrary constant). (The same definition was used for intracellular Ca^{2+} waves in the fire–diffuse–fire model of Sect. 4.3.2.) Substituting into (5.78), gives

$$\frac{dv_j}{dt} = -v_j + I_0 + g\sum_{k\in\mathbf{Z}} W(j-k)\Phi(t-k\Delta). \tag{5.79}$$

Analytically speaking, it is convenient to consider a continuum version of the model. Therefore, introduce a lattice spacing d and set $v(x,t) = v_{x/d}(t)$, $w(x-y) = W([x-y]/d)$, $T(y) = T_{y/d}$. Moreover, rescale the coupling constant according to $g \to gd$. Taking the continuum limit $d \to 0$ and $\Delta \to 0$ such that the speed $d/\Delta = c$ is fixed, then $T(y) = y/c$ and we obtain the continuum IF equation

$$\frac{\partial v(x,t)}{\partial t} = I_0 - v(x,t) + g\int_{-\infty}^{\infty} w(x-y)\Phi(t-y/c)dy. \tag{5.80}$$

Equation (5.80) is supplemented by the reset condition $v(x,t^+) = 0$ whenever $v(x,t) = 1$. In the following, we set $I_0 = 0$, assume that g is a positive coupling parameter, and $W(x)$ is a positive, symmetric, monotonically decreasing function of $|x|$ with $\int_0^\infty W(x)dx < \infty$. Typical choices for such a weight function are

$$w(x) = \frac{1}{\sqrt{2\pi\sigma^2}}\mathrm{e}^{-x^2/2\sigma^2} \quad \text{(Gaussian)}, \qquad w(x) = \frac{1}{2\sigma}\mathrm{e}^{-|x|/\sigma} \quad \text{(exponential)}. \tag{5.81}$$

For concreteness, we choose the exponential function, although the basic results will not depend on the precise form of $w(x)$.

In order to determine the velocity c of a solitary pulse, multiply both sides of (5.80) by e^t and integrate over the interval $-\infty < t \le T(x) = x/c$ using the threshold condition $v(x,T(x)) = 1$. This generates a self-consistency condition for c of the form [62, 167]

$$\begin{aligned} 1 &= g\int_{-\infty}^{x/c} \mathrm{e}^t \left[\int_{-\infty}^{\infty} w(x-y)\Phi(t-y/c)dy\right]dt \\ &= g\int_0^{\infty} w(x)\mathrm{e}^{-x/c}\int_0^{x/c} \mathrm{e}^t\,\Phi(t)dtdx. \end{aligned} \tag{5.82}$$

The second line is obtained by noting that $\Phi(t-y/c)=0$ for $y>ct$, reversing the order of integration,

$$\int_{-\infty}^{x/c} dt \int_{-\infty}^{ct} dy \to \int_{-\infty}^{x} dy \int_{y/c}^{x/c} dy,$$

and performing a change of variables. In the case of an exponential weight function, the integration over x and t can be performed explicitly by Fourier expanding $\Phi(t)$ and using the analyticity properties of $\tilde{\Phi}(\omega)=\int_{-\infty}^{\infty} e^{-i\omega t}\Phi(t)dt$, namely, that $\tilde{\Phi}(\omega)$ is analytic in the lower-half complex ω-plane since $\Phi(t)=0$ for $t\le 0$. After performing a contour integral, we obtain the result

$$1=\frac{gc}{2(\sigma+c)}\tilde{\Phi}(-ic/\sigma). \tag{5.83}$$

Suppose that $\Phi(t)$ is given by the α function (5.23) together with a finite axonal propagation delay τ_a:

$$\Phi(t)=\alpha^2(t-\tau_a)e^{-\alpha(t-\tau_a)}H(t-\tau_a), \tag{5.84}$$

where H is the Heaviside function. Substitution into (5.83) leads to the following implicit equation for the propagation velocity of a solitary pulse:

$$1=\frac{g\alpha^2 c}{2(\sigma+c)}\frac{e^{-c\tau_a/\sigma}}{(\alpha+c/\sigma)^2}. \tag{5.85}$$

In the absence of axonal delays ($\tau_a=0$) and large c, the velocity scales according to a power law $c\sim\alpha\sigma\sqrt{g/2}$ [167]. This form of power law is consistent with the behavior observed in more detailed computational models [228]. The velocity c is plotted as a function of the coupling g in Fig. 5.19. It can be seen that for fixed α and τ_a there exists a critical coupling $g_s(\alpha,\tau_a)$ such that there are no traveling pulse solutions for $g<g_s$ and two solutions for $g>g_s$. Using linear stability analysis (see below), one finds that for the given parameter values, the lower (upper) solution branch is unstable (stable).

The (local) asymptotic stability of a solitary wave can be determined by considering perturbations of the firing times. For simplicity, we will only consider linear stability analysis based upon perturbations traveling at the same speed as the wave itself, that is, perturbations of the single neuron firing times $T(x)$. It is possible that there are further instabilities associated with global bifurcations where, for example, certain neurons fire more than once, fail to fire, or fire out of sequence. Suppose that $T(x)=x/c+\phi(x)$ with $\phi(x)=\phi_0(x)$ for $x\le 0$ and $\phi_0(x)$ a prescribed, bounded function on $(-\infty,0]$. Asymptotic stability then corresponds to the condition $\phi(x)\to 0$ as $x\to\infty$ for arbitrary nonuniform initial data $\phi_0(x)$. Integrating (5.80) over the interval $(-\infty,T(x)]$ gives

$$e^{x/c+\phi(x)}=g\int_{-\infty}^{x/c+\phi(x)} e^{t}\int_{-\infty}^{\infty} w(x-x')\Phi(t-x'/c-\phi(x'))dx'dt.$$

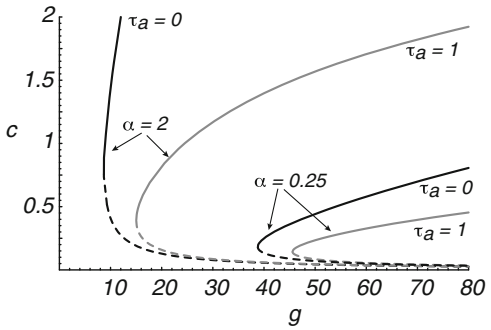

Fig. 5.19 Variation of the speed c of a traveling pulse as a function of the synaptic coupling g for different values of the inverse rise-time α and axonal delay τ_a. *Solid (dashed) lines* correspond to stable (unstable) branches. The external input is taken to be $I_0 = 0$ and the range of the exponential weight function is $\sigma = 1$

Expanding to first order in $\phi(x)$ and imposing (5.82) leads to the linear integral equation

$$\int_{-\infty}^{0} \mathrm{e}^{t} \left[\int_{-\infty}^{\infty} w(x-x') \Phi'(t + [x-x']/c) \left[\phi(x) - \phi(x') \right] dx' \right] dt = 0. \tag{5.86}$$

Substitution of a solution of the form $\phi(x) = \mathrm{e}^{\lambda x}$ then yields the characteristic equation (after reversing the order of integration and performing a change of variables)

$$\mathscr{H}(\lambda) \equiv \int_{0}^{\infty} \left[\mathrm{e}^{-\lambda x} - 1 \right] w(x) f(x/c) dx = 0, \tag{5.87}$$

with

$$f(\tau) = \int_{0}^{\tau} \mathrm{e}^{-(\tau - t)} \Phi'(t) dt. \tag{5.88}$$

Asymptotic stability then holds if all nonzero solutions λ have negative real part. Such solutions depend indirectly on the coupling g via the speed c, which satisfies (5.82). Equation (5.87) can be evaluated using Fourier analysis and, up to an irrelevant constant factor,

$$\mathscr{H}(\lambda) = P(c[\sigma^{-1} + \lambda]) - P(c/\sigma), \tag{5.89}$$

$$P(z) = \frac{z}{2(1+z)} \tilde{\Phi}(-iz). \tag{5.90}$$

Note that $P(z)$ is real when z is real, and $P(z) \to 0$ as $|z| \to \infty$. The stability of the fast and slow solution branches displayed in Fig 5.19. can be determined from the following theorem [62]:

Theorem 5.1. *Let $\mathscr{C}_+$ and $\mathscr{C}_-$ denote, respectively, the fast and slow solution branches $c = c_\pm(g)$, $g \geq g_s$, of the self-consistency condition (5.83) for the velocity of a solitary pulse, assuming a unimodal response function $\Phi(t)$. Here g_s is the critical coupling for the existence of a solitary wave. Denote the time to peak of $\Phi(t)$ by τ_{max}. The following stability results then hold: (i) The branch $\mathscr{C}_-$ is unstable for all τ_{max} and τ_a. (ii) The branch $\mathscr{C}_+$ is stable for all τ_{max} in the case of zero axonal delays, $\tau_a = 0$. (iii) In the case of large axonal delays and fast synapses (small τ_{max}), there exists a Hopf bifurcation point g_h such that $c_+(g)$ is stable (unstable) for $g > g_h$ ($g_s \leq g < g_h$).*

We sketch a proof. First, note that (5.83) can be written in the more compact form

$$1 = g(c)P(c/\sigma), \tag{5.91}$$

where the dependence on the coupling as a function of c has been made explicit. Now decompose $\lambda = a + ib$ and differentiate (5.89) with respect to a for $b = 0$:

$$\partial \mathscr{H}(a,0)/\partial a|_{a=0} = \sigma^{-1} P'(c/\sigma).$$

Similarly, differentiating (5.91) with respect to c shows that

$$0 = g'(c)P(c/\sigma) + g(c)P'(c/\sigma).$$

It follows that

$$\text{sign}\,[\partial \mathscr{H}(a,0)/\partial a|_{a=0}] = -\text{sign}[g'(c)].$$

Hence, $\partial H(a,0)/\partial a|_{a=0} > 0$ when $dg/dc < 0$, that is, when $c \in \mathscr{C}_-$. Since $\lim_{a\to\infty} \mathscr{H}(a,0) = -P(c) < 0$, it follows that $H(a,0)$ must cross the positive a-axis at least once when $c \in \mathscr{C}_-$. This implies that $H(a,0) = 0$ has at least one solution for $a > 0$ and, hence, that the branch $\mathscr{C}_-$ is unstable. Second, assuming that the delay kernel $\Phi(t)$ is unimodal with a maximum at τ_{max}, it follows from (5.88) that $f(\tau) > 0$ for $0 < \tau < \tau_{max}$. The real part of (5.89) can then be decomposed as

$$\text{Re}[\mathscr{H}(\lambda)] = \int_0^{c\tau_{\max}} \left[e^{-ax} - 1\right] w(x) f(x/c) dx + \int_{c\tau_{\max}}^{\infty} \left[e^{-\lambda x} - 1\right] w(x) f(x/c) dx.$$

with the first term on the right-hand side positive definite. Since $w(x)$ is a monotonically decreasing function of x, it follows that the second term becomes negligible when $c\tau_{max}$ is sufficiently large. In other words, $\mathscr{H}(\lambda) \neq 0$ and hence the upper branch $\mathscr{C}_+$ is stable in the large-c limit. It can also be established that $\mathscr{H}(a,0) = 0$ does not have any positive definite solutions when $c \in \mathscr{C}_+$ so that the upper branch is stable with respect to static bifurcations. The proof is completed by establishing conditions for the occurrence of a Hopf instability on the upper branch. This requires searching for solutions $a = 0, b \neq 0$ of (5.89).

It turns out that for the parameter values chosen in Fig. 5.19, the upper branch is stable. However, one finds that for larger values of the axonal delay τ_a, a continuous solitary pulse can become unstable as the axonal delay is increased. This is illustrated in Fig. 5.20, where the fast and slow solution branches are plotted as a function of τ_a. Interestingly, Golomb and Ermentrout [230] have demonstrated that in the regime where the continuous wave is unstable, lurching (pulsating) waves propagate with discontinuous, periodic spatiotemporal characteristics; see Fig 5.21. Space is now spontaneously divided into discrete spatial intervals of length Δx, and

$$T(x + \Delta x) = T(x) + \Delta t, \tag{5.92}$$

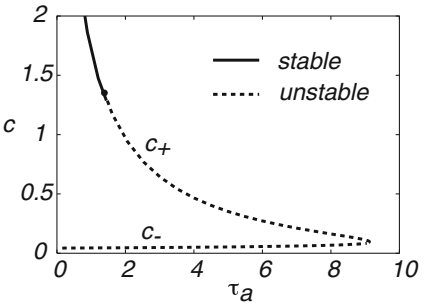

Fig. 5.20 Fast and slow velocity branches as a function of the axonal delay τ_a for fixed α and g. The stable slow branch undergoes a Hopf instability at a critical value of axonal delay

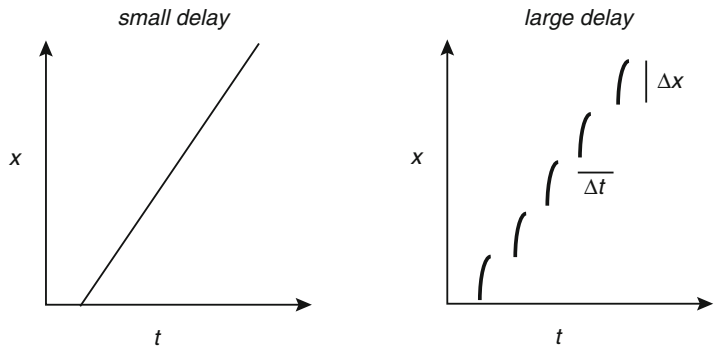

Fig. 5.21 Schematic illustration of the difference between continuous and lurching pulses in an excitatory IF network with delays. Each IF neuron only fires a single spike at a time as indicated by the *solid curves*

where Δt is the period of a lurching cycle. Hence, the average speed of the pulse is $c = \Delta x/\Delta t$. Suppose that the lurching wave starts at $x = 0$ and $T(0) = 0$. The firing time of the neuron at x is then

$$T(x) = n\Delta t + f(\hat{x}), \tag{5.93}$$

where n is the integer part of $T(x)/\Delta t$ and $\hat{x} = x - n\Delta x$. The function f specifies how the firing times vary within a single lurch, and is defined on the interval $[0.L)$ with $f(0) = 0$. One also finds that lurching waves can persist in regions where the continuous wave does not exist and, for certain choices of weight kernel $w(x)$ such as a step function, the two types of wave may coexist (bistability) [230]. It follows that $T(x) - x/c = f(\hat{x}) - \hat{x}/c$ is a Δx-periodic function of x. Interestingly, the possible correlation between the nature of wave propagation and the effective size of discrete delays is suggestive of the observed differences between the spread of activity in cortical and thalamic slices; see Sect. 5.4.3.

There have also been a number of studies of 2D spiking networks. For example, Kistler et al. analyzed solitary waves and periodic wave trains in an excitable network based on the so-called spike response model [337], which is essentially an integrated version of the IF model. However, there were a few important differences between their treatment and the analysis of IF networks reviewed above. First, they effectively took the activity of a solitary pulse propagating in the x-direction, say, to be $c^{-1}\Phi(t-x/c)$ rather than $\Phi(ct-x)$. The additional factor of c^{-1} results in only one solution branch for $c=c(g)$ rather than two as found in [62, 167]. It is not clear that there is any biophysical justification for this additional factor, given the interpretation of $\Phi(t)$ as a synaptic impulse response function; see Sect. 1.4. Second, their stability analysis was mainly based on studying changes in local field potentials, which is not sufficient to guarantee asymptotic stability with respect to more general perturbations of the firing times as considered above. In particular, it does not take into account the full spectrum of the linearized firing time map, which is crucial in establishing the occurrence of Hopf instabilities. The numerical results presented in [337] did, however, reveal a rich repertoire of geometrical waves such as spirals and target patterns. Spontaneous spiral waves have also been observed in a stochastic IF network [117]. Finally, the existence of stable traveling pulses in a synaptically coupled IF network has been linked to the empirical observation of traveling pulses in disinhibited brain slices and with epileptiform activity following brain trauma. However, as in the case of oscillatory IF networks, it is not clear what the appropriate level of modeling should be. That is, whether the fundamental physiological element of a synaptically coupled network, discrete or continuous, is a single neuron or a local population of neurons. We will consider the latter case in Chaps. 6 and 7.

5.4.2 *Traveling Pulses in Networks of Excitatory and Inhibitory Spiking Neurons*

It is also possible to extend the above analysis to a 1D network of excitatory (E) and inhibitory IF neurons, in which there are fast (AMPA) and slow (NMDA) excitatory synapses [229]; see Fig. 5.22. The generalization of the continuum model (5.80) takes the form

$$\frac{\partial v_\alpha(x,t)}{\partial t} = I_\alpha - v_\alpha(x,t) + \sum_{\gamma=f,s} g_{\alpha E}^{\gamma} \int_{-\infty}^{\infty} w_{\alpha E}(x-y)\Phi_{\alpha E}^{\gamma}(t-T_E(y))dy$$
$$-g_{\alpha I}\int_{-\infty}^{\infty} w_{\alpha I}(x-y)\Phi_{\alpha I}(t-T_I(y))dy \tag{5.94}$$

for $\alpha=E,I$. Here $v_\alpha(x,t)$ describes the time-dependent membrane potential of the α-type neuron at x, $w_{\alpha\beta}(x)$ represents the synaptic weight density from neurons of type β to neurons of type α, and the synaptic filters are taken to be exponentials

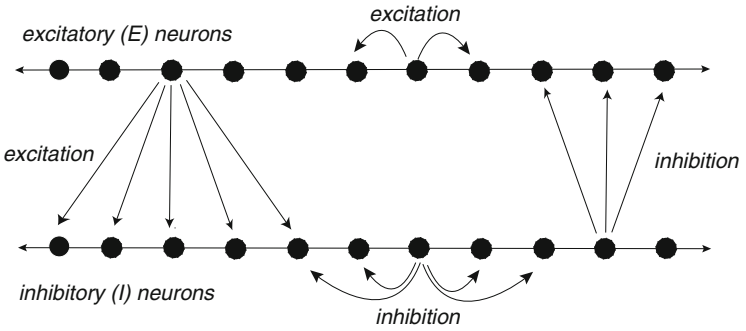

Fig. 5.22 Cortical network model consisting of a 1D layer of excitatory neurons reciprocally coupled to a 1D layer of inhibitory layers

$$\Phi_{\alpha\beta} = \frac{1}{\tau_{\alpha\beta}} \exp(-t/\tau_{\alpha\beta}) H(t). \tag{5.95}$$

The additional superscript γ for excitatory synapses specifies whether the excitatory synapse is fast ($\gamma = f$) or slow ($\gamma = s$). For concreteness, the synaptic weights are also taken to be exponentials,

$$w_{\alpha\beta} = \frac{1}{\sigma_{\alpha\beta}} \exp(-|x|/\sigma_{\alpha\beta}). \tag{5.96}$$

Again it is assumed that each neuron at x only fires once and the corresponding firing times are denoted by $T_\alpha(x)$ for $\alpha = E, I$. The spatial and temporal scales are fixed by taking $\sigma_{EE} = 1$ and the membrane time constants to be unity. Numerical simulations establish that there are two types of stable traveling pulses. One is a *fast pulse* that is similar to the continuous pulse found in the excitatory network—its speed increases as inhibition decreases. The other is a continuous *slow pulse* that is characterized by a much smaller velocity and by the fact that the inhibitory cells fire before their neighboring excitatory cells [229]. Moreover, in a narrow range of parameters, the two solutions coexist (bistability).

The analysis of existence and stability of traveling pulses proceeds along similar lines to the excitatory case [229], so we will only summarize the results. Integrating (5.94) with respect to t and imposing the threshold conditions $v_\alpha(T_\alpha) = \kappa_\alpha$ gives the pair of equations

$$\begin{aligned} \kappa_\alpha = &\sum_{\gamma=f,s} g^\gamma_{\alpha E} \int_{-\infty}^{\infty} w_{\alpha E}(x') G^\gamma_{\alpha E}[T_\alpha(x) - T_E(x-x')] dx' \\ &- g_{\alpha I} \int_{-\infty}^{\infty} w_{\alpha I}(x') G_{\alpha I}[T_\alpha(x) - T_I(x-x')] dx', \end{aligned} \tag{5.97}$$

where

$$G_{\alpha\beta}(t) = \int_0^t \Phi_{\alpha\beta}(s) ds. \tag{5.98}$$

It is also required that the voltage be below threshold prior to firing, $V_\alpha(x,t) < \kappa_\alpha$ for $t < T_\alpha(x)$. A traveling pulse solution with velocity c is defined according to

$$T_E(x) = \frac{x}{c}, \quad T_I(x) = \frac{x}{c} + \zeta, \tag{5.99}$$

where ζ is the shift in the firing times of the inhibitory neurons relative to the excitatory neurons, so that $\zeta < 0$ means that the I cells fire before the corresponding E cells. Substituting such a solution into (5.97) and using the explicit expressions for w and G yield two algebraic equations for the two unknowns c, ζ. Existence of a traveling pulse then reduces to the problem of solving for c, ζ. Similarly, stability of a solution is determined by substituting

$$T_E(x) = \frac{x}{c} + \phi_E(x), \quad T_I(x) = \frac{x}{c} + \zeta + \phi_I(x), \tag{5.100}$$

into (5.97), expanding to first order in $\phi_{E,I}$ and analyzing the spectrum of the resulting linear operator. The quantitative results that emerge from such an analysis are summarized in Fig. 5.23. A number of additional points are as follows [229]:

1. The fast pulses are the continuation of the waves found in excitatory networks. The E neuron typically fires before or just after neighboring I cells. They are robust solutions that can be generated by a strong localized current injection.
2. Slow waves are characterized by I cells firing significantly before neighboring E cells. Although slow waves can exist in the absence of slow excitation, the presence of the latter greatly expands the basin of attraction and the possibility of inducing a slow wave with a localized perturbation.
3. There exists a bistable regime and a regime in which there is a continuous transition from fast to slow waves.
4. It is also possible to find parameter regimes in which there are lurching waves and other more irregular solutions.

The possibility for a cortical network to sustain two propagation velocities has also been observed in a much more detailed conductance-based model [122], with slow waves observed in the presence of inhibition and fast waves in the absence of inhibition. The more detailed model also showed that inhibitory neurons always fired before excitatory neurons during the propagation of slow waves. One limitation of the IF network study was that, in order to make the mathematical analysis tractable, it was necessary to impose the constraint that each neuron fired only one spike. On the other hand, the biophysical model can simulate the propagation of a pulse that represents the onset of a long-lasting active spiking (up) state and the transition to an inactive (down) state. Neurons within the pulse fire coherently at a rate of around 10 Hz. Repetitive stimulus-invoked or spontaneous activation of a local population resulted in the rhythmic slow oscillations (< 1 Hz) between up and down states observed in EEG recordings during slow-wave sleep [602] and in vitro slice studies [549]. There is still a debate regarding the precise mechanisms for the spontaneous transitions between the up and down states, although they are likely to involve some combination of intrinsic membrane properties and slow/fast synaptic interactions [27, 122, 419, 488, 549].

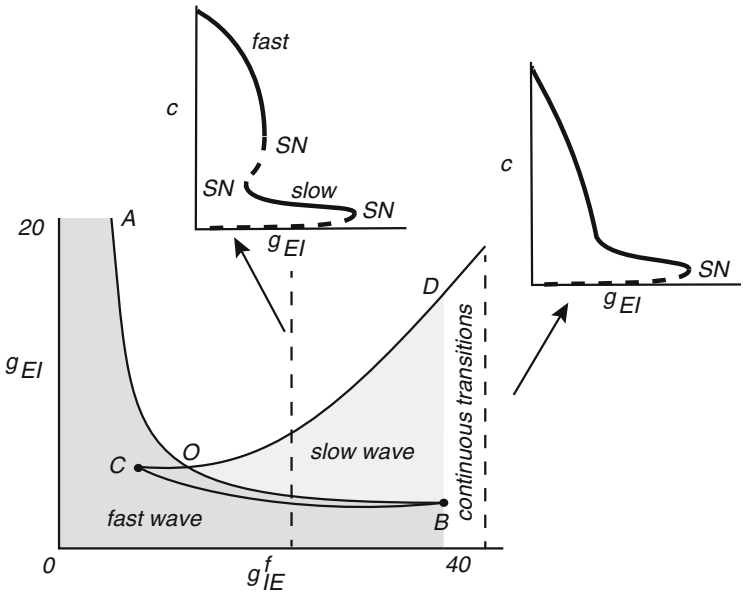

Fig. 5.23 Sketch of phase diagram showing the existence of stable fast and slow waves in the (g^f_{IE}, g_{EI}) plane for $g^s_{EE} = 10$, $g^f_{EE} = 12$, and $g^s_{IE} = 0$. The ranges of the synaptic weights are taken to be $\sigma_{EE} = 1 = \sigma_{IE}, \sigma_{II} = 0.5 = \sigma_{IE}$, and the thresholds are $\kappa_E = \kappa_I = 1$. Assuming the membrane time constants are unity, $\tau^s_{EE} = \tau^s_{IE} = 5/3$, $\tau^f_{EE} = \tau^f_{IE} = 1/12$, and $\tau_{II} = \tau_{EI} = 4/15$. The *solid lines* show saddle–node (SN) bifurcation curves: along AB a stable/unstable pair of fast waves coalesce, along CD a stable/unstable pair of slow waves coalesce, and along OB the unstable fast wave coalesces with the stable slow wave. A stable fast wave exists in the *dark-shaded domain*, a stable slow wave exists in the *light-shaded domain*, and the waves coexist in the region OCB (bistability). The points B, C are codimension two-cusp bifurcation points. The insets show the bifurcation diagram with respect to g_{EI} for two different values of g^f_{IE} (not shown to scale). In particular, the right-hand inset illustrates the case of a continuous transition from a fast to a slow wave with the latter disappearing in an SN. The parameter regime over which slow waves exists shrinks significantly in the absence of slow excitation ($g^s_{IE} \to 0$), partly due to the fact that the slow wave can destabilize via a Hopf bifurcation

5.4.3 Spiking Model of Thalamic Spindle Waves

As we have already highlighted, computational and experimental studies of disinhibited neocortical slices indicate that neuronal discharges propagate continuously at a velocity $c \sim 10$ cm/s [228]. Axonal delays are relatively small. On the other hand, in models of thalamic slices, composed of excitatory thalamocortical (TC) neurons and inhibitory reticular (RE) thalamic neurons, waves propagate in a lurching manner at a velocity $c \sim 1$ cm/s [232, 334, 349]. This is thought to form the basic mechanism for the generation of 7–14 Hz spindle oscillations during the onset of sleep. Each recruitment cycle of the lurching waves has two stages (see Fig. 5.24): (i) a new group of inhibitory RE cells is excited by synapses from TC cells, and this

RE group then inhibits a new group of TC cells; (ii) the new recruited TC cells rebound from hyperpolarization and fire a burst of spikes, which further recruit more RE cells during the next cycle. One can reduce the two-layer thalamic model to a single-layer excitatory network with a large effective delay ($\tau_a \approx 100$ ms) caused by the time needed for a TC cell to rebound from inhibition [230, 525]. If such a network is modeled in terms of an IF network with delays, then one can obtain lurching waves, as discussed at the end of Sect. 5.3. A more detailed analysis of the post-inhibitory rebound mechanism underlying the generation of continuous and lurching waves in thalamic networks has been carried out using conductance-based [153, 232, 620] and integrate-and-fire-or-burst models [128]. We briefly describe the latter model.

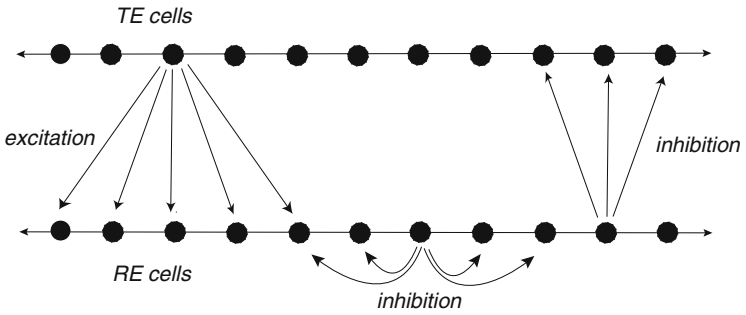

Fig. 5.24 Two-layer thalamic model. Inhibitory reticular (RE) cells inhibit excitatory thalamocortical (TC) cells, and TC cells excite RE cells. RE cells also mutually inhibit each other but this has a relatively small effect on discharge propagation

Several models of bursting neurons include a low-threshold calcium T-current [657]. Such a current is slowly activated when the neuron is sufficiently hyperpolarized so that it can cause the neuron to fire a burst of action potentials when released from sustained inhibition, so-called *post-inhibitory* rebound. Recently the integrate-and-fire model has been extended to incorporate this slow acting T-current leading to the aptly named *integrate-and-fire-or-burst* (IFB) model [128, 138, 589]. The current balance equation for the model is

$$C\frac{dv}{dt} = -I - I_L - I_T, \tag{5.101}$$

where C is a membrane capacitance, I represents external or synaptic current, and $g_L(v - v_L)$ is a leakage current with constant conductance g_L and reversal potential v_L. The low-threshold Ca^{2+} current is given by

$$I_T = g_T h(t)(v - v_T)H(v - v_h), \tag{5.102}$$

where H is a Heaviside function and the slow variable h has the dynamics

$$\frac{dh}{dt} = \begin{cases} -h/\tau_-, & v \geq v_h \\ (1-h)/\tau_+, & v < v_h. \end{cases} \tag{5.103}$$

The variable h, which represents slow de-inactivation of the low-threshold Ca^{2+} conductance, relaxes to zero with time constant τ_- when $v \geq v_h$ and relaxes to unity with time constant τ_+ when $v < v_h$. Since $v_h < v_r < \kappa$, where κ is the firing threshold and v_r is the rest level, it follows that sustained hyperpolarization is required in order that the potential crosses the v_h boundary from above, resulting in an increase in h. If the cell is then released from inhibition so that v recrosses the threshold v_h from below, a nonzero I_T current is generated that can depolarize the cell and produce a burst of spikes. In the absence of such hyperpolarization, the system acts as a regular integrate-and-fire neuron. For an appropriate choice of parameters, it has been shown that the IFB model under periodic stimulation exhibits excellent agreement with experimental results obtained from intracellular recordings of thalamic relay cells [589]. In the case of a constant external input, it is possible to obtain an exact solution of the IFB model in terms of characteristic curves [105]. Taking the ratio of (5.101) and (5.103) in the Ca^{2+} de-inactivated region ($v < v_h$), we have (for $C = 1$)

$$\frac{dv}{dh} = \tau_+ \frac{I_0 + g_L(v_L - v)}{1 - h}, \tag{5.104}$$

whereas, in the Ca^{2+} inactivated region ($v < v_h$),

$$\frac{dv}{dh} = -\tau_- \frac{I_0 + g_L(v_L - v) + g_T h(v_T - v)}{h}. \tag{5.105}$$

A sketch of a typical solution for $v = v(h)$ in both regimes is shown in Fig. 5.25; see [105] for a more detailed analysis.

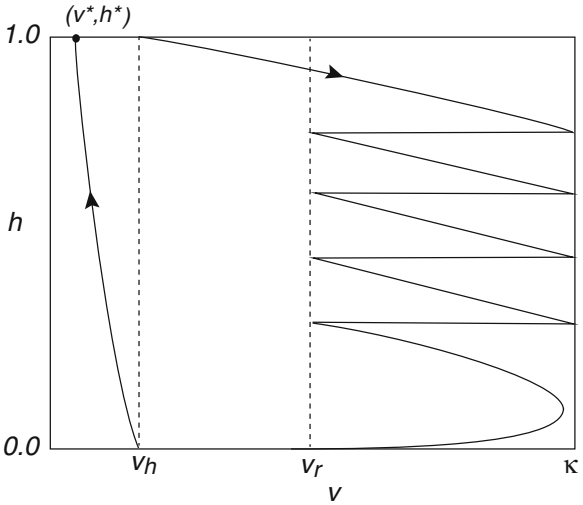

Fig. 5.25 Illustrative sketch of typical characteristic curves for an IFB neuron driven by a subthreshold constant input. A burst of four spikes arises when the neuron crosses the threshold v_h from below. Bursting ceases when h has decreased sufficiently so that the voltage v can no longer cross the firing threshold κ. Once v decreases below v_h, h increases to its equilibrium value $h^* = 1$ where $v = v^* < v_h$

A network version of the IFB model can be constructed along similar lines to a standard IF model [128]. Let (v_i, h_i) denote the voltage and slow inactivation variable of neuron i. Equation (5.101) becomes (for $C = 1$)

$$\frac{dv_i}{dt} = u_i(t) - g_L(v_i - v_L) - g_T h_i(t)(v_i - v_T)H(v_i - v_h), \tag{5.106}$$

where h_i evolves according to (5.103) and $u_i(t)$ is the total synaptic current into neuron i:

$$u_i(t) = \sum_j w_{ij} \sum_m \Phi(t - T_j^m), \tag{5.107}$$

with the firing times T_j^m determined by (5.2). Equation (5.106) is supplemented by the reset condition (5.57). In principle, one could now investigate the existence and stability of continuous and lurching waves in a one-dimensional network of IFB neurons by taking a continuum limit along the lines of Sect. 5.4.1. However, the analysis is still nontrivial unless some further approximation is made such as taking the synapses to be slow so that the spiking model can be reduced to a rate-based model [128]. Nevertheless, it can be shown that a single-layer inhibitory network of IFB neurons with v_h below the resting potential can support lurching waves, whereas a corresponding excitatory network with v_h above the resting potential supports continuous waves. In terms of the two-layer network shown in Fig. 5.24, the former can be interpreted as a thalamic network with TRN-mediated inhibition while the former corresponds to a TRN network with thalamus-mediated excitation.

Chapter 6
Population Models and Neural Fields

In this chapter we show how to construct population-based models of synaptically coupled neural networks, distinguishing between voltage-based and activity-based versions [71, 168]. We also consider the important issue of how noise at the single-cell level (Poisson-like spiking statistics) relates to noise at the population level. In particular, we describe a neural master equation formulation of stochastic population dynamics. One biological motivation for population-based models is that neurons in cortex tend to be organized into tightly coupled groups known as cortical columns, in which the cells share similar functional properties (Sects. 5.1 and 8.1). Another important feature of cortex is that it is spatially organized at both the anatomical and functional levels, which can be modeled in terms of spatially structured networks of interacting populations. In the continuum limit, such models can be described in terms of neural field equations. The advantage of a continuum rather than a discrete representation of spatially structured networks is that various techniques from the analysis of PDEs presented in Part I can be adapted to the study of neural field models of cortex (Chaps. 7 and 8).

6.1 Population Averaging and Rate Models

Suppose that a network of synaptically coupled spiking neurons is partitioned into a set of P homogeneous populations labeled $\alpha = 1,\ldots,P$, with $N_\alpha = N$ neurons in each population. (It is straightforward to relax this assumption by taking $N_\alpha = \mathcal{O}(N)$.) Let χ denote the population function that maps the single neuron index $i = 1,\ldots,N$ to the population index α to which neuron i belongs: $\chi(i) = \alpha$. Furthermore, suppose the synaptic interactions between populations are the same for all neuron pairs. (Relaxing this assumption can lead to additional sources of stochasticity as explored in [184, 632].) Denote the sequence of firing times of the jth neuron by $\{T_j^m, m \in \mathbf{Z}\}$. The net synaptic current into postsynaptic neuron i due to innervation by the spike train from presynaptic neuron j, with $\chi(i) = \alpha, \chi(j) = \beta$, is taken to have the general form $N^{-1}\sum_m \Phi_{\alpha\beta}(t - T_j^m)$, where $N^{-1}\Phi_{\alpha\beta}(t)$ represents

P.C. Bressloff, *Waves in Neural Media: From Single Neurons to Neural Fields*,
Lecture Notes on Mathematical Modelling in the Life Sciences,
DOI 10.1007/978-1-4614-8866-8_6,

the temporal filtering effects of synaptic and dendritic processing of inputs from any neuron of population β to any neuron of population α; see Sect. 1.4.2. Assuming that all synaptic inputs sum linearly, the total synaptic input to the soma of the ith neuron is

$$u_i(t) = \sum_\beta \frac{1}{N} \sum_{j;\chi(j)=\beta} \Phi_{\alpha\beta}(t - T_j^m) = \int_{-\infty}^t \sum_\beta \Phi_{\alpha\beta}(t-t') \frac{1}{N} \sum_{j;\chi(j)=\beta} a_j(t')dt' \tag{6.1}$$

for all $\chi(i) = \alpha$, where $a_j(t) = \sum_{m\in\mathbf{Z}} \delta(t - T_j^m)$. That is, $a_j(t)$ represents the output spike train of the jth neuron in terms of a sum of Dirac delta functions. In order to obtain a closed set of equations, we have to determine the firing times T_i^m given by Eq. (5.2), where $v_i(t)$ evolves according to conductance-based model (5.1). It follows that, since the right-hand side of (6.1) is independent of i, we can set $u_i(t) = u_\alpha(t)$ for all $p(i) = \alpha$ with

$$u_\alpha(t) = \sum_{\beta=1}^P \int_{-\infty}^t \Phi_{\alpha\beta}(t-t') a_\beta(t')dt', \tag{6.2}$$

and $a_\alpha(t)$ is the output activity of the αth population:

$$a_\alpha(t) = \frac{1}{N} \sum_{j;\chi(j)=\alpha} a_j(t). \tag{6.3}$$

We now assume that each homogeneous population is close to a so-called asynchronous state, in which the spike trains of different neurons within a homogeneous population are uncorrelated (see Sect. 6.3.1). The population activity a_α is then approximately constant, which means that the synaptic currents are also slowly varying functions of time. It follows that a_α can track the input current according to $a_\alpha(t) = F(u_\alpha(t))$, where F is a population gain function [2, 86, 87, 213]. Substituting this approximation into (6.2) leads to the closed system of equations

$$u_\alpha(t) = \sum_{\beta=1}^P \int_{-\infty}^t \Phi_{\alpha\beta}(t-t') F[u_\beta(t')]dt', \tag{6.4}$$

(Note, however, the asynchronous state only exists in the thermodynamic limit so that for finite N we expect statistical fluctuations around the asynchronous state; see Sect. 6.4.) A rate equation identical in form to (6.4) was derived in Sect. 5.3 for an IF network with slow synapses, except that it involved single neuron labels rather than the population labels α, β. As highlighted elsewhere [71, 168], Eq. (6.4) can be reduced to a system of ordinary differential equations provided that we place rather mild restrictions on the time dependence of $\Phi_{\alpha\beta}(t)$. First, suppose that $\Phi_{\alpha\beta}(t) = w_{\alpha\beta}\Phi_\alpha(t)$ where $w_{\alpha\beta}$ denotes the mean synaptic strength of connections from population β to neuron α and $\Phi_\alpha(t)$ determines the time course of the input, which is assumed to depend only on properties of the postsynaptic population

α. Furthermore, suppose that there exists a differential operator $\mathbb{L}_\alpha$ such that (see also (5.76))

$$\mathbb{L}_\alpha \Phi_\alpha(t) = \delta(t). \tag{6.5}$$

Applying the operator $\mathbb{L}_\alpha$ to both sides of equation (6.4) then leads to a system of differential equations for the population currents $u_\alpha(t)$:

$$\mathbb{L}_\alpha u_\alpha(t) = \sum_{\beta=1}^{P} w_{\alpha\beta} F_\beta(u_\beta(t)). \tag{6.6}$$

Note that we could easily convert the synaptic current $u_\alpha(t)$ into an input voltage $v_\alpha(t) = u_\alpha(t)/\sigma$ using an effective input conductance σ, for example. Thus Eq. (6.6) is often referred to as a voltage equation and forms the basis of most classical neural networks such as the Hopfield model [288]. On the other hand, if the time course of the inputs depends only on presynaptic parameters, $\Phi_{\alpha\beta}(t) = w_{\alpha\beta}\Phi_\beta(t)$, with Φ_β having inverse differential operator $\mathbb{L}_\beta$, then we obtain a system of differential equations for the so-called synaptic drives:

$$z_\alpha(t) = \int_{-\infty}^{t} \Phi_\alpha(t-t') F_\alpha(u_\alpha(t'))dt'. \tag{6.7}$$

That is, applying the differential operator $\mathbb{L}_\alpha$ to Eq. (6.7) and using $u_\alpha(t) = \sum_{\beta=1}^{P} w_{\alpha\beta} z_\beta(t)$ leads to the activity-based model

$$\mathbb{L}_\alpha z_\alpha(t) = F_\alpha\left(\sum_{\beta=1}^{P} w_{\alpha\beta} z_\beta(t)\right). \tag{6.8}$$

The differential operator $\mathbb{L}_\alpha$ appearing in Eqs. (6.6) and (6.8) is often taken to be first order in time:

$$\mathbb{L}_\alpha = \frac{\partial}{\partial t} + \frac{1}{\tau_\alpha}, \tag{6.9}$$

with inverse kernel $\Phi_\alpha(t) = H(t)\mathrm{e}^{-t/\tau_\alpha}$. In order to relate the effective time constant τ_α to membrane and synaptic time constants, let us assume for simplicity that all synapses are sufficiently close to the soma so that the dendrite simply acts as a first-order low-pass filter and set (with $V_{\text{rest}} = 0$)

$$\Phi_{\alpha\beta}(t) = \sigma_\alpha r_{m,\alpha} V_{\text{syn},\beta} \bar{g}_{\alpha\beta} H(t) \int_0^t \mathrm{e}^{-(t-s)/\tau_{m,\alpha}} h_\beta(s)ds,$$

with

$$h_\beta(s) = \frac{\tau_{d,\beta}}{\tau_{d,\beta} - \tau_{r,\beta}} (\mathrm{e}^{-s/\tau_{d,\beta}} - \mathrm{e}^{-s/\tau_{r,\beta}}).$$

We have made explicit that the reversal potential V_{syn} and synaptic rise/fall times $\tau_{r,d}$ only depend on the particular class of synapses innervated by the presynaptic population β, whereas the membrane time constant τ_m, resistance r_m, and conductance σ are solely properties of the postsynaptic population α. Only the maximum

conductance $\bar{g}$ is specific to the particular synapses $\beta \to \alpha$. The various constant factors can be combined to define the synaptic weight $w_{\alpha\beta}$. In particular, $w_{\alpha\beta} \sim V_{\text{syn},\beta}$ so that the sign of $V_{\text{syn},\beta}$ (relative to the resting potential) determines whether the synapse is excitatory or inhibitory. If $\tau_m \gg \tau_r, \tau_d$, then the time course is effectively independent of the presynaptic label β, and we have the voltage-based model (6.6) with first-order operator $\mathbb{L}_\alpha$ and $\tau_\alpha = \tau_m$. On the other hand, if $\tau_d \gg \tau_m, \tau_r$, then we obtain the activity-based model with $\tau_\alpha = \tau_d$. Although the reduction to a rate-based model is a major simplification of the full conductance-based model, it is still possible to incorporate various additional physiological features.

1. *Synaptic depression.* In order to incorporate synaptic depression we need to return to the single neuron level. Equation (6.1) is modified according to

$$\begin{aligned} u_i(t) &= \sum_\beta \frac{1}{N} \sum_{j;\chi(j)=\beta} \Phi_{\alpha\beta}(t - T_j^m) q_{ij}(t - T_j^m) \\ &= \int_{-\infty}^t \sum_\beta \Phi_{\alpha\beta}(t-t') \left[\frac{1}{N} \sum_{j;\chi(j)=\beta} a_j(t') q_{ij}(t') \right] dt' \end{aligned}$$

with q_{ij} evolving according to an equation of the form (1.45), which we write as

$$\frac{dq_{ij}}{dt} = \frac{1 - q_{ij}}{\tau_q} - (1-\gamma) q_{ij}(t) a_j(t).$$

Averaging the latter equation with respect to $j, \chi(j) = \beta$, and introducing the compact notation

$$\langle f(t) \rangle_\beta = \frac{1}{N} \sum_{j;\chi(j)=\beta} f_j(t),$$

we have the pair of equations

$$u_i(t) = \int_{-\infty}^t \sum_\beta \Phi_{\alpha\beta}(t-t') \langle a(t') q_i(t') \rangle_\beta dt' \tag{6.10}$$

and

$$\frac{d\langle q_i \rangle_\beta}{dt} = \frac{1 - \langle q_i \rangle_\beta}{\tau_q} - (1-\gamma) \langle a(t) q_i(t) \rangle_\beta.$$

We now make the mean-field approximation

$$\langle a(t) q_i(t) \rangle_\beta = a_\beta(t) \langle q_i(t) \rangle_\beta \tag{6.11}$$

Since all averaged depression variables $\langle q_i(t) \rangle_\beta, i = 1, \ldots, N\}$ for fixed β now have a common input drive $a_\beta(t)$, it follows that

$$\tau_q \frac{d(\langle q_i(t) \rangle_\beta - \langle q_{i'}(t) \rangle_\beta)}{dt} = -[\langle q_i(t) \rangle_\beta - \langle q_{i'}(t) \rangle_\beta],$$

and thus $\langle q_i(t)\rangle_\beta \to \langle q_{i'}(t)\rangle_\beta = q_\beta(t)$ for all $i,i' = 1,\ldots,N$. In other words, after an initial transient of duration τ_q, we can identify all depression variables associated with a given presynaptic population β. If we now assume that $\Phi_{\alpha\beta}(t) = w_{\alpha\beta}\Phi_\beta(t)$, we can introduce the synaptic drives (6.7) and derive the modified activity-based model [25, 617, 637, 644]:

$$\mathbb{L}_\alpha z_\alpha(t) = F_\alpha\left(\sum_{\beta=1}^{P} w_{\alpha\beta}q_\beta(t)z_\beta(t)\right), \tag{6.12}$$

with

$$\frac{dq_\alpha}{dt} = \frac{1-q_\alpha(t)}{\tau_q} - (1-\gamma)q_\alpha(t)F_\alpha\left(\sum_{\beta=1}^{P} w_{\alpha\beta}q_\beta(t)z_\beta(t)\right). \tag{6.13}$$

The corresponding voltage-based model is

$$\mathbb{L}_\alpha u_\alpha(t) = \sum_{\beta=1}^{P} w_{\alpha\beta}q_\beta(t)F_\beta(u_\beta(t)). \tag{6.14}$$

with

$$\frac{dq_\alpha}{dt} = \frac{1-q_\alpha(t)}{\tau_q} - (1-\gamma)q_\alpha(t)F_\alpha(u_\alpha(t)). \tag{6.15}$$

2. *Axonal propagation delays.* In the above derivation of rate-based models, we have assumed that the spiking of a presynaptic neuron has an instantaneous effect on downstream postsynaptic neurons. This neglects the fact that action potentials take time to propagate along an axon to innervate a synaptic terminal. Let us denote the corresponding axonal delay of a synapse $\alpha \to \beta$ by $\tau_{\alpha\beta}$. The integral equation (6.2) is modified according to

$$u_\alpha(t) = \sum_{\beta=1}^{P}\int_{-\infty}^{t} \Phi_{\alpha\beta}(t-t')a_\beta(t'-\tau_{\alpha\beta})dt'. \tag{6.16}$$

The corresponding voltage-based model then takes the form of a system of delay differential equations,

$$\mathbb{L}_\alpha u_\alpha(t) = \sum_{\beta=1}^{P} w_{\alpha\beta}F_\beta(u_\beta(t-\tau_{\alpha\beta})), \tag{6.17}$$

and similarly for the activity-based model.

3. *Adaptive threshold dynamics.* Another biophysical process that can be incorporated into rate-based models is spike frequency adaptation. Spike frequency adaptation causes a neuron's firing rate to decay to a submaximal level and occurs when a potassium current, presumably activated by elevated intracellular

calcium, hyperpolarizes the membrane voltage [35, 396, 604]. This afterhyperpolarization current has a time constant of around 40–120 ms. Spike frequency adaptation can be introduced as a negative current $-c_i$ on the right-hand side of the conductance-based model equation (5.1). Assuming that $c_i(t)$ varies slowly relative to the voltage $v_i(t)$, it can be shown that c_i effectively acts as an adaptive threshold that varies linearly with the firing rate [35]. In the case of a network of homogeneous populations, each neuron within a given population fires at the same mean rate so that we can identify $c_i = c_\alpha$ for all i such that $\chi(i) = \alpha$. Hence, the voltage-based model becomes

$$\mathbb{L}_\alpha u_\alpha(t) = \sum_{\beta=1}^{P} w_{\alpha\beta} F_\beta(u_\beta(t) - c_\beta(t)). \tag{6.18}$$

with

$$\frac{dc_\alpha}{dt} = -\frac{c_\alpha(t)}{\tau_c} + \gamma_c F_\alpha(u_\alpha(t) - c_\alpha(t)). \tag{6.19}$$

6.2 E–I Oscillator Networks

One of the simplest population-based networks, which is often taken to be a fundamental module in large-scale models of cortex, is a pair of mutually coupled local populations of excitatory and inhibitory neurons known as an E–I network; see Fig. 6.1. An E–I network has the important property of exhibiting limit cycle oscillations and can thus act as a basic oscillatory element in network models of cortical phase waves, as an alternative to single spiking neurons (Sect. 5.2). An activity-based version of an E–I network takes the form (for first-order synapses)

$$\begin{aligned} \frac{da_E}{dt} &= -a_E + F\left(w_{EE}a_E - w_{EI}a_I + h_E\right) \\ \frac{da_I}{dt} &= -a_I + F\left(w_{IE}a_E - w_{II}a_I + h_I\right), \end{aligned} \tag{6.20}$$

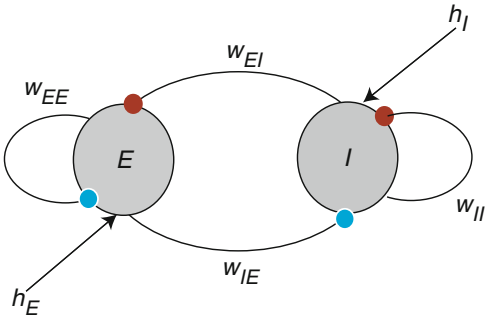

Fig. 6.1 Two-population E–I network

where h_E, h_I represent constant background inputs. For simplicity, we set $\tau_E = \tau_I = 1$. The bifurcation structure of the two-population model given by Eq. (6.20) has been analyzed in detail elsewhere [55]. An equilibrium (a_E^*, a_I^*) is obtained as a solution of the pair of equations

$$\begin{aligned} a_E^* &= F\left(w_{EE}a_E^* - w_{EI}a_I^* + h_E\right) \\ a_I^* &= F\left(w_{IE}a_E^* - w_{II}a_I^* + h_I\right). \end{aligned} \tag{6.21}$$

These can be inverted to yield

$$\begin{aligned} h_E &= F^{-1}(a_E^*) - w_{EE}a_E^* + w_{EI}a_I^* \\ h_I &= F^{-1}(a_I^*) - w_{IE}a_E^* + w_{II}a_I^*. \end{aligned} \tag{6.22}$$

As a further simplification, take the gain function F to be the simple sigmoid $F(u) = (1+\mathrm{e}^{-u})^{-1}$. Using the fact that the sigmoid function then satisfies $F' = F(1-F)$ and applying the fixed-point equations allows one to represent the associated Jacobian in the form

$$\Delta = \begin{pmatrix} -1 + w_{EE}a_E^*(1-a_E^*) & -w_{EI}a_E^*(1-a_E^*) \\ w_{IE}a_I^*(1-a_I^*) & -1 - w_{II}a_I^*(1-a_I^*) \end{pmatrix}.$$

An equilibrium will be stable provided that the eigenvalues $\lambda_\pm$ of Δ have negative real parts, where

$$\lambda_\pm = \frac{1}{2}\left(\mathrm{Tr}\,\Delta \pm \sqrt{[\mathrm{Tr}\,\Delta]^2 - 4\mathrm{Det}\,\Delta}\right). \tag{6.23}$$

This leads to the stability conditions $\mathrm{Tr}\,\Delta < 0$ and $\mathrm{Det}\,\Delta > 0$. In order to construct a phase diagram in the (h_E, h_I)-plane for a fixed weight matrix $\mathbf{w}$, we express a_I^* as a function of a_E^* by imposing a constraint on the eigenvalues $\lambda_\pm$ and then substitute the resulting function into Eq. (6.22). This yields bifurcation curves in the (h_E, h_I)-plane that are parameterized by a_E^*, $0 < a_E^* < 1$; see Fig. 6.2. For example, the constraint

$$\mathrm{Tr}\,\Delta \equiv -2 + w_{EE}a_E^*(1-a_E^*) - w_{II}a_I^*(1-a_I^*) = 0 \tag{6.24}$$

with $\mathrm{Det}\,\Delta > 0$ determines Hopf bifurcation curves where a pair of complex conjugate eigenvalues cross the imaginary axis. Since the trace is a quadratic function of a_E^*, a_I^*, we obtain two Hopf branches. Similarly, the constraint $\mathrm{Det}\,\Delta = 0$ with $\mathrm{Tr}\,\Delta < 0$ determines saddle–node or fold bifurcation curves where a single real eigenvalue crosses zero. The saddle–node curves have to be determined numerically, since the determinant is a quartic function of a_E^*, a_I^*.

Now consider a network of synaptically coupled E–I modules or subnetworks, with each module labeled by the discrete index n:

$$\frac{da_E^n}{dt} = -\frac{a_E^n}{\tau_E} + F\left(\sum_m \left[w_{EE}(n,m)a_E^m - w_{EI}(n,m)a_I^m + h_E\right]\right) \tag{6.25a}$$

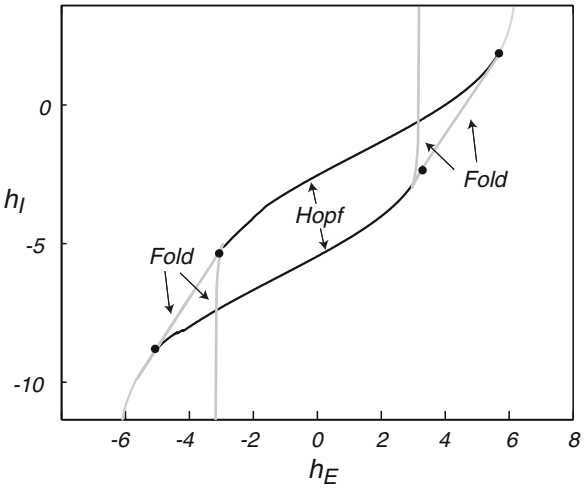

Fig. 6.2 Phase diagram of two-population Wilson–Cowan model (6.20) for fixed set of weights $w_{EE} = 11.5, w_{IE} = w_{EI} = 10, , w_{II} = -2$. The *dots* correspond to Takens–Bogdanov bifurcation points

$$\frac{da_I^n}{dt} = -\frac{a_I^n}{\tau_I} + F\left(\sum_m [w_{IE}(n,m)a_E^m - w_{II}(n,m)a_I^m + h_I]\right), \tag{6.25b}$$

Suppose that synaptic interactions within a local E–I network are stronger than those between E–I networks. That is, we write

$$w_{ab}(n,m) = w_{ab}\delta_{nm} + \varepsilon J_{ab}(n,m)(1-\delta_{nm})$$

with $\varepsilon \ll 1$. Substituting into (6.25) and Taylor expanding to $\mathscr{O}(\varepsilon)$ then gives

$$\begin{aligned}\frac{da_E^n}{dt} &= -a_E^n + F\left([w_{EE}a_E^n - w_{EI}a_I^n + h_E]\right) \\ &\quad + \varepsilon F'\left([w_{EE}a_E^n - w_{EI}a_I^n + h_E]\right)\sum_{m\neq n}[J_{EE}(n,m)a_E^m - J_{EI}(n,m)a_I^m]\end{aligned} \tag{6.26a}$$

$$\begin{aligned}\frac{da_I^n}{dt} &= -a_I^n + F\left([w_{IE}a_E^n - w_{II}a_I^n + h_I]\right) \\ &\quad + \varepsilon F'\left([w_{IE}a_E^n - w_{II}a_I^n + h_E]\right)\sum_{m\neq n}[J_{IE}(n,m)a_E^m - J_{II}(n,m)a_I^m]\end{aligned} \tag{6.26b}$$

One can view the synaptic interaction between E–I modules as weak perturbations of the underlying limit cycle oscillators, which suggests carrying out a phase reduction of (6.26) along the lines of Sects. 1.2 and 5.2. In order to proceed, it is first necessary to determine the phase-resetting curve (PRC) of an individual E–I network. Suppose that each uncoupled E–I network operates in a parameter regime where the mean-field equations (6.20) support a stable limit cycle. For concreteness, take a point in parameter space between the two Hopf curves in Fig. 6.2, namely,

$(h_E, h_I) = (0, -4)$. A plot of the oscillation in phase space is shown in Fig. 6.3(a) and the components Z_E, Z_I of the corresponding PRC are shown in Fig. 6.3(b). Note that both components are approximately sinusoidal so that the E–I network acts as a type II oscillator.

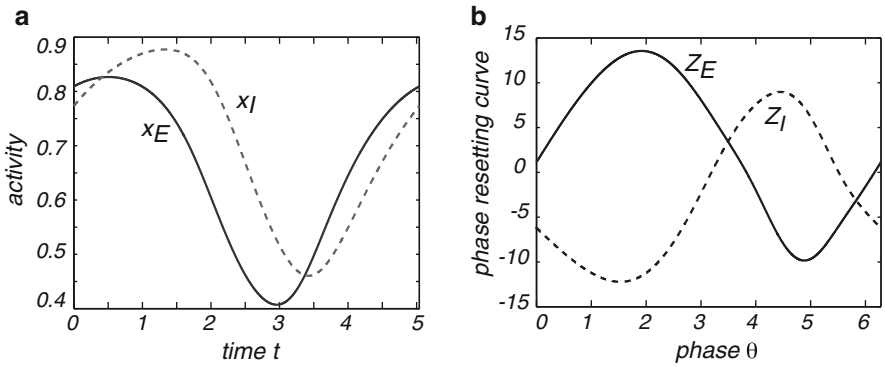

Fig. 6.3 (**a**) Trajectories along the limit cycle of an E–I network: $x_E(t)$ (*solid curve*) and $x_I(t)$ (*dashed curve*). Parameters are $w_{EE} = 11.5, w_{IE} = -w_{EI} = 10$, $w_{II} = -2$, $h_E = 0$, and $h_I = -4$. Also $F(u) = 1/(1+\mathrm{e}^{-u})$. (**b**) Corresponding components Z_E and Z_I of the phase-resetting curve

The next step is to rewrite (6.26) in the more compact form

$$\frac{d\mathbf{a}^n}{dt} = -\mathbf{a}^n + \mathbf{f}(\mathbf{a}^n) + \varepsilon \mathbf{g}(\mathbf{a}^n)^T \sum_{m \neq n} \mathbf{J}(n,m)\mathbf{a}^m, \tag{6.27}$$

where $\mathbf{a}^n = (a_E^n, a_I^n)^T$, $\mathbf{f} = (f_E, f_I)$, $\mathbf{g} = (g_E, g_I)$,

$$f_p(\mathbf{a}) = F(w_{pE}a_E - w_{pI}a_I + h_p), \quad g_p(\mathbf{a}) = F'(w_{pE}a_E - w_{pI}a_I + h_p), \quad p = E, I.$$

Phase reduction now proceeds using the method of isochrones as described in Sect. 1.2. Let $\Theta(\mathbf{a})$ represent the isochronal mapping in a neighborhood of an uncoupled limit cycle oscillator and denote the natural frequency by ω_0. Then

$$Z_E(\theta) = \frac{\partial \Theta(\mathbf{a}^*(\theta))}{\partial a_E}, \quad Z_I(\theta) = \frac{\partial \theta(\mathbf{a}^*(\theta))}{\partial a_I}, \tag{6.28}$$

where $\mathbf{a}^*$ is a point on the limit cycle. Applying the phase reduction procedure to (6.27) with $\theta_n = \Theta(\mathbf{a}^n)$, we have

$$\frac{d\theta_n}{dt} = \omega_0 + \varepsilon \sum_{p,q=E,I} Z_p(\theta_n) g_p(\theta_n) \sum_m J_{pq}(n,m) a_q^*(\theta_m). \tag{6.29}$$

Here, all quantities are evaluated on the limit cycles so that $g_p(\theta_n) = g_p(a^*(\theta_n))$ etc. Finally, averaging over one period $\Delta_0 = 2\pi/\omega_0$ gives the phase equations

$$\frac{d\theta_n}{dt} = \omega_0 + \varepsilon \sum_{p,q=E,I} \left[\sum_m J_{pq}(n,m) H_{pq}(\theta_m - \theta_n) \right], \tag{6.30}$$

with phase interaction functions

$$H_{pq}(\phi) = \frac{1}{2\pi}\int_0^{2\pi} Z_p(\theta-\phi)g_p(\theta-\phi)a_q^*(\theta)d\theta. \tag{6.31}$$

Given the phase equations, one can investigate the existence and stability of phase-locked states, including phase waves, along identical lines to the analysis of waves on a chain in Sect. 5.2.2. Note that phase-coupled E–I networks have been used to study the phenomenon of stimulus-induced oscillations and synchrony in primary visual cortex model, where each E–I network is interpreted as a cortical column consisting of reciprocally coupled populations of excitatory and inhibitory neurons [239, 560].

6.3 Firing Rates, Asynchronous States, and Spiking Statistics

6.3.1 The Asynchronous State in a Homogeneous Spiking Network

One of the major assumptions in the derivation of rate-based population models in Sect. 6.1 was that each homogeneous population is in an asynchronous state. Here we consider the existence and stability of an asynchronous state in a large, globally coupled network of IF neurons [2, 213]. Consider the following synaptically coupled network of nonlinear IF neurons (see also Sect. 5.3):

$$\frac{dv_i}{dt} = G(v_i) + \frac{\varepsilon}{N}\sum_{j=1}^{N}\int_{-\infty}^{\infty}\Phi(t'-\tau_d)\sum_m \delta(t-t'-T_j^m)dt', \tag{6.32}$$

with Φ given by the alpha function (5.23), τ_d a discrete axonal delay and ε determines the strength of coupling. We take a threshold $v_\kappa = 1$ and a reset $v_r = 0$. In the case of global coupling, we can express the sum over delta functions in terms of the population activity variable

$$a(t) = \sum_{j=1}^{N}\sum_m \delta(t-T_j^m) \tag{6.33}$$

so that

$$\frac{dv_i}{dt} = G(v_i) + \varepsilon u(t), \tag{6.34}$$

where $u(t) = \int_{-\infty}^{\infty}\Phi(t'-\tau_d)a(t-t')dt'$. Now suppose that there exists an asynchronous state $a(t) = a_0$. (Strictly speaking, such a state only exists in the thermodynamic limit $N \to \infty$.) Since Φ is normalized to unity it follows that $u(t) = a_0$ as well (ignoring transients). An implicit equation for a_0 is then obtained by integrating equation (6.34) between successive firing times:

$$\frac{1}{a_0} = \int_0^1 \frac{du}{G(u) + \varepsilon a_0}. \tag{6.35}$$

We will assume that there exists a unique solution to this equation for given G and ε. If G depends on a uniform external input I, then this yields the population gain function F with $a_0 = F(I)$.

In order to study the stability of the asynchronous state, it is convenient to carry out the change of variables

$$y_i = a_0 \int_0^{v_i} \frac{du}{G(u) + \varepsilon a_0}, \tag{6.36}$$

with $0 < y_i < 1$ such that Eq. (6.34) becomes

$$\frac{dy_i}{dt} = a_0 + \Gamma(y_i)[u(t) - a_0] \tag{6.37}$$

and

$$\Gamma(y) = \frac{a_0 \varepsilon}{G(y) + a_0 \varepsilon}. \tag{6.38}$$

We also incorporate the effects of synaptic noise by including an additive white noise term $\xi_i(t)$,

$$\frac{dy_i}{dt} = a_0 + \Gamma(y_i)[u(t) - a_0] + \xi_i(t), \tag{6.39}$$

with

$$\langle \xi_i(t) \rangle = 0, \quad \langle \xi_i(t) \xi_j(t') \rangle = \sigma^2 \delta_{ij} \delta(t - t'). \tag{6.40}$$

(Note that diffusive fluctuations of the membrane potential due to stochastic background activity would lead to an additive white noise term in Eq.(6.34) rather than in Eq. (6.40). The corresponding stochastic equation for y_i would then involve multiplicative noise, which is much harder to analyze.) In the presence of noise the variable y_i can become negative so $-\infty < y_i < 1$. The Langevin equation (6.40) has an associated Fokker–Planck equation

$$\frac{\partial}{\partial t} p(y,t) = -\frac{\partial}{\partial y} J(y,t), \tag{6.41}$$

where $J(y,t)$ is the probability flux

$$J(y,t) = [a_0 + \Gamma(y)[u(t) - a_0]]\, p(y,t) - \frac{\sigma^2}{2} \frac{\partial}{\partial y} p(y,t). \tag{6.42}$$

This is supplemented by the boundary conditions arising from reset:

$$p(1,t) = 0, \quad J(1,t) = a(t), \tag{6.43}$$

$$p(0^+,t) = p(0^-,t), \quad J(0^+,t) - J(0^-,t) = a(t). \tag{6.44}$$

We also require $p(-\infty,t)=0$ and $J(-\infty,t)=0$. The steady-state solution of the Fokker–Planck equation is $J(y,t)=a_0$ and $p(y,t)=p_0(y)$ with

$$p_0(y)=\begin{cases} e^{2a_0y/\sigma^2}-e^{2a_0(y-1)/\sigma^2}, & y<0 \\ 1-e^{2a_0(y-1)/\sigma^2}, & 0<y<1 \end{cases}. \tag{6.45}$$

The stability of the steady state can be determined by setting

$$p(y,t)=p_0(y)+\rho(y)e^{\lambda t}, \quad a(t)=a_0+a_1e^{\lambda t} \tag{6.46}$$

and expanding to first order in ρ, a_1. This gives the eigenvalue equation

$$\lambda\rho(y)=\frac{\sigma^2}{2}\frac{\partial^2}{\partial y^2}\rho(y)-a_0\frac{\partial}{\partial y}\rho(y)-a_1\tilde{\Phi}(\lambda)\frac{\partial}{\partial y}[\Gamma(y)p_0(y)], \tag{6.47}$$

where $\tilde{\Phi}(\lambda)$ is the Laplace transform

$$\tilde{\Phi}(\lambda)=\int_0^\infty \Phi(t-\tau_d)e^{-\lambda t}=\frac{\alpha^2}{(\lambda+\alpha)^2}e^{\tau_d\lambda}. \tag{6.48}$$

Defining the function

$$h(y)=a_1\tilde{\Phi}(\lambda)\frac{\partial}{\partial y}[\Gamma(y)p_0(y)], \tag{6.49}$$

we can write Eq. (6.47) as the inhomogeneous equation

$$[\mathscr{L}\rho(y)\equiv\left[\frac{\sigma^2}{2}\frac{\partial^2}{\partial y^2}-a_0\frac{\partial}{\partial y}\right]\rho(y)=\lambda\mathbf{1}]\rho(y)+h(y;\lambda). \tag{6.50}$$

This inhomogeneous equation can be solved in terms of the associated one-dimensional Green's function satisfying $[\mathscr{L}-\lambda\mathbf{1}]\mathscr{G}(y,y';\lambda)=\delta(y-y')$ and $\mathscr{G}(1,y',\lambda)=0$:

$$\rho(y)=\int_{-\infty}^{1}\mathscr{G}(y,y';\lambda)h(y';\lambda)dy'-a_1\mathscr{G}(y,0;\lambda) \tag{6.51}$$

with

$$\mathscr{G}(y,y';\lambda)=\begin{cases} A\left(e^{\mu_+(\lambda)[y-1]}-e^{-\mu_-(\lambda)[y-1]}\right)e^{\mu_-(\lambda)[y'-1]}, & y'<y<1 \\ A\left(e^{\mu_-(\lambda)[y'-1]}-e^{-\mu_+(\lambda)[y'-1]}\right)e^{\mu_+(\lambda)[y-1]}, & y<y', \end{cases} \tag{6.52}$$

where

$$A=\frac{2}{\sigma^2}\frac{1}{\mu_++\mu_-}, \tag{6.53}$$

$$\mu_\pm(\lambda)=\frac{1}{\sigma^2}\left[\sqrt{a_0^2+2\lambda\sigma^2}\pm a_0\right]. \tag{6.54}$$

Note that the term $a_1\mathscr{G}(y,0;\lambda)$ ensures that the flux discontinuity at $y=0$ is satisfied. Finally, an implicit equation for the eigenvalues λ can be obtained by substituting Eq. (6.49) into (6.51) and imposing the boundary condition $J(1,t)=a(t)$, which corresponds to the following first-order condition:

$$-\frac{\sigma^2}{2}\frac{\partial}{\partial y}\rho(y,t)|_{y=1}=a_1. \tag{6.55}$$

The resulting characteristic equation is [2]

$$\left(e^{\mu_-(\lambda)}-1\right)=\mu_-(\lambda)\tilde{\Phi}(\lambda)\int_{-\infty}^{1}p_0(y)\Gamma(y)e^{\mu_-(\lambda)y}dy. \tag{6.56}$$

In the zero noise limit $\sigma\to 0$, we have $\mu_-(\lambda)\to\lambda/a_0$ and $p_0(y)\to 1$ for $0<y<1$ and is zero otherwise. Thus, Eq. (6.56) becomes

$$\left(e^{\lambda/a_0}-1\right)=\frac{\lambda}{a_0}\tilde{\Phi}(\lambda)\int_{0}^{1}\Gamma(y)e^{\lambda y/a_0}dy. \tag{6.57}$$

In the weak coupling regime, solutions of Eq. (6.57) are of the form $\lambda=2\pi i n a_0+\Lambda_n$ for integer n with $\Lambda_n=\mathscr{O}(\varepsilon)$. The term Λ_n can be calculated by performing a perturbation expansion in the coupling ε. The lowest-order contribution is simply determined by setting $\lambda=2\pi i n a_0$ on the right-hand side of Eq. (6.57). In the case of a linear IF model with $G(u)=I-u$, we have $\Gamma(y)=e^{y/a_0}$ so that

$$\Lambda_n=\varepsilon\left(\frac{2\pi i n a_0}{1+2\pi i n a_0}\right)\tilde{\Phi}(2\pi i n a_0)+\mathscr{O}(\varepsilon^2). \tag{6.58}$$

We then have the following stability results in the absence of noise [2, 213]:

(i) For zero axonal delays ($\tau_d=0$) and excitatory coupling ($\varepsilon>0$), the asynchronous state is stable with respect to excitation of the nth mode if and only if $\alpha<\alpha_n$ where

$$\alpha_n=-1+\sqrt{1+4n^2\pi^2a_0^2} \tag{6.59}$$

Hence, it is stable for sufficiently slow synapses, that is, $\alpha<\alpha_1$. The asynchronous state is always unstable in the case of inhibitory coupling since the condition for stability with respect to the nth harmonic is now $\alpha>\alpha_n$, which cannot be satisfied for all n.

(ii) The asynchronous state is almost always unstable for nonzero delays (in the noise-free case).

(iii) For large n, $|\Lambda_n|\sim 1/n^2$ so that higher harmonics grow or decay slowly.

Note that although the zero delay case is a singular limit in the absence of noise, it becomes non-singular for arbitrarily small amounts of noise, where instabilities

with respect to higher harmonics are suppressed [2, 213]. One finds that for sufficiently high noise levels the asynchronous state is always stable. Reducing the noise for fixed delay induces an instability due to excitation of one of the harmonic modes with frequency $\omega \approx \omega_n = 2\pi n a_0$. A bifurcation at $\omega \approx \omega_1$ implies that the period of the resulting collective oscillation is identical to the period of the individual oscillators. Higher harmonics correspond to instabilities of the asynchronous state that lead to the formation of cluster states [213, 231]: each neuron fires with mean rate a_0, but the population of neurons splits up into several groups that fire in sequence so that the overall activity exhibits faster oscillations. Finally, note that fast oscillations are also found in sparsely connected random networks [87].

6.3.2 Balanced Networks and Neural Variability

It is well known that the spike trains of individual cortical neurons in vivo tend to be very noisy, having interspike interval (ISI) distributions that are close to Poisson [179, 593]. Indeed, one observes trial-to-trial variability in spike trains, even across trials in which external stimuli are identical. This raises a number of important issues. First, neurons are continuously bombarded by thousands of synaptic inputs, many of which are uncorrelated, so that an application of the law of large numbers would suggest that total input fluctuations are small. This would make it difficult to account for the Poisson-like behavior of individual neurons, even when stochastic ion channel fluctuations (Sect. 1.5) or random synaptic background activity is taken into account. For example, in the homogeneous spiking network analyzed above, the spike trains of individual neurons can be quite regular even when the population activity is asynchronous. Conversely, irregularity in spiking at the single-cell level can coexist with regular firing rates at the population level. However, there is growing evidence that noise can play a significant role at the network level. For example, noise appears to be present during perceptual decision making [656] and bistable perception, the latter being exemplified by perceptual switching during binocular rivalry [436, 578, 663]; see Sect. 8. Noise also contributes to the generation of spontaneous activity during resting states [148, 152]. At the level of large-scale neural systems, as measured with functional MRI (fMRI) imaging, this ongoing spontaneous activity reflects the organization of a series of highly coherent functional networks that may play an important role in cognition. Another issue is the possible computational role of pairwise and higher-order statistical correlations between the spike trains of distinct neurons, that is, whether or not it is necessary to go beyond firing rates.

One paradigm for exploring these various issues is the so-called balanced network [567, 645, 650]. In such networks, each neuron is driven by a combination of strong excitation and strong inhibition, which mainly cancel each other out, so that the remaining fluctuations occasionally and irregularly push the neuron over the firing threshold. Even in the absence of any external sources of noise, the resulting deterministic dynamics is chaotic and neural outputs are Poisson-like. Interestingly,

there is some experimental evidence that cortical networks can operate in a balanced regime [391]. Another emergent feature of balanced networks is that they can support an asynchronous state characterized by large variability in single neuron spiking and yet arbitrarily small pairwise correlations even in the presence of substantial amounts of shared inputs [519]. Thus there is a growing consensus that the trial-to-trial irregularity in the spiking of individual neurons is often unimportant, and that information is typically encoded in firing rates. (Such rates could be a measure of population activity as in Sect. 6.1 or correspond to the rates of individual neurons modeled as inhomogeneous Poisson processes; see below.) There is then another level of neural variability, namely, trail-to-trial variations in the firing rates themselves. Recent physiological data shows that the onset of a stimulus reduces firing rate fluctuations in cortical neurons while having little or no effect on spiking variability [119]; see Fig. 6.4. Litwin-Kumar and Doiron have recently shown how these two levels of stochastic variability can emerge in a chaotic balanced network of randomly connected spiking neurons, in which a small amount of clustered connections induces firing rate fluctuations superimposed on spontaneous spike fluctuations [387].

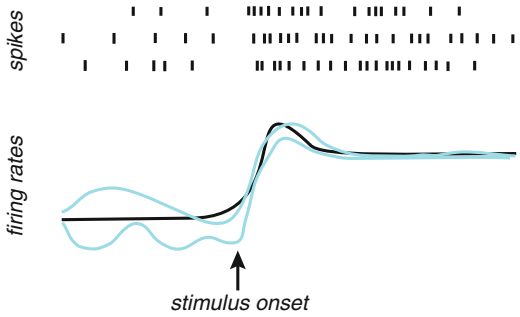

Fig. 6.4 Neurons can exhibit double stochasticity. Trial-to-trial variability in spike trains (shown as raster plots) can coexist with trial-to-trial variability in the firing rate (shown as continuous *gray curves*). Trial-averaged firing rate is the *black curve*. Following stimulus onset, the variability in the firing rate is reduced

6.3.3 Spike Statistics and the Poisson Process

Given the ubiquity of Poisson processes in spiking neuron models and its relevance to neural master equations (see Sect. 6.4), it is useful to consider these processes in a little more detail. Suppose that a neuron emits a sequence of spikes at times $t_1, t_2, \ldots, t_n$. One way to characterize this sequence statistically is in terms of the probability density $\rho(t_1, \ldots t_n)$ of finding such a sequence over many experimental trials. In other words, the probability of having a sequence of n spikes in the interval $[0, T]$ with the ith spike falling between the times t_i and $t_i + \Delta t$

is $P[t_1,\ldots t_n] = \rho(t_1,\ldots t_n)\Delta t^n$. In principle, the probability of an event occurring, namely, the firing of the next spike, could depend on the entire history of past spikes. If this dependence only extends to the previous spike so that the interspike intervals are statistically independent, then the stochastic process is said to be a *renewal process*. If there is no dependence at all on preceding spikes so that the firing times are themselves independent, then we have a *Poisson process*.

Consider a sequence of spikes generated by a homogeneous Poisson process, that is, one with a time-independent mean firing rate r. Divide a given time interval T into M bins of size $\Delta t = T/M$ and assume that ΔT is small enough so that the probability of finding two spikes within any one bin can be neglected. Then the probability $P_T[n]$ of finding n spikes over the interval T is given by

$$P_T[n] = \lim_{\Delta t\to 0} \frac{M!}{(M-n)!n!}(r\Delta t)^n(1-r\Delta t)^{M-n}$$

This consists of the probability $(r\Delta t)^n$ of finding n spikes in n specific bins multiplied by the probability $(1-r\Delta t)^{M-n}$ of not finding spikes in the remaining bins. The binomial factor is the number of ways of choosing n out of M bins with spikes. Using the approximation $M-n \approx M = T/\Delta t$ and defining $\varepsilon = -r\Delta t$, we have that

$$\lim_{\Delta t\to 0}(1-r\Delta t)^{M-n} = \lim_{\varepsilon\to 0}\left((1+\varepsilon)^{1/\varepsilon}\right)^{-rT} = \mathrm{e}^{-rT}.$$

For large M, $M!/(M-n)! \approx M^n = (T/\Delta t)^n$, so that we obtain the Poisson distribution

$$P_T[n] = \frac{(rT)^n}{n!}\mathrm{e}^{-rT}$$

Given that there are n independent spikes over the interval $[0,T]$, the probability that these spikes lie within specified bins of size Δt is $n!(\Delta t/T)^n$. Hence

$$\rho(t_1,\ldots t_n) = n!\left(\frac{1}{T}\right)^n P_T[n] = r^n\mathrm{e}^{-rT} \tag{6.60}$$

Also note that the fastest way to generate a sequence of Poisson spikes for constant r is to iterate the firing times $t_{n+1} = t_n - \log(x_{rand})/r$ with x_{rand} uniformly distributed over $[0,1]$.

A simple method for calculating the moments of the Poisson distribution is to introduce the moment-generating function

$$g(s) = \sum_{n=0}^{\infty} P_T[n]\mathrm{e}^{sn}$$

Differentiating with respect to s shows that

$$\left.\frac{d^k g(s)}{ds^k}\right|_{s=0} = \langle n^k\rangle$$

The generating function for the Poisson process can be evaluated explicitly as

$$g(s) = \exp(-rT)\exp(rT\mathrm{e}^{s})$$

from which we deduce that

$$\langle n \rangle = rT, \quad \sigma_n^2 = rT$$

Another useful quantity is the interspike interval (ISI) distribution. Suppose that a spike was last fired at time T^n. The probability of a homogeneous Poisson process generating the next spike in the interval $T^n + \tau \leq T^{n+1} \leq T^n + \tau + \Delta\tau$ is equal to the probability that no spike is fired for a time τ, which is $P_\tau[0] = \mathrm{e}^{-r\tau}$ multiplied by the probability $r\Delta\tau$ of generating a spike within the following interval $\Delta\tau$:

$$\mathbf{Pr}[\tau \leq T^{n+1} - T^n \leq \tau + \Delta\tau] = r\Delta\tau\mathrm{e}^{-r\tau}$$

The ISI probability density is thus an exponential, $\rho(\tau) = r\mathrm{e}^{-r\tau}$. It follows that the mean interspike interval is

$$\langle \tau \rangle = \int_0^\infty r\mathrm{e}^{-r\tau}\tau d\tau = \frac{1}{r}$$

and the variance is

$$\sigma_\tau^2 = \int_0^\infty r\mathrm{e}^{-r\tau}\tau^2 d\tau - \langle \tau \rangle^2 = \frac{1}{r^2}$$

The ratio of the standard deviation to the mean is called the *coefficient of variation*

$$C_V = \frac{\sigma_\tau}{\langle \tau \rangle}$$

It follows that for a homogeneous Poisson process $C_V = 1$.

How well do Poisson statistics describe experimentally measured spike trains? One often finds that for ISIs longer than about 10 msec, the ISI distribution is indeed approximately exponential. However, for shorter intervals, there is a rapid decrease in the distribution reflecting the fact that neurons are refractory immediately after

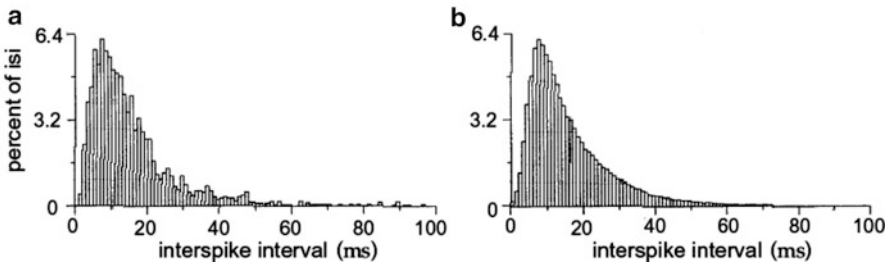

Fig. 6.5 (**a**) Interspike interval distribution from a neuron from the MT cortical visual area of a macaque monkey responding to a moving image. (**b**) Interspike interval generated with a Poisson model with a stochastic refractory period. Redrawn from [20]

firing. This is illustrated in Fig. 6.5. The data can be fitted more accurately by a gamma distribution

$$p[\tau] = \frac{r(r\tau)^k e^{-r\tau}}{k!} \tag{6.61}$$

Alternatively, one can introduce a refractory period into a standard Poisson model. Note that C_V values extracted from the spike trains of cortical neurons also take values around unity, provided that the mean interspike interval is not too small [593].

It is possible to generalize the above Poisson model to the case of a time-dependent rate $r(t)$. The simplest way to analyze this inhomogeneous Poisson process is to consider the probability distribution $\rho(t_1, \ldots t_n)$. This is given by the product of the probabilities $r(t_i)\Delta t$ that the neuron fires within the time intervals $t_i \leq t \leq t_i + \Delta t$ and the probabilities of not firing during the interspike intervals. The latter is given by

$$\mathbf{Pr}[\text{no spikes in } (t_i, t_{i+1})] = \prod_{m=1}^{M} (1 - r(t_i + m\Delta t)\Delta t)$$

where we have partitioned the interval (t_i, t_{i+1}) into M bins of size Δt. Taking the logarithm,

$$\log \mathbf{Pr}[\text{no spikes in } (t_i, t_{i+1})] = \sum_{m=1}^{M} \log(1 - r(t_i + m\Delta t)\Delta t) \approx -\sum_{m=1}^{M} r(t_i + m\Delta t)\Delta t$$

Taking the limit $\Delta t \to 0$ and exponentiating again shows that

$$\mathbf{Pr}[\text{no spikes in } (t_i, t_{i+1})] = \exp\left(-\int_{t_i}^{t_{i+1}} r(t)dt\right)$$

Hence

$$\rho(t_1, \ldots t_n) = \prod_{i=1}^{n} r(t_i) \exp\left(-\int_0^T r(t)dt\right) \tag{6.62}$$

In the case of a time-dependent rate, one generates x_{rand} at each time step and a spike is fired if $r(t)\Delta t > x_{rand}$.

6.4 Stochastic Population Models

The discussion of neural variability in Sect. 6.3 motivates the incorporation of noise directly into rate-based models, without explicitly modeling spike variability. One approach is to introduce noise into a rate-based network model using extrinsic noise sources [21, 84, 184, 297]. An alternative approach is to assume that noise arises intrinsically as a collective population effect. A number of methods involve carrying out some form of dimension reduction of a network of synaptically coupled spiking neurons. These include population density methods [395, 468, 477], mean-field the-

ories [21, 86, 87], and Boltzmann-like kinetic theories [90, 100, 517]. However, such methods tend to consider either fully connected or sparsely connected networks and simplified models of spiking neurons such as the integrate-and-fire (IF) model. Nevertheless, as discussed in Sect. 6.3, one important feature of spiking networks is that they can support an asynchronous state in which individual neurons exhibit Poisson-like statistics, whereas the total population activity can be expressed in terms of a characteristic activation or gain function [2, 86, 87, 213, 519]. Formally speaking, the asynchronous state only exists in the thermodynamic limit $N \to \infty$, where N determines the size of the population. This then suggests a possible source of intrinsic noise at the network level arises from fluctuations about the asynchronous state due to finite size effects [57, 220, 412, 425, 597]; this is distinct from intrinsic noise at the single-cell level due to channel fluctuations and it is assumed that the latter is negligible at the population level. The presence of finite size effects has motivated the development of a closer analogy between intrinsic noise in biochemical networks (including ion channel kinetics) and neural networks [68, 69, 72], based on extensions of the neural master equation introduced by Buice et al. [91, 92]; see also [473]. In this section, we describe the master equation framework for stochastic neural population dynamics.

6.4.1 Neural Master Equations

One way to incorporate intrinsic noise at the population level is to treat the output activity of a local homogeneous population as a discrete stochastic variable $A_\alpha(t)$ rather than the instantaneous firing rate $a_\alpha = F(u_\alpha)$ [68, 91, 92]:

$$A_\alpha(t) = \frac{N_\alpha(t)}{N\Delta t}, \tag{6.63}$$

where $N_\alpha(t)$ is the number of neurons in the αth population that fired in the time interval $[t-\Delta t, t]$ and Δt is the width of a sliding window that counts spikes. The discrete stochastic variables $N_\alpha(t)$ are taken to evolve according to a one-step jump Markov process:

$$N_\alpha(t) \to N_\alpha(t) \pm 1: \quad \text{transition rate } \omega_\pm(U_\alpha(t), N_\alpha(t)), \tag{6.64}$$

with the synaptic current $U_\alpha(t)$ given by (for exponential synapses)

$$\tau dU_\alpha(t) = \left[-U_\alpha(t) + \sum_{\beta=1}^{M} w_{\alpha\beta} A_\beta(t) \right] dt, \tag{6.65}$$

where, for convenience, we have rescaled the weights according to $w_{\alpha\beta} \to w_{\alpha\beta}/\tau$. The transition rates are taken to be (cf. [68])

$$\omega_+(u_\alpha,n_\alpha)\to\omega_+(u_\alpha)=\frac{N\Delta t}{\tau_a}F(u_\alpha),\quad \omega_-(u_\alpha,n_\alpha)\to\omega_-(n_\alpha)=\frac{n_\alpha}{\tau_a}. \tag{6.66}$$

We see that the transition rate ω_+ depends on U_α, with the latter itself coupled to the associated jump Markov according to Eq. (6.65), which is only defined between jumps, during which $U_\alpha(t)$ evolves deterministically. Hence, the resulting stochastic process defined by Eqs. (6.63), (6.64), (6.65) and (6.66) provides an example of a stochastic hybrid system at the population neuron level, just as stochastic ion channel gating provides an example at the molecular level (Sect. 1.5). It is important to note that the time constant τ_a cannot be identified directly with membrane or synaptic time constants. Instead, it determines the relaxation rate of a local population to the instantaneous firing rate.

A. Case $\tau\to 0$ (fast synapses). In the limit $\tau\to 0$, Eq. (6.65) implies that the continuous variables $U_\alpha(t)$ can be eliminated by setting $U_\alpha(t)=\sum_\beta w_{\alpha\beta}A_\alpha(t)$. This then leads to a pure birth–death process for the discrete variables $N_\alpha(t)$. That is, let $P(\mathbf{n},t)=\text{Prob}[\mathbf{N}(t)=\mathbf{n}]$ denote the probability that the network of interacting populations has configuration $\mathbf{n}=(n_1,n_2,\ldots,n_M)$ at time $t,t>0$, given some initial distribution $P(\mathbf{n},0)$ with $0\le n_\alpha\le N$. The probability distribution then evolves according to the birth–death master equation [68, 91, 92]

$$\frac{dP(\mathbf{n},t)}{dt}=\sum_\alpha\left[(\mathbb{T}_\alpha-1)\left(\omega_\alpha^-(\mathbf{n})P(\mathbf{n},t)\right)+(\mathbb{T}_\alpha^{-1}-1)\left(\omega_\alpha^+(\mathbf{n})P(\mathbf{n},t)\right)\right], \tag{6.67}$$

where

$$\omega_\alpha^+(\mathbf{n})=\frac{N\Delta t}{\tau_a}F\left(\sum_\beta w_{\alpha\beta}n_\alpha/N\Delta t\right),\quad \omega_\alpha^-(\mathbf{n})=\frac{n_\alpha}{\tau_a}, \tag{6.68}$$

and $\mathbb{T}_\alpha$ is a translation operator: $\mathbb{T}_\alpha^{\pm 1}F(\mathbf{n})=F(\mathbf{n}_{\alpha\pm})$ for any function F with $\mathbf{n}_{\alpha\pm}$ denoting the configuration with n_α replaced by $n_\alpha\pm 1$. Equation (6.67) is supplemented by the boundary conditions $P(\mathbf{n},t)\equiv 0$ if $n_\alpha=N+1$ or $n_\alpha=-1$ for some α. The neural master equation (6.67) has two versions depending on the choice of Δt. First, fixing $\Delta t=1$ leads to the Bressloff version of the master equation. For large but finite N, the master equation (6.67) can be approximated by a Fokker–Planck equation using a Kramers–Moyal or system-size expansion, so that the population activity A_α evolves according to a Langevin equation [68]. Introduce the rescaled variables $a_\alpha=n_\alpha/N$ and corresponding transition rates $\Omega_\alpha^-(\mathbf{a})=a_\alpha/\tau_a$ and $\Omega_\alpha^+(\mathbf{a})=\tau_\alpha^{-1}F\left(\sum_\beta w_{\alpha\beta}a_\beta\right)$. Carrying out a Kramers–Moyal expansion to second order then leads to the multivariate FP equation

$$\frac{\partial P(\mathbf{a},t)}{\partial t}=-\sum_{\alpha=1}^M\frac{\partial}{\partial a_\alpha}\left[\mathscr{A}_\alpha(\mathbf{a})P(\mathbf{a},t)\right]+\frac{1}{2N}\sum_{\alpha=1}^M\frac{\partial^2}{\partial a_\alpha^2}\left[\mathscr{B}_\alpha(\mathbf{a})P(\mathbf{a},t)\right] \tag{6.69}$$

with

$$\mathscr{A}_\alpha(\mathbf{a})=\Omega_\alpha^+(\mathbf{a})-\Omega_\alpha^-(\mathbf{a}),\quad \mathscr{B}_\alpha(\mathbf{a})=\Omega_\alpha^+(\mathbf{a})+\Omega_\alpha^-(\mathbf{a}). \tag{6.70}$$

The solution to the Fokker–Planck equation (6.69) determines the probability density function for a corresponding stochastic process $\mathbf{A}(t)=(A_1(t),\ldots,A_M(t))$, which evolves according to a neural Langevin equation or SDE of the form

$$dA_\alpha = \mathscr{A}_\alpha(\mathbf{A})dt + \frac{1}{\sqrt{N}} b_\alpha(\mathbf{A})dW_\alpha(t). \tag{6.71}$$

with $b_\alpha(\mathbf{x})^2 = \mathscr{B}_\alpha(\mathbf{x})$. Here $W_\alpha(t)$ denotes an independent Wiener process such that

$$\langle dW_\alpha(t)\rangle = 0, \quad \langle dW_\alpha(t)dW_\beta(s)\rangle = \delta_{\alpha,\beta}\delta(t-s)dtds. \tag{6.72}$$

In the thermodynamic limit $N \to \infty$, we recover the activity-based mean-field equation

$$\tau_\alpha \frac{da_\alpha}{dt} = \mathscr{A}_\alpha(\mathbf{a}) = -a_\alpha(t) + F(\sum_\beta w_{\alpha\beta} a_\alpha(t)). \tag{6.73}$$

Note that the multiplicative noise in Eq. (6.71) is interpreted in the sense of Ito, which follows from the form of the FP equation (6.69); see Sect. 1.7.

A rigorous probabilistic treatment of the thermodynamic limit of the neural master equation has also been developed [89], extending previous work on chemical master equations [351]. However, as we noted within the context of stochastic ion channels in Sect. 1.5, the diffusion approximation breaks down when considering noise-induced transitions between multistage states. It is then necessary to use a WKB approximation of the master equation together with matched asymptotics [69]. The second version of the neural master equation, which was introduced by Buice et al. [91, 92], is obtained by taking the limit $N \to \infty, \Delta t \to 0$ such that $N\Delta t = 1$. In this case there is no small parameter that allows one to construct a Langevin approximation to the master equation. Nevertheless, it is possible to determine the moment hierarchy of the master equation using path integral methods or factorial moments, based on the observation that the network operates in a Poisson-like regime. The role of the sliding window size Δt is crucial in understanding the difference between the two versions of the master equation. First, it should be emphasized that the stochastic models are keeping track of *changes* in population spiking activity. If the network is operating close to an asynchronous state for large N, then one-step changes in population activity could occur relatively slowly, so there is no need to take the limit $\Delta t \to 0$. On the other hand, if population activity is characterized by a Poisson process, then it is necessary to take the limit $\Delta t \to 0$ in order to maintain a one-step process. However, given the existence of an arbitrarily small time scale Δt, it is no longer clear that one is justified in ignoring synaptic dynamics by taking the limit $\tau \to 0$ in Eq. (6.65).

B. Case $\tau \gg \tau_a > 0$ (stochastic hybrid system). Now suppose that $\tau > 0$ in the full stochastic model given by (6.63)–(6.66), with $N \to \infty$, $\Delta t \to 0$ such that $N\Delta t = 1$. Denote the random state of the full model at time t by $\{(U_\alpha(t), N_\alpha(t)); \alpha = 1,\ldots,M\}$. Introduce the corresponding probability density

$$\text{Prob}\{U_\alpha(t) \in (u_\alpha, u_\alpha + du), N_\alpha(t) = n_\alpha; \alpha = 1, \ldots, M\} = p(\mathbf{u}, \mathbf{n}, t)d\mathbf{u}, \quad (6.74)$$

with $\mathbf{n} = (n_1, \ldots, n_M)$ and $\mathbf{u} = (u_1, \ldots, u_M)$. It follows from Eqs. (6.63)–(6.66) that the probability density evolves according to the Chapman–Kolmogorov (CK) equation [82]

$$\begin{aligned} &\frac{\partial p}{\partial t} + \frac{1}{\tau}\sum_\alpha \frac{\partial [v_\alpha(\mathbf{u}, \mathbf{n}) p(\mathbf{u}, \mathbf{n}, \mathbf{t})]}{\partial u_\alpha} \\ &\quad = \frac{1}{\tau_a}\sum_\alpha \left[(\mathbb{T}_\alpha - 1)\left(\omega_-(n_\alpha) p(\mathbf{u}, \mathbf{n}, t)\right) + (\mathbb{T}_\alpha^{-1} - 1)\left(\omega_+(u_\alpha) p(\mathbf{u}, \mathbf{n}, t)\right)\right], \end{aligned} \quad (6.75)$$

with

$$\omega_+(u_\alpha) = F(u_\alpha), \quad \omega_-(n_\alpha) = n_\alpha, \quad v_\alpha(\mathbf{u}, \mathbf{n}) = -u_\alpha + \sum_\beta w_{\alpha\beta} n_\beta. \quad (6.76)$$

Equation (6.75) can be rewritten in the more compact form (see also (1.143))

$$\frac{\partial p}{\partial t} = -\frac{1}{\tau}\sum_{\alpha=1}^{M} \frac{\partial}{\partial u_\alpha}(v_\alpha(\mathbf{u}, \mathbf{n}) p(\mathbf{u}, \mathbf{n}, t)) + \frac{1}{\tau_a}\sum_{\mathbf{m}} A(\mathbf{n}, \mathbf{m}; \mathbf{u}) p(\mathbf{u}, \mathbf{m}, t). \quad (6.77)$$

The drift "velocities" $v_\alpha(\mathbf{u}, \mathbf{n})$ for fixed $\mathbf{n}$ represent the piecewise deterministic synaptic dynamics according to

$$\tau \frac{du_\alpha}{dt} = v_\alpha(\mathbf{u}, \mathbf{n}), \quad \alpha = 1, \ldots, M, \quad (6.78)$$

and A represents the $\mathbf{u}$-dependent transition matrix for the jump Markov process.

For fixed $\mathbf{u}$, the matrix $A(\mathbf{n}, \mathbf{m}; \mathbf{u})$ is irreducible (which means that there is a nonzero probability of transitioning, possibly in more than one step, from any state to any other state in the jump Markov process) and has a simple zero eigenvalue. In particular, $\sum_{\mathbf{n}} A(\mathbf{n}, \mathbf{m}; \mathbf{u}) = 0$ for all $\mathbf{m}$, that is, $\mathbf{n} = (1, 1, \ldots, 1)^T$ is the left null vector of A. The Perron–Frobenius theorem (for large but finite N) ensures that all other eigenvalues of A are negative and the continuous-time Markov process for fixed $\mathbf{u}$,

$$\frac{dp(\mathbf{u}, \mathbf{n}, t)}{dt} = \frac{1}{\tau_a}\sum_{\mathbf{m} \in I} A(\mathbf{n}, \mathbf{m}; \mathbf{u}) p(\mathbf{u}, \mathbf{m}, t),$$

has a globally attracting steady-state $\rho(\mathbf{u}, \mathbf{n})$ such that $p(\mathbf{u}, \mathbf{n}, t) \to \rho(\mathbf{u}, \mathbf{n})$ as $t \to \infty$. The steady-state equation is

$$\begin{aligned} 0 &= \sum_{\mathbf{m}} A(\mathbf{n}, \mathbf{m}; \mathbf{u}) \rho(\mathbf{u}, \mathbf{m}) \\ &= \sum_{\alpha=1}^{M} \left[(n_\alpha + 1)\rho(\mathbf{u}, \mathbf{n} + \mathbf{e}_\alpha) - n_\alpha \rho(\mathbf{u}, \mathbf{n}) + F(u_\alpha)(\rho(\mathbf{u}, \mathbf{n} - \mathbf{e}_\alpha) - \rho(\mathbf{u}, \mathbf{n}))\right], \end{aligned}$$

where $[\mathbf{e}_\alpha]_\beta = \delta_{\alpha,\beta}$. The solution can be factorized as $\rho(\mathbf{u},\mathbf{n}) = \prod_{\beta=1}^{M} \rho_1(u_\beta, n_\beta)$ with

$$0 = \sum_{\alpha=1}^{M} \left[\prod_{\beta\neq\alpha} \rho_1(u_\beta, n_\beta) \right] [J(u_\alpha, n_\alpha + 1) - J(u_\alpha, n_\alpha)],$$

where

$$J(u,n) = n\rho_1(u,n) - F(u)\rho_1(u,n-1).$$

Since $\rho_1(u,-1) \equiv 0$, it follows that $J(u,n) = 0$ for all n. Hence,

$$\rho_1(u,n) = \rho(u,0) \prod_{m=1}^{n} \frac{F(u)}{m} = \rho(u,0) \frac{F(u)^n}{n!}, \tag{6.79}$$

and the corresponding normalized density is a Poisson process with rate $F(u)$

$$\rho_1(u,n) = \mathrm{e}^{-F(u)} \frac{F(u)^n}{n!}. \tag{6.80}$$

There are two time scales in the CK equation (6.75), the synaptic time constant τ and the time constant τ_a, which characterizes the relaxation rate of population activity. In the limit $\tau \to 0$ for fixed τ_a, Eq. (6.75) reduces to the neural master equation (6.67) with $\mathbf{u} = \mathbf{u}(\mathbf{n})$ such that $v_\alpha(\mathbf{u}(\mathbf{n}),\mathbf{n}) = 0$. On the other hand, if $\tau_a \to 0$ for fixed τ, then we obtain deterministic voltage- or current-based mean-field equations

$$\begin{aligned} \tau \frac{du_\alpha}{dt} &= \langle v_\alpha \rangle(\mathbf{u}(t)) \equiv \sum_{\mathbf{n}} v_\alpha(\mathbf{u}(t),\mathbf{n}) \rho(\mathbf{u}(t),\mathbf{n}) \\ &= -u_\alpha(t) + \sum_{\beta=1}^{M} w_{\alpha\beta} \sum_{\mathbf{n}} n_\beta \rho(\mathbf{u}(t),\mathbf{n}). \end{aligned} \tag{6.81}$$

Since $\rho(\mathbf{u},\mathbf{n})$ is given by product of independent Poisson processes with rates $F(u_\alpha)$, consistent with the operating regime of the Buice *et. al.* master equation [91, 92], it follows that

$$\langle n_\beta \rangle = F(u_\beta), \tag{6.82}$$

and (6.81) reduces to the standard voltage- or current-based activity equation. Now suppose that the network operates in the regime $0 < \tau_a/\tau \equiv \varepsilon \ll 1$, for which there are typically a large number of transitions between different firing states $\mathbf{n}$ while the synaptic currents $\mathbf{u}$ hardly change at all. This suggests that the system rapidly converges to the (quasi) steady state $\rho(\mathbf{u},\mathbf{n})$, which will then be perturbed as $\mathbf{u}$ slowly evolves. The resulting perturbations can be analyzed using a quasi-steady-state (QSS) diffusion or adiabatic approximation, in which the CK equation (6.75) is approximated by a Fokker–Planck equation [82]; see Sect. 1.6. However, when considering escape from a metastable state, it is necessary to use the WKB method outlined in Sect. 1.6, as will be illustrated below.

6.4.2 Metastability in a One-Population Model

One of the useful features of the master equation formulation of stochastic population dynamics is that one can apply methods previously used to analyze jump Markov processes at the cellular level. We will illustrate this by considering a first passage time (FPT) problem for a one-population version of the CK equation (6.75), which exhibits bistability in the deterministic limit [82]. This is analogous to the problem of spontaneous action potential generation presented in Sect. 1.6. In the case of a single homogeneous population of excitatory neurons, (6.75) becomes

$$\frac{\partial p}{\partial t}+\frac{\partial [v(u,n)p(u,n,t)]}{\partial u}=\frac{1}{\varepsilon}\sum_m A(n,m;u)p(u,m,t) \tag{6.83}$$

with drift term

$$v(u,n)=-u+n, \tag{6.84}$$

and tridiagonal transition matrix

$$A(n,n-1;u)=F(u),\quad A(n,n;u)=-F(u)-n,\quad A(n,n+1;u)=n+1. \tag{6.85}$$

As shown in Sect. 6.4.1, the steady-state density for A is given by a Poisson process,

$$\rho(u,n)=\frac{[F(u)]^n \mathrm{e}^{-F(u)}}{n!}, \tag{6.86}$$

and the mean-field equation obtained in the $\varepsilon\to 0$ limit is

$$\frac{du}{dt}=\sum_{n=0}^{\infty} v(u,n)\rho(u,n)=-u+F(u). \tag{6.87}$$

If F is given by the sigmoid (1.14), it is straightforward to show that (6.87) exhibits bistability for a range of thresholds and gains; see Fig. 6.6.

The CK equation (6.83) is identical in form to (1.143) under the change of variables $u\to v$, where v is voltage, and $v(u,n)\to F(v,n)$. It follows that the general analysis developed in Sect. 1.6 can be applied directly to the stochastic neural population model. In particular, the escape rate λ_0 from the low activity state u_- is given by (1.191). As in the case of stochastic ion channels, there are three basic steps needed in order to evaluate λ_0 using the particular form of the drift v and transition matrix A [72]:

(1) Find the unique nontrivial positive eigenfunction $\psi_n(u)=R^{(0)}(u,n)$ and associated eigenvalue $\mu(u)=-\Phi_0'(u)$. In the case of the neural population model, Eq. (1.171) takes the explicit form

$$F(u)\psi_{n-1}(u)-(F(u)+n)\psi_n(u)+(n+1)\psi_{n+1}(u)=\mu(-u+n)\psi_n(u). \tag{6.88}$$

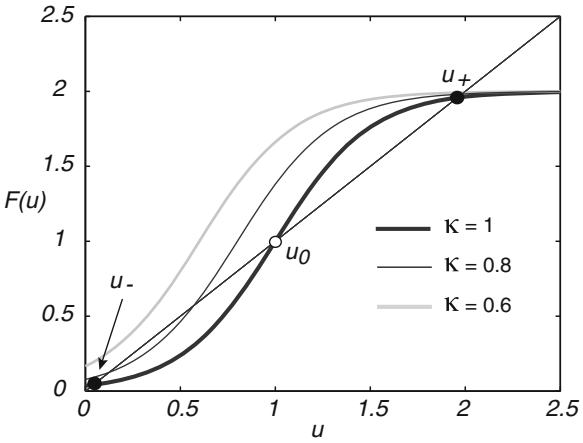

Fig. 6.6 Bistability in the deterministic network satisfying $\dot{u} = -u + F(u)$ with F given by the sigmoid (1.14) for gain $\eta = 4$ and threshold $\kappa = 1.0$, $F_0 = 2$. There exist two stable fixed points $u_\pm$ separated by an unstable fixed point u_0. As the threshold κ is reduced the network switches to a monostable regime

Trying a solution for ψ of the form

$$\psi_n(u) = \frac{\Lambda(u)^n}{n!} \tag{6.89}$$

yields the following equation relating Λ and the corresponding eigenvalue μ:

$$\left[\frac{F(u)}{\Lambda} - 1\right] n + \Lambda - F(u) = \mu(u)(-u + n).$$

We now collect terms independent of n and linear in n, respectively, to obtain the pair of equations

$$\mu = \left[\frac{F(u)}{\Lambda} - 1\right], \quad \Lambda = F(u) - \mu u.$$

We deduce that

$$\Lambda = u, \quad \mu = \left[\frac{F(u)}{u} - 1\right], \tag{6.90}$$

and the normalized eigenfunction is

$$\psi_n(u) = \frac{u^n}{n!} \mathrm{e}^{-u}. \tag{6.91}$$

Note that $\mu(u)$ vanishes at the fixed points u_-, u_* of the mean-field equation (6.87) with $\mu(u) > 0$ for $0 < u < u_-$ and $\mu(u) < 0$ for $u_- < u < u_*$. Moreover, comparing Eq. (6.86) with (6.91) establishes that $\psi_n(u) = \rho(u,n)$ at the fixed points $u_*, u_\pm$. In conclusion $R^{(0)}(u,n) = \psi_n(u)$ and the effective potential Φ_0 is given by

$$\Phi_0(u) = -\int_{u_-}^{u^*} \mu(y)dy. \tag{6.92}$$

The effective potential is defined up to an arbitrary constant, which has been fixed by setting $\Phi_0(u_-) = 0$.

(2) Determine the null eigenfunction $\eta_n(u) = S(u,n)$ of Eq. (1.174), which becomes

$$F(u)\eta_{m+1} - (F(u)+m)\eta_m + m\eta_{m-1} = \mu(u)[-u+m]\eta_m. \tag{6.93}$$

Trying a solution of the form $\eta_m = \Gamma^m$ yields

$$(F(u))\Gamma - (F(u)+m) + m\Gamma^{-1} = \mu(u)[-u+m]. \tag{6.94}$$

Γ is then determined by canceling terms linear in m, which finally gives

$$\eta_n(u) = \left(\frac{u}{F(u)}\right)^n. \tag{6.95}$$

(3) Calculate the generalized eigenvector $\zeta_n = \hat{S}(u_*,n)$ of Eq. (1.186), which reduces to

$$F(u_*)\zeta_{n+1} + n\zeta_{n-1} - (F(u_*)+n)\zeta_n = u_* - n. \tag{6.96}$$

It is straightforward to show that this has the solution $\zeta_n = n$ (up to an arbitrary constant that does not contribute to the principal eigenvalue). It follows from Eq. (6.86) that the factor $B(u_*)$ defined by (1.190) is

$$\begin{aligned} B(u_*) &= \sum_{n=0}^{\infty} \rho(u_*,n)\left[-u_*n + n^2\right] \\ &= \left[-u_*\langle n\rangle + \langle n^2\rangle\right]. \end{aligned} \tag{6.97}$$

Recall that $\rho(u,n)$ is given by a Poisson density with rate $F(u)$, which implies that $\langle n^2\rangle = \langle n\rangle + \langle n\rangle^2$ with $\langle n\rangle = F(u)$. Therefore,

$$B(u_*) = F(u_*)\left[2F(u_*) - u_*\right], \tag{6.98}$$

which reduces to $B(u_*) = F(u_*)^2$ since $u^* = F(u^*)$ at a fixed point.

It is instructive to compare the effective potential Φ_0 obtained using the WKB approximation with the potential obtained using the FP equation (1.146) based on the QSS approximation. First, substitute (6.86), (6.84), and (6.85) into Eqs. (1.147) and (1.148) under the change of variables $u \to v$ and $v(u,n) \to F(v,n)$. We find that $Z(u,n) = n\rho(u,n)$ so that

$$\mathscr{D}(u) = [-u\langle n\rangle + w\langle n^2\rangle] = B(u). \tag{6.99}$$

The steady-state solution of the FP equation (1.146) takes the form $C(u) \sim \exp^{-\hat{\Phi}_0(u)/\varepsilon}$ with stochastic potential

$$\hat{\Phi}_0(u) = -\int^u \frac{\mathscr{F}(y)}{\mathscr{D}(y)}dy = -\int^u \frac{-y+F(y)}{wF(y)[2F(y)-y]}dy. \tag{6.100}$$

Note that $\hat{\Phi}_0$ differs from the potential Φ_0, Eq. (6.92), obtained using the more accurate WKB method. Equations (6.90) and (6.92) show that the latter has the integral form

$$\Phi_0(u) = -\int^u \frac{1}{w}\left[\frac{wF(y)}{y} - 1\right]dy. \tag{6.101}$$

Thus, there will be exponentially large differences between the steady states for small ε.

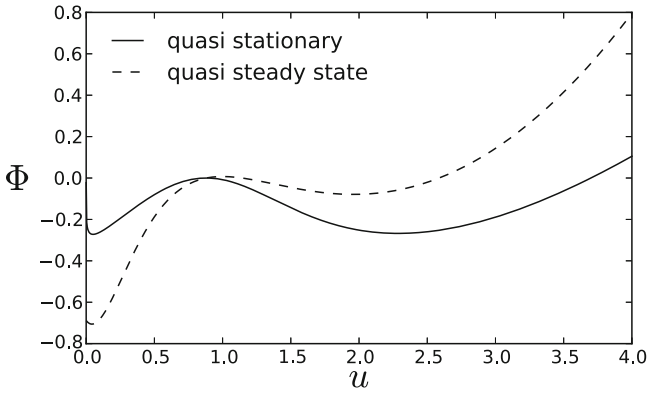

Fig. 6.7 Comparison of the double-well potentials $\Phi_0(u)$ and $\hat{\Phi}_0(u)$ obtained using the quasistationary approximation and the QSS diffusion approximation, respectively [82]. Parameter values are chosen so that deterministic network is bistable: $F_0 = 2.3$, $\gamma = 4$, and $\kappa = 1$

In Fig. 6.7, we plot the potential function Φ_0 of Eq. (6.101), which is obtained using the quasistationary approximation in a parameter regime for which the underlying deterministic network is bistable. We also plot the corresponding potential function $\hat{\Phi}_0$ of Eq. (6.100), under the QSS diffusion approximation. The differences between the two lead to exponentially large differences in estimates for the mean exit times when ε is small. The mean exit time from the left and right well is shown in Fig. 6.8. Solid curves show the analytical approximation $T \sim 1/\lambda_0$, where λ_0 is given by (1.191), as a function of $1/\varepsilon$. For comparison, the mean exit time computed from averaged Monte Carlo simulations of the full stochastic system is shown as symbols. As expected, the log of the mean exit time is an asymptotically linear function of $1/\varepsilon$, and this is confirmed by Monte Carlo simulations. The slope is determined by the depth of the potential well, and the vertical shift is determined by the prefactor. Also shown is the corresponding MFPT calculated using the QSS diffusion approximation (dashed curves), which is typically several orders of magnitude out and validates the relative accuracy of the quasistationary approximation.

One of the applications of noise-induced transitions between metastable states in a stochastic population model is to the study of switching between up and down states during slow-wave sleep; see Sect. 5.1. For example, Holcman and Tsodyks

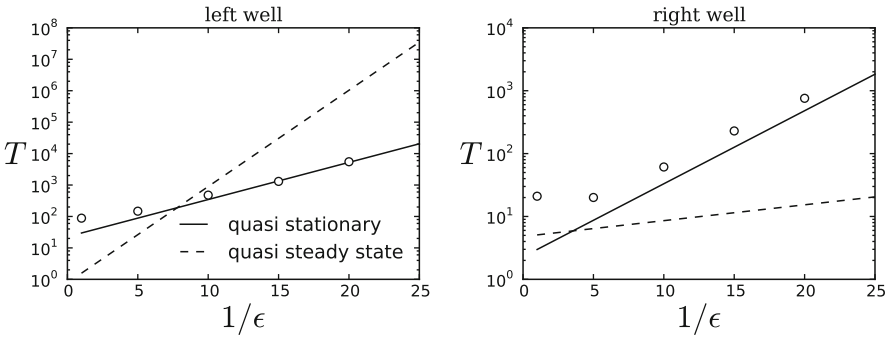

Fig. 6.8 Mean exit time from the left and right well calculated using the quasistationary approximation (*solid line*) and the QSS diffusion approximation (*dashed line*) [82]. The *open circles* represent data points obtained by numerically solving the corresponding jump velocity Markov process using the Gillespie algorithm. Parameter values are the same as in Fig. 6.7

[282] consider an extension of the deterministic one-population model (6.87) by including the effects of synaptic depression and extrinsic noise. The voltage-based model equations take the form

$$\tau \frac{du}{dt} = -u + qw\chi F(u) + \sqrt{\tau}\sigma\xi(t) + I(t) \tag{6.102a}$$

$$\frac{dq}{dt} = \frac{1-q}{\tau_q} - \chi q F(V), \tag{6.102b}$$

where $q(t)$ is the depression variable, $\xi(t)$ is a white noise term, $I(t)$ is an external input, and the constant χ is known as a utilization parameter. The firing rate function is taken to be a linear threshold function $F(V) = \eta[u-\kappa]_+$. In the absence of noise ($\sigma = 0$) and external inputs ($I = 0$), the deterministic system undergoes a series of bifurcations as the weight w is increased. For sufficiently small w, there exists a globally attracting stable fixed point which is a low activity or down state. At a critical value of w, a saddle and unstable node appear, with the latter undergoing a subcritical Hopf bifurcation at a second critical value of w—this generates a stable up state inside an unstable limit cycle. The system then exhibits bistability such that noise-induced transitions from the down to the up state have to cross both the separatrix of the saddle and the unstable limit cycle. The resulting fluctuations in activity are suggestive of slow-wave oscillations observed in cortical slices [549].

6.4.3 Metastability in a Two-Population Model

It turns out that the analysis of metastability in a one-population model can be extended to higher-dimensional networks [72]. Consider, for example, the E–I network of Sect. 6.2. The corresponding CK equation (6.75) becomes

$$\frac{\partial p}{\partial t} = -\frac{\partial}{\partial x}(vp) - \frac{\partial}{\partial y}(\tilde{v}p) + \frac{1}{\varepsilon}\sum_{\mathbf{m}} A(\mathbf{n},\mathbf{m};\mathbf{x})p(\mathbf{x},\mathbf{n}) \tag{6.103}$$

where $\mathbf{x} = (x,y)$, $\mathbf{n} = (n_x,n_y)$, the drift terms are

$$v(x,n_x,n_y) = -x + [w_{EE}n_x - w_{EI}n_y], \tag{6.104}$$
$$\tilde{v}(y,n_x,n_y) = -y + [w_{IE}n_x - w_{II}n_y], \tag{6.105}$$

and A has the nonzero components

$$A(n_x,n_y,n_x-1,n_y;\mathbf{x}) = F(x), \quad A(n_x,n_y,n_x,n_y-1;\mathbf{x}) = F(y), \tag{6.106}$$

$$A(n_x,n_y,n_x+1,n_y;\mathbf{x}) = n_x+1, \quad A(n_x,n_y,n_x,n_y+1;\mathbf{x}) = n_y+1, \tag{6.107}$$

and

$$A(n_x,n_y,n_x,n_y;\mathbf{x}) = -[F(x)+F(y)+n_x+n_y]. \tag{6.108}$$

Here x and y denote the excitatory and inhibitory population variables a_E, a_I, respectively. In the limit $\varepsilon \to 0$, we recover the deterministic equations (6.20). However, in contrast to Sect. 6.2, it is now assumed that the E–I network operates in a bistable regime as illustrated in Fig. 6.9.

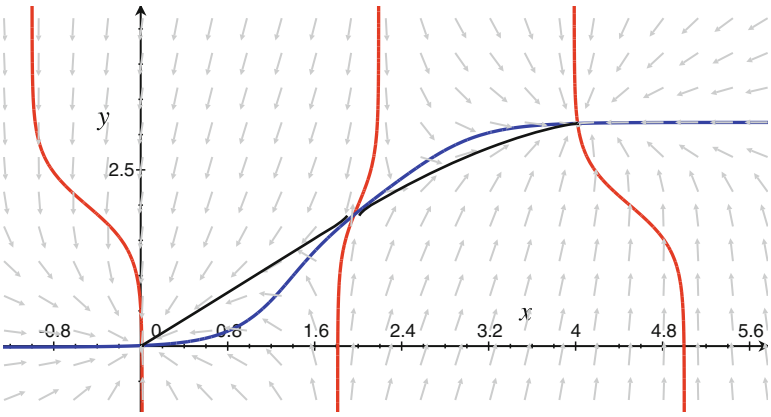

Fig. 6.9 Bistability in an E–I network. The x-nullcline through the saddle is its stable manifold and acts as the separatrix Σ between the two stable fixed points. Two deterministic trajectories are shown (directed *black curves*), starting from either side of the unstable saddle and ending at a stable fixed point. Parameter values are $F_0 = 1$, $\gamma = 3$, $\kappa = 2$, $w_{EE} = 5$, $w_{EI} = 1$, $w_{IE} = 9$, and $w_{II} = 6$

Again the MFPT can be identified as the inverse of the principal eigenvalue λ_0 of the associated linear operator on the right-hand side of (6.103). However, now the analysis is more complicated, since one has to consider stochastic trajectories crossing different points along the separatrix Σ between the two metastable states.

Nevertheless, the various steps in the calculation of λ_0 proceed along similar lines to the one-population model. That is, a spectral projection method can be used to express λ_0 in terms of the inner product of a quasistationary density with a corresponding adjoint eigenfunction. The former can be calculated using a WKB approximation, except that now one has to determine the stochastic potential Φ_0 by solving an equation of the form [82]

$$\mathscr{H} \equiv -x\mathscr{P}_x - y\mathscr{P}_y - F(x) - F(y) + \Lambda_x(x, \mathscr{P}_x, \mathscr{P}_y) + \Lambda_y(y, \mathscr{P}_x, \mathscr{P}_y) = 0, \quad (6.109)$$

where

$$\mathscr{P}_x = \frac{\partial \Phi_0}{\partial x} \quad \mathscr{P}_y = \frac{\partial \Phi_0}{\partial y}, \quad (6.110)$$

and

$$\Lambda_x = \frac{F(x)}{1 - w_{EE}\mathscr{P}_x - w_{IE}\mathscr{P}_y}, \quad \Lambda_y = \frac{F(y)}{1 + w_{EI}\mathscr{P}_x + w_{II}\mathscr{P}_y} \quad (6.111)$$

Mathematically speaking, Eq. (6.109) is identical to a stationary Hamilton–Jacobi equation for a classical particle with $\mathscr{H}$ identified as the Hamiltonian (see also Sect. 4.4). A trajectory of the particle is given by the solution of Hamilton's equations

$$\begin{aligned} \frac{dx}{dt} &= \frac{\partial \mathscr{H}}{\partial \mathscr{P}_x}, \quad \frac{dy}{dt} = \frac{\partial \mathscr{H}}{\partial \mathscr{P}_y}, \\ \frac{d\mathscr{P}_x}{dt} &= -\frac{\partial \mathscr{H}}{\partial x}, \quad \frac{d\mathscr{P}_y}{dt} = -\frac{\partial \mathscr{H}}{\partial y} \end{aligned} \quad (6.112)$$

Here t is treated as a parameterization of trajectories rather than as a real-time variable. Given a solution curve $(x(t), y(t))$, known as a ray, the potential Φ_0 can be determined along the ray by solving the equation

$$\frac{d\Phi_0}{dt} \equiv \frac{\partial \Phi_0}{\partial x}\frac{dx}{dt} + \frac{\partial \Phi_0}{\partial y}\frac{dy}{dt} = \mathscr{P}_x\frac{dx}{dt} + \mathscr{P}_y\frac{dy}{dt}. \quad (6.113)$$

Thus, Φ_0 can be identified as the action along a zero-energy trajectory. One numerically solves for Φ_0 by considering Cauchy data in a neighborhood of the stable fixed point (x_-, y_-) [82].

The rays $(x(t), y(t))$ (i.e., solutions to Hamilton's equations (6.112) in the (x, y) plane) have an important physical meaning. The trajectory of the ray is the most likely trajectory or path leading away from a point in the neighborhood of a stable fixed point [160]. The rays shown in Fig. 6.10 are obtained by integrating Hamilton's equations (6.112) . These trajectories are only valid in one direction: away from the stable fixed points. For parameter values considered in Fig. 6.10, rays originating from the neighborhood of each stable fixed point cover separate regions, so that the most likely paths between points in each region are connected by deterministic trajectories starting at the boundary between the two regions. Note that this boundary is not the separatrix (gray curve). For example, a trajectory initially at the left fixed point which crosses the separatrix at the saddle would most likely follow

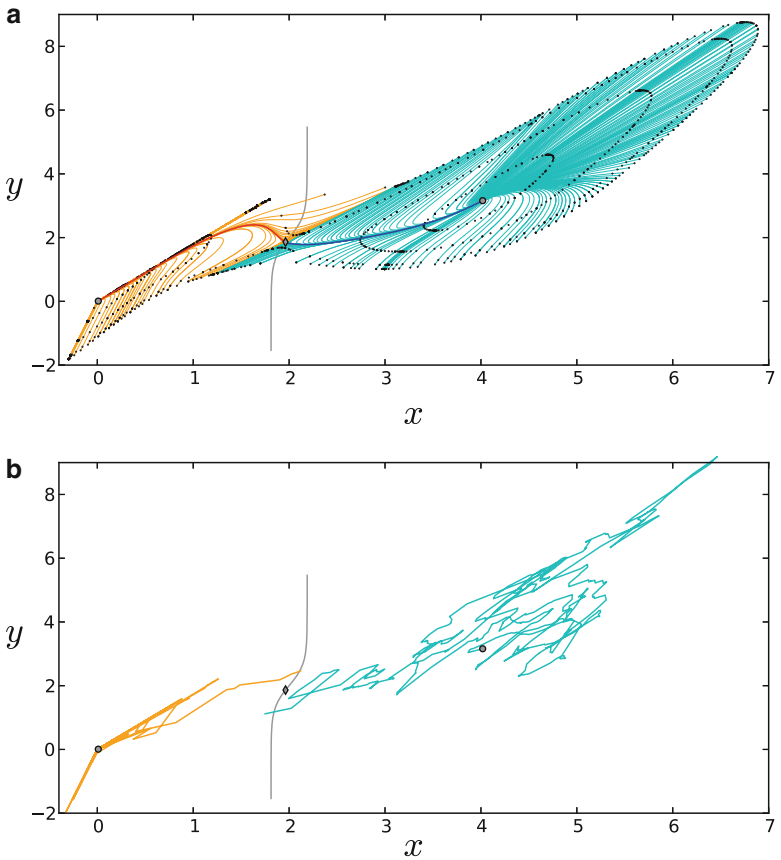

Fig. 6.10 (**a**) Characteristic paths of maximum likelihood for the 2D model. Rays originating from the left (right) stable fixed point are shown in *orange* (*cyan*), with the ray connecting to the saddle shown in *red* (*blue*). The *gray curve* is the separatrix Σ. Level curves of constant $\Phi_0(x,y)$ are shown as *black dots*. Each ray has four dots for different values of $\Phi_0(x,y)$. Rays originating from the left fixed point have dots at $\Phi = 0.1, 0.2, \Phi_* + 0.01, \Phi_* + 0.02$, and rays originating from the right fixed point have dots at $\Phi_0 = 0.19, 0.23, 0.28, 0.30$, where $\Phi_* = \Phi(x_*, y_*) = 0.28$. All rays terminate at $\Phi_0 = \Phi_* + 0.02$. (**b**) Sample trajectories of the two-population velocity jump Markov process, whose associated probability density evolves according to (6.83), are computed using the Gillespie algorithm with $\varepsilon = 0.05$ and $N\Delta t = 1$. (The maximum likelihood paths are independent of ε.) Other parameter values are the same as in Fig. 6.9 [72]

a ray towards the saddle and then follow a deterministic trajectory to the right fixed point. If a trajectory crosses the separatrix away from the saddle, it is most likely to cross the separatrix above the saddle when starting from the left fixed point and below the saddle when starting from the right fixed point. In Fig. 6.11, the probability density function for the y coordinate of the point on the separatrix reached by an exit trajectory is shown for each well (square symbols show the histogram for exit from the left well and likewise, 'o' symbols for the right well). Each density function is

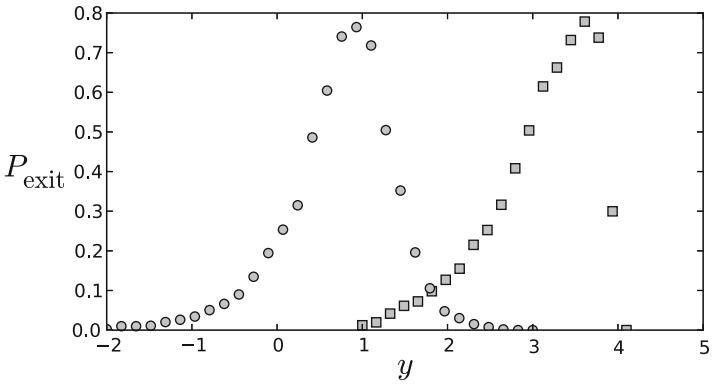

Fig. 6.11 The probability density for the exit point (y coordinate) where the separatrix is crossed by an exiting trajectory. Results are obtained by 10^2 Monte Carlo simulation with the same parameters as used in Fig. 6.9, with $\varepsilon = 0.08$. The *square* symbols show trajectories from the left well, and 'o' symbols show trajectories from the right well

peaked away from the saddle point, showing a phenomena known as saddle point avoidance [398, 559]. As $\varepsilon \to 0$, the two peaks merge at the saddle point. Although one might expect the saddle point to be the most likely exit point, since it is the point on the separatrix where the potential Φ_0 takes its minimum value, Fig. 6.11 shows that this is not necessarily true. Even though the most likely exit point is shifted from the saddle, the value of the potential around the saddle point still dominates the mean first exit time.

6.5 Spatially Structured Networks and Neural Fields

So far we have not made any assumptions about the topology of the underlying neural network, that is, the structure of the weight matrix $\mathbf{W}$ with components w_{ij}. If one looks at a region of cortex such as primary visual cortex (V1), one finds that it has a characteristic spatial structure, in which a high density of neurons (10^5 per mm^3 in primates) are distributed according to an approximately two-dimensional (2D) architecture. That is, the physical location of a vertical column of neurons within the two-dimensional cortical sheet often reflects the specific information processing role of that population of neurons. For example, in V1 there is an orderly retinotopic mapping of the visual field onto the cortical surface, with left and right halves of the visual field mapped onto right and left visual cortices, respectively. Superimposed upon this are additional two-dimensional maps reflecting the fact that neurons respond preferentially to stimuli with particular features such as local orientation [613]. (A more detailed description of the functional architecture of V1 is given in Sect. 8.1.) This suggests labeling neurons according to their spatial location in cortex. We now give a heuristic argument for how such labeling leads to a continuum neural field model of cortex, following along similar lines to Gerstner and Kistler [214].

For simplicity, consider a population of neurons distributed along a one-dimensional axis. (Extensions to higher dimensions proceed in a similar fashion.) Suppose that we partition space into segments of length d such that the number of neurons in segment $[nd,(n+1)d]$ is $N=\rho d$ where ρ is the cell density. We treat neurons in that interval as a homogeneous population of cells (cortical column) labeled by the integer n and assume that synaptic interactions between the nth and mth populations only depend on the discrete locations of the populations on the line. Writing $\Phi_{nm}(t)=\rho d\Phi(nd,md,t)$ and $u_n(t)=u(nd,t)$, Eq. (6.4) becomes

$$u(nd,t)=\rho d\sum_m\int_{-\infty}^{t}\Phi(nd,md,t-t')F(u(md,t'))dt'.$$

Taking the limit $d\to 0$, the summation on the right-hand side can be replaced by an integral to give

$$u(x,t)=\int_{-\infty}^{\infty}\int_{-\infty}^{t}\Phi(x,y,t-t')F(u(y,t'))dt'dy, \tag{6.114}$$

where we have absorbed the factor ρ into Φ. Following our derivation of the discrete voltage-based model (6.6), suppose that we can decompose the integral kernel as

$$\Phi(x,y,t)=w(x,y)\Phi(t),\quad \Phi(t)=\mathrm{e}^{-t/\tau}H(t).$$

That is, we assume that there is only one type of neuron so that the temporal kernel $\Phi(t)$ is independent of the presynaptic label y and the postsynaptic label x. Applying the differential operator $\mathbb{L}_t=\partial_t+\tau^{-1}$ to the integral equation for u then leads to the scalar neural field equation

$$\frac{\partial}{\partial t}u(x,t)=-\frac{u(x,t)}{\tau}+\int_{-\infty}^{\infty}w(x,y)F(u(y,t))dy. \tag{6.115}$$

Alternatively, we could have applied the differential operator $\mathbb{L}_t$ to the corresponding synaptic drive $z(x,t)=\int_{-\infty}^{t}\Phi(t-t')F(u(x,t'))dt'$ to obtain the activity-based neural field model

$$\frac{\partial}{\partial t}z(x,t)=-\frac{z(x,t)}{\tau}+F\left(\int_{-\infty}^{\infty}w(x,y)z(y,t)dy\right). \tag{6.116}$$

Following the same basic procedure, it is straightforward to incorporate into the neural field equation (6.115) or (6.116) additional features such as synaptic depression [329–331], adaptive thresholds [135, 329], and axonal propagation delays [16, 139, 296, 307, 382, 528, 603]. For example, a voltage-based neural field equation with synaptic depression takes the form

$$\begin{aligned}\frac{\partial}{\partial t}u(x,t)&=-\frac{u(x,t)}{\tau}+\int_{-\infty}^{\infty}w(x,y)q(y,t)F(u(y,t))dy,\\ \frac{\partial}{\partial t}q(x,t)&=\frac{1-q(x,t)}{\tau_q}-\beta q(x,t)F(u(x,t)),\end{aligned} \tag{6.117}$$

with $\beta = 1-\gamma$. In the case of axonal delays, $\tau_{ij} \to \tau(x,y)$ in the continuum limit. Assuming that an action potential propagates with constant speed v along the axon, then $\tau(x,y) = |x-y|/v$ so that the voltage-based equation (6.115) becomes

$$\frac{\partial}{\partial t}u(x,t) = -\frac{u(x,t)}{\tau} + \int_{-\infty}^{\infty} w(x,y)F(u(y,t-|x-y|/v))dy. \tag{6.118}$$

Two-dimensional versions of these various models are obtained by taking $x \to \mathbf{x} = (x_1,x_2)$ and $y \to \mathbf{y} = (y_1,y_2)$ with $d\mathbf{y} = dy_1 dy_2$.

Now suppose that there are M classes of neuron distributed along the line labeled by the population index $a = 1,\ldots M$. Equation (6.114) then generalizes to the multi-population integral equation

$$u_a(x,t) = \int_{-\infty}^{\infty}\int_{-\infty}^{t}\sum_{b=1}^{M} \Phi_{ab}(x,y,t-t')F_b(u_b(y,t'-|x-y|/v_{ab}))dt'dy. \tag{6.119}$$

We have included axonal delays with v_{ab} the conduction velocity along axonal projections from neurons of type b to neurons of type a. Assuming that $\Phi_{ab}(x,y,t) = w_{ab}(x,y)\Phi(t)$ with $\Phi(t) = \mathrm{e}^{-t/\tau}H(t)$, we obtain multi-population neural field equations:

$$\frac{\partial u_a}{\partial t} = -\frac{u_a(x,t)}{\tau} + \sum_{b=1}^{M}\int_{-\infty}^{\infty} w_{ab}(x,y)F_b(u_b(y,t-|x-y|/v_{ab}))dy, \tag{6.120}$$

and

$$\frac{\partial z_a}{\partial t} = -\frac{z_a(x,t)}{\tau} + F_b\left(\sum_{b=1}^{M}\int_{-\infty}^{\infty} w_{ab}(x,y)z_b(y,t-|x-y|/v_{ab})dy\right) \tag{6.121}$$

for $a = 1,\ldots,M$. The latter is a version of the *Wilson–Cowan equations* for cortical dynamics [675, 676]. Note that all synapses innervated by a particular type of neuron have the same sign. That is, if type b neurons are excitatory (inhibitory), then $w_{ab}(x,y) \geq 0$ ($w_{ab}(x,y) \leq 0$) for all $a = 1,\ldots,M$ and (x,y). Thus, one of the major reasons for considering more than one class of neuron is to incorporate both excitatory and inhibitory synapses. It can be argued that since excitatory and inhibitory synapses tend to have different time courses in response to action potentials, one should take $\Phi_{ab}(x,y,t) = w_{ab}(x,y)\Phi_b(t)$, suggesting that the activity-based model (6.121) with $\tau \to \tau_a$ is more biologically realistic than the voltage-based model, at least in the case of excitatory–inhibitory networks [173]. However, in practice, both versions of the neural field equations are used to model cortical dynamics. Since both versions exhibit very similar types of solution, and since most analytical results have been obtained for voltage-based neural fields, we will mainly focus on the latter.

Under certain additional simplifying assumptions, it is possible to incorporate inhibition into the scalar neural field equations (6.115) or (6.116) [505]. For example, consider a two-population model ($M = 2$) of excitatory ($a = E$) and

inhibitory ($a = I$) neurons evolving according to the pair of continuum voltage-based equations

$$\frac{\partial u_E}{\partial t} = -\frac{u_E(x,t)}{\tau_E} + \int_{-\infty}^{\infty} w_{EE}(x,y) F_E(u_E(y,t))dy + \int_{-\infty}^{\infty} w_{EI}(x,y) F_I(u_I(y,t))dy \tag{6.122a}$$

$$\frac{\partial u_I}{\partial t} = -\frac{u_I(x,t)}{\tau_I} + \int_{-\infty}^{\infty} w_{IE}(x,y) F_E(u_E(y,t))dy + \int_{-\infty}^{\infty} w_{II}(x,y) F_I(u_I(y,t))dy, \tag{6.122b}$$

with $w_{EE}, w_{IE} \geq 0$ and $w_{EI}, w_{II} \leq 0$. Now suppose that $w_{II} \equiv 0$, $F_I(u_I) = u_I/\tau_I$ and $\tau_I \ll \tau_E$. It follows that we can eliminate u_I by setting

$$u_I(x) \sim \tau_I \int_{-\infty}^{\infty} w_{IE}(x,y) F_E(u_E(y,t))dy,$$

which leads to a scalar equation for u_E of the form (6.115) with effective weight distribution

$$w(x,y) = w_{EE}(x,y) + \int_{-\infty}^{\infty} w_{EI}(x,y') w_{IE}(y',y)dy'. \tag{6.123}$$

It is then possible for $w(x,y)$ to change sign as a function of x, y. (Often w is modeled as a difference of Gaussians or exponentials—the so-called Mexican hat weight distribution.) The reduced model can be used to investigate the effects of inhibition on stationary solutions and propagating waves. However, in contrast to the full two-population model, it does not support oscillatory solutions (in the absence of axonal delays, higher-order synapses, or some form of adaptation such as synaptic depression).

It is important to emphasize that there does not currently exist a multi-scale analysis of conductance-based neural networks that provides a rigorous derivation of neural field equations, although some progress has been made in this direction [100, 147, 184, 307, 675, 676]. One crucial step in the derivation of neural field equations presented here was the assumption of slowly varying synaptic currents, which is related to the assumption that there is not significant coherent activity at the level of individual spikes. This allowed us to treat the output of a neuron (or population of neurons) as an instantaneous firing rate. A more rigorous derivation would need to incorporate the mean-field analysis of local populations of stochastic spiking neurons into a larger-scale cortical model and to carry out a systematic form of coarse graining or homogenization in order to generate a continuum neural field model. Nevertheless, the heuristic approach does provide a framework for relating parameters of neural field equations to biophysical parameters such as membrane/synaptic time constants and axonal delays and also prescribes how to incorporate additional physiological processes such as synaptic depression and spike frequency adaptation. Moreover, neural field models make it possible to explore the dependence of cortical dynamics on the detailed anatomy of local and long-range synaptic connections. It is often assumed that w depends on the Euclidean distance between interacting cells within the 2D cortical sheet so that

$w(\mathbf{x},\mathbf{y}) = w(|\mathbf{x}-\mathbf{y}|)$. However, this is an oversimplification of the detailed architecture of cortex [64–66, 308, 526]; see Sect. 8.1. A related simplification is to take axonal delays to depend on Euclidean distance according to $|\mathbf{x}-\mathbf{y}|/v$, where v is the speed of propagation.

It is also possible to construct continuum neural field equations for stochastic population models. For the sake of illustration, consider the Langevin equation (6.71), except we simplify the multiplicative noise by additive noise σdW_α for constant noise strength σ. The continuum limit of Eq. (6.71) proceeds as follows. First, set $A_\alpha(t) = A(\alpha\Delta d,t)$ and $w_{\alpha\beta} = \rho\Delta d w(\alpha\Delta d,\beta\Delta d)$ where ρ is a synaptic density and Δd is an infinitesimal length scale. We also assume that the noise strength $\sigma_\alpha = \sigma/\sqrt{\Delta d}$ and define $W_\alpha(t)/\sqrt{\Delta d} = W(\alpha\Delta d,t)$. Taking the limit $\Delta d \to 0$ with $\tau_\alpha = \hat{\tau}$ for all α gives

$$\hat{\tau} dA(x,t) = \left[-A(x,t) + F\Big(\int w(x-y)A(y,t)dy\Big)\right]dt + \sigma dW(x,t) \tag{6.124}$$

with

$$\langle dW(x,t)\rangle = 0, \quad \langle dW(x,t)dW(y,t)\rangle = \delta(x-y)dt. \tag{6.125}$$

Similarly, we can write down a stochastic version of a voltage-based neural field equation, namely,

$$\tau dU(x,t) = [-U(x,t) + \int w(x-y)F(U(y,t))dy]dt + \sigma dW(x,t) \tag{6.126}$$

From a numerical perspective, any computer simulation would involve rediscretizing space and then solving a time-discretized version of the resulting stochastic differential equation. On the other hand, in order to investigate analytically the effects of noise on spatiotemporal dynamics, it is more useful to work directly with stochastic neural fields. One can then adapt various PDE methods for studying noise in spatially extended systems [546], as illustrated in Sect. 7.4. Recently, Buice and Cowan [91] have used path integral methods and renormalization group theory to establish that a stochastic neural field model based on a continuum version of a birth–death master equation belongs to the universality class of directed percolation and consequently exhibits power law behavior, suggestive of many measurements of spontaneous cortical activity in vitro and in vivo [30, 508]; see Sect. 9.5. Although the existence of power law behavior is still controversial [28], the application of path integral methods provides yet another example of how analytical techniques familiar in the study of PDEs are being adapted to studies of continuum neural fields. (For reviews on path integral methods for stochastic differential equations see [115, 618, 698].)

Finally, note that several groups have constructed equivalent PDE models for neural fields with axonal propagation delays, which take the form of damped inhomogeneous wave equations [307, 382, 467, 527, 528, 603]. The basic idea is to assume a particular form for the synaptic weight distribution and to use Fourier transforms. Consider, for example, a 2D version of the multi-population integral

equation (6.119). Suppose that $\Phi_{ab}(\mathbf{x},\mathbf{y},t) = w_{ab}(|\mathbf{x}-\mathbf{y}|)\Phi(t)$ and introduce the auxiliary field

$$\Psi_{ab}(\mathbf{x},t) = \int_{\mathbb{R}^2} w_{ab}(|\mathbf{x}-\mathbf{y}|)F_b(\mathbf{y},t-|\mathbf{x}-\mathbf{y}|/v_{ab})d\mathbf{y},$$

where we have set $F_b(\mathbf{y},t) = F_b(u_b(\mathbf{y},t))$. Fourier transforming this equation with

$$\hat{\Psi}_{ab}(k,\omega) = \int_{\mathbb{R}^2}\int_{-\infty}^{\infty} \mathrm{e}^{-i(\mathbf{k}\cdot\mathbf{r}+\omega t)}\Psi_{ab}(\mathbf{x},t)dt\,d\mathbf{x},$$

and

$$w_{ab}(r) = \frac{w_{ab}^0}{2\pi}\mathrm{e}^{-r/\sigma_{ab}},$$

we find that

$$\hat{\Psi}_{ab}(k,\omega) = w_{ab}^0\frac{\mathscr{A}_{ab}(\omega)}{(\mathscr{A}_{ab}(\omega)^2+k^2)^{3/2}}\hat{F}_b(k,\omega)$$

with $\mathscr{A}_{ab}(\omega) = 1/\sigma_{ab} + i\omega/v_{ab}$. If one now makes a long-wavelength approximation by Taylor expanding the denominator of the above equation about $k=0$ and rearranging to give $(\mathscr{A}_{ab}(\omega)^2 + 3k^2/2)\hat{\Psi}_{ab}(k,\omega) = \hat{F}_b(k,\omega)$, one can then apply the inverse Fourier transform to derive the damped wave equation

$$\left[\left(\frac{1}{\sigma_{ab}}+\frac{1}{v_{ab}}\partial_t\right)^2 - \frac{3}{2}\nabla^2\right]\Psi_{ab}(\mathbf{x},t) = w_{ab}^0F_b(u_b(\mathbf{x},t)).$$

The current $u_a(\mathbf{x},t)$ is then related to the field $\Psi_{ab}(\mathbf{x},t)$ according to

$$u_a(\mathbf{x},t) = \int_{-\infty}^{t}\Phi(t-t')\sum_b\Psi_{ab}(\mathbf{x},t')dt',$$

which can itself be converted to a PDE by applying the inverse operator $\mathbb{L}_t$. There have also been various extensions of the PDE theory including improvements upon the long-wavelength approximation [142] and incorporation of network inhomogeneities [526]. The damped wave equation (6.127) and its generalizations have been used extensively to study large-scale phenomena such as EEG rhythms, where axonal propagation delays are important [60, 467]; see also Sect. 9.4. PDE models have also been used to study single and multi-bump stationary solutions of scalar neural field equations, in which the time-independent equations reduce to fourth-order differential equations with a Hamiltonian structure [355, 356].

Chapter 7
Waves in Excitable Neural Fields

In Sect. 5, we showed how both solitary pulses and oscillatory phase waves could occur in a synaptically coupled network of spiking neurons, where the fundamental element of the network was a single neuron. Hence, whether the network acted as an excitable or an oscillatory medium depended primarily on the intrinsic properties of the individual neurons. In this chapter, we focus on waves in excitable neural fields, where the fundamental network element is a local population of cells (see Sect. 6), and show how many of the PDE methods and results for the analysis of waves in reaction–diffusion equations (see part I) can be extended to the nonlocal integrodifferential equations of neural field theory. We begin by analyzing the existence and stability of solitary traveling fronts in a 1D scalar neural field. (Since there is strong vertical coupling between layers of a cortical column, it is possible to treat a thin vertical cortical slice as an effective 1D medium.) In order to relate the models to experiments on disinhibited cortical slices (Sect. 5.1), we assume that the weight distribution is purely excitatory. This is also motivated by the observation that epileptic seizures are often associated with greatly enhanced levels of recurrent excitation [430] (Sect. 9.4). We then extend the analysis to the case of traveling pulses, which requires the inclusion of some form of local negative feedback mechanism such as synaptic depression or spike frequency adaptation. Next we describe two approaches to analyzing wave propagation failure in inhomogeneous neural media: one based on homogenization theory [79, 332] and the other on interfacial dynamics [132]. This is followed by a discussion of wave propagation in stochastic neural fields.

It is useful to emphasize here that there are two main approaches to analyzing the spatiotemporal dynamics of neural field equations. The first method is based on the original work of Amari [8], in which one establishes the existence of nonlinear traveling wave solutions by explicit construction. This is possible if one takes the firing rate function F to be the Heaviside (1.15). It is also possible to study the linear stability of such solutions by constructing an associated Evans function, whose zeros determine the spectrum of the resulting linear operator [134, 552, 696]. The constructive approach of Amari [8] has been particularly useful in providing explicit insights into how spatiotemporal network dynamics depends on the structure

P.C. Bressloff, *Waves in Neural Media: From Single Neurons to Neural Fields*,
Lecture Notes on Mathematical Modelling in the Life Sciences,
DOI 10.1007/978-1-4614-8866-8_7,

of the synaptic weight kernel as well as various physiological parameters. Moreover, in certain cases, it is possible to use singular perturbation methods [504, 505] or fixed-point theorems [172, 336] to extend results for neural fields with Heaviside nonlinearities to those with more realistic sigmoidal nonlinearities; see also [136]. The second method is based on bifurcation theory, following the original work of Ermentrout and Cowan [169], in which one investigates the emergence of spatially periodic stationary and oscillatory patterns through a combination of linear stability analysis, weakly nonlinear analysis, symmetric bifurcation theory, and numerical simulations, as reviewed in [67, 71, 167]. Rigorous functional analytical techniques combined with numerical bifurcation schemes have also been used to study the existence and (absolute) stability of stationary solutions for a general class of neural field models with smooth firing rate functions [185, 642]. As far as we are aware, these methods have not yet been applied to traveling wave solutions of neural field equations.

7.1 Traveling Fronts in a Scalar Neural Field

7.1.1 Propagating Fronts in a Bistable Neural Field

We begin by using Amari's constructive method [8] to analyze the existence of traveling front solutions in a scalar neural field equation. Similar analyses are found in Refs. [76, 134, 504]. We assume a Heaviside rate function (1.15) and an excitatory weight distribution of the form $w(x,y) = w(x-y)$ with $w(x) \geq 0$ and $w(-x) = w(x)$. We also assume that $w(x)$ is a monotonically decreasing function of x for $x \geq 0$. A common choice is the exponential weight distribution

$$w(x) = \frac{1}{2\sigma} \mathrm{e}^{-|x|/\sigma}, \tag{7.1}$$

where σ determines the range of synaptic connections. The latter tends to range from 100 μm to 1 mm. The resulting neural field equation is

$$\frac{\partial u(x,t)}{\partial t} = -u(x,t) + \int_{-\infty}^{\infty} w(x-x')F(u(x',t))dx', \tag{7.2}$$

with $F(u) = H(u-\kappa)$. We have fixed the units of time by setting $\tau = 1$. If τ is interpreted as a membrane time constant, then $\tau \sim 10$ msec. In order to construct a traveling front solution of (7.2), we introduce the traveling wave coordinate $\xi = x - ct$, where c denotes the wave speed, and set $u(x,t) = U(\xi)$ with $\lim_{\xi \to -\infty} U(\xi) = U_+ > 0$ and $\lim_{\xi \to \infty} U(\xi) = 0$ such that $U(\xi)$ only crosses the threshold κ once. Here $U_+ = \int_{-\infty}^{\infty} w(y)dy$ is a spatially uniform fixed-point solution of (7.2). Since Eq. (7.2) is equivariant with respect to uniform translations, we are free to take the threshold crossing point to be at the origin, $U(0) = \kappa$, so that $U(\xi) < \kappa$ for $\xi > 0$ and $U(\xi) > \kappa$ for $\xi < 0$. Substituting this traveling front solution into Eq. (7.2) then gives

$$-cU'(\xi)+U(\xi)=\int_{-\infty}^{0} w(\xi-\xi')d\xi'=\int_{\xi}^{\infty} w(x)dx\equiv W(\xi), \tag{7.3}$$

where $U'(\xi)=dU/d\xi$. Multiplying both sides of the above equation by $e^{-\xi/c}$ and integrating with respect to ξ leads to the solution

$$U(\xi)=e^{\xi/c}\left[\kappa-\frac{1}{c}\int_{0}^{\xi} e^{-y/c}W(y)dy\right]. \tag{7.4}$$

Finally, requiring the solution to remain bounded as $\xi\to\infty$ ($\xi\to-\infty$) for $c>0$ (for $c<0$) implies that κ must satisfy the condition

$$\kappa=\frac{1}{|c|}\int_{0}^{\infty} e^{-y/|c|}W(\mathrm{sign}(c)y)dy. \tag{7.5}$$

Thus, one of the useful aspects of the constructive method is that it allows us to derive an explicit expression for the wave speed as a function of physiological parameters such as firing threshold and range of synaptic connections. In the case of the exponential weight distribution (7.1), the relationship between wave speed c and threshold κ is

$$c=\frac{\sigma}{2\kappa}[1-2\kappa]\ (\text{for } \kappa<0.5),\quad c=\frac{\sigma}{2}\frac{1-2\kappa}{1-\kappa}\ (\text{for } 0.5<\kappa<1). \tag{7.6}$$

This establishes the existence of a unique front solution for fixed κ, which travels to the right ($c>0$) when $\kappa<0.5$ and travels to the left ($c<0$) when $\kappa>0.5$. As we will show below, the traveling front is stable.

Given the existence of a traveling front solution for a Heaviside rate function, it is possible to extend the analysis to a smooth sigmoid nonlinearity using a continuation method [172]. We briefly summarize the main result. Consider the scalar neural field equation (7.2) with F given by the sigmoid function (1.14) and $w(x)$ nonnegative and symmetric with normalization $\int_{-\infty}^{\infty} w(x)dx=1$. Suppose that the function $\tilde{F}(u)=-u+F(u)$ has precisely three zeros at $u=U_{\pm},U_0$ with $U_-<U_0<U_+$ and $\tilde{F}'(U_{\pm})<0$. It can then be shown that (modulo uniform translations) there exists a unique traveling front solution $u(x,t)=U(\xi)$, $\xi=x-ct$, with

$$-cU'(\xi)+U(\xi)=\int_{-\infty}^{\infty} w(\xi-\xi')F(U(\xi'))d\xi', \tag{7.7}$$

and $U(\xi)\to U_{\pm}$ as $\xi\to\mp\infty$ [172]. Moreover, the speed of the wave satisfies

$$c=\frac{\Gamma}{\int_{-\infty}^{\infty}U'(\xi)^2F'(U(\xi))d\xi}, \tag{7.8}$$

where $F'(U)=dF/dU$ and

$$\Gamma=\int_{U_-}^{U_+}\tilde{F}(U)dU. \tag{7.9}$$

Since the denominator of Eq. (7.8) is positive definite, the sign of c is determined by the sign of the coefficient Γ. In particular, if the threshold $\kappa = 0.5$ and the gain of the sigmoid $\eta > 4$ (see Eq. (1.14), then there exists a pair of stable homogeneous fixed points with $U_- = -U_+$, which in turn implies that $\Gamma = 0$ and the front solution is stationary. Note that this analysis has been extended to a more general form of nonlocal equations by Chen [108].

7.1.2 Wave Stability and Evans Functions

Suppose that the scalar neural field equation (7.2) has a traveling wave solution $u(x,t) = U(\xi), \xi = x - ct$ with $c > 0$. Following Coombes and Owen [134], it is convenient to rewrite the neural field equation in the integral form

$$u(x,t) = \int_{-\infty}^{\infty} \int_0^{\infty} w(y)\Phi(s)F(u(x-y,t-s))dsdy, \tag{7.10}$$

with $\Phi(t) = \mathrm{e}^{-t}H(t)$. For this representation, the front solution satisfies

$$U(\xi) = \int_{-\infty}^{\infty} \int_0^{\infty} w(y)\Phi(s)F(U(\xi - y + cs)dsdy. \tag{7.11}$$

In order to determine the stability of the front solutions, we transform to traveling wave coordinates by setting $u(x,t) = U(\xi,t) = U(\xi) + \varphi(\xi,t)$, and Taylor expand to first order in φ. This leads to the linear integral equation

$$\varphi(\xi,t) = \int_{-\infty}^{\infty} \int_0^{\infty} w(y)\Phi(s)F'(U(\xi - y + cs))\varphi(\xi - y + cs, t-s)dsdy. \tag{7.12}$$

We now seek solutions of Eq. (7.12) of the form $\varphi(\xi,t) = \varphi(\xi)\mathrm{e}^{\lambda t}$, $\lambda \in \mathbb{C}$, which leads to the eigenvalue equation $\varphi = \mathbb{L}(\lambda)\varphi$. That is,

$$\varphi(\xi) = \int_{-\infty}^{\infty} \int_{\xi - y}^{\infty} w(y)\Phi((s+y-\xi)/c)\mathrm{e}^{-\lambda(s+y-\xi)/c}F'(U(s))\varphi(s)\frac{ds}{c}dy, \tag{7.13}$$

where we have performed the change of variables $cs + \xi - y \to s$. The linear stability of the traveling front can then be determined in terms of the spectrum $\sigma(\mathbb{L}(\lambda))$.

Following appendix section 2.7, we assume that the eigenfunctions $\varphi \in L^2(\mathbb{R})$ and introduce the resolvent operator $\mathscr{R}(\lambda) = [\mathbb{L}(\lambda) - I]^{-1}$, where I denotes the identity operator. We can then decompose the spectrum $\sigma(\mathscr{L})$ into the disjoint sum of the discrete spectrum and the essential spectrum. Given the spectrum of the linear operator defined by Eq. (7.13), the traveling wave is said to be linearly stable if [551]

$$\max\{\mathrm{Re}(\lambda) : \lambda \in \sigma(\mathscr{L}), \lambda \neq 0\} \leq -K \tag{7.14}$$

for some $K > 0$, and $\lambda = 0$ is a simple eigenvalue of λ. The existence of at least one zero eigenvalue is a consequence of translation invariance. Indeed, differentiating equation (7.11) with respect to ξ shows that $\varphi(\xi) = U'(\xi)$ is an eigenfunction solution of Eq. (7.13) with $\lambda = 0$. As in the case of PDEs (see Sect. 2.4), the discrete spectrum may be associated with the zeros of an Evans function. A number of authors have applied the Evans function construction to neural field equations [134, 198, 506, 536, 552, 696], as well as more general nonlocal problems [314]. Moreover, for neural fields with Heaviside firing rate functions, the Evans function can be calculated explicitly. This was first carried out by Zhang [696], who applied the method of variation of parameters to the linearized version of the integrodifferential Eq. (7.2), and was subsequently extended using a more direct integral formulation by Coombes and Owen [134].

Construction of Evans function. Setting $F(U) = H(U - \kappa)$ in Eq. (7.12) and using the identity

$$H'(U(\xi) - \kappa) = \delta(U(\xi) - \kappa) = \frac{\delta(\xi)}{|U'(0)|} \tag{7.15}$$

gives

$$\varphi(\xi) = \frac{\varphi(0)}{c|U'(0)|} \int_{-\infty}^{\infty} w(y) \Phi((y-\xi)/c) \mathrm{e}^{-\lambda(y-\xi)/c} dy. \tag{7.16}$$

In order to obtain a self-consistent solution at $\xi = 0$, we require that

$$\varphi(0) = \frac{\varphi(0)}{c|U'(0)|} \int_{0}^{\infty} w(y) \Phi(y/c) \mathrm{e}^{-\lambda y/c} dy, \tag{7.17}$$

We have used the fact that $\Phi(y) = 0$ for $y < 0$, which is a consequence of causality. Hence, a nontrivial solution exists provided that $\mathscr{E}(\lambda) = 0$, where

$$\mathscr{E}(\lambda) = 1 - \frac{1}{c|U'(0)|} \int_{0}^{\infty} w(y) \Phi(y/c) \mathrm{e}^{-\lambda y/c} dy. \tag{7.18}$$

Equation (7.18) can be identified with the Evans function for the traveling front solution of the scalar neural field equation (7.10). It is real valued if λ is real. Furthermore, (i) the complex number λ is an eigenvalue of the operator $\mathscr{L}$ if and only if $\mathscr{E}(\lambda) = 0$, and (ii) the algebraic multiplicity of an eigenvalue is equal to the order of the zero of the Evans function [134, 552, 696]. We briefly indicate the proof of (i) for $\Phi(t) = \mathrm{e}^{-t} H(t)$. Equation (7.16) becomes

$$\begin{aligned} \varphi(\xi) &= \frac{\varphi(0)}{c|U'(0)|} \mathrm{e}^{(\lambda+1)\xi/c} \int_{\xi}^{\infty} w(y) \mathrm{e}^{-(\lambda+1)y/c} dy, \\ &= \varphi(0) \left[1 - \frac{1}{c|U'(0)|} \int_{0}^{\xi} w(y) \mathrm{e}^{-(\lambda+1)y/c} dy \right] \mathrm{e}^{(\lambda+1)\xi/c}, \end{aligned}$$

which in the limit $\xi \to \infty$ gives

$$\lim_{\xi \to \infty} \varphi(\xi) = \varphi(0) \mathscr{E}(\lambda) \lim_{\xi \to \infty} \mathrm{e}^{(\lambda+1)\xi/c}.$$

Assuming that $\mathrm{Re}\lambda > -1$ (which turns out to be to the right of the essential spectrum), then $\varphi(\xi)$ will be unbounded as $\xi \to \infty$ unless $\mathscr{E}(\lambda) = 0$. That is, if $\mathscr{E}(\lambda) = 0$, then $\varphi(\xi)$ is normalizable, the resolvent operator is not invertible and λ is an eigenvalue.

It is also straightforward to show that $\mathscr{E}(0) = 0$, which we expect from translation invariance. First, setting $F(U) = H(U - \kappa)$ in Eq. (7.11) and differentiating with respect to ξ show that

$$U'(\xi) = -\frac{1}{c}\int_{-\infty}^{\infty} w(y)\Phi((y-\xi)/c)dy. \tag{7.19}$$

Thus, defining

$$\mathscr{H}(\lambda) = \int_0^{\infty} w(y)\Phi(y/c)\mathrm{e}^{-\lambda y/c}dy, \tag{7.20}$$

we see that $c|U'(0)| = \mathscr{H}(0)$ and, hence,

$$\mathscr{E}(\lambda) = 1 - \frac{\mathscr{H}(\lambda)}{\mathscr{H}(0)}. \tag{7.21}$$

It immediately follows that $\mathscr{E}(0) = 0$.

In order to determine the essential spectrum, consider the inhomogeneous equation

$$\varphi(\xi) - \frac{\varphi(0)}{c|U'(0)|}\int_{-\infty}^{\infty} w(y)\Phi((y-\xi)/c)\mathrm{e}^{-\lambda(y-\xi)/c}dy = h(\xi) \tag{7.22}$$

for some normalizable smooth function h on $\mathbb{R}$. Assuming that λ does not belong to the discrete spectrum, $\mathscr{E}(\lambda) \neq 0$, we can expresses the constant $\varphi(0)$ in terms of $h(0)$ by setting $\xi = 0$ in Eq. (7.22): $\varphi(0) = h(0)/\mathscr{E}(\lambda)$. Thus,

$$\varphi(\xi) = h(\xi) + \frac{1}{\mathscr{E}(\lambda)}\frac{h(0)}{c|U'(0)|}\int_{-\infty}^{\infty} w(y)\Phi((y-\xi)/c)\mathrm{e}^{-\lambda(y-\xi)/c}dy. \tag{7.23}$$

Fourier transforming this equation using the convolution theorem gives

$$\hat{\varphi}(k) = \hat{h}(k) + \frac{1}{\mathscr{E}(\lambda)}\frac{h(0)}{c|U'(0)|}\hat{\omega}(k)\hat{\Phi}(kc + i\lambda), \tag{7.24}$$

where

$$\hat{\varphi}(k) = \int_{-\infty}^{\infty} \varphi(y)\mathrm{e}^{iky}dy \tag{7.25}$$

etc. Now suppose that for a given value of k, there exists $\lambda = \lambda(k)$ for which $[\hat{\Phi}(kc + i\lambda(k))]^{-1} = 0$. It follows that the right-hand side of Eq. (7.24) blows up if $\lambda = \lambda(k)$, that is, the dispersion curve belongs to the essential spectrum.

For the sake of illustration, let us calculate the zeros of the Evans function in the case of the exponential weight function (7.1). Substituting $\Phi(t) = \mathrm{e}^{-t}$ and $w(y) = \mathrm{e}^{-|y|/\sigma}/2\sigma$ in Eq. (7.20) gives

$$\mathscr{H}(\lambda) = \frac{1}{2\sigma}\frac{1}{\sigma^{-1} + \lambda/c + 1/c}$$

so that [134]

$$\mathscr{E}(\lambda) = \frac{\lambda}{c/\sigma + 1 + \lambda}. \tag{7.26}$$

It follows that $\lambda = 0$ is the only zero of the Evans function and it is a simple root (since $\mathscr{E}'(0) > 0$). Furthermore, in the particular case $\Phi(t) = \mathrm{e}^{-t}$, we have $[\tilde{\Phi}(kc + i\lambda)]^{-1} = 1 - ikc + \lambda$ so that the essential spectrum is $\lambda(k) = -1 + ikc$, that is, a vertical line in the complex plane at $\mathrm{Re}\lambda = -1$. It follows that the

corresponding traveling front (it it exists) is stable. This example illustrates one of the powerful features of the constructive method based on Heavisides. Not only is it possible to construct exact traveling wave solutions and derive formulae for the speed of the wave, but one can also explicitly construct the Evans function that determines wave stability. The method extends to multi-population neural field models, neural fields with axonal propagation delays, and adaptive neural fields [134]. (Although taking the high-gain limit of a smooth firing rate function is not very realistic from a biological perspective, one finds that many of the basic features of traveling waves persist for finite gain.) In the particular case of axonal delays, it can be shown that delays reduce the speed of a wave but do not affect its stability properties. For example, given a right-moving traveling front solution of the scalar neural field equation (6.118) with $\tau = 1$ and exponential weights, one finds that the speed of the wave is [134, 139]

$$c = \sigma \frac{1-2\kappa}{2\kappa + \sigma(1-2\kappa)/v},$$

where v is the propagation speed along an axon, and the Evans function is

$$\mathscr{E}(\lambda) = \frac{\lambda}{c/\sigma + (1-c/v) + \lambda}.$$

7.1.3 Pulled Fronts

So far we have assumed that the scalar neural field operates in a bistable regime analogous to the FitzHugh–Nagumo equations; see Sect. 2. However, as we explored within the context of CaMKII translocation waves (Sect. 3.2), Fisher-like reaction–diffusion equations support traveling waves propagating into unstable states, resulting in pulled fronts (Sect. 3.3). It turns out that it is also possible to observe pulled fronts in an activity-based version of a scalar neural field equation [70, 132]:

$$\tau \frac{\partial a(x,t)}{\partial t} = -a(x,t) + F\left(\int_{-\infty}^{\infty} w(x-x')a(x',t)dx' \right). \tag{7.27}$$

with $a(x,t) \geq 0$ for all (x,t). Note that the restriction to positive values of a is a feature shared with population models in ecology or evolutionary biology, for example, where the corresponding dependent variables represent number densities. Indeed, Eq. (7.27) has certain similarities with a nonlocal version of the Fisher–KPP equation, which takes the form [238]

$$\tau \frac{\partial p(x,t)}{\partial t} = D\frac{\partial^2 p(x,t)}{\partial x^2} + \mu p(x,t)\left(1 - \int_{-\infty}^{\infty} K(x-x')p(x',t)dx'\right). \tag{7.28}$$

One major difference from a mathematical perspective is that Eq. (7.28) supports traveling fronts even when the range of the interaction kernel K goes to zero, that is, $K(x) \to \delta(x)$, since we recover the standard local Fisher–KPP equation (3.44) [191, 345]. In particular, as the nonlocal interactions appear nonlinearly in Eq. (7.28), they do not contribute to the linear spreading velocity in the leading edge of the front. On the other hand, nonlocal interactions play a necessary role in the generation of fronts in the neural field equation (7.27).

Suppose that $F(a)$ in Eq. (7.27) is a positive, bounded, monotonically increasing function of a with $F(0) = 0$, $\lim_{a\to 0^+} F'(a) = 1$ and $\lim_{a\to\infty} F(a) = \kappa$ for some positive constant κ. For concreteness, we take

$$F(a) = \begin{cases} 0, & a \le 0 \\ a, & 0 < a \le \kappa \\ \kappa, & a > \kappa. \end{cases} \tag{7.29}$$

A homogeneous fixed-point solution a^* of Eq. (7.27) satisfies

$$a^* = F(W_0 a^*), \quad W_0 = \int_{-\infty}^{\infty} w(y)dy. \tag{7.30}$$

In the case of the given piecewise linear firing rate function, we find that if $W_0 > 1$, then there exists an unstable fixed point at $a^* = 0$ (absorbing state) and a stable fixed point at $a^* = \kappa$; see Fig. 7.1(a). The construction of a front solution linking the stable and unstable fixed points differs considerably from that considered in neural fields with sigmoidal or Heaviside nonlinearities [8, 167], where the front propagates into a metastable state; see Fig 7.1(b). Following the PDE theory of fronts propagating into unstable states [544] (see Sect. 3.3), we expect there to be a continuum of front velocities and associated traveling wave solutions.

Recall that a conceptual framework for studying such solutions is the linear spreading velocity c^*, which is the asymptotic rate with which an initial localized perturbation spreads into an unstable state based on the linear equations obtained by linearizing the full nonlinear equations about the unstable state. Therefore, linearizing equation (7.27) about $a = 0$ gives

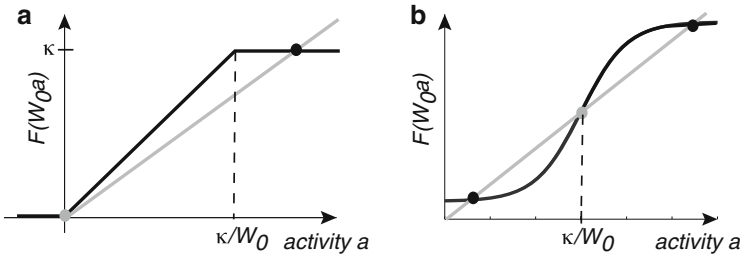

Fig. 7.1 Plots of firing rate function. Intercepts of $y = F(W_0 a)$ with the straight line $y = a$ determine homogeneous fixed points. (**a**) Piecewise linear rate function (7.29) showing the existence of an unstable fixed point at $a = 0$ and a stable fixed point at $a = \kappa$. (**b**) Sigmoidal rate function $F(a) = 2/(1 + e^{-2[a-\kappa]})$ showing the existence of two stable fixed points separated by an unstable fixed point

$$\frac{\partial a(x,t)}{\partial t} = -a(x,t) + \int_{-\infty}^{\infty} w(x-x')a(x',t)dx'. \tag{7.31}$$

Note that if $a(x,0) \geq 0$ for all x, then Eq. (7.31) ensures that $a(x,t) \geq 0$ for all x and $t > 0$. One way to see this is to note from Eq. (7.31) that $a(x,t+\Delta t) = (1-\Delta t)a(x,t) + \Delta t \int_{-\infty}^{\infty} w(x-x')a(x',t)dx'$. Assuming positivity of the solution at time t and using the fact that the neural field is purely excitatory ($w(x) \geq 0$ for all x), it follows that $a(x,t+\Delta t)$ is also positive. An arbitrary initial condition $a(x,0)$ will evolve under Eq. (7.31) as

$$a(x,t) = \int_{-\infty}^{\infty} G(x-y,t)a(y,0)dy, \tag{7.32}$$

where $G(x,t)$ is Green's function

$$G(x,t) = \int_{-\infty}^{\infty} \mathrm{e}^{ikx - i\omega(k)t} \frac{dk}{2\pi}, \quad \omega(k) = i[\tilde{w}(k) - 1], \tag{7.33}$$

and $\tilde{w}(k)$ is the Fourier transform of the weight distribution $w(x)$. Hence, the solution can be written in the form of Eq. (3.102):

$$a(x,t) = \int_{-\infty}^{\infty} \tilde{a}_0(k)\mathrm{e}^{i[kx - \omega(k)t])} \frac{dk}{2\pi}. \tag{7.34}$$

with $\tilde{a}_0$, the Fourier transform of the initial condition $a(x,0)$.

Given a sufficiently steep initial condition, for which the Fourier transform $\tilde{a}(k)$ is analytic, the asymptotic behavior of $a(x,t)$ can be obtained from the large-time asymptotics of $G(x,t)$ based on steepest descents. It immediately follows from the analysis of the Fisher equation in Sect. 3.3 that the linear spreading velocity c^* is given by $c^* = c(\lambda^*)$ where

$$c(\lambda) = \frac{\mathrm{Im}(\omega(i\lambda))}{\lambda}, \quad \left.\frac{dc(\lambda)}{d\lambda}\right|_{\lambda=\lambda^*} = 0. \tag{7.35}$$

Using the fact that the Fourier transform of the weight distribution is real valued, we find that

$$c(\lambda) = \frac{1}{\lambda}\left[\mathscr{W}(\lambda) - 1\right], \tag{7.36}$$

where $\mathscr{W}(\lambda) = \hat{W}(\lambda) + \hat{W}(-\lambda)$ and $\hat{W}(\lambda)$ is the Laplace transform of $w(x)$:

$$\hat{W}(\lambda) = \int_0^{\infty} w(y)\mathrm{e}^{-\lambda y}dy. \tag{7.37}$$

We are assuming that $w(y)$ decays sufficiently fast as $|y| \to \infty$ so that the Laplace transform $\hat{W}(\lambda)$ exists for bounded, negative values of λ. This holds in the case of a Gaussian weight distribution

$$w(x) = \frac{W_0}{\sqrt{2\pi\sigma^2}} \mathrm{e}^{-x^2/2\sigma^2}, \tag{7.38}$$

since

$$\mathscr{W}(\lambda) = \int_{-\infty}^{\infty} w(y)\mathrm{e}^{-\lambda y} dy = \frac{W_0}{\sqrt{2\pi\sigma^2}} \int_{-\infty}^{\infty} \mathrm{e}^{-y^2/2\sigma^2} \mathrm{e}^{-\lambda y} dy = W_0 \mathrm{e}^{\lambda^2\sigma^2/2}.$$

Hence,

$$c(\lambda) = \frac{W_0 \mathrm{e}^{\lambda^2\sigma^2/2} - 1}{\lambda}. \tag{7.39}$$

If $W_0 > 1$ (necessary for the zero activity state to be unstable), then $c(\lambda)$ is a positive unimodal function with $c(\lambda) \to \infty$ as $\lambda \to 0$ or $\lambda \to \infty$ and a unique minimum at $\lambda = \lambda_0$ with λ_0 the solution to the implicit equation

$$\lambda_0{}^2 = \frac{W_0 - \mathrm{e}^{-\lambda_0{}^2\sigma^2/2}}{\sigma^2 W_0}. \tag{7.40}$$

Example dispersion curves are shown in Fig. 7.2(a) for various values of the Gaussian weight amplitude W_0. Combining Eqs. (7.39) and (7.40) shows that

$$\frac{c_0}{\lambda_0} = \sigma^2 W_0 \mathrm{e}^{\lambda_0{}^2\sigma^2/2} = \sigma^2(\lambda_0 c_0 + 1), \tag{7.41}$$

so that

$$\lambda_0 = \frac{1}{2}\left[-\frac{1}{c_0} + \sqrt{\frac{1}{c_0{}^2} + \frac{4}{\sigma^2}}\right]. \tag{7.42}$$

Assuming that the full nonlinear system supports a pulled front (see Sect. 3.3), then a sufficiently localized initial perturbation (one that decays faster than $\mathrm{e}^{-\lambda_0 x}$) will asymptotically approach the traveling front solution with the minimum wave speed $c_0 = c(\lambda_0)$. Note that $c_0 \sim \sigma$ and $\lambda_0 \sim \sigma^{-1}$. In Fig. 7.2(b), we show an asymptotic front profile obtained by numerically solving the neural field equation (7.27) when $W_0 = 1.2$. The corresponding displacement of the front is a linear function of time with a slope consistent with the minimal wave speed $c_0 \approx 0.7$ of the corresponding dispersion curve shown in Fig. 7.2(a). This wave speed is independent of κ.

The asymptotic analysis of the linear equation (7.31) also shows that, given a sufficiently localized initial condition, $|a(x,t)| \sim \mathrm{e}^{-\lambda^*\xi}\psi(\xi,t)$ as $t \to \infty$, where $\xi = x - c^*t$ and the leading-edge variable $\psi(\xi,t)$ is given by

$$\psi(\xi,t) \approx \frac{\mathrm{e}^{-\xi^2/(4\mathscr{D}t)}}{\sqrt{4\pi\mathscr{D}t}} \tag{7.43}$$

with

$$\mathscr{D} = -\frac{\omega_i''(i\lambda^*)}{2} = \frac{\lambda^*}{2}\left.\frac{d^2c(\lambda)}{d\lambda^2}\right|_{\lambda^*}. \tag{7.44}$$

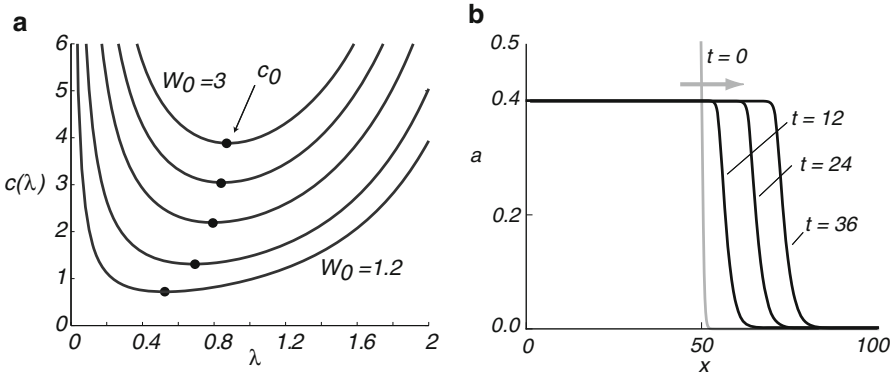

Fig. 7.2 (**a**) Velocity dispersion curves $c = c(\lambda)$ for a pulled front solution of the neural field equation (7.27) with piecewise linear firing rate function (7.29) and a Gaussian weight distribution with amplitude W_0 and width σ. Here $\sigma = 1.0$, $\kappa = 0.4$ and $W_0 = 1, 2, 1.5, 2.0, 2.5, 3.0$. *Black dots* indicate minimum wave speed c_0 for each value of W_0. (**b**) Snapshots of the front profile evolving from an initial condition consisting of a steep sigmoid function of unit amplitude (*gray curve*). Here $W_0 = 1.2$

Positivity of $\mathscr{D}$ follows from the fact that λ^* is a minimum of $c(\lambda)$. However, as shown by Ebert and van Saarloos [162], although the spreading of the leading edge under linearization gives the right qualitative behavior, it fails to match correctly the traveling front solution of the full nonlinear system. In particular, the asymptotic front profile takes the form $\mathscr{A}(\xi) \sim \xi e^{-\lambda^* \xi}$ for $\xi \gg 1$. The factor of ξ reflects the fact that at the saddle point the two branches of the velocity dispersion curve $c(\lambda)$ meet, indicating a degeneracy. In order to match the $\xi e^{-\lambda^* \xi}$ asymptotics of the front solution with the leading-edge solution, it is necessary to take the leading-edge function $\psi(x,t)$ to be the so-called dipole solution of the diffusion equation [162]:

$$\psi(x,t) = -\partial_\xi \frac{e^{-\xi^2/(4\mathscr{D}t)}}{\sqrt{4\pi\mathscr{D}t}} = \xi \frac{e^{-\xi^2/(4\mathscr{D}t)}}{\sqrt{2\pi}(2\mathscr{D}t)^{3/2}}. \tag{7.45}$$

Putting all of this together, if the neural field equation supports a pulled front, then the leading edge should relax asymptotically as

$$|a| \sim \xi e^{-\lambda^* \xi} e^{-\xi^2/(4\mathscr{D}t)} t^{-3/2} \tag{7.46}$$

with $\xi = x - c^* t$. Finally, writing

$$e^{-\lambda^* \xi} t^{-3/2} = e^{-\lambda^*[x - v^* t - X(t)]}, \quad X(t) = -\frac{3}{2\lambda^*} \ln t \tag{7.47}$$

suggests that to leading order, the velocity relaxes to the pulled velocity c^* according to (see also [162])

$$v(t) = c^* + \dot{X}(t) = c^* - \frac{3}{2\lambda^* t} + h.o.t. \tag{7.48}$$

7.2 Traveling Pulses in Adaptive Neural Fields

Traveling fronts are not particularly realistic, since populations of cells do not stay in the excited state forever. Hence, rather than a traveling front, propagating activity in cortex is usually better described as a traveling pulse. (One example where fronts rather than pulses occur is wave propagation during binocular rivalry [83, 312, 369, 678]; see Sect. 8.) One way to generate a traveling pulse is to include some form of synaptic inhibition, provided that it is not too strong [8]. However, even in the absence of synaptic inhibition, most neurons possess intrinsic negative feedback mechanisms that slowly bring the cell back to resting voltages after periods of high activity. Possible nonlinear mechanisms include synaptic depression or spike frequency adaptation as discussed in Sect. 6.1. However, most analytical studies of traveling pulses in neural field models have been based on a simpler linear form of adaptation introduced by Pinto and Ermentrout [504]. (For an analysis of waves in neural fields with nonlinear adaptation, see, e.g., [135, 329].) The linear adaptation model is given by

$$\frac{\partial u(x,t)}{\partial t} = -u(x,t) + \int_{-\infty}^{\infty} w(x-x')F(u(x',t))dx' - \beta q(x,t) \tag{7.49a}$$

$$\frac{1}{\varepsilon}\frac{\partial q(x,t)}{\partial t} = -q(x,t) + u(x,t), \tag{7.49b}$$

where ε and β determine the rate and amplitude of linear adaptation. We first show how to construct a traveling pulse solution of Eq. (7.49) in the case of a Heaviside rate function $F(u) = H(u-\kappa)$, following the particular formulation of [198, 696]. We then indicate how singular perturbation methods can be used to construct a traveling pulse for smooth F, as carried out by Pinto and Ermentrout [504]. The introduction of adaptation means that the neural field can support fronts or pulses, depending on whether there exist one or two stable homogeneous fixed points; see Fig. 7.3. We will focus on the latter here. Note, however, that linear (or nonlinear) adaptation can have a nontrivial effect on the propagation of traveling fronts [76, 80]. This is due to the occurrence of a symmetry breaking front bifurcation analogous to that found in reaction–diffusion systems [251, 252, 524, 561]. That is, a stationary front can undergo a supercritical pitchfork bifurcation at a critical rate of adaptation, leading to bidirectional front propagation. As in the case of reaction–diffusion systems, the front bifurcation acts as an organizing center for a variety of nontrivial dynamics including the formation of oscillatory fronts or breathers. The latter can occur, for example, through a Hopf bifurcation from a stationary front in the presence of a weak stationary input inhomogeneity [76].

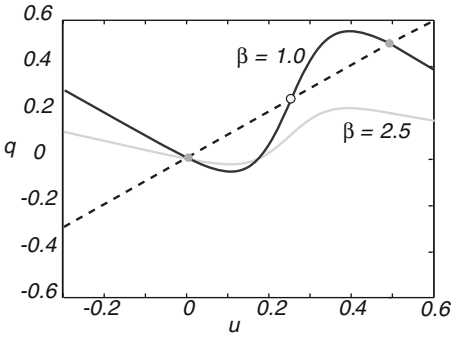

Fig. 7.3 Plot of nullclines for space-clamped planar system $\dot{u} = -u + F(u) - \beta u$, $\varepsilon^{-1}\dot{q} = -q + u$ with $F(u) = 1/(1+\mathrm{e}^{-\eta(u-\kappa)})$. Nullcline $q = -u + F(u)]/\beta$ for $\beta = 1.0$ ($\beta = 2.5$) intercepts straight nullcline $q = u$ at three fixed points (one fixed point) and the corresponding spatially extended network acts as a bistable (excitable) medium. Other parameters are $\eta = 20, \kappa = 0.25$

7.2.1 Exact Traveling Pulse Solution

Without loss of generality, let us consider a right-moving traveling pulse solution of the form $(u(x,t), q(x,t)) = (U(x-ct), Q(x-ct))$ with $U(\pm\infty), Q(\pm\infty) = 0$ and $U(-\Delta) = U(0) = \kappa$; see Fig. 2.1(b). Here c, Δ denote the speed and width of the wave, respectively. We also assume that $U(\xi) > \kappa$ for $\xi \in (-\Delta, 0)$ and $U(\xi) < \kappa$ for $\xi < -\Delta$ and $\xi > 0$. Substituting this solution into Eq. (7.49) with $\xi = x - ct$ then gives

$$\begin{aligned} -cU'(\xi) + U(\xi) + \beta Q(\xi) &= \int_{-\Delta}^{0} w(\xi - \xi')d\xi' \\ -cQ'(\xi) + \varepsilon[Q(\xi) - U(\xi)] &= 0. \end{aligned} \tag{7.50}$$

It is useful to rewrite Eq. (7.50) in the matrix form

$$\begin{pmatrix} 1 & \beta \\ -\varepsilon & \varepsilon \end{pmatrix} \begin{pmatrix} U \\ Q \end{pmatrix} - c\partial_\xi \begin{pmatrix} U \\ Q \end{pmatrix} = [W(\xi) - W(\xi + \Delta)] \begin{pmatrix} 1 \\ 0 \end{pmatrix} \tag{7.51}$$

with $W(\xi) = \int_\xi^\infty w(x)dx$. We proceed by diagonalizing the left-hand side of Eq. (7.51) using the right eigenvectors $\mathbf{v}$ of the matrix

$$\mathbf{M} = \begin{pmatrix} 1 & \beta \\ -\varepsilon & \varepsilon \end{pmatrix}. \tag{7.52}$$

These are given by $\mathbf{v}_\pm = (\varepsilon - \lambda_\pm, \varepsilon)^T$ with corresponding eigenvalues

$$\lambda_\pm = \frac{1}{2}\left[1 + \varepsilon \pm \sqrt{(1+\varepsilon)^2 - 4\varepsilon(1+\beta)}\right]. \tag{7.53}$$

We will assume that ε is sufficiently small so that $\beta < (1-\varepsilon)^2/4\varepsilon$ and consequently $\lambda_\pm$ are real. (For a discussion of the effects of complex eigenvalues $\lambda_\pm$ see [580].) Note that $\mathbf{v}_\pm e^{\lambda_\pm \xi/c}$ are the corresponding null vectors of the linear operator on the left-hand side of Eq. (7.51). Performing the transformation

$$\begin{pmatrix} \tilde{U} \\ \tilde{Q} \end{pmatrix} = \mathbf{T}^{-1} \begin{pmatrix} U \\ Q \end{pmatrix}, \quad \mathbf{T} = \begin{pmatrix} \mathbf{v}_+ & \mathbf{v}_- \end{pmatrix}, \tag{7.54}$$

then gives the pair of equations

$$\begin{aligned} -c\partial_\xi \tilde{U} + \lambda_+ \tilde{U} &= \eta_+ [W(\xi) - W(\xi + \Delta)] \\ -c\partial_\xi \tilde{Q} + \lambda_- \tilde{Q} &= \eta_- [W(\xi) - W(\xi + \Delta)] \end{aligned}$$

with $\eta_\pm = \mp 1/(\lambda_+ - \lambda_-)$. Integrating the equation for $\tilde{U}$ from $-\Delta$ to ∞, we have

$$\tilde{U}(\xi) = e^{\lambda_+ \xi/c} \left[\tilde{U}(-\Delta) e^{\Delta \lambda_+/c} - \tfrac{\eta_+}{c} \int_{-\Delta}^{\xi} e^{-\lambda_+ \xi'/c} [W(\xi') - W(\xi' + \Delta)] d\xi' \right].$$

Finiteness of $\tilde{U}$ in the limit $\xi \to \infty$ requires the term in square brackets to cancel. Hence, we can eliminate $\tilde{U}(-\Delta)$ to obtain the result

$$\tilde{U}(\xi) = \frac{\eta_+}{c} \int_0^\infty e^{-\lambda_+ \xi'/c} [W(\xi' + \xi) - W(\xi' + \xi + \Delta)] d\xi'. \tag{7.55}$$

Similarly,

$$\tilde{Q}(\xi) = \frac{\eta_-}{c} \int_0^\infty e^{-\lambda_- \xi'/c} [W(\xi' + \xi) - W(\xi' + \xi + \Delta)] d\xi'. \tag{7.56}$$

Performing the inverse transformation $U = (\varepsilon - \lambda_+)\tilde{U} + (\varepsilon - \lambda_-)\tilde{Q}$ we have

$$U(\xi) = \frac{1}{c} \int_0^\infty \left[\chi_+ e^{-\lambda_+ \xi'/c} + \chi_- e^{-\lambda_- \xi'/c} \right] [W(\xi' + \xi) - W(\xi' + \xi + \Delta)] d\xi', \tag{7.57}$$

with $\chi_\pm = (\varepsilon - \lambda_\pm)\eta_\pm$. The threshold conditions $U(-\Delta) = \kappa$ and $U(0) = \kappa$ then yield a pair of equations whose solutions determine existence curves relating the speed c and width Δ of a pulse to the threshold κ [134, 198, 504].

For the sake of illustration, let w be given by the exponential function (7.1). In the domain $\xi > 0$, there is a common factor of $e^{-\xi/\sigma}$ in the integrand of Eq. (7.57) so that $U(\xi) = \kappa e^{-\xi/\sigma}$ for $\xi > 0$ provided that

$$\kappa = \frac{1}{2} \frac{\sigma(c + \varepsilon\sigma)(1 - e^{-\Delta/\sigma})}{c^2 + c\sigma(1+\varepsilon) + \sigma^2 \varepsilon(1+\beta)}. \tag{7.58}$$

(Note that for zero negative feedback ($\beta = 0$), Eq. (7.58) reduces to the formula for wave speed of a front in the limit $\Delta \to \infty$.) On the other hand, when $\xi < 0$, one has to partition the integral of Eq. (7.57) into the separate domains $\xi' > |\xi|$,

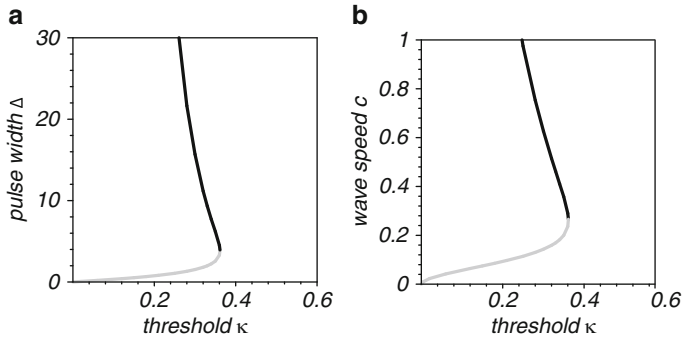

Fig. 7.4 Existence of right-moving traveling pulses in the case of the excitatory network (7.49) with linear adaptation for an exponential weight distribution (7.1). Here $\sigma = 1, \varepsilon = 0.01$ and $\beta = 2.5$. (**a**) Plot of pulse width Δ against threshold κ. (**b**) Plot of wave speed c against threshold κ. Stable (unstable) branches indicated by *black* (*gray*) curves

$|\xi| - \Delta < \xi' < |\xi|$ and $\xi' < |\xi| - \Delta$. This then determines the second threshold condition as well as the asymptotic behavior of $U(\xi)$ in the limit $\xi \to -\infty$:

$$U(\xi) = A_+ e^{\lambda_+ \xi/c} + A_- e^{\lambda_- \xi/c} + A_0 e^{\sigma\xi}. \tag{7.59}$$

where the amplitudes $A_\pm$ and A_0 can be determined from matching conditions at the threshold crossing points [198, 504]. Note that the leading edge of the pulse is positive, whereas the trailing edge is negative due to the effects of adaptation. One finds that for sufficiently slow negative feedback (small ε) and large β there exist two pulse solutions: one narrow and slow and the other wide and fast. This is illustrated in Fig. 7.4. Note that a numerical value of $c \sim 1$ in dimensionless units ($\sigma = \tau = 1$) translates into a physical speed of 60–90 mm/s if the membrane time constant $\tau = 10$ msec and the range of synaptic connections is $\sigma = 600$–$900\,\mu$m. Numerically, the fast solution is found to be stable [504], and this can be confirmed analytically using an Evans function construction [134, 198, 507]; see below. Finally, note that one of the predictions of the neural field model is that the speed of wave propagation should increase as the threshold decreases [504]. Interestingly, this has been confirmed experimentally by applying electric fields to a disinhibited rat cortical slice [521]. The experimental setup is shown in Fig. 7.5. A positive (negative) electric field increases (decreases) the speed of wave propagation by altering the effective excitability of layer V pyramidal neurons. Such neurons have long apical dendrites and are easily polarizable by the electric field.

Construction of Evans function. Rewrite the neural field equation (7.49) in the integral form

$$u(x,t) = \int_{-\infty}^{\infty} \int_0^{\infty} w(y) \Phi(s) F(u(x-y, t-s)) ds dy - \beta \int_0^{\infty} \Psi(s) u(x, t-s) ds, \tag{7.60}$$

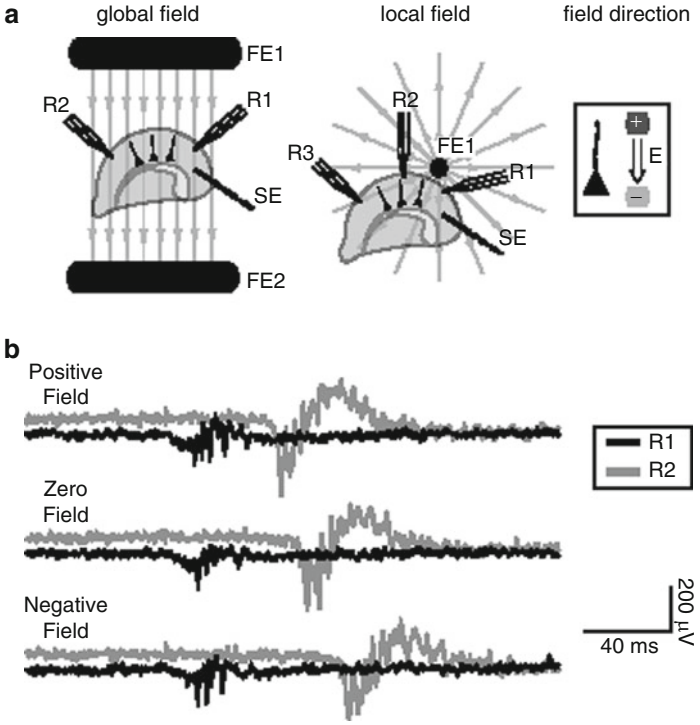

Fig. 7.5 (**a**) Rat cortical slices are bathed in picrotoxin (a $GABA_A$ blocker) and a stimulation electrode (SE) is placed in layers 5–6 to initiate epileptiform bursts. An electric field is applied globally or locally across the slice using Ag/AgCl electrodes (FE1,FE2). Layer five neurons have long apical dendrites and are easily polarizable by an electric field, which controls the effective firing threshold of the neuron. (**b**) The time for an activity pulse to travel between two recording electrodes R1 and R2 depends on the applied electric field, reflecting the dependence of wave speed on the effective firing threshold. [Adapted from Richardson, Schiff and Gluckman [521]]

with $\Phi(t) = \mathrm{e}^{-t}H(t)$ and $\Psi(t) = \int_0^t \Phi(s)\mathrm{e}^{-\varepsilon(t-s)}ds$. Linearizing about the pulse solution by setting $u(x,t) = U(\xi) + \varphi(\xi)\mathrm{e}^{\lambda t}$ gives

$$\varphi(\xi) = \int_{-\infty}^{\infty}\int_{\xi-y}^{\infty} w(y)\Phi((s+y-\xi)/c)\mathrm{e}^{-\lambda(s+y-\xi)/c}F'(U(s))\varphi(s)\frac{ds}{c}dy$$
$$-\beta\int_{\xi}^{\infty}\Psi((s-\xi)/c)\mathrm{e}^{-\lambda(s-\xi)/c}\varphi(s)\frac{ds}{c}. \tag{7.61}$$

Proceeding along similar lines to the analysis of front stability in Sect. 7.1, we set $F(U) = H(U-\kappa)$ and use the identity

$$H'(U(\xi)-\kappa) = \delta(U(\xi)-\kappa) = \frac{\delta(\xi)}{|U'(0)|} + \frac{\delta(\xi+\Delta)}{|U'(-\Delta)|}. \tag{7.62}$$

This gives

$$\varphi(\xi)+\beta\int_{\xi}^{\infty}\Psi((s-\xi)/c)\mathrm{e}^{-\lambda(s-\xi)/c}\varphi(s)\frac{ds}{c} \tag{7.63}$$
$$=\frac{\varphi(0)}{c|U'(0)|}\mathscr{H}(\lambda,\xi)+\frac{\varphi(-\Delta)}{c|U'(-\Delta)|}\mathscr{H}(\lambda,\xi+\Delta)$$

where

$$\mathscr{H}(\lambda,\xi)=\int_{\xi}^{\infty}w(y)\Phi((y-\xi)/c)\mathrm{e}^{-\lambda(y-\xi)/c}dy. \tag{7.64}$$

Let $\hat{\mathscr{H}}(\lambda,k)$ denote the Fourier transform of $\mathscr{H}(\lambda,\xi)$ and $\hat{\mathscr{G}}(\lambda,k)$ denote the Fourier transform of $\Psi(\xi/c)\mathrm{e}^{-\xi/c}$. Using Fourier transforms and the convolution theorem, Eq. (7.63) can then be rewritten as

$$\varphi(\xi)=\frac{\varphi(0)}{c|U'(0)|}\mathscr{B}(\lambda,\xi)+\frac{\varphi(-\Delta)}{c|U'(-\Delta)|}\mathscr{B}(\lambda,\xi+\Delta), \tag{7.65}$$

with $\mathscr{B}(\lambda,\xi)$ the inverse transform of

$$\hat{\mathscr{B}}(\lambda,k)=\frac{\hat{\mathscr{H}}(\lambda,k)}{[1+\beta\hat{\mathscr{G}}(\lambda,-k)/c]}. \tag{7.66}$$

Finally, the eigenvalues λ are determined by setting $\xi=0,-\Delta$ and solving the resulting matrix equation $\mathbf{f}=\mathscr{M}(\lambda)\mathbf{f}$ with $\mathbf{f}=(\varphi(0),\varphi(-\Delta))$ and

$$\mathscr{M}(\lambda)=\frac{1}{c}\begin{pmatrix}\frac{\mathscr{B}(\lambda,0)}{|U'(\xi_1)|} & \frac{\mathscr{B}(\lambda,\Delta)}{|U'(-\Delta)|}\\ \frac{\mathscr{B}(\lambda,-\Delta)}{|U'(0)|} & \frac{\mathscr{B}(\lambda,0)}{|U'(-\Delta)|}\end{pmatrix}. \tag{7.67}$$

It follows that the eigenvalues λ are zeros of the Evans function

$$\mathscr{E}(\lambda)=\mathrm{Det}[\mathbf{1}-\mathscr{M}(\lambda)], \tag{7.68}$$

where $\mathbf{1}$ denotes the identity matrix.

7.2.2 *Singularly Perturbed Pulse Solution*

In the case of slow adaptation ($\varepsilon\ll 1$), Pinto and Ermentrout [504] showed how to construct a traveling pulse solution of Eq. (7.49) for a smooth firing rate function F by exploiting the existence of traveling front solutions of the corresponding scalar equation (7.2). The method is analogous to the construction of traveling pulses in the FitzHugh–Nagumo equation [316]; see Sect.2.3. The basic idea is to analyze separately the fast and slow time behavior of solutions to Eq. (7.49) expressed in traveling wave coordinates:

$$-c\frac{dU(\xi)}{d\xi}=-U(\xi)-\beta Q(\xi)+\int_{-\infty}^{\infty}w(\xi-\xi')F(U(\xi'))d\xi', \tag{7.69}$$

$$-c\frac{dQ(\xi)}{d\xi}=\varepsilon[-Q(\xi)+U(\xi)]. \tag{7.70}$$

We will assume the normalization $\int_{-\infty}^{\infty} w(y)dy = 1$. In the case of fast time, the slow adaptation is taken to be constant by setting $\varepsilon = 0$ so that we have the inner layer equations

$$-c\frac{dU(\xi)}{d\xi} = -U - \beta Q_0 + \int_{-\infty}^{\infty} w(\xi - \xi')F(U(\xi'))d\xi', \tag{7.71}$$

$$-c\frac{dQ(\xi)}{d\xi} = 0. \tag{7.72}$$

Since $Q(\xi) = Q_0$ is a constant, the term βQ_0 can be absorbed into the threshold of the firing rate function F by making the shift $U(\xi) \to U(\xi) + \beta Q_0$. Hence Eq. (3.55) is equivalent to the scalar equation (7.7), which supports the propagation of traveling fronts. In the case of slow time, we introduce the compressed variable $\zeta = \varepsilon\xi$ so that

$$-c\varepsilon\frac{dU(\zeta)}{d\zeta} = -U(\zeta) - \beta Q(\zeta) + \frac{1}{\varepsilon}\int_{-\infty}^{\infty} w([\zeta - \zeta']/\varepsilon)F(U(\zeta'))d\zeta', \tag{7.73}$$

$$-c\frac{dQ(\zeta)}{d\zeta} = -Q(\zeta) + U(\zeta). \tag{7.74}$$

In the limit $\varepsilon \to 0$, we have

$$\frac{1}{\varepsilon}w([\zeta - \zeta']/\varepsilon) \to \delta(\zeta - \zeta')$$

so that first equation becomes

$$\beta Q(\zeta) = -U(\zeta) + F(U(\zeta)) \tag{7.75}$$

Inverting this equation yields two branches $U = g_{\pm}(Q)$. Hence we obtain a slow time or outer layer equation on each branch (see Fig. 7.6):

$$\frac{dQ}{d\zeta} = \frac{1}{c}[Q - g_{\pm}(Q)] \tag{7.76}$$

The construction of the traveling pulse now proceeds by matching inner and outer solutions [504]. This can be visualized by considering the nullclines of the space-clamped version of Eq. (7.49); see Fig. 7.6. We assume that the gain of F and the strength β of adaptation are such that there is only a single fixed point of the space-clamped system:

I Starting at the unique fixed point, use the fast inner equations and the existence results of [172] to construct a leading front solution at $Q = Q_0$ with speed c_0 and matching conditions $\lim_{\xi \pm \infty} U(\xi) = g_{\pm}(Q_0)$.

II Use the slow outer equations to determine dynamics of Q along upper branch $U = g_{+}(Q)$

III The solution leaves upper branch at some point Q_1. Once again use the fast inner equations and [172] to construct a trailing front solution with speed c_1 and matching conditions

$$\lim_{\xi \pm \infty} U(\xi) = g_{\mp}(Q_1)$$

IV Finally, use the slow outer equations to determine the return to the fixed point along the lower branch.

In order to establish the existence of a traveling pulse solution, it remains to find a value Q_1 for which $c_1 = -c_0$ so that the leading and trailing edges of the pulse move at the same speed and thus the pulse maintains its shape as it propagates. (Since Q_0 is known, so is c_0.) Adapting the formula for the wave speed obtained in [172], we have

$$c_1 = -\frac{\Gamma}{\int_{-\infty}^{\infty} U'^2(\xi) F'(U(\xi)) d\xi}, \qquad \Gamma = \int_{g_-(Q_1)}^{g_+(Q_1)} [-U - Q_1 + F(U)] dU. \quad (7.77)$$

Unfortunately, it is not possible to derive a closed form expression for the wave speed. However, the existence of a matching speed can be established provided that certain additional assumptions are made regarding the shape of the firing rate function; see [504] for more details.

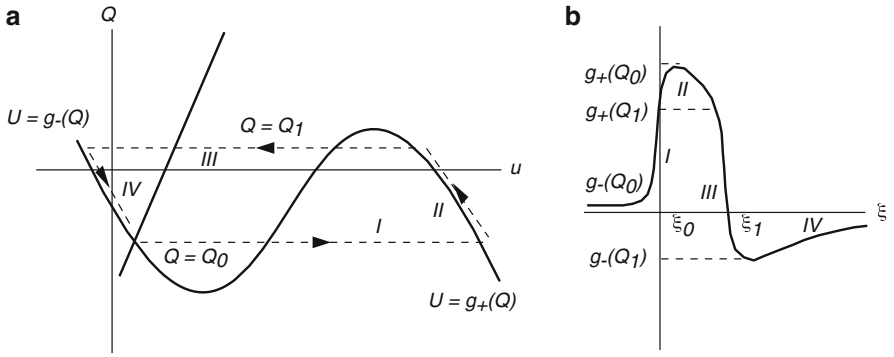

Fig. 7.6 Singular perturbation construction of a traveling pulse in (**a**) the phase plane and (**b**) traveling wave coordinates. See text for details

7.3 Wave Propagation in Heterogeneous Neural Fields

Most studies of neural field theory assume that the synaptic weight distribution only depends upon the distance between interacting populations, that is, $w(x,y) = w(|x-y|)$. This implies translation symmetry of the underlying integrodifferential equations (in an unbounded or periodic domain) and an excitatory network can support the propagation of solitary traveling waves. However, if one looks more closely at the anatomy of cortex, it is clear that its detailed microstructure is far from homogeneous. For example, to a first approximation, primary visual cortex (V1) has a periodic-like microstructure on the millimeter length scale, reflecting the existence of various stimulus feature maps; see Sect. 8.1. This has motivated a number of

studies concerned with the effects of a periodically modulated weight distribution on wave propagation in neural fields [64, 132, 332].

We first consider the voltage-based neural field equation (6.115) with periodically modulated weight distribution

$$w(x,y) = w(x-y)[1+\rho K(y/\varepsilon)], \tag{7.78}$$

where ρ is the amplitude of the periodic modulation and ε is the period with $K(x) = K(x+1)$ for all x. It will also be assumed that if $\rho = 0$ (no periodic modulation), then the resulting homogeneous network supports a traveling front solution of speed c_0 as analyzed in Sect. 7.1.1. We will describe two alternative methods for analyzing the effects of periodic wave modulation: one based on averaging theory for small ε [79], which adapts the method use to study the propagation failure in myelinated axons (Sect. 2.5), and the other based on analyzing interfacial dynamics [132]. Both approaches make use of the observation that for sufficiently small ρ, numerical simulations of the inhomogeneous network show a front-like wave separating high and low activity states. However, the wave does not propagate with constant speed, but oscillates periodically in an appropriately chosen moving frame. This pulsating front solution satisfies the periodicity condition $u(x,t) = u(x+\varepsilon, t+T)$ so that we can define the mean speed of the wave to be $c = \varepsilon/T$. We will then consider the effects of periodically modulated weights on the propagation of pulled fronts in an activity-based neural field equation, extending the Hamilton–Jacobi method used in the analysis of CaMKII waves in Sect. 3.2.

7.3.1 Averaging Theory

Suppose that the period ε of weight modulations is much smaller than the range of synaptic interactions $\varepsilon \ll \sigma$. (We fix the length scales by setting $\sigma = 1$.) Following the analysis of saltatory waves along myelinated axons (Sect. 2.5) and [318, 319], we want any inhomogeneous terms to be $\mathcal{O}(\varepsilon)$. Therefore, after substituting Eq. (7.78) into (6.115), we integrate by parts to obtain the equation

$$\begin{aligned}\frac{\partial u(x,t)}{\partial t} &= -u(x,t) + \int_{-\infty}^{\infty} w(x-x')F(u(x',t))dx' \\ &\quad + \varepsilon \int_{-\infty}^{\infty} \mathscr{K}(x'/\varepsilon)\left[w'(x-x')F(u(x',t)) - w(x-x')\frac{\partial F(u(x',t))}{\partial x'}\right]dx'.\end{aligned} \tag{7.79}$$

Here $\mathscr{K}'(x) = \rho K(x)$ with $\mathscr{K}$ only having to be defined up to an arbitrary constant. Motivated by the existence of pulsating front solutions, we perform the change of variables $\xi = x - \phi(t)$ and $\tau = t$. Equation (7.79) becomes

$$\frac{\partial u}{\partial \tau} = -u(\xi,\tau) + \int_{-\infty}^{\infty} w(\xi-\xi')F(u(\xi',\tau))d\xi' + \phi' \frac{\partial u(\xi,\tau)}{\partial \xi} \tag{7.80}$$
$$+\varepsilon \int_{-\infty}^{\infty} \mathscr{K}\left(\frac{\xi'+\phi}{\varepsilon}\right)\left[w'(\xi-\xi')F(u(\xi',\tau)) - w(\xi-\xi')\frac{\partial F(u(\xi',\tau))}{\partial \xi'}\right] d\xi'.$$

Next perform the perturbation expansions

$$u(\xi,\tau) = U(\xi) + \varepsilon u_1(\xi,\tau) + \varepsilon^2 u_2(\xi,\tau) + \ldots, \tag{7.81}$$

$$\phi'(\tau) = c_0 + \varepsilon \phi_1'(\tau) \tag{7.82}$$

where $U(\xi)$ is the unique traveling wave solution of the corresponding homogeneous equation (7.7) with unperturbed wave speed $c = c_0$. The first-order term u_1 satisfies the inhomogeneous linear equation

$$-\frac{\partial u_1(\xi,\tau)}{\partial \tau} + \mathbb{L}u_1(\xi,\tau) = -\phi_1'(\tau)U'(\xi) + h_1(\xi,\phi/\varepsilon) \tag{7.83}$$

where

$$\mathbb{L}u(\xi) = c_0 \frac{du(\xi)}{d\xi} - u(\xi) + \int_{-\infty}^{\infty} w(\xi-\xi')F'(U(\xi'))u(\xi')d\xi' \tag{7.84}$$

and

$$h_1 = \int_{-\infty}^{\infty} \mathscr{K}\left(\frac{\xi'+\phi}{\varepsilon}\right)\left[-w'(\xi-\xi')F(U(\xi')) + w(\xi-\xi')\frac{dF(U(\xi'))}{d\xi'}\right] d\xi'. \tag{7.85}$$

The linear operator $\mathbb{L}$ has a one-dimensional null-space spanned by U'. The existence of U' as a null vector follows immediately from differentiating both sides of Eq. (7.7) with respect to ξ, whereas its uniqueness can be shown using properties of positive linear operators [172]. Therefore, a bounded solution of Eq. (7.83) with respect to ξ and τ will only exist if the right-hand side of Eq. (7.83) is orthogonal to all elements of the null-space of the adjoint operator $\mathbb{L}^\dagger$. The latter is defined with respect to the inner product

$$\int_{-\infty}^{\infty} u(\xi)\mathbb{L}v(\xi)d\xi = \int_{-\infty}^{\infty} \left[\mathbb{L}^\dagger u(\xi)\right] v(\xi)d\xi \tag{7.86}$$

where $u(\xi)$ and $v(\xi)$ are arbitrary integrable functions. Hence,

$$\mathbb{L}^\dagger u(\xi) = -c\frac{du(\xi)}{d\xi} - u(\xi) + F'(U(\xi)) \int_{-\infty}^{\infty} w(\xi-\xi')u(\xi')d\xi'. \tag{7.87}$$

It can be proven that $\mathbb{L}^\dagger$ also has a one-dimensional null-space [172], that is, it is spanned by some function $V(\xi)$. Equation (7.83) thus has a bounded solution if and only if

$$B_0\phi_1'(\tau) = \int_{-\infty}^{\infty} V(\xi)h_1(\xi,\phi/\varepsilon)d\xi \tag{7.88}$$

where

$$B_0 = \int_{-\infty}^{\infty} V(\xi)U'(\xi)d\xi. \tag{7.89}$$

Note that B_0 is strictly positive since V and U' can be chosen to have the same sign [172]. Substituting for h_1 using Eqs. (7.85) and (7.82) and performing an integration by parts leads to a differential equation for the phase ϕ:

$$\frac{d\phi}{d\tau} = c + \varepsilon\Phi_1\left(\frac{\phi}{\varepsilon}\right), \tag{7.90}$$

where

$$\Phi_1\left(\frac{\phi}{\varepsilon}\right) = \frac{1}{B_0}\int_{-\infty}^{\infty}\int_{-\infty}^{\infty} w(\xi-\xi')\mathscr{K}\left(\frac{\xi'+\phi}{\varepsilon}\right) \times\left[V'(\xi)F(U(\xi'))+V(\xi)\frac{dF(U(\xi'))}{d\xi'}\right]d\xi' d\xi. \tag{7.91}$$

The phase equation (7.90) is identical in form to the one derived in Sect. 2.5 for wave propagation along myelinated axons; see Eq. (2.72). It implies that there are two distinct types of behavior. If the right-hand side of Eq. (7.90) is strictly positive, then there exists a pulsating front of the approximate form $U(x-\phi(t))$ and the average speed of propagation is $c = \varepsilon/T$ with

$$T = \int_0^{\varepsilon} \frac{d\phi}{c+\varepsilon\Phi_1\left(\frac{\phi}{\varepsilon}\right)}. \tag{7.92}$$

On the other hand, if the right-hand side of Eq. (7.90) vanishes for some ϕ, then there is wave propagation failure.

In the case of a Heaviside firing rate function $F(u) = H(u-\kappa)$, it is possible to derive an explicit expression for the wave speed c [64]. The solution for the unperturbed wave front $U(\xi)$ was derived in Sect. 7.1, so it is only necessary to determine the solution $V(\xi)$ of the adjoint equation (7.87), which becomes

$$cV'(\xi)+V(\xi) = -\frac{\delta(\xi)}{U'(0)}\int_{-\infty}^{\infty} w(\xi')V(\xi')d\xi'. \tag{7.93}$$

This can be integrated to give

$$V(\xi) = -H(\xi)\mathrm{e}^{-\xi/c}. \tag{7.94}$$

Given the solutions for $U(\xi)$ and $V(\xi)$, it can then be shown that (7.91) reduces to the form

$$B_0\Phi_1\left(\frac{\phi}{\varepsilon}\right) = W(0)\mathscr{K}\left(\frac{\phi}{\varepsilon}\right) + \int_0^\infty \mathscr{K}\left(\frac{\phi-\xi}{\varepsilon}\right)\left[\frac{W(\xi)}{c} - w(\xi)\right]d\xi, \quad (7.95)$$

where

$$W(\xi) = \int_0^\infty \mathrm{e}^{-y/c_0} w(y+\xi)dy \equiv -cU'(\xi), \quad (7.96)$$

and

$$B_0 = \frac{1}{c_0}\int_0^\infty \mathrm{e}^{-\xi/c_0} W(\xi)d\xi. \quad (7.97)$$

Keeping only the lowest-order contribution to Φ_1, Eq. (7.92) reduces to

$$T = \int_0^\varepsilon \frac{d\phi}{c_0 + \varepsilon\Gamma(c_0)A\left(\frac{\phi}{\varepsilon}\right)} \quad (7.98)$$

with $\Gamma(c_0) = W(0)/B_0$. For the sake of illustration, suppose that the periodic modulation functions K and A are pure sinusoids. Setting $A(x) = \rho\sin(2\pi x)/(2\pi)$ in Eq. (7.98) we find that

$$T = \frac{\varepsilon}{\sqrt{c_0^2 - \varepsilon^2\rho^2\Gamma(c_0)^2}} \quad (7.99)$$

and, hence,

$$c = \sqrt{c_0^2 - \varepsilon^2\rho^2\Gamma(c_0)^2/(2\pi)^2}. \quad (7.100)$$

This establishes that a sinusoidally varying heterogeneous neural medium only supports a propagating wave if the velocity c_0 of the (unique) solution of the corresponding homogeneous medium satisfies the inequality

$$c_0 \geq \varepsilon\rho\Gamma(c_0). \quad (7.101)$$

For the particular example of an exponential distribution (7.1) with $\sigma = 1$, we have $c_0 = (1-2\kappa)/(2\kappa)$ and $\Gamma(c_0) = 1 + c_0$ so that

$$c = c_0\sqrt{1 - \gamma_0\rho^2\varepsilon^2}, \quad \gamma_0 = \frac{1}{2\pi(2\kappa-1)}. \quad (7.102)$$

The above averaging method can also be extended to the case of periodically modulated traveling pulses (pulsating pulses) (see [332]), in which there are two

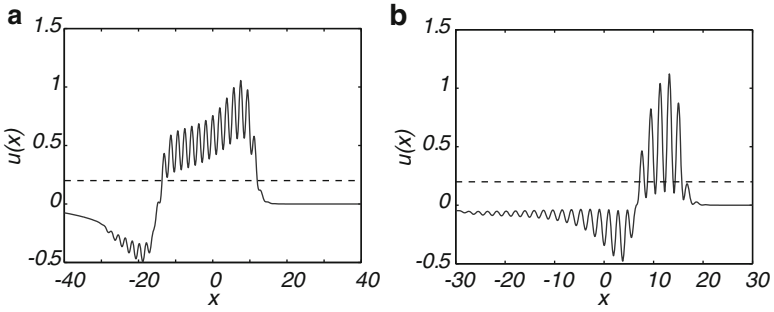

Fig. 7.7 Pulsating pulse solutions in a 1D excitatory neural field with linear adaptation and Heaviside firing rate function; see Eq. (7.49). The threshold is $\kappa = 0.2$, strength of adaptation is $\beta = 2.0$, and adaptation rate constant is $\varepsilon = 0.04$. The weight distribution is given by $w(x,y) = \rho w(x-y)\sin(2\pi x/\varepsilon)$ with $2\pi\varepsilon = 0.3$ and $w(x)$ an exponential weight function. (**a**) Single-bump solution for $\rho = 0.3$. The interior of the pulse consists of non-propagating, transient ripples. (**b**) Multi-bump solution for $\rho = 0.8$. The solitary pulse corresponds to the envelope of a multiple bump solution, in which individual bumps are non-propagating and transient. The disappearance of bumps at one end and the emergence of new bumps at the other end generate the propagation of activity [332]

threshold crossing points. One simplifying assumption of the analysis is that, in the presence of periodically modulated weights, additional threshold crossing points do not occur. However, numerical solutions of a neural field equation with linear adaptation have shown that in the case of large amplitude modulations, a pulsating pulse can develop multiple threshold crossing points [332]. That is, the traveling wave represents the envelope of a multi-bump solution, in which individual bumps are non-propagating and transient; see Fig. 7.7. The appearance (disappearance) of bumps at the leading (trailing) edge of the pulse generates the coherent propagation of the pulse. Wave propagation failure occurs when activity is insufficient to maintain bumps at the leading edge.

7.3.2 Interfacial Dynamics

The averaging method provides a reasonable estimate for the mean wave speed and the critical amplitude ρ for wave propagation failure, provided that the spatial period $\varepsilon \ll 1$. As shown by Coombes and Laing [132] in the case of a Heaviside firing rate function, a more accurate estimate for the wave speed for larger values of ε can be obtained by analyzing the dynamics of the interface between high and low activity states, provided that the amplitude of periodic modulations is not too large [132]. The basic idea is to change to a co-moving frame of the unperturbed system, $u = u(\xi,t)$ with $\xi = x - c_0 t$ such that Eq. (6.115) becomes

$$-c_0 u_\xi + u_t = -u + \int_{-\infty}^{\infty} w(\xi + c_0 t, y) F(u(y - c_0 t, t) dy, \tag{7.103}$$

with w given by Eq. (7.78) and $F(u) = H(u-\kappa)$. The moving interface (level set) is then defined according to the threshold condition

$$u(\xi_0(t),t) = \kappa. \tag{7.104}$$

Differentiating with respect to t then determines the velocity of the interface in the co-moving frame according to

$$\frac{d\xi_0}{dt} = -\frac{u_t(\xi_0(t),t)}{u_\xi(\xi_0(t),t)}. \tag{7.105}$$

As in the previous averaging method, suppose that for $\rho = 0$, there exists a traveling front solution $U(\xi)$ of the homogeneous equation (7.7) with speed c_0. Now make the approximation $u_\xi(\xi_0(t),t) = U'(0)$, which is based on the assumption that for small amplitudes ρ, the slope of the traveling front varies sufficiently slowly. Setting $\xi = \xi_0(t)$ in Eq. (7.103) and using Eq. (7.3), it is then straightforward to show that [132]

$$\frac{d\xi_0}{dt} = \rho c_0 \frac{\displaystyle\int_0^\infty w(y)K(\xi_0 + c_0 t - y)}{\displaystyle\kappa - \int_0^\infty w(y)dy}. \tag{7.106}$$

In order to match up with the previous method, let $K(x) = \sin(2\pi x/\varepsilon)$ and $w(x) = \mathrm{e}^{-|x|}/2$. Then $c_0 = (1-2\kappa)/(2\kappa)$ and [132]

$$\frac{d\xi_0}{dt} = c_0\rho\gamma(\varepsilon)\sin\left[\frac{2\pi}{\varepsilon}(\xi_0(t)+c_0 t) + \phi_0(\varepsilon)\right], \tag{7.107}$$

with

$$\gamma(\varepsilon) = \frac{1}{2\kappa-1}\frac{1}{\sqrt{1+(2\pi/\varepsilon)^2}}, \quad \tan\phi_0(\varepsilon) = \frac{2\pi}{\varepsilon}. \tag{7.108}$$

The final step is to look for a T-periodic solution of Eq. (7.107) such that $\xi_0(t) = \xi_0(t+T)$. Setting $x_0 = \xi_0 + c_0 t$ with $x_0 \in [0,\varepsilon]$ and integrating gives

$$\int_0^{x_0} \frac{dx}{1+\rho\gamma\sin(2\pi x/\sigma+\phi)} = c_0 t. \tag{7.109}$$

This may be evaluated using a half-angle substitution,

$$c_0 t = \frac{\varepsilon}{\pi}\frac{1}{\sqrt{1-\rho^2\gamma^2}}\tan^{-1}\frac{z}{\sqrt{1-\rho^2\gamma^2}}\Bigg|_{z_0(0)+\rho\gamma}^{z_0(t)+\rho\gamma}, \tag{7.110}$$

where $z_0(t) = \tan[(2\pi x_0(t)/\varepsilon + \phi)/2]$ and $x_0(0) = 0$. A self-consistent pulsating front solution is then obtained by imposing the condition $\varepsilon = x_0(T)$, which then determines the effective speed $c = \varepsilon/T$ to be

$$c = c_0\sqrt{1-\rho^2\gamma(\varepsilon)^2}. \tag{7.111}$$

Note that on Taylor expanding $\gamma(\varepsilon)$ to first order in ε, Eq. (7.111) recovers the corresponding result (7.102) obtained using averaging theory. However, the expression derived using interfacial dynamics is more accurate when the period ε increases, provided that the amplitude ρ does not become too large.

7.3.3 Hamilton–Jacobi Dynamics and Slow Spatial Heterogeneities

We now turn to the effects of periodically modulated weights on the propagation of pulled front solutions of the activity-based neural field equation (7.27). In the case of high-frequency modulation, Coombes and Laing [132] adapted previous work by Shigesada et al. on pulsating fronts in reaction–diffusion models of the spatial spread of invading species into heterogeneous environments [574, 575]. (In Sect. 3.2.2 we applied the theory of pulsating fronts to CaMKII translocation waves along spiny dendrites.) We briefly sketch the basic steps in the analysis. First, substitute the periodically modulated weight distribution (7.78) into Eq. (7.27) and linearize about the leading edge of the wave where $a(x,t) \sim 0$:

$$\frac{\partial a(x,t)}{\partial t} = -a(x,t) + \int_{-\infty}^{\infty} w(x-y)[1+K(y/\varepsilon)]a(y,t)dy. \tag{7.112}$$

Now assume a solution of the form $a(x,t) = A(\xi)P(x)$, $\xi = x - ct$ with $A(\xi) \to 0$ as $\xi \to \infty$ and $P(x+2\pi\varepsilon) = P(x)$. Substitution into Eq. (7.112) then gives

$$-cP(x)A'(\xi) = -P(x)A(\xi) + \int_{-\infty}^{\infty} w(x-y)[1+K(y/\varepsilon)]P(y)A(\xi-[x-y])dy. \tag{7.113}$$

Taking $A(\xi) \sim \mathrm{e}^{-\lambda\xi}$ and substituting into the above equation yields a nonlocal version of the Hill equation:

$$(1+c\lambda)P(x) = \int_{-\infty}^{\infty} \mathrm{e}^{\lambda[x-y]} w(x-y)[1+K(y/\varepsilon)]P(y)dy. \tag{7.114}$$

In order to determine the minimal wave speed, it is necessary to find a bounded periodic solution $P(x)$ of Eq. (7.114), which yields a corresponding dispersion relation $c = c(\lambda)$, whose minimum with respect to λ can then be determined (assuming it exists). One way to obtain an approximate solution to Eq. (7.114) is to use Fourier methods to derive an infinite matrix equation for the Fourier coefficients of

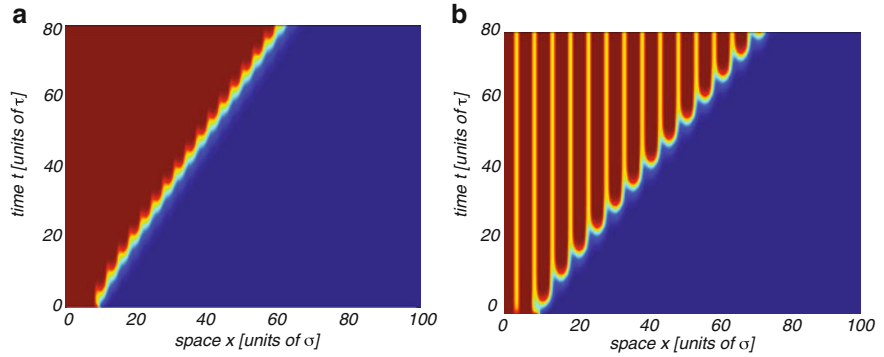

Fig. 7.8 Space–time contour plots of a pulsating front solution of the neural field equation (7.112) with piecewise linear firing rate function (7.29), Gaussian weight distribution (7.38), and a $2\pi\varepsilon$-periodic modulation of the synaptic weights, $K(x) = \cos(x/\varepsilon)$. (**a**) $\varepsilon = 0.5$ and (**b**) $\varepsilon = 0.8$. Other parameters are $W_0 = 1.2$, $\sigma = 1.0$, and $\kappa = 0.4$

the periodic function $P(x)$ and then to numerically solve a finite truncated version of the matrix equation. This is the approach followed in [132]. The matrix equation takes the form

$$(1 + c\lambda)P_m = \mathscr{W}(\lambda - im/\varepsilon)P_m + \mathscr{W}(\lambda - im/\varepsilon)\sum_l K_l P_{m-l}, \tag{7.115}$$

where $K(x/\varepsilon) = \sum_n K_n e^{imx/\varepsilon}$, $P(x) = \sum_n P_n e^{imx/\varepsilon}$, and $\mathscr{W}(p) = \hat{W}(p) + \hat{W}(-p)$ with $\hat{W}(p)$, the Laplace transform of $w(x)$. One finds that the mean velocity of a pulsating front increases with the period $2\pi\varepsilon$ of the synaptic modulations [132]. This is illustrated in Fig. 7.8, which shows space–time plots of a pulsating front for $\varepsilon = 0.5$ and $\varepsilon = 0.8$.

Now suppose that there is a slowly varying spatial modulation of the synaptic weight distribution (relative to the range of synaptic interactions). (Although we do not have a specific example of long-wavelength modulations in mind, we conjecture that these might be associated with inter-area cortical connections. For example, it has been shown that heterogeneities arise as one approaches the V1/V2 border in visual cortex, which has a number of effects including the generation of reflected waves [688].) In the case of slow modulations, one can extend the Hamilton–Jacobi theory of sharp interfaces developed originally for PDEs (see [178, 203, 204, 212, 421] and Sect. 3.3.2) to the case of neural fields [70]. In order to illustrate this, consider a heterogeneous version of the activity-based neural field equation (7.27) of the form

$$\frac{\partial a(x,t)}{\partial t} = -a(x,t) + F\left(\int_{-\infty}^{\infty} w(x-x')J(\varepsilon x')a(x',t)dx'\right), \tag{7.116}$$

in which there is a slow (nonperiodic) spatial modulation $J(\varepsilon x)$ of the synaptic weight distribution with $\varepsilon \ll 1$.

Recall from Sect. 3.3.2 that the first step in the Hamilton–Jacobi method is to rescale space and time in Eq. (7.116) according to $t \to t/\varepsilon$ and $x \to x/\varepsilon$ [178, 204, 421]:

$$\varepsilon \frac{\partial a(x,t)}{\partial t} = -a(x,t) + F\left(\frac{1}{\varepsilon}\int_{-\infty}^{\infty} w([x-x']/\varepsilon)J(x')a(x',t)dx'\right). \tag{7.117}$$

Under this hyperbolic rescaling, the front region where the activity $a(x,t)$ rapidly increases as x decreases from infinity becomes a step as $\varepsilon \to 0$; see Fig. 7.2(b). This motivates introducing the WKB approximation

$$a(x,t) \sim \mathrm{e}^{-G(x,t)/\varepsilon} \tag{7.118}$$

with $G(x,t) > 0$ for all $x > x(t)$ and $G(x(t),t) = 0$. The point $x(t)$ determines the location of the front and $c = \dot{x}$. Substituting (3.85) into Eq. (7.117) gives

$$-\partial_t G(x,t) = -1 + \frac{1}{\varepsilon}\int_{-\infty}^{\infty} w([x-x']/\varepsilon)J(x')\mathrm{e}^{-[G(x',t)-G(x,t)]/\varepsilon}dx'. \tag{7.119}$$

We have used the fact that for $x > x(t)$ and $\varepsilon \ll 1$, the solution is in the leading edge of the front so that F can be linearized. Equation (7.119) can be simplified using the method of steepest descents [70]; see below. This yields the equation

$$-\partial_t G(x,t) = -1 + \tilde{w}(i\partial_x G(x,t))J(x), \tag{7.120}$$

where $\tilde{w}(k)$ is the Fourier transform of $w(x)$:

$$w(x) = \int_{-\infty}^{\infty} \tilde{w}(k)\mathrm{e}^{ikx}\frac{dk}{2\pi}. \tag{7.121}$$

Equation (7.120) is formally equivalent to the Hamilton–Jacobi equation

$$\partial_t G + H(\partial_x G, x) = 0 \tag{7.122}$$

with corresponding Hamiltonian

$$H(p,x) = -1 + \tilde{w}(ip)J(x) \tag{7.123}$$

where $p = \partial_x G$ is interpreted as the conjugate momentum of x, and $\tilde{w}(ip) = \mathscr{W}(p)$. It follows that the Hamilton–Jacobi equation (7.122) can be solved in terms of the Hamilton equations

$$\frac{dx}{ds} = \frac{\partial H}{\partial p} = J(x)\mathscr{W}'(p) = J(x)[\hat{W}'(p) - \hat{W}'(-p)] \tag{7.124}$$

$$\frac{dp}{ds} = -\frac{\partial H}{\partial x} = -J'(x)\mathscr{W}(p). \tag{7.125}$$

Let $X(s;x,t), P(s;x,t)$ denote the solution with $x(0) = 0$ and $x(t) = x$. We can then determine $G(x,t)$ according to

$$G(x,t) = -E(x,t)t + \int_0^t P(s;x,t)\dot{X}(s;x,t)ds. \tag{7.126}$$

Here

$$E(x,t) = H(P(s;x,t), X(s;x,t)), \tag{7.127}$$

which is independent of s due to conservation of "energy," that is, the Hamiltonian is not an explicit function of time.

Steepest descent calculation of G. The derivation of Eq. (7.120) using steepest descents proceeds as follows. First, substituting the Fourier transfer (7.121) into (7.119) and reversing the order of integration gives

$$-\partial_t G(x,t) = -1 + \frac{1}{\varepsilon}\int_{-\infty}^{\infty}\int_{-\infty}^{\infty} \tilde{w}(k)J(x')\mathrm{e}^{-S(k,x';x,t)/\varepsilon}dx'\frac{dk}{2\pi}, \tag{7.128}$$

where

$$S(k,x';x,t) = ik(x'-x) + G(x',t) - G(x,t). \tag{7.129}$$

Exploiting the fact that ε is small, we perform steepest descents with respect to the x' variable with (k,x,t) fixed. Let $x' = z(k,t)$ denote the stationary point for which $\partial S/\partial x' = 0$, which is given by the solution to the implicit equation

$$ik + \partial_x G(x',t) = 0. \tag{7.130}$$

Taylor expanding S about this point (assuming it is unique) gives to second order

$$\begin{aligned} S(k,x';x,t) &\approx S(k,z(k,t);x,t) + \frac{1}{2}\frac{\partial^2 S}{\partial x'^2}\bigg|_{x'=z(k,t)}(x'-z(k,t))^2 \\ &= ik[z(k,t)-x] + G(z(k,t),t) - G(x,t) \\ &\quad - \frac{1}{2}\partial_{xx}G(z(k,t),t)(x'-z(k,t))^2. \end{aligned} \tag{7.131}$$

Substituting into Eq. (7.128) and performing the resulting Gaussian integral with respect to x' yields the result

$$\begin{aligned} -\partial_t G(x,t) = -1 + \frac{1}{\varepsilon}\int_{-\infty}^{\infty}\sqrt{\frac{2\pi\varepsilon}{\partial_{xx}G(z(k,t),t)}}\tilde{w}(k)J(z(k,t)) \\ \times \mathrm{e}^{-\left(ik[z(k,t)-x] + G(z(k,t),t) - G(x,t)\right)/\varepsilon}\frac{dk}{2\pi}. \end{aligned} \tag{7.132}$$

This can be rewritten in the form

$$-\partial_t G(x,t) = -1 + \frac{1}{\sqrt{2\pi\varepsilon}}\int_{-\infty}^{\infty}\tilde{w}(k)J(z(k,t))\mathrm{e}^{-\hat{S}(k;x,t)/\varepsilon}dk, \tag{7.133}$$

where

$$\hat{S}(k;x,t) = ik[z(k,t)-x] + G(z(k,t),t) - G(x,t) + \frac{\varepsilon}{2}\ln\partial_{xx}G(z(k,t),t). \tag{7.134}$$

The integral over k can also be evaluated using steepest descents. Thus, Taylor expand $\hat{S}$ to second order about the stationary point $k = k(x,t)$, which is the solution to the equation

$$0 = \frac{\partial \hat{S}}{\partial k} = i[z(k,t) - x] + \frac{\partial z(k,t)}{\partial k}\left[ik + \partial_x G(z(k,t),t) + \frac{\varepsilon}{2}\frac{\partial_{xxx} G(z(k,t),t)}{\partial_{xx} G(z(k,t),t)}\right]. \tag{7.135}$$

It follows from Eqs. (7.130) and (7.135) that $z(k(x,t),t) = x + \mathscr{O}(\varepsilon)$ and so

$$k(x,t) = i\partial_x G(x,t) + \mathscr{O}(\varepsilon). \tag{7.136}$$

Moreover,

$$\hat{S}(k;x,t) \approx \frac{1}{2}\left.\frac{\partial^2 \hat{S}}{\partial k^2}\right|_{k=k(x,t)} (k - k(x,t))^2. \tag{7.137}$$

Substituting into Eq. (7.133) and performing the Gaussian integral with respect to k gives to leading order in ε

$$-\partial_t G(x,t) = -1 + \frac{1}{\sqrt{i\partial_{xx} G(x,t)\partial_k z(k(x,t),t)}}\tilde{w}(k(x,t))J(x). \tag{7.138}$$

Finally, setting $x' = z(k,t)$ in Eq. (7.130) and differentiating with respect to k show that $\partial_{xx} G(z(k,t),t)\partial_k z(k,t) = -i$ and we obtain Eq. (7.120).

Given $G(x,t)$, the location $x(t)$ of the front at time t is determined by the equation $G(x(t),t) = 0$. Differentiating with respect to t shows that $\dot{x}\partial_x G + \partial_t G = 0$. Let us begin by rederiving the wave speed for a homogeneous neural field by setting $J(x) \equiv 1$. In this case, $dp/ds = 0$ so that $p = \lambda_0$ independently of s. Hence, $x(s) = xs/t$, which implies that

$$\dot{x} = \frac{dx}{ds} = \mathscr{W}'(\lambda_0). \tag{7.139}$$

On the other hand,

$$\dot{x} = -\frac{\partial_t G}{\partial_x G} = \frac{-1 + \mathscr{W}(\lambda_0)}{\lambda_0}. \tag{7.140}$$

Combining these two results means that λ_0 is given by the minimum of the function

$$c(\lambda) = \frac{-1 + \mathscr{W}(\lambda)}{\lambda} \tag{7.141}$$

and $c_0 = c(\lambda_0)$. This recovers the result of Sect. 7.1.3. Thus, in the case of a Gaussian weight distribution, λ_0 is related to c_0 according to Eq. (7.42). Now suppose that there exists a small-amplitude, slow modulation of the synaptic weights $J(x) = 1 + \beta f(x)$ with $\beta \ll 1$. We can then obtain an approximate solution of Hamilton's Eqs. (7.124) and (7.125) and the corresponding wave speed using regular perturbation theory along analogous lines to a previous study of the F–KPP equation [421]. We find (see below) that

$$x(t) = c_0 t + \frac{\beta \mathscr{W}(\lambda_0)}{c_0 \lambda_0} \int_0^{c_0 t} f(y)dy + \mathscr{O}(\beta^2). \tag{7.142}$$

Here c_0 is the wave speed of the homogeneous neural field ($\beta = 0$), which is given by $c_0 = c(\lambda_0)$ with λ_0 obtained by minimizing the function $c(\lambda)$ defined by Eq. (7.141); see Eq. (7.42). Finally, differentiating both sides with respect to t and inverting the hyperbolic scaling yields

$$c \equiv \dot{x}(t) = c_0 + \frac{\beta \mathscr{W}(\lambda_0)}{\lambda_0} f(\varepsilon c_0 t) + \mathscr{O}(\beta^2). \tag{7.143}$$

The analytical results agree reasonably well with numerical simulations, provided that ε is sufficiently small [70]. In Fig. 7.9(a) we show snapshots of a pulled front in the case of a homogeneous network with Gaussian weights (7.38) and piecewise linear firing rate function (7.29). Space and time units are fixed by setting the range of synaptic weights $\sigma = 1$ and the time constant $\tau = 1$. A corresponding space–time plot is given in Fig. 7.9(b), which illustrates that the speed of the front asymptotically approaches the calculated minimal wave speed c_0. (Note that pulled fronts take an extremely long time to approach the minimal wave speed at high levels of numerical accuracy, since the asymptotics are algebraic rather than exponential in time [162].) In Figs. 7.9(c,d) we plot the corresponding results in the case of an inhomogeneous network. For the sake of illustration, the synaptic heterogeneity is taken to be a linear function of displacement, that is, $J(x) = 1 + \varepsilon(x - l)$, and $\beta = \varepsilon$. Equation (7.142) implies that

$$\begin{aligned} x(t) &= l + c_0 t + \frac{\varepsilon^2 \mathscr{W}(\lambda_0)}{2c_0\lambda_0}[(c_0 t)^2 - 2c_0 l t] \\ &= l + \left[c_0 - \frac{\varepsilon^2 l(c_0\lambda_0 + 1)}{\lambda_0}\right] t + \frac{\varepsilon^2 c_0(c_0\lambda_0 + 1)}{2\lambda_0} t^2, \end{aligned} \tag{7.144}$$

where we have used Eq. (7.141) and assumed that the initial position of the front is $x(0) = l$. Hence, the perturbation theory predicts that a linearly increasing modulation in synaptic weights results in the leading edge of the front tracing out a downward parabola in a space–time plot for times $t \ll \mathscr{O}(1/\varepsilon^2)$. This is consistent with numerical simulations for $\varepsilon^2 = 0.005$, as can be seen in the space–time plot of Fig. 7.9(d).

Perturbation calculation of wave speed. Introduce the perturbation expansions

$$x(s) = x_0(s) + \beta x_1(s) + \mathscr{O}(\beta^2), \quad p(s) = p_0(s) + \beta p_1(s) + \mathscr{O}(\beta^2) \tag{7.145}$$

and substitute into Eqs. (7.124) and (7.125). Taylor expanding the nonlinear function $f(x)$ about x_0 and $\mathscr{W}(p) = \hat{W}(p) + \hat{W}(-p)$ about p_0 then leads to a hierarchy of equations, the first two of which are

$$\dot{p}_0(s) = 0, \quad \dot{x}_0(s) = \mathscr{W}'(p_0), \tag{7.146}$$

and

$$\dot{p}_1(s) = -f'(x_0)\mathscr{W}(p_0), \quad \dot{x}_1(s) = \mathscr{W}''(p_0)p_1(s) + f(x_0)\mathscr{W}'(p_0), \tag{7.147}$$

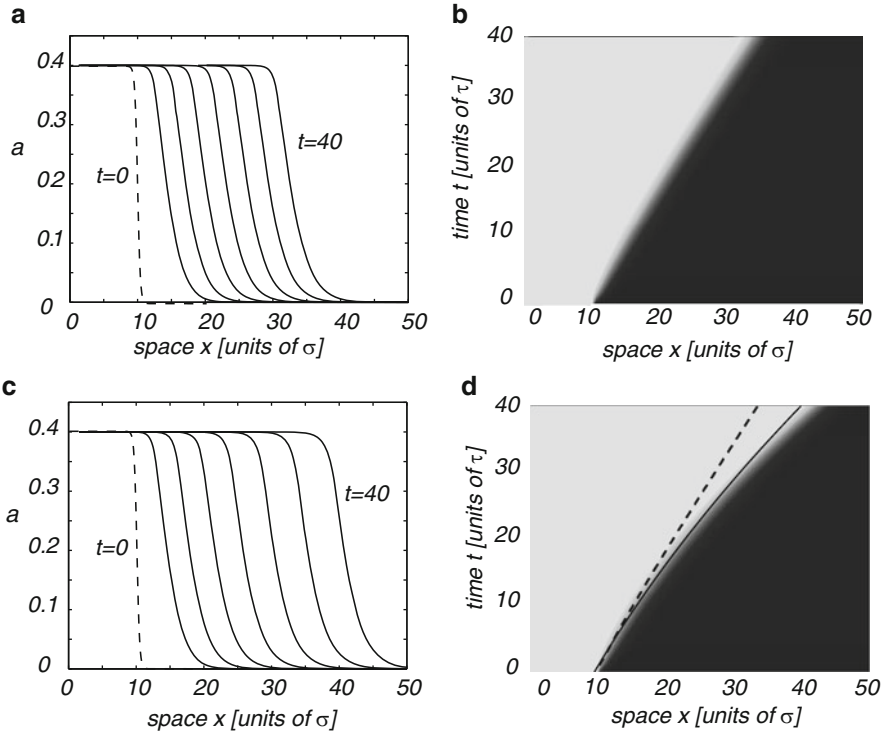

Fig. 7.9 (**a**) Propagating front in a homogeneous network with Gaussian weights (7.38) and piecewise linear rate function (7.29). Parameter values are $W_0 = 1.2, \sigma = 1, \kappa = 0.4$. The initial condition is taken to be a steep sigmoid $a(x,0) = 0.5/(1+\exp(-\eta(x-l)))$ with $\eta = 5$ and $l = 10$. (**a**) Snapshots of wave profile at time intervals of width $\Delta t = 5$ from $t = 10$ to $t = 40$. (**b**) Space–time contour plot. Wave speed asymptotically approaches the minimum c_0 of the velocity dispersion curve given by Eq. (7.39). (**c**,**d**) Propagating front in a network with a linear heterogeneity in the synaptic weights, $J(x) = 1 + \varepsilon(x-l)$, $l = 10$, and $\varepsilon^2 = 0.005$. Other parameters as in (**a**,**b**). (**c**) Snapshots of wave profile at time intervals of width $\Delta t = 5$ from $t = 10$ to $t = 40$. (**d**) Space–time contour plot. Wave speed increases approximately linearly with time, so the position $x(t)$ of front evolves according to a downward parabola. Theoretical curve based on the perturbation calculation is shown by the *solid curve*. The trajectory of the front in the corresponding homogeneous case is indicated by the *dashed curve*

These are supplemented by the Cauchy conditions $x_0(0) = 0, x_0(t) = x$ and $x_n(0) = x_n(t) = 0$ for all integers $n \geq 1$. Equations (7.146) have solutions of the form

$$p_0(s) = \lambda, \quad x_0(s) = \mathscr{W}'(\lambda)s + B_0 \tag{7.148}$$

with λ, B_0 independent of s. Imposing the Cauchy data then implies that $B_0 = 0$ and λ satisfies the equation

$$\mathscr{W}'(\lambda) = x/t. \tag{7.149}$$

At the next order,

$$p_1(s) = -\mathscr{W}(\lambda)\frac{t}{x}f(xs/t) + A_1, \tag{7.150}$$

$$x_1(s) = -\mathscr{W}''(\lambda)\mathscr{W}(\lambda)\frac{t^2}{x^2}\int_0^{xs/t} f(y)dy + \int_0^{xs/t} f(y)dy + \mathscr{W}''(\lambda)A_1 s + B_1, \tag{7.151}$$

with A_1, B_1 independent of s. Imposing the Cauchy data then implies that $B_1 = 0$ and

$$A_1 = A_1(x,t) = \mathscr{W}(\lambda)\frac{t}{x^2}\int_0^x f(y)dy - \frac{1}{t\mathscr{W}''(\lambda)}\int_0^x f(y)dy. \tag{7.152}$$

Given these solutions, the energy function $E(x,t)$ is

$$\begin{aligned} E(x,t) &= -1 + [1 + \beta f(x_0 + \beta x_1 + \ldots)]\mathscr{W}(\lambda + \beta p_1 + \ldots) \\ &= -1 + \mathscr{W}(\lambda) + \beta[\mathscr{W}'(\lambda)p_1(s) + f(x_0(s))\mathscr{W}(\lambda)] + \mathscr{O}(\beta^2). \end{aligned} \tag{7.153}$$

Substituting for $x_0(s)$ and $p_1(s)$ and using the condition $\mathscr{W}'(\lambda) = x/t$, we find that

$$E(x,t) = -1 + \mathscr{W}(\lambda) + \beta\frac{x}{t}A_1(x,t) + \mathscr{O}(\beta^2), \tag{7.154}$$

which is independent of s as expected. Similarly,

$$\begin{aligned} \int_0^t p(s)\dot{x}(s)ds &= \lambda x + \beta\mathscr{W}'(\lambda)\int_0^t p_1(s)ds + \mathscr{O}(\beta^2) \\ &= \lambda x + \beta\frac{\mathscr{W}'(\lambda)}{\mathscr{W}''(\lambda)}\int_0^t \left[\dot{x}_1(s) - \mathscr{W}'(\lambda)f(\mathscr{W}'(\lambda)s)\right]ds + \mathscr{O}(\beta^2) \\ &= \lambda x - \beta\frac{\mathscr{W}'(\lambda)}{\mathscr{W}''(\lambda)}\int_0^x f(y)dy + \mathscr{O}(\beta^2). \end{aligned} \tag{7.155}$$

Hence, to first order in β,

$$G(x,t) = t - \mathscr{W}(\lambda)t + \lambda x - \beta\mathscr{W}(\lambda)\frac{t}{x}\int_0^x f(y)dy. \tag{7.156}$$

We can now determine the wave speed c by imposing the condition $G(x(t),t) = 0$ and performing the perturbation expansions $x(t) = x_0(t) + \beta x_1(t) + \mathscr{O}(\beta^2)$ and $\lambda = \lambda_0 + \beta\lambda_1 + \mathscr{O}(\beta^2)$. Substituting into Eq. (7.156) and collecting terms at $\mathscr{O}(1)$ and $\mathscr{O}(\beta)$ leads to Eq. (7.142).

7.4 Wave Propagation in Stochastic Neural Fields

In Sect. 6.4 we constructed stochastic neuronal population models based on a master equation formulation. However, continuum versions of these models are difficult to analyze even under a diffusion approximation, due to the nonlocal nature of the multiplicative noise terms; see Eq. (6.71). Therefore, in this section, we analyze the effects of noise on wave propagation in stochastic neural fields with local multiplicative noise, extending the PDE methods outlined in Sect. 2.6. This form of noise can also be interpreted in terms of parametric fluctuations in the firing threshold [58].

7.4.1 Spontaneous Front Propagation

Consider the following stochastic neural field equation: $U(x,t)$

$$dU(x,t) = \left[-U(x,t) + \int_{-\infty}^{\infty} w(x-y)F(U(y,t))dy\right]dt + \varepsilon^{1/2} g(U(x,t))dW(x,t). \tag{7.157}$$

We assume that $dW(x,t)$ represents an independent Wiener process such that

$$\langle dW(x,t)\rangle = 0, \quad \langle dW(x,t)dW(x',t')\rangle = 2C([x-x']/\lambda)\delta(t-t')dtdt', \tag{7.158}$$

where $\langle\cdot\rangle$ denotes averaging with respect to the Wiener process. Here λ is the spatial correlation length of the noise such that $C(x/\lambda) \to \delta(x)$ in the limit $\lambda \to 0$, and ε determines the strength of the noise, which is assumed to be weak. Moreover, the multiplicative noise term is taken to be of Stratonovich form. The analysis of Eq. (7.157) proceeds along similar lines to the analysis of the stochastic bistable equation in Sect. 2.6; see also [70]. First, using Novikov's theorem, we rewrite Eq. (7.157) so that the fluctuating term has zero mean:

$$dU(x,t) = \left[h(U(x,t)) + \int_{-\infty}^{\infty} w(x-y)F(U(y,t))dy\right]dt + \varepsilon^{1/2} dR(U,x,t), \tag{7.159}$$

where

$$h(U) = -U + \varepsilon C(0) g'(U) g(U) \tag{7.160}$$

and

$$dR(U,x,t) = g(U)dW(x,t) - \varepsilon^{1/2} C(0) g'(U) g(U) dt. \tag{7.161}$$

The stochastic process R has the variance

$$\langle dR(U,x,t)dR(U,x',t)\rangle = \langle g(U(x,t))dW(x,t)g(U(x',t)dW(x',t)\rangle + \mathscr{O}(\varepsilon^{1/2}). \tag{7.162}$$

The next step in the analysis is to express the solution U of Eq. (7.159) as a combination of a fixed wave profile U_0 that is displaced by an amount $\Delta(t)$ from its uniformly translating position $\xi = x - c_\varepsilon t$ and a time-dependent fluctuation Φ in the front shape about the instantaneous position of the front:

$$U(x,t) = U_0(\xi - \Delta(t)) + \varepsilon^{1/2}\Phi(\xi - \Delta(t), t). \tag{7.163}$$

The wave profile U_0 and associated wave speed c_ε are obtained by solving the modified deterministic equation

$$-c_\varepsilon \frac{dU_0}{d\xi} - h(U_0(\xi)) = \int_{-\infty}^{\infty} w(\xi - \xi')F(U_0(\xi'))d\xi', \tag{7.164}$$

As in Sect. 2.6, Eq. (7.164) is chosen so that that to leading order, the stochastic variable $\Delta(t)$ undergoes unbiased Brownian motion with

$$\langle \Delta(t) \rangle = 0, \quad \langle \Delta(t)^2 \rangle = 2D(\varepsilon)t \tag{7.165}$$

where the diffusion coefficient $D(\varepsilon) = \mathscr{O}(\varepsilon)$ can be calculated using perturbation analysis (see below).

Perturbation calculation of diffusivity $D(\varepsilon)$. Substitute the decomposition (7.163) into Eq. (7.159) and expand to first order in $\mathscr{O}(\varepsilon^{1/2})$:

$$\begin{aligned}
&-c_\varepsilon U_0'(\xi-\Delta(t))dt - U_0'(\xi-\Delta(t))d\Delta(t) + \varepsilon^{1/2}\left[d\Phi(\xi-\Delta(t),t) - c_\varepsilon \Phi'(\xi-\Delta(t),t)dt\right] \\
&\quad -\varepsilon^{1/2}\Phi'(\xi-\Delta(t),t)d\Delta(t) \\
&\quad = h(U_0(\xi-\Delta(t)))dt + h'(U_0(\xi-\Delta(t)))\varepsilon^{1/2}\Phi(\xi-\Delta(t),t)dt \\
&\quad + \int_{-\infty}^{\infty} w(\xi-\xi')\left(F(U_0(\xi'-\Delta(t))) + F'(U_0(\xi'-\Delta(t)))\varepsilon^{1/2}\Phi(\xi'-\Delta(t),t)\right)d\xi' dt \\
&\quad + \varepsilon^{1/2} dR(U_0(\xi-\Delta(t)),\xi,t) + \mathscr{O}(\varepsilon).
\end{aligned}$$

Imposing Eq. (7.164), after shifting $\xi \to \xi - \Delta(t)$, and dividing through by $\varepsilon^{1/2}$ then gives

$$\begin{aligned}
d\Phi(\xi-\Delta(t),t) = \hat{L}\circ\Phi(\xi-\Delta(t),t)dt + \varepsilon^{-1/2}U_0'(\xi-\Delta(t))d\Delta(t) \\
+ dR(U_0(\xi-\Delta(t),\xi,t) + \mathscr{O}(\varepsilon^{1/2}),
\end{aligned} \tag{7.166}$$

where $\mathbb{L}$ is the non-self-adjoint linear operator

$$\mathbb{L}\circ A(\xi) = c_\varepsilon \frac{dA(\xi)}{d\xi} + h'(U_0(\xi))A(\xi) + \int_{-\infty}^{\infty} w(\xi-\xi')F'(U_0(\xi'))A(\xi')d\xi' \tag{7.167}$$

for any function $A(\xi) \in L^2(\mathbb{R})$. Finally, for all terms in Eq. (7.166) to be of the same order, we require that $\Delta(t) = \mathscr{O}(\varepsilon^{1/2})$. It then follows that $U_0(\xi-\Delta(t)) = U_0(\xi) + \mathscr{O}(\varepsilon^{1/2})$ and Eq. (7.166) reduces to

$$d\Phi(\xi,t) = \mathbb{L}\circ\Phi(\xi,t)dt + \varepsilon^{-1/2}U_0'(\xi)d\Delta(t) + dR(U_0(\xi),\xi,t) + \mathscr{O}(\varepsilon^{1/2}). \tag{7.168}$$

It can be shown that for a sigmoid firing rate function and exponential weight distribution, the operator $\mathbb{L}$ has a 1D null-space spanned by $U_0'(\xi)$ [172]. (The fact that $U_0'(\xi)$ belongs to the null-space follows immediately from differentiating equation (7.164) with respect to ξ.) We then have the solvability condition for the existence of a nontrivial solution of Eq. (7.168), namely, that the inhomogeneous part is orthogonal to all elements of the null-space of the adjoint operator $\mathbb{L}^\dagger$. The latter is almost identical in form to Eq. (7.87):

$$\mathbb{L}^\dagger B(\xi) = -c_\varepsilon \frac{dB(\xi)}{d\xi} + h'(U_0(\xi))B(\xi) + F'(U_0(\xi))\int_{-\infty}^{\infty} w(\xi-\xi')B(\xi')d\xi'. \tag{7.169}$$

Hence, $\mathbb{L}^\dagger$ has a one-dimensional null-space that is spanned by some function $\mathscr{V}(\xi)$. Taking the inner product of both sides of Eq. (7.168) with respect to $\mathscr{V}(\xi)$ then leads to the solvability condition

$$\int_{-\infty}^{\infty} \mathscr{V}(\xi)\left[U_0'(\xi)d\Delta(t) + \varepsilon^{1/2}dR(U_0,\xi,t)\right]d\xi = 0. \tag{7.170}$$

Thus $\Delta(t)$ satisfies the stochastic differential equation (SDE)

$$d\Delta(t) = -\varepsilon^{1/2} \frac{\int_{-\infty}^{\infty} \mathscr{V}(\xi) dR(U_0, \xi, t) d\xi}{\int_{-\infty}^{\infty} \mathscr{V}(\xi) U_0'(\xi) d\xi}. \tag{7.171}$$

Using the lowest-order approximation $dR(U_0, \xi, t) = g(U_0(\xi)) dW(\xi, t)$, we deduce that $\Delta(t)$ is a Wiener process with effective diffusion coefficient

$$D(\varepsilon) = \varepsilon \frac{\int_{-\infty}^{\infty} \int_{-\infty}^{\infty} \mathscr{V}(\xi) \mathscr{V}(\xi') g(U_0(\xi)) g(U_0(\xi')) \langle dW(\xi, t) dW(\xi', t) \rangle d\xi d\xi'}{\left[\int_{-\infty}^{\infty} \mathscr{V}(\xi) U_0'(\xi) d\xi \right]^2} \tag{7.172}$$

In the case of a Heaviside rate function $F(U) = H(U - \kappa)$ and multiplicative noise $g(U) = g_0 U$, the effective speed c_ε and diffusion coefficient $D(\varepsilon)$ can be calculated explicitly [70]. (The constant g_0 has units of $\sqrt{\text{length}/\text{time}}$.) The deterministic equation (7.164) for the fixed profile U_0 then reduces to

$$-c_\varepsilon \frac{dU_0}{d\xi} + U_0(\xi)\gamma(\varepsilon) = \int_{-\infty}^{\infty} w(\xi - \xi') H(U_0(\xi') - \kappa) d\xi', \tag{7.173}$$

with

$$\gamma(\varepsilon) = (1 - \varepsilon g_0^2 C(0)), \tag{7.174}$$

This is identical in structure to Eq. (7.3) for the deterministic neural field modulo the rescaling of the decay term. The analysis of the wave speeds proceeds along similar lines to Sect. 7.1. Thus, multiplying both sides of Eq. (7.173) by $\mathrm{e}^{-\xi\gamma(\varepsilon)/c_\varepsilon}$ and integrating with respect to ξ gives

$$U_0(\xi) = \mathrm{e}^{\xi\gamma(\varepsilon)/c_\varepsilon} \left[\kappa - \frac{1}{c_\varepsilon} \int_0^\xi \mathrm{e}^{-y\gamma(\varepsilon)/c_\varepsilon} W(y) dy \right]. \tag{7.175}$$

Finally, requiring the solution to remain bounded as $\xi \to \infty$ ($\xi \to -\infty$) for $c_\varepsilon > 0$ (for $c_\varepsilon < 0$) implies that κ must satisfy the condition

$$\kappa = \frac{1}{|c_\varepsilon|} \int_0^\infty \mathrm{e}^{-y\gamma(\varepsilon)/|c_\varepsilon|} W(\mathrm{sign}(c_\varepsilon) y) dy. \tag{7.176}$$

Hence, in the case of the exponential weight distribution (7.1), we have

$$c_\varepsilon = \frac{\sigma}{2\kappa} [1 - 2\kappa\gamma(\varepsilon)] \tag{7.177}$$

for $c_\varepsilon > 0$, and

$$c_\varepsilon = \frac{\sigma\gamma(\varepsilon)}{2} \frac{1 - 2\kappa\gamma(\varepsilon)}{1 - \kappa\gamma(\varepsilon)}, \tag{7.178}$$

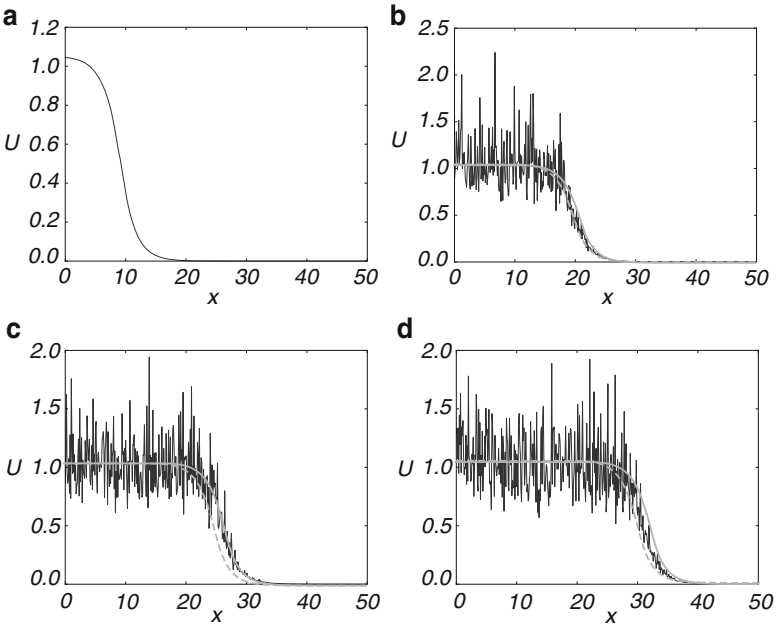

Fig. 7.10 Numerical simulation showing the propagation of a front solution of the stochastic neural field equation (7.157) for Heaviside weight function $F(U) = H(U - \kappa)$ with $\kappa = 0.35$, exponential weight function (7.1) with $\sigma = 2$, and multiplicative noise $g(U) = U$. Noise strength $\varepsilon = 0.005$ and $C(0) = 10$. The wave profile is shown at successive times (**a**) $t = 0$ (**b**) $t = 12$ (**c**) $t = 18$ and (**d**) $t = 24$, with the initial profile at $t = 0$ given by the solution to Eq. (7.164). In numerical simulations we take the discrete space and time steps $\Delta x = 0.1, \Delta t = 0.01$. The deterministic part U_0 of the stochastic wave is shown by the *solid gray curves* and the corresponding solution in the absence of noise ($\varepsilon = 0$) is shown by the *dashed gray curves*

for $c_\varepsilon < 0$. Assuming that $0 \leq \gamma(\varepsilon) \leq 1$, we see that multiplicative noise shifts the effective velocity of front propagation in the positive ξ direction.

In order to calculate the diffusion coefficient, it is first necessary to determine the null vector $\mathscr{V}(\xi)$ of the adjoint linear operator $\mathbb{L}^\dagger$ defined by Eq. (7.169). Setting $F(U) = H(U - \kappa)$ and $g(U) = g_0 U$, we obtain an adjoint equation almost identical to (7.93):

$$c_\varepsilon \mathscr{V}'(\xi) + \gamma(\varepsilon)\mathscr{V}(\xi) = -\frac{\delta(\xi)}{U_0'(0)} \int_{-\infty}^{\infty} w(\xi')\mathscr{V}(\xi')d\xi'. \tag{7.179}$$

Hence, this has the solution

$$\mathscr{V}(\xi) = -H(\xi)\exp(-\Gamma(\varepsilon)\xi), \quad \Gamma(\varepsilon) = \frac{\gamma(\varepsilon)}{c_\varepsilon}, \tag{7.180}$$

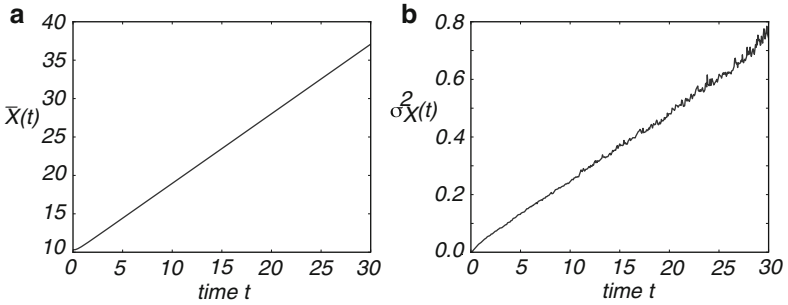

Fig. 7.11 Plot of (**a**) mean $\overline{X}(t)$ and (**b**) variance $\sigma_X^2(t)$ of front position as a function of time, averaged over $N = 4096$ trials. Same parameter values as Fig. 7.10

and Eq. (7.172) reduces to the form

$$D(\varepsilon) = \varepsilon \frac{\displaystyle\int_0^\infty \mathrm{e}^{-2\Gamma(\varepsilon)\xi} U_0(\xi)^2 d\xi}{\left[\displaystyle\int_0^\infty \mathrm{e}^{-\Gamma(\varepsilon)\xi} U_0'(\xi) d\xi\right]^2}. \tag{7.181}$$

In the case of an exponential weight distribution, $U_0(\xi)$ has the explicit form

$$U_0(\xi) = \begin{cases} \dfrac{1}{2c_\varepsilon} \dfrac{\sigma e^{-\xi/\sigma}}{1+\sigma\Gamma(\varepsilon)} & \xi \geq 0 \\ \dfrac{1}{2c_\varepsilon}\left[\dfrac{2e^{\xi\Gamma(\varepsilon)}}{\Gamma(\varepsilon)\left(-1+\sigma^2\Gamma(\varepsilon)^2\right)} + \dfrac{2}{\Gamma(\varepsilon)} + \dfrac{\sigma \mathrm{e}^{\xi/\sigma}}{1-\sigma\Gamma(\varepsilon)}\right] & \xi < 0, \end{cases} \tag{7.182}$$

and the integrals in (7.181) can be evaluated explicitly to give

$$D(\varepsilon) = \frac{1}{2}\varepsilon\sigma g_0^2(1+\sigma\Gamma(\varepsilon)). \tag{7.183}$$

In Fig. 7.10 we show the temporal evolution of a single stochastic wave front, which is obtained by numerically solving the stochastic neural field equation (7.157) for $F(U) = H(U-\kappa)$, $g(U) = U$ and an exponential weight distribution w. In order to numerically calculate the mean location of the front as a function of time, we carry out a large number of level set position measurements. That is, we determine the positions $X_a(t)$ such that $U(X_a(t),t) = a$, for various level set values $a \in (0.5\kappa, 1.3\kappa)$ and then define the mean location to be $\overline{X}(t) = \mathbb{E}[X_a(t)]$, where the expectation is first taken with respect to the sampled values a and then averaged over N trials. The corresponding variance is given by $\sigma_X^2(t) = \mathbb{E}[(X_a(t) - \bar{X}(t))^2]$. In Fig. 7.11 we plot $\overline{X}(t)$ and $\sigma_X^2(t)$ as a function of t. It can be seen that both vary linearly with t, consistent with the assumption that there is a diffusive-like displacement of the front from its uniformly translating position at long time scales. The slopes of these curves then determine the effective wave speed and diffusion coefficient according

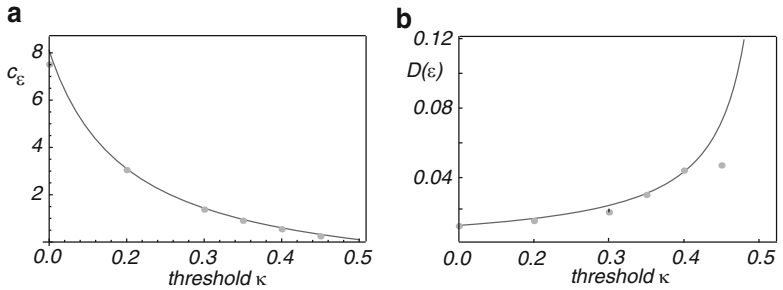

Fig. 7.12 Plot of (**a**) wave speed c_ε and (**b**) diffusion coefficient $D(\varepsilon)$ as a function of threshold κ. Numerical results (*solid dots*) are obtained by averaging over $N = 4,096$ trials starting from the initial condition given by Eq. (7.182). Corresponding theoretical predictions (*solid curves*) for c_ε and $D(\varepsilon)$ are based on Eqs. (7.177) and (7.181), respectively. Other parameters as in Fig. 7.10

to $\overline{X}(t) \sim c_\varepsilon t$ and $\sigma_X^2(t) \sim 2D(\varepsilon)t$. In Fig. 7.12 we plot the numerically estimated speed and diffusion coefficient for various values of the threshold κ and compare these to the corresponding theoretical curves obtained using the above analysis. It can be seen that there is excellent agreement with our theoretical predictions provided that κ is not too large. As $\kappa \to 0.5$, the wave speed decreases towards zero so that the assumption of relatively slow diffusion breaks down.

7.4.2 Stimulus-Locked Fronts

So far we have assumed that the underlying deterministic neural field equation is homogeneous in space so that there exists a family of traveling front solutions related by a uniform shift. Now suppose that there exists an external front-like input that propagates at a uniform speed v, so that the deterministic equation (7.2) becomes

$$\frac{\partial u(x,t)}{\partial t} = -u(x,t) + \int_{-\infty}^{\infty} w(x-x')F(u(x',t))dx' + I(x-vt), \tag{7.184}$$

where the input is taken to be a positive, bounded, monotonically decreasing function of amplitude $I_0 = I(-\infty) - I(\infty)$. The resulting inhomogeneous neural field equation can support a traveling front that locks to the stimulus, provided that the amplitude of the stimulus is sufficiently large [198]. Consider, in particular, the case of a Heaviside firing rate function $F(u) = H(u-\kappa)$. (See [174] for an extension to the case of a smooth sigmoid function F.) We seek a traveling wave solution $u(x,t) = \mathscr{U}(\xi)$ where $\xi = x - vt$ and $\mathscr{U}(\xi_0) = \kappa$ at a single threshold crossing point $\xi_0 \in \mathbb{R}$. The front is assumed to travel at the same speed as the input (stimulus-locked front). If $I_0 = 0$, then we recover the homogeneous equation (7.2) and ξ_0 becomes a free parameter, whereas the wave propagates at the natural speed $c(\kappa)$ given by Eq. (7.6). Substituting the front solution into Eq. (7.184) yields

$$-v\frac{d\mathscr{U}(\xi)}{d\xi} = -\mathscr{U}(\xi) + \int_{-\infty}^{\xi_0} w(\xi-\xi')d\xi' + I(\xi). \tag{7.185}$$

This can be solved for $v>0$ by multiplying both sides by the integrating factor $v^{-1}\mathrm{e}^{-v\xi}$ and integrating over the interval $[\xi,\infty)$ with $U(\xi)\to 0$ as $\xi\to\infty$ to give

$$\mathscr{U}(\xi) = \frac{1}{v}\int_{\xi}^{\infty} e^{(\xi-\xi')/v}[W(\xi'-\xi_0)+I(\xi')]d\xi',$$

with $W(\xi)$ defined according to Eq. (7.3). Similarly, for $v<0$, we multiply by the same integrating factor and then integrate over $(-\infty,\xi]$ with $U(\xi)\to W_0$ as $\xi\to-\infty$ to find

$$\mathscr{U}(\xi) = -\frac{1}{v}\int_{-\infty}^{\xi} e^{(\xi-\xi')/v}[W(\xi'-\xi_0)+I(\xi')]d\xi'.$$

The threshold crossing condition $\mathscr{U}(\xi_0)=\kappa$ then determines the position ξ_0 of the front relative to the input as a function of speed v, input amplitude I_0, and threshold κ.

One of the interesting features of stimulus-locked fronts is that they are much more robust to noise [70]. In order to show this, consider the following stochastic version of Eq. (7.184):

$$\begin{aligned} dU(x,t) = &\left[-U(x,t)+\int_{-\infty}^{\infty} w(x-y)F(U(y,t))dy + I(x-vt)\right]dt \\ &+\varepsilon^{1/2}g(U(x,t))dW(x,t). \end{aligned} \tag{7.186}$$

Proceeding along identical lines to the case of freely propagating fronts, Eq. (7.186) is first rewritten so that the fluctuating term has zero mean:

$$dU(x,t) = \left[h(U(x,t))+\int_{-\infty}^{\infty} w(x-y)F(U(y,t))dy+I(x-vt)\right]dt+\varepsilon^{1/2}dR(U,x,t), \tag{7.187}$$

and h and R are given by Eqs. (7.160) and (7.161), respectively. The stochastic field $U(x,t)$ is then decomposed according to Eq. (7.163) with U_0 a front solution of

$$-v\frac{dU_0}{d\xi} - h(U_0(\xi)) - I(\xi) = \int_{-\infty}^{\infty} w(\xi-\xi')F(U_0(\xi'))d\xi'. \tag{7.188}$$

It is assumed that the fixed profile U_0 is locked to the stimulus (has speed v). However, multiplicative noise still has an effect on U_0 by generating an ε-dependent threshold crossing point ξ_ε such that $U_0(\xi_\varepsilon)=\kappa$.

Proceeding to the next order and imposing equation (7.188), we find that $\Delta(t)=\mathscr{O}(\varepsilon^{1/2})$ and

$$d\Phi(\xi,t) = \mathbb{L}\circ\Phi(\xi,t)dt + \varepsilon^{-1/2}U_0'(\xi)d\Delta(t) + dR(U_0,\xi,t) + \varepsilon^{-1/2}I'(\xi)\Delta(t)dt \tag{7.189}$$

where $\mathbb{L}$ is the non-self-adjoint linear operator (7.167) with $c_\varepsilon \to v$. The last term on the right-hand side of Eq. (7.189) arises from the fact that in Eq. (7.163), U_0 and Φ are expressed as functions of $\xi - \Delta(t)$ and $I(\xi) = I(\xi - \Delta(t) + \Delta(t)) \approx I(\xi - \Delta(t)) + I'(\xi - \Delta(t))\Delta(t)$. A nontrivial solution of Eq. (7.189) exists if and only if the inhomogeneous part is orthogonal to the null vector $\Psi(\xi)$ of the adjoint operator $\mathbb{L}^\dagger$ defined by Eq. (7.169) with $c_\varepsilon \to v$. Taking the inner product of both sides of Eq. (7.189) with respect to $\Psi(\xi)$ thus leads to the solvability condition

$$\int_{-\infty}^{\infty}\Psi(\xi)\left[U_0'(\xi)d\Delta(t) + I'(\xi)\Delta(t)dt + \varepsilon^{1/2}dR(U_0,\xi,t)\right]d\xi = 0. \tag{7.190}$$

It follows that, to leading order, $\Delta(t)$ satisfies the Ornstein–Uhlenbeck equation

$$d\Delta(t) + A\Delta(t)dt = d\hat{W}(t), \tag{7.191}$$

where

$$A = \frac{\int_{-\infty}^{\infty}\Psi(\xi)I'(\xi)d\xi}{\int_{-\infty}^{\infty}\Psi(\xi)U_0'(\xi)d\xi}, \tag{7.192}$$

and

$$\hat{W}(t) = -\varepsilon^{1/2}\frac{\int_{-\infty}^{\infty}\Psi(\xi)g(U_0(\xi))W(\xi,t)d\xi}{\int_{-\infty}^{\infty}\Psi(\xi)U_0'(\xi)d\xi}. \tag{7.193}$$

Note that $A > 0$ for $I_0 > 0$, since both $U_0(\xi)$ and $I(\xi)$ are monotonically decreasing functions of ξ. Moreover

$$\langle d\hat{W}(t)\rangle = 0, \quad \langle d\hat{W}(t)d\hat{W}(t)\rangle = 2D(\varepsilon)dt \tag{7.194}$$

with $D(\varepsilon)$ given by Eq. (7.172). Using standard properties of an Ornstein–Uhlenbeck process [210], we conclude that

$$\langle\Delta(t)\rangle = \Delta(0)\mathrm{e}^{-At}, \quad \langle\Delta(t)^2\rangle - \langle\Delta(t)\rangle^2 = \frac{D(\varepsilon)}{A}\left[1-\mathrm{e}^{-2At}\right]. \tag{7.195}$$

In particular, the variance approaches a constant $D(\varepsilon)/A$ in the large t limit, rather than increasing linearly with time as found for freely propagating fronts.

In order to illustrate the above analysis, take $g(U) = g_0U$ for the multiplicative noise term and set $F(U) = H(U-\kappa)$. The deterministic Eq. (7.188) for the profile U_0 then reduces to

$$-v\frac{dU_0}{d\xi} + U_0(\xi)[1-\varepsilon g_0^2C(0)] + I(\xi) = \int_{-\infty}^{\infty}w(\xi-\xi')H(U_0(\xi')-\kappa)d\xi'. \tag{7.196}$$

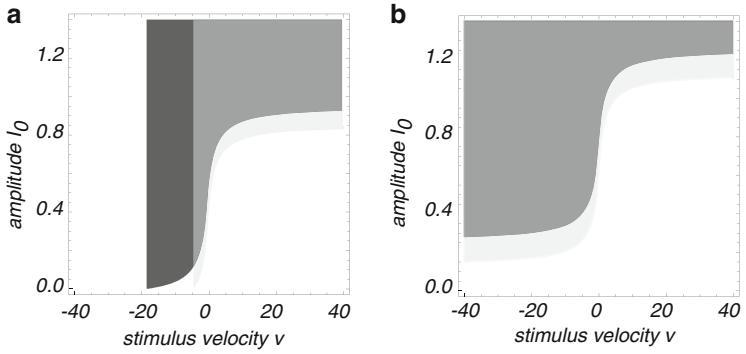

Fig. 7.13 Plot of existence regions of a stimulus-locked front without noise ($\gamma = 1$, *dark gray*) and in the presence of noise ($\gamma = 0.9$, *light gray*) with overlapping regions indicated by *medium gray*. Stimulus taken to be of the form $I(x,t) = I_0 H(-\xi), \xi = x - vt$ with amplitude I_0 and speed v. Other parameter values as in Fig. 7.10. (**a**) $\kappa = 0.95$: spontaneous fronts exist in the absence of a stimulus ($I_0 = 0$). (**b**) $\kappa = 1.25$: there are no spontaneous fronts

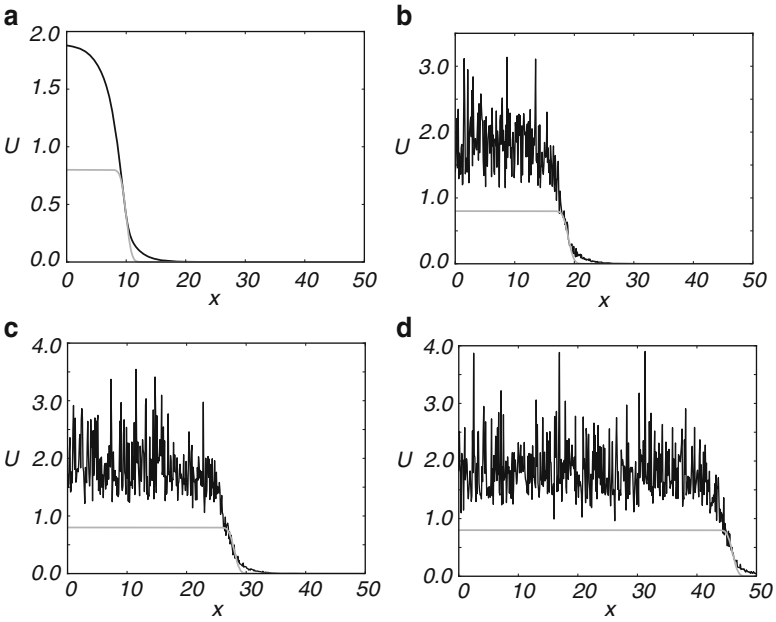

Fig. 7.14 Numerical simulation showing the propagation of a stimulus-locked wave-front solution (*black curves*) of the stochastic neural field equation (7.186) for Heaviside weight function $F(U) = H(U - \kappa)$ with $\kappa = 0.35$, exponential weight function (7.1) with $\sigma = 2$, and multiplicative noise $g(U) = U$. The external input (*gray curves*) is taken to be of the form $I(x,t) = I_0 \mathrm{Erfc}[x - vt]$ with amplitude $I_0 = 0.4$ and speed $v = 1.5$. Noise strength $\varepsilon = 0.005$ and $C(0) = 10$. The wave profile is shown at successive times (**a**) $t = 0$ (**b**) $t = 6$ (**c**) $t = 12$ and (**d**) $t = 24$, with the initial profile at $t = 0$ given by the solution U_0 of Eq. (7.188). In numerical simulations we take the discrete space and time steps $\Delta x = 0.1, \Delta t = 0.01$

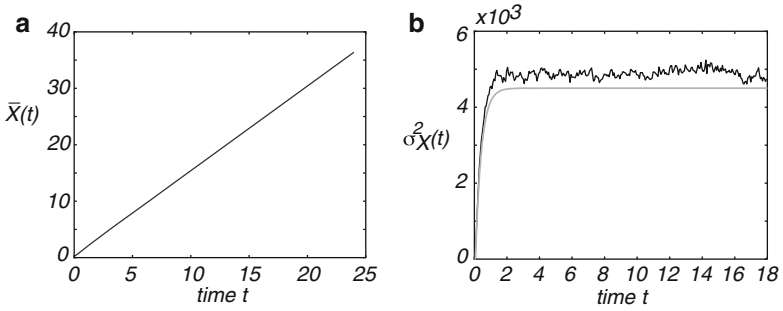

Fig. 7.15 Plot of (**a**) mean $\overline{X}(t)$ and (**b**) variance $\sigma_X^2(t)$ of the position of a stimulus-locked front as a function of time, averaged over $N = 4096$ trials. Smooth gray curve in (b) indicates theoretical prediction of variance. Stimulus taken to be of the form $I(x,t) = I(x-ct) = I_0\text{Erfc}[x-vt]$ with amplitude $I\_0 = 0.4$ and speed $v = 1.5$. Other parameter values as in Fig. 7.10

Existence of front solution proceeds along identical lines to Sect. 7.1, except now the speed v is fixed, whereas the threshold crossing point ξ_0, say, is no longer arbitrary due to the breaking of translation symmetry. The point ξ_0 is determined by the threshold condition $U_0(\xi_0) = \kappa$ and will depend on the noise strength ε. In Fig. 7.13 we show existence regions in the (v, I_0)-plane for stimulus-locked fronts when $I(\xi) = I_0 H(-\xi)$, that is, for a step function input of speed v and amplitude I_0. This illustrates the fact that multiplicative noise leads to an ε-dependent shift in the existence regions. In Fig. 7.14 we show the temporal evolution of a single stimulus-locked front, which is obtained by numerically solving the Langevin equation (7.186) for $F(U) = H(U-\kappa)$, $g(U) = U$ and an exponential weight distribution w. Numerically speaking, it is convenient to avoid discontinuities in the input by taking $I(x,t) = I_0\text{Erfc}[x-vt]$ rather than a Heaviside. The corresponding mean $\overline{X}(t)$ and variance $\sigma_X^2(t)$ of the position of the front, which are obtained by averaging over level sets as outlined in Sect. 7.4.1, are shown in Fig. 7.15. It can be seen that, as predicted by the analysis, $\overline{X}(t)$ varies linearly with t with a slope equal to the stimulus speed $v = 1.5$. Moreover, the variance $\sigma_X^2(t)$ approaches a constant value as $t \to \infty$, which is comparable to the theoretical value $D(\varepsilon)/A$ evaluated for the given input. Thus, we find that stimulus-locked fronts are much more robust to noise than freely propagating fronts, since the variance of the mean position saturates as $t \to \infty$. Consequently, stimulus locking persists in the presence of noise over most of the parameter range for which stimulus locking is predicted to occur.

7.4.3 Stochastic Pulled Fronts

In the case of the F–KPP equation with multiplicative noise, one finds that the stochastic wandering of a pulled front about its mean position is subdiffusive with $\text{var}\Delta(t) \sim t^{1/2}$, in contrast to the diffusive wandering of a front propagating into a

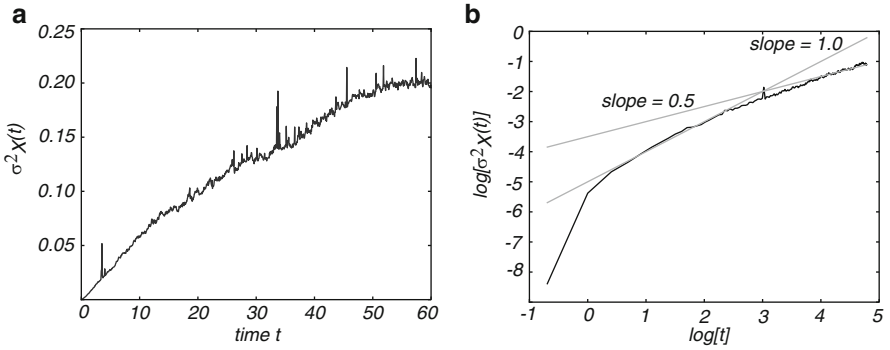

Fig. 7.16 (**a**) Plot of variance $\sigma_X^2(t)$ of the position of a stochastic pulled front as a function of time. (**b**) Log-log plot of variance $\sigma_X^2(t)$ as a function of time t. Noise amplitude $\varepsilon = 0.005$ and $\kappa = 0.8$. Other parameter values as in Fig. 7.2

metastable state for which $\mathrm{var}\Delta(t) \sim t$ [530]. Such scaling is a consequence of the asymptotic relaxation of the leading edge of the deterministic pulled front. Since pulled front solutions of the neural field equation (7.27) exhibit similar asymptotic dynamics (see Eq. (7.46)), it suggests that there will also be subdiffusive wandering of these fronts in the presence of multiplicative noise. In order to illustrate this, consider the stochastic neural field equation

$$dA(x,t) = \left[-A(x,t)+F\left(\int_{-\infty}^{\infty} w(x-y)A(y,t)dy\right)\right]dt+\varepsilon^{1/2}g_0A(x,t)dW(x,t) \quad (7.197)$$

with $W(x,t)$ a Wiener process satisfying Eq. (2.84). Note that the noise term has to vanish when $A(x,t) = 0$, since the firing rate A is restricted to be positive. Hence, the noise has to be multiplicative. Formally speaking, one can carry over the analysis of the Langevin equation (7.157). First, decompose the solution along similar lines to Eq. (2.96):

$$A(x,t) = A_0(\xi - \Delta(t)) + \varepsilon^{1/2}\Phi(\xi - \Delta(t),t) \quad (7.198)$$

with $\xi = x - c_\varepsilon t$, with the fixed front profile A_0 satisfying the deterministic equation

$$-c_\varepsilon \frac{dA_0}{d\xi} + A_0(\xi)[1 - \varepsilon g_0^2 C(0)] = F\left(\int_{-\infty}^{\infty} w(\xi - \xi')A_0(\xi')d\xi'\right). \quad (7.199)$$

The effective velocity c_ε of the front is given by the minimum of the dispersion curve

$$c_\varepsilon(\lambda) = \frac{1}{\lambda}\left[\hat{W}(\lambda) + \hat{W}(-\lambda) - [1 - \varepsilon g_0^2 C(0)]\right]. \quad (7.200)$$

Fluctuations thus shift the dispersion curve to higher velocities. However, it is no longer possible to derive an expression for the diffusion coefficient $D(\varepsilon)$ along the lines of Eq. (7.172), since both numerator and denominator would diverge for a pulled front. This reflects the asymptotic behavior of the leading edge of the front.

It is also a consequence of the fact that there is no characteristic time scale for the convergence of the front velocity to its asymptotic value, which means that it is not possible to separate the fluctuations into a slow wandering of front position and fast fluctuations of the front shape [162, 486]. Nevertheless, numerical simulations of Eq. (7.197) with F given by the piecewise linear firing rate (7.29) are consistent with subdiffusive wandering of the front. In Fig. 7.16(a), we plot the variance $\sigma_X^2(t)$ of the position of a pulled front solution of Eq. (7.197), which are obtained by averaging over level sets along identical lines to Sect. 7.4.1. It can be seen that the variance appears to exhibit subdiffusive behavior over longer time scales. This is further illustrated by plotting a log-log plot of $\sigma_X^2(t)$ against time t; see Fig. 7.16(b). At intermediate time scales, the slope of the curve is approximately equal to one, consistent with normal diffusion, but at later times the slope decreases, indicating subdiffusive behavior.

7.5 Traveling Waves in 2D Oscillatory Neural Fields

Troy and Shusterman [580, 634] have shown how a neural field model with strong linear adaptation (see Eq. (7.49)) can act as an oscillatory network that supports 2D target patterns and spiral waves consistent with experimental studies of tangential cortical slices [292]. (For the analysis of spiral waves in the corresponding excitable regime, see [354].) However, since the linear form of adaptation used in these studies is not directly related to physiological models of adaptation, it is difficult to ascertain whether or not the strength of adaptation required is biologically reasonable. This motivated a more recent study of spiral waves in a 2D neural

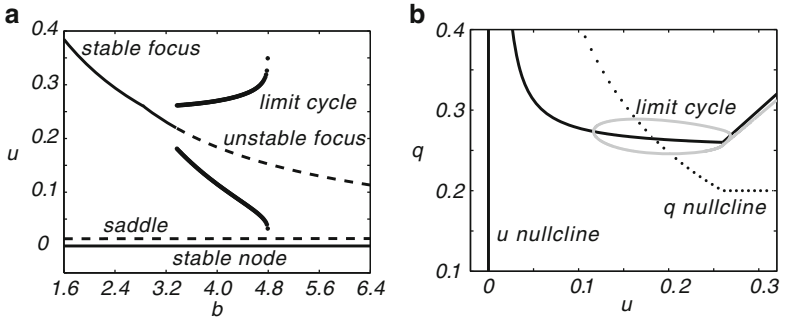

Fig. 7.17 Limit cycle oscillations in the space-clamped system (7.202) for a piecewise linear firing rate function (1.16) with threshold $\kappa = 0.01$ and gain $\eta = 4$. (**a**) Bifurcation diagram showing fixed points u of the system as a function of β for $\tau_q = 80$. (**b**) Corresponding phase-plane plot of q versus u (*gray curve*) for $\beta = 4$, showing that the system supports a stable limit cycle [329]

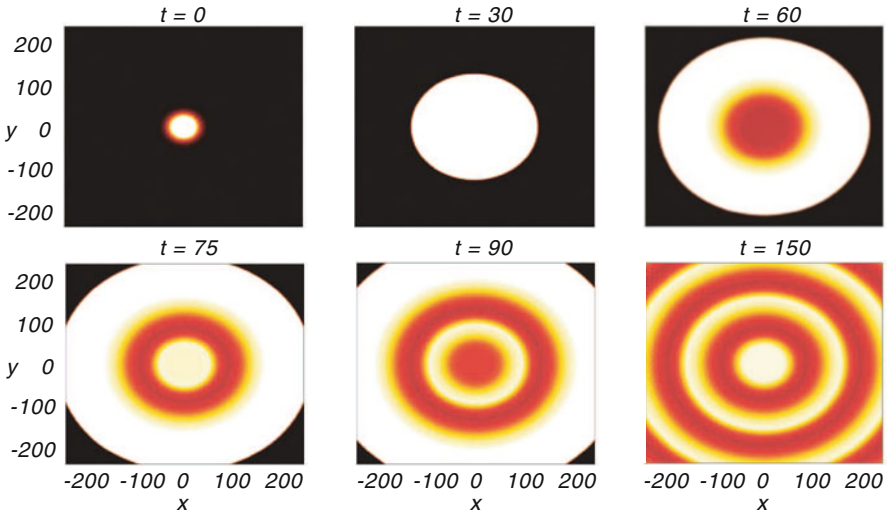

Fig. 7.18 Target patterns in a 2D neural field with synaptic depression induced by an initial conditional stimulus specified by Eq. (7.203) at $t = 0$, where $\chi = 1$ and $\zeta = 25$. Initially, an activated state spreads radially outward, across the entire medium as a traveling front. Then, the localized oscillating core of activity emits a target wave with each oscillation cycle. Eventually, these target waves fill the domain. Each target wave can be considered as a phase shift in space of the oscillation throughout the medium; they travel with the same speed as the initial front. Parameters are $\tau_q = 80$, $\beta = 4$, $\eta = 4$, and $\kappa = 0.01$ [330]

medium involving a nonlinear, physiologically based form of adaptation, namely, synaptic depression [330]. The latter model is given by

$$\begin{aligned} \frac{\partial u(\mathbf{r},t)}{\partial t} &= -u(\mathbf{r},t) + \int w(|\mathbf{r}-\mathbf{r}'|)q(\mathbf{r}',t)F(u(\mathbf{r}',t))d\mathbf{r}' \\ \frac{\partial q(\mathbf{r},t)}{\partial t} &= \frac{1-q(\mathbf{r},t)}{\tau_q} - \beta q(\mathbf{r},t)F(u(\mathbf{r},t)). \end{aligned} \tag{7.201}$$

The radially symmetric excitatory weight distribution is taken to be an exponential, $w(r) = \mathrm{e}^{-r}/2\pi$. It can be shown that the space-clamped model

$$\dot{u}(t) = -u(t) + q(t)F(u(t)), \quad \dot{q}(t) = \frac{1-q(t)}{\tau_q} - \beta q(t)F(u(t)), \tag{7.202}$$

supports limit cycle oscillations provided that the firing rate function has finite gain. For example, in the case of the piecewise linear firing rate function (1.16), oscillations arise via a subcritical Hopf bifurcation of a high activity fixed point; see Fig. 7.17. One then finds that the full network model (7.201) supports a spatially localized oscillating core that periodically emits traveling pulses [330]. Such dynamics can be induced by taking an initial condition of the form

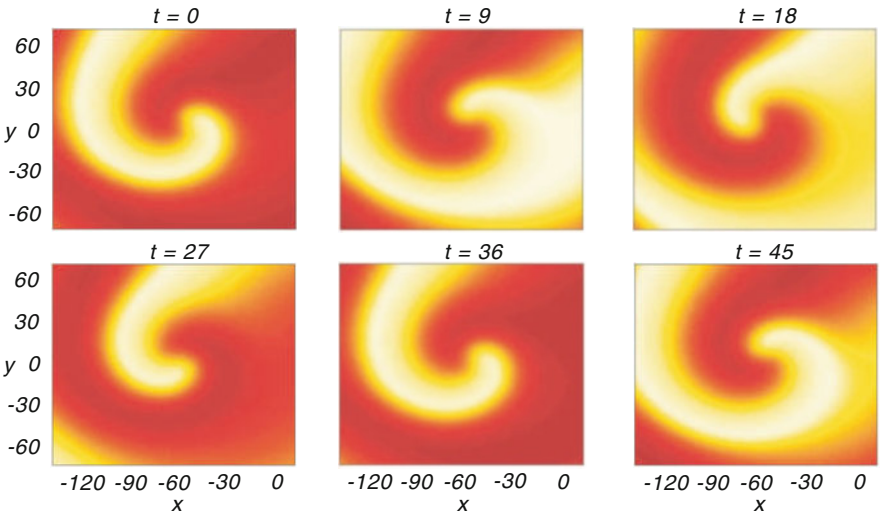

Fig. 7.19 Spiral wave generated by shifting the phase of the top and bottom halves of the target pattern shown in Fig. 7.18. The period of the spiral wave oscillation is roughly the same as the period of the oscillation in the space-clamped system. All patches of neurons are oscillating at the same frequency, but phase-shifted as coordinates are rotated about the central phase singularity [330]

$$(u(\mathbf{r},0),q(\mathbf{r},0)) = (\chi e^{-(x^2+y^2)/\zeta^2},1), \tag{7.203}$$

where χ and ζ parameterize the amplitude and spatial constant of the initial state. An example of a pulse-emitting core is shown in Fig. 7.18, which oscillates at a frequency of roughly 3 Hz. Pulses are emitted each cycle and travel at a speed of roughly 30 cm/s, which is determined by the period of the oscillations; the latter is set by the time constant of synaptic depression. The initial emission of spreading activity appears as a traveling front which propagates from the region activated by the input current into the surrounding region of zero activity; it travels at the same speed as the subsequent target waves. The front converts each region of the network into an oscillatory state that is phase-shifted relative to the core, resulting in the appearance of a radially symmetric target pattern. Spiral waves can also be induced by breaking the rotational symmetry of pulse emitter solutions [330]. More specifically, if the target pattern produced by the emitter has the top and bottom halves of its domain phase-shifted, then the dynamics evolves into two counterrotating spirals on the left and right halves of the domain. Closer inspection of one of these spirals reveals that it has a fixed center about which activity rotates indefinitely as shown in Fig. 7.19.

A very different mechanism for generating periodic waves in a 1D or 2D neural field model is through the combination of adaptation and a spatially localized input [196, 197]. Recall from Sect. 7.2 that a 1D excitatory neural field with adaptation supports the propagation of solitary traveling pulse, which can be induced by perturbing the system with a transient localized pulse. (In contrast to the previous example, we are assuming that the neural field operates in an excitable regime.)

In the case of a 2D network with radially symmetric weights, such a pulse will produce a single expanding circular wave. Now suppose that a 2D localized pulse persists in the form of a radially symmetric Gaussian input $I(\mathbf{r}) = I_0 \mathrm{e}^{-r^2/\sigma^2}$—this could either represent an external stimulus or a localized region of depolarization. As one might expect, for sufficiently large input amplitude I_0, the neural field supports a radially symmetric stationary pulse or bump centered about the input. Such a bump is not self-sustaining, however, since if the input is removed, then the bump disappears as well. This then raises the question as to what happens to the stability of the bump as the input amplitude is slowly decreased. One finds that the bump first undergoes a Hopf instability as I_0 is decreased, leading to the formation of a spatially localized oscillating pulse or *breather* [196]. Interestingly, as the input amplitude is further reduced, the breather can undergo a secondary instability such that it now acts as an oscillating core that emits circular target waves. Thus, a spatially localized stationary input provides a mechanism for the formation of a network pacemaker oscillator. A linear stability analysis establishes that the primary instability is due to the growth of radially symmetric eigenmodes. A similar bifurcation scenario also occurs in a neural field with lateral inhibition, except that now the Hopf bifurcation typically involves the growth of nonradially symmetric eigenmodes, resulting in asymmetric breathers and rotating waves [197].

Chapter 8
Neural Field Model of Binocular Rivalry Waves

Binocular rivalry is the phenomenon whereby perception switches back and forth between different images presented to the two eyes. The resulting fluctuations in perceptual dominance and suppression provide a basis for noninvasive studies of the human visual system and the identification of possible neural mechanisms underlying conscious visual awareness [46, 47]. Various psychophysical experiments have demonstrated that the switch between a dominant and suppressed visual percept propagates as a traveling front for each eye [312, 369, 678]. In this chapter we show how the neural field theory presented in Chap. 7 can be used to model the phenomenon of binocular rivalry waves [83, 663].

8.1 Binocular Rivalry Waves and the Structure of Primary Visual Cortex

We begin by summarizing several important properties of neurons and their functional organization within primary visual cortex (V1), and then review some of the experimental findings regarding binocular rivalry.

8.1.1 Functional Architecture of V1

V1 is the first cortical area to receive visual information from the retina (see Fig. 8.1). The output from the retina is conveyed by ganglion cells whose axons form the optic nerve. The optic nerve conducts the output spike trains of the retinal ganglion cells to the lateral geniculate nucleus (LGN) of the thalamus, which acts as a relay station between retina and primary visual cortex (V1). Prior to arriving at the LGN, some ganglion cell axons cross the midline at the optic chiasm. This allows the left and right sides of the visual fields from both eyes to be represented on the right and left sides of the brain, respectively. Note that signals from the left and

P.C. Bressloff, *Waves in Neural Media: From Single Neurons to Neural Fields*,
Lecture Notes on Mathematical Modelling in the Life Sciences,
DOI 10.1007/978-1-4614-8866-8_8,

right eyes are segregated in the LGN and in input layers of V1. This means that the corresponding LGN and cortical neurons are monocular, in the sense that they only respond to stimuli presented to one of the eyes but not the other (ocular dominance).

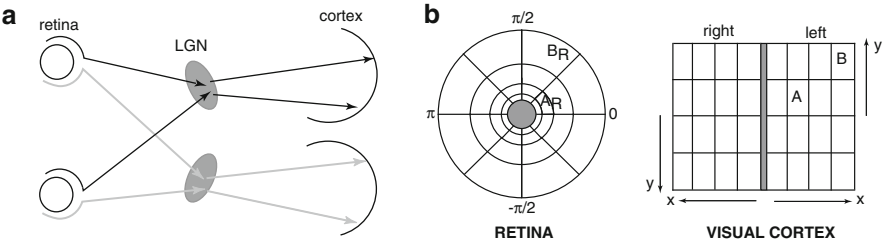

Fig. 8.1 (**a**) Visual pathways from the retina through the lateral geniculate nucleus (LGN) of the thalamus to the primary visual cortex (V1). (**b**) Schematic illustration of the complex logarithmic mapping from retina to V1. Foveal region in retina is indicated by *gray disk*. Regions A_R and B_R in the visual field are mapped to regions A and B in cortex

One of the striking features of the early visual system is that the visual world is mapped onto the cortical surface in a topographic manner. This means that neighboring points in a visual image evoke activity in neighboring regions of visual cortex. Moreover, one finds that the central region of the visual field has a larger representation in V1 than the periphery, partly due to a nonuniform distribution of retinal ganglion cells. The retinotopic map is defined as the coordinate transformation from points in the visual world to locations on the cortical surface and can be approximated by a complex logarithm [562]. Superimposed upon the retinotopic map are additional maps reflecting the fact that neurons respond preferentially to stimuli with particular features [613]. Neurons in the retina, LGN, and primary visual cortex respond to light stimuli in restricted regions of the visual field called their classical receptive fields (RFs). Patterns of illumination outside the RF of a given neuron cannot generate a response directly, although they can significantly modulate responses to stimuli within the RF via long-range cortical interactions (see below). The RF is divided into distinct ON and OFF regions. In an ON (OFF) region illumination that is higher (lower) than the background, light intensity enhances firing. The spatial arrangement of these regions determines the selectivity of the neuron to different stimuli. For example, one finds that the RFs of most V1 cells are elongated so that the cells respond preferentially to stimuli with certain preferred orientations (see Fig. 8.2). Similarly, the width of the ON and OFF regions within the RF determines the optimal spacing of alternating light and dark bars to elicit a response, that is, the cell's spatial frequency preference.

In recent years much information has accumulated about the spatial distribution of orientation selective cells in V1 [216]. One finds that orientation preferences rotate smoothly over the surface of V1, so that approximately every 300 µm the same preference reappears, i.e., the distribution is π-periodic in the orientation preference angle. One also finds that cells with similar feature preferences tend to arrange

themselves in vertical columns so that to a first approximation the layered structure of cortex can be ignored. A more complete picture of the two-dimensional distribution of both orientation preference and ocular dominance in layers 2/3 has been obtained using optical imaging techniques [50, 51, 53]. The basic experimental procedure involves shining light directly on to the surface of the cortex. The degree of light absorption within each patch of cortex depends on the local level of activity. Thus, when an oriented image is presented across a large part of the visual field, the regions of cortex that are particularly sensitive to that stimulus will be differentiated. The topography revealed by these methods has a number of characteristic features [469]; see Fig. 8.2b: (i) Orientation preference changes continuously as a function of cortical location, except at singularities or *pinwheels*. (ii) There exist *linear zones*, approximately $750 \times 750\,\mu m^2$ in area (in primates), bounded by pinwheels, within which iso-orientation regions form parallel slabs. (iii) Linear zones tend to cross the borders of ocular dominance stripes at right angles; pinwheels tend to align with the centers of ocular dominance stripes. These experimental findings suggest that there is an underlying periodicity in the microstructure of V1 with a period of approximately 1 mm (in cats and primates). The fundamental domain of this approximate periodic (or quasiperiodic) tiling of the cortical plane is the hypercolumn [293, 294, 377], which contains two sets of orientation preferences $\theta \in [0, \pi)$ per eye, organized around a pair of singularities; see Fig. 8.2b.

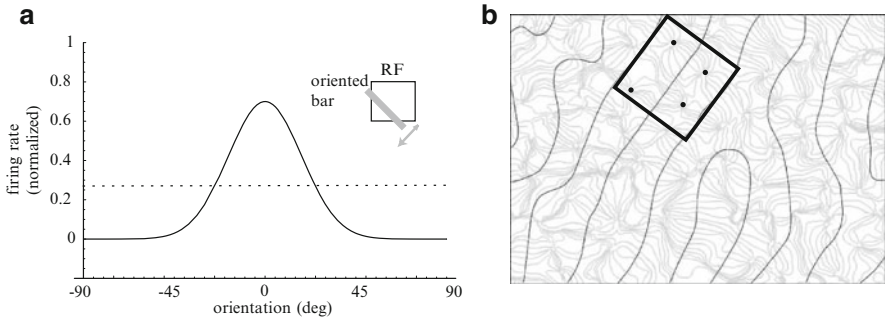

Fig. 8.2 (**a**) Schematic illustration of an orientation tuning curve of a V1 neuron. Average firing rate is plotted as a function of the orientation of a bar stimulus that is moved back and forth within the receptive field (RF) of the neuron. The peak of the orientation tuning curve corresponds to the orientation preference of the cell. (**b**) Schematic illustration of iso-orientation (*light*) and ocular dominance (*dark*) contours in a region of primate V1. A cortical hypercolumn consists of two orientation singularities or pinwheels per ocular dominance column

Within each hypercolumn, neurons with sufficiently similar orientations tend to excite each other, whereas those with sufficiently different orientations inhibit each other, and this serves to sharpen a particular neuron's orientation preference [34, 188]. There are also longer-range horizontal or lateral connections that link cells in different hypercolumns [218, 531]. Optical imaging combined with labeling techniques has generated considerable information concerning the pattern of

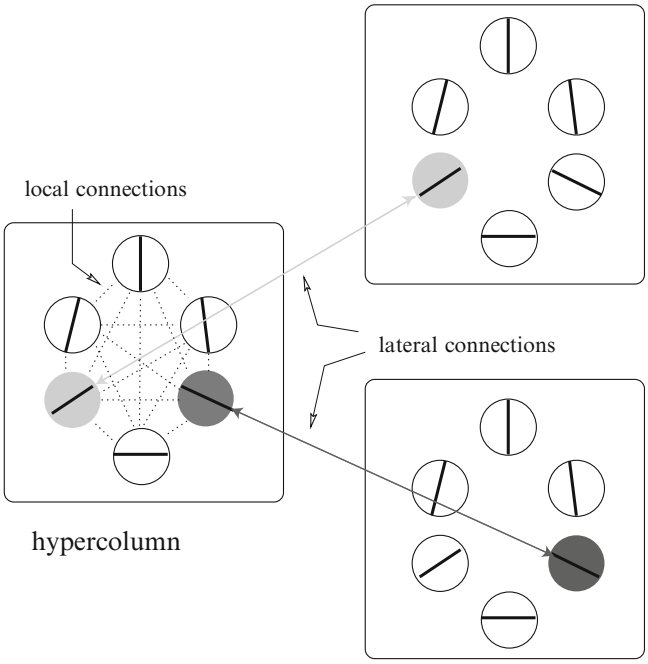

Fig. 8.3 Schematic illustration of anisotropic horizontal connections. Orientation selective cells within a hypercolumn tend to connect to all neighbors in a roughly isotropic fashion. On the other hand, longer-range horizontal connections link cells between hypercolumns with similar orientation preferences along a particular visuotopic axis

these connections in superficial layers of V1 [56, 401, 691]. In particular, one finds that the horizontal connections are patchy and tend to link cells with similar feature preferences. Moreover, in certain animals such as tree shrew and cat, there is a pronounced anisotropy in the distribution of patchy connections, with differing iso-orientation patches preferentially connecting to neighboring patches in such a way as to form continuous contours following the topography of the retinotopic map [56]. This is illustrated schematically Fig. 8.3. That is, the major axis of the horizontal connections tends to run parallel to the visuotopic axis of the connected cells' common orientation preference. There is also a clear anisotropy in the patchy connections of primates [11, 583]. However, in these cases most of the anisotropy can be accounted for by the fact that V1 is expanded in the direction orthogonal to ocular dominance columns [11]. Nevertheless, it is possible that when this expansion is factored out, there remains a weak anisotropy correlated with orientation selectivity. Moreover, patchy feedback connections from higher-order visual areas in primates are strongly anisotropic [11]. Stimulation of a hypercolumn via lateral connections modulates rather than initiates spiking activity [278], suggesting that the long-range interactions provide local cortical processes with contextual information about the global nature of stimuli. As a consequence horizontal and feedback

connections have been invoked to explain a wide variety of context-dependent visual processing phenomena [11, 217]. In summary, the functional relationship between stimulus feature preferences and synaptic connections within V1 suggests that V1 is a likely substrate of many simple examples of binocular rivalry, such as those involving sinusoidal grating stimuli.

8.1.2 Binocular Rivalry

The perception of ambiguous figures is a well-known phenomenon where, in response to a single fixed image, a subject switches back and forth between two rival percepts; see Fig. 8.4. In the case of binocular rivalry, fixed but different images are presented to the two eyes. Rather than perceiving a superposition of the two images, a subject typically sees the left-eye image, say, which then switches to the right-eye image in an alternating fashion. Although binocular rivalry has been studied for hundreds of years, only recently have experimentalists clarified some of its specific statistical properties using a combination of psychophysics and brain imaging [47, 48]:

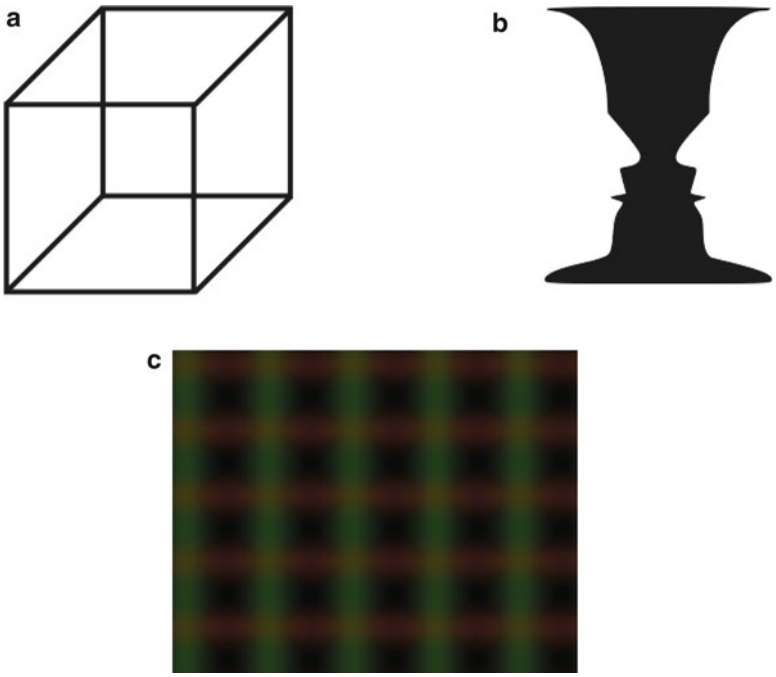

Fig. 8.4 Ambiguous figures. (**a**) Necker cube. (**b**) Faces/vase. (**c**) Monocular rivalry between a horizontal orange grating and a vertical green grating. [Reproduced from Wikimedia Commons (public domain)]

1. Increasing the "strength" of one of the rival figures (brighter, moving rather than stationary, more densely contoured) increases the percentage of time that it is dominant. However, this tends to occur due to a decrease in the periods of suppression of the enhanced figure rather than an increase in its dominance periods [199, 390]. The stimulus dependence of rivalry was summarized in a series of postulates by Levelt [378].
2. The switching from one percept to the next during binocular rivalry occurs stochastically, with the switching times distributed according to a gamma distribution [390]. A number of studies suggest that there are little or no correlations between one dominance time and the next [59, 372].
3. Attention to a particular stimulus may prolong the dominance time of the attended stimulus [270]. Experimental evidence suggests that this correlation may hold true when the subject practices repeatedly [114]. However, the non-attended stimulus will eventually appear in the observer's perception, no matter how strongly attention is focused on the other. The fact that attention can bias the outcomes of binocular rivalry suggests that higher level visual areas may play a modulatory role in the phenomenon [674]. Attention may increase the apparent contrast of the attended stimulus or simply boost the activity of one of two competing neural populations [114].
4. The "tilt aftereffect" is still observed when vertical and tilted lines are rivalrous stimuli [306]; the tilt aftereffect is the phenomenon by which staring at a slightly tilted line will make a vertical line appear to be tilted in the opposite direction if viewed immediately after. Since the neural substrate of this phenomenon is known to reside in primary visual cortex (V1), this suggests that binocular rivalry can involve V1.
5. Perceptual dominance transitions are not instantaneous; rather they emerge in a wavelike fashion, originating at one region of a figure and spreading from there throughout the rest of the figure [312, 369, 678].

Several different methods of recording neural activity in subjects during binocular rivalry have also been employed in an effort to isolate the specific sites of its encoding. In monkeys, single-electrode recordings have been employed to track electrical activity during binocular rivalry tasks [47]. Evidence of an elevation in some cells' firing rates has been found in the V1, V2, and V4 regions of visual cortex, and these correspond well with the monkey's reported perception of a stimulus [376]. Thus, it appears that several areas of visual cortex may be involved. However, single-unit recordings have yet to reveal changes in the firing rate of LGN neurons that correspond to the perceptual changes of binocular rivalry [373]. In humans, less invasive techniques such as scalp recordings and functional magnetic resonance imaging (fMRI) have helped to localize brain regions whose activity reflects the experience of binocular rivalry. Visually evoked potentials measured on the scalp during a binocular rivalry task reveal that potential waveforms associated with each stimulus possess a time course very closely linked to the subject's perceptual observation [85]. A number of fMRI studies have verified there are changes in the blood-oxygen-level-dependent (BOLD) signals in V1 that correspond to the perceived switching in stimulus dominance [369, 510, 626]. It is likely that the site of binocular rivalry de-

pends on the nature of the rivalrous images. Indeed, some theories propose that there may be a hierarchy of visual areas involved so that there is a competition between either eye's input as well as between differing patterns [627, 674].

One way to observe and measure the speed of perceptual waves in psychophysical experiments of binocular rivalry [369, 678] is to take the rival images to be a low-contrast radial grating presented to one eye and a high-contrast spiral grating presented to the other eye. Each image is restricted to an annular region of the visual field centered on the fixation point of the observer, thus effectively restricting wave propagation to the one dimension around the annulus. Switches in perceptual dominance can then be triggered using a brief rapid increase in stimulus contrast within a small region of the suppressed low-contrast grating. This induces a perceptual traveling wave in which the observer perceives the local dominance of the low-contrast image spreading around the annulus. The observer presses a key when the perceptual wave reaches a target area at a fixed distance from the trigger zone, and this determines the wave speed [369, 678]. Since the rival images consist of oriented gratings, one might expect that primary visual cortex (V1) plays some role in the generation of binocular rivalry waves. Indeed, it has been shown using fMRI that there is a systematic correspondence between the spatiotemporal dynamics of activity in V1 and the time course of perceptual waves [369]. However, it has not been established whether the waves originate in V1 or are evoked by feedback from extrastriate cortex. Recently Kang et al. [312, 313] have developed a new psychophysical method for studying binocular rivalry waves that involves periodic perturbations of the rival images consisting of linear gratings. An observer tracks rivalry within a small, central region of spatially extended rectangular grating patterns, while alternating contrast triggers are presented repetitively in the periphery of the rival patterns. The basic experimental setup is illustrated in Fig. 8.5. A number of interesting results have been obtained from these studies. First, over a range of trigger frequencies, the switching between rival percepts within the central regions is entrained to the triggering events. Moreover, the optimal triggering frequency depends on the natural frequency of spontaneous switching (in the absence of triggers). Second, the latency between triggering event and perceptual switching increases approximately linearly with the distance between the triggering site and the central region being tracked by the observer, consistent with the propagation of a traveling front. Third, the speed of the traveling wave across observers covaries with the spontaneous switching rate.

8.2 Competitive Network Models of Binocular Rivalry

The above psychophysical experiments suggest that binocular rivalry waves consist of two basic components: the switching between rivalrous left-/right-eye states and the propagation of the switched state across a region of cortex. Let us first focus on the switching mechanism by neglecting spatial effects. Suppose, for the sake of illustration, that a horizontally oriented grating is presented to the left eye and a vertically oriented grating is presented to the right eye. This triggers rivalry due to the combination of orientation and eye-specific cross-inhibition in V1. During left-eye

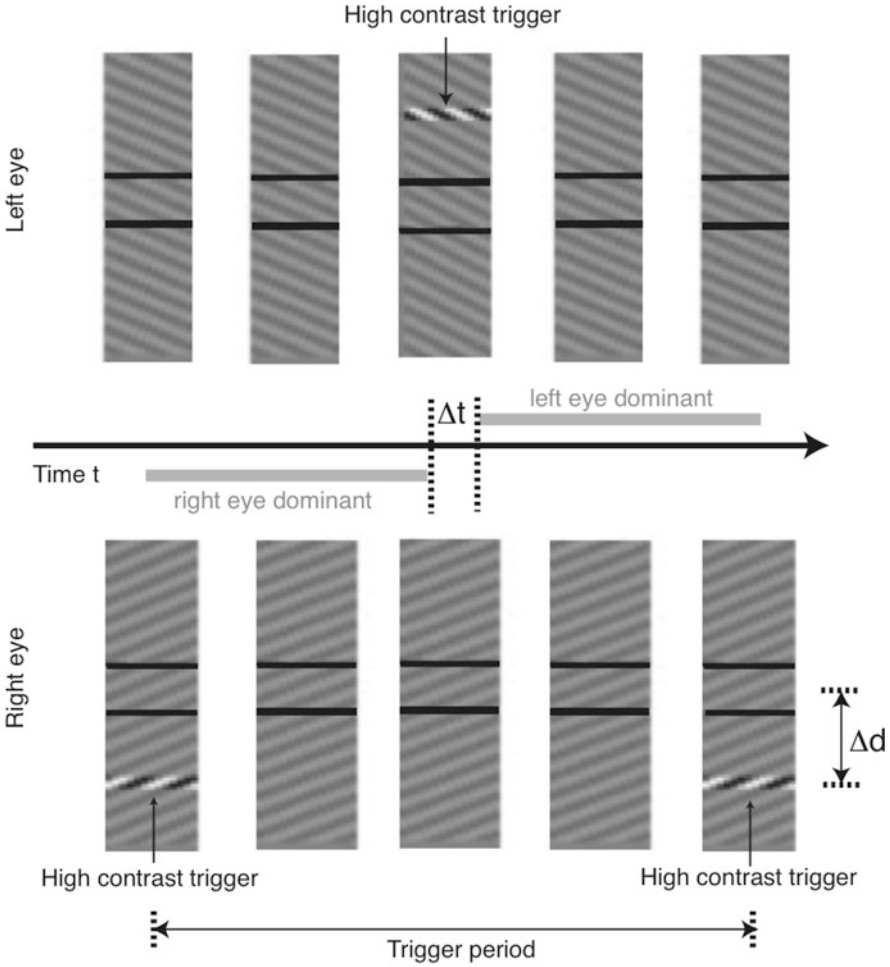

Fig. 8.5 Schematic diagram illustrating experimental protocol used to study binocular rivalry waves [312]. High-contrast triggers are presented periodically in anti-phase within the upper extended region of one grating pattern and within the lower region of the rival pattern. Subject simply reports perceptual alternations in rival dominance within the central monitoring region indicated by the *horizontal black lines* on each pattern. The monitoring region is a distance Δd from the trigger region, which can be adjusted. If Δt is the latency between the triggering event and the subsequent observation of a perceptual switch, then the speed c of the wave is given by the slope of the plot $\Delta d = c\Delta t$

stimulus dominance, it is assumed that a group of the left-eye neurons that respond to horizontal orientations are firing persistently, while right-eye neurons are suppressed by cross-inhibitory connections. Of course, there may still be some low-rate firing of the right-eye neurons, but it will be less than the firing rate of the left-eye horizontally tuned neurons [47]. Following this, some slow adaptive process causes a switch so that right-eye vertical orientation neurons fire persistently, suppressing

the left-eye neurons resulting in a repetitive cycle of perceptual dominance between the left- and right-eye stimuli. The competitive network architecture of reciprocal inhibition paired with slow adaptation (Fig. 8.6) has been used extensively to model oscillations in binocular rivalry [199, 328, 355, 577, 578, 586, 619, 678]. (In some versions of the model, recurrent excitation is omitted.) In most cases a firing rate model appears sufficient to capture the elevation in neuronal spiking associated with the dominant stimulus.

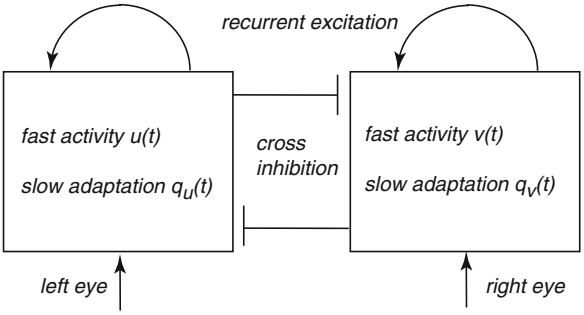

Fig. 8.6 Schematic diagram of a competitive network architecture for rivalry oscillations [355, 577, 678], consisting of two homogeneous populations of cells: one driven by left-eye stimuli and the other by right-eye stimuli. Recurrent connections within each population are assumed to be excitatory, whereas connections between the two populations are inhibitory (cross-inhibition). Each network is described by two variables: a fast activity variable and a slow adaptation variable

It remains an open question as to which slow adaptive process is most responsible for the eventual switching of one stimulus dominance to the other [577]. The mechanism of spike frequency adaptation has been suggested, since it can curtail excitatory activity in a single neuron [355, 678]. Spike frequency adaptation is the process by which a hyperpolarizing current is switched on due to a buildup of a certain ion, like calcium, within the cell due to repetitive firing [604]; see Sect. 4.1. The maximal firing rate of a neuron is lowered as a result. In the case of binocular rivalry, this may cause the dominant population to eventually drop its firing rate so that cross-inhibition suppressing the other population is then low enough for the suppressed populations to rekindle its firing rate into dominance. Since the recently released population is not adapted, it can then remain in dominance and suppress the other population for a period of time roughly equal to the time constant of spike frequency adaptation [355, 392, 678]. Another proposed switching mechanism is that the inhibitory synapses from one eye's neurons to the other's undergo synaptic depression; see Sect. 1.3. (More precisely, synaptic depression tends to be associated only with excitatory synapses, so that inclusion of depressing inhibitory connections would have to be mediated by excitatory connections innervating local interneurons, for example.) If inhibitory synapses remain repeatedly active, due to one eye's neurons suppressing the others, eventually most of those synapses' resources will be used up, the effect of inhibition will be weakened and the suppressed population will escape [328, 355, 577]. Synaptic depression could also occur in the excitatory recurrent connections. For concreteness, we will take slow adaptation to

arise from synaptic depression in all synaptic weights; however, the specific choice of adaptation does not affect the main results.

Let $u(t)$ and $v(t)$ denote the activity variables of the left- and right-eye populations at time t. The rate-based equations for a competitive network model with synaptic depression can be constructed as follows [328]:

$$\tau \frac{du(t)}{dt} = -u(t) + I_u(t) + \overline{w}_e q_u(t) F(u(t)) - \overline{w}_i q_v(t) F(v(t)), \tag{8.1}$$

$$\tau_s \frac{dq_u(t)}{dt} = 1 - q_u(t) - \beta q_u(t) F(u(t)), \tag{8.2}$$

and

$$\tau \frac{dv(t)}{dt} = -v(t) + I_v(t) + \overline{w}_e q_v(t) F(v(t)) - \overline{w}_i q_u(t) F(u(t)), \tag{8.3}$$

$$\tau_s \frac{dq_v(t)}{dt} = 1 - q_v(t) - \beta q_v(t) F(v(t)), \tag{8.4}$$

where the positive constants $\overline{w}_e$ and $\overline{w}_i$ denote the strengths of recurrent excitatory and cross-inhibitory connections, I_u, I_v denote the input stimuli from the left and right eyes, and F is a firing rate function that is taken to be the sigmoid (1.14). The depression variables q_u, q_v satisfy a rate-based version of (1.45); see also (6.15). In anticipation of the analysis of traveling front solutions of a spatially extended version of the model, we will take the high gain limit of F to obtain the Heaviside function $F(u) = H(u - \kappa)$. In this limit, the existence and stability of fixed-point solutions of (8.1) and (8.4) can be analyzed explicitly [328].

Suppose that $I_u = I_v = I$ with I constant. It turns out that there are four possible homogeneous fixed points and all are stable. First, there is the *off state* $U^* = V^* = I$, which occurs when $I < \kappa$, that is, the input is not strong enough to activate either population. Second there is the *on state* or *fusion state*, where both populations are simultaneously active:

$$(U^*, V^*) = \left(\frac{\overline{w}_e - \overline{w}_i}{1+\beta} + I, \frac{\overline{w}_e - \overline{w}_i}{1+\beta} + I \right), \quad (Q_u^*, Q_v^*) = \left(\frac{1}{1+\beta}, \frac{1}{1+\beta} \right),$$

and occurs when $I > \kappa - (\overline{w}_e - \overline{w}_i)/(1+\beta)$. This case is more likely for very strong depression (β large), since cross-inhibition will be weak, or when the local connections are strong and excitation-dominated. Finally there are two *winner-takes-all* (WTA) states in which one population dominates the other: the left-eye dominant state

$$(U^*, V^*) = \left(\frac{\overline{w}_e}{1+\beta} + I, I - \frac{\overline{w}_i}{1+\beta} \right), \quad (Q_u^*, Q_v^*) = \left(\frac{1}{1+\beta}, 1 \right),$$

and the right-eye dominant state

$$(U^*, V^*) = \left(I - \frac{\overline{w}_i}{1+\beta}, \frac{\overline{w}_e}{1+\beta} + I \right), \quad (Q_u^*, Q_v^*) = \left(1, \frac{1}{1+\beta} \right).$$

The WTA states exist provided that

$$I > \kappa - \frac{\overline{w}_e}{1+\beta}, \quad I < \kappa + \frac{\overline{w}_i}{1+\beta}.$$

This will occur in the presence of weak depression (β small) and strong cross-inhibition such that depression cannot exhaust the dominant hold one population has on the other. It can also be shown that (8.1)–(8.4) also support homogeneous limit cycle oscillations in which there is periodic switching between left- and right-eye dominance consistent with binocular rivalry [328]. Since all the fixed points are stable, it follows that such oscillations cannot arise via a standard Hopf bifurcation. Indeed, one finds bistable regimes where a rivalry state coexists with a fusion state as illustrated in Fig. 8.7. (Such behavior persists in the case of smooth sigmoid firing rate functions, at least for sufficiently high gain [328].) For a detailed discussion of the various bifurcation scenarios in competitive neural networks see [435, 563, 577].

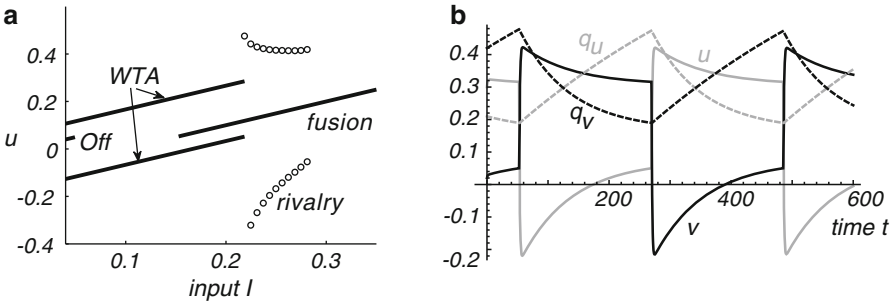

Fig. 8.7 (**a**) Bifurcation diagram showing homogeneous solutions for the left population activity u as a function of the input amplitude I. *Solid lines* represent stable states, whereas *circles* represent the maximum and minimum of rivalry oscillations. It can be seen that there are regions of off/WTA bistability, WTA/fusion bistability, and fusion/rivalry bistability. Parameters are $\tau_s = 500$, $\kappa = 0.05$, $\beta = 5$, $\overline{w}_e = 0.4$, and $\overline{w}_i = 1$. (**b**) Homogeneous oscillatory solution in which there is spontaneous periodic switching between left- and right-eye dominance. Plot against time of the left-eye neural field u (*solid gray*) and the right-eye neural activity v (*solid black*) together with the corresponding depression variables q_u (*dashed gray*) and q_v (*dashed black*)

In order to take into account the propagation of activity seen in binocular rivalry waves, it is necessary to introduce a spatially extended network model. Therefore, suppose that the neuronal populations responding to stimuli from the left eye, say, are distributed on a one-dimensional (1D) lattice and are labeled according to the integer n; a second 1D network responds to stimuli from the right eye; see Fig. 8.8. In terms of the functional architecture of V1, one can interpret the nth left-/right-eye populations as consisting of neurons in a given hypercolumn that respond maximally to the distinct stimuli presented to the two eyes at a particular coarse-grained location in space. In the case of the orientated grating stimuli used by Kang et al. [312, 313] (see Fig. 8.5), this would mean neurons whose orientation

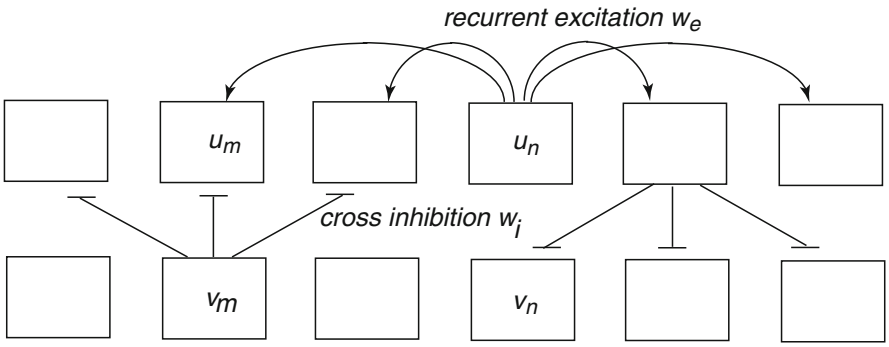

Fig. 8.8 Schematic diagram of a competitive neural network consisting of two sets of populations distributed along a 1D lattice. Recurrent connections within each 1D network are assumed to be excitatory, whereas connections between the two networks are inhibitory (cross-inhibition). Slow adaptation is incorporated into the model by taking the network connections to exhibit synaptic depression

preference coincides with the stimulus orientation presented to a given eye. Since the orientation does not change along the length of the grating, all neurons receive the same external drive. Letting $u_n, v_n, q_{u,n}, q_{v,n}$ denote the activity and depression variables of the nth left- and right-eye networks, we have

$$\tau \frac{du_m}{dt} = -u_m + I_u + \sum_n [[w_e]_{mn} q_{u,n} F(u_n) - [w_i]_{mn} q_{v,n} F(v_n)] \tag{8.5}$$

$$\tau_s \frac{dq_{u,m}}{dt} = 1 - q_{u,m} - \beta q_{u,m} F(u_m) \tag{8.6}$$

and

$$\tau \frac{dv_m}{dt} = -v_m + I_v + \sum_n [[w_e]_{mn} q_{v,n} F(v_n) - [w_i]_{mn} q_{u,n} F(u_n)] \tag{8.7}$$

$$\tau_s \frac{dq_{v,m}}{dt} = 1 - q_{v,m} - \beta q_{v,m} F(v_m). \tag{8.8}$$

Here $[w_e]_{mn}$ is the strength of excitation from the nth to the mth population with the same eye preference, and $[w_i]_{mn}$ is the strength of cross-inhibition between populations with opposite eye preferences. The weights are typically assumed to decrease with distance of separation $|m-n|$ according to an exponential or Gaussian distribution. Note that a similar network architecture was previously considered in a computational model of binocular rivalry waves [313, 678], in which cross-inhibition was mediated explicitly by interneurons and, rather than including depressing synapses, the excitatory neurons were taken to exhibit spike frequency adaptation. Numerical simulations of the model showed that the network supported traveling waves consistent with those observed numerically under physiologically reasonable parameter regimes.

8.3 Neural Field Model

Although the discrete lattice model presented in Sect. 8.2 is directly amenable to numerical simulations, it is difficult to derive any analytical results for the model that generate, for example, explicit expressions for how the wave speed depends on network parameters. Therefore, in this section we turn to a neural field model that can be constructed by taking an appropriate continuum limit of (8.5) and (8.8) [83, 663]. Introduce a lattice spacing a, and write $[w_e]_{nm} = aw_e(na,ma)$, $u_n(t) = u(na,t)$, etc. Substituting into (8.5)–(8.8) and taking the continuum limit $a \to 0$ such that $na \to x$ and $ma \to y$, the discrete sums can be replaced by integrals to give the neural field model

$$\tau \frac{du(x,t)}{dt} = -u(x,t) + I_u + \int_{-\infty}^{\infty} w_e(x-x')q_u(x',t)F(u(x',t))dx' - \int_{-\infty}^{\infty} w_i(x-x')q_v(x',t)F(v(x',t))dx' \tag{8.9a}$$

$$\tau_s \frac{dq_u(x,t)}{dt} = 1 - q_u(x,t) - \beta q_u(x,t)F(u(x,t)) \tag{8.9b}$$

and

$$\tau \frac{dv(x,t)}{dt} = -v(x,t) + I_v + \int_{-\infty}^{\infty} w_e(x-x')q_v(x',t)F(v(x',t))dx' - \int_{-\infty}^{\infty} w_i(x-x')q_u(x',t)F(u(x',t))dx' \tag{8.10a}$$

$$\tau_s \frac{dq_v(x,t)}{dt} = 1 - q_v(x,t) - \beta q_v(x,t)F(v(x,t)), \tag{8.10b}$$

assuming that the weights only depend on the distance between interacting populations. For concreteness, the distributions w_e and w_i are both taken to be Gaussians:

$$w_e(r) = \frac{\overline{w}_e}{\sqrt{2\pi\sigma_e^2}} e^{-\frac{r^2}{2\sigma_e^2}}, \quad w_i(r) = \frac{\overline{w}_i}{\sqrt{2\pi\sigma_i^2}} e^{-\frac{r^2}{2\sigma_i^2}}. \tag{8.11}$$

Following [83], assume that $\sigma_e > \sigma_i$ (longer-range excitation) and fix the length scale by setting $\sigma_e = 2$, $\sigma_i = 1$. Assuming that excitation spans a single hypercolumn, σ_e should be the same approximate size as a hypercolumn, that is, of the order 200 μm. We also take $\tau = 1$ in units of the membrane time constant, which is typically of the order 10 ms.

8.3.1 Rivalry Waves in a Deterministic Neural Field Model

The next step is to interpret the binocular rivalry wave seen in the experiments of Kang et al. [312, 313] as a traveling wave-front solution of the neural field equations (8.9) and (8.10), in which a high activity state invades the suppressed left-eye

network, say, while retreating from the dominant right-eye network; see Fig. 8.9. Such a wave is defined as

$$u(x,t) = U(x-ct), \quad v(x,t) = V(x-ct), \tag{8.12}$$

where c is the wave speed and $\xi = x - ct$ is a traveling wave coordinate together with the asymptotic conditions

$$(U(\xi),V(\xi)) \to \mathbf{X}_L \text{ as } \xi \to -\infty, \quad (U(\xi),V(\xi)) \to \mathbf{X}_R \text{ as } \xi \to \infty \tag{8.13}$$

with $U(\xi)$ a monotonically decreasing function of ξ and $V(\xi)$ a monotonically increasing function of ξ. Here $\mathbf{X}_L$ ($\mathbf{X}_R$) represents a homogeneous left-eye (right-eye) dominant state. Given the asymptotic behavior of the solution and the requirements of monotonicity, we see that $U(\xi)$ and $V(\xi)$ each cross threshold at a single location, which may be different for the two eyes. Exploiting translation invariance, we take $U(0) = \kappa$ and $V(d) = \kappa$.

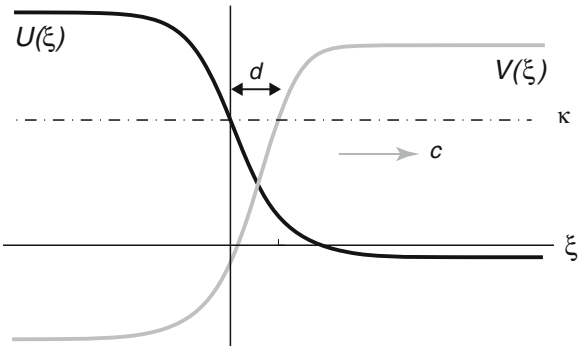

Fig. 8.9 Sketch of a right-moving traveling wave solution in which a high activity state invades the suppressed left-eye network while retreating from the dominant right-eye network. *Wave* is shown in a moving frame $\xi = x - ct$

It is possible to construct an exact traveling wave solution of equations (8.9) and (8.10) by taking f to be the Heaviside function (1.15) and making the adiabatic approximation that $q_u(x,t) = Q_u, q_v(x,t) = Q_v$ with Q_u, Q_v constants [83]. The latter is based on the assumption that adaptation is sufficiently slow so that the wave traverses cortex in a time $T_l \ll \tau_s$. Substituting the traveling wave solution (8.12) into (8.9a) and (8.10a) with fixed Q_u, Q_v and $F(u) = H(u-\kappa)$ leads to the equations

$$-c\frac{dU}{d\xi} + U = Q_u \int_{-\infty}^{0} w_e(\xi - \xi')d\xi' - Q_v \int_{d}^{\infty} w_i(\xi - \xi')d\xi' + I \tag{8.14a}$$

$$-c\frac{dV}{d\xi} + V = Q_v \int_{d}^{\infty} w_e(\xi - \xi')d\xi' - Q_u \int_{-\infty}^{0} w_i(\xi - \xi')d\xi' + I. \tag{8.14b}$$

where, for simplicity, we have set $I_u = I_v = I$. Multiplying both sides of (8.14a) and (8.14b) by $e^{-\xi/c}$, integrating with respect to ξ and imposing the threshold conditions gives

$$U(\xi) = e^{\xi/c}\left[\kappa - \frac{1}{c}\int_0^{\xi} e^{-z/c}\Psi_d(z)dz - I(1-e^{-\xi/c})\right], \tag{8.15a}$$

$$V(\xi) = e^{(\xi-d)/c}\left[\kappa - \frac{1}{c}\int_0^{\xi-d} e^{-z/c}\Phi_d(-z)dz - I(1-e^{-(\xi-d)/c})\right] \tag{8.15b}$$

for $\xi > 0$, with Ψ and Φ defined by

$$\Psi_d(z) = Q_u\int_z^{\infty} w_e(y)dy - Q_v\int_{-\infty}^{z-d} w_i(y)dy. \tag{8.16}$$

$$\Phi_d(z) = Q_v\int_z^{\infty} w_e(y)dy - Q_u\int_{-\infty}^{z-d} w_i(y)dy. \tag{8.17}$$

Finally, requiring that the wave solution remain bounded as $\xi \to \infty$ (assuming $c > 0$) yields the pair of threshold conditions

$$\kappa = \int_0^{\infty} e^{-s}\Psi_d(cs)ds + I, \quad \kappa = \int_0^{\infty} e^{-s}\Phi_d(-cs)ds + I. \tag{8.18}$$

In the particular case $Q_u = Q_v = 1$ (no synaptic depression), the above equations have no solution for $c \neq 0$, that is, there does not exist a traveling wave solution [83]. This follows from setting $Q_u = Q_v = 1$ in (8.18) and subtracting the pair of equations to obtain

$$\int_0^{\infty} e^{-s}\left[\Psi_d(cs) - \Psi_d(-cs)\right]ds = 0.$$

The latter equation has no solution for $c \neq 0$, since

$$\Psi_d(cs) - \Psi_d(-cs) = -\int_{-cs}^{cs} w_e(y)dy - \int_{-cs-d}^{cs-d} w_i(y)dy < 0$$

for all $s \in [0,\infty)$. On the other hand, slow synaptic depression with $Q_u \neq Q_v$ breaks the symmetry of the threshold crossing conditions, leading to a unique solution for c, d as a function of the network parameters. Moreover, one can establish that the traveling front is linearly stable by constructing the corresponding Evans function along similar lines to Sect. 7.1.2 [83]. The threshold conditions can also be used to simplify the expressions for the wave profile, namely,

$$U(\xi) = \frac{1}{c}\int_0^{\infty} e^{-z/c}\Psi_d(z+\xi)dz + I \tag{8.19a}$$

$$V(\xi) = \frac{1}{c}\int_0^{\infty} e^{-z/c}\Phi_d(-z-\xi+d)dz + I. \tag{8.19b}$$

Example plots of the wave speed are shown in Fig. 8.10. Baseline parameter values are chosen so that spontaneous oscillations and traveling fronts coexist as found experimentally [312, 313]. The model wave speed is of the order $c = 1$ in dimensionless units, that is, $c = \sigma_e/2\tau$ where σ_e is the range of excitation and τ is the membrane time constant. Taking σ_e to be of the order 200 μm and τ to be of the order 10 ms yields a wave speed of around 10 mm/s, which is consistent with the speeds observed experimentally. (In the psychophysical experiments of Kang et al., binocular rivalry waves took approximately 0.8 s to traverse 2 degrees of the visual field. The magnification factor in humans throughout the foveal region is approximately 0.4 cm/deg, which corresponds to 0.8 cm of cortex.) Figure 8.10 shows that the speed of the wave is a decreasing function of the threshold κ and an increasing function of the input amplitude I; the latter is consistent with what is found experimentally when the stimulus contrast is increased [312, 313]. Yet another experimental result that emerges from the model is that the wave speed covaries with the frequency of spontaneous rivalry oscillations [83].

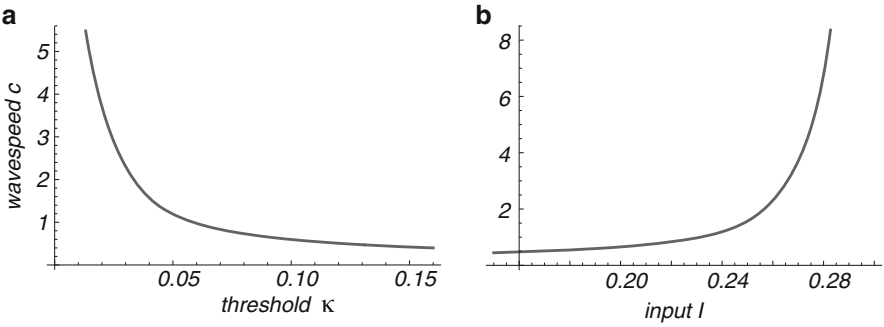

Fig. 8.10 Plot of wave speed c in units of $\sigma_e/(2\tau)$ as a function of (**a**) the threshold κ and (**b**) the external input strength I. The default parameters are taken to be $\overline{w}_i = 1, \overline{w}_e = 0.4, \sigma_i = 1, \sigma_e = 2, \beta = 5, \kappa = 0.05, I = 0.24, Q_u = 0.42, Q_v = 0.25$ and the corresponding wave speed is $c = 1.2$. For this set of parameters, the network operates in a regime that supports both traveling waves and homogeneous oscillatory solutions, that is, spontaneous switching occurs in the absence of traveling waves

8.3.2 Effects of Extrinsic Noise in the Fast Activity Variables

As highlighted in Sect. 8.1, the switching between rivalrous images has a stochastic component. This motivates studying a stochastic version of the neural field model (8.9), which, in the adiabatic limit of fixed depression variables, takes the form of an SPDE for the stochastic activity variables $U(x,t)$ and $V(x,t)$ [663]:

$$dU = \left[-U + Q_u \int_{-\infty}^{\infty} w_e(x-y)F[U(y,t)]dy - Q_v \int_{-\infty}^{\infty} w_i(x-y)F[V(y,t)]dy + I_u\right] dt + \varepsilon^{\frac{1}{2}} g(U) \circ dW_u \tag{8.20a}$$

$$dV = \left[-V + q_v \int_{-\infty}^{\infty} w_e(x-y)F[V(y,t)]dy - Q_u \int_{-\infty}^{\infty} w_i(x-y)F[U(y,t)]dy + I_v\right]dt$$
$$+\varepsilon^{\frac{1}{2}} g(V) \circ dW_v. \tag{8.20b}$$

with Q_u, Q_v fixed. Here W_u, W_v represent independent Wiener processes such that [see (7.158)]

$$\langle dW_{\{u,v\}}(x,t)\rangle = 0, \quad \langle dW_i(x,t)dW_j(x',t')\rangle = 2\delta_{i,j}C([x-x']/\lambda)\delta(t-t')dtdt', \tag{8.21}$$

where $i,j = u,v$ and $\langle\cdot\rangle$ denotes averaging with respect to the Wiener processes. The effects of extrinsic noise on binocular rivalry waves can be analyzed using the multiple time-scale method described in Sect. 2.6 for PDEs and Sect. 7.4 for neural fields [663]. First, (8.20) and (8.20b) are rewritten so that the fluctuating terms have zero mean according to Novikov's theorem. Then (U,V) is expressed as a fixed wave profile (U_0,V_0) that is displaced by an amount $\Delta(t)$ from its uniformly translating position $\xi = x - c_\varepsilon t$ and a time-dependent fluctuation (U_1,V_1) in the wave shape about its instantaneous position:

$$U(x,t) = U_0(\xi - \Delta(t)) + \varepsilon^{1/2}U_1(\xi - \Delta(t),t), \tag{8.22a}$$
$$V(x,t) = V_0(\xi - \Delta(t)) + \varepsilon^{1/2}V_1(\xi - \Delta(t),t). \tag{8.22b}$$

The wave profile (U_0,V_0) and associated wave speed c_ε are obtained by solving the deterministic equations (8.14) with the decay terms U and V replaced by $h(U)$ and $h(V)$, where $h(U) = -U + \varepsilon C(0)g'(U)g(U)$. By carrying out a perturbation expansion in ε and imposing a solvability condition, one finds that $\Delta(t)$ is given by a Wiener process with

$$\langle \Delta(t)\rangle = 0, \quad \langle \Delta(t)^2\rangle = 2D(\varepsilon)t, \tag{8.23}$$

The diffusion coefficient $D(\varepsilon)$ is

$$D(\varepsilon) = \varepsilon \frac{\int_{-\infty}^{\infty} \left(\mathscr{V}_1(\xi)^2 g(U_0(\xi))^2 + \mathscr{V}_2(\xi)^2 g(V_0(\xi))^2\right) d\xi}{\left[\int_{-\infty}^{\infty} \left(\mathscr{V}_1(\xi)U_0'(\xi) + \mathscr{V}_2(\xi)V_0'(\xi)\right) d\xi\right]^2}, \tag{8.24}$$

where $\mathscr{V} = (\mathscr{V}_1, \mathscr{V}_2)^T$ is the null vector of the adjoint linear operator $\mathbb{L}^\dagger = (\mathbb{L}_u^\dagger, \mathbb{L}_v^\dagger)^T$

$$\mathbb{L}_u^\dagger(B_1,B_2) = -c_\varepsilon \frac{dB_1}{d\xi} + h'(U_0)B_1 + F'(U_0)Q_u \int_{-\infty}^{\infty} w_e(\xi - \xi')B_1(\xi')d\xi'$$
$$-F'(V_0)Q_v \int_{-\infty}^{\infty} w_i(\xi - \xi')B_2(\xi')d\xi' \tag{8.25}$$

and

$$\mathbb{L}_v^\dagger(B_1,B_2) = -c_\varepsilon \frac{dB_2}{d\xi} + h'(V_0)B_2 + F'(V_0)Q_v \int_{-\infty}^{\infty} w_e(\xi-\xi')B_2(\xi')d\xi' \\ -F'(U_0)Q_u \int_{-\infty}^{\infty} w_i(\xi-\xi')B_1(\xi')d\xi'. \tag{8.26}$$

It is important to point out that, in contrast to traveling front solutions of scalar neural field equations (see Sect. 7.4), we are now considering composite wave solutions consisting of an invading front in the left-eye network, say, co-moving with a retreating front in the right-eye network. Thus in addition to the center-of-mass of the composite wave, which moves with speed c in the absence of noise, there is an additional degree of freedom corresponding to the "width" of the composite wave. [In the case of a Heaviside rate function, the width is determined by the threshold crossing point d; see (8.18).] For simplicity, we assume that the width of the composite wave is only weakly affected by the noise; this is consistent with what is found numerically [663].

8.3.3 Explicit Results for a Heaviside Rate Function

In order to illustrate the above analysis, we consider a particular example where the mean speed c_ε and diffusion coefficient $D(\varepsilon)$ can be calculated explicitly. That is, set $g(U) = g_0 U$ for the multiplicative noise term and take $F(U) = H(u-\kappa)$. The deterministic equations for U_0, V_0 can be solved along identical lines to (8.14a) and (8.14b) and lead to the modified threshold conditions

$$\kappa = \frac{1}{\gamma(\varepsilon)} \int_0^\infty \mathrm{e}^{-s} \Psi_d(cs/\gamma(\varepsilon))ds + I, \quad \kappa = \frac{1}{\gamma(\varepsilon)} \int_0^\infty \mathrm{e}^{-s} \Phi_d(-cs/\gamma(\varepsilon))ds + I, \tag{8.27}$$

where $\gamma(\varepsilon) = 1 - \varepsilon C(0) g_0^2$. The corresponding wave profiles are

$$U(\xi) = \frac{1}{c} \int_0^\infty \mathrm{e}^{-z\gamma/c} \Psi_d(z+\xi)dz + I \tag{8.28a}$$

$$V(\xi) = \frac{1}{c} \int_0^\infty \mathrm{e}^{-z\gamma/c} \Phi_d(-z-\xi+d)dz + I. \tag{8.28b}$$

It immediately follows that both the speed c and displacement d depend on the noise strength ε. In order to calculate the diffusion coefficient, it is first necessary to determine the null vector $\mathscr{V}(\varepsilon)$ of the adjoint linear operator $\mathbf{L}^\dagger$. Substituting $F(U) = H(U-\kappa)$ and $g(U) = g_0 U$ in (8.25) and (8.26) shows that the components of $\mathscr{V}$ satisfy the simultaneous equations

$$c\frac{d\mathscr{V}_1}{d\xi} + \gamma(\varepsilon)\mathscr{V}_1 = \frac{\delta(\xi)}{|U_0'(0)|} Q_u \int_{-\infty}^{\infty} w_e(z)\mathscr{V}_1(z)dz \\ -\frac{\delta(\xi-d)}{|V_0'(d)|} Q_v \int_{-\infty}^{\infty} w_i(z-d)\mathscr{V}_2(z)dz \tag{8.29}$$

$$c\frac{d\mathscr{V}_2}{d\xi}+\gamma(\varepsilon)\mathscr{V}_2=-\frac{\delta(\xi)}{|U_0'(0)|}Q_u\int_{-\infty}^{\infty}w_i(z)\mathscr{V}_1(z)dz \\ +\frac{\delta(\xi-d)}{|V_0'(d)|}Q_v\int_{-\infty}^{\infty}w_e(z-d)\mathscr{V}_2(z)dz. \tag{8.30}$$

Proceeding along similar lines to Sect. 7.4, we make the ansatz that

$$\begin{aligned}\mathscr{V}_1(\xi) &= \mathscr{A}_1\mathrm{e}^{-\gamma\xi/c}H(\xi)-\mathscr{B}_1\mathrm{e}^{-\gamma[\xi-d]/c}H(\xi-d),\\ \mathscr{V}_2(\xi) &= -\mathscr{A}_2\mathrm{e}^{-\gamma\xi/c}H(\xi)+\mathscr{B}_2\mathrm{e}^{-\gamma[\xi-d]/c}H(\xi-d).\end{aligned}$$

Substituting back into the adjoint equations yields algebraic conditions for the constant coefficients $\mathscr{A}_j,\mathscr{B}_j$:

$$\mathscr{A}_1 = \frac{Q_u}{|U_0'(0)|}\left(\mathscr{A}_1\Omega_e[0]-\mathscr{B}_1\Omega_e[d]\right) \tag{8.31}$$

$$\mathscr{B}_1 = \frac{Q_v}{|V_0'(d)|}\left(\mathscr{B}_2\Omega_i[0]-\mathscr{A}_2\Omega_i[-d]\right) \tag{8.32}$$

$$\mathscr{A}_2 = \frac{Q_u}{|U_0'(0)|}\left(\mathscr{A}_1\Omega_i[0]-\mathscr{B}_1\Omega_i[d]\right) \tag{8.33}$$

$$\mathscr{B}_2 = \frac{Q_v}{|V_0'(d)|}\left(\mathscr{B}_2\Omega_e[0]-\mathscr{A}_2\Omega_e[-d]\right), \tag{8.34}$$

where

$$\Omega_j[x]=\int_0^{\infty}\mathrm{e}^{-z\gamma/c}w_j(x+z)dz,\quad j=e,i. \tag{8.35}$$

Differentiating (8.28a) and (8.28b) with respect to ξ and using (8.16) and (8.17) show that

$$U_0'(0)=-Q_u\Omega_e[0]-Q_v\Omega_i[-d]<0, \tag{8.36}$$

and

$$V_0'(d)=Q_v\Omega_e[0]+Q_u\Omega_i[d]>0. \tag{8.37}$$

We have also used the fact that the weight distributions $w_e(x),w_i(x)$ are even functions of x. Substituting these derivatives into (8.31) and (8.34) gives

$$\mathscr{B}_2=-\frac{Q_v\Omega_e[-d]}{Q_u\Omega_i[d]}\mathscr{A}_2,\quad \mathscr{B}_1=-\frac{Q_v\Omega_i[-d]}{Q_u\Omega_e[d]}\mathscr{A}_1. \tag{8.38}$$

It follows from (8.33) and (8.38) that $\mathscr{A}_2,\mathscr{B}_1,\mathscr{B}_2$ can all be expressed as constant multiples of $\mathscr{A}_1$, with the latter determined by normalizing the null vector.

It can be verified that the various assumptions used in the above analysis are reasonable by carrying out numerical simulations of the full system given by (8.20a), (8.20b), (8.9a) and (8.9b) with $Q_{u,v}\to q_{u,v}$ [663]. In particular it can be checked that fluctuations in the separation between the left- and right-eye fronts are negligible in the long time limit. An illustration of the progression of a stochastic composite front is shown in Fig. 8.11. The corresponding mean $\overline{X}(t)$ and variance $\sigma_X^2(t)$ of wave position as a function of time are plotted in Fig. 8.12 using level sets as

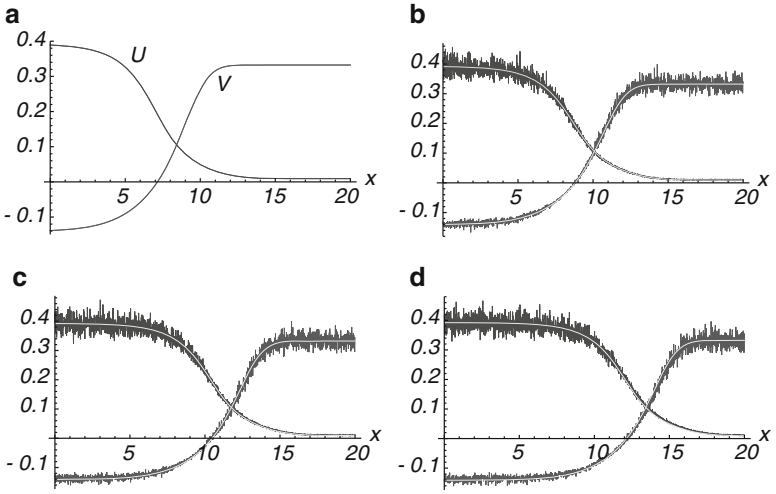

Fig. 8.11 Effects of multiplicative noise in the activity variables. Simulation of the activity variables $u(x,t)$ and $v(x,t)$ for (**a**) t=0, (**b**) t=1, (**c**) t=2, (**d**) t=3. The continuous lines are the functions $U_0(x-ct)$ and $V_0(x-ct)$ which were found by solving (2.97). The functions U_0 and V_0 were also used for the initial condition. Parameter values were $a_i = 1, a_e = 0.4, \sigma_i = 1, \sigma_e = 2, \beta = 5, \kappa = 0.05, I = 0.24, \varepsilon = 0.006$ with spatial and temporal grid sizes both being 0.01

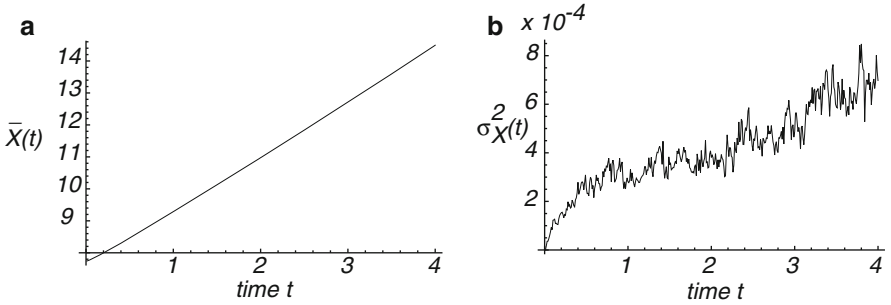

Fig. 8.12 (**a**) Mean and (**b**) variance of the wave position for an ensemble of 128 stochastic simulations. Parameters were the same as Fig. 8.11

explained in Sect. 7.4.1. It can be seen that $\overline{X}(t)$ varies linearly with t, consistent with the assumption that there is constant speed wave, $\overline{X}(t) \sim c_\varepsilon t$. The variance initially increases rapidly with respect to t, but then follows linear behavior consistent with a diffusive-like displacement of the wave from its uniformly translating position at long time scales, $\sigma_X^2(t) \sim 2D(\varepsilon)t$. The initial sharp increase in the variance results from the fact that the left and right fronts do move slightly with respect to each other, resulting in higher-order behavior. However, one finds numerically that this component of the variance is small and bounded so that it becomes negligible as time increases.

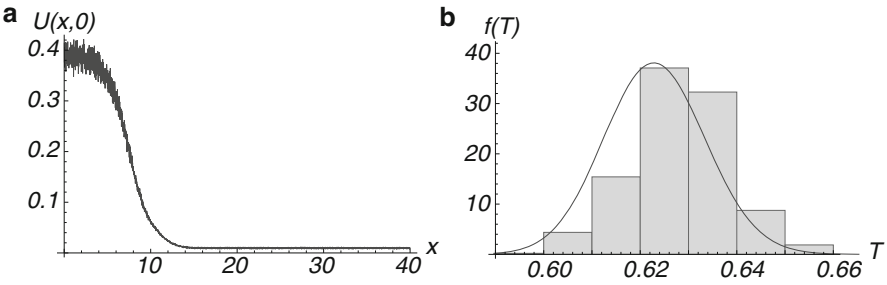

Fig. 8.13 (**a**) Snapshot of a stochastic traveling wave (only left-eye activity is shown). (**b**) First passage time distribution for the wave to travel a distance $L = 1$, starting from the wave profile in (**a**). Parameter values were $a_i = 1, a_e = 0.4, \sigma_i = 1, \sigma_e = 2, \beta = 5, \kappa = 0.05, I = 0.24, \varepsilon = 0.006$ with spatial and temporal grid sizes both being 0.01.The best fit inverse Gaussian $\mathscr{F}(T;\mu,\lambda)$ for the histogram gives the parameters $\mu = 0.62, \lambda = 2200$ which is in very good agreement with the theoretical predictions of $\mu = L/c = 0.6, \lambda = L^2/D = 2100$

The above analysis predicts that the wave position will follow a Brownian motion, which implies that the time taken for a wave to travel a distance $L > 0$ has a distribution given by the standard first passage time formula for Brownian motion with drift c. That is, let T_L denote the first passage time for the wave to travel a distance L: $cT_L + \Delta(T_L) = L$ given $\Delta(0) = 0$. Then the first passage time density is given by an inverse Gaussian or Wald distribution:

$$f(T_L) = \mathscr{F}(T_L; \frac{L}{c}, \frac{L^2}{D}), \tag{8.39}$$

where

$$\mathscr{F}(T;\mu,\lambda) = \left[\frac{\lambda}{2\pi T^3}\right]^{1/2} \exp\left(-\frac{\lambda(T-\mu)^2}{2\mu^2 T}\right). \tag{8.40}$$

Figure 8.13 shows the first passage time distribution generated over a large number of simulations for an initial condition given by a fully developed stochastic traveling wave. Consistent with the analysis, the distribution can be fitted by an inverse Gaussian. However, it has been assumed that the predominant source of noise is in the activity variables. Now suppose that the main source of noise is in the depression variables. Once again assume that a traveling wave crosses cortex significantly faster than the relaxation time of synaptic depression, so that q_u and q_v can be taken to be constant with respect to time during passage of the wave. However, they are no longer constant with respect to space nor with respect to trials, that is, $q_u = Q_u(x)$ and $q_v = Q_v(x)$ with Q_u, Q_v random variables of x. So although the wave itself will travel deterministically in a given trial, the functions $Q_u(x)$ and $Q_v(x)$ will be different across trials. In several experimental studies [312, 313] of binocular rivalry waves, a dominance switch was induced about halfway through a normal dominance cycle by locally changing the contrast in the depressed stimulus. The latter can be represented by increasing the input strength I over a small region of the model. This suggests taking q_u and q_v to evolve according to

$$\tau_s dq_u(x,t) = [1 - q_u(x,t)]\,dt + \eta\, dW_{q_u}(x,t), \tag{8.41a}$$

$$\tau_s dq_v(x,t) = [1 - q_v - \beta q_v]\,dt + \eta\, dW_{q_v}(x,t) \tag{8.41b}$$

over the time interval $[t_0, T]$. It is assumed that a switch from left- to right-eye dominance occurs at $t = t_0$ so that $u(x,t) < \kappa$ and $v(x,t) > \kappa$ for $t \in (t_0, T)$. The time T is then chosen so that the system is about $2/3$ of the way through a rivalry oscillation, such that $Q_u(x) = q_u(x,T)$ and $Q_v(x) = q_v(x,T)$. (Similar results were obtained for different cycle lengths and choices of T away from the beginning or end of a cycle.) Thus, the quenched random variables $Q_u(x)$ and $Q_v(x)$ are obtained by taking a snapshot of two lines of independent Ornstein–Uhlenbeck processes. Averaging over many trials, it is found numerically that the first passage time distribution is still well approximated by an inverse Gaussian distribution; see Fig. 8.14 and [663].

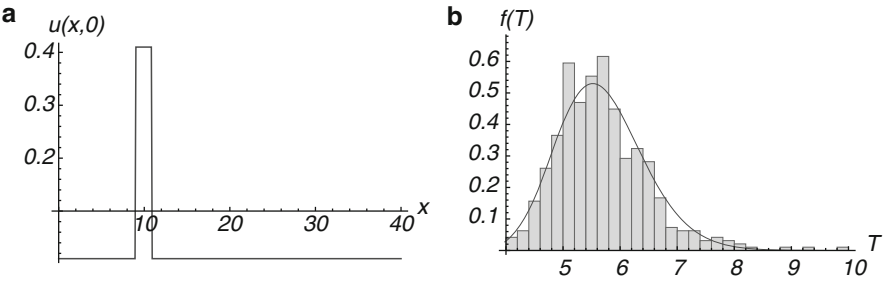

Fig. 8.14 Effects of quenched noise in the depression variables. (**a**) Initial condition given by a right-eye dominant homogeneous steady state perturbed by a narrow square pulse of left-eye activity. (**b**) First passage time distribution for a wave to travel a distance $L = 6$ starting from the initial condition shown in (**a**). Parameter values were $a_i = 1, a_e = 0.4, \sigma_i = 1, \sigma_e = 2, \beta = 5, \kappa = 0.05, I = 0.24, \eta = 0.037\langle Q\rangle$, where $\langle Q\rangle$ is the spatial average of the quenched depression variables (to make the results comparable with multiplicative noise). The spatial grid size $\Delta x = 0.1$ and the temporal grid step is $\Delta t = 0.01$. The *solid curve* in (**b**) is the best fit inverse Gaussian

In summary, we have illustrated one application of neural field theory, namely, to the phenomenon of binocular rivalry waves. Formulating the problem in terms of continuum neural field equations allows one to study the short time behavior associated with the propagation of eye dominance from an analytical perspective, both for deterministic and stochastic waves. In the deterministic case, one finds that some form of slow adaptation such as synaptic depression is needed in order to provide a symmetry breaking mechanism that allows propagation of a binocular rivalry wave [83]. That is, the equations for the left- and right-eye networks have to be different on the time scales during which traveling waves propagate. One implication of this is that purely noise-driven switching between rivalrous states in the absence of adaptation could not by itself generate rivalry waves, since it would not produce bias in the appropriate direction. However, noise does have a significant effect on binocular rivalry waves in the presence of slow adaptation. In particular, the analysis predicts that motion of the wave in the presence of noise in the activity variables has a diffusive component that leads to a distribution of first passage times given by an inverse Gaussian. A similar distribution of first passage times occurs for quenched noise in the depression variables [83].

8.4 Modeling Primary Visual Cortex Using 2D Neural Fields

The neural field model of binocular rivalry waves introduced in Sect. 8.3 is based on a very simple model of V1. In particular, it is a 1D model that ignores any correlations between long-range horizontal connections and stimulus feature maps. Such simplifications are reasonable as a first step, particularly when modeling the psychophysical experiments of Kang et al. [312, 313]. However, in order to account for the dependence of wave velocity on the orientation patterns of annular stimuli in the experiments of Wilson et al. [678], for example, it is necessary to consider a more detailed, 2D model of V1 that takes into account such correlations. In the final section of this chapter, we briefly describe one possible approach, which is based on a neural field model of coupled hypercolumns [71, 79].

8.4.1 2D Planar Model

For the sake of illustration, consider a 2D scalar neural field (without any slow adaptation) of the form

$$\frac{\partial u(\mathbf{r},t)}{\partial t} = -u(\mathbf{r},t) + \int w(\mathbf{r},\mathbf{r}')F(u(\mathbf{r}',t))d\mathbf{r}'. \tag{8.42}$$

Almost all 2D neural field models take $w(\mathbf{r},\mathbf{r}') = w(|\mathbf{r}-\mathbf{r}'|)$ so that w is invariant with respect to the Euclidean group $\mathbf{E}(2)$ of rigid body transformations in the plane. That is,

$$\gamma \cdot w(\mathbf{r},\mathbf{r}') = w(\gamma^{-1}\cdot\mathbf{r},\gamma^{-1}\cdot\mathbf{r}') = w(\mathbf{r},\mathbf{r}')$$

for all $\gamma \in \mathbf{E}(2)$. The Euclidean group is composed of the (semi-direct) product of $\mathbf{O}(2)$, the group of planar rotations $\mathbf{r} \to R_\varphi \mathbf{r}$ and reflections $(x,y) \to (x,-y)$, with $\mathbb{R}^2$, the group of planar translations $\mathbf{r} \to \mathbf{r}+\mathbf{s}$. Here

$$R_\varphi = \begin{pmatrix} \cos\varphi & -\sin\varphi \\ \sin\varphi & \cos\varphi \end{pmatrix}, \quad \varphi \in [0,2\pi). \tag{8.43}$$

However, one of the immediate implications of the existence of regularly repeating feature maps and patchy horizontal (or feedback) connections (Sect. 8.1.1) is that one can no longer treat the weight distribution w in the neural field equation (8.42) as Euclidean invariant. That is, one has to consider a more general weight distribution of the form

$$w(\mathbf{r},\mathbf{r}') = w(|\mathbf{r}-\mathbf{r}'|) + \rho w^{\Delta}(\mathscr{F}(\mathbf{r}),\mathscr{F}(\mathbf{r}')), \tag{8.44}$$

where $\mathscr{F}(\mathbf{r})$ denotes a cortical feature map, w^{Δ} represents the dependence of excitatory horizontal connections on the feature preferences of the presynaptic and postsynaptic neuron populations, and ρ is a positive coupling parameter. The local connections span a single hypercolumn, whereas the patchy horizontal connections link cells with similar feature preferences in distinct hypercolumns.

In the absence of long-range connections ($\rho = 0$), the resulting weight distribution is invariant under the action of the Euclidean group. However, the long-range connections break Euclidean symmetry due to correlations with the feature map $\mathscr{F}(\mathbf{r})$. A certain degree of symmetry still remains under the approximation that the feature map is periodic. For example, Fig. 8.2b suggests partitioning V1 into a set of hypercolumns organized around a lattice of orientation pinwheels. Therefore, suppose we treat the distribution of pinwheels as a regular planar lattice L. The resulting weight distribution for $\rho \neq 0$ is then doubly periodic with respect to L:

$$w(\mathbf{r}+\ell,\mathbf{r}'+\ell) = w(\mathbf{r},\mathbf{r}') \tag{8.45}$$

for all $\ell \in L$. Additional symmetries may also exist depending on the particular form of w^{Δ}. There are number of distinct ways in which w^{Δ} may depend on the underlying feature map $\mathscr{F}$. The first reflects the "patchiness" of the horizontal connections that link cells with similar feature preferences. In the case of a periodic feature map, this may be implemented by taking [65, 66, 526]

$$w^{\Delta}(\mathscr{F}(\mathbf{r}),\mathscr{F}(\mathbf{r}')) = \sum_{\ell\in\mathscr{L}} J_{\ell}\Delta(\mathbf{r}-\mathbf{r}'-\ell), \tag{8.46}$$

where $\Delta(\mathbf{r})$ is some localized unimodal function that is maximal when $\mathbf{r} = 0$, thus ensuring that presynaptic and postsynaptic cells with similar feature preferences are connected. The width of Δ determines the size of the patches and $J_{\ell}, \ell \neq 0$ is a monotonically decreasing function of ℓ. In this particular example, the patchy horizontal connections break continuous rotation symmetry down to the discrete rotation symmetry of the lattice. On the other hand, continuous translation symmetry (homogeneity) still holds, since w^{Δ} only depends on the relative separation $\mathbf{r}-\mathbf{r}'$ in cortex.

However, if the anisotropy of horizontal connections is taken into account (Fig. 8.3), then continuous translation symmetry is broken as well. That is, the direction of anisotropy is correlated with the orientation preference map and thus rotates periodically across cortex [56]. Anisotropy can be incorporated into the model by modifying the weight distribution w^{Δ} along the following lines [75, 79]:

$$w^{\Delta}(\mathscr{F}(\mathbf{r}),\mathscr{F}(\mathbf{r}')) = \sum_{\ell\in\mathscr{L}} J_{\ell}\mathscr{A}_{\mathscr{F}(\mathbf{r}')}(\ell)\Delta(\mathbf{r}-\mathbf{r}'-\ell), \tag{8.47}$$

with

$$\mathscr{A}_{\mathscr{F}(\mathbf{r})}(\ell) = \frac{1}{4\eta(\mathbf{r})}\left(H[\eta(\mathbf{r}) - |\arg\ell - \theta(\mathbf{r})|] + H[\eta(\mathbf{r}) - |\arg\ell - \theta(\mathbf{r}) - \pi|]\right), \tag{8.48}$$

where $\theta(\mathbf{r})$ denotes the orientation preference map. The second term takes account of the fact that $\theta \in [0,\pi)$ whereas $\arg\ell \in [0,2\pi)$. The parameter $\eta(\mathbf{r})$ determines the degree of anisotropy, that is, the angular spread of the horizontal connections around the axis joining cells with similar orientation preferences. The degree of anisotropy is also likely to depend on position $\mathbf{r}$ relative to pinwheels, since populations of

cells around pinwheels have zero average orientation preference so that one expects the corresponding distribution of weights to be isotropic, in contrast to cells in the linear zones of the orientation preference map; see Fig. 8.2. In conclusion, at the submillimeter length scale, there is an approximately periodic modulation of the synaptic connections that can lead to a periodically varying heterogeneous medium. We have already explored one implication of this in a simpler 1D model of traveling waves in a heterogeneous neural field (see Sect. 7.3), namely, that it can cause wave propagation failure [79, 132, 332]. Another consequence of such an inhomogeneity is that it can lead to the pinning of a spatially periodic pattern to the underlying lattice of pinwheels [65, 66].

8.4.2 Coupled Hypercolumn Model

Treating the distribution of pinwheels as a regular lattice does not take into account the considerable degree of disorder in the distribution of feature preferences across cortex. One way to avoid such complexity is to collapse each hypercolumn into a single point (through some form of spatial coarse graining) and to treat V1 as a continuum of hypercolumns [78, 79]. Thus cortical position $\mathbf{r}$ is replaced by the pair $\{\mathbf{r}, \mathscr{F}\}$ with $\mathbf{r} \in \mathbb{R}^2$ now labeling the hypercolumn at (coarse-grained) position $\mathbf{r}$ and $\mathscr{F}$ labeling the feature preferences of neurons within the hypercolumn. Let $u(\mathbf{r}, \mathscr{F}, t)$ denote the activity of a neuronal population at $(\mathbf{r}, \mathscr{F})$, and suppose that u evolves according to the neural field equation

$$\frac{\partial u(\mathbf{r}, \mathscr{F}, t)}{\partial t} = -u(\mathbf{r}, \mathscr{F}, t) + \int_{\mathbb{R}^2} \int w(\mathbf{r}, \mathscr{F} | \mathbf{r}', \mathscr{F}') F(u(\mathbf{r}', \mathscr{F}', t)) D\mathscr{F}' d\mathbf{r}', \tag{8.49}$$

with $D\mathscr{F}'$ an appropriately defined measure on feature space. We decompose w into local and long-range parts by assuming that the local connections mediate interactions within a hypercolumn, whereas the patchy horizontal connections mediate interactions between hypercolumns:

$$w(\mathbf{r}, \mathscr{F} | \mathbf{r}', \mathscr{F}') = \delta(\mathbf{r} - \mathbf{r}') w(\mathscr{F}, \mathscr{F}') + \rho J(|\mathbf{r} - \mathbf{r}'|) \mathscr{A}_{\mathscr{F}'}(\mathbf{r} - \mathbf{r}') w^{\Delta}(\mathscr{F}, \mathscr{F}'), \tag{8.50}$$

where $w(\mathscr{F}, \mathscr{F}')$ and $w^{\Delta}(\mathscr{F}, \mathscr{F}')$ represent the dependence of the local and long-range interactions on the feature preferences of the pre- and postsynaptic cell populations, and $J(\mathbf{r})$ with $J(0) = 0$ is a positive function that determines the variation in the strength of the long-range interactions with cortical distance. We have also included the anisotropy factor $\mathscr{A}_{\mathscr{F}}$ of (8.48). The advantage of collapsing each hypercolumn to a single point in the cortical plane is that a simpler representation of the internal structure of a hypercolumn can be developed that captures the essential tuning properties of the cells as well as incorporating the modulatory effects of long-range connections.

For the sake of illustration, suppose that we identify $\mathscr{F}$ in (8.49) and (8.50) with the orientation preference $\theta \in [0,\pi)$ of cells within a hypercolumn. The weight distribution (8.50) is taken to have the form [79]

$$\begin{aligned} w(\mathbf{r},\theta|\mathbf{r}',\theta') &= \delta(\mathbf{r}-\mathbf{r}')w(\theta-\theta') \\ &\quad +\rho J(|\mathbf{r}-\mathbf{r}'|)\mathscr{P}(\arg(\mathbf{r}-\mathbf{r}')-\theta)w^{\Delta}(\theta-\theta') \end{aligned} \tag{8.51}$$

with

$$\mathscr{P}(\psi) = \frac{1}{4\eta}[H(\eta-|\psi|)+H(\eta-|\psi-\pi)|]. \tag{8.52}$$

(Note that the direction $\arg(\mathbf{r}-\mathbf{r}')$ can be taken to be correlated with either θ or θ', since w^{Δ} is a sharply peaked function.) The functions $w(\theta)$ and $w^{\Delta}(\theta)$ are assumed to be even, π-periodic functions of θ, with corresponding Fourier expansions

$$\begin{aligned} w(\theta) &= w_0 + 2\sum_{n\geq 1} w_n \cos 2n\theta \\ w^{\Delta}(\theta) &= w_0^{\Delta} + 2\sum_{n\geq 1} w_n^{\Delta} \cos 2n\theta. \end{aligned} \tag{8.53}$$

The distribution $w^{\Delta}(\theta)$ is taken to be a positive, narrowly tuned distribution with $w^{\Delta}(\theta)=0$ for all $|\theta|>\theta_c$ and $\theta_c \ll \pi/2$; the long-range connections thus link cells with similar orientation preferences. Equation (8.49) then describes a continuum of coupled ring networks, each of which corresponds to a version of the so-called ring model of orientation tuning [34, 74, 595]. If there is no orientation-dependent anisotropy, then the weight distribution (8.51) is invariant with respect to the symmetry group $\mathbf{E}(2)\times\mathbf{O}(2)$ where $\mathbf{O}(2)$ is the group of rotations and reflections on the ring S^1 and $\mathbf{E}(2)$ is the Euclidean group acting on $\mathbb{R}^2$. The associated group action is

$$\begin{aligned} \zeta\cdot(\mathbf{r},\theta) &= (\zeta\mathbf{r},\theta), \qquad \zeta\in\mathbf{E}(2) \\ \xi\cdot(\mathbf{r},\theta) &= (\mathbf{r},\theta+\xi) \\ \kappa\cdot(\mathbf{r},\theta) &= (\mathbf{r},-\theta). \end{aligned} \tag{8.54}$$

Invariance of the weight distribution can be expressed as

$$\gamma\cdot w(\mathbf{r},\theta|\mathbf{r}',\theta) = w(\gamma^{-1}\cdot(\mathbf{r},\theta)|\gamma^{-1}\cdot(\mathbf{r}',\theta')) = w(\mathbf{r},\theta|\mathbf{r}',\theta')$$

for all $\gamma\in\Gamma$ where $\Gamma=\mathbf{E}(2)\times\mathbf{O}(2)$. Anisotropy reduces the symmetry group Γ to $\mathbf{E}(2)$ with the following *shift–twist* action on $\mathbb{R}^2\times S^1$ [64, 78]:

$$\begin{aligned} \mathbf{s}\cdot(\mathbf{r},\theta) &= (\mathbf{r}+\mathbf{s},\theta) \\ \xi\cdot(\mathbf{r},\theta) &= (R_\xi\mathbf{r},\theta+\xi) \\ \kappa\cdot(\mathbf{r},\theta) &= (R_\kappa\mathbf{r},-\theta), \end{aligned} \tag{8.55}$$

where R_ξ denotes the planar rotation through an angle ξ and R_κ denotes the reflection $(x_1,x_2)\mapsto(x_1,-x_2)$. It can be seen that the discrete rotation operation comprises

a translation or *shift* of the orientation preference label θ to $\theta + \xi$, together with a rotation or *twist* of the position vector $\mathbf{r}$ by the angle ξ. The fact that the weight distribution is invariant with respect to this shift–twist action has important consequences for the global dynamics of V1 in the presence of anisotropic horizontal connections [79].

Finally, one can write down a 2D neural field model for binocular rivalry waves based on a continuum of coupled hypercolumns for left- and right-eye preferences. Ignoring the effects of anisotropy and taking an adiabatic approximation for the depression variables, such a model takes the form

$$\begin{aligned}\frac{\partial u}{\partial t} &= -u(\mathbf{r},\theta,t) + \int_0^{2\pi} w(\theta-\theta')F(u(\mathbf{r},\theta',t)d\theta' \\ &\quad + Q_u \int_{-\infty}^{\infty} J_e(|\mathbf{r}-\mathbf{r}'|)F(u(\mathbf{r}',\theta,t)d\mathbf{r}' - Q_v \int_{-\infty}^{\infty} J_i(|\mathbf{r}-\mathbf{r}'|)F(v(\mathbf{r}',\theta,t)d\mathbf{r}'\end{aligned}$$

$$\begin{aligned}\frac{\partial v}{\partial t} &= -v(\mathbf{r},\theta,t) + \int_0^{2\pi} w(\theta-\theta')F(v(\mathbf{r},\theta',t)d\theta' \\ &\quad + Q_v \int_{-\infty}^{\infty} J_e(|\mathbf{r}-\mathbf{r}'|)F(v(\mathbf{r}',\theta,t)d\mathbf{r}' - Q_u \int_{-\infty}^{\infty} J_i(|\mathbf{r}-\mathbf{r}'|)F(u(\mathbf{r}',\theta,t)d\mathbf{r}'.\end{aligned}$$

An interesting issue is then how to define a traveling wave solution for such a model that combines orientation tuning within a hypercolumn due to the effects of the local weight distribution w with a variation of activity across hypercolumns in the form of a traveling front.

Part III
Development and Disease

Chapter 9
Waves in the Developing and the Diseased Brain

In this final chapter we discuss various wave phenomena in the developing and diseased brain. We begin by describing two examples of intercellular developmental waves: Ca^{2+} waves in radial glial cells, which coordinate cell division and cell migration during early development, and spontaneous retinal waves, which are thought to contribute to the activity-dependent development of circuits in visual cortex. We then consider the possible role of traveling waves in the maturation of neurons from sphere-like cells to polarized cells consisting of a single axon and several shorter dendrites. In particular, we consider some new wave phenomena including wave-pinning and cytoskeletal actin waves. Switching to the case of pathological waves in the diseased brain, we focus on two examples: cortical spreading depression, which is often associated with migraine auras, and epilepsy. In the former case, we review reaction–diffusion models of spreading depression that track changes in the concentration of extracellular ions such as K^+, and show how kinematic wave theory can be used to model the progression of a migraine aura across the visual field. It is also necessary to determine the effective diffusion of ions in the extracellular space, which can be carried out using the theory of porous media, for example. Epilepsy is a vast field in its own right, so we will focus on how changes in network structure can result in abnormal cortical states such as seizure-like activity or population bursting. We also consider recent work on characterizing normal and abnormal brain states according to how close the cortex is to a critical state. This leads to another approach to studying the propagation of activity in cortex, based on the theory of branching processes. We finish by discussing the spread of protein aggregates in neurodegenerative diseases such as Alzheimer's disease, Parkinson's disease, and Huntington's disease. There is growing experimental evidence that such spread has parallels with the neuropathogenesis of prion diseases, in which the infected agent is a misfolded protein aggregate.

P.C. Bressloff, *Waves in Neural Media: From Single Neurons to Neural Fields*,
Lecture Notes on Mathematical Modelling in the Life Sciences,
DOI 10.1007/978-1-4614-8866-8_9,

9.1 Intercellular Waves in Neural Development

9.1.1 Calcium Waves in Early Development

There is growing experimental evidence that intercellular Ca^{2+} waves play an important role in early neural development [146, 368, 498, 666, 697]. In order to describe such findings, it is first necessary to give a short overview of the early stages of development. During embryogenesis a strip of specialized cells called the *notochord* induces epithelial cells of the *ectoderm* directly above it to transform into the primitive nervous system known as the *neuroepithelium*; see Fig. 9.1. The latter then wrinkles and folds over to form a hollow tube (the *neural tube*), which is the precursor of the brain and spinal cord. Meanwhile, the ectoderm and endoderm continue to curve around and fuse beneath the embryo to create the body cavity, completing the transformation of the embryo from a flattened disk to a three-dimensional body. Cells originating from the fused tips of the neuroectoderm (*neural crest cells*) migrate to various locations throughout the embryo, where they initiate the development of the peripheral nervous system including the retina. As neurogenesis

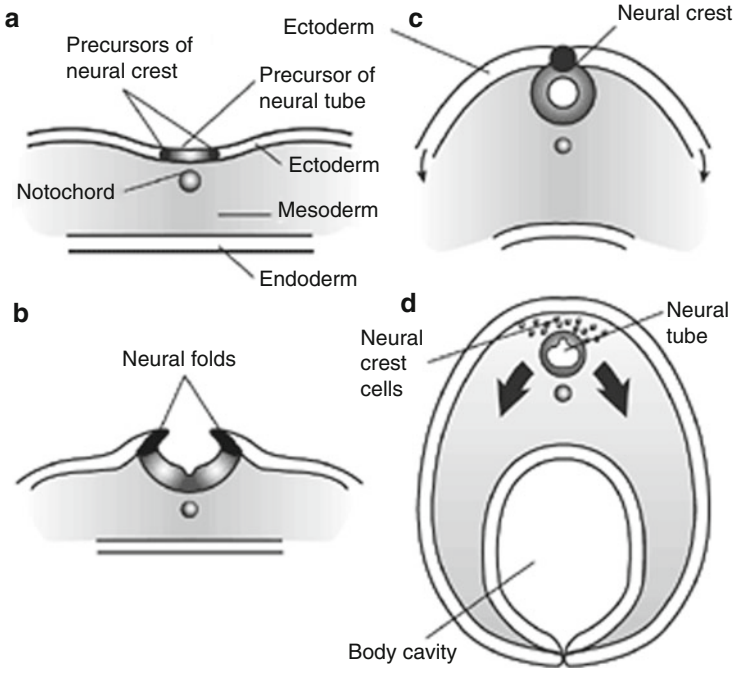

Fig. 9.1 Formation of the neural tube (cross view). See text for details. (**a**) Induction of neuroepithelium. (**b**, **c**) Folding of the neuroepithelium to form the neural tube. (**d**) Formation of 3D body structure and migration of neural crest cells [Reproduced from Wikimedia Commons (public domain)]

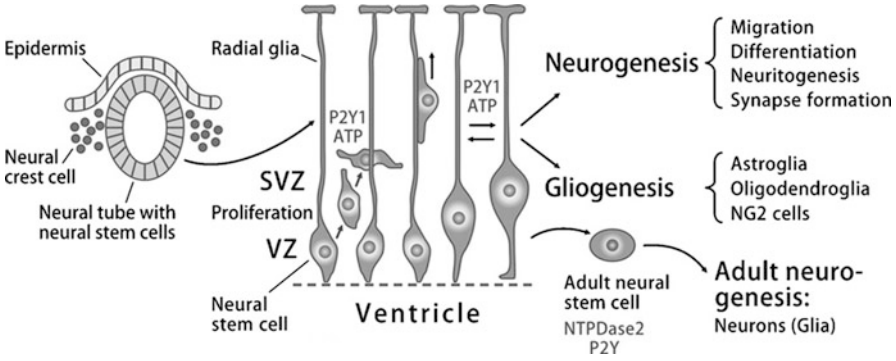

Fig. 9.2 Transformation of neuroepithelial cells in the neural tube into radial glial cells, which are the progenitors of neurons and glial cells. Their radial projections also guide cell migration from the ventricular zone (*VZ*) or inner surface of the neural tube to the outer surface. Cortical cells are also produced in the subventricular zone (*SVZ*). During early neurogenesis, intercellular ATP signaling is essential for the migration of SVZ progenitors from the VZ to the SVZ. During late neurogenesis, ATP released from cortical radial glia mediates Ca^{2+} waves that are essential for VZ proliferation (Adapted from [697])

proceeds, neuroepithelial cells of the neural tube transform into *radial glial cells*, also known as progenitor cells, which ultimately give rise to neurons and glial cells; see Fig. 9.2 and [514]. The cell body of radial glial cells is found in the *ventricular zone* (VZ), or inner surface of the neural tube, and has a radial extension that projects near the border of the marginal zone, or outer surface. After asymmetrical division, their daughter cells migrate along the radial projections and differentiate into neurons. At the onset of cortical neurogenesis, a second proliferating population of progenitor cells appears in a new layer known as the subventricular zone (SVZ), which generates both neurons and glial cells. Finally, towards the end of cortical neurogenesis, radial glial cells retract their extensions to become astrocytes. In summary, radial glial cells function as stem cells for neurogenesis and as scaffolding that guides the migration of neurons out of the ventricular zone. Moreover, the process of radial migration occurs in an "inside-out manner." In other words, cells that arrive the earliest (the oldest ones) form the deepest layer of the cortex, whereas the late-arriving (the youngest) neurons form the outermost layer.

An experimental study of embryonic rat cortical slices provides strong evidence that ATP-mediated calcium waves, which propagate between radial glial cells in the ventricular zone, are involved in the modulation of cell proliferation [666]. The predominant mechanism for the intracellular Ca^{2+} waves appears to be paracrine signaling, in which gliotransmission leads to the release of ATP via gap hemichannels, which diffuses and binds to metabotropic P2Y receptors. This activates a G-protein-mediated IP_3 signaling pathway, which leads to an increase in intracellular Ca^{2+}; see Sect. 4.5. As suggested in [666], one possible function of ATP-mediated Ca^{2+} waves during neurogenesis is that it could coordinate the cell cycle. Recall that the cell cycle consists of four distinct phases or stages G1–S–G2–M; see Fig. 9.3. Here G1 and G2 are *gap* phases, while S is the *synthesis* stage where DNA replication

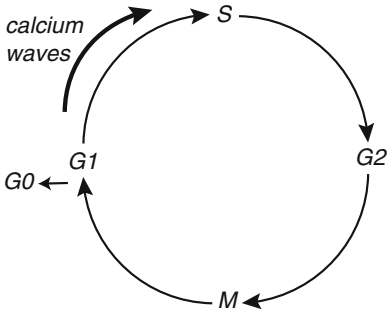

Fig. 9.3 Phases of the cell cycle: mitosis (*M*), Gap1 (*G1*), Gap2 (*G2*), and synthesis (*S*). *G0* represents the quiescent phase where cells exit the cell cycle either temporarily or permanently. Calcium waves can coordinate cells to enter the S phase

occurs. The M phase consists of two tightly coupled processes: *mitosis*, in which the cell's chromosomes are divided into two, and *cytokinesis*, in which the cell's cytoplasm divides in half forming distinct cells. Activation of each phase is dependent on the proper progression and completion of the previous one. Cells that have temporarily or reversibly stopped dividing are said to have entered a state of quiescence called the G0 phase. It is known that increases in intracellular Ca^{2+} are required for a cell to enter the S and M phases [42]. For example, during the G1 phase Ca^{2+} may drive a cell to reenter the S phase rather than exit the cell cycle. Experimentally blocking intercellular Ca^{2+} waves in the ventricular zone using ATP receptor antagonists appears to decrease cell proliferation without blocking Ca^{2+} elevations in individual cells [666]. Hence, one function of the intercellular waves could be to generate Ca^{2+} increases that help a nearby cluster of cells to enter the S phase in a coordinated manner. This hypothesis is also supported by the experimental observation that ventricular zone waves appear to be triggered by cells in the S phase [666]. In addition to S phase coordination, it is possible that intercellular Ca^{2+} waves also regulate differential gene expression [246], as suggested by the observation that the frequency of Ca^{2+} waves increases as neurogenesis proceeds.

Intercellular Ca^{2+} waves are also found in early developmental stages of structures in the peripheral nervous system such as the retina [146, 498, 499]. The developing retina is a layered structure whose outermost layer, the *retinal pigment epithelium* (RPE), is essential for the development of the underlying neural layers. The layer closest to the RPE is called the ventricular zone where, similar to the developing cortex, progenitor cells divide and differentiate to form the neurons and glia of the fully developed retina. ATP-mediated Ca^{2+} waves propagate in the RPE, possibly triggered by a single epithelial cell, and arise via the same paracrine signaling mechanism as Ca^{2+} waves in developing cortex; see Fig. 9.4. Diffusing ATP molecules released from the RPE also bind to P2Y receptors on the progenitor cells within the ventricular zone, which enhances cell proliferation and speeds up mitosis. It also appears that ATP from the RPE, possibly in combination with the action of neurotransmitters from differentiated neurons, can induce

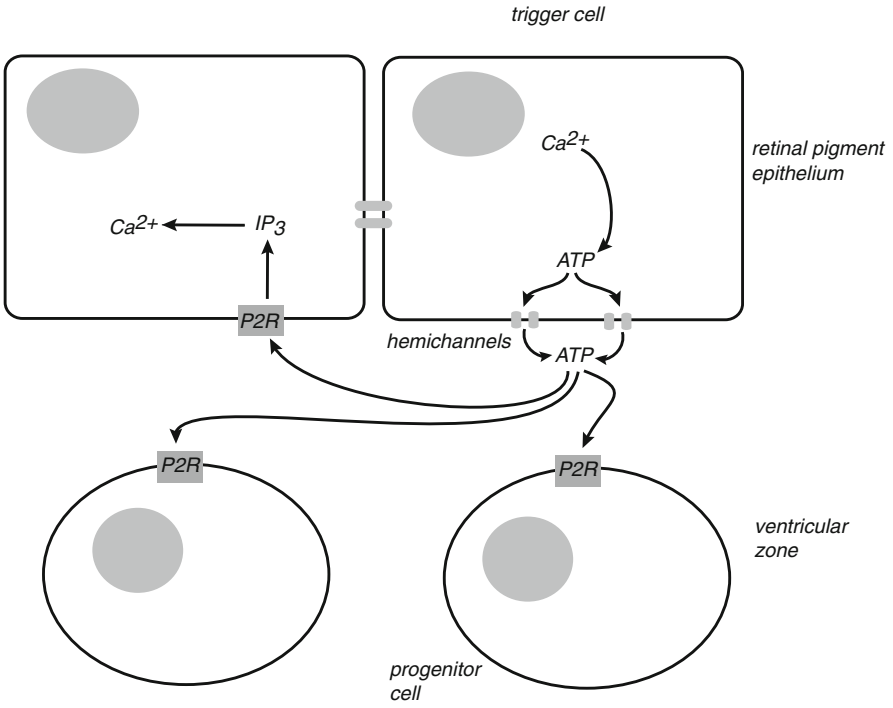

Fig. 9.4 ATP-mediated Ca^{2+} wave in radial pigment epithelium. ATP released from hemichannels diffuses and binds to metabotropic receptors (P2Rs) in neighboring epithelial cells leading to the release of intracellular Ca^{2+} from internal stores. The ATP also binds to P2Rs of progenitor cells in the ventricular zone, thus promoting cell proliferation

Ca^{2+} waves in the ventricular zone [498, 614]. The propagation of ventricular Ca^{2+} waves, which is probably mediated by gap-junction coupling between progenitors rather than paracrine signaling, can also modulate cell proliferation within a cluster of progenitor cells.

9.1.2 Retinal Waves in Later Development

The fully developed retina located at the back of the eye converts patterns of light activity from a visual image into neural spiking activity. The first stage is the conversion of light into graded neural activity by photoreceptors. Such activity is then modulated by both vertical and horizontal neuronal pathways via synaptic and gap-junction coupling, before reaching the *retinal ganglion cells* (RGCs). These form the output layer of the retina, which transmits the resulting pattern of spiking activity along the optic nerve to the brain; see also Sect. 8.1.1. Following the very early stages of development discussed at the end of the previous section, but before photoreceptors are visually responsive, the retina has already formed a layered

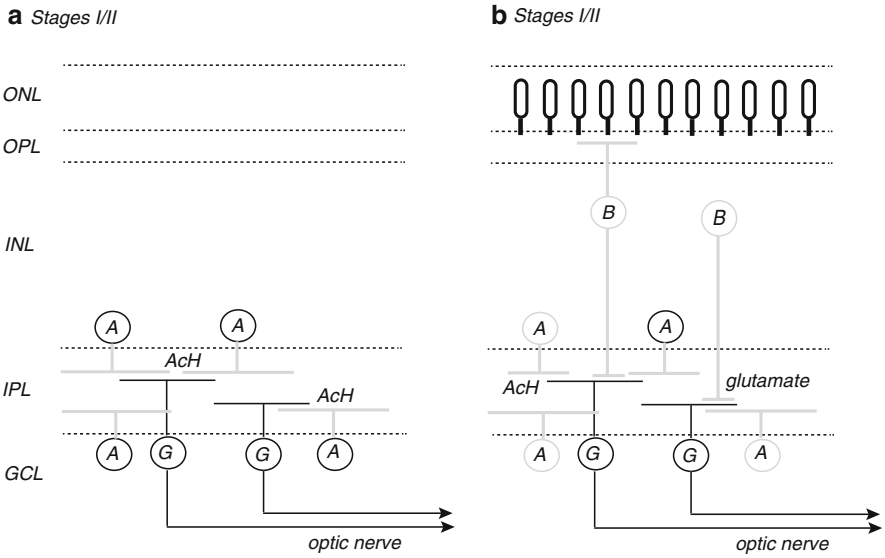

Fig. 9.5 Simplified schematic of neural circuits that mediate retinal waves during (**a**) stages I/II and (**b**) stage III. The retina is partitioned into three main layers: outer nuclear layer (*ONL*), inner nuclear layer (*INL*), and ganglion cell layer (*GCL*). There are also two layers of interconnecting processes: inner plexiform layer (*IPL*) and outer plexiform layer (*OPL*). During stages I/II, spontaneous retinal waves between retinal ganglion cells (*G*) are driven mainly by the interactions between ganglion cells and cholinergic amacrine cells (*A*). In stage III, waves are predominantly driven by glutamatergic bipolar cells (*B*), which are connected to photoreceptors in the ONL

structure with distinct classes of differentiated neurons, including RGCs. Although the RGCs are not yet driven by visual stimuli, they are far from silent, firing spontaneous bursts of action potentials that travel across the retinal surface as retinal waves; see the reviews [190, 222, 682]. Interestingly, such spontaneous rhythmic activity occurs in many other developing neural circuits [49, 471], including the cochlea [633], spinal cord [260, 472], cerebellum [661], hippocampus [32], and cortex [326]. There is growing evidence that the resulting spontaneous depolarizations, and corresponding increases in intracellular Ca^{2+} (via voltage-gated ion channels rather than release from intracellular stores), play an important role in driving many aspects of development, including axon guidance, cell differentiation, local circuit formation, and the emergence of sensory maps. These phenomena have been extensively studied in the retina, where upregulating or blocking retinal waves has a major affect on the development of visual circuits [190, 315, 416, 682] and has led to the suggestion that retinal waves are crucial for the normal development of the retinotopic map and the segregation of eye dominance in the cortex. However, their precise role still remains controversial. We briefly summarize some of the main properties of retinal waves at various stages of development and describe a number of theoretical models; see also [222].

Retinal waves can initiate at any retinal location due to spontaneous activation of a local cluster of cells and form non-repeating propagation boundaries that are determined, in part, by refractory effects. The waves can be categorized into three distinct developmental stages [615]. During stages I and II, the retina has only a few functional cell types and the waves arise via a coupled network of RGCs and *amacrine cells* forming the inner retina; see Fig. 9.5a. Stage I waves are mediated by the neuromodulator adenosine and by gap junctions, since very few synapses have formed. Stage II waves first appear at the onset of synaptogenesis and are primarily mediated by the neurotransmitter *acetylcholine*; they have a characteristic refractory period so that following passage of a retinal wave over a section of retina, another wave can only propagate across the same section after tens of seconds have elapsed. Stage I waves tend to be faster and occur more frequently than stage II waves. The transition to stage III occurs when vertical *bipolar cells* form synaptic connections with RGCs and the neurotransmitter glutamate becomes involved in mediating retinal waves; see Fig. 9.5b. Although acetylcholine continues to be involved as well, the nicotinic receptors found in stage II are replaced by muscarinic receptors. One finds that stage III waves are comparable in speed to stage II waves, but are smaller and less frequent. In certain species (e.g., the mouse), the retina first becomes sensitive to light near the onset of stage III, whereas in other species (e.g., the rabbit) light sensitivity occurs later. Spontaneous retinal waves generally disappear after eye opening, although in the turtle they can persist in diminished form for several weeks. Finally, retinal waves tend to have speeds in the range 100–300 μm/s, which are much slower than waves found in disinhibited cortical slices, for example; see Chap. 7. On the other hand, the speeds are much faster than processes based on the extracellular diffusion of signaling molecules.

Most computational studies of retinal waves have focused on developmental stage II and are based on networks of cholinergically coupled amacrine cells. The first such model also included a layer of RGCs that acted as a low-pass filter of the spontaneous activity generated in the amacrine layer [94]. The basic mechanism of the model was that amacrine cells would spontaneously depolarize and excite neighboring cells, after which they would enter a refractory state of fixed duration. A propagating wave was initiated whenever a sufficiently large local cluster of amacrine cells spontaneously became active and the surrounding medium contained a sufficient number of non-refractory cells. In spite of the model's simplicity, containing only two free parameters (an activation threshold and the probability of spontaneous activation), it could generate patterns of non-repeating waves that were statistically similar to experimental data. However, the model was not robust to changes in parameters, that is, it had to be finely tuned. An alternative model of retinal waves was proposed by Godfrey and Swindale [223], who took the refractory period of amacrine cells to be activity dependent. This provided a more robust model and did not require an RGC layer to generate biologically plausible waves. A more biophysically detailed model of the roles of cholinergic coupling, noise, and refractory period in the generation of retinal waves in amacrine circuits has subsequently been developed by Hennig et al. [271]. An individual amacrine cell is now described in terms of a conductance-based model, which consists of a voltage-gated Ca^{2+} current that supports spontaneous bursting, and a slow after-hyperpolarization

(AHP) current that prevents further bursting. Moreover, the duration of the AHP current is taken to increase with the level of depolarization. Thus, during passage of a wave, strong synaptic coupling between adjacent amacrine cells generates a stronger depolarization than intrinsic bursts in an isolated cell, which in turn causes a longer-lasting refractory period due to AHP currents. Thus, the effective network connectedness is dynamically regulated in such a way that the network can operate close to a percolation threshold, which means that the distribution of propagation events (frequency and duration) exhibits power-law behavior consistent with some experimental observations [271]; see also Sect. 9.5.

9.2 Traveling Waves, the Cytoskeleton, and Cell Polarization

9.2.1 Neuronal Polarization and the Cytoskeleton

Cell polarization refers to the breaking of cell symmetry and is an essential process in various cell types, including migration of fibroblasts during wound healing, asymmetric cell growth or division, and the functional maturation of neurons. Neurons are among the most polarized cells due to their compartmentalization into a thin, long axon and several shorter, tapered dendrites (Sect. 1.1). Experimental studies of neuronal polarization have mainly been performed on dissociated, embryonic cortical and hippocampal neurons or on postnatal cerebellar granule neurons. Such studies have identified three basic stages of polarization [13, 452, 509, 581]; see Fig. 9.6. Cultured neurons initially attach to their substrate as round spheres

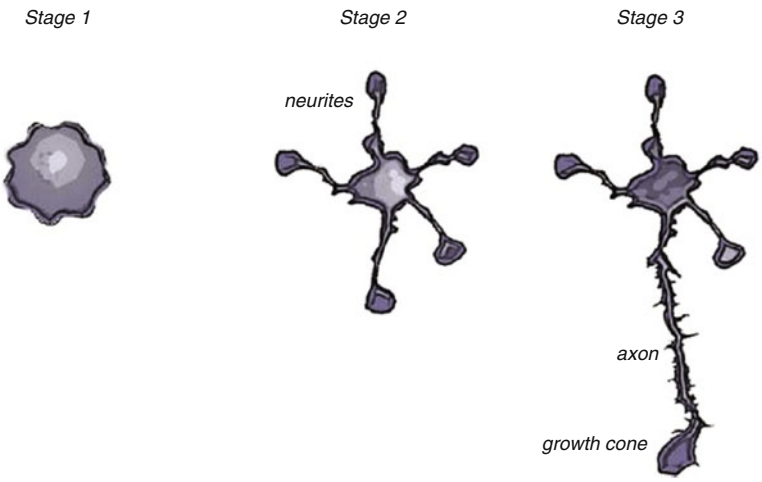

Fig. 9.6 Stages of neuronal polarization. A neuron attaches to the substrate as a round sphere surrounded by actin-rich lamellipodia and filopodia (stage 1). Growth cones formation by the consolidation of lamellipodia leads to the establishment of several neurites (stage 2). One neurite starts to elongate rapidly and forms the axon (stage 3)

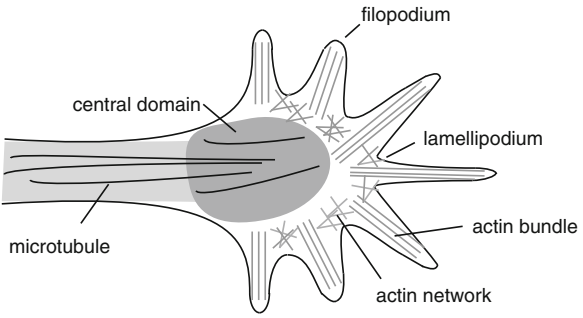

Fig. 9.7 Schematic diagram of growth cone showing cytoskeletal structures

surrounded by actin-rich structures such as *lamellipodia* (mesh-like actin sheets) and *filopodia* (packed actin bundles) (stage 1). Lamellipodia then coalesce to form *growth cones*, followed by the establishment of several short processes, called *neurites* (stage 2). Eventually one of the neurites starts to grow more rapidly to become the axon (stage 3), while the other neurites remain short and develop into dendrites at later stages of maturation. During the development of a neuron, the cytoskeleton plays a fundamental role (as does intracellular transport [289]). Since neurite formation is a key event in neuronal polarization, it is instructive to describe the role of the cytoskeleton during the elongation of neurites.

The growth cone at the mobile tip of an elongating neurite or axon contains microtubules within a central domain (C-domain) and actin filaments within the peripheral domain (P-domain); see Fig. 9.7. The microtubules provide the structural backbone of the shaft and a substrate for intracellular transport to the growth cone. They polymerize with their growing ends pointed towards the leading edge of the growth cone. Actin filaments within the P-domain form filopodia and lamellipodia that shape and direct the motility of the growth cone. In both structures, the actin filaments face with their barbed (growing) ends towards the plasma membrane. Polymerization of actin filaments towards the leading edge causes the extension and protrusion of the growth cone. This creates a force that pushes the actin network and the tightly linked plasma membrane backwards (retrograde flow) and hinders the invasion of the microtubules into the P-domain. The retrograde flow is also enhanced by the action of myosin molecular motors, which drag the actin cytoskeleton back towards the C-domain where actin filaments depolymerize at their pointed ends. If there is a balance between actin polymerization in the P-domain and retrograde flow, then there is no elongation. However, signals from surface adhesion receptors bound to a substrate can suppress the retrograde flow of actin filaments, shifting the balance towards polymerization-driven forward motion that involves both actin filaments and microtubules. (This signaling mechanism can in turn be modulated by external chemoattractant cues during axon guidance [394, 470].) The growth of a neurite proceeds in three stages [225, 432]. First, enhanced polymerization in the P-domain pushes the growth cone forward (protrusion phase). Second, an actin-free

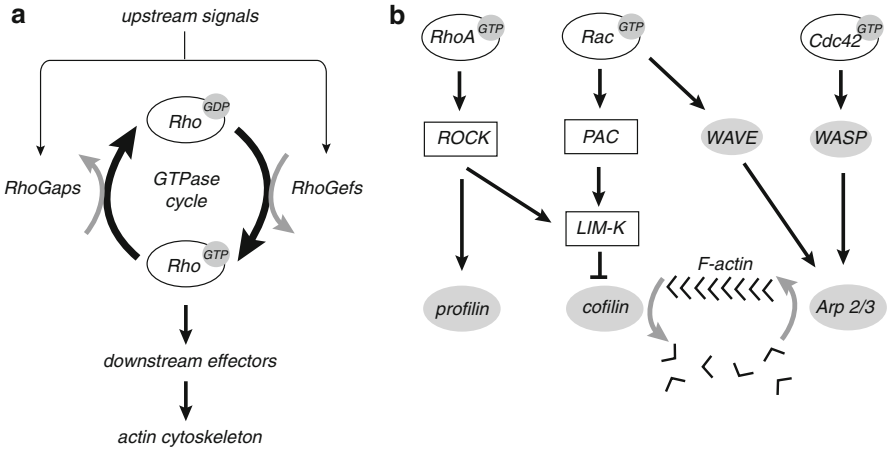

Fig. 9.8 (**a**) The Rho GTPase cycle. (**b**) Simplified signaling pathways from GTPases RhoA, Rac, and Cdc42 to actin accessory proteins cofilin and Arp 2/3 that regulate actin polymerization in the growth cone (Redrawn from Luo [394])

zone is created by a combination of cytoskeletal restructuring and actin disassembly so that the retrograde flow no longer hinders the advancement of microtubules into this zone (engorgement phase). Third, vesicles and organelles enter the newly created zone via intracellular transport, resulting in an elongation of the neurite shaft (consolidation phase).

One class of signaling molecule that appears to play an important role in the polarization and migration of many different cell types is *Rho GTPases* [235, 254]. These act as intracellular molecular switches that cycle between an active GTP-bound form and an inactive GDP-bound form; see Fig. 9.8a. Guanine nucleotide exchange factors (RhoGEFs) facilitate the conversion from GDP-bound to GTP-bound form, whereas GTPase-activating proteins (RhoGAPs) enhance GTP hydrolysis and are thus negative regulators. RhoGEFs and RhoGAPs are both regulated by upstream signals. A major downstream target of the Rho GTPase signaling pathways is the actin cytoskeleton within the growth cone [254, 394, 452]. (There is growing evidence that the GTPases also regulate microtubules [13], although we will not discuss this here.) A variety of actin accessory proteins mediate the different components of actin dynamics within the growth cone and can be activated by the various signaling pathways associated with neuronal polarization. We describe a few of the major players; see [452, 483] for more details.

First, the *actin-related proteins 2 and 3* (Arp2/3) *complex* stimulates actin polymerization by creating new nucleation cores. The Arp2/3 complex is activated by members of the *Wiskott–Aldrich syndrome protein* (WASP) family protein (WAVE) complex, which localizes to lamellipodia where it facilitates actin polymerization. The WAVE complex is activated by the small GTPase *Rac1*, which modulates the actin cytoskeleton dynamics by controlling the formation of lamellipodia. Filopodia formation, on the other hand, is regulated by another member of the small GTPases, called *Cdc42*. A second important accessory protein is *cofilin*, a member of the

actin-depolymerizing factor (ADF)/cofilin family, which modifies actin dynamics by increased severing and depolymerization of actin filaments via its binding to the non-barbed (pointed) ends. Cofilin is inhibited when phosphorylated by LIM-kinase, which is itself activated by Pak-kinase. Since the latter is a downstream target of Rac1 and Cdc42, it follows that Rac1 and Cdc42 inhibit actin depolymerization by downregulating cofilin. At first sight, one would expect the reduction of cofilin to counter the affects of Arp2/3. However, the extent to which cofilin enhances or reduces cell protrusion depends on the spatial and temporal scale over which it operates [150]. It turns out that the overall effect of Rac1 and Cdc42 is to increase actin dynamics thus promoting neurite growth. This is opposed by the action of a third type of GTPase known as *RhoA*, which tends to stabilize the actin network by activating ROCK-kinase, which promotes *profilin* (an actin-binding protein that catalyzes polymerization) and suppresses cofilin. A summary of the basic signaling pathways is given in Fig. 9.8b.

9.2.2 Wave-Pinning and Cell Polarity in a Bistable Reaction–Diffusion Model

We now turn to a reaction–diffusion model of cell polarity developed and analyzed by Keshet et al. [305, 438, 439]; see also [478, 482]. Although the model was originally constructed in order to understand the mechanisms of cell polarization in motile cells such as fibroblasts, it is possible that similar mechanisms occur prior to the sprouting of a new neurite during stage 2 (neuritogenesis). The basic idea is to use reaction–diffusion equations to describe the spatiotemporal dynamics of Rho GTPases such as Rac1, Cdc42, and RhoA, which are known to cycle between active membrane-bound forms and inactive cytosolic forms. One finds that a transient and localized stimulus can be spatially amplified, leading to a robust partitioning of the cell into a front and back, where the concentration of the active forms is high and low, respectively. Mathematically speaking, the emergence of cell polarization can be understood in terms of front propagation in a bistable reaction–diffusion system (Sect. 2.2) with the following additional features [438, 439]: (1) the inactive and active states have unequal rates of diffusion; (2) the total amount of each GTPase is conserved. Consequently, a local stimulus induces a propagating front that decelerates as it propagates across the cell so that it becomes stationary, a process known as *wave-pinning*; the stationary front persists in the absence of the stimulus and represents a polarized cell. Note that the wave-pinning mechanism is distinct from the diffusion-driven Turing mechanism found in other reaction–diffusion models of cell polarization [417, 482, 609]. One of the basic differences is that in the latter class of models, a homogeneous state becomes unstable to arbitrarily small fluctuations and the nonlinear reaction terms support the growth of a spatially varying pattern via a Turing stability. For a recent application of the Turing mechanism to neurite formation, see [420].

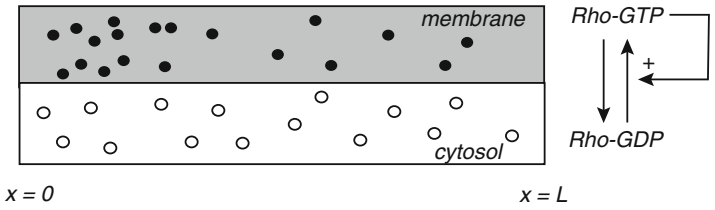

Fig. 9.9 Schematic diagram of wave-pinning model showing spatial distribution of membrane-bound active and cytosolic inactive forms of Rho GTPase

The simplest version of the model considers a single Rho GTPase that can transition between inactive and active forms diffusing in a bounded 1D domain of length L [438]; see Fig. 9.9. Let $a(x,t)$ and $b(x,t)$ be the concentrations of the active/inactive states. Then

$$\frac{\partial a}{\partial t} = D_a \frac{\partial^2 a}{\partial x^2} + f(a,b), \tag{9.1a}$$

$$\frac{\partial b}{\partial t} = D_b \frac{\partial^2 b}{\partial x^2} - f(a,b), \tag{9.1b}$$

Since the rate of diffusion of the membrane-bound (active) state is significantly slower than that of the cytosolic (inactive) state, $D_a \ll D_b$. The nonlinear function $f(a,b)$ represents the difference between the rates of activation and inactivation of the Rho GTPase. Assuming there is cooperative positive feedback in the activation of the protein, which is modeled as a Hill function of index 2, then

$$f(a,b) = b\left(k_0 + \frac{\gamma a^2}{K^2 + a^2}\right) - k_- a. \tag{9.2}$$

It can be checked that for a range of uniform concentrations of the inactive state, $b_{\min} < b < b_{\max}$, the space-clamped version of the model exhibits bistability with two stable fixed points $a_\pm(b)$ separated by an unstable fixed point $a_0(b)$. Equation (9.1) is supplemented by no-flux boundary conditions at the ends of the domain:

$$\left.\frac{\partial a}{\partial x}\right|_{x=0,L} = 0, \quad \left.\frac{\partial b}{\partial x}\right|_{x=0,L} = 0. \tag{9.3}$$

It follows that there is mass conservation of the total amount of Rho GTPase, that is,

$$\int_0^L (a+b)dx = C. \tag{9.4}$$

The mathematical explanation of wave-pinning proceeds as follows [438]. First, since $D_b \gg D_a$ and there are no-flux boundary conditions, one can assume that b rapidly diffuses to establish a uniform concentration within the bounded domain $[0,L]$; b then changes on a slower time scale as the a dynamics evolves

(quasi-steady-state approximation). Thus, on short time scales b can be treated as a fixed global parameter of a scalar equation for $a(x,t)$ given by (9.1a). Suppose that initially $b_{\min} < b < b_{\max}$, so (9.1a) is bistable. On an infinite domain, the bistable equation supports the propagation of a traveling front linking the stable fixed point $a_+(b), a_-(b)$ (see Sect. 2.2). That is, for $-\infty < x < \infty$ there exists a monotonically decreasing solution $a(x,t) = A(\xi)$, $\xi = x - ct$ with $\lim_{\xi\to-\infty} A(\xi) = a_+(b)$ and $\lim_{\xi\to\infty} A(\xi) = a_-(b)$. Moreover the wave speed satisfies $c = c(b)$ with [see also (2.19)]

$$c(b) = \frac{\displaystyle\int_{a_-}^{a_+} f(a,b)da}{\displaystyle\int_{-\infty}^{\infty} (\partial A/\partial\xi)^2 d\xi}. \tag{9.5}$$

Note that the wave speed depends on the global parameter b. Since the denominator of (9.5) is always positive, the sign of $c(b)$ will depend on the sign of $I(b) \equiv \int_{a_-}^{a_+} f(a,b)da$, which has a geometrical interpretation in terms of the difference between the area of the curve $y = f(a,b)$ above the straight line $y = k_- a$ and the area below; see Fig. 9.10. In the case of a sufficiently sharp front that is away from the boundaries, these results carry over to the bounded domain $[0,L]$.

Now suppose that a transient stimulus near the edge of the cell at $x = 0$ triggers at time $t = 0$ a traveling front as described above. This implies that $b_{\min} < b(0) < b_{max}$ and $I(b(0)) > 0$. As the front starts to propagate into the interior of the cell, it converts a greater fraction of the domain from $a \approx a_-(b)$ to $a \approx a_+(b)$. From the conservation condition (9.4), it follows that the approximately uniform concentration $b(t)$ of the inactive state decreases, eventually reaching a critical value b_c, $b_{\min} < b_c < b_{\max}$, for which

$$I(b_c) \equiv \int_{a_-}^{a_+} f(a,b_c)da = 0, \tag{9.6}$$

and wave-pinning occurs. The basic steps are illustrated in Fig. 9.10.

Asymptotic Analysis of Wave-Pinning. As shown by Mori et al. [439], it is possible to analyze wave-pinning in more detail using a multi-time-scale analysis. The first step is to nondimensionalize (9.1):

$$\varepsilon\frac{\partial a}{\partial t} = \varepsilon^2\frac{\partial^2 a}{\partial x^2} + f(a,b), \tag{9.7a}$$

$$\varepsilon\frac{\partial b}{\partial t} = D\frac{\partial^2 b}{\partial x^2} - f(a,b), \tag{9.7b}$$

with $x \in [0,1]$ and $0 < \varepsilon \ll 1$. In order to look at the dynamics on short time scales, set $\tau = t/\varepsilon$ and introduce the asymptotic expansions $a \sim a_0 + \varepsilon a_1 + \ldots$ and $b \sim b_0 + \varepsilon b_1 + \ldots$. This yields the following pair of equations for a_0 and b_0:

$$\frac{\partial a_0}{\partial\tau} = f(a_0,b_0), \tag{9.8a}$$

$$\frac{\partial b_0}{\partial\tau} = D\frac{\partial^2 b_0}{\partial x^2} - f(a_0,b_0). \tag{9.8b}$$

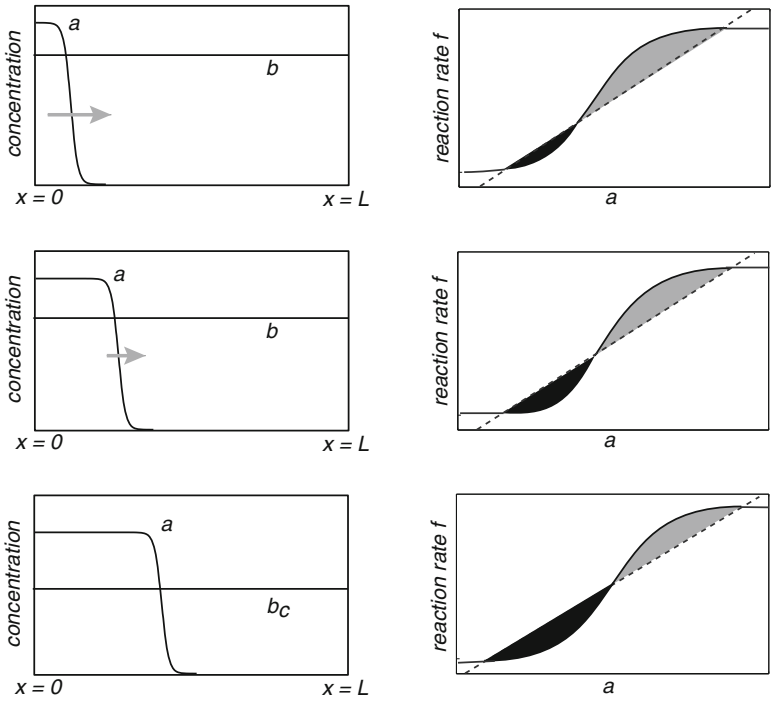

Fig. 9.10 Schematic diagram explaining the mechanism of wave-pinning developed in [438]. A sequence of snapshots of the traveling front (*left column*) showing that as the front advances into the domain, the background concentration b of the inactive state decreases so that the front decelerates until it becomes stationary. The corresponding geometric construction of $I(b)$ (*right column*), which is given by the difference of the *shaded areas*, shows that $I(b)$ is initially positive but vanishes at the critical value b_c

Suppose that $b_{\min} < b_0 < b_{\max}$ so that $f(a_0, b_0)$ is bistable with respect to a_0. Equation (9.8a) implies that $a_0 \to a_+(b_0)$ or $a_0 \to a_-(b_0)$ at each point $x \in [0,1]$. Assume initial conditions in which there exists a single sharp transition layer linking a_+ to a_- (a traveling front).

Let $\phi(t)$ be the position of the transition layer with respect to the slower time scale t. Divide the domain $[0,1]$ into inner and outer regions, with the latter given by $[0, \phi(t) - \mathcal{O}(\varepsilon)) \cup (\phi(t) + \mathcal{O}(\varepsilon), 1]$. Taking the limit $\varepsilon \to 0$ in (9.1), with $a \sim a_0 + \varepsilon a_1 + \ldots$, $b \sim b_0 + \varepsilon b_1 + \ldots$, and restricting x to the outer layer, we have

$$0 = f(a_0, b_0), \tag{9.9a}$$

$$0 = D\frac{\partial^2 b_0}{\partial x^2} - f(a_0, b_0). \tag{9.9b}$$

Adding these two equations immediately implies that $\partial^2 b_0 / \partial x^2 = 0$. Combining this with the no-flux boundary conditions, it follows that

$$b_0(x,t) = \begin{cases} b_L(t) & 0 \le x < \phi(t) - \mathcal{O}(\varepsilon), \\ b_R(t) & \phi(t) + \mathcal{O}(\varepsilon) < x \le 1. \end{cases} \tag{9.10}$$

with $b_{L,R}(t)$ independent of x. The corresponding solution for a_0 is

$$a_0(x,t) = \begin{cases} a_+(b_L) & 0 \le x < \phi(t) - \mathcal{O}(\varepsilon), \\ a_-(b_R) & \phi(t) + \mathcal{O}(\varepsilon) < x \le 1. \end{cases} \tag{9.11}$$

In order to determine the solution in the inner layer near the front, introduce the stretched coordinate $\xi = (x - \phi(t))/\varepsilon$, and set

$$A(\xi,t) = a([x-\phi(t)]/\varepsilon, t), \quad B(\xi,t) = b([x-\phi(t)]/\varepsilon, t) \tag{9.12}$$

Introduce the asymptotic expansion $A \sim A_0 + \varepsilon A_1 + \ldots$ and similarly for B and ϕ. Substitution into (9.7) and expansion to lowest order in ε then gives

$$\frac{\partial^2 A_0}{\partial \xi^2} + \frac{d\phi_0}{dt}\frac{\partial A_0}{\partial \xi} + f(A_0, B_0) = 0, \tag{9.13a}$$

$$\frac{\partial^2 B_0}{\partial \xi^2} = 0. \tag{9.13b}$$

The solution of (9.13b) is of the form

$$B_0 = \alpha_1(t)\xi + \alpha_2(t), \tag{9.14}$$

where $\alpha_{1,2}(t)$ are determined by matching the inner (B_0) and outer (b_0) solutions according to

$$\lim_{\xi \to -\infty} B_0(\xi) = b_L, \quad \lim_{\xi \to \infty} B_0(\xi) = b_R. \tag{9.15}$$

The matching conditions can only be satisfied if B_0 is constant in the inner layer, which means that the inactive state is uniform throughout the whole domain, $B_0 = b_0$. The next step is to determine the inner solution for A_0, given that B_0 is ξ-independent. That is, we have to solve the boundary value problem (9.13a) with matching conditions:

$$\lim_{\xi \to -\infty} A_0(\xi) = a_+(b_0), \quad \lim_{\xi \to \infty} A_0(\xi) = a_-(b_0). \tag{9.16}$$

The inner solution thus corresponds to the standard front solution of a bistable equation with

$$\frac{d\phi_0}{dt} \equiv c(b_0) = \frac{\displaystyle\int_{a_-(b_0)}^{a_+(b_0)} f(a, b_0)\, da}{\displaystyle\int_{-\infty}^{\infty} (\partial A_0/\partial \xi)^2 d\xi}, \tag{9.17}$$

see (9.5).

The final step is to incorporate the conservation condition (9.4), which to lowest order in ε becomes

$$\int_0^1 a_0 dx + b_0 = C. \tag{9.18}$$

The integral term can be approximated by substituting for a_0 using the outer solution:

$$\begin{aligned} \int_0^1 a_0 dx &= \int_0^{\phi(t)-\mathcal{O}(\varepsilon)} a_0 dx + \int_{\phi(t)+\mathcal{O}(\varepsilon)}^1 a_0 dx + \mathcal{O}(\varepsilon) \\ &= a_+(b_0)\phi_0(t) + a_-(b_0)(1-\phi_0(t)) + \mathcal{O}(\varepsilon). \end{aligned}$$

Combining the various results, the analysis of a traveling front solution of (9.7) reduces to the problem of solving the ODE system [439]

$$\frac{d\phi_0}{dt} = c(b_0), \quad b_0 = C - a_+(b_0)\phi_0(t) - a_-(b_0)(1-\phi_0(t)). \tag{9.19}$$

These equations can be used to establish that the front slows down and eventually stops to form a stable stationary front. In particular, differentiating the second relation in (9.19) with respect to t shows that

$$\left(1 + \frac{da_+(b_0)}{db}\phi_0 + \frac{da_-(b_0)}{db}(1-\phi_0)\right)\frac{db_0}{dt} = -[a_+(b_0) - a_-(b_0)]\frac{d\phi_0}{dt}. \tag{9.20}$$

Differentiating the condition $f(a_\pm(b), b) = 0$ with respect to b and imposing the condition that $f(a,b)$ is bistable, it can be established that $1 + da_\pm/db > 0$. Since $0 < \phi_0 < 1$ and $a_+(b_0) > a_-(b_0)$, it follows from (9.20) that db_0/dt and $d\phi_0/dt$ have opposite signs. Hence, as the front advances, b_0 decreases until the front stalls at a critical value b_c for which $c(b_c) = 0$. The corresponding front position is ϕ_c with

$$b_c = C - a_+(b_c)\phi_c - a_-(b_c)(1-\phi_c). \tag{9.21}$$

Explicit conditions for wave-pinning can be obtained if the reaction term f is taken to be a cubic

$$f(a,b) = a(1-a)(a-1-b), \tag{9.22}$$

rather than the Hill function (9.2). In this case, the speed of the front solution in the inner layer can be calculated explicitly (see Sect. 2.2), so that (9.19) becomes

$$\frac{d\phi_0}{dt} = \frac{b_0 - 1}{\sqrt{2}}, \quad b_0 = C - (1+b_0)\phi_0. \tag{9.23}$$

It follows that the wave stops when $b_0 = 1 \equiv b_c$ and the stall position is $\phi_c = (C-1)/2$. Finally, note that Mori et al. [439] also extend the asymptotic analysis to the case of multiple transition layers and carry out a bifurcation analysis to determine parameter regimes for which wave-pinning occurs.

One interesting issue is to what extent the wave-pinning mechanism differs from the phenomenon of wave propagation failure due to spatial discretization, as occurs in myelinated axons, for example (Sect. 2.5). This is particularly important given that any numerical simulation of the wave-pinning model involves the introduction of a spatial grid, and the wave becomes more sensitive to discretization effects as it slows down. A careful numerical study has shown that wave-pinning and propagation failure are distinct effects [655]. In the same study, a stochastic version of the wave-pinning model was also considered, which takes into account fluctuations in the number of active and inactive molecules at low concentrations. It was found that when the total number of molecules is lowered, wave-pinning behavior is lost due to a broadening of the transition layer as well as increasing fluctuations in the pinning position.

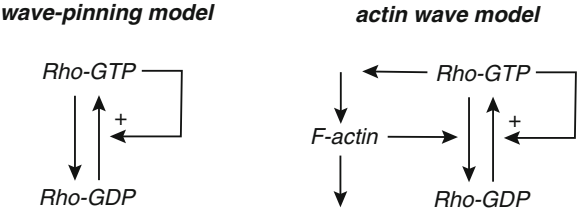

Fig. 9.11 Schematic diagram showing the basic pathways involved in the wave-pinning model [438] and actin wave model [286]

9.2.3 Actin Waves

There are a number of intracellular wavelike phenomena associated with the maturation of single neurons. First, localized Ca^{2+} transients occur in the growth cone of developing neurons [233, 234, 245]. Although they spread passively by diffusion rather than actively, they are often referred to as growth cone Ca^{2+} waves. These waves regulate the rate of neurite extension, which is inversely proportional to their frequency, since elevations in intracellular Ca^{2+} concentration above baseline slow any growth. Second, a neuron-wide Ca^{2+} wave propagating from the growth cone of an axon to the soma mediates reversal of neuronal migration in response to a repulsive extracellular cue (Slit-2) [247]. It is hypothesized that Slit-2 receptor activation at the leading edge of the growth cone triggers the Ca^{2+} wave, which propagates to the soma, resulting in a front-to-rear gradient of Ca^{2+} concentration. This gradient in turn causes (by some yet-to-be-identified mechanism) a redistribution of the GTPase RhoA towards the rear of soma, a process necessary for establishing the reversed direction of migration. (One possibility is that the calcium wave acts as a trigger for a polarization wave similar to the one discussed in Sect. 9.2.2.) We will focus on another type of wave, namely, an actin wave propagating along the axon shaft of neurites during cell maturation. In developing hippocampal neurons, neurites undergo periodic extensions and retractions, which correlate with the propagation of growth cone-like structures that originate in the soma and propagate down the neurites [194, 542, 543]. The waves travel at a speed of around 3 μm/min, transporting actin and associated proteins such as cofilin down the neurite shaft to the growth cone. Waves occur in all neurites during maturation stage 2, but become more frequent in the emerging axon during the transition from stage 2 to stage 3 [194]. This coincides with an engorgement and increased dynamics of the axon's growth cone. Interestingly, growth cone-like actin waves have also been observed during the regeneration of injured axons in cultured hippocampal neurons [155].

Actin waves are found in a number of other cell types including *Dictyostelium* [643], neutrophils [665], and fibroblasts (see the review [7]). Indeed, most current models of actin waves are based on studies of nonneuronal cells. They also tend to be rather complicated, containing details regarding the distribution of actin lengths or orientations, for example [103, 157, 643]. Here we will consider a simpler model of actin waves that extends the wave-pinning model of Mori et al. by coupling the Rho

GTPase signaling module to a module representing the assembly and disassembly of actin polymers (F-actin) [286]; see Fig. 9.11. More specifically, active Rho GTPase promotes the polymerization of F-actin which feeds back to enhance the inactivation of Rho GTPase (negative feedback). In order to incorporate the effects of negative feedback, the kinetic rate function (9.2) is modified according to

$$f(a,b,u) = b\left(k_0 + \frac{\gamma a^3}{K^3 + a^3}\right) - k_-\left(s_1 + s_2\frac{u}{u_0+u}\right)a, \tag{9.24}$$

where u is the concentration of F-actin and s_1, s_2, u_0 are additional parameters. If $s_2 = 0$ and $s_1 = 1$, then we recover the previous wave-pinning model with f having a hill coefficient of $n = 3$ rather than $n = 2$. (Although $n = 2$ also works, the choice $n = 3$ gives more robust waves). It remains to specify the F-actin dynamics. It is assumed that F-actin is nucleated from an infinite reservoir of actin monomers with concentration M, at a rate that is proportional to the concentration of active Rho GTPase. Thus, neglecting the diffusion of F-actin,

$$\frac{\partial u}{\partial t} = \varepsilon[k_n M - k_s u], \tag{9.25}$$

where εk_n is the nucleation rate and εk_s is the disassembly rate.

Extensive numerical simulations show that the actin wave model supports a wide range of spatiotemporal dynamics not found in the wave-pinning model, including solitary traveling pulses, periodic wave trains, persistent reflecting waves, and more exotic localized patterns [286]. In order to characterize the parameter dependence of these various patterns, Holmes et al. [286] considered the nonlinear stability of homogeneous steady states with respect to non-infinitesimal localized perturbations. This analysis identified two distinct stability regimes: an *excitable* regime where a pattern can only be triggered by a perturbation whose amplitude exceeds some threshold and an *unstable* regime where arbitrarily small noise can induce a pattern. Traveling pulses occur in the excitable regime, where the negative feedback due to F-actin plays a role analogous to the refractory variable in the FitzHugh–Nagumo equations (see Chap. 2). On the other hand, wave trains occur in the unstable regime, and reflecting waves occur in both regimes. As with other models of actin waves, the motivating examples are from nonneuronal cells. However, it is possible that the solitary traveling pulse could represent the growth cone-like wave seen in developing neurites [194, 542, 543].

9.2.4 Diffusion-Based Model of Neurite Symmetry Breaking

A major unresolved issue is how a single axon is specified among equally potential neurites, that is, what is the underlying symmetry breaking mechanism for neurite differentiation? During stage 3, the cytoskeleton of the emerging axonal growth cone becomes more dynamic and less dense (due to the action of Rac1 and Cdc42,

say), whereas the actin cytoskeleton of the other growth cones remains more stable and maintains a denser network (due to the action of RhoA, say). Consequently, microtubules are hindered from entering the growth cone of the inhibited neurites, whereas they can advance into the P-domain of the axon thus stimulating elongation. An emerging hypothesis [9, 13, 193, 629] is that neurite extension and retraction are controlled by positive and negative signaling molecules (morphogens) respectively, which diffuse within neurites to regulate the behavior of actin filaments and microtubules or to influence cargo transport. In particular, it is hypothesized that prior to neurite differentiation, positive and negative feedback mechanisms are balanced; this balance can be broken by an external cue or by spontaneous intrinsic fluctuations, resulting in the enhancement of positive feedback within a single neurite that elongates to form an axon; simultaneously, the activated neurite generates a strong negative feedback signal that prevents other neurites from forming a second axon. A discussion of various candidate signaling cascades that could support autocatalytic (positive feedback) processes in growth cones can be found elsewhere [9, 13]. Here we will describe a particular model of neurite differentiation due to Toriyama et al. [629], which is based on the transport of a protein called *Shootin1*. Shootin1 is thought to be an upstream regulator of various signaling molecules responsible for neuronal polarization [576]. The model is motivated by the experimental observation that Shootin1 is actively transported from the soma to growth cones as discrete boluses within actin waves [628]. The active anterograde transport combines with diffusive retrograde transport in such a way that Shootin1 accumulates in the growth cones in a neurite length-dependent manner [629]. Moreover, during the stage 2/3 transition, Shootin1 predominantly accumulates in the nascent axon. The observation that Shootin1 can induce neurite outgrowth by regulating actin retrograde flow [576] suggests that the asymmetric accumulation of Shootin1 is one of the critical events in neurite differentiation.

Consider a developing neuron that consists of N neurites labeled $i = 1,\ldots,N$, each having length L_i; see Fig. 9.12a. Let C_0 denote the concentration of Shootin1 in the soma and C_i the concentration in the ith growth cone. The diffusion coefficient of Shootin is around $350\,\mu m^2/min$ so that the diffusion time constant $\tau = L^2/D$ is around 1 min for a typical neurite length of $L = 20\,\mu m$. Given that the volumes of the cell body (V_S) and growth cone (V) are large compared to the volume of a thin neurite shaft, it follows that changes in Shootin1 concentration within the growth cone and soma occur on a slower time scale than the formation of a concentration gradient along a neurite. Hence, one can assume as a first approximation that the diffusive retrograde flow is in quasi-equilibrium. This means that the diffusive flux J_i along the jth neurite is approximately uniform so that the net flux from the growth cone is

$$J_i(t) = \frac{D}{L_i}(C_i(t) - C_0(t)). \tag{9.26}$$

For simplicity, the propagation of actin waves is not modeled explicitly; rather, the waves are treated as sequences of discrete stochastic events corresponding to

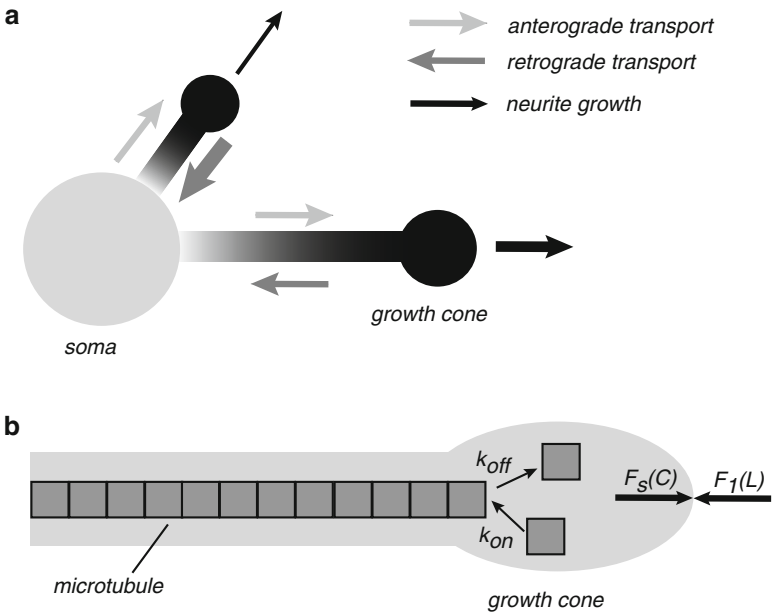

Fig. 9.12 Model of diffusion-based neurite growth due to Toriyama et al. [629]. (**a**) A concentration gradient of Shootin1 is set up along each dendrite due to the combination of active anterograde flow and length-dependent retrograde diffusion. Accumulation of Shootin1 in a growth cone sets up a positive feedback loop for neurite growth. Neurite competition for resources leads to symmetry breaking where one neurite grows at the expense of all the others. (**b**) Neurite growth is regulated by the balance between a Shootin1-induced traction force $F_S(C)$ and a length-dependent neurite tensional force $F_1(L)$

Gaussian-like packets of Shootin1 delivered to a neurite's growth cone at random times T_j^n and amplitudes a_j^n. Thus, the active transport in neurite j is represented as a sum of discrete events

$$\Gamma_j(t) = \frac{V_S}{V} \sum_n a_j^n g(t - T_j^n). \tag{9.27}$$

with $g(t)$ a normalized Gaussian of width σ. The amplitudes and delivery times are modeled by gamma distributions fitted to the experimental data [629]. Combining (9.26) and (9.27), the Shootin1 concentration in the jth growth cone evolves as

$$\frac{dC_i}{dt} = -\frac{AD}{VL_i}(C_i - C_0) + \Gamma_j(t). \tag{9.28}$$

(For simplicity, the growth cone volume V and cross-sectional shaft area A is taken to be the same for each neurite.)

The next component of the model specifies how the accumulation of Shootin1 in the growth cone regulates neurite growth; see Fig. 9.12b. It is assumed that

growth is determined primarily by the balance between two mechanical forces: a Shootin1-dependent traction force $F_S(C)$ and a neurite length-dependent tensional force $F_1(L)$. The former is taken to be a Hill function

$$F_S(C) \sim \frac{C^h}{K_s^h + C^h}, \tag{9.29}$$

for constants K_s, h, while the latter is approximated as a logarithmic Hill-like function,

$$F_1(L) \sim \frac{\ln(L/L_0)}{\ln(L/L_0) + \ln(K_1/L_0)} \tag{9.30}$$

for constants K_1, L_0. The growth velocity of the ith neurite is determined as

$$\frac{dL_i}{dt} = \delta(k_i^{\text{on}} M - k_i^{\text{off}}), \tag{9.31}$$

where δ is the size of a tubulin monomer (the basic building block of microtubules), M is the intracellular concentration of tubulin, and k_i^{on} and k_i^{off} are the rates of polymerization and depolymerization, respectively. From the thermodynamics analysis of a simple ratchet model of polymerization [434], it can be shown that the ratio of the on and off rates depends on the net force $F = F_1(L) - F_s(C)$ according to

$$\frac{k^{\text{off}}(F)}{k^{\text{on}}(F)} = \frac{k^{\text{off}}(0)}{k^{\text{on}}(0)} e^{F\delta/k_B T}, \tag{9.32}$$

where k_B is the Boltzmann constant and T is absolute temperature. Fitting to experimental data suggests that the on rate is approximately independent of F. Hence, setting $F_i = F_1(L_i) - F_s(C_i)$, $k_i^{\text{on}} = k_{\text{on}}$ and $k_i^{\text{off}} = k^{\text{off}}(F_i) = k_{\text{off}} e^{F_i\delta/k_B T}$, we have

$$\frac{dL_i}{dt} = \delta \left[k_{\text{on}} M - k_{\text{off}} e^{-[F_s(C_i) - F_1(L_i)]\delta/k_B T} \right]. \tag{9.33}$$

As it stands, if C_0 and M were fixed (reflecting an unlimited supply of tubulin and Shootin1), then each neurite would independently undergo a positive feedback loop in which an increase in neurite length L_i would slow the rate of retrograde diffusion, the growth cone concentration C_i of Shootin1 would increase, and this would in turn speed up the rate of growth. However, the neurites actually compete for a finite amount of resources. If S is the total amount of Shootin1 in the neuron and V_0 is the volume of the soma, then

$$S = V_0 C_0 + V \sum_{j=1}^{N} C_j. \tag{9.34}$$

Hence, as a neurite grows, it depletes the level of Shootin1, which inhibits the growth of the other neurites. There is also competition for tubulin monomers, which can be expressed as

$$T = V_{\text{tot}} M + \rho \sum_{j=1}^{N} L_j, \tag{9.35}$$

where $V_{\text{tot}} = V_0 + NV$, T is the total amount of cellular tubulin and ρ is a parameter that determines how much tubulin is needed to build a neurite of a given length. Finally, experimental data indicates that both T and S are upregulated, that is, they are slowly increasing functions of time that can be fitted by a time-dependent function of the form $S(t) \sim \alpha_s + \gamma_s/(1 + \beta_s t^{-2.5})$ for constants $\alpha_s, \beta_s, \gamma_s$, and similarly for $T(t)$. Numerical simulations of the full model, with parameter values based on studies of cultured hippocampal neurons, robustly exhibits spontaneous symmetry breaking and the formation of an axon [629]. The model also reproduces various atypical behaviors observed in cultured neurons. For example, applying mechanical tension to a single neurite during stage 2 results in its axonal specification, overexpression of Shootin1 induces the formation of multiple axons, and repression of Shootin1 inhibits polarization.

Finally, note that the Toriyama et al. model can be viewed as one of a class of models for neurite differentiation that involve competition among neurites for a pool of proteins involved in neuronal polarization. The first models of this type [479, 548, 640] simply took the rate of elongation to be proportional to the intracellular concentration of the protein (possibly tubulin) at the neurite tip. One prediction of these models is that the rate at which a neuron polarizes to form an axon should increase with the number of neurites. However, a recent experiment establishes that the time to polarize is independent of the number of neurites [680], which is consistent with another recent model of neurite differentiation based on the transport of the protein HRas rather than Shootin1 [193]. It turns out that all of the models exhibit independence of the number of neurites N, provided that the expression of the relevant protein increases with N [680], which was one of the assumptions in [193].

9.3 Spreading Depression

Cortical spreading depression (SD) is a complex wave of transient depolarization of neurons and glial cells that propagates slowly across cortical and subcortical gray matter at speeds of 1–5 mm/min [93, 365, 407, 461, 596]. It occurs as a response to various forms of brain damage or pathology [237], including focal ischemia, traumatic brain injury, and seizure activity. There is also strong evidence that SD is a correlate or cause of *migraine with aura*, where a light scintillation in the visual field propagates before disappearing to be replaced by a sustained headache [358, 639]. Although SD does not usually damage brain tissue, if it arises repeatedly during stroke or head trauma, then it may promote neuronal damage. One of the characteristic features of SD is a large increase in extracellular K^+ and a dramatic decrease in extracellular Ca^{2+} and other ions. Simultaneously, the DC surface potential of electroencephalogram (EEG) undergoes a negative shift of around 19 mV that lasts 30 s, followed by a smaller but longer positive voltage shift. At the cellular level, the slow shift in potential coincides with a period of membrane depolarization followed by a longer period of hyperpolarization. A comprehensive picture of the precise

physiological and chemical processes underlying the generation of SD is still lacking. However, a number of mechanisms are thought to contribute, including diffusion and membrane transport of ions, chemical synapses and neurotransmitters, spatial buffering, gap junctions, and osmotic effects [433].

Although SD waves are associated with populations of cells, they have several properties in common with propagating action potentials in the axons of single neurons (Chap. 2): (1) they are essentially all-or-none phenomena; (2) they travel with approximately constant speed and wave form; (3) they involve membrane depolarization; (4) they exhibit refractoriness; (5) multiple waves can be generated from a sustained stimulus and colliding waves can annihilate. Phenomenologically speaking, the general characteristics of a solitary SD wave can be reproduced by appropriately parameterized Fitzhugh–Nagumo equations, for example, with the principal dependent variable being extracellular K^+ concentration rather than membrane potential. However, such a model fails to give insights into the underlying physiological mechanisms and is thus not useful for developing clinical treatments for associated pathologies such as migraine. Indeed, there are a number of significant differences between SD waves and action potentials: (1) space and time scales are much longer for SD waves; (2) SD wave propagation mainly involves ionic fluxes through synaptic rather than non-synaptic membrane; (3) there are substantial changes in extracellular ion concentrations during passage of an SD wave; (4) the recovery phase of SD involves active transport mechanisms such as ion pumps.

9.3.1 Tuckwell–Miura Model

The first physiologically based mathematical model of SD waves was introduced by Tuckwell and Miura [638]. It centers on the idea that an initial large increase in extracellular K^+ would depolarize presynaptic terminals, resulting in the release of neurotransmitter. This would then open K^+ channels in the postsynaptic membrane of a neuron, leading to the flux of additional K^+ into the extracellular space. The resulting regenerative process would support the propagation of an SD wave. The model of Tuckwell and Miura is a bidomain continuum model (see Sect. 4.2), in which the concentration of ions in the extracellular and intracellular domains are taken to coexist at every point in space. This is a reasonable approximation given that the spatial scale of an SD wave is much larger than the size of individual neurons. Ions are free to diffuse over significant distances within the extracellular space, whereas intracellular ions can only diffuse within a cellular domain that is negligible compared to the scale of SD waves. Thus the effective diffusivity of intracellular ions is taken to be zero. Another assumption of the model is that the equilibrium membrane potentials for neighboring presynaptic and postsynaptic membranes are approximately the same and are thus taken to have the common value $V(x,t)$. This can be justified by first noting that during passage of an SD wave, the changes in intracellular ion concentrations are negligible, since the ratio of the intracellular to

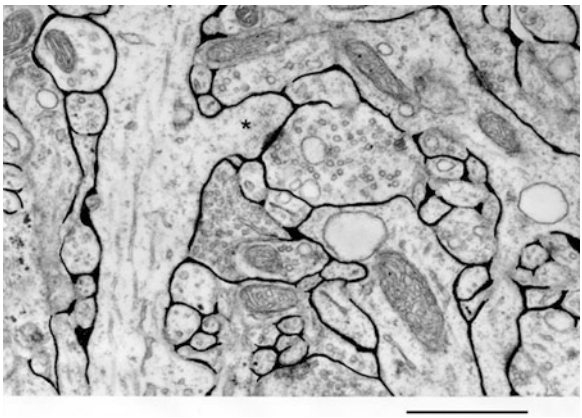

Fig. 9.13 Electron micrograph of a small region of the cerebral cortex of a rat illustrating the small volume fraction of the extracellular space, which is indicated by the black areas between cells. (Note, however, that the extracellular space may have been reduced in size as a consequence of the histological processing.) The *asterisk* indicates a dendritic spine, which is joined by a synaptic cleft to a presynaptic terminal containing several small round vesicles filled with neurotransmitter. Some of the round profiles adjoining the dendrite are likely to be unmyelinated axons cut in cross section. The *scale bar* represents a distance of approximately 1 µm (Adapted from [461])

extracellular volumes is large; see Fig. 9.13. Second, the local equilibrium membrane potential of a neuron is given by the Hodgkin–Katz formula

$$V = \frac{k_B T}{q} \ln \left[\frac{K^{\text{out}} + p_{\text{Na}} Na^{\text{out}} + p_{\text{Cl}} Cl^{\text{in}}}{K^{\text{in}} + p_{\text{Na}} Na^{\text{in}} + p_{\text{Cl}} Cl^{\text{out}}} \right]. \tag{9.36}$$

Here (K^{out}, Na^{out}, Cl^{out}) and (K^{in}, Na^{in}, Cl^{in}) denote the extracellular and intracellular concentrations of potassium, sodium, and chloride, respectively, q is the charge of a proton, and p_{Na}, p_{Cl} are the ratios of the sodium and chloride membrane permeabilities to the potassium permeability. It follows that the membrane potential $V(x,t)$ simply tracks the extracellular ion concentrations, which are common to presynaptic and postsynaptic neurons.

Let c_j^{out} and c_j^{in} denote the extracellular and intracellular concentration of ion species j, with $j = 1,2,3,4$ corresponding to sodium, chloride, potassium, and calcium, respectively. The basic model equations are then of the general form (in one space dimension) [638]

$$\frac{\partial c_j^{out}}{\partial t} = D_j \frac{\partial^2 c_j^{out}}{\partial x^2} + g_j(V - V_j) + P_j, \tag{9.37a}$$

$$\frac{\partial c_j^{in}}{\partial t} = -\frac{\alpha}{1-\alpha} \left[g_j(V - V_j) + P_j \right]. \tag{9.37b}$$

Here D_j is the extracellular diffusion coefficient of the jth ion species, V_j is the corresponding Nernst potential for an ion with charge modulus q_j,

$$V_j = \frac{k_B T}{q_j} \ln\left(\frac{c_j^{out}}{c_j^{in}}\right), \tag{9.38}$$

g_j is an effective conductance, and P_j represents the contribution of active transport mechanisms (pumps). Conservation of ions implies that the non-diffusive rate of change of each extracellular concentration is the negative of the rate of change of the corresponding intracellular concentration, scaled by a factor $\alpha/(1-\alpha)$, where α is the "volume" fraction of the extracellular space. In principle, the contribution to the conductance g_j could come from channels at both synaptic and non-synaptic sites. However, it is assumed that exchange of ions between the extracellular and intracellular domains during passage of an SD wave occurs predominantly at synaptic sites. First, the Ca^{2+} conductance is taken to be presynaptic and a sigmoidal function of voltage

$$g_4 = g_4(V) \equiv g_0\,(1+\tanh[\eta\,(V+\kappa)])\,, \tag{9.39}$$

for constants g_0, κ, η. A large increase in the extracellular K^+ concentration generates a positive shift in the equilibrium potential V given by (9.36). The resulting depolarization leads to an influx of presynaptic Ca^{2+}, which causes the release of neurotransmitter. (For simplicity, only one type of neurotransmitter is considered here.) The rate of release is taken to be proportional to the calcium current. However, since such an event lasts a small time interval of size τ_r, the effective concentration of extracellular neurotransmitter is approximated by

$$T(x,t) = k_4 \tau_r g_4(V(x,t))(V(x,t) - V_4), \tag{9.40}$$

where k_4 is a constant. On the other hand, the conductance associated with the other ions is assumed to arise from the binding of neurotransmitter to postsynaptic receptors according to

$$g_j(x,t) = k_j T(x,t), \quad j = 1,2,3, \tag{9.41}$$

with constants k_j. Finally, the pump rates are given by exponential functions of the ion concentrations:

$$P_j = f_j(1 - \mathrm{e}^{-r_j(c_j^{\mathrm{out}} - \bar{c}_j)}), \tag{9.42}$$

for constants $f_j, r_j, \bar{c}_j$ with $\bar{c}_j$, the resting extracellular concentration. Note that $f_1 < 0$ for potassium and $f_j > 0$ for all the other ions, since the potassium pump maintains a higher intracellular concentration. Equations (9.36)–(9.42) determine the full version of the Tuckwell–Miura model [638]. It is also possible to consider a simplified version of the model, in which the sodium and chloride concentrations are kept fixed.

Using physiologically based parameter values, the Tuckwell–Miura model produces a wave speed of around 1 mm/min and a wave form consistent with experimental findings. However, it is necessary to take into account the effects of tortuosity, that is, the effective increase in path length for diffusion of ions around cells. This introduces a scaling factor of around 1.5 for the diffusion coefficient of ions in aqueous solution. One way to estimate the tortuosity of brain tissue as well as the volume fraction of the extracellular space is to use the theory of porous

media [461, 616]; see Sect. 9.3.2. The heterogeneous and anisotropic nature of brain tissue means that extending the Tuckwell–Miura model to higher dimensions is nontrivial, since one would need to determine an effective diffusion tensor. Nevertheless, the model has the advantage of being relatively simple and amenable to mathematical analysis. For example, one of the interesting mathematical features of the model is that there exists a family of rest states that depend continuously on a set of parameters. This degeneracy implies that traveling waves have a number of properties that are not present in the case of isolated rest points [686]. For example, a localized disturbance can lead to a pair of outward propagating waves that slow down and reverse direction before ultimately colliding and annihilating each other. Since the introduction of the Tuckwell–Miura model, which focused on extracellular diffusion and membrane ion currents, a number of other mechanisms have been identified as possible contributors to the initiation and propagation of SD waves:

1. *Gap junctions.* Experiments have shown that pharmacological blockade of gap junctions slows or even prevents the propagation of retinal SD waves [359, 406, 448]. As we described in Sect. 4.5, there is extensive gap-junction coupling between astrocytes. However, it would appear that SD waves still occur in the absence of astrocytes [360]. More specifically, destroying many astrocytes using the toxin fluorocitrate only reduces the effectiveness of SD by 50%. This motivated Shapiro [568] to develop a detailed biophysical model of SD waves, in which gap-junction coupling between neurons played a major role in the transport of K^+. Unfortunately, there is no evidence for such widespread gap-junction coupling between neurons. In addition, it is possible that after application of toxins, there are still a sufficient number of intact astrocytes to support some level of SD.

2. *Neuron–astrocyte networks.* There is growing experimental evidence that SD waves involve both neurons and astrocytes acting together via the release of ATP and glutamate. First, intercellular Ca^{2+} waves precede SD but blocking these waves by gap-junction inhibitors does not prevent SD [501]. On the other hand, SD is blocked by antagonists to NMDA receptors suggesting a role for glutamate signaling. Second, a large amount of ATP is released from astrocytes during SD [118, 558]. This is consistent with the observation that the ATP antagonist heptanol completely prevents SD in hippocampus [360], presumably by blocking paracrine signaling. It is also known that glutamate can stimulate the release of ATP from astrocytes [667] and, conversely, activation of purinergic receptors by ATP can induce glutamate (and possibly ATP) release from astrocytes [187]. These experimental results have led to a model of SD waves [38], in which a wave of ATP propagates with the astrocyte Ca^{2+} wave, resulting in an accompanying wave of glutamate release from the astrocytes. The glutamate acts on NMDA receptors in the postsynaptic membrane of neurons, which triggers the large depolarization characteristic of SD together with the presynaptic release of additional glutamate from neurons. The latter acts on neighboring astrocytes to initiate the release of additional ATP. Hence, one has a regenerative mechanism for the propagation of ATP and glutamate, resulting in an SD wave. Note that one

major assumption of the model is that glutamate and ATP can be released from astrocytes via Ca^{2+}-independent pathways [250, 659].

3. *Spatial buffering.* Another well-known role of astrocytes is in the regulation of extracellular K^+ by several mechanisms including the action of Na^+/K^+–ATPase pumps and K^+ ion channels [109, 211, 601]. The spatial buffering of K^+ by astrocytes has only been studied within the context of small perturbations away from the resting state rather than the large excursions that occur during the passage of an SD wave. Nevertheless, it is possible that spatial buffering can account for the range of wave speeds observed during SD. The central mechanism for spatial K^+ buffering via ion channels is that a local increase in extracellular K^+ causes a local depolarization of glial cell membranes, which then spreads electrotonically to other glial cells via gap junctions. There is thus an influx of extracellular K^+ into glia at the original site of enhanced extracellular K^+ and an efflux of K^+ into the extracellular space at distal sites where extracellular K^+ is close to the resting level. In other words, there is a rapid net transport of K^+ from sites of high extracellular concentration to sites of low extracellular concentration, which is mediated by ion channels and gap-junction coupling of astrocytes.
4. *Cell swelling.* A number of models of SD waves have taken into account the effects of cell swelling that results from ions crossing neuronal membranes leading to osmotic stresses [568, 596]. This reduces the volume fraction of the extracellular space.

9.3.2 Brain Tissue as a Porous Medium

Diffusion in the extracellular space occurs in the narrow gaps between cells (neurons and glia) and is analogous to diffusion in a porous medium consisting of two phases such as water in the sandy bed of a river [503]. The connection with porous media can be exploited to estimate the effective diffusivity of ions moving in the extracellular space; see the reviews [461, 616]. One immediate observation is that if one were to draw a line through a section of brain tissue (see Fig. 9.13), one would find that the extracellular concentration is a discontinuous function of position along the line. In order to construct continuum reaction–diffusion models such as Tuckwell–Miura, it is necessary to carry out some form of spatial averaging using either homogenization theory (see Sect. 4.6) or volume averaging. Although the former approach is more rigorous, we will describe the latter approach here following [461], since it is more intuitive. The first step is to partition brain tissue into a set of representative elementary volumes (REVs) that are sufficiently large to include a sufficient range of cellular elements for averaging, yet sufficiently small to allow a local description of averaged quantities. Consider an arbitrary REV with center $\mathbf{x}$ relative to a fixed origin and local coordinates $\boldsymbol{\xi}$ about the center; see Fig. 9.14. (One can view $\boldsymbol{\xi}$ and $\mathbf{x}$ as microscopic and macroscopic coordinates, respectively.) Suppose that each REV is composed of two phases σ, ω corresponding, respectively, to

the extracellular and intracellular domains and occupying the volumes V_σ, V_ω. Let $V = V_\sigma + V_\omega$ be the total volume of the REV and let $\alpha = V_\sigma/V$ be the volume fraction of the extracellular space. Derivation of an effective diffusion equation in the extracellular space now proceeds by applying a spatial averaging theorem to Fick's law and the particle conservation equation.

Spatial averaging theorem. This relates the average of the divergence of a microscopic quantity to the divergence of a macroscopic (averaged) quantity [240, 503]. Let $\mathbf{F}$ denote a microscopic state vector that is a function of time t and position $\mathbf{x}+\xi$ within the REV centered at $\mathbf{x}$. Applying the divergence theorem to the volume occupied by extracellular space V_σ, we have

$$\int_{V_\sigma} \nabla \cdot \mathbf{F} dV_\xi = \int_{S_\sigma} \mathbf{F} \cdot \mathbf{n}_\sigma dS_\xi + \int_{S_{\sigma\omega}} \mathbf{F} \cdot \mathbf{n}_\sigma dS_\xi, \tag{9.43}$$

where $\mathbf{n}_\sigma$ is the unit normal vector on the boundary of the σ phase pointing outwards. Introduce the index function χ such that $\chi(\mathbf{x}+\xi) = 1$ if $\mathbf{x}+\xi$ lies in the σ phase and is zero otherwise. We can then write the first term on the right-hand side as $\int_{\partial V} (\mathbf{F}\chi) \cdot \mathbf{n}_\sigma dS_\xi$ where ∂V is the exterior boundary of the REV. Applying the divergence theorem to the whole volume V then gives

$$\int_{V_\sigma} \nabla \cdot \mathbf{F} dV_\xi = \int_V \nabla_\xi \cdot (\mathbf{F}\chi) dV_\xi + \int_{S_{\sigma\omega}} \mathbf{F} \cdot \mathbf{n}_\sigma dS_\xi. \tag{9.44}$$

Since $\mathbf{F}\chi$ is a function of $\mathbf{x}+\xi$, we can replace ∇_ξ by $\nabla_\mathbf{x}$ and take the divergence operator outside the volume integral with respect to ξ:

$$\int_{V_\sigma} \nabla \cdot \mathbf{F} dV_\xi = \nabla_\mathbf{x} \cdot \int_V (\mathbf{F}\chi) dV_\xi + \int_{S_{\sigma\omega}} \mathbf{F} \cdot \mathbf{n}_\sigma dS_\xi. \tag{9.45}$$

Finally, noting that the index function χ restricts the first integral on the right-hand side to the domain V_σ, we have (after dividing through by V), the spatial averaging theorem [240]

$$\langle \nabla \cdot \mathbf{F} \rangle = \nabla \cdot \langle \mathbf{F} \rangle + \frac{1}{V} \int_{S_{\sigma\omega}} \mathbf{F} \cdot \mathbf{n}_\sigma dS_\xi, \tag{9.46}$$

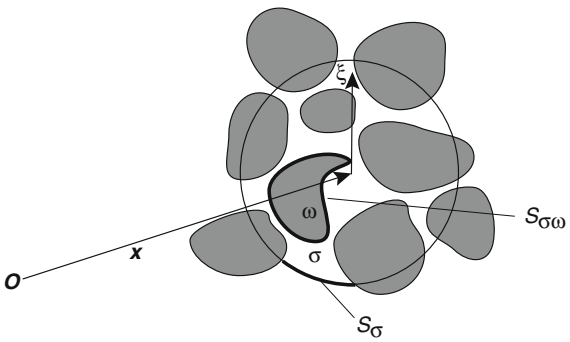

Fig. 9.14 A representative elementary volume (*REV*) composed of σ and ω phases and centered at $\mathbf{x}$. The interface between the phases is denoted by $S_{\sigma\omega}$ and the surfaces that make up the boundary of the REV are denoted by S_σ and S_ω, respectively

where

$$\langle f \rangle = \frac{1}{V} \int_{V_\sigma} f dV \tag{9.47}$$

for any function f. The spatial averaging theorem for a scalar quantity ψ may then be obtained by setting $\mathbf{F}(\mathbf{x}+\xi) = \psi(\mathbf{x}+\xi)\mathbf{a}$ with $\mathbf{a}$ an arbitrary constant vector:

$$\langle \nabla \psi \rangle = \nabla \langle \psi \rangle + \frac{1}{V} \int_{S_{\sigma\omega}} \psi \mathbf{n}_\sigma dS_\xi. \tag{9.48}$$

Fick's law for the diffusive flux $\mathbf{J}$ in a homogeneous medium takes the form

$$\mathbf{J} = -D\nabla c, \tag{9.49}$$

where D is the diffusion coefficient and $c(\mathbf{x},t)$ is the concentration of the diffusing particles at position $\mathbf{x}$ and time t. Combining this with particle conservation,

$$\frac{\partial c}{\partial t} + \nabla \cdot \mathbf{J} = 0, \tag{9.50}$$

then recovers the standard diffusion equation. Now suppose that Fick's law only applies to particles located within the extracellular space, which is a multiply connected 3D domain. One would then need to solve the associated diffusion equation within each simply connected component of extracellular space supplemented by surface boundary conditions. An alternative approach is to apply the spatial averaging theorem to Fick's law and the conservation equation to obtain a macroscopic version of the diffusion equation. First, we have

$$\langle \mathbf{J} \rangle = -D\langle \nabla c \rangle = -D\nabla \langle c \rangle + \frac{1}{V} \int_A c\mathbf{n} dS, \tag{9.51}$$

where the area integral is over the interfaces A between the extracellular and intracellular spaces. The nontrivial part of the analysis is determining the surface integrals, which corresponds to the problem of determining the effective diffusion tensor by solving the cell equations in homogenization theory; see Sect. 4.6. Nevertheless, the surface integral reduces to the general form [374]

$$\frac{1}{V} \int_A c\mathbf{n} dS = (\mathbf{K} - \mathbf{I})\nabla \langle c \rangle, \tag{9.52}$$

where $\mathbf{K}$ is a second-order tensor and $\mathbf{I}$ is the identity. It follows that Fick's law for a porous medium takes the form

$$\mathbf{J} = -\mathbf{D}^* \nabla \langle c \rangle, \tag{9.53}$$

where $\mathbf{D}^* = D\mathbf{K}$ is an effective diffusion tensor. In the special case of an isotropic medium, this reduces to scalar diffusion coefficient $D^* = D/\lambda^2$, where λ is the tortuosity. Similarly, volume averaging the particle conservation equation gives

$$\left\langle \frac{\partial c}{\partial t} \right\rangle + \langle \nabla \cdot \mathbf{J} \rangle = 0. \tag{9.54}$$

Applying the spatial averaging theorem to the divergence of the flux implies that

$$\langle \nabla \cdot \mathbf{J} \rangle = \nabla \cdot \langle \mathbf{J} \rangle + \frac{1}{V} \int_A \mathbf{J} \cdot \mathbf{n} dS.$$

In the case of impermeable cell membranes, $\mathbf{J} \cdot \mathbf{n} = 0$, whereas for permeable membrane

$$\mathbf{J} \cdot \mathbf{n} = g(c - c_{in}) \tag{9.55}$$

where g is an effective permeability and c_{in} is the local mean intracellular concentration. For simplicity, we focus on the impermeable case. Assuming that the interfaces A are fixed, that is, ignoring osmotic effects and cell swelling, then

$$\left\langle \frac{\partial c}{\partial t} \right\rangle = \frac{\partial \langle c \rangle}{\partial t}.$$

Collecting the various results finally gives in the isotropic case

$$\frac{\partial \langle c \rangle}{\partial t} = D^* \nabla^2 \langle c \rangle - \phi k(\langle c \rangle - c_{\text{in}}), \tag{9.56}$$

where $\phi = \int_A dS/V$ is a surface-to-volume ratio.

9.3.3 Migraine Auras

In this section we describe the relationship between SD and migraine aura. See also the review by Dahlem and Chronicle [144]. A characteristic feature of migraine is an episodic headache of moderate to severe intensity, which is usually unilateral (one side of the brain) and pulsating in nature. In the West, the lifetime prevalence of migraine is around 33 % in women and 13 % in men. In the case of migraine with aura, the migraine attack is preceded by a sensory hallucination called aura that usually lasts for less than half an hour. Consider, in particular, the classical visual aura that occurs in approximately 25–30 % of patients. Such an aura typically starts with a *scotoma* forming near the central region of the visual field; a scotoma (Greek for darkness) is an area of visual field in which there is partially or severely reduced visual acuity that is surrounded by a field of normal vision. The scotoma, which initially has indistinct boundaries, expands into a sickle or C-shaped region whose advancing edge contains a zigzag pattern of bright lines and shapes oriented at 60° to each other. The patterns are often called fortification patterns, since they are reminiscent of baroque city ramparts. An illustration of a fortification pattern is shown in Fig. 9.15, which has been superimposed upon a photograph of moose taken in the author's backyard. The fortification pattern becomes more distinct as it expands into the visual periphery, before disappearing at the edge of the visual field. The aura rarely returns during a single migraine event and leaves no noticeable permanent disruption of vision. Note that the fortification pattern at the leading edge of

Fig. 9.15 Illustration of a fortification pattern within the scotoma of a classical migraine aura

a scotoma reflects a short first phase of intense neuronal excitation, which precedes the prolonged phase of depressed neural activity that is associated with the scotoma. The existence of two phases is consistent with early studies of SD waves [93].

One of the important features of the migraine aura is that it clearly corresponds to a physiological wave propagating across the visual cortex. Moreover, the detailed structure of the fortification pattern appears to reflect the functional organization of the cortex, including its topographic organization and finer-scale feature maps; see Sect. 8.1.1. Indeed, it is now generally accepted that the fortification pattern provides a direct view of the layout of orientation columns in human visual cortex. Interestingly, many of these observations were anticipated by the psychologist Lashley in 1941 [363]. The first link between migraine aura and SD waves was made in 1945 [366], and there is now considerable experimental evidence supporting such a link [237]. There is also growing evidence that patients susceptible to SD waves have hyperexcitable visual cortices [441].

The progression of the scotoma across the visual cortex can be modeled using a kinematic theory of wave propagation in two-dimensional excitable media [145]. Such a model describes the propagation of a wave front in terms of the motion of curves with free ends, without detailed knowledge of the underlying reaction–diffusion equations [426]. Wave propagation is analyzed by assuming that the normal velocity c of the wave depends solely on the front curvature and by taking into account an additional tangential velocity γ that describes the growth rate of the front at its open ends. To motivate the curvature dependence of the normal velocity, consider a 2D version of the FitzHugh–Nagumo equations (Sect. 2.3)

$$\frac{\partial v}{\partial t} = f(v,w) + D\nabla^2 v, \tag{9.57a}$$

$$\varepsilon^{-1}\frac{\partial w}{\partial t} = -w + v. \tag{9.57b}$$

In particular, consider a circular target pattern in which the leading edge of a traveling pulse forms a circle of radius R at time t, with R much larger than the width of the pulse. $K = 1/R$ is then the curvature of the circular front. Introducing polar coordinates (r, ϕ) with the origin at the center of the target pattern, we have

$$\frac{\partial v}{\partial t} = f(v,w) + \frac{D}{r}\frac{\partial v}{\partial r} + D\frac{\partial^2 v}{\partial r^2}, \tag{9.58a}$$

$$\varepsilon^{-1}\frac{\partial w}{\partial t} = -w + v. \tag{9.58b}$$

Since $\partial v/\partial r$ is negligible outside the transition layers of the pulse, we can replace D/r by D/R on the right-hand side of (9.58a). Writing the circular wave solution as $v = V(\xi)$, $w = W(\xi)$ with $\xi = r - ct$, yields the pair of equations

$$-(c + DK)V' = f(V,W) + DV'', \tag{9.59a}$$

$$-\frac{c}{\varepsilon}W' = -W + V, \tag{9.59b}$$

with $V' = dV/d\xi$, etc. These equations are equivalent to the 1D FN equations in the moving frame of a pulse traveling with speed $c_0 = c + DK$, under the rescaling $\varepsilon \to (c + DK)\varepsilon/c$. Approximating c_0 by the singular solution of the 1D FN equations (see Sect. 2.3), we deduce that the speed of the circular front is a linear function of the curvature [426]

$$c(K) = c_0 - DK. \tag{9.60}$$

This result extends locally to a more general curved front, by partitioning the curve into small segments approximated by circular arcs. Assuming that there are no self-intersections, the curve can be represented in polar coordinates as $r = r(\phi)$ and there is now a phase-dependent curvature $K(\phi)$. Unfortunately, there is no general theory for the form of the tangential velocity γ. Following [145], we will take γ to be a linearly decreasing function of the curvature at the end point (Fig. 9.16):

$$\gamma(K) = \gamma_0(1 - K/K_c), \tag{9.61}$$

up to some critical curvature K_c.

If both $c(K)$ and $\gamma(K)$ are known, then one can determine the evolution of an arbitrary initial excitation pattern, at least numerically. An analytical solution is only possible when c and γ are linear function of the curvature and the initial front is circular symmetric. The basic kinematic theory proceeds as follows [145, 426]. Suppose that the curvature of a point a on the front at time t is K_a, and introduce a local polar coordinate system (r, ϕ) with the origin at the center of curvature from point a. Note that $r' = r'' = 0$ at a where $r' = \partial r/\partial\phi$. The curve in a neighborhood of a is given by a function $r(\phi, t)$ with $r(0,t) = r_a = 1/K_a$. Over a short time interval dt, the neighborhood of point a moves to a neighborhood of point b with the new curve segment

$$r(\phi, t + dt) = r(\phi, t) + c(\phi, t)dt, \quad c(\phi, t) = c(K(\phi, t)). \tag{9.62}$$

Given a local polar representation of a curve, its local curvature is given by the formula

$$K = \frac{r^2 + r'^2 - rr''}{[r^2 + r'^2]^{3/2}}. \tag{9.63}$$

The curvature K_b can then be determined by substituting for $r(\phi, t+dt)$ using (9.62), expanding to first order in dt, and setting $\phi = 0$:

$$K_b = K_a - \left(c(K_a)K_a^2 + K_a^2 \left.\frac{\partial^2 c}{\partial \phi^2}\right|_{\phi=0} \right) dt. \tag{9.64}$$

In order to integrate this equation, it is necessary to replace ϕ by the intrinsic arc-length coordinate l using $dl = r_a d\phi$. Assuming that a is an intrinsic distance l from one free end and taking $K_a = K(l,t)$, $K_b - K_a = dK(l,t)$ gives

$$dK = -\left[K^2 c(K) + \frac{\partial^2 c}{\partial l^2} \right] dt. \tag{9.65}$$

Note that the points a, b have different values for their intrinsic coordinate, since a circular wave propagating outwards increases its arc length and the arc length is measured with respect to an end point of a curve that may be growing or shrinking. It follows that the difference in arc length between the points a and b is

$$dl = \left[\int_0^l K(s,t)c(K(s,t))ds \right] dt + \gamma(0,t)dt. \tag{9.66}$$

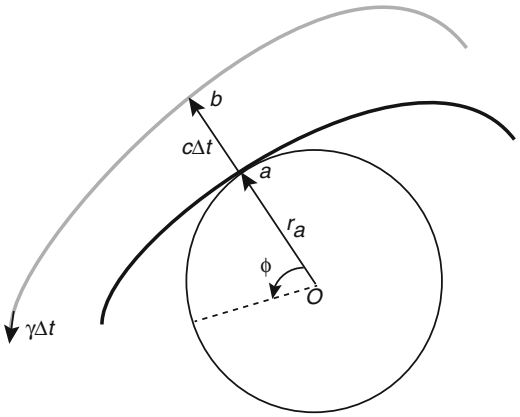

Fig. 9.16 Front position at two successive times $t, t+\Delta t$. Normal velocity at a given point on the front at time t is c and the tangential velocity at an end point is γ

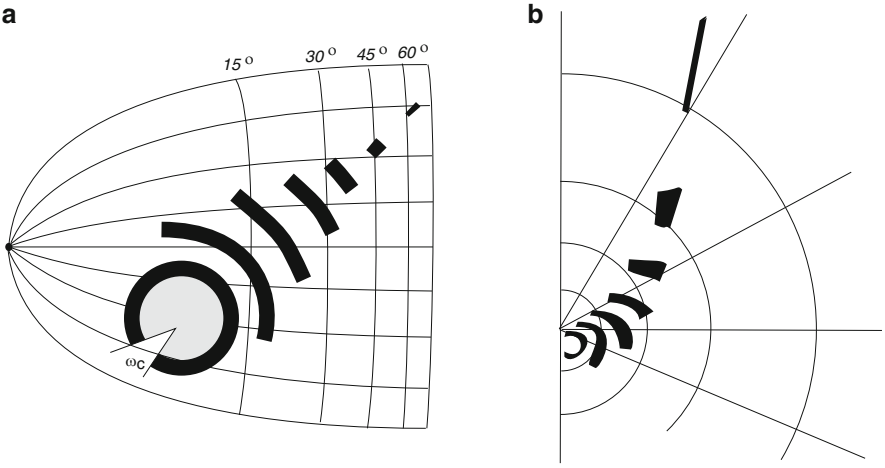

Fig. 9.17 (**a**) Propagation of a front across one half of primary visual cortex. Away from the focus, horizontal and vertical lines in cortex transform under the inverse retinotopic map to radii and concentric circles in the corresponding visual hemifield. (**b**) Progression of scotoma across the visual hemifield, which is obtained by applying the inverse retinotopic map to the propagating cortical front in (a)

Since $K = K(l,t)$, we have the alternative expression for dK,

$$dK = \frac{\partial K}{\partial l} dl + \frac{\partial K}{\partial t} dt. \tag{9.67}$$

with dl given by (9.66). Comparing (9.65) with (9.66) and (9.67) finally yields the integrodifferential equation [145, 426]

$$\frac{\partial K}{\partial t} + \left[\int_0^l K(s,t) c(K(s,t)) ds + \gamma(0,t) \right] \frac{\partial K}{\partial l} = -c(K) K^2 - \frac{\partial^2 c}{\partial l^2}. \tag{9.68}$$

Dahlem and Muller applied the above kinematic theory to a circular arc propagating in the visual cortex under the assumptions that $c \approx c_0$ and γ are given by (9.61). The initial front is taken to be an arc of small radius r_0, which means that $K > K_c$ and $\gamma < 0$, that is, the end points, shrink as a function of time. Since the normal velocity is approximately independent of curvature, the front at time t is still a circular arc, but its arc length $l(t)$ has shrunk. Setting $K(t) = 1/r(t)$ with $r(t) = r_0 + c_0 t$ and $c(K) = c_0$, (9.66) implies that

$$\frac{dl}{dt} = \frac{V_0 l}{r} + G_0 \left(1 - \frac{1}{r k_c} \right).$$

Let $\omega = l/r$ be the angle subtended by the arc. Then

$$\frac{d\omega}{dr} = G_0 \left(\frac{1}{r} - \frac{1}{r^2 k_c} \right),$$

so that integrating with respect to r gives

$$\omega(r) = \omega(1/k_c) + G_0 \left(\ln(rk_c) + \frac{1}{rk_c} - 1 \right). \tag{9.69}$$

Using the analytical expression for the propagation of a circular arc across visual cortex, it is possible to determine the progression of a corresponding scotoma across the visual hemifield by applying the inverse retino-cortical map; see Sect. 8.1.1. This construction was carried out by Dahlem and Muller [145], and an illustrative sketch of their results is shown in Fig. 9.17. Finally, note that it is also possible to reproduce fortification patterns by introducing a region of enhanced neural excitability in the leading edge of the propagating front and superimposing this onto an orientation preference map. The resulting activity pattern of orientation-selective neurons was used to generate a set of population vectors that determined the distribution of oriented edges in the visual field [144].

9.4 Epilepsy

Epilepsy is the world's most common serious brain disorder, affecting around 50 million people [348, 430, 594]. Although there have been major advances in the medical and surgical treatment of epileptic seizures, almost a third of patients are untreatable and, even in successful cases, there can be serious side effects. Traditionally, epilepsy has been divided into two main categories: *primary generalized seizures* that arise simultaneously across large parts of the brain and *focal* or *partial* seizures that initially occur within a localized area of the brain but may subsequently propagate to other brain regions. If the latter does not cause a disruption of consciousness or cognitive abilities, then it is referred to as a simple seizure, otherwise it is called complex. In reality, there is probably a spectrum of different types of seizure with overlapping or related mechanisms for the initiation, propagation, and termination of the seizure [507]. Most studies of epilepsy have focused on the molecular, anatomical, and cellular processes underlying the development of epilepsy (epileptogenesis) and the initiation of seizures [125, 415]. Much of this work has been based on in vitro and in vivo animal models.

In the cortex and hippocampus, a stereotypical signature of focal epileptiform activity is the *interictal spike* that occurs between seizures (*ictal* activity). Interictal spikes are brief bursts of synchronized activity that last around 100 ms and which show up as sharp spikes in EEG recordings and as large amplitude depolarizations at the intracellular level. The spike appears to be initiated in deep layer V of the cortex, which contains a subset of pyramidal neurons that can intrinsically generate high-frequency bursts of up to five action potentials at 200–350 Hz and resemble in some ways the up states of the slow (< 1Hz) oscillations seen in cortical slices [549]; see Sect. 5.1. Recurrent excitation mediated by glutamatergic synapses then leads to a rapid spread of activity both vertically and horizontally through a large

local network of neurons. Activity is finally terminated by a combination of local recurrent GABA inhibition, Ca^{2+}-dependent AHP currents, and possibly synaptic depression [415]. In the hippocampus, pyramidal neurons in the CA3 region appear to be the substrate for intrinsic bursters. There are two competing theories for the primary cause of the large depolarization that initiates an interictal spike. The first assumes that there is an excessive synchronous synaptic activation of essentially normal pyramidal neurons due to rewiring of excitatory connections or removal of inhibition, for example, whereas the second proposes that the excitability properties of the neurons exhibiting strong depolarizations are altered such that normal synaptic drive results in an abnormal response. Until recently, the first theory was predominant, but now there is growing experimental evidence that several forms of epilepsy involve genetically determined ion channel defects that alter intrinsic excitability [41]. A third possible cause of epileptiform activity has also recently emerged, namely, neuron–astrocyte interactions [311, 564, 647, 668]. As discussed in Sect. 4.5, astrocytes are in a position to induce local synchronization of neurons via gliotransmission of glutamate and gap-junction coupling, which could be a precursor of larger-scale epileptiform activity. Alternatively, excessive swelling of astrocytes through the intake of water could reduce the volume of the extracellular space, thus increasing the concentration of extracellular K^+ and resulting in a depolarization of surrounding neurons, see also our discussion of spreading depression in Sect. 9.3.

Another ongoing debate concerns the precise role of interictal spikes in epileptogenesis? At the cellular level, the transition to seizure-like activity is typically associated with a prolonged depolarization and high-frequency repetitive firing around 10–20 Hz [415]. This *tonic phase* of a seizure is often followed by a period of irregular periodic bursts known as the *clonic phase*, in which there is very little action potential activity between bursts. Finally, the clonic phase is succeeded by a relatively quite *postictal depression phase*, during which the membrane potential is hyperpolarized. One hypothesis is that interictal spikes promote epileptogenesis, which is motivated by the observation that in certain animal models interictal spikes arise in a latent period prior to spontaneous seizures [599]. The main idea is that persistent abnormal interictal activity over a period of time leads to the formation of new excitatory connections and a strengthening of existing excitatory circuits via Hebbian plasticity, both of which ultimately reinforce the epileptic state. A completely opposite proposal is that although interictal spikes resemble patterns of spiking activity during seizures, they are independent events such that, in certain cases, the occurrence of interictal activity can actually reduce the likelihood of seizures; the latter effect has been observed in some brain slice experiments [18]. Yet another hypothesis is that deafferentation following brain trauma, for example, engages homeostatic synaptic plasticity mechanisms, which strengthen connections between intact neurons ultimately leading to seizures; interictal spikes could then be an intermediate stage in the progression to full seizure-like activity [290, 463]. In order to help resolve these issues, a number of computational models have explored how epileptogenesis depends on changes in network structure [159, 437, 451, 646].

Recent advances in human brain imaging such as functional magnetic resonance imaging (fMRI) and diffusion-tensor imaging, together with more traditional electrophysiological methods such as *electroencephalogram* recordings and chronic multielectrode implants, have led to a rapid increase in large-scale brain models of epilepsy [522, 594]. Broadly speaking, such models focus either on the global temporal dynamics of primary generalized seizures [60, 529, 582] or on characterizing the types of large-scale brain networks that support generalized seizures and the propagation of focal seizures [348, 375]. Two major types of generalized seizure are *tonic–clonic* (grand mal) seizures (see above) and *absence* (petit mal) seizures. The latter are generated in the thalamocortical loop, where reticular thalamic neurons are recruited by the neocortex and then inhibit thalamocortical neurons; see Sect. 5.4.3. The subsequent activation of various ionic currents generates post-inhibitory rebound bursting in the thalamocortical neurons, which project onto and excite neocortical neurons, resulting in a repeating cycle of spiking activity at around 3 Hz [415]. Since primary generalized seizures occur across large parts of the brain, it is reasonable as a first approximation to consider a nonspatial (mean-field) model of interacting neural populations (Chap. 6). The resulting model can be described by a system of ODEs, and bifurcation theory can be used to analyze the onset of seizures and to identify electrophysiological differences between tonic–clonic and absence seizures [60, 529, 582]. At least two different bifurcation scenarios have been identified [522]: (1) a change in some control parameter transitions the dynamical system from a normal state to a seizure state or (2) a change in a control parameter moves the brain from a normal state to a bistable state, in which both normal and seizure states coexist. In the latter case, the switch to the seizure state would require changes in some intrinsic physiological process such as the sleep–wake cycle or an external drive such as a stroboscope. One potential clinical application of these ODE models is that they generate time series that can be directly compared to EEG recordings and, in principle, could be used to predict the onset of seizures.

In this section, we focus on network aspects of epilepsy. (For a comprehensive review of computational models of epilepsy, see the book by Soltesz and Staley [594].) We begin by summarizing some basic network theory that is particularly relevant to brain networks. We then review recent work on identifying structural and functional brain networks that support epileptiform bursts and seizures. Ultimately, one would like to incorporate such findings in neural field models of wave propagation (Chap. 7), in order to better understand the spread of epileptiform activity in the human brain.

9.4.1 Basics of Network Theory

Much of the modern theory of networks was stimulated by the discovery of small-world networks in 1998 [662] and scale-free networks in 1999 [23], both of which will be defined below. There are a number of excellent reviews of modern network theory [52, 459], including several that are tailored towards brain networks [541,

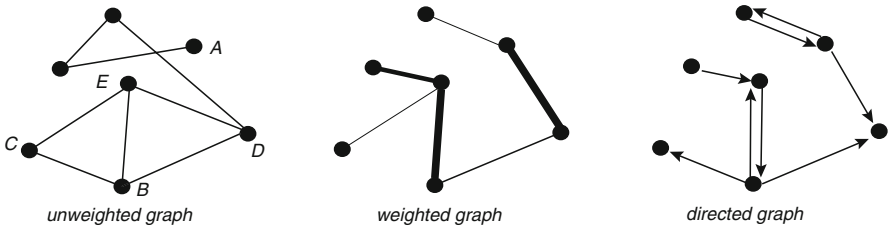

Fig. 9.18 Graph representation of a network in terms of vertices and edges. The vertex B in the unweighted graph has degree $k = 3$ with neighbors C, D, E. The clustering coefficient of B is 2/3, since there is a maximum of three edges between the neighbors but only CE and ED exist, whereas CD is missing. The shortest path length from A to C is $d = 5$

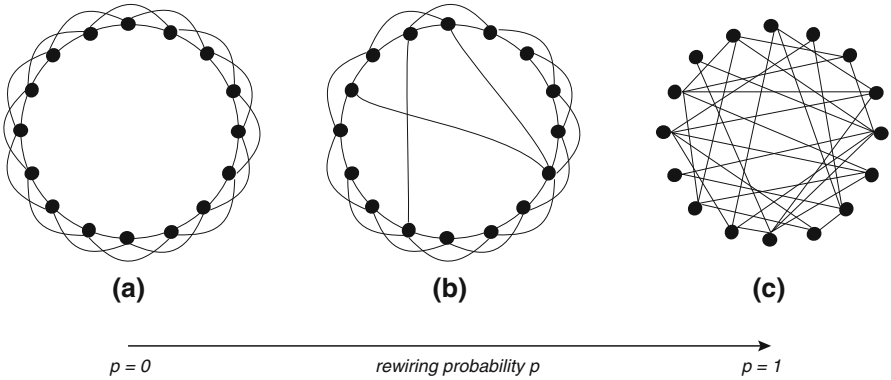

Fig. 9.19 Three basic network types illustrated by the ring network of Watts and Strogatz [662]. (**a**) The ordered network has $N = 16$ vertices and each vertex is connected to $k = 4$ neighbors. (**b**) and (**c**) The small-world and random networks are constructed by randomly reconnecting edges with rewiring probability p. For small values of p one obtains a small-world network, whereas a completely random network is created when $p = 1$

600]; we will follow [600]. An abstract representation of a network, whether it is a neural network, a social network, or a communications network, is a graph. The latter consists of a set or *vertices* (or nodes) and set of *edges* or connections. The connectivity structure of the graph is specified by an *adjacency matrix* $\mathbf{A}$ with $A_{ij} = 1$ if the vertices i and j are linked by an edge; otherwise $A_{ij} = 0$. The number of edges ending at given vertex is called the *degree* k of the vertex. The probability $P(k)$ that a randomly chosen vertex has degree k is called the degree distribution and is an important factor in determining network properties. If the direction of information flow along each edge is unimportant, then the graph is said to be *undirected* and $\mathbf{A}$ is a symmetric matrix; otherwise it is *directed*; in the latter case the degree distribution of incoming and outgoing edges may be distinct. Graphs where all edges are treated equally are said to be *unweighted*, whereas if each edge is assigned a weight to signify its strength or efficacy, then the graph is *weighted*; see Fig. 9.18.

There are two measures that are frequently used to characterize the structure of an unweighted graph, namely, the *clustering coefficient* C and the *characteristic path*

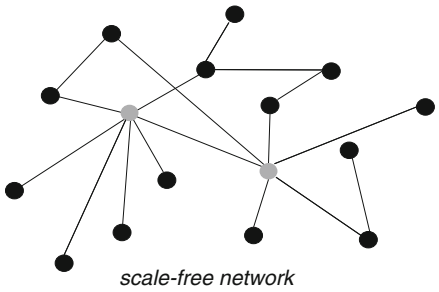

Fig. 9.20 Scale-free network with two hubs *shaded gray*

length L. The clustering coefficient C_i of a vertex i with degree k_i is typically defined as the ratio of the number of existing edges between neighbors of i (those directly connected to i) and the maximum possible number of such edges. Thus,

$$C_i = \frac{\sum_{j,k\in\mathcal{N}} A_{ij}A_{jk}A_{ki}}{k_i(k_i-1)}. \tag{9.70}$$

with $0 \leq C_i \leq 1$. An equivalent definition of C_i is that it determines the number of completed triangles with i as one of the vertices. The clustering coefficient of the graph is then obtained by averaging C_i over all vertices:

$$C = \frac{1}{N}\sum_{i=1}^{N} C_i. \tag{9.71}$$

The clustering coefficient is a local measure of network structure that characterizes the degree of resilience to random errors, since if $C \approx 1$, then removal of a single vertex has a minimal affect on the connectivity pattern of the other vertices. The second important measure of an unweighted graph is the characteristic path length. The path length or distance d_{ij} between two vertices i and j is the minimal number of edges that have to be traversed in order to go from i to j. The characteristic path length of a graph is then defined to be the mean of the path lengths between all vertex pairs:

$$L = \frac{1}{N(N-1)}\sum_{i,j,i\neq j} d_{ij}. \tag{9.72}$$

Using the degree distribution, clustering coefficient, and path length, one can distinguish between four different types of graph: ordered, small world, random, and scale-free. The first three cases can be illustrated using a 1D network on a ring, which was introduced by Watts and Strogatz [662], see Fig. 9.19. Initially each vertex is connected to k nearest neighbors ($k/2$ on either side) to form an *ordered network*. (Higher-dimensional versions of an ordered network could be generated using a regular lattice.) Ordered networks have a high C and a high L; in the ring network of Fig. 9.19a with $k = 4$ and $N = 16$, we have $C = 3/4$ and $L = N/2k$. Now suppose that with a probability p, edges are chosen at random, detached at one end, and then reconnected to another, randomly chosen vertex. For small p, one thus obtains a *small-world network*, which has a C close to an ordered network but a very small path length close to that of a random network. As p is increased, more

and more edges are randomly reconnected until finally all connections are random when $p = 1$. A random network has small C and small L. The fourth type of network is a *scale-free network*, which has a power-law degree distribution $P(k)$. This was originally formulated in terms of model for network growth by Barabasi and Albert [23]. They assumed that the probability that a newly added edge will connect to a vertex depends upon the current degree of the edge. In other words, vertices with a large number of edges (large degree) are more likely to be assigned even more edges. A network with this form of growth are characterized by a degree distribution of the form $P(k)) \sim k^{-1/\alpha}$; the original scale-free network of Barabasi and Albert has $\alpha = 3$. It turns out that many real-world networks appear to be scale-free, including the World Wide Web and collaboration networks of researchers. Scale-free networks not only can have very small path lengths [$L \sim \ln(\ln(N))$], but may also have a smaller clustering coefficient than small-world networks. Another interesting feature of scale-free networks is that they typically have a few vertices with extremely high degrees, which act as network *hubs*; see Fig. 9.20.

9.4.2 Epilepsy and Network Structure

One major research topic in modern network theory is the relationship between topological network characteristics and network dynamics, particularly synchronization [52]. A number of studies have investigated how the synchronization of coupled conductance-based or integrate-and-fire (IF) neurons depends on the rewiring probability of a small-world network [353, 409, 535]. Here the neural oscillators are placed at the vertices of the graph and the edges correspond to synaptic connections. Roughly speaking, ordered networks exhibit coherent oscillations but slow system response, whereas random networks have fast response properties but cannot support coherent oscillations. On the other hand, small-world networks support coherent oscillations and a fast system response. The dependence of synchronization on network topology has also been investigated within the context of epilepsy [159, 437, 451, 646]. In particular, Netoff et al. [451] based their study on results from hippocampal slice experiments indicating that short synchronous bursts tend to be seen in the CA3 region, where there is a relatively high degree of recurrent excitation, whereas seizure-like activity is found in the more sparsely connected CA1 region [450]. They modeled a small-world ring network (with $N = 3000$; $k = 30$ for CA1 and $k = 90$ for CA3) consisting of various types of stochastic model neurons such as IF and Hodgkin–Huxley. The neurons were assumed to be initially in a quiescent state, so that network activity was kindled by spontaneous action potentials that propagated as waves around the ring; the pattern of activity that emerged then depended on the number of long-range connections, as well as the interplay between noise and refractoriness. It was found that as the rewiring probability was increased, the model network displayed normal spiking behavior (low, sustained population firing rate), then seizure-like activity (significantly higher, sustained firing rates with a relatively low level of coherence), and finally bursting (waxing and waning of synchronous activity). Moreover, the transition from seizures

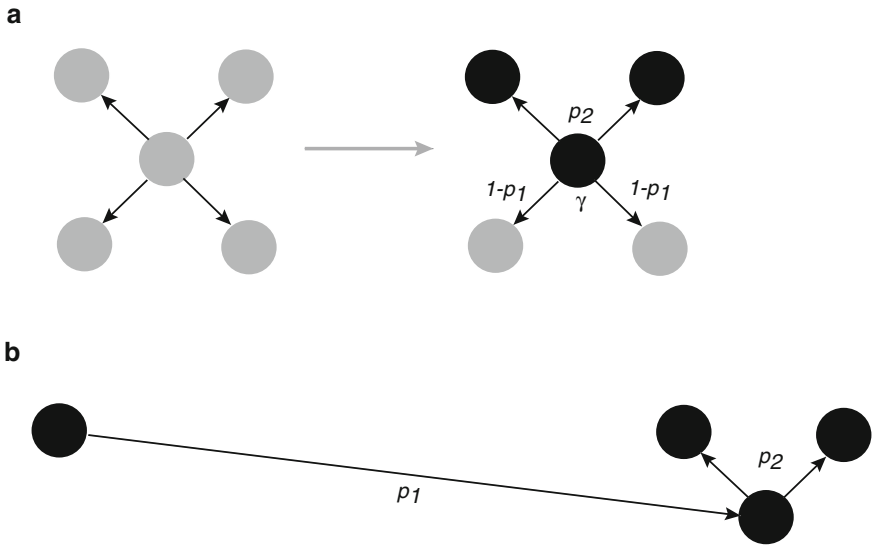

Fig. 9.21 Two mechanisms for spontaneous wave generation in the model of Netoff et al. [451]. Excitable (active) neurons are indicated by *gray* (*black*) disks. (**a**) An excitable neuron fires spontaneously at a rate γ and triggers at least two of its neighbors to fire with probability p_2: the probability that a neighbor does not fire is $1 - p_1$. (**b**) An active neuron with a random long-range connection induces an excitable neuron to fire with probability p_1, which in turn triggers at least two of its neighbors to fire with probability p_2

to synchronized bursting occurred at a lower value of p for higher degree k, that is, for the CA3 model.

Netoff et al. [451] also introduced a reduced model of propagating activity, under the assumption that the number of neurons N is much larger than the number of refractory or active neurons. This model takes the form of a discrete birth–death process for the number of spontaneous waves X_n at the nth time step:

$$X_{n+1} = f(X_n) = X_n + \omega_+(X_n) - \omega_-(X_n), \tag{9.73}$$

where $\omega_\pm$ are the birth and death rates. Suppose that each neuron in the network has k neighbors and if a given presynaptic neuron fires then there is a probability p_1 that this induces a given postsynaptic neuron to fire. A local spontaneous wave is generated if at least two neighboring postsynaptic neurons fire (see Fig. 9.21), with associated probability

$$p_2 = 1 - (1 - p_1)^k - kp_1(1 - p_1)^{k-1}.$$

It follows that the rate at which new waves are generated in one time step by local interactions is

$$\Gamma_n = \gamma E_n p_2,$$

where E_n is the number of excitable neurons and γ is the spontaneous rate at which each neuron fires. The latter is taken to be

$$E_n = N - \alpha X_n(1+R). \tag{9.74}$$

Here $\alpha = k/2 - 1$ is the mean number of active neurons in a wave front and R is the number of time steps each neuron remains refractory in the wake of a wave. A second contribution to the birth rate comes from the long-range connections in the ring network, which takes the form

$$\hat{\Gamma_n} = 2\alpha X_n k p \left(\frac{p_1 p_2 E_n}{N} \right).$$

The first factor is the number of long-range connections with active presynaptic neurons for a given rewiring probability p and the second factor is the probability that such a connection results in the formation of a wave emerging from the postsynaptic neuron. Putting these results together, we have

$$\omega_+(X_n) = \Gamma_n + \hat{\Gamma_n} = E_n \left[\frac{2\alpha X_n k p p_1 p_2}{N} + \gamma p_2 \right]. \tag{9.75}$$

Since E_n is an affine function of X_n, the total birth rate is a quadratic function of X_n. Finally, the death rate is assumed to be

$$\omega_-(X_n) = \frac{2\alpha X_n}{E_n}, \tag{9.76}$$

and is based on an estimate of how often waves collide and annihilate.

Sketches of the function f for various rewiring probabilities are shown in Fig. 9.22. For sufficiently small rewiring probability p there exists a unique stable

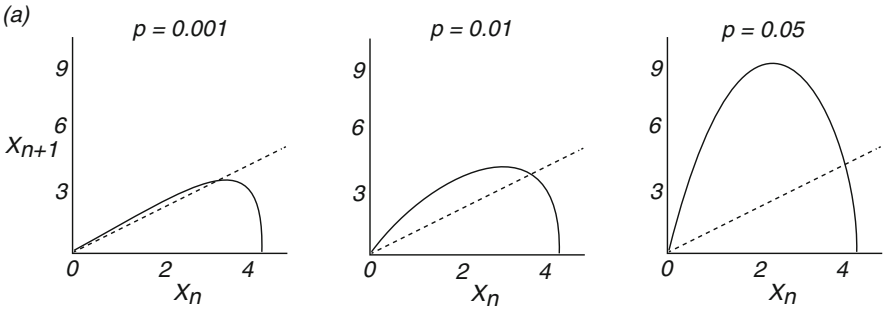

Fig. 9.22 Birth–death process for activity in a ring network [451]. The map $f : X_n \to X_{n+1}$ describing the evolution of the number X_n of spontaneous waves is sketched for several values of the rewiring probability p. Other parameter values are $\gamma = 0.0315, p_1 = 0.025, k = 90, N = 3000$. There is a unique fixed point, which is weakly attracting for small p, strongly attracting for intermediate p, and unstable for large p

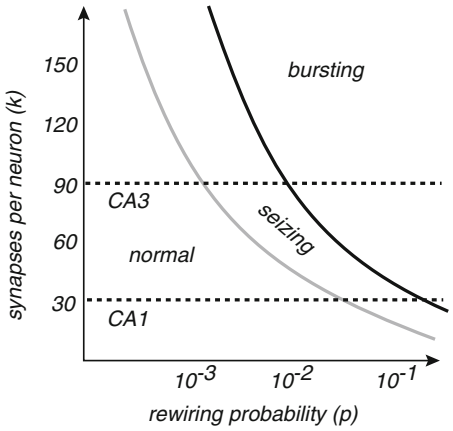

Fig. 9.23 Sketch of phase diagram for the reduced model of Netoff et al. [451]. The phase boundaries separating normal, seizing, and bursting states are plotted in the (p,k)-plane. The *black* (*gray*) boundary curve is obtained from the 1D map [$(R+1)$-dimensional map]. For a range of rewiring probabilities the CA3 network with $k = 90$ is in a bursting state, whereas the CA1 network with $k = 30$ is in a seizing state

fixed point $X^* = f(X^*)$, which is only weakly attracting. At each time step the number of waves remains approximately constant, that is, waves are rarely born or destroyed. This implies that there is a low rate of spontaneous wave generation consistent with normal brain activity. For larger p, the fixed point becomes strongly attracting and the number of waves increases, which is interpreted as a seizure state. Finally, for even larger values of p, the fixed point becomes unstable via a flip bifurcation, and new waves are generated rapidly, suggestive of a bursting state. (True population bursting cannot be realized in the reduced model under the restriction that the number of refractory neurons is much smaller than N, since termination of a population burst requires most of the network to enter a refractory state.)The one-dimensional map captures quite well the transition boundary between the seizing and bursting states. However, in order to capture the transition between the normal and oscillatory seizing state, it is necessary to consider a more accurate model of refractory dynamics by replacing (9.74) with

$$E_n = N - \alpha X_n - \alpha \sum_{m=1}^{R} X_{n-m}. \tag{9.77}$$

This leads to an $(R+1)$th-order map that can undergo a Hopf bifurcation resulting in stable oscillations. A typical phase diagram for the model is shown in Fig. 9.23.

Changes in network structure are not necessary, however, for abnormal rhythms to occur. Motivated by the observation that epileptiform bursting activity often arises following severe head trauma, Volman et al. [646] studied a computational model of traumatized cortex, in which a significant fraction of neurons had their afferent

inputs reduced (deafferented neurons). Hence, the model could be viewed as a population of intact neurons embedded in a sea of traumatized neurons. Homeostatic synaptic plasticity was incorporated into the model so that following deafferentation, the remaining intact neurons strengthened their connections within the intact subnetwork, as well as their efferents to traumatized neurons. The authors found that this resulted in the emergence of interictal bursts propagating across the cortical network, provided that the density of intact neurons was relatively high so that they could also trigger activity in deafferented neurons. Thus the transition to bursting involved a strengthening of the intact subnetwork rather than a topological restructuring. Indeed, the level of bursting was found to be weakly dependent on properties of the subnetwork such as its clustering coefficient and path length [646]; a much more critical factor was the density of intact neurons.

The above examples correspond to structural or anatomical network models, in which the vertices of a given network are taken to be individual neurons and the edges correspond to physical synaptic connections. At this microscopic scale, the only complete structural network that has been mapped is for the 302 neurons of the nematode worm *C. elegans* [669]. Such a feat remains intractable for the human brain, which consists of more than 10^{10} neurons and 10^{12} synapses, although non-invasive neuroimaging techniques such as *magnetic resonance imaging* (MRI) can be used to construct coarser-grained macroscopic structural networks in humans. An alternative representation of brain networks has been gaining increasing attention, namely, one involving functional networks [5, 598, 600]. A functional network represents the coupling between dynamical activity recorded from separate brain areas. It is based on the assumption that statistical correlations between the time series of electrophysiological or metabolic activity reflect functional interactions between neurons or populations of neurons in different brain regions. Clearly functional connectivity depends on the underlying structural connectivity, but they need not be identical. A variety of neuroimaging methods have been used to construct functional networks at different spatial and temporal scales, ranging from single unit recordings to fMRI. One of the ongoing challenges in establishing a functional brain network is choosing the most appropriate coupling measure (two-point correlations, Granger causality) and determining the threshold value above which the level of coupling constitutes an edge [500]. Roughly speaking, experimental observations of focal seizures indicate that functional networks acquire larger path lengths and clustering coefficients at seizure onset and become more small world during seizure propagation and more random at seizure termination [348]. However, contradictory results have also been obtained, probably reflecting the fact that epilepsy is a complex, heterogeneous phenomenon.

9.5 Neuronal Avalanches, Criticality, and Branching Processes

Another characterization of large-scale brain activity that has gained prominence in recent years is the extent to which the cortex operates close to criticality [29, 31, 113, 508, 573]. Roughly speaking, criticality at the network level means that the

network is in a balanced state with regard to the propagation of activity induced by the spontaneous spiking of individual neurons. As a simple *gedanken* experiment [573], imagine a fully connected network of N neurons and let p denote the probability that each neuron in the network fires in response to a single spike. The parameter p represents a variety of neurobiological factors that could contribute to the efficacy of a single action potential, including the relative number of excitatory and inhibitory neurons, the strength of excitatory versus inhibitory synapses, the intrinsic excitability of neurons, and the strength of neuromodulators. Clearly, if $p \ll 1/N$, then activity in the network quickly dies out, and it is said to be in the *subcritical regime*. On the other hand, if $p \gg 1/N$, then a single spike almost surely ignites a runaway chain of spiking events that never terminates, and we have a *supercritical regime*. Finally, if $p = 1/N$, then one spike is likely to cause one subsequent spike, so that there is reverberating activity in the network that does not overwhelm the network with a hypersynchronous state—the *critical* regime. Within the context of epilepsy, the basic idea is that the normal brain operates close to a critical state, whereas the epileptic brain deviates significantly from criticality during seizures, due to a failure in the underlying homeostatic mechanisms that maintain the critical state [291, 418].

The concept of criticality has its origins in the statistical physics of equilibrium phase transitions. A classical example is the phase transition from paramagnetism to ferromagnetism in an iron bar magnet as the temperature T crosses a critical threshold from above, known as the Curie temperature T_c. The *Ising model* treats the bar magnet as a lattice of electrons, each of which can be in one of two "spin" states represented by an arrow pointing up (north) or pointing down (south)—the arrows can be viewed as microscopic bar magnets. Nearest-neighbor interactions between the spins favor spin alignment (order), whereas thermal fluctuations favor disalignment (disorder). Both processes occur in order to minimize the free energy of the system, the first by reducing the interaction energy and the second by increasing the entropy. At low temperatures ($T < T_c$), the ordering effects of coupling dominate and the iron bar exhibits macroscopic magnetization due to most spins pointing in the same direction; see Fig. 9.24. On the other hand, at high temperatures ($T > T_c$) the disordering effects of thermal fluctuations win out and the spins point in random directions so there is no net magnetization. At the critical point $T = T_c$ there is a

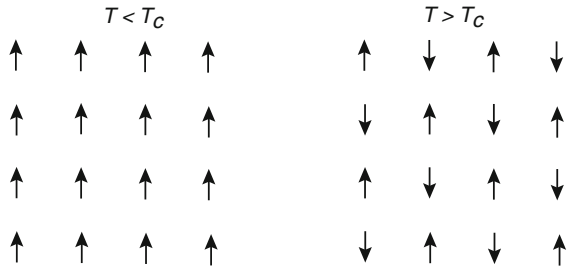

Fig. 9.24 Diagram illustrating an ordered ($T < T_c$) and a disordered ($T > T_c$) alignment of spins in the 2D Ising model, where T_c is the Curie temperature at criticality

balance between the two effects. (Technically speaking, this so-called second-order phase transition occurs on a 2D or 3D lattice but not a 1D lattice.) Although there is now no global order, there will be local domains where all the spins point up and other domains where all the spins point down. At the critical temperature there is a broad distribution of domain sizes, and the domains are themselves dynamically shifting and changing size. An important signature of criticality in equilibrium phase transitions is that various physical quantities exhibit power-law behavior. In the case of the Ising model, this includes the distribution of domain sizes and the two-point correlation matrix, which is defined according to

$$C_{ij} = \langle (s_i - \langle s_i \rangle)(s_j - \langle s_j \rangle) \rangle. \tag{9.78}$$

Here $s_i = \pm 1$ denotes the up/down state of the spin at lattice site i, and the angled brackets indicate time averaging. Thus $(s_i - \langle s_i \rangle)$ represents the size of fluctuations of the ith spin about its average at a given time. It follows that C_{ij} will only be large if s_i and s_j both fluctuate (some disorder) and these fluctuations are coordinated in the same direction (some order). As one might expect, C_{ij} only becomes large in a domain where these two effects are balanced, that is, close to criticality. One finds that $C_{ij} \sim \mathrm{e}^{-|i-j|/\Gamma}$, where Γ is known as the *correlation length* and

$$\Gamma \sim \frac{1}{|T - T_c|^{\alpha}}. \tag{9.79}$$

That is, the correlation length diverges as the system approaches the critical temperature T_c according to a power law with critical exponent α. (In fact, the critical exponent α differs on either side of the critical point.) An important feature of power laws is that they show no characteristic scale—they are scale-free. Moreover, they are a signature of universality, in the sense that a large class of systems that differ at the microscopic level exhibit the same macroscopic behavior close to criticality—they belong to the same *universality class*.

Extending the notion of criticality to biological networks such as the cortex is nontrivial, not only given the fact that these networks are complex and heterogeneous but also because they operate far from thermodynamic equilibrium. Nevertheless, criticality can be understood in a dynamical sense, as suggested by the previous

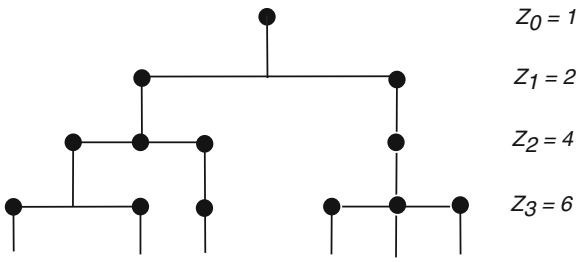

Fig. 9.25 Illustration of a branching process with three generations

gedanken experiment concerning spike avalanches, and evidence (but not proof) of criticality can be obtained by observing power laws in experimental data. The first substantive study of power-law distributions at the network level arose from multielectrode array recordings in cell cultures and acute brain slices [29]. Bursts of spontaneous activity were observed such that if the number of electrodes activated in each distinct burst were counted, then the burst sizes were distributed according to a power law. That is, denoting the burst size by l,

$$P(l) \sim l^{-\alpha} \tag{9.80}$$

with $\alpha \approx 1.5$. The index value of 1.5 can be understood using the theory of branching processes [264, 364]; see below. Since these initial findings, power-law distributions of these so-called neuronal avalanches have been observed in a variety of animal models, both in vitro and in vivo, using both multielectrode recordings and imaging methods such as fMRI; see the reviews [31, 573]. In spite of these results, there is still some controversy regarding their interpretation, both in terms of whether or not the statistical data is truly given by power laws and in terms of the causes of power-law-like behavior [28, 631]. Nevertheless, neuronal avalanches and the theory of branching processes provide another interesting framework for understanding the propagation of activity in networks. In the following we sketch how to obtain the observed power law from a classical branching process, following [364].

A simple branching process is a discrete Markov model for the evolution of a population, which in the neural context would correspond to the progression of spiking events in a neuronal avalanche. Let Z_n denote the number of members (events) of the nth generation (time step). Each member of the nth generation gives birth to a family, which could be empty, of members of the $(n+1)$th generation with the following assumption: the family sizes of the individuals of the branching process are independent identically distributed random variables [264]. An example realization of a branching process is shown in Fig. 9.25. A useful method for analyzing a branching process is to use generating functions. Let $G_n(s) = \mathbb{E}(s^{Z_n})$ be the generating function of the random variable Z_n with probability distribution $\mathbb{P}(Z_n = m)$. A number of results can now be established.

1. *Recursive structure of generating functions.* Each member of the $(n+1)$th generation has a unique ancestor in the nth generation such that

$$Z_{n+1} = X_1 + X_2 + \ldots + X_{Z_n},$$

where X_i is the size of the family produced by the ith member of the mth generation. It follows that

$$\begin{aligned} G_{n+1}(s) &= \mathbb{E}(s^{Z_{n+1}}) = \mathbb{E}(s^{X_1+\ldots+X_{Z_n}}) \\ &= \sum_{n=0}^{\infty} \mathbb{E}(s^{X_1+\ldots+X_m} | Z_n = m)\mathbb{P}(Z_n = m) \end{aligned}$$

$$
\begin{aligned}
&= \sum_{n=0}^{\infty} \mathbb{E}(s^{X_1} s^{X_2} \ldots^{X_m} | Z_n = m) \mathbb{P}(Z_n = m) \\
&= \sum_{n=0}^{\infty} \left[\prod_{j=1}^{m} \mathbb{E}(s^{X_j}) \right] \mathbb{P}(Z_n = m) \\
&= \sum_{n=0}^{\infty} [G_1(s)]^m \mathbb{P}(Z_n = m) = G_n(G_1(s)).
\end{aligned}
$$

Iterating this resulting and dropping the subscript on G_1, we have the recurrence relation

$$G_n(s) = G_{n-1}(G(s)) = G(G(\ldots(G(s))\ldots)). \tag{9.81}$$

2. *Mean and variance.* Let $\mu = \mathbb{E}(Z_1)$ and $\sigma^2 = \mathrm{var}(Z_1)$. In order to determine the mean and variance of Z_n, we use the recursive structure of the generating functions. First,

$$\mathbb{E}(Z_n) = G_n'(1) = \frac{d}{ds} G(G_{n-1}(s)) \bigg|_{s=1} = G'(1) G_{n-1}'(s) = \mu G_{n-1}'(s).$$

Iterating this result shows that

$$\mathbb{E}(Z_n) = \mu^n. \tag{9.82}$$

Similarly,

$$\mathbb{E}(Z_n(Z_n - 1)) = G_n''(1) = G''(1) G_{n-1}'(1)^2 + G'(1) G_{n-1}''(1).$$

This gives the iterative result

$$\mathrm{var}(Z_n) = \sigma^2 \mu^{2n-2} + \mu \, \mathrm{var}(Z_{n-1}),$$

from which one finds that

$$\mathrm{var}(Z_n) = \begin{cases} n\sigma^2 & \text{if } \mu = 1 \\ \dfrac{\sigma^2(\mu^n - 1)\mu^{n-1}}{\mu - 1} & \text{if } \mu \neq 1. \end{cases} \tag{9.83}$$

3. *Total number of individuals.* Let T_n be the total number of individuals up to and including the nth generation. Then

$$
\begin{aligned}
\mathbb{E}(T_n) &= \mathbb{E}(Z_0 + Z_1 + Z_2 + \ldots + Z_n) \\
&= 1 + \mathbb{E}(Z_1) + \mathbb{E}(Z_2) + \ldots + \mathbb{E}(Z_n) \\
&= 1 + \mu + \mu^2 + \ldots + \mu^n \\
&= \begin{cases} \frac{\mu^{n+1} - 1}{\mu - 1}, & \mu \neq 1, \\ n + 1, & \mu = 1. \end{cases}
\end{aligned}
$$

It follows that

$$\lim_{n\to\infty} \mathbb{E}(T_n) = \begin{cases} \infty, & \mu \geq 1, \\ \frac{1}{1-\mu}, & \mu < 1. \end{cases}$$

Let $H_n(s) = \mathbb{E}(s^{T_n})$ be the generating function for the random variable T_n. The generating functions satisfy the recurrence relation

$$H_{n+1}(s) = sG(H_n(s)). \tag{9.84}$$

4. *Probability of extinction.* One important property of a branching process is whether or not it eventually becomes extinct, that is, $Z_n = 0$ for some finite n. We can define the probability of extinction η according to

$$\eta = \lim_{n\to\infty} \mathbb{P}(Z_n = 0). \tag{9.85}$$

It can be shown that η is the smallest nonnegative root of the equation $s = G(s)$. Moreover, $\eta = 1$ if $\mu < 1$ (extinction occurs almost surely), whereas $\eta < 1$ if $\mu > 1$ (there is a nonzero probability that there is persistent growth). Moreover, if $\mu = 1$, then $\eta = 1$ provided that the variance of the family size distribution has a strictly positive variance. In light of our discussion of criticality, $\mu = 1$ is a critical point separating a subcritical regime ($\mu < 1$) from a supercritical regime ($\mu > 1$).

For the sake of illustration, consider a geometric branching process where the distribution of family sizes is given by $\mathbb{P}(Z_1 = k) \equiv f(k) = qp^k$ with $q = 1 - p$. In this case, one can calculate the generating function and other quantities explicitly:

$$G(s) = q(1-ps)^{-1}, \quad \mu = \frac{p}{q}, \quad \sigma^2 = \frac{p^2}{q^2} + \frac{p}{q}. \tag{9.86}$$

Moreover, it can be shown by induction that

$$G_n(s) = \begin{cases} \dfrac{n-(n-1)s}{n+1-ns} & \text{if } p = q = \frac{1}{2}, \\ \dfrac{q[p^n - q^n - ps(p^{n-1} - q^{n-1})]}{p^{n+1} - q^{n+1} - ps(p^n - q^n)} & \text{if } p \neq q. \end{cases} \tag{9.87}$$

It follows that

$$\mathbb{P}(Z_n = 0) = G_n(0) = \begin{cases} \dfrac{n}{n+1} & \text{if } p = q, \\ \dfrac{q(p^n - q^n)}{p^{n+1} - q^{n+1}} & \text{if } p \neq q, \end{cases} \tag{9.88}$$

and, hence, $\eta = 1$ if $p \leq q$ and $\eta = q/p$ if $p > q$. We conclude that for a geometric branching process, extinction occurs almost surely if $\mathbb{E}(Z_1) = \mu = p/q \leq 1$,

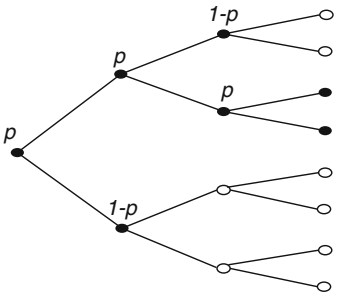

Fig. 9.26 Branching process for the propagation of activity during an avalanche. Activity propagates to a pair of descendants with probability p, whereas it fails to propagate with probability $1-p$. *Black* nodes are active and *white* nodes are inactive

otherwise there is a finite probability of persistent growth. In light of our discussions of criticality and avalanches, we can identify the regime $p < q$ as subcritical, the regime $p > q$ as supercritical, and the point $p = q = 1/2$ as critical.

In the case of neuronal avalanches, a more appropriate branching process is one where each node has two descendants and activity can propagate to the descendants with probability p [29, 364]; see Fig. 9.26. Thus Z_n denotes the number of active members of the nth generation (burst size) with $0 \leq Z_n \leq 2^n$. For this process $f(k) = (1-p)\delta_{k,0} + p\delta_{k,2}$. It follows that

$$G(s) = 1 - p + ps^2, \quad \mu = 2p, \quad \sigma^2 = 4p(1-p), \tag{9.89}$$

and the critical point is at $p = 1/2$. The total number of events T_n is the burst size, whose distribution can be determined from the generating function $H_n(s)$. For the given branching process, $H_n(s)$ satisfies the recurrence relation (see (9.84))

$$H_{n+1}(s) = s[(1-p) + pH_n(s)^2]. \tag{9.90}$$

The solution of this recurrence relation for $n \geq 1$ is approximately [264, 364]

$$H_n(s) = \frac{1 - \sqrt{1 - 4s^2p(1-p)}}{2sp}. \tag{9.91}$$

Expanding as a power series in s and comparing with the definition of $H_n(s)$, one finds that for $1 \ll l < n$, the distribution of avalanche sizes l is given by

$$P(l) \equiv \mathbb{P}(T_n = l) = \frac{\sqrt{2(1-p)/p}}{\sqrt{\pi} l^{3/2}} \mathrm{e}^{-l/l_c(p)}, \tag{9.92}$$

with

$$l_c(p) = -\frac{2}{\ln[4p(1-p)]}. \tag{9.93}$$

For $l > n$ one finds that $P(l)$ decays exponentially. This then establish the 3/2 power-law behavior at the critical point $p = 1/2$, since $1/l_c(1/2) = 0$ and

$$P(l) \sim \sqrt{\frac{2}{\pi}} l^{-3/2} \tag{9.94}$$

for $1 \ll l < n$ and n is large. Also note that at criticality $\mu = 1$, which is consistent with the experimental observation that the ratio of the number of active descendant electrodes to the number of active ancestor electrodes is around one [29].

9.6 Protein Aggregate Spreading in Neurodegenerative Diseases

There is growing experimental evidence suggesting that there are parallels between prion disease pathogenesis and other, more common neurodegenerative diseases that are typically not thought to be infectious, including Alzheimer's disease, Parkinson's disease, frontal-lobe dementia, and Huntington's disease [284, 300, 371]. Prion diseases are fatal neurodegenerative diseases that rose to prominence during the BSE epidemic in England in the 1980s, where there was thought to be a possible transmission pathway from infected animals to humans. Unlike classical infective agents such as bacteria or viruses, prion diseases involve an agent consisting solely of a misfolded protein or *prion* [513]. Pathologically folded prion protein (PrP*) corrupts normally folded PrP via a fixed conformational change, which usually leads to the formation of protein aggregates, and this process propagates across brain cells at a speed of around 0.1–1mm per day. The initial cause could be an external infective agent or, more commonly, the spontaneous formation of PrP* aggregates. Recent molecular, cellular, and animal studies suggest that the intercellular propagation of protein misfolding also occurs for a variety of aggregate-prone proteins that are linked to noninfective neurodegenerative diseases [262, 533, 565, 566]. These include amyloid-β and tau (Alzheimer's disease), α-synuclein (Parkinson's diseases), and huntingtin (Huntington's disease).

The conformational change of a normally folded protein tends to occur via direct contact with a misfolded protein aggregate. This process is commonly called *aggregate seeding* or *seeded polymerization* [300]. If the resulting protein aggregate is small, then it remains soluble, whereas larger aggregates precipitate out of solution under physiological conditions. Two distinct morphological types of aggregate can be identified: *amorphous aggregates* and *amyloid fibrils*. The former have an irregular granular appearance when viewed under an electron microscope, whereas the latter consist of highly ordered and repetitive structures in which all the polypeptides adopt a common fold. Amyloid fibrillogenesis consists of multiple stages, involving nucleation, polymerization, elongation, and aggregate seeding. It used to be thought that mature amyloid fibrils were ultimately responsible for the toxic effects of protein aggregates. However, there is a widening consensus that it is the non-fibrillar assemblies in early stages of amyloid formation that are particularly toxic. The monomers of proteins such as tau and α-synuclein are found within the cytosol of cells. This means that the spread of such protein aggregates

requires the internalization of the corresponding fibrils in order to seed the formation of new aggregates. The newly formed aggregates must then be released back into the extracellular space. The precise mechanisms of internalization and externalization are currently unknown. Such processes are not required for prions and amyloid-β within cells, since they are both exposed to the extracellular space. Hence, the latter proteins can diffuse intracellularly and then infect a neighboring cell directly.

So far there has been very little modeling work on the spread of protein aggregates. Here we will review a reaction–diffusion model for the propagation of prion disease in the brain [411]. The simplest version of the model uses a heterodimer model for prion–prion interactions, in which one molecule of normal PrP (denoted by A) combines with one molecule of PrP* (denoted by B) to form two molecules of B:

$$A + B \to AB \to BB \to B + B. \tag{9.95}$$

For simplicity, this is represented as a single-step reaction with rate k_{AB}:

$$A + B \underset{k_{AB}}{\to} 2B. \tag{9.96}$$

The molecules also degrade at rates k_A and k_B, respectively, with $k_A > k_B$ since PrP* is more resistant to the action of proteases. If the reaction kinetics are combined with classical diffusion on a 1D domain $x \in [0, L]$, then we obtain the reaction–diffusion system

$$\frac{\partial a}{\partial t} = \gamma_0 - k_A a - k_{AB} ab + D_A \frac{\partial^2 a}{\partial x^2} \tag{9.97a}$$

$$\frac{\partial b}{\partial t} = k_{AB} ab - k_B b + D_B \frac{\partial^2 b}{\partial x^2}, \tag{9.97b}$$

where $a(x,t)$ and $b(x,t)$ denote the concentration of normal and misfolded PrP at time $t > 0$ and location x. The corresponding diffusivities are D_A, D_B, and γ_0 represents a constant rate of production of PrP. Equations (9.97) are supplemented by no-flux boundary conditions at the ends of the domain. The resulting model belongs to the same class of PDE as the Fisher–KPP equation (3.44) and the CaMKII model (3.43) of Sect. 3.2. In particular, it supports a spreading wave in the form of a pulled front. Suppose that the system is initially in a stable, homogeneous steady-state $a(x,0) = a^* = \gamma_0/k_A, b(x,0) = 0$. A local transient increase in b at one end of the domain will induce a propagating front whose speed can be determined by linearizing about the steady state in the leading edge of the wave where $a \approx a^*$ (Sects. 3.2 and 3.3). The resulting linear equation for b is

$$\frac{\partial b}{\partial t} = Kb + D_B \frac{\partial^2 b}{\partial x^2} \tag{9.98}$$

with $K = k_{AB} a^* - k_B$. Taking $b(x,t) = B(x - ct) = B(\xi)$ gives the ODE $-cB' = KB + DB''$. The latter has a solution of the form (neglecting boundary effects) $b(\xi) =$

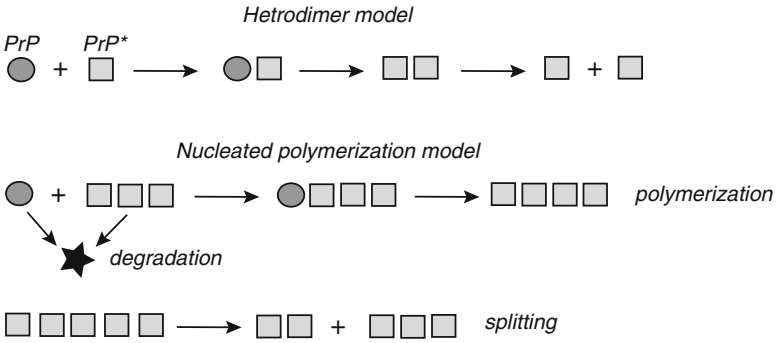

Fig. 9.27 Schematic illustration of the heterodimer and nucleated polymerization models of prion reaction kinetics

$Ce^{-\lambda\xi}$ with

$$c = c(\lambda) \equiv \frac{K}{\lambda} + D_B\lambda. \tag{9.99}$$

Finally, minimizing $c(\lambda)$ with respect to λ yields the minimum speed

$$c_{\min} = \sqrt{D_B K} = \sqrt{D_B(k_{AB}\gamma_0/k_A - k_B)}. \tag{9.100}$$

This is the asymptotic speed of the front induced by a localized perturbation.

The above model suffers from at least two major simplifications, as highlighted by Matthaus [411]. First, the heterodimer model is not a good description of aggregate seeding, which involves the interaction between PrP* polymers of various lengths and normal PrP monomers. Second, as in the case of cortical spreading depression (Sect. 9.3), the brain should really be treated as a highly heterogeneous medium. Focusing on the first issue, one can replace the heterodimer reaction scheme by a nucleated polymerization model [263, 408], in which the infective agent is not a single molecule of PrP* but a PrP* oligomer (short polymer of misfolded PrP). Consider, in particular, the model of Masel et al. [408], which is illustrated in Fig. 9.27. There are a number of steps in the formulation of the kinetic model:

1. Denote a PrP* polymer of size m (m monomer subunits) by B_m. Polymers below a critical size n (the nucleation length) are unstable and are assumed to disintegrate instantaneously into m monomers ($m < n$). The nucleation of new stable PrP* polymers is neglected.
2. When a PrP molecule A comes in contact with a PrP* polymer of size m, $m \geq n$, it forms a polymer of size $m+1$:

$$B_m + A \underset{k_{AB}}{\rightarrow} B_{m+1}$$

with the rate k_{AB} independent of m.

3. A polymer of size $m, m \geq n$, can split into two pieces of sizes $m-k$ and k:

$$B_m \underset{\beta}{\to} B_{m-k} + B_k$$

with the rate β independent of m and k. If the resulting pieces are smaller than the nucleation length, then they immediately disintegrate.

4. PrP is produced at a rate γ_0 and degrades at a rate k_A. All PrP* polymers degrade at a rate k_B.

Let a be the concentration of PrP monomers and b_m denote the concentration of PrP* polymers of size m. Using the law of mass action, the above kinetic scheme can be expressed in terms of the following system of ODES [408]:

$$\frac{da}{dt} = \gamma_0 - k_A a - k_{AB} a \sum_{m \geq n} b_m + 2\beta \sum_{k=1}^{n-1} k \sum_{m \geq k+1} b_m, \tag{9.101a}$$

$$\frac{db_m}{dt} = k_{AB} a (b_{m-1} - b_m) - k_B b_m - \beta(m-1) b_m + 2\beta \sum_{l \geq m+1} b_l \tag{9.101b}$$

for $m \geq n$, and $b_m \equiv 0$ for $m < n$. It turns out that this infinite hierarchy of equations can be reduced to a closed system of three ODES by summation. Defining

$$b = \sum_{m \geq n} b_m, \quad z = \sum_{m \geq n} m b_m, \tag{9.102}$$

one finds that

$$\frac{da}{dt} = \gamma_0 - k_A a - k_{AB} ab + n(n-1)\beta b, \tag{9.103a}$$

$$\frac{db}{dt} = -k_B b - \beta z - (2n-1)\beta b, \tag{9.103b}$$

$$\frac{dz}{dt} = k_{AB} ab - k_B z - n(n-1)\beta b. \tag{9.103c}$$

The reaction kinetics given by the system of (9.101) can be incorporated into a reaction–diffusion model for the spread of prion disease by adding the terms $D_A \partial^2 a/\partial x^2$ and $D_m \partial^2 b_m/\partial x^2$ to the right-hand sides of (9.101a) and (9.101b), respectively [411]. Numerical simulations confirm that the extended model also supports propagating fronts. (Note that since the cytosolic diffusion coefficient D_m will depend on polymer size m, it is not possible to use summation to reduce (9.103) to a small closed system of coupled RD equations.)

Finally, we briefly consider the issue of diffusion. The 1D model can capture the intracellular diffusion of prions along a single nerve. However, applying a homogeneous and isotropic 3D diffusion equation to the spread on larger spatial scales fails to take into account the fact that neurons form complex networks, which include both local connections to neighbors and long-range connections. That is, one has to consider epidemic diseases on complex networks such as the scale-free

and small-world networks defined in Sect. 9.4.1. Some insights into the spread of diseases on networks have been obtained by considering standard models of epidemics such as the susceptible–infected (SI) model [26, 411, 458]. In the latter model, each individual is represented by a vertex of the network, and the edges represent the connections between individuals along which the infection may spread. (In a prion model each vertex would be a neuron and each edge a nerve fiber, say.) The total population N (number of vertices) is kept fixed so that $N = S(t) + I(t)$, where $S(t)$ and $I(t)$ are the number of susceptible and infected individuals, respectively.

A first approach to analyzing the SI model is to use a mean-field description [26]. That is, all the vertices are treated equivalently, which means that the average density $i(t) = I(t)/N$ of infected individuals satisfies

$$\frac{di(t)}{dt} = \lambda \langle k \rangle i(t)[1 - i(t)]. \tag{9.104}$$

The above equation can be interpreted as follows: the growth rate of infected individuals is proportional to a constant spreading rate, λ, the density of susceptible vertices, $s(t) = 1 - i(t)$, and the number of infected individuals in contact with any susceptible vertex. The mean-field approximation takes the latter to be the product of the mean number of neighbors $\langle k \rangle$ and the average density $i(t)$. Note that if the initial density i_0 of infected individuals is small, then one can drop the quadratic term in (9.104) and deduce that the leading behavior at small times is $i(t) \sim i_0 e^{t/\tau_H}$ with $\tau_H = 1/(\lambda \langle k \rangle)$. The time constant τ_H determines the initial rate at which the disease spreads. The mean-field approximation does not take into account fluctuations arising from fluctuations in the degree k of vertices. In order to proceed further, it is necessary to consider the evolution equation for the average density of infected vertices of degree k, $i_k(t) = I_k(t)/N_k$, where N_k and I_k are the total number and infected number of k-vertices. Thus

$$\frac{di_k(t)}{dt} = \lambda k[1 - i_k(t)]\Gamma_k(t), \tag{9.105}$$

where $\Gamma_k(t)$ is the density of infected individuals that are neighbors of a k-vertex. As a further simplification, suppose that $\Gamma_k = \Gamma$ for all k (a so-called uncorrelated network). Let $P(k)$ be the degree distribution of the network (Sect. 9.4.1). The probability that a susceptible vertex is connected to an infected vertex of degree k' is proportional to the number of edges emanating from the latter. Since at least one edge is likely to be connected to another infected vertex, it follows that this number is $k' - 1$. One thus obtains the result [26]

$$\Gamma(t) = \frac{1}{\langle k \rangle} \sum_{k'} (k' - 1) P(k') i_{k'}(t). \tag{9.106}$$

Differentiate this equation with respect to t and use (9.105). Dropping quadratic terms in the early stages of the epidemic yields the pair of equations

$$\frac{di_k}{dt} = \lambda k \Gamma(t), \quad \frac{d\Gamma}{dt} = \lambda \left(\frac{\langle k^2 \rangle}{\langle k \rangle} - 1 \right) \Gamma(t). \tag{9.107}$$

Finally, assume uniform initial conditions $i_k(0) = i_0$ for all k. The pair of (9.107) can then be solved in terms of $i(t) = \sum_k P(k) i_k(t)$ according to

$$i(t) = i_0 \left[1 + \frac{\langle k \rangle^2 - \langle k \rangle}{\langle k^2 \rangle - \langle k \rangle} \left(\mathrm{e}^{t/\tau} - 1 \right) \right], \tag{9.108}$$

with new time constant

$$\tau = \frac{\langle k \rangle}{\lambda \left(\langle k^2 \rangle - \langle k \rangle \right)}. \tag{9.109}$$

In the case of a Poisson degree distribution for which $\mathrm{var}[k] = \langle k \rangle$, we recover the mean-field result $\tau = 1/(\lambda \langle k \rangle)$. On the other hand, for a scale-free network with $P(k) \sim k^{-\gamma}$, $2 < \gamma < 3$, we find that $\langle k^2 \rangle \to \infty$ as $N \to \infty$. In other words, for large scale-free networks, there is approximately an instantaneous rise in the number of infected.

References

1. Abbott, L.F., Marder, E.: Modelling small networks. In: Koch, C., Segev, I. (eds.) Methods in Neuronal Modelling, pp. 361–410, 2nd edn. MIT Press, Cambridge (1998)
2. Abbott, L.F., van Vresswijk, C.: Asynchronous states in networks of pulse–coupled oscillators. Phys. Rev. E **48**(2), 1483–1490 (1993)
3. Abbott, L.F., Fahri, E., Gutmann, S.: The path integral for dendritic trees. Biol. Cybern. **66**, 49–60 (1991)
4. Abbott, L.F., Varela, J.A., Sen, K., Nelson, S.B.: Synaptic depression and cortical gain control. Science **275**, 220–224 (1997)
5. Aertsen, A.M.H.J., Gerstein, G.L., Habib, M.K., Palm, G.: Dynamics of neuronal firing correlation: modulation of 'effective connectivity'. J. Neurophysiol. **61**, 900–917 (1989)
6. Alexander, G., Crutcher, M.: Functional architecture of basal ganglia circuits: neural substrates of parallel processing. Trends. Neurosci. **13**, 266–271 (1990)
7. Allard, J., Moginler, A.: Traveling waves in actin dynamics and cell motility. Curr. Opin. Cell Biol. **25**, 107–115 (2013)
8. Amari, S.: Dynamics of pattern formation in lateral inhibition type neural fields. Biol. Cybern. **27**, 77–87 (1977)
9. Andersen, S.S., Bi, G.Q.: Axon formation: a molecular model for the generation of neuronal polarity. Bioessays **22**, 172–179 (2000)
10. Andersen, P., Morris, R., Amaral, D., Bliss, T., O'Keefe, J.: The Hippocampus Book. Oxford University Press, Oxford (2008)
11. Angelucci, A., Levitt, J.B., Walton, E.J.S., Hupe, J.M., Bullier, J., Lund, J.S.: Circuits for local and global signal integration in primary visual cortex. J. Neurosci. **22**, 8633–8646 (2002)
12. Antic, S.D., Zhou, W.L., Moore, A.R., Short, S.M., Ikonomu, K.D.: The decade of the dendritic NMDA spike. J. Neurosci. Res. **88**, 2991–3001 (2010)
13. Arimura, N., Kaibuchi, K.: Neuronal polarity: from extracellular signals to intracellular mechanisms. Nat. Rev. Neurosci **8**, 194–205 (2007)
14. Armero, J., Casademunt, J., Ramirez-Piscina, L., Sancho, J.M.: Ballistic and diffusive corrections to front propagation in the presence of multiplicative noise. Phys. Rev. E **58**, 5494–5500 (1998)
15. Aronson, D.G., Weinberger, H.F.: Multidimensional nonlinear diffusion arising in population genetics. Adv. Math. **30**, 33–76 (1978)
16. Atay, F.M., Hutt, A.: Stability and bifurcations in neural fields with finite propagation speed and general connectivity. SIAM J. Appl. Math. **65**, 644–646 (2005)
17. Austin, T.D.: The emergence of the deterministic Hodgkin-Huxley equations as a limit from the underlying stochastic ion-channel mechanism. Ann. Appl. Prob. **18**, 1279–1325 (2006)
18. Avoli, M., de Curtis, G.B.M.: Do interictal spikes sustain seizures and epileptogenesis. Epilepsy Currents **6**, 203–207 (2006)

P.C. Bressloff, *Waves in Neural Media: From Single Neurons to Neural Fields*,
Lecture Notes on Mathematical Modelling in the Life Sciences,
DOI 10.1007/978-1-4614-8866-8, © Springer Science+Business Media New York 2014

19. Baer, S.M., Rinzel, J.: Propagation of dendritic spikes mediated by excitable spines: a continuum theory. J. Neurophysiol. **65**, 874–890 (1991)
20. Bair, W., Koch, C., Newsome, W.T., Britten, K.H.: Power spectrum analysis of bursting cells in area MT in the behaving monkey. J. Neurosci. **14**, 2870–2893 (1994)
21. Baladron, J., Fasoli, D., Faugeras, O., Touboul, J.: Mean field description of and propagation of chaos in recurrent multipopulation networks of Hodgkin-Huxley and FitzHugh-Nagumo neurons. J. Math. Neuro. **2**, 10 (2012)
22. Ballesteros-Yanez, I., Benavides-Piccione, R., Elston, G.N., Yuste, R., DeFelipe, J.: Density and morphology of dendritic spines in mouse neocortex. Neurosci. **138**, 403–409 (2006)
23. Barabasi, A.L., Albert, R.: Emergence of scaling in random networks. Science **286**, 509–512 (1999)
24. Baras, F., Mansour, M., Malek, M., Pearson, J.E.: Microscopic simulation of chemical bistability in homogeneous systems. J. Chem. Phys. **105**, 8257–8261 (1996)
25. Bart, E., Bao, S., Holcman, D.: Modeling the spontaneous activity of the auditory cortex. J. Comput. Neurosci. **19**, 357–378 (2005)
26. Barthelemy, M., Barrat, A., Pastor-Satorras, R., Vespignani2, A.: Velocity and hierarchical spread of epidemic outbreaks in scale-free networks. Phys. Rev. Lett. **92**, 178701 (2004)
27. Bazhenov, M., Timofeev, I., Steriade, M., Sejnowski, T.J.: Model of thalamocortical slow-wave sleep oscillations and transitions to activated states. J. Neurosci. **22**, 8691–8704 (2002)
28. Bedard, C., Destexhe, A.: Macroscopic models of local field potentials the apparent 1/f noise in brain activity. Biophys. J. **96**, 2589–2603 (2009)
29. Beggs, J.M., Plenz, D.: Neuronal avalanches in neocortical circuits. J. Neurosci. **23**, 11167–11177 (2003)
30. Beggs, J.M., Plenz, D.: Neuronal avalanches are diverse and precise activity patterns that are stable for many hours in cortical slice cultures. J. Neurosci. **24**, 5216–5229 (2004)
31. Beggs, J.M., Timme, N.: Being critical of criticality in the brain. Front. Physiol. **3 (163)**, 1–14 (2012)
32. Ben-Ari, Y.: Developing networks play a similar melody. Trend. Neurosci. **24**, 353–360 (2001)
33. Ben-Jacob, E., Brand, H., Dee, G., Kramer, L., Langer, J.S.: Pattern propagation in nonlinear dissipative systems. Physica D **14**, 348–364 (1985)
34. Ben-Yishai, R., Bar-Or, R.L., Sompolinsky, H.: Theory of orientation tuning in visual cortex. Proc. Nat. Acad. Sci. **92**, 3844–3848 (1995)
35. Benda, J., Herz, A.V.M.: A universal model for spike-frequency adaptation. Neural Comput. **15**, 2523–2564 (2003)
36. Benguria, R., Depassier, M.: Variational characterization of the speed of propagation of fronts for the nonlinear diffusion equation. Comm. Math. Phys. **175**, 221–227 (1996)
37. Bennett, M.R., Farnell, L., Gibson, W.G.: A quantitative model of purinergic junctional transmission of calcium waves in astrocyte networks. Biophys. J. **89**, 2235–2250 (2005)
38. Bennett, M.R., Farnell, L., Gibson, W.G.: A quantitative model of cortical spreading depression due to puringenic and gap-junction transmission in astrocyte networks. Biophys. J. **95**, 5648–5660 (2008)
39. Benucci, A., Frazor, R., Carandini, M.: Standing waves and traveling waves distinguish two circuits in visual cortex. Neuron **55**, 103–17 (2007)
40. Berestycki, H., Hamel, F., Roques, L.: Analysis of the periodically fragmented environment model: II-biological invasions and pulsating travelling fronts. J. Math. Biol. **51**, 75–113 (2005)
41. Bernard, C., Anderson, A., Becker, A., Poolos, N.P., Beck, H., Johnston, D.: Acquired dendritic channelopathy in temporal lobe epilepsy. Science **305**, 532–535 (2004)
42. Berridge, M.J.: Calcium signalling and cell proliferation. Bioessays **17**, 491–500 (1995)
43. Berridge, M.J.: Neuronal calcium signaling. Neuron **21**, 13–26 (1998)
44. Berridge, M.J., Lipp, P., Bootman, M.D.: The versatility and universality of calcium signalling. Nat. Rev. Mol. Cell Biol. **1**, 11–21 (2000)

45. Bertram, R., Smith, G.D., Sherman, A.: Modeling study of the effects of overlapping calcium microdomains on neurotransmitter release. Biophys. J. **76**, 735–750 (1999)
46. Blake, R.: A primer on binocular rivalry, including current controversies. Brain Mind **2**, 5–38 (2001)
47. Blake, R., Logothetis, N.: Visual competition. Nat. Rev. Neurosci. **3**, 1–11 (2002)
48. Blake, R., Wilson, H.R.: Binocular vision. Vis. Res. **51**, 754–770 (2011)
49. Blakenship, A.G., Feller, M.B.: Mechanisms underlying spontaneous patterned activity in developing neural circuits. Nat. Rev. Neurosci. **11**, 18–29 (2010)
50. Blasdel, G.G.: Orientation selectivity, preference, and continuity in monkey striate cortex. J. Neurosci. **12**, 3139–3161 (1992)
51. Blasdel, G.G., Salama, G.: Voltage-sensitive dyes reveal a modular organization in monkey striate cortex. Nature **321**, 579–585 (1986)
52. Boccaletti, S., Latora, V., Moreno, Y., Chavez, M., Hwang, D.U.: Complex networks: Structure and dynamics. Phys. Rep. **424**, 175–308 (2006)
53. Bonhoeffer, T., Grinvald, A.: Orientation columns in cat are organized in pinwheel like patterns. Nature **364**, 166–146 (1991)
54. Boonstra, T., Daffertshofer, A., Breakspear, M., Beek, P.: Multivariate time-frequency analysis of electromagnetic brain activity during bimanual motor learning. Neuroimage **36**, 370–377 (2007)
55. Borisyuk, R., Kirillov, A.B.: Bifurcation analysis of a neural network model. Biol. Cybern. **66**, 319–325 (1992)
56. Bosking, W.H., Zhang, Y., Schofield, B., Fitzpatrick, D.: Orientation selectivity and the arrangement of horizontal connections in tree shrew striate cortex. J. Neurosci. **17**, 2112–2127 (1997)
57. Boustani, S.E., Destexhe, A.: A master equation formalism for macroscopic modeling of asynchronous irregular activity states. Neural Comput. **21**, 46–100 (2009)
58. Brackley, C.A., Turner, M.S.: Random fluctuations of the firing rate function in a continuum neural field model. Phys. Rev. E **75**, 041913 (2007)
59. Brascamp, J.W., van Ee, R., Noest, A.J., Jacobs, R.H., van den Berg, A.V.: The time course of binocular rivalry reveals a fundamental role of noise. J. Vision **6**, 1244–1256 (2006)
60. Breakspear, M., Roberts, J.A., Terry, J.R., Rodrigues, S., Mahant, N., Robinson, P.A.: A unifying explanation of primary generalized seizures through nonlinear brain modeling and bifurcation analysis. Cereb. Cortex **16**, 1296–1313 (2006)
61. Bressloff, P.C.: Resonantlike synchronization and bursting in a model of pulse-coupled neurons with active dendrites. J. Comput. Neurosci. **6**, 237–249 (1999)
62. Bressloff, P.C.: Synaptically generated wave propagation in excitable neural media. Phys. Rev. Lett. **82**, 2979–2982 (1999)
63. Bressloff, P.C.: Traveling waves and pulses in a one-dimensional network of integrate-and-fire neurons. J. Math. Biol. **40**, 169–183 (2000)
64. Bressloff, P.C.: Traveling fronts and wave propagation failure in an inhomogeneous neural network. Physica D **155**, 83–100 (2001)
65. Bressloff, P.C.: Bloch waves, periodic feature maps and cortical pattern formation. Phys. Rev. Lett. **89**, 088101 (2002)
66. Bressloff, P.C.: Spatially periodic modulation of cortical patterns by long-range horizontal connections. Physica D **185**, 131–157 (2003)
67. Bressloff, P.C.: Pattern formation in visual cortex. In: Chow, C.C., Gutkin, B., Hansel, D., Meunier, C., Dalibard, J. (eds.) Les Houches 2003: Methods and Models in Neurophysics, pp. 477–574. Elsevier, Amsterdam (2005)
68. Bressloff, P.C.: Stochastic neural field theory and the system-size expansion. SIAM J. Appl. Math. **70**, 1488–1521 (2009)
69. Bressloff, P.C.: Metastable states and quasicycles in a stochastic Wilson-Cowan model of neuronal population dynamics. Phys. Rev. E **85**, 051903 (2010)
70. Bressloff, P.C.: From invasion to extinction in heterogeneous neural fields. J. Math. Neurosci. **2**(6), 1–27 (2012)
71. Bressloff, P.C.: Spatiotemporal dynamics of continuum neural fields. J. Phys. A **45**, 033001 (109 pp.) (2012)

72. Bressloff, P.C.: Propagation of CaMKII translocation waves in heterogeneous spiny dendrites. J. Math. Biol. **66**, 1499–1525 (2013)
73. Bressloff, P.C., Coombes, S.: Dynamics of strongly coupled spiking neurons. Neural Comput. **12**, 91–129 (2000)
74. Bressloff, P.C., Cowan, J.D.: Amplitude equation approach to contextual effects in visual cortex. Neural Comput. **14**, 493–525 (2002)
75. Bressloff, P.C., Cowan, J.D.: The visual cortex as a crystal. Physica D **173**, 226–258 (2002)
76. Bressloff, P.C., Folias, S.E.: Front bifurcations in an excitatory neural network. SIAM J. Appl. Math. **65**, 131–151 (2005)
77. Bressloff, P.C., Dwyer, V.M., Kearney, M.J.: Sum-over-paths approach to diffusion on trees. J. Phys. A **29**, 1881–1896 (1996)
78. Bressloff, P.C., Cowan, J.D., Golubitsky, M., Thomas, P.J.: Scalar and pseudoscalar bifurcations: pattern formation on the visual cortex. Nonlinearity **14**, 739–775 (2001)
79. Bressloff, P.C., Cowan, J.D., Golubitsky, M., Thomas, P.J., Wiener, M.: Geometric Visual Hallucinations, Euclidean Symmetry and the Functional Architecture of Striate Cortex. Phil. Trans. Roy. Soc. Lond. B **356**, 299–330 (2001)
80. Bressloff, P.C., Folias, S.E., Prat, A., Li, Y.X.: Oscillatory waves in inhomogeneous neural media. Phys. Rev. Lett. **91**, 178101 (2003)
81. Bressloff, P.C., Newby, J.: Quasi-steady state analysis of motor-driven transport on a two-dimensional microtubular network. Phys. Rev. E **83**, 061139 (2011)
82. Bressloff, P.C., Newby, J.M.: Metastability in a stochastic neural network modeled as a velocity jump Markov process. SIAM J. Appl. Dyn. Sys. **12**, 1394–1435 (2013)
83. Bressloff, P.C., Webber, M.: Neural field model of binocular rivalry waves. J. Comput. Neurosci. **32**, 233–252 (2012)
84. Bressloff, P.C., Webber, M.A.: Front propagation in stochastic neural fields. SIAM J. Appl. Dyn. Syst. **11**, 708–740 (2012)
85. Brown, R.J., Norcia, A.M.: A method for investigating binocular rivalry in real-time with the steady state VEP. Vision Res. **37**, 2401–2408 (1997)
86. Brunel, N.: Dynamics of sparsely connected networks of excitatory and inhibitory spiking neurons. J. Comput. Neurosci **8**, 183–208 (2000)
87. Brunel, N., Hakim, V.: Fast global oscillations in networks of integrate–and–fire neurons with low firing rates. Neural Comput. **11**, 1621–1671 (1999)
88. Buckwar, E., Riedler, M.G.: An exact stochastic hybrid model of excitable membranes including spatio-temporal evolution. J. Math. Biol. **63**, 1051–1093 (2011)
89. Buckwar, E., Riedler, M.G.: Laws of large numbers and langevin approximations for stochastic neural field equations. J. Math. Neurosci. **3**(1), 1–54 (2013)
90. Buice, M.A., Chow, C.C.: Effective stochastic behavior in dynamical systems with incomplete information. Phys. Rev. E **84**, 051120 (2011)
91. Buice, M., Cowan, J.D.: Field-theoretic approach to fluctuation effects in neural networks. Phys. Rev. E **75**, 051919 (2007)
92. Buice, M., Cowan, J.D., Chow, C.C.: Systematic fluctuation expansion for neural network activity equations. Neural Comp. **22**, 377–426 (2010)
93. Bures, J., Buresova, O., Krivanek, J.: The Mechanisms and Applications of Leao's Spreading Depression of Electrical Activity. Academia, Prague (1974)
94. Butts, D.A., Feller, M.B., Shatz, C.J., Rokshar, D.S.: Retinal waves are governed by collective network properties. J. Neurosci. **19**, 3580–3593 (1999)
95. Butz, E.G., Cowan, J.D.: Transient potentials in dendritic systems of arbitrary geometry. Biophys. J. **14**, 661–689 (1974)
96. Buzsaki, G.: Hippocampal sharp waves: their origin and significance. Brain Res. **398**, 242–252 (1986)
97. Buzsaki, G.: Theta oscillations in the hippocampus. Neuron **33**, 325–40 (2002)
98. Buzsaki, G.: Rhythms of the Brain. Oxford University Press, Oxford (2006)
99. Byrne, J.H., Roberts, J.L.: From Molecules to Networks: An Introduction to Cellular and Molecular Neuroscience. Elsevier, Amsterdam (2004)

100. Cai, D., Tao, L., Shelley, M., McLaughlin, D.W.: An effective kinetic representation of fluctuation–driven neuronal networks with application to simple and complex cells in visual cortex. Proc. Natl. Acad. Sci. USA **101**, 7757–7562 (2004)
101. Campbell, K., Gotz., M.: Radial glia: multi-purpose cells for vertebrate brain development. Trend. Neurosci. **25**, 235–238 (2002)
102. Cantrell, R.S., Cosner, C.: Spatial Ecology Via Reaction-Diffusion Equations. Wiley, Chichester (2003)
103. Carlsson, A.E.: Dendritic actin filament nucleation causes traveling waves and patches. Phys. Rev. Lett. **104**, 228102 (2010)
104. Carpenter, G.: A geometric approach to singular perturbation problems with applications to nerve impulse equations. J. Diff. Eqns. **23**, 335–367 (1977)
105. Casti, A.R.R., Ormutag, A., Sornborger, A., Kaplan, E., Knight, B., Victor, J., Sirovich, L.: A population study of integrate–and–fire–or burst neurons. Neural Comput. **14**, 957–986 (2002)
106. Charles, A.C., Merrill, J.E., Dickson, E.R., Sanderson, M.J.: Intercellular signaling in glial cells: calcium waves and oscillations in response to mechanical stimulation and glutamate. Neuron **6**, 983–992 (1991)
107. Charles, A.C., Naus, C.C., Zhu, D., Kidder, G.M., Dirksen, E.R., Sanderson, M.J.: Intercellular calcium signaling via gap junctions in glioma cells. J. Cell. Biol. **118**, 195–201 (1992)
108. Chen, X.: Existence, uniqueness, and asymptotic stability of traveling waves in nonlocal evolution equations. Adv. Diff. Eqns. **2**, 125 (1997)
109. Chen, K.C., Nicholson, C.: Spatial buffering of potassium ions in brain extracellular space. Biophys. J. **78**, 2776–2797 (2000)
110. Cheng, H., Lederer, W.J.: Calcium sparks. Physiol. Rev. **88**, 1491–1545 (2008)
111. Cheng, H., Lederer, M.R., Lederer, W.J., Cannell, M.B.: Calcium sparks and waves in cardiac myocytes. Am. J. Physiol. **270**, C148–C159 (1996)
112. Chervin, R.D., Pierce, P.A., Connors, B.W.: Periodicity and directionality in the propagation of epileptiform discharges across neocortex. J. Neurophysiol. **60**, 1695–1713 (1988)
113. Chialvo, D.: Emergent complex neural dynamics. Nat. Phys. **6**, 744–750 (2010)
114. Chong, S.C., Tadin, D., Blake, R.: Endogenous attention prolongs dominance durations in binocular rivalry. J. Vision **5**, 1044–1012 (2005)
115. Chow, C.C., Buice, M.: Path integral methods for stochastic differential equations. arXiv nlin/105966v1 (2011)
116. Chow, C.C., White, J.A.: Spontaneous action potentials due to channel fluctuations. Biophys. J. **71**, 3013–3021 (1996)
117. Chu, P.H., Milton, J.G., Cowan, J.D.: Connectivity and the dynamics of integrate-and-fire neural networks. Int. J. Bif. Chaos **4**, 237–243 (1994)
118. Chuquet, J., Hollander, L., Nimchinsky., E.A.: High-resolution in vivo imaging of the neurovascular unit during spreading depression. J. Neurosci. **27**, 4036–4044 (2007)
119. Churchland, M.M., et al.: Stimulus onset quenches neural variability: a widespread cortical phenomenon. Nat. Neurosci. **13**, 369–378 (2010)
120. Citri, A., Malenka, R.C.: Synaptic plasticity: multiple forms, functions, and mechanisms. Neuropsychopharmacol. **33**, 18–41 (2008)
121. Cohen, A.H., Ermentrout, G.B., Kiermel, T., Kopell, N., Sigvardt, K.A., Williams, T.L.: Modeling of intersegmental coordination in the lamprey central pattern generator for motion. Trend. Neurosci. **15**, 434–438 (1992)
122. Compte, A., Sanchez-Vives, M.V., McCormick, D.A., Wang, X.J.: Cellular and network mechanisms of slow oscillatory activity (<1 Hz) and wave propagations in a cortical network model. J. Neurophysiol. **89**, 2707–2725 (2003)
123. Collingridge, G.L., Peineau, S., Howland, J.G., Wang, Y.T.: Long-term depression in the CNS. Nat. Rev. Neurosci. **11**, 459–473 (2010)
124. Compte, A., Reig, R., Descalzo, V.F., Harvey, M.A., Puccini, G.D., Sanchez-Vives, M.V.: Spontaneous high-frequency (10–80 Hz) oscillations during up states in the cerebral cortex in vitro. J. Neurosci. **28**, 13828–13844 (2008)

125. Connors, B.W., Amitai, Y.: Epilespy: Models, mechanisms and concepts. In: Schwartkroin, P.A. (ed.) Generation of Epileptiform Discharge by Local Circuits of Neocortex, pp. 388–423. Cambridge University Press, Cambridge (1993)
126. Connors, B.W., Long, M.A.: Electrical synapses in the mammalian brain. Annu. Rev. Neurosci. **27**, 393–418 (2004)
127. Coombes, S.: The effects of ion pumps on the speed of traveling waves in the fire-diffuse-fire model of Ca^{2+} release. Bull. Math. Biol. **63**, 1–20 (2001)
128. Coombes, S.: Dynamics of synaptically coupled integrate-and-fire-or-burst neuron. Phys. Rev. E **67**, 041910 (2003)
129. Coombes, S., Bressloff, P.C.: Solitary waves in a model of dendritic cable with active spines. SIAM J. Appl. Math. **61**, 432–453 (2000)
130. Coombes, S., Bressloff, P.C.: Saltatory waves in the spike-diffuse-spike model of active dendritic spines. Phys. Rev. Lett. **91**, 028102 (2003)
131. Coombes, S., Bressloff, P.C. (eds.): Bursting: The Genesis of Rhythm in the Nervous System. World Scientific Press, London (2005)
132. Coombes, S., Laing, C.R.: Pulsating fronts in periodically modulated neural field models. Phys. Rev. E **83**, 011912 (2011)
133. Coombes, S., Lord, G.J.: Intrinsic modulation of pulse-coupled integrate-and-fire neurons. Phys. Rev. E **56**(5), 5809–5818 (1997)
134. Coombes, S., Owen, M.R.: Evans functions for integral neural field equations with Heaviside firing rate function. SIAM J. Appl. Dyn. Syst. **4**, 574–600 (2004)
135. Coombes, S., Owen, M.R.: Bumps, breathers, and waves in a neural network with spike frequency adaptation. Phys. Rev. Lett. **94**, 148102 (2005)
136. Coombes, S., Schmidt, H.: Neural fields with sigmoidal firing rates: approximate solutions. Discret. Contin. Dyn. Syst. Ser. A **28**, 1369–1379 (2010)
137. Coombes, S., Timofeeva, Y.: Sparks and waves in a stochastic fire-diffue-fire model of Ca^{2+} release. Phy. Rev. E **68**, 021915 (2003)
138. Coombes, S., Owen, M.R., Smith, G.D.: Mode-locking in a periodically forced integrate-and-fire-or-burst neuron model. Phys. Rev. E **64**, 041914 (2001)
139. Coombes, S., Lord, G.J., Owen, M.R.: Waves and bumps in neuronal networks with axo-dendritic synaptic interactions. SIAM J. Appl. Dyn. Sys. **5**, 552–574 (2003)
140. Coombes, S., Hinch, R., Timofeeva, Y.: Receptors, sparks and waves in a fire-diffuse-fire framework for Ca^{2+} release. Prog. Biophys. Mol. Biol. **85**, 197–216 (2004)
141. Coombes, S., Timofeeva, Y., Svensson, C.M., Lord, G.J., Josic, K., Cox, S.J., Colbert, C.M.: Branching dendrites with resonant membrane: a "sum-over-trips" approach. Biol. Cybern. **97**, 137–149 (2007)
142. Coombes, S., Venkov, N.A., Bojak, I., Liley, D.T.J., Laing, C.R.: Modeling electrocortical activity through improved local approximations of integral neural field equations. Phys. Rev. E **76**, 051901 (2007)
143. Cornell-Bell, A.H., Finkbeiner, S.M., Cooper, M.S., Smith, S.J.: Glutamate induces calcium waves in cultured astrocytes: long-range glial signaling. Science **247**, 470–473 (1990)
144. Dahlem, M.A., Chronicle, E.P.: A computational perspective on migraine aura. Prog. Neurobiol. **74**, 351–361 (2004)
145. Dahlem, M.A., Muller, S.C.: Migraine aura dynamics after reverse retinotopic mapping of weak excitation waves in the primary visual cortex. Biol. Cybern. **88**, 419–424 (2003)
146. Dale, N.: Dynamic ATP signalling and neural development. J. Physiol. **586**, 2429–2436 (2008)
147. Deco, G., Jirsa, V., Robinson, P.A., Breakspear, M., Friston, K.: The dynamic brain: from spiking neurons to neural masses and cortical fields. PLoS Comput. Biol. **4**, e1000092 (2008)
148. Deco, G., Jirsa, V.K., McIntosh., A.R.: Emerging concepts for the dynamical organization of resting-state activity in the brain. Nat. Rev. Neurosci. **12**, 43–56 (2011)
149. Delaney, K.R., Galperin, A., Fee, M.S., Flores, J.A., Gervais, R., Tank, D.W., Kleinfeld, D.: Waves and stimulus-modulated dynamics in an oscillating olfactory network. Proc. Natl. Acad. Sci. USA **91**, 669–673 (1994)

150. Delorme, V., Machacek, M., DerMardirossian, C., Anderson, K.L., Wittmann, T., Hanein, D., Waterman-Storer, C., Danuser, G., Bokoch, G.M.: Cofilin activity downstream of Pak1 regulates cell protrusion efficiency by organizing lamellipodium and lamella actin networks. Dev. Cell. **13**, 646–662 (2007)
151. Derkach, V., Barria, A., Soderling, T.R.: Ca^{2+}/calmodulin-kinase II enhances channel conductance of α-amino-3-hydroxyl-5-methyl-4-isoxazoleproprionate type glutamate receptors. Proc. Nat. Acad. Sci. (USA) **96**, 3269–3274 (1999)
152. Destexhe, A., Contreras., D.: Neuronal computations with stochastic network states. Science **314**, 85–90 (2006)
153. Destexhe, A., Sejnowski, T.J.: Thalamocortical Assemblies: How Ion Channels, Single Neurons and Large-Scale Networks Organize Sleep Oscillations. Oxford University Press, Oxford (2001)
154. Destexhe, A., Mainen, Z.F., Sejnowski, T.J.: Synthesis of models for excitable membranes synaptic transmission and neuromodulation using a common kinetic formalism. J. Comput. Neurosci. **1**, 195–231 (1994)
155. Difato, F., Tsushima, H., Pesce, M., Benfenati, F., Blau, A., Chieregatti, E.: The formation of actin waves during regeneration after axonal lesion is enhanced by BDNF. Sci. Rep. **1 (183)**, 1–18 (2011)
156. Dockery, J.D., Keener, J.P.: Diffusive effects on dispersion in excitable media. SIAM J. Appl. Dyn. **49**, 539–566 (1989)
157. Doubrovinski, K., Kruse, K.: Cytoskeletal waves in the absence of molecular motors. Europhys. Lett. **83**, 18003 (2008)
158. van Drongelen, W., Lee, H.C., Stevens, R.L., Hereld, M.: Propagation of seizure-like activity in a model of neocortex. J. Clin. Neurophysiol. **24**, 182–188 (2007)
159. Dyhrfjeld-Johnsen, J., Santhakumar, V., Morgan, R.J., Huerta, R., Tsimring, L., Soltesz, I.: Topological determinants of epileptogenesis in large-scale structural and functional models of the dentate gyrus derived from experimental data. J. Neurophysiol. **97**, 1566–1587 (2007)
160. Dykman, M.I., Mori, E., Ross, J., Hunt, P.M.: Large fluctuations and optimal paths in chemical kinetics. J. Chem. Phys. A **100**, 5735–5750 (1994)
161. Earnshaw, B.A., Bressloff, P.C.: Diffusion-activation model of CaMKII translocation waves in dendrites. J. Comput. Neurosci. **28**, 77–89 (2010)
162. Ebert, U., van Saarloos, W.: Front propagation into unstable states: universal algebraic convergence towards uniformly translating pulled fronts. Physica D **146**, 1–99 (2000)
163. Edwards, J.R., Gibson, W.G.: A model for Ca^{2+} waves in networks of glial cells incorporating both intracellular and extracellular communication pathways. J. Theor. Biol. **263**, 45–58 (2010)
164. Elgart, V., Kamenev, A.: Rare event statistics in reaction–diffusion systems. Phys. Rev. E **70**, 041106 (2004)
165. Elmer, C.E., Vleck, E.S.V.: Analysis and computation of traveling waves solutions of bistable differential-difference equations. Nonlinearity **12**, 771–798 (1999)
166. Ermentrout, G.B.: The behaviour of rings of coupled oscillators. Journal of Mathematical Biology **23**, 55–74 (1985)
167. Ermentrout, G.B.: The analysis of synaptically generated travelling waves. J. Comput. Neurosci. **5**, 191–208 (1998)
168. Ermentrout, G.B.: Neural networks as spatio-temporal pattern-forming systems. Rep. Prog. Phy. **61**, 353–430 (1998)
169. Ermentrout, G.B., Cowan, J.: A mathematical theory of visual hallucination patterns. Bio. Cybern. **34**, 137–150 (1979)
170. Ermentrout, G.B., Kleinfeld, D.: Traveling electrical waves in cortex: insights from phase dynamics and speculation on a computational role. Neuron **29**, 33–44 (2001)

171. Ermentrout, G.B., Kopell, N.: Frequency plateaus in a chain of weakly coupled oscillators. SIAM J. Appl. Math. **15**, 215–237 (1984)
172. Ermentrout, G.B., McLeod, J.B.: Existence and uniqueness of travelling waves for a neural network. Proc. Roy. Soc. Edin. A **123**, 461–478 (1993)
173. Ermentrout, G.B., Terman, D.: Mathematical Foundations of Neuroscience. Springer, Berlin (2010)
174. Ermentrout, G.B., Jalics, J.Z., Rubin, J.E.: Stimulus-driven traveling solutions in continuum neuronal models with a general smooth firing rate function. SIAM J. Appl. Math. **70**, 3039–3064 (2010)
175. Escudero, C., Kamanev, A.: Switching rates of multistep reactions. Phys. Rev. E **79**, 041149 (2009)
176. Escudero, C., Rodriguez, J.A.: Persistence of instanton connections in chemical reactions with time–dependent rates. Phys. Rev. E **77**, 011130 (2008)
177. Evans, J.: Nerve axon equations IV: The stable and unstable impulse. Ind. Univ. Math. J. **24**, 1169–1190 (1975)
178. Evans, L.C., Sougandis, P.E.: A PDE approach to geometric optics for certain semilinear parabolic equations. Ind. Univ. Math. J. **38**, 141–172 (1989)
179. Faisal, A.A., Selen, L.P.J., Wolpert, D.M.: Noise in the nervous system. Nat. Rev. Neurosci. **9**, 292 (2008)
180. Falcke, M.: On the role of stochastic channel behavior in intracellular Ca^{2+} dynamics. Biophys. J. **84**, 42–56 (2003)
181. Falcke, M.: Reading the patterns in living cells - the physics of Ca^{2+} signaling. Adv. Phys. **53**, 255–440 (2004)
182. Falcke, M., Tsimiring, L., Levine, H.: Stochastic spreading of intracellular Ca^{2+} release. Phys. Rev. E **62**, 2636–2643 (2000)
183. Fath, G.: Propagation failure of traveling waves in a discrete bistable medium. Physica D **116**, 176–190 (1998)
184. Faugeras, O., Touboul, J., Cessac, B.: A constructive mean–field analysis of multi–population neural networks with random synaptic weights and stochastic inputs. Frontiers in Comp. Neurosci. **3**, 1–28 (2009)
185. Faugeras, O., Veltz, R., Grimbert, F.: Persistent neural states: Stationary localized activity patterns in nonlinear continuous n-population, q-dimensional neural networks. Neural Comput. **21**, 147–187 (2009)
186. Fellin, T., Pascual, O., Gobbo, S., Pozzan, T., Haydon, P.G., Carmignoto, G.: Neuronal synchrony mediated by astrocytic glutamate through activation of extrasynaptic NMDA receptors. Neuron **43**, 729–743 (2004)
187. Fellin, T., Pozzan, T., Carmignoto., G.: Purinergic receptors mediate two distinct glutamate release pathways in hippocampal astrocytes. J. Biol. Chem. **281**, 4274–4284 (2006)
188. Ferster, D., Miller, K.: Neural mechanisms of orientation selectivity in the visual cortex. Annual review of neuroscience **23**(1), 441–471 (2000)
189. Fianco, T.A., McCarthy, K.D.: Intracellular astrocyte calcium waves in situ increase the frequency of spontaneous AMPA receptor currents in CA1 pyramidal cells. J. Neurosci. **24**, 722–732 (2004)
190. Firth, S.I., Wang, C.T., Feller, M.B.: Retinal waves: mechanisms and function in visual system development. Cell Calcium **37**, 425–432 (2005)
191. Fisher, R.A.: The wave of advance of advantageous genes. Ann. Eugenics **7**, 353–369 (1937)
192. FitzHugh, R.: Impulses and physiological states in theoretical models of nerve membrane. Biophys. J. **1**, 445–466 (1960)
193. Fivaz, M., Bandara, S., Inoue, T., Meyer, T.: Robust neuronal symmetry-breaking by Ras-triggered local positive feedback. Curr. Biol. **18**, 44–50 (2008)
194. Flynn, K.C., Pak, C.W., Shaw, A.E., Bradke, F., Bamburg, J.R.: Growth cone-like waves transport actin and promote axonogenesis and neurite branching. Dev. Neurobiol. **69**, 761–779 (2009)

195. Fogelson, A., Zucker, R.S.: Presynaptic calcium diffusion from various arrays of single channels. implications for transmitter release and synaptic facilitation. Biophys. J. **48**, 1003–1017 (1985)
196. Folias, S.E., Bressloff, P.C.: Breathing pulses in an excitatory neural network. SIAM J. Appl. Dyn. Syst. **3**, 378–407 (2004)
197. Folias, S.E., Bressloff, P.C.: Breathers in two–dimensional neural media. Phys. Rev. Lett. **95**, 208107 (2005)
198. Folias, S.E., Bressloff, P.C.: Stimulus–locked traveling pulses and breathers in an excitatory neural network. SIAM J. Appl. Math. **65**, 2067–2092 (2005)
199. Fox, R., Rasche, F.: Binocular rivalry and reciprocal inhibition. Attention Percept. Psychophys. **5**(4), 215–217 (1969)
200. Fox, R.F., Lu, Y.N.: Emergent collective behavior in large numbers of globally coupled independent stochastic ion channels. Phys. Rev. E **49**, 3421–3431 (1994)
201. Franci, A., Drion, G., Sepulchre, R.: An organizing center in a planar model of neuronal excitability. SIAM J. Appl. Dyn. Sys. **11**, 1698–1722 (2013)
202. Franks, K.M., Sejnowski, T.J.: Complexity of calcium signaling in synaptic spines. Bioessays **24**, 1130–1144 (2002)
203. Freidlin, M.I.: Limit theorems for large deviations and reaction-diffusion equations. Ann. Prob. **13**, 639–675 (1985)
204. Freidlin, M.I.: Geometric optics approach to reaction–diffusion equations. SIAM J. Appl. Math. **46**, 222–232 (1986)
205. Freidlin, M.I., Wentzell, A.D.: Random Perturbations of Dynamical Systems. Springer, New York (1984)
206. Friedman, A., Craciun, G.: A model of intracellular transport of particles in an axon. J. Math. Biol. **51**, 217–246 (2005)
207. Friedman, A., Hu, B.: Uniform convergence for approximate traveling waves in linear reaction-hyperbolic systems. Ind. Univ. Math. J. **56**, 2133–2158 (2007)
208. Fusi, S., Drew, P.J., Abbott, L.F.: Cascade models of synaptically stored memories. Neuron **45**, 599–611 (2005)
209. Garcia-Ojalvo, J., Sancho, J.M.: External fluctuations in a pattern-forming instability. Phys. Rev. E **53**, 5680–5689 (1996)
210. Gardiner, C.W.: Handbook of Stochastic Methods, 4th edn. Springer, Berlin (2009)
211. Gardner-Medwin, A.R.: Analysis of potassium dynamics in mammalian brain tissue. J. Physiol. (Lond) **335**, 393–462 (1983)
212. Gartner, J., Freidlin, M.I.: On the propagation of concentration waves in periodic and random media. Soviet Math. Dokl. **20**, 1282–1286 (1979)
213. Gerstner, W., van Hemmen, J.L.: Coherence and incoherence in a globally coupled ensemble of pulse–emitting units. Phys. Rev. Lett. **71**(3), 312–315 (1993)
214. Gerstner, W., Kistler, W.: Spiking Neuron Models. Cambridge University Press, Cambridge (2002)
215. Gerstner, W., van Hemmen, J.L., Cowan, J.D.: What matters in neuronal locking? Neural Comput. **8**, 1689–1712 (1996)
216. Gilbert, C.D.: Horizontal integration and cortical dynamics. Neuron **9**, 1–13 (1992)
217. Gilbert, C.D., Das, A., Ito, M., Kapadia, M., Westheimer, G.: Spatial integration and cortical dynamics. Proc. Nat. Acad. Sci. USA **93**, 615–622 (1996)
218. Gilbert, C.D., Wiesel, T.N.: Clustered intrinsic connections in cat visual cortex. J. Neurosci. **3**, 1116–1133 (1983)
219. Gilboa, G., Chen, R., Brenner, N.: History–dependent multiple-time-scale dynamics in a single-neuron model. J. Neurosci. **25**, 6479–6489 (2005)
220. Ginzburg, I., Sompolinsky, H.: Theory of correlations in stochastic neural networks. Phys. Rev. E **50**, 3171–3191 (1994)
221. Glass, L., Mackey, M.C.: From Clocks to Chaos. Princeton University Press, Princeton (1988)
222. Godfrey, K.B., Eglen, S.J.: Theoretical models of spontaneous activity generation and propagation in the developing retina. Mol. Biosyst. **5**, 1527–1535 (2009)

223. Godfrey, K.B., Swindale, N.V.: Retinal wave behavior through activity-dependent refractory periods. PLoS Comp. Biol. **3 (11)**, 2408–2420 (2007)
224. Goel, P., Sneyd, J., Friedman, A.: Homogenization of the cell cytoplasm: the calcium bidomain equations. SIAM Nultiscal. Model Simul. **5**, 1045–1062 (2006)
225. Goldberg, J.L.: How does an axon grow? Genes Dev. **17**, 941–958 (2003)
226. Golding, N.L., Staff, N.P., Spruston, N.: Dendritic spikes as a mechanism for cooperative long-term potentiation. Nature **418**, 326–331 (2002)
227. Goldwyn, J.H., Shea-Brown, E.: The what and where of adding channel noise to the Hodgkin-Huxley equations. PLoS Comp. Biol. **7 (11)**, e1002247 (2011)
228. Golomb, D., Amitai, Y.: Propagating neuronal discharges in neocortical slices: Computational and experimental study. J. Neurophysiol. **78**, 1199–1211 (1997)
229. Golomb, D., Ermentrout, G.: Bistability in pulse propagation in networks of excitatory and inhibitory populations. Phys. Rev. Lett. **86**, 4179–4182 (2001)
230. Golomb, D., Ermentrout, G.B.: Continuous and lurching traveling waves in neuronal networks with spatially-decaying connectivity and delay. Proc. Natl. Acad Sci. USA **96**, 13480–13485 (1999)
231. Golomb, D., Rinzel, J.: Clustering in globally coupled inhibitory neurons. Physica D **72**, 259–282 (1994)
232. Golomb, D., Wang, X.J., Rinzel, J.: Propagation of spindle waves in a thalamic slice model. J. Neurophysiol. **75**, 750–769 (1996)
233. Gomez, T.M., Spitzer, N.C.: Regulation of growth cone behavior by calcium: New dynamics to earlier perspectives. J. Neurobiol. **44**, 174–183 (1999)
234. Gomez, T.M., Zheng, J.Q.: The molecular basis for calcium-dependent axon pathfinding. Nat. Rev. Neurosci. **7**, 115–125 (2006)
235. Gonzalez-Billault, C., Munoz-Llancao, P., Henriquez, D.R., Wojnacki, J., Conde, C., Caceres, A.: The role of small GTPases in neuronal morphogenesis and polarity. Cytoskeleton **69**, 464–485 (2012)
236. Gordon, G.R., Baimoukhametova, D.V., Hewitt, S.A., Kosala, W.R.A., Rajapaksha, J.S., Fisher, T.E., Bains, J.S.: Noropinephrine triggers release of glial ATP to increase postsynaptic efficacy. Nat. Neurosci. **8**, 1078–1086 (2005)
237. Gorji, A.: Spreading depression: A review of the clinical relevance. Brain Res. Revs. **38**, 33–60 (2001)
238. Gourley, S.A.: Travelling front solutions of a nonlocal fisher equation. J. Math Biol. **41**, 272–284 (2000)
239. Grannan, E.R., Kleinfeld, D., Sompolinsky, H.: Stimulus dependent synchronization of neuronal assemblies. Neural Comput. **5**, 550–569 (1993)
240. Gray, W.G., Lee, P.C.Y.: On the theorems for local volume averaging of multiphase systems. Int. J. Multiphase Flow **3**, 333–340 (1977)
241. Greenstein, J.L., Hinch, R., Winslow, R.L.: Mechanisms of excitation-contraction coupling in an integrative model of the cardiac ventricular myocyte. Biophys. J. **90**, 77–91 (2006)
242. Grindrod, P.: Patterns and Waves: The Theory and Application of Reaction-Diffusion Equations. Clarendon Press, Oxford (1991)
243. Grinvald, A., Lieke, E.E., Frostig, R.D., Hildesheim, R.: Cortical point-spread function and long-range lateral interactions revealed by real-time optical imaging of macaque monkey primary visual cortex. J. Neurosci. **14**, 2545–2568 (1994)
244. Groff, J.R., DeRemigio, H., Smith, G.D.: Stochastic methods in neuroscience, chap. 2. In: Markov Chain Models of Ion Channels and Calcium Release Sites, pp. 29–64. Oxford University Press, Oxford (2009)
245. Gu, X., Olson, E.C., Spitzer, N.: Spontaneous neuronal calcium spikes and waves during early differentiation. . J. Neurosci. **14**, 6325–6335 (1994)
246. Gu, X., Spitzer, N.C.: Breaking the code: regulation of neuronal differentiation by spontaneous calcium transients. Dev. Neurosci. **19**, 33–41 (1997)
247. Guan, C.B., Xu, H.T., Jin, M., Yuan, X.B., Poo, M.M.: Long-range Ca^{2+} signaling from growth cone to soma mediates reversal of neuronal migration induced by Slit-2. Cell **129**, 385–395 (2007)

248. Guckenheimer, J., Holmes, P.J.: Nonlinear Oscillations, Dynamical Systems and Bifurcations of Vector Fields. Springer, New York (1983)
249. Guthrie, P.B., Knappenberger, J., Segal, M., Bennett, M.V., , Charles, A.C., Kater, S.B.: ATP released from astrocytes mediates glial calcium waves. J. Neurosci. **19**, 520–528 (1999)
250. Haas, B., Schipke, C.G., Peters, O., Sohl, G., Willecke, K., Kettenmann, H.: Activity-dependent ATP-waves in the mouse neocortex are independent from astrocytic calcium waves. Cereb. Cortex **16**, 237–246 (2006)
251. Hagberg, A., Meron, E.: Pattern formation in non–gradient reaction–diffusion systems: the effects of front bifurcations. Nonlinearity **7**, 805–835 (1994)
252. Hagberg, A., Meron, E., Rubinstein, I., Zaltzman., B.: Controlling domain patterns far from equilibrium. Phys. Rev. Lett. **76**, 427–430 (1996)
253. Halassa, M.M., Fellin, T., Haydon, P.G.: The tripartite synapse: roles for gliotransmission in health and disease. Trend. Mol. Med. **13**, 54–63 (2007)
254. Hall, A.: Rho GTPases and the actin cytoskeleton. Science **279**, 509–514 (1998)
255. Han, F., Caporale, N., Dan, Y.: Reverberation of recent visual experience in spontaneous cortical waves. Neuron **60**, 321–327 (2008)
256. Hanggi, P., Grabert, H., Talkner, P., Thomas, H.: Bistable systems: master equation versus Fokker–Planck modeling. Z. Physik B **28**, 135 (1984)
257. Hanggi, P., Talkner, P., Borkovec, M.: Reaction-rate theory: fifty years after Kramers. Rev. Mod. Phys. **62**, 251–341 (1990)
258. Hansel, D., Mato, G., Meunier, C.: Synchrony in excitatory neural networks. Neural Comput. **7**, 2307–2337 (1995)
259. Hansen, M., Boltano, S., Dirksen, E.R., Sanderson, M.J.: Intercellular calcium signaling induced by extracellular adenosine 5-triphosphate and mechanical stimulation in airway epithelial cells. J. Cell. Sci. **106**, 995–1004 (1993)
260. Hanson, M.G., Landmesser, L.T.: Chracaterization of the circuits that generate spontaneous episodes of activity in the early embryonic mouse spinal cord. J. Neurosci. **23**, 587–600 (2003)
261. Hanson, P.I., Meyer, T., Stryer, L., Schulman, H.: Dual role of calmodulin in autophosphorylation of multifunctional cam kinase may underlie decoding of calcium signal. Neuron **12**, 943–956 (1994)
262. Hardy, J.: A hundred years of Alzheimer's disease research. Neuron **52**, 3–13 (2006)
263. Harper, J.D., Lansbury, P.T. Jr.: Models of amyloid seeding in Alzheimer's disease and scrapie: mechanistic truths and physiological consequences of the time-dependent solubility of amyloid proteins. Annu. Rev. Biochem. **66**, 385–407 (1997)
264. Harris, T.E.: The theory of branching processes. Dover, New York (1989)
265. Harris-White, M.E., Zanotti, S.A., Frautschy, S.A., Charles, A.C.: Spiral intercellular calcium waves in hippocampal slice cultures. J. Neurophysiol. **79**, 1045–1052 (1998)
266. Hassinger, T.D., Guthrie, P.B., Atkinson, P.B., Bennett, M.V., Kater, S.B.: An extracellular signaling component in propagation of astrocytic calcium waves. Proc. Natl. Acad. Sci. USA **93**, 13268–13273 (1996)
267. Hastings, S.P.: The existence of progressive wave solutions to the Hodgkin-Huxley equations. Arc. Rat. Mech. Anal. **60**, 229–257 (1975)
268. Haydon, P.G.: Glia: listening and talking to the synapse. Nat. Rev. Neurosci. **2**, 185–193 (2000)
269. Heitmann, S., Gong, P., Breakspear, M.: A computational role for bistability and traveling waves in motor cortex. Front. Comp. Neurosci. **6 (67)**, 1–15 (2012)
270. von Helmholtz, H.: Treatise on physiological optics. Dover, New York (1866)
271. Hennig, M.H., Adams, C., Willshaw, D., Sernagor, E.: Early-stage waves in the retinal network emerge close to a critical state transition between local and global functional connectivity. J. Neurosci. **29**, 1077–1086 (2009)
272. Hill, S., Tononoi, G.: Modeling sleep and wakefulness in the thalamocortical system. J. Neurophysiol. **93**, 1671–1698 (2005)

273. Hill, A.A.V., Masino, M.A., Calabrese, R.L.: Intersegmental coordination of rhythmic motor patterns. J. Neurophysiol. **90**, 531–538 (2003)
274. Hillen, T., Othmer, H.: The diffusion limit of transport equations derived from velocity-jump processes. SIAM J. Appl. Math. **61**, 751–775 (2000)
275. Hinch, E.J.: Perturbation Methods. Cambridge University Press, Cambridge (1991)
276. Hinch, R.: A mathematical analysis of the generation and termination of calcium sparks. Biophys. J. **86**, 1293–1307 (2004)
277. Hinch, R., Chapman, S.J.: Exponentially slow transitions on a Markov chain: the frequency of calcium sparks. Eur. J. Appl. Math. **16**, 427–446 (2005)
278. Hirsch, J.D., Gilbert, C.D.: Synaptic physiology of horizontal connections in the cat's visual cortex. J. Physiol. Lond. **160**, 106–154 (1991)
279. Hodgkin, A.L., Huxley, A.F.: A quantitative description of membrane and its application to conduction and excitation in nerve. J. Physiol. **117**, 500–544 (1952)
280. Hofer, T., Politi, A., Heinrich, R.: Intercellular Ca^{2+} wave propagation through gap-junctional Ca^{2+} diffusion: a theoretical study. Biophys. J. **80**, 75–87 (2001)
281. Hofer, T., Venance, L., Giaume, C.: Control and plasticity of intercellular calcium waves in astrocytes: a modeling approach. J. Neurosci. **22**, 4850–4859 (2002)
282. Holcman, D., Tsodyks, M.: The emergence of up and down states in cortical networks. PLoS Comp. Biol. **2(3)**, 0174–0181 (2006)
283. Holcman, D., Schuss, Z., Korkotian, E.: Calcium dynamics in dendritic spines and spine motility. Biophys. J. **87**, 81–91 (2004)
284. Holmes, B.B., Diamond, M.I.: Cellular mechanisms of protein aggregate propagation. Curr. Opin. Neuro. **25**, 721–726 (2012)
285. Holmes, E.E., Lewis, M.A., Banks, J.E., Veit, R.R.: Partial differential equations in ecology: spatial interactions and population dynamics. Ecology **75**, 17–29 (1994)
286. Holmes, W.R., Carlsson, A.E., Edelstein-Keshet, L.: Regimes of wave type patterning driven by refractory actin feedback: transition from static polarization to dynamic wave behaviour. Phys. Biol. **9**, 046005 (2012)
287. Hoogland, T.M., Kuhn, B., Gobel, W., Huang, W., Nakai, J., Helmchen, F., Flint, J., Wang, S.S.: Radially expanding transglial calcium waves in the intact cerebellum. Proc. Natl. Acad. Sci. USA **106**, 3496–3501 (2009)
288. Hopfield, J.J.: Neurons with graded response have collective computational properties like those of two–state neurons. Proc. Natl. Acad. Sci. USA **81**, 3088–3092 (1984)
289. Horton, A.C., Ehlers, M.D.: Neuronal polarity and trafficking. Neuron **40**, 277–295 (2003)
290. Houweling, A.R., Bazhenov, M., Timofeev, I., Steriade, M., Sejnowski, T.J.: Homeostatic synaptic plasticity can explain post-traumatic epileptogenesis in chronically isolated neocortex. Cereb. Cortex **15**, 834–845 (2005)
291. Hsu, D., Tang, A., Hsu, M., Beggs, J.M.: Simple spontaneously active Hebbian learning model: homeostatsis of activity and connectivity, and consequences for learining and epileptogenesis. Phys. Rev. E **76**, 041909 (2007)
292. Huang, X., Troy, W.C., Yang, Q., Ma, H., Laing, C.R., Schiff, S.J., Wu, J.: Spiral waves in disinhibited mammalian neocortex. J. Neurosci. **24**, 9897–9902 (2004)
293. Hubel, D.H., Wiesel, T.N.: Sequence regularity and geometry of orientation columns in the monkey striate cortex. J. Comp. Neurol. **158**, 267–294 (1974)
294. Hubel, D.H., Wiesel, T.N.: Uniformity of monkey striate cortex: A parallel relationship between field size, scatter, and magnification factor. J. Comp. Neurol. **158**, 295–306 (1974)
295. Hudson, A., Schulman, H.: Neuronal Ca^{2+}/calmodulin-dependent protein kinase II: the role of structure and autoregulation in cellular function. Annu. Rev. Biochem. **71**, 473–510 (2002)
296. Hutt, A., Bestehorn, M., Wennekers, T.: Pattern formation in intracortical neuronal fields. Network **14**, 351–368 (2003)
297. Hutt, A., Longtin, A., Schimansky-Geier, L.: Additive noise-induces Turing transitions in spatial systems with application to neural fields and the Swift-Hohenberg equation. Physica D **237**, 755–773 (2008)
298. Iacobas, D.A., Suadicani, S.O., Spray, D.C., Scemes, E.: A stochastic two-dimensional model of intercellular Ca^{2+} wave spread in glia. Biophys. J. **90**, 24–41 (2006)

299. Idan, S., Rinzel, J., Gordon, M.S. (eds.): The Theoretical Foundations of Dendritic Function: Selected Papers of Wilfrid Rall with Commentaries. MIT Press, Cambridge (1995)
300. Invernizzi, G., Papaleo, E., Sabate, R., Ventura, S.: Protein aggregation: Mechanisms and functional consequences. Int. J. Biochem. Cell Biol. **44**, 1541–1554 (2012)
301. Izhikevich, E.: Dynamical Systems in Neuroscience: The Geometry of Excitability and Bursting. MIT Press, Cambridge (2006)
302. Jacobs, K.: Stochastic Processes for Physicists. Cambridge University Press, Cambridge (2010)
303. Jaffe, D.B., Brown, T.H.: Metabotropic glutamate receptor activation induces calcium waves within hippocampal dendrites. J. Neurophysiol. **72**, 471–474 (1994)
304. Jahr, C., Stevens, C.: A quantitative description of NMDA receptor-channel kinetic behavior. J. Neurosci. **10**, 1830–1837 (1990)
305. Jilkine, A., Maree, A.F.M., Edelstein-Keshet, L.: Mathematical model for spatial segregation of the Rho-family GTPases based on inhibitory crosstalk. Bull. Math. Biol. **68**, 1169–1211 (2007)
306. Jin, D.Z., Dragoi, V., Sur, M., Seung, H.S.: Tilt aftereffect and adaptation-induced changes in orientation tuning and visual cortex. J. Neurosci. **94**, 4038–4050 (2005)
307. Jirsa, V.K., Haken, H.: A derivation of a macroscopic field theory of the brain from the quasi-microscopic neural dynamics. Physica D **99**, 503–526 (1997)
308. Jirsa, V.K., Kelso, J.A.S.: Spatiotemporal pattern formation in neural systems with heterogeneous topologies. Phys. Rev. E **62**, 8462–8465 (2000)
309. van Kampen, N.G.: Stochastic Processes in Physics and Chemistry. North-Holland, Amsterdam (1992)
310. Kang, M., Othmer, H.G.: Spatiotemporal characteristics of calcium dynamics in astrocytes. Chaos **19**, 037116 (2009)
311. Kang, N., Xu, J., Xu, Q., Nedergaard, M., Kang, J.S.: Astrocytic glutamate release-induced transient depolarization and epileptiform discharges in hippocampal CA1 pyramidal neuron. J. Neurophysiol. **94**, 4121–4130 (2005)
312. Kang, M., Heeger, D.J., Blake, R.: Periodic perturbations producing phase-locked fluctuations in visual perception. J. Vision **9(2):8**, 1–12 (2009)
313. Kang, M., Lee, S.H., Kim, J., Heeger, D.J., Blake, R.: Modulation of spatiotemporal dynamics of binocular rivalry by collinear facilitation and pattern-dependent adaptation. J. Vision **10(11):3**, 1–15 (2010)
314. Kapitula, T., Kutz, N., Sandstede, B.: The Evans function for nonlocal equations. Ind. Univ. Math. J. **53**, 1095–1126 (2004)
315. Katz, L.C., Shatz, C.J.: Synaptic activity and the construction of cortical circuits. Science **274**, 1133–1138 (1996)
316. Keener, J.P.: Waves in excitable media. SIAM J. Appl. Math. **39**, 528–548 (1981)
317. Keener, J.P.: Propagation and its failure in coupled systems of discrete excitable cells. SIAM J. Appl. Math **31**, 269–276 (1987)
318. Keener, J.P.: Homogenization and propagation in the bistable equation. Physica D **136**, 1–17 (2000)
319. Keener, J.P.: Propagation of waves in an excitable medium with discrete release sites. SIAM J. Appl. Math. **61**, 317–314 (2000)
320. Keener, J.P.: Stochastic calcium oscillations. Math. Med. Biol. **23**, 1–25 (2006)
321. Keener, J.P., Newby, J.M.: Perturbation analysis of spontaneous action potential initiation by stochastic ion channels. Phy. Rev. E **84**, 011918 (2011)
322. Keener, J., Sneyd, J.: Mathematical Physiology I: Cellular Physiology, 2nd edn. Springer, New York (2009)
323. Keener, J.P., Hoppensteadt, F.C., Rinzel, J.: Integrate–and–fire models of nerve membrane response to oscillatory input. SIAM J. Appl. Math. **41**(3), 503–517 (1981)
324. Keizer, J., Smith, G.D.: Spark-to-wave transition: saltatory transmission of calcium waves in cardiac myocytes. Biophys. Chem. **72**, 87–100 (1998)
325. Keizer, J., Smith, G.D., Ponce-Dawson, S., Pearson, J.E.: Saltatory propagation of Ca^{2+} waves by Ca^{2+} sparks. Biophys. J. **75**, 595–600 (1998)

326. Khazipov, R., Luhmann, H.J.: Early patterns of electrical activity in the developing cerebral cortex of humans and rodents. Trend. Neurosci. **29**, 414–419 (2006)
327. Khovanov, I.A., Polovinkin, A.V., Luchinsky, D.G., McClintock, P.V.E.: Noise-induced escape in an excitable system. Phys. Rev. E **87**, 032116 (2013)
328. Kilpatrick, Z.P., Bressloff, P.C.: Binocular rivalry in a competitive neural network with synaptic depression. SIAM J. Appl. Dyn. Syst. **9**, 1303–1347 (2010)
329. Kilpatrick, Z.P., Bressloff, P.C.: Effects of synaptic depression and adaptation on spatiotemporal dynamics of an excitatory neuronal network. Physica D **239**, 547–560 (2010)
330. Kilpatrick, Z.P., Bressloff, P.C.: Spatially structured oscillations in a two-dimensional neuronal network with synaptic depression. J. Comp. Neurosci. **28**, 193–209 (2010)
331. Kilpatrick, Z.P., Bressloff, P.C.: Stability of bumps in piecewise smooth neural fields with nonlinear adaptation. Physica D **239**, 1048–1060 (2010)
332. Kilpatrick, Z.P., Folias, S.E., Bressloff, P.C.: Traveling pulses and wave propagation failure in inhomogeneous neural media. SIAM J. Appl. Dyn. Syst. **7**, 161–185 (2008)
333. Kim, H.G., Connors, B.W.: Apical dendrites of the neocortex: correlation between sodium and calcium-dependent spiking and pyramidal cell morphology. J. Neurosci. **13**, 5301–5311 (1993)
334. Kim, U., Bal, T., McCormick, D.A.: Spindle waves are propagating synchronized oscillations in the ferret LGN in vitro. J. Neurophysiol. **74**, 1301–1323 (1995)
335. Kinezaki, N., Kawasaki, K., Takasu, F., Shigesada, N.: Modeling biological invasions into periodically fragmented environments. Theor. Popul. Biol. **64**, 291–302 (2003)
336. Kishimoto, K., Amari, S.: Existence and stability of local excitations in homogeneous neural fields. J. Math. Biol. **7**, 303–318 (1979)
337. Kistler, W.M., Seitz, R., van Hemmen, J.L.: Modeling collective excitations in cortical tissue. Physica D **114**, 273–295 (1998)
338. Kleinfeld, D., Delaney, K.R., Fee, M.S., Flores, J.A., Tank, D.W., Gelperin, A.: Dynamics of propagating waves in the olfactory network of a terrestrial mollusc: an electrical and optical study. J. Neurophysiol. **72**, 1402–1419 (1994)
339. Knessl, C., Mangel, M., Matkowsky, B.J., Schuss, Z., Tier, C.: An asymptotic solution of the Kramers-Moyal equation and first passage time problems for Markov jump processes. Phys. Rev. E **29**, 3359–3369 (1984)
340. Knessl, C., Matkowsky, B.J., Schuss, Z., Tier, C.: An asymptotic theory of large deviations for Markov jump processes. SIAM J. Appl. Math. **46**, 1006–1028 (1985)
341. Koch, C.: Cable theory in neurons with active, linearized membranes. Biol. Cybern. **50**, 15–33 (1984)
342. Koch, C.: Biophysics of Computation. Oxford University Press, New York (1999)
343. Koch, C., Zador, A.M.: The function of dendritic dendritic spines. devices subserving biochemical rather than electrical compartmentalization. J. Neurosci. **13**, 413–422 (1993)
344. Koch, C., Poggio, T., Torre, V.: Nonlinear interactions in a dendritic tree: localization, timing and role in information processing. Proc. Nat. Acad. Sci. (USA) **80**, 2799–2802 (1983)
345. Kolmogorff, A., Petrovsky, I., Piscounoff, N.: Étude de l'équation de la diffusion avec croissance de la quantité de matière et son application à un problème biologique. Moscow Univ. Bull. Math. **1**, 1–25 (1937)
346. Konur, S., Rabinowitz, D., Fenstermaker, V.L., Yuste, R.: Systematic regulation of spine sizes and densities in pyramidal neurons. J. Neurobiol. **56**, 95–112 (2003)
347. Kopell, N., Ermentrout, G.B.: Symmetry and phase-locking in chains of weakly coupled oscillators. Comm. Pure Appl. Math. **39**, 623–660 (1986)
348. Kramer, M.A., Cash, S.S.: Epilepsy as a disorder of cortical network organization. Neuroscientist **18**, 360–372 (2012)
349. von Krosigk, M., Bal, T., McCormick, D.: Cellular mechanisms of a synchronized oscillation in the thalamus. Science **261**, 361–364 (1993)
350. Kuramoto, Y.: Chemical Oscillations, Waves and Turbulence. Springer, New-York (1984)
351. Kurtz, T.G.: Limit theorems for a sequence of jump Markov processes approximating ordinary differential equations. J. Appl. Prob. **8**, 344–356 (1971)

352. Kurtz, T.G.: Limit theorems and diffusion approximations for density dependent Markov chains. Math. Prog. Stud. **5**, 67 (1976)
353. Lago-Fernandez, L.F., Huerta, R., Corbacho, F., Siguenza, J.A.: Fast response and temporal coherent oscillations in small-world networks. Phys. Rev. Lett. **84**, 2758–2761 (2000)
354. Laing, C.R.: Spiral waves in nonlocal equations. SIAM J. Appl. Dyn. **4**, 588–606 (2005)
355. Laing, C.R., Chow, C.C.: A spiking neuron model for binocular rivalry. J. Comput. Neurosci. **12**, 39–53 (2002)
356. Laing, C.R., Troy, W.C.: PDE methods for nonlocal models. SIAM J. Appl. Dyn. Syst. **2**, 487–516 (2003)
357. Lam, Y.W., Cohen, L.B., Wachowiak, M., Zochowski, M.R.: Odors elicit three different oscillations in the turtle olfactory bulb. J. Neurosci. **20**, 749–762 (2000)
358. Lance, J.W.: Current concepts of migraine pathogenesis. Neurology **43**, 11–15 (1993)
359. Largo, C., Cuevas, P., Somjen, G., Rio, R.M., Herreras, O.: The effect of depressing glial function in rat brain in situ on ion homeostasis, synaptic transmission, and neuronal survival. J. Neurosci. **16**, 1219–1229 (1996)
360. Largo, C., Ibarz, J.M., Herreras, O.: Effects of the gliotoxin fluorocitrate on spreading depression and glial membrane potential in rat brain in situ. J. Neurophysiol. **78**, 295–307 (1997)
361. Larkum, M.E., Zhu, J.J., Sakmann, B.: A new cellular mechanism for coupling inputs arriving at different cortical layers. Nature **398**, 338–341 (1999)
362. Larkum, M.E., Nevian, T., Sandler, M., Polsky, A., Schiller, J.: Synaptic integration in tuft dendrites of layer 5 pyramidal neurons: a new unifying principle. Science **325**, 756–760 (2009)
363. Lashley, K.: Patterns of cerebral integration indicated by scotomas of migraine. Arch. Neurol. Pyschiatry **46**, 331–339 (1941)
364. Lauritsen, K.B., Zapperi, S., Stanley, H.E.: Self-organized branching processes: avalanche models with dissipation. Phys. Rev. E **54**, 2483–2488 (1996)
365. Leao, A.A.P.: Spreading depression of activity in the cerebral cortex. J. Neurophysiol. **10**, 409–414 (1944)
366. Leao, A.A.P., Morrisson, R.S.: Propagation of spreading cortical depression. J. Neurophysiol. **8**, 33–45 (1945)
367. Lechleiter, J., Girard, S., Peralta, E., Clapham, D.: Spiral calcium wave propagation and annihilation in *xenopus laevis* oocytes. Science **252**, 123–126 (1991)
368. Leclerc, C., Neant, I., Moreau, M.: The calcium: an early signal that initiates the formation of the nervous system during early embryogenesis. Front. Mol. Neurosci. **5 (64)**, 1–12 (2012)
369. Lee, S.H., Blake, R., Heeger, D.J.: Traveling waves of activity in primary visual cortex during binocular rivalry. Nat. Neurosci. **8**, 22–23 (2005)
370. Lee, S.J., Escobedo-Lozoya, Y., Szatmari, E.M., Yasuda, R.: Activation of CaMKII in single dendritic spines during long-term potentiation. Nature **458**, 299–304 (2009)
371. Lee, S.J., Lim, H.S., Masliah, E., Lee, H.J.: Protein aggregate spreading in neurodegerative diseases: problems and perspectives. Neuro. Res. **70**, 339–348 (2011)
372. Lehky, S.R.: Binocular rivalry is not chaotic. Proc. Roy. Soc. Lond. Biol Sci. **259**, 71–76 (1995)
373. Lehky, S.R.: No binocular rivalry in the LGN of alert macaque monkeys. Vis. Res. **36**, 1225–1234 (1996)
374. Lehner, F.K.: On the validity of Fick's law for transient diffusion through a porous medium. Chem. Eng. Sci. **34**, 821–825 (1977)
375. Lemieux, L., Daunizeau, J., Walker, M.C.: Concepts of connectivity and human epileptic activity. Front. Syst. Neurosci. **5 (12)**, 1–13 (2011)
376. Leopold, D.A., Logothetis, N.K.: Activity changes in early visual cortex reflect monkeys' percepts during binocular rivalry. Nature **379**, 549–553 (1996)
377. LeVay, S., Nelson, S.B.: Columnar organization of the visual cortex. In: Leventhal, A.G. (ed.) The Neural Basis of Visual Function, pp. 266–315. CRC Press, Boca Raton (1991)
378. Levelt, W.J.M.: On Binocular Rivalry. Institute for Perception RVO–TNO, Soesterberg, The Netherlands (1965)
379. Leybaert, L., Paemeleire, K., Strahonja, A., Sanderson, M.J.: Inositol-trisphosphate-dependent intercellular calcium signaling in and between astrocytes and endothelial cells. Glia **24**, 398–407 (1998)

380. Leybaert, L., Sanderson, M.J.: Intercellular Ca^{2+} waves: mechanisms and function. Physiol. Rev. **92**, 1359–1392 (2012)
381. Li, Y., Rinzel, J.: Equations for $InsP_3$ receptor-mediated calcium oscillations derived from a detailed kinetic model: a Hodgkin-Huxley like formalism. J. Theor. Biol. **166**, 461–473 (1994)
382. Liley, D.J.T., Cadusch, P.J., Dafilis, M.P.: A spatially continuous mean field theory of electrocortical activity. Network **13**, 67–113 (2002)
383. Linder, B., Garcia-Ojalvo, J., Neiman, A., Schimansky-Geier, L.: Effects of noise in excitable systems. Phys. Rep. **392**, 321–424 (2004)
384. Lisman, J.E.: Relating hippocampal circuitry to function: recall of memory sequences by reciprocal dentate-CA3 interactions. Neuron **22**, 233–242 (1999)
385. Lisman, J.: Long-term potentiation: outstanding questions and attempted synthesis. Phil. Trans. R. Soc. Lond. B **358**, 829–842 (2003)
386. Lisman, J.E., Schulman, H., Cline, H.: The molecular basis of CaMKII function in synaptic and behavioral memory. Nat. Rev. Neurosci. **3**, 175–190 (2002)
387. Litwin-Kumar, A., Doiron, B.: Slow dynamics and high variability in balanced cortical networks with clustered connections. Nat. Neurosci. **15**, 1498–1505 (2012)
388. Liu, Q.S., Xu, Q., Kang, G.A.J., Nedergaard, M.: Astrocyte-mediated activation of neuronal kainate receptors. Proc. Natl. Acad Sci. USA **101**, 3172–3177 (2004)
389. Llano, I., González, J., Caputo, C., Lai, F.A., Blayney, L.M., Tan, Y.P., Marty, A.: Presynaptic calcium stores underlie large-amplitude miniature IPSCs and spontaneous calcium transients. Nat. Neurosci. **3**, 1256–1265 (2000)
390. Logothetis, N.K., Leopold, D.A., Sheinberg, D.L.: What is rivalling during binocular rivalry? Nature **380**, 621–624 (1996)
391. London, M., Roth, A., Beeren, L., Hausser, M., Latham, P.E.: Sensitivity to perturbations in vivo implies high noise and suggests rate coding in cortex. Nature **466**, 123–127 (2010)
392. Loxley, P., Robinson, P.: Soliton model of competitive neural dynamics during binocular rivalry. Phys. Rev. Lett. **102**(25), 258701 (2009)
393. Lubenov, E.V., Siapas, A.G.: Hippocampal theta oscillations are travelling waves. Nature **459**, 534–539 (2009)
394. Luo, L.: Actin cytoskeleton regulation in neuronalmorphogenesis and structural plasticity. Ann. Rev. Cell Dev. Biol. **18**, 601–635 (2002)
395. Ly, C., Tranchina, D.: Critical analysis of a dimension reduction by a moment closure method in a population density approach to neural network modeling. Neural Comput. **19**, 2032–2092 (2007)
396. Madison, D.V., Nicoll, R.A.: Control of the repetitive discharge of rat CA1 pyramidal neurones in vitro. J. Physiol. **354**, 319–331 (1984)
397. Magee, J.C., Johnston, D.: Characterization of single voltage-gated Na^+ and Ca^{2+} channels in apical dendrites of rat CA1 pyramidal neurons. J. Physiol. **487**, 67–90 (1995)
398. Maier, R.S., Stein, D.L.: Limiting exit location distribution in the stochastic exit problem. SIAM J. Appl. Math **57**, 752–790 (1997)
399. Maier, N., Nimmrich, V., Draguhn, A.: Cellular and network mechanisms underlying spontaneous sharp wave–ripple complexes in mouse hippocampal slices. J. Physiol. **550**, 873–887 (2003)
400. Major, G., Polsky, A., Denk, W., Schiller, J., Tank, D.W.: Spatiotemporally graded NMDA spike/plateau potentials in basal dendrites of neocortical pyramidal neurons. J. Neurophysiol. **99**, 2584–2601 (2008)
401. Malach, R., Harel, Y.A.M., Grinvald, A.: Relationship between intrinsic connections and functional architecture revealed by optical imaging and in vivo targeted biocytin injections in primate striate cortex. Proc. Natl. Acad. Sci. USA **90**, 0469–10473 (1993)
402. Malenka, R.C., Bear, M.F.: LTP and LTD: an embarrassment of riches. Neuron **44**, 5–21 (2004)
403. Manita, S., Ross, W.N.: Synaptic activation and membrane potential changes modulate the frequency of spontaneous elementary Ca^{2+} releases events in the dendrites of pyramidal neurons. J. Neurosci. **29**, 7833–7845 (2009)

404. Marder, E., Calabrese, R.L.: Principles of rhythmic motor pattern generation. Physiol. Rev. **76**, 687–717 (1996)
405. Markram, H., Tsodyks, M.: Redistribution of synaptic efficacy between neocortical pyramidal neurons. Nature **382**, 807–810 (1996)
406. Martins-Ferreira, H., Ribeiro, I.J.: Biphasic effects of gap junctional uncoupling agents on the propagation of retinal spreading depression. Braz. J. Med. Biol. Res. **28**, 991–994 (1995)
407. Martins-Ferreira, H., Nedergaard, M., Nicholson, C.: Perspectives on spreading depression. Brain Res. Rev. **32**, 215–234 (2000)
408. Masel, J., Jansen, V.A.A., Nowak, M.A.: Quantifying the kinetic parameters of prion replication. Biophys. Chem. **77**, 139–15 (1999)
409. Masuda, N., Aihara, K.: Global and local synchrony of coupled neurons in small-world networks. Biol. Cybern. **90**, 302–309 (2004)
410. Mataga, N., Mizuguchi, Y., Hensch, T.K.: Experience-dependent pruning of dendritic spines in visual cortex by tissue plasminogen activator. Neuron **44**, 1031–1041 (2004)
411. Matthaus, F.: Diffusion versus network models as descriptions for the spread of prion diseasess in the brain. J. Theor. Biol. **240**, 104–113 (2006)
412. Mattia, M., Guidice, P.D.: Population dynamics of interacting spiking neurons. Phys. Rev. E **66**, 051917 (2002)
413. Matus, A.: Actin plasticity in dendritic spines. Science **290**, 754–758 (2000)
414. Mayer, M.L., Westbrook, G.L., Guthrie, P.B.: Voltage-dependent block by Mg2+ of NMDA responses in spinal cord neurone. Nature **309**, 261–263 (1984)
415. McCormick, D.A., Contreras, D.: On the cellular and network bases of epileptic seizures. Annu. Rev. Physiol. **63**, 815–846 (2001)
416. McLaughlin, T., Torborg, C.L., Feller, M.B., O'Leary, D.D.M.: Retinotopic map refinement requires spontaneous retinal waves during a brief critical period of development. Neuron **40**, 1147–1160 (2003)
417. Meinhardt, H.: Orientation of chemotactic cells and growth cones: models and mechanisms. J. Cell. Sci. **112**, 2867–2874 (1999)
418. Meisel, C., Storch, A., Hallmeyer-Elgner, S., Bullmore, E., Gross, T.: Failure of adaptive self-organized criticality during epileptic seizure attacks. PLoS Comp. Biol. **8**, e1002312 (2012)
419. Melamed, O., Barak, O., Silberberg, G., Markram, H., Tsodyks, M.: Slow oscillations in neural networks with facilitating synapses. J. Comp. Neurosci. **25**, 308–316 (2008)
420. Menchon, S.A., Gartner, A., Roman, P., Dotti, C.G.: Neuronal (bi)polarity as a self-organized process enhanced by growing membrane. PLoS One **6**(9), e24190 (2011)
421. Mendez, V., Fort, J., Rotstein, H.G., Fedotov, S.: Speed of reaction-diffusion fronts in spatially heterogeneous media. Phys. Rev. E **68**, 041105 (2003)
422. Mendez, V., Fedotov, S., Horsthemke, W.: Reaction-Transport Systems. Springer, Berlin (2010)
423. Meng, X., Huguet, G., Rinzel, J.: Type III excitability, slope sensitivity and coincidence detection. Disc. Cont. Dyn. Systs, **32**, 2729–2757 (2012)
424. Meunier, C., d'Incamps, B.L.: Extending cable theory to heterogeneous dendrites. Neural Comput. **20**, 1732–1775 (2008)
425. Meyer, C., van Vreeswijk, C.: Temporal correlations in stochastic networks of spiking neurons. Neural Comput. **14**, 369–404 (2002)
426. Mikhailov, A.S., Davydov, V.A., Zykov, V.S.: Complex dynamics of spiral waves and motion of curves. Physica D **70**, 1–39 (1994)
427. Miller, J.P., Rall, W., Rinzel, J.: Synaptic amplification by active membrane in dendritic spines. Brain Res. **325**, 325–330 (1985)
428. Miller, L.D., Golarai, J.J.P., Connor, J.: Ca^{2+} release from intracellular stores induced by afferent stimulation of CA3 pyramidal neurons in hippocampal slices. J. Neurophysiol. **76**, 554–562 (1996)
429. Millhauser, G.L., Salpeter, E.E., Oswald, R.E.: Diffusion model of ion–channel gating and the origin of power–law distributions from single–channel recordings. Proc. Natl. Acad. Sci. USA **85**, 1503–1507 (1988)

430. Milton, J., Jung, P.: Epilepsy as a Dynamic Disease. Springer, Berlin (2003)
431. Mirollo, R.E., Strogatz, S.H.: Synchronisation of pulse–coupled biological oscillators. SIAM J. Appl. Math. **50**(6), 1645–1662 (1990)
432. Mitchison, T., Kirschner., M.: Cytoskeletal dynamics and nerve growth. Neuron **1**, 761–772 (1988)
433. Miura, R., Huang, H., Wylie, J.: Cortical spreading depression: An enigma. Eur. Phys. J. Special Topics **147**, 287–302 (2007)
434. Mogilner, A., Oster, G.: Cell motility driven by actin polymerization. Biophys. J. **71**, 3030–3045 (1996)
435. Moldakarimov, S., Rollenhagen, J.E., Olson, C.R., Chow, C.C.: Competitive dynamics in cortical responses to visual stimuli. J. Neurophysiol. **94**, 3388–3396 (2005)
436. Moreno-Bote, R., Rinzel, J., Rubin, N.: Noise-induced alternations in an attractor network model of perceptual bistability. J. Neurophysiol. **98**, 1125–1139 (2007)
437. Morgan, R.J., Soltesz, I.: Nonrandom connectivity of the epileptic dentate gyrus predicts a major role for neuronal hubs in seizures. Proc. Natl. Acad. Sci. USA **105**, 6179–6184 (2008)
438. Mori, Y., Jilkine, A., Edelstein-Keshet, L.: Wave-pinning and cell polarity from a bistable reaction-diffusion system. Biophys. J. **94**, 3684–3697 (2008)
439. Mori, Y., Jilkine, A., Edelstein-Keshet, L.: Asymptotic and bifurcation analysis of wave-pinning in a reaction-diffusion model for cell polarization. SIAM J. Appl. Math. **71**, 1401–1427 (2011)
440. Morris, C., Lecar, H.: Voltage oscillations in the barnacle giant muscle fiber. J. Biophys. **35**, 193–213 (1981)
441. Mulleners, W.M., Chronicle, E.P., Palmer, J.E., Koehler, P.J., Vredeveld, J.W.: Visual cortex excitability in migraine with and without aura. Headache **41**, 565–572 (2001)
442. Muller, L., Destexhe, A.: Propagating waves in thalamus, cortex and the thalamocortical system: experiments and models. J. Physiol. (Paris) **106**, 222–238 (2012)
443. Mullins, O.J., Hackett, J.T., Buchanan, J.T., Friesen, W.O.: Neuronal control of swimming behavior: Comparison of vertebrate and invertebrate model systems. Prog. Neurobiol. **93**, 244–269 (2011)
444. Murray, J.D.: Mathematical Biology, vol. I, II. Springer, Berlin (2002)
445. Naeh, T., Klosek, M.M., Matkowsky, B.J., Schuss, Z.: A direct approach to the exit problem. SIAM J. Appl. Math. **50**, 595–627 (1990)
446. Nagumo, J., Armoto, S., Yoshizawa, S.: An active pulse transmission line simulating nerve axon. Proc. Inst. Radio Eng. **50**, 2061–2070 (1964)
447. Nakamura, T., Barbara, J.G., Nakamura, K., Ross, W.N.: Synergistic release of Ca^{2+} from IP_3 sensitive stores evoked by synaptic activation of mGluRs paired with backpropagating action potentials. Neuron **24**, 727–737 (1999)
448. Nedergaard, M., Cooper, A.J., Goldman, S.A.: Gap junctions are required for the propagation of spreading depression. J. Neurobiol. **28**, 433–444 (1995)
449. Nedergaard, M., Ransom, B., Goldman, S.A.: New roles for astrocytes: redefining the functional architecture of the brain. Trend. Neurosci. **26**, 523–530 (2003)
450. Netoff, T.I., Schiff, S.J.: Decreased neuronal synchronization during experimental seizures. J. Neurosci. **22**, 7297–7307 (2002)
451. Netoff, T.I., Clewely, R., Arno, S., Keck, T., White, J.A.: Epilepsy in small-world networks. J. Neurosci. **24**, 8075–8083 (2004)
452. Neukirchen, D., Bradke, F.: Neuronal polarization and the cytoskeleton. Sem. Cell. Dev. Biol. **22**, 825–833 (2011)
453. Newby, J.M., Bressloff, P.C.: Local synaptic signalling enhances the stochastic transport of motor-driven cargo in neurons. Phys. Biol. **7**, 036004 (2010)
454. Newby, J.M., Bressloff, P.C.: Quasi-steady state reduction of molecular-based models of directed intermittent search. Bull. Math. Biol. **72**, 1840–1866 (2010)
455. Newby, J., Chapman, J.: Metastable behavior in Markov processes with internal states: breakdown of model reduction techniques. J. Math. Biol. published online, DOI: 10.1007/s00285-013-0723-1 (2013)

456. Newby, J.M., Bressloff, P.C., Keeener, J.P.: The effect of potassium channels on spontaneous action potential initiation by stochastic ion channels. Phys. Rev. Lett. **111**, 128–101 (2013)
457. Newman, E.A.: Propagation of intercellular calcium waves in retinal astrocytes and Muller cells. J. Neurosci. **21**, 2215–2223 (2001)
458. Newman, M.E.J.: Spread of epidemic disease on networks. Phys. Rev. E **66**, 016128 (2002)
459. Newman, M.E.J.: The structure and function of complex networks. SIAM Rev. **45**, 167–256 (2003)
460. Newman, E.A., Zahs, K.R.: Calcium waves in retinal glial cells. Science **275**, 844–847 (1997)
461. Nicholson, C.: Diffusion and related transport mechanisms in brain tissue. Rep. Prog. Phys. **64**, 815–884 (2001)
462. Nimchinsky, E.A., Sabatini, B.L., Svoboda, K.: Structure and function of dendritic spines. Ann. Rev. Physiol. **64**, 313–353 (2002)
463. Nita, D.A., Cisse', Y., Timofeev, I., Steriade, M.: Increased propensity to seizures after chronic cortical deafferentation in vivo. J. Neurophysiol. **95**, 902–913 (2006)
464. Noble, J.V.: Geographic and temporal development of plagues. Nature **250**, 726–729 (1974)
465. Novikov, E.A.: Functionals and the random-force method in turbulence theory. Sov. Phys. JETP **20**, 1290 (1965)
466. Nowak, L., Bregestovski, P., Ascher, P., Herbet, A., Prochiantz, A.: Magnesium gates glutamate-activated channels in mouse central neurones. Nature **307**, 462–465 (1984)
467. Nunez, P.I.: Neocortical dynamics and human EEG rhythms. Oxford University Press, New York (1995)
468. Nykamp, D., Tranchina, D.: A population density method that facilitates large–scale modeling of neural networks: analysis and application to orientation tuning. J. Comp. Neurosci. **8**, 19–50 (2000)
469. Obermayer, K., Blasdel, G.G.: Geometry of orientation and ocular dominance columns in monkey striate cortex. J. Neurosci. **13**, 4114–4129 (1993)
470. O'Donnell, M., Chance, R.K., Bashaw, G.J.: Axon growth and guidance: Receptor regulation and signal transduction. Ann. Rev. Neurosci. **32**, 383–412 (2009)
471. O'Donovan, M.J.: The origin of spontaneous activity in developing networks of the vertebrate nervous system. Curr. Opin. Neuro. **9**, 94–104 (1999)
472. O'Donovan, M.J., Chub, N., Wenner, P.: Mechanisms of spontaneous activity in the developing retina. J. Neurobiol. **37**, 131–145 (1998)
473. Ohira, T., Cowan, J.D.: Stochastic neurodynamics and the system size expansion. In: Ellacott, S., Anderson, I.J. (eds.) Proceedings of the First International Conference on Mathematics of Neural Networks, pp. 290–294. Academic, New York (1997)
474. O'Keefe, J., Dostrovsky, J.: The hippocampus as a spatial map. preliminary evidence from unit activity in the freely moving rat. Brain Res. **34**, 171–174 (1971)
475. O'Keefe, J., Recce, M.L.: Phase relationship between hippocampal place units and the EEG theta rhythm. Hippocampus **3**, 317–330 (1993)
476. Oksendal, B.: Stochastic Differential Equations: An Introduction with Applications. Springer, New York (2007)
477. Omurtag, A., Knight, B.W., Sirovich, L.: On the simulation of large populations of neurons. J. Comput. Neurosci. **8**, 51–63 (2000)
478. Onsum, M., Rao, C.V.: A mathematical model for neutrophil gradient sensing and polarization. PLoS Comput. Biol. **3**, e36 (2007)
479. Ooyen, A.V., Graham, B.P., Ramakers, G.J.A.: Competition for tubulin between growing neurites during development. Neurocomputing **38**, 73–78 (2001)
480. Oray, S., Majewska, A., Sur, M.: Dendritic spine dynamics are regulated by monocular deprivation and extracellular matrix degredation. Neuron **44**, 1021–1030 (2004)
481. Othmer, H., Dunbar, S., Alt, W.: Models of dispersal in biological systems. J. Math. Biol. **26**, 263–298 (1988)
482. Otsuji, M., Ishihara, S., Co, C., Kaibuchi, K., Mochizuki, A., Kuroda, S.: A mass conserved reaction-diffusion system captures properties of cell polarity. PLoS Comput. Biol. **3**, e108 (2007)

483. Pak, C.W., Flynn, K.C., Bamburg, J.R.: Actin-binding proteins take the reins in growth cones. Nat. Rev. Neurosci. **9**, 136–147 (2008)
484. Pakdaman, K., Thieullen, M., Wainrib, G.: Fluid limit theorems for stochastic hybrid systems with application to neuron models. J. Appl. Prob. **24**, 1 (2010)
485. Panatier, A., Theodosis, D.T., Mothet, J.P., Touquet, B., Pollegioni, L., Poulain, D.A., Oliet, S.H.: Glia-derived D-serine controls NMDA receptor activity and synaptic memory. Cell **125**, 775–784 (2006)
486. Panja, D.: Effects of fluctuations on propagating fronts. Phys. Rep. **393**, 87–174 (2004)
487. Papanicolaou, G.C.: Asymptotic analysis of transport processes. Bull. Amer. Math. Soc. **81**, 330–392 (1975)
488. Parga, N., Abbott, L.F.: Network model of spontaneous activity exhibiting synchronous transitions between up and down states. Front. Neurosci. **1**, 57–66 (2007)
489. Parker, I., Ivorra, I.: Localized all-or-none calcium liberation by inositol triphosphate. Science **250**, 977–979 (1990)
490. Parker, I., Yao, Y.: Regenerative release of calcium from functionally discrete subcellular stores by inositol triphosphate. Proc. Roy. Soc. Lond. B **246**, 269–274 (1991)
491. Parpura, V., Basarsky, T.A., Liu, F., Jeftinija, K., Jeftinija, S., Haydon, P.G.: Glutamate-mediated astrocyte-neuron signalling. Nature **369**, 744–747 (1994)
492. Parri, H.R., Gould, T.M., Crunelli, V.: Spontaneous astrocytic Ca^{2+} oscillations in situ drive NMDAR-mediated neuronal excitation. Nat. Neurosci. **4**, 803–81 (2001)
493. Pascual, O., Casper, K.B., Kubera, C., Zhang, J., Revilla-Sanchez, R., Sul, J.Y., Takano, H., Moss, S.J., McCarthy, K., Haydon, P.G.: Astrocytic purinergic signaling coordinates synaptic networks. Science **310**, 113–116 (2005)
494. de Pasquale, F., Gorecki, J., Poielawski., J.: On the stochastic correlations in a randomly perturbed chemical front. J. Phys. A **25**, 433 (1992)
495. Paullet, J.E., Ermentrout, G.B.: Stable rotating waves in two-dimensional discrete active media. SIAM J. Appl. Math. **54**, 1720–1744 (1994)
496. Pavliotis, G.A., Stuart, A.M.: Multiscale Methods: Averaging and Homogenization. Springer, New York (2008)
497. Pearson, J.E., Ponce-Dawson, S.: Crisis on skid row. Physica A **257**, 141–148 (1998)
498. Pearson, R., Catsicas, M., Becker, D., Mobbs, P.: Purinergic and muscarinic modulation of the cell cycle and calcium signaling in the chick retinal ventricular zone. J. Neurosci. **22**, 7569–7579 (2002)
499. Pearson, R.A., Dale, N., Llaudet, E., Mobbs, P.: ATP released via gap junction hemichannels from the pigment epithelium regulates neural retinal progenitor proliferation. Neuron **46**, 731–744 (2005)
500. Pereda, E., Quiroga, R., Bhattacharya, J.: Nonlinear multivariate analysis of neurophysiological signals. Prog. Neurobiol. **77**, 1–37 (2005)
501. Peters, O., Schipke, C.G., Hashimoto, Y., Kettenmann, H.: Different mechanisms promote astrocyte Ca^{2+} waves and spreading depression in the mouse neocortex. J. Neurosci. **23**, 9888–9896 (2003)
502. Pikovsky, A., Rosenblum, M., Kurths, J.: Synchronization: A Universal Concept in Nonlinear Sciences. Cambridge University Press, Cambridge (2003)
503. Pinder, G.F., Gray, W.G.: Essentials of Multiphase Flow and Transport in Porous Media. Wiley, New York (2008)
504. Pinto, D., Ermentrout, G.B.: Spatially structured activity in synaptically coupled neuronal networks I: traveling fronts and pulses. SIAM J. Appl. Math **62**, 206–225 (2001)
505. Pinto, D., Ermentrout, G.B.: Spatially structured activity in synaptically coupled neuronal networks II: lateral inhibition and standing pulses. SIAM J. Appl. Math. **62**, 226–243 (2001)
506. Pinto, D., Jackson, R.K., Wayne, C.E.: Existence and stability of traveling pulses in a continuous neuronal network. SIAM J. Appl. Dyn. Syst. **4**, 954–984 (2005)
507. Pinto, D., Patrick, S.L., Huang, W.C., Connors, B.W.: Initiation, propagation, and termination of epileptiform activity in rodent neocortex in vitro involve distinct mechanisms. J. Neurosci. **25**, 8131–8140 (2005)
508. Plenz, D., Thiagarajan, T.C.: The organizing principles of neuronal avalanches: cell assemblies in the cortex? Trend. Neurosci. **30**, 101–110 (2007)

509. Polleux, F., Snider, W.: Initiating and growing an axon. Cold Spring Harb Perspect Biol **2**, a001925 (2010)
510. Polonsky, A., Blake, R., Braun, J., Heeger, D.J.: Neuronal activity in human primary visual cortex correlates with perception during binocular rivalry. Nat. Neurosci. **3**, 1153–1159 (2000)
511. Ponce, S.J., Keizer, J., Pearson, J.E.: Fire-diffuse-fire model of dynamics of intracellular calcium waves. Proc. Nat. Acad. Sci. USA **96**, 6060–6063 (1999)
512. Prechtl, J.C., Cohen, L.B., Pesaran, B., Mitra, P.P., Kleinfeld, D.: Visual stimuli induce waves of electrical activity in turtle cortex. Proc. Natl. Acad. Sci. USA **94**, 7621–7626 (1997)
513. Prusiner, S.B.: Prions. Proc. Nat. Acad. Sci. (USA) **95**, 13363–13383 (1998)
514. Rakic, P.: Elusive radial glial cells: historical and evolutionary perspective. Glia **43**, 19–32 (2003)
515. Rall, W., Snir, H.A.: Cable theory for dendritic neurons. In: Koch, C., Segev, I. (eds.) Methods in Neuronal Modelling, 2nd edn. MIT Press, Cambridge (1998)
516. Ramirez, O.A., Couve, A.: The endoplasmic reticulum and protein trafficking in dendrites and axons. Trend. Cell. Biol. **21**, 219–227 (2011)
517. Rangan, A.V., Kovacic, G., Cai, D.: Kinetic theory for neuronal networks with fast and slow excitatory conductances driven by the same spike train. Phys. Rev. E **77**, 041915 (2008)
518. Reed, M.C., Venakides, S., Blum, J.J.: Approximate traveling waves in linear reaction-hyperbolic equations. SIAM J. Appl. Math. **50**(1), 167–180 (1990)
519. Renart, A., de la Rocha, J., Bartho, P., Hollender, L., Parga, N., Reyes, A., Harris, K.D.: The asynchronous state in cortical circuits. Science **327**, 587–590 (2010)
520. Rhodes, P.: The properties and implications of NMDA spikes in neocortical pyramidal cells. J. Neurosci. **26**, 6704–6715 (2006)
521. Richardson, K.A., Schiff, S.J., Gluckman, B.J.: Control of traveling waves in the mammalian cortex. Phys. Rev. Lett. **94**, 028103 (2005)
522. Richardson, M.P.: Large scale brain models of epilepsy: dynamics meets connectomics. Epilepsy (2012)
523. Rinzel, J., Maginu, K.: Kinematic analysis of wave pattern formation in excitable media. In: Pacault, A., Vidal, C. (eds.) Non-Equilibrium Dynamics in Chemical Systems. Springer, Berlin (1984)
524. Rinzel, J., Terman, D.: Propagation phenomena in a bistable reaction–diffusion system. SIAM J. Appl. Math. **42**, 1111–1137 (1982)
525. Rinzel, J., Terman, D., Wang, X., Ermentrout, B.: Propagating activity patterns in large-scale inhibitory neuronal networks. Science **279**, 1351–1355 (1998)
526. Robinson, P.A.: Patchy propagator, brain dynamics, and the generation of spatially structured gamma oscillations. Phys. Rev. E **73**, 041904 (2006)
527. Robinson, P.A., Rennie, C.J., Wright, J.J.: Propagation and stability of waves of electrical activity in the cerebral cortex. Phys. Rev. E **56**, 826–840 (1997)
528. Robinson, P.A., Rennie, C.J., Wright, J.J., Bahramali, H., Gordon, E., Rowe, D.I.: Prediction of electroencephalographic spectra from neurophysiology. Phys. Rev. E **63**, 021903 (2001)
529. Robinson, P.A., Rennie, C.J., Rowe, D.L.: Dynamics of large-scale brain activity in normal arousal states and epileptic seizures. Phys. Rev. E **65**, 041924 (2002)
530. Rocco, A., Ebert, U., van Saarloos, W.: Subdiffusive fluctuations of "pulled" fronts with multiplicative noise. Phys. Rev. E. **65**, R13–R16 (2000)
531. Rockland, K.S., Lund, J.: Intrinsic laminar lattice connections in primate visual cortex. J. Comp. Neurol. **216**, 303–318 (1983)
532. Rose, J., Jin, S.X., Craig, A.M.: Heterosynaptic molecular dynamics: locally induced propagating synaptic accumulation of CaM Kinase II. Neuron **61**, 351–358 (2009)
533. Ross, C.A., Poirier, M.A.: Protein aggregation and neurodegenerative disease. Nat. Med. **10**(Suppl.), S10–S17 (2004)
534. Ross, W.N.: Understanding calcium waves and sparks in central neurons. Nat. Rev. Neurosci. **13**, 157–168 (2012)
535. Roxin, A., Riecke, H., Solla, S.A.: Self-sustained activity in a small-world network of excitable neurons. Phys. Rev. Lett. **92**, 198101 (2004)

536. Rubin, J.E.: A nonlocal eigenvalue problem for the stability of a traveling wave in a neuronal medium. Discret. Contin. Dyn. Syst. **10**, 925–940 (2004)
537. Rubin, J., Terman, D.: Geometric singular perturbation analysis of neuronal dynamics. In: Fiedler, B. (ed.) Handbook of Dynamical Systems: Towards Applications, vol. 2. Elsevier, Amsterdam (2002)
538. Rubin, J.E., Terman, D.: Explicit maps to predict activation order in multiphase rhythms of a coupled cell network. J. Math. Neurosci. **2**, 4 (2012)
539. Rubin, J., Wechselberger, M.: Giant squid-hidden canard: the 3d geometry of the Hodgkin–Huxley model. Biol. Cybern. **97**, 5–32 (2007)
540. Rubin, J., Wechselberger, W.: The selection of mixed-mode oscillations in a Hodgkin-Huxley model with multiple timescales. Chaos **18**, 015105 (2008)
541. Rubinov, M., Sporns, O.: Complex network measures of brain connectivity: Uses and interpretations. Neuroimage **52**, 1059–1069 (2010)
542. Ruthel, G., Banker, G.: Actin-dependent anterograde movement of growth-cone-like structures along growing hippocampal axons: A novel form of axonal transport? Cell Motil. Cytoskel. **40**, 160–173 (1998)
543. Ruthel, G., Banker, G.: Role of moving growth cone-like wave structures in the outgrowth of cultured hippocampal axons and dendrites. J. Neurobiol. **39**, 97–106 (1999)
544. van Saarloos, W.: Front propagation into unstable states. Phys. Rep. **386**, 29–222 (2003)
545. Saez, J.C., Berthoud, V.M., Branes, M.C., Martinez, A.D., Beyer., E.C.: Plasma membrane channels formed by connexins: their regulation and functions. Physiol. Rev. **83**, 1359–1400 (2003)
546. Sagues, F., Sancho, J.M., Garcia-Ojalvo, J.: Spatiotemporal order out of noise. Rev. Mod. Phys. **79**, 829–882 (2007)
547. Saitoh, T., Schwartz, J.H.: Phosphorylation-dependent subcellular translocation of a Ca^{2+}/calmodulin-dependent protein kinase produces an autonomous enzyme in aplysia neurons. J. Cell. Biol. **100**, 835–842 (1985)
548. Samuels, D.C., Hentschel, H.G.E., Fine, A.: The origin of neuronal polarization: a model of axon formation. Phil. Trans. R. Soc. Lond. B **351**, 1147–1156 (1996)
549. Sanchez-Vives, M.V., McCormick, D.A.: Cellular and network mechanisms of rhythmic recurrent activity in neocortex. Nat. Neurosci. **3**, 1027–1034 (2000)
550. Sanderson, M.J., Charles, A.C., Dirksen, E.R.: Mechanical stimulation and intercellular communication increases intracellular Ca^{2+} in epithelial cells. Cell. Regul. **1**, 585–596 (1990)
551. Sandstede, B.: Stability of travelling waves. In: Handbook of Dynamical Systems, vol. 2, pp. 983–1055. North-Holland, Amsterdam (2002)
552. Sandstede, B.: Evans functions and nonlinear stability of traveling waves in neuronal network models. Int. J. Bifur. Chaos Appl. Sci. Eng. **17**, 2693–2704 (2007)
553. Sato, T.K., Nauhaus, I., Carandini, M.: Traveling waves in visual cortex. Neuron **75**, 218–229 (2012)
554. Scemes, E., Giaume, C.: Astrocyte calcium waves: what they are and what they do. Glia **54**, 716–725 (2006)
555. Schiller, J., Schiller, Y., Stuart, G., Sakmann, B.: Calcium action potentials restricted to distal apical dendrites of rat neocortical pyramidal neurons. J. Physiol. **505**, 605–616 (1997)
556. Schiller, J., Major, G., Koester, H.J., Schiller, Y.: NMDA spikes in basal dendrites of cortical pyramidal neurons. Nature **404**, 285–289 (2000)
557. Schimansky-Geier, L., Mikhailov, A.S., Ebeling., W.: Effects of fluctuations on plane front propagation in bistable nonequilibrium systems. Ann. Phys. **40**, 277 (1983)
558. Schock, S.C., Munyao, N., Yakubchyk, Y., Sabourin, L.A., Hakim, A.M., Ventureyra, E.C.G., Thompson, C.S.: Cortical spreading depression releases ATP into the extracellular space and purinergic receptor activation contributes to the induction of ischemic tolerance. Brain Res. **1168**, 129–138 (2007)
559. Schuss, Z.: Theory and applications of stochastic processes: an analytical approach. In: Applied Mathematical Sciences, vol. 170. Springer, New York (2010)
560. Schuster, H.G., Wagner, P.: A model for neuronal oscillations in visual cortex. Biol. Cybern. **64**, 77–82 (1990)

561. Schutz, P., Bode, M., Purwins, H.G.: Bifurcations of front dynamics in a reaction-diffusion system with spatial inhomogeneities. Physica D **82**, 382–397 (1995)
562. Schwartz, E.: Spatial mapping in the primate sensory projection: analytic structure and relevance to projection. Biol. Cybern. **25**, 181–194 (1977)
563. Seely, J., Chow, C.C.: Role of mutual inhibition in binocular rivalry. J. Neurophysiol. **106**, 2136–2150 (2011)
564. Seifert, G.: Astrocyte dysfunction in neurological disorders; a molecular perspective. Nat. Rev. Neurosci. **7**, 194–206 (2006)
565. Selkoe, D.J.: Folding proteins in fatal way. Nature **426**, 900–904 (2003)
566. Selkoe, D.J.: Cell biology of protein misfolding: the examples of Alzheimer's and Parkinson's diseases. Nat. Cell Biol. **6**, 1054–1061 (2004)
567. Shadlen, M.N., Newsome, W.T.: Noise, neural codes and cortical organization. Curr. Opin. Neurobiol. **4**, 569–579 (1994)
568. Shapiro, B.E.: Osmotic forces and gap junctions in spreading depression: A computational model. J. Comp. Neurosci. **10**, 99–120 (2001)
569. Shen, K., Meyer, T.: Dynamic control of CaMKII translocation and localization in hippocampal neurons by NMDA receptor simulation. Science **284**, 162–166 (1999)
570. Shen, K., Tereul, M.N., Subramanian, K., Meyer, T.: CaMKIIβ functions as an F-actin targeting module that localizes CaMKIIα/β heterooligomers to dendritic spines. Neuron **21**, 593–606 (1998)
571. Shepherd, G.M.: The dendritic spine: a multifunctional unit. J. Neurophysiol. **75**, 2197–2210 (1996)
572. Shepherd, G.M., Brayton, R.K., Miller, J.P., Segev, I., Rinzel, J., Rall, W.: Signal enhancement in distal cortical dendrites by means of interactions between active dendritic spines. Proc. Natl. Acad. Sci. USA **82**, 2192–2195 (1985)
573. Shew, W.L., Plenz, D.: The functional benefits of criticality in the cortex. Neuroscientist **19**, 88–100 (2012)
574. Shigesada, N., Kawasaki, K., Teramoto, E.: Traveling periodic waves in heterogeneous environments. Theor. Popul. Biol. **30**, 143–160 (1986)
575. Shigesada, N., Kawasaki, K.: Biological invasions: theory and practice. Oxford University Press, Oxford (1997)
576. Shimada, T., Toriyama, M., Uemura, K., Kamiguchi, H., Sugiura, T., Watanabe, N., Inagaki, N.: Shootin1 interacts with actine retrograde flow and L1-CAM to promote axon outgrowth. J. Cell. Biol. **181**, 817–829 (2008)
577. Shpiro, A., Moreno-Bote, R., Rubin, N., Rinzel, J.: Dynamical characteristics common to neuronal competition models. J. Neurophysiol. **97**, 37–54 (2007)
578. Shpiro, A., Curtu, R., Rinzel, J., Rubin, N.: Balance between noise and adaptation in competition models of perceptual bistability. J Comp. Neurosci. **27**, 462–473 (2009)
579. Shuai, J.W., Jung, P.: Stochastic properties of Ca^{2+} release of Inositol 1,4,5-Triphosphate receptor clusters. Biophys. J. **83**, 87–97 (2002)
580. Shusterman, V., Troy, W.C.: From baseline to epileptiform activity: a path to synchronized rhythmicity in large-scale neural networks. Phys. Rev. E **77**, 061911 (2008)
581. Silva, J.S.D., Dotti, C.G.: Breaking the neuronal sphere: regulation of the actin cytoskeleton in neuritogenesis. Nat. Rev. Neurosci. **3**, 694–704 (2002)
582. Silva, F.H.L.D., Blanes, W., Kalitzin, S.N., Parra, J., Suffczynski, P., Velis, D.N.: Dynamical diseases of brain systems: different routes to epileptic seizures. IEEE Trans. Biomed. Eng. **50**, 540–548 (2003)
583. Sincich, L.C., Blasdel, G.G.: Oriented axon projections in primary visual cortex of the monkey. J. Neurosci. **21**, 4416–4426 (2001)
584. Sinha, S.R.: Basic mechanisms of sleep and epilespy. J. Clin. Neurophysiol. **28**, 103–110 (2011)
585. Sjostrom, P.J., Rancz, E.A., Roth, A., Hausser, M.: Dendritic excitability and synaptic plasticity. Physiol. Rev. **88**, 769–840 (2008)
586. Skinner, F., Kopell, N., Marder, E.: Mechanisms for oscillation and frequency control in reciprocally inhibitory model neural networks. J. Comput. Neurosci. **1**, 69–87 (1994)

587. Smaily, M.E., Hamel, F., Roques, L.: Homogenization and influence of fragmentation in a biological invasion model. Discret. Contin. Dyn. Syst. Ser. A **25**, 321–342 (2009)
588. Smith, G.D.: Modeling the stochastic gating of ion channels. In: Fall, C., Marland, E.S., wagner, J.M., Tyson, J.J. (eds.) Computational Cell Biology, chap. 11. Springer, New York (2002)
589. Smith, G.D., Cox, C.L., Sherman, S.M., Rinzel, J.: Fourier analysis of sinusoidally driven thalamocortical relay neurons and a minimal integrate-and-burst model. J. Neurophysiol. **83**, 588–610 (2000)
590. Sneyd, J., Charles, A.C., Sanderson, M.J.: A model for the propagation of intercellular calcium waves. Amer. J. Physiol. cell physiol. **266**, C293–C302 (1994)
591. Sneyd, J., Wetton, B.T., Charles, A.C., Sanderson, M.J.: Intercellular calcium waves mediated by diffusion of inositol trisphosphate: a two-dimensional model. Am. J. Physiol. Cell Physiol. **268**, C1537–C1545 (1995)
592. Sneyd, J., Dale, P.D., Duffy, A.: Traveling waves in buffered systems: applications to calcium waves. SIAM J. Appl. Math. **58**, 1178–1192 (1998)
593. Softky, W.R., Koch, C.: Cortical cell should spike regularly but do not. Neural Comput. **4**, 643–646 (1992)
594. Soltesz, I., Staley, K.: Computational Neuroscience in Epilepsy. Academic, San Diego (2008)
595. Somers, D.C., Nelson, S., Sur, M.: An emergent model of orientation selectivity in cat visual cortical simple cells. J. Neurosci. **15**, 5448–5465 (1995)
596. Somjen, G.G.: Mechanisms of spreading depression and hypoxic spreading depression-like depolarization. Physiol. Rev. **81**, 1065–1096 (2001)
597. Soula, H., Chow, C.C.: Stochastic dynamics of a finite-size spiking neural network. Neural Comput. **19**, 3262–3292 (2007)
598. Sporns, O.: Networks of the Brain. MIT Press, Cambridge (2010)
599. Staley, K.J., Dudek, F.E.: Interictal spikes and epileptogenesis. Epilepsy Currents **6**, 199–202 (2006)
600. Stam, C.J., Reijeneveld, J.C.: Graph theoretical analysis of complex networks in the brain. Nonlin. Biomed. Phys. **1 (3)**, 1–19 (2007)
601. Steinberg, B., Wang, Y.Q., Huang, H., Miura, R.: Spatial buffering mechanism: Mathematical model and computer simulations. Math. Biosci. Eng. **2**, 675–702 (2005)
602. Steriade, M., McCormick, D.A., Sejnowski, T.J.: Thalamocortical oscillations in the sleeping and aroused brain. Science **262**, 679–685 (1993)
603. Steyn-Ross, M.L., Sleigh, D.A.S.R.J.W., Whiting, D.R.: Theoretical predictions for spatial covariance of the electroencephalographic signal during the anesthetic-induced phase transition: Increased correlation length and emergence of spatial self-organization. Phys. Rev. E **68**, 021902 (2003)
604. Stocker, M., Krause, M., Pedarzani, P.: An apamin-sensitive Ca^{2+}-activated K^+ current in hippocampal pyramidal neurons. Proc. Natl. Acad. Sci. USA **96**, 4662–4667 (1999)
605. Strack, S., Choi, S., Lovinger, D.M., Colbran, R.J.: Translocation of autophosphorylated calcium/calmodulin-dependent protein kinase II to the postsynaptic density. J. Biol. Chem. **272**, 13467–13470 (1997)
606. Stuart, G.J., Sakmann, B.: Active propagation of somatic action potentials into neocortical pyramidal cell dendrites. Nature **367**, 69–72 (1994)
607. Stuart, G., Spruston, N., Hausser, M.: Dendrites. Oxford University Press, New York (1999)
608. Stuart, G., Spruston, N., Hausser, M. (eds.): Dendrites. Oxford University Press, Oxford (2007)
609. Subramanian, K., Narang, A.: A mechanistic model for eukaryotic gradient sensing: spontaneous and induced phosphoinositide polarization. J. Theor. Biol. **231**, 49–67 (2004)
610. Sun, W., McConnell, E., Pare, J.F., Xu, Q., Chen, M., Peng, W., Lovatt, D., Han, X., Y.Smith, Nedergaard, M.: Glutamate-dependent neuroglial calcium signaling differs between young and adult brain. Science **339**, 197–200 (2013)
611. Sutherland, G.R., McNaughton, B.: Memory trace reactivation in hippocampal and neocortical neuronal ensembles. Curr. Opin. Neurobiol. **10**, 180–186 (2000)

612. Swillens, S., Dupont, G., Combettes, L., Champeil, P.: From calcium blips to calcium puffs: theoretical analysis of the requirement for interchannel communication. Proc. Nat. Acad. Sci. (USA) **96**, 13750–13755 (1999)
613. Swindale, N.V.: The development of topography in the visual–cortex: A review of models. Network **7**, 161–274 (1996)
614. Syed, M.M., Lee, S., He, S., Zhou, Z.J.: Spontaneous waves in the ventricular zone of developing mammalian retina. J. Neurophysiol. **91**, 1999–2009 (2004)
615. Syed, M.M., Lee, S., Zheng, J., Zhou, Z.J.: Stage-dependent dynamics and modulation of spontaneous waves in the developing rabbit retina. J. Physiol. **560**, 533–549 (2004)
616. Sykova, E., Nicholson, C.: Diffusion in brain extracellular space. Physiol. Rev. **88**, 1277–1340 (2008)
617. Tabak, J., Senn, W., O'Donovan, M.J., Rinzel, J.: Modeling of spontaneous activity in developing spinal cord using activity-dependent depression in an excitatory network. J. Neurosci. **20**, 3041–3056 (2000)
618. Tauber, U.C.: Field-theory approaches to nonequilibrium dynamics. Lect. Notes Phys. **716**, 295–348 (2007)
619. Taylor, A., Cottrell, G., Kristan Jr, W.: Analysis of oscillations in a reciprocally inhibitory network with synaptic depression. Neural comput. **14**(3), 561–581 (2002)
620. Terman, D.H., Ermentrout, G.B., Yew, A.C.: Propagating activity patterns in thalamic neuronal networks. SIAM J. Appl. Math **61**, 1578–1604 (2003)
621. Thul, R., Coombes, S., Smith, G.D.: Sensitisation waves in a bidomain fire-diffuse-fire model of intracellular Ca^{2+} dynamics. Physica D **238**, 2142–2152 (2009)
622. Thul, R., Smith, G.D., Coombes, S.: A bidomain threshold model of propagating calcium waves. J. Math. Biol. **56**, 435–463 (2008)
623. Tian, G.F., , Hooman, A., Takano, T., Xu, Q., Peng, W., Lin, J., Oberheim, N., Lou, N., Zielke, R., Kang, J., Nedergaard, M.: An astrocytic basis of epilepsy. Nat. Med. **11**, 973–981 (2005)
624. Timofeeva, Y.: Traveling waves in a model of quasi-active dendrites with active spines. Physica D **239**, 494–503 (2010)
625. Timofeeva, Y., Lord, G.J., Coombes, S.: Spatio-temporal filtering properies of a dendritic cable with active spines: a modeling study in the spike-diffuse-spike framework. J. Comput. Neurosci. **21**, 293–306 (2006)
626. Tong, F., Engel, S.A.: Interocular rivalry revealed in the human cortical blind-spot representation. Nature **411**, 195–199 (2001)
627. Tong, F., Meng, M., Blake, R.: Neural bases of binocular rivalry. Trend. Cog. Sci. **10**, 502–511 (2006)
628. Toriyama, M., Shimada, T., Kim, K.B., Mitsuba, M., Nomura, E., Katsuta, K., Sakumura, Y., Roepstorff, P., Inagaki, N.: Shootin1: a protein involved in the organization of an asymmetric signal for neuronal polarization. J. Cell Biol. **175**, 147–157 (2006)
629. Toriyama, M., Sakumura, Y., Shimada, T., Ishii, S., Inagaki, N.: A diffusion-based neurite length-sensing mechanism involved in neuronal symmetry breaking. Mol. Syst. Biol. **6**, 1–16 (2010)
630. Torquato, S.: Random Heterogeneous Materials. Springer, New York (2002)
631. Touboul, J., Destexhe, A.: Can power-law scaling and neuronal avalanches arise from stochastic dynamics? PLoS One **5**, 14 (2010)
632. Touboul, J., Hermann, G., Faugeras, O.: Noise–induced behaviors in neural mean field dynamics. SIAM J. Appl. Dyn. Sys. **11**, 49–81 (2012)
633. Tritsch, N.X., Yi, E., Gale, J.E., Glowatzki, E., Bergles, D.E.: The origin of spontaneous activity in the developing auditory system. Nature **450**, 50–55 (2007)
634. Troy, W.C., Shusterman, V.: Patterns and features of families of traveling waves in large-scale neuronal networks. SIAM J. Appl. Dyn. Syst. **6**, 263–292 (2007)
635. Tsai, J.C., Sneyd, J.: Are buffers boring? uniqueness and asymptotical sttability of traveling wave fronts in the buffered bistable equation. J. Math. Biol. **54**, 513–553 (2007)
636. Tsai, J.C., Sneyd, J.: Traveling waves in the buffered FitzHugh-Nagumo model. SIAM J. Appl. Math. **71**, 1606–1636 (2011)

637. Tsodyks, M., Pawelzik, K., Markram, H.: Neural networks with dynamic synapses. Neural Comput. **10**, 821–835 (1998)
638. Tuckwell, H.C., Miura, R.M.: A mathematical model for spreading cortical depression. Biophys. J. **23**, 257–276 (1978)
639. Vecchia, D., Pietrobon, D.: Migrain: a disorder of brain excitatory-inhibitory balance? Trend. Neurosci. **35**, 507–520 (2012)
640. Veen, M.V., Pelt, J.V.: Neuritic growth rate described by modelling microtubule dynamics. Bull. Math. Biol. **56**, 249–273 (1994)
641. Vellela, M., Qian, H.: Stochastic dynamics and non-equilibrium thermodynamics of a bistable chemical system: the Schlögl model revisited. J. R. Soc. Interface **6**, 925–940 (2009)
642. Veltz, R., Faugeras, O.: Local/global analysis of the stationary solutions of some neural field equations. SIAM J. Appl. Dyn. Syst. **9**, 954–998 (2010)
643. Vicker, M.G.: Eukaryotic cell locomotion depends on the propagation of self-organized reaction-diffusion waves and oscillations of actin filament assembly. J. Expt. Cell Res. **275**, 54–66 (2002)
644. Vladimirski, B.B., Tabak, J., ODonovan, M.J., Rinzel, J.: Episodic activity in a heterogeneous excitatory network, from spiking neurons to mean field. J. Comp. Neurosci. **25**, 39–63 (2008)
645. Vogels, T.P., Abbott, L.F.: Signal propagation and logic gating in networks of integrate-and-fire neurons. J. Neurosci. **25**, 10786–10795 (2005)
646. Volman, V., Sejnowski, T.J., Bazhenov, M.: Topological basis of epileptogenesis in a model of severe cortical trauma. J. Neurophysiol. **106**, 1933–1942 (2011)
647. Volman, V., Bazhenov, M., Sejnowski, T.J.: Computational models of neuron-astrocyte interaction in epilepsy. Front. Comp. Neurosci. **6**(58), 1–10 (2012)
648. Volpert, V., Petrovskii, S.: Reaction-diffusion waves in biology. Phys. Life Rev. **6**, 267–310 (2009)
649. van Vreeswijk, C.: Partial synchronization in populations of pulse-coupled oscillators. Phys. Rev. E. **54**(5), 5522–5537 (1996)
650. van Vreeswijk, C., Sompolinsky, H.: Chaotic balanced state in a model of cortical circuits. . Neural Comput. **10**, 1321–1371 (1998)
651. van Vreeswijk, C., Ermentrout, G.B., Abbott, L.F.: When inhibition not excitation synchronizes neural firing. J. Comput. Neurosci. **1**, 313–321 (1994)
652. Vuyst, E.D., Wang, N., Decrock, E., Bock, M.D., Vinken, M., Moorhem, M.V., Lai, C., Culot, M., Rogiers, V., Cecchelli, R., Naus, C.C., Evans, W.H., Leybaert, L.: Ca^{2+} regulation of connexin 43 hemichannels in C6 glioma and glial cells. Cell Calcium **46**, 176–187 (2009)
653. Wagner, J., Sneyd, J.: Effects of rapid buffers on Ca^{2+} diffusion and Ca^{2+} oscillations. Biophys. J. **67**, 447–456 (1994)
654. Wainrib, G., Thieullen, M., Pakdaman, K.: Reduction of stochastic conductance-based neuron models with time-scales separation. J. Comput. Neurosci. **32**, 327–46 (2012)
655. Walther, G.R., Maree, A.F., Edelstein-Keshet, L., Grieneisen, V.A.: Deterministic versus stochastic cell polarisation through wave-pinning. Bull. Math. Biol. **74**, 2570–2599 (2012)
656. Wang, X.J.: Decision making in recurrent neuronal networks. Neuron **60**, 215–234 (2008)
657. Wang, X.J., Rinzel, J.: Alternating and synchronous rhythms in reciprocally inhibitory model neurons. Neural Comput. **4**, 84–97 (1992)
658. Wang, S.S., Denk, W., Hausser, M.: Coincidence detection in single dendritic spines mediated by calcium release. Nat. Neurosci. **3**, 1266–1273 (2000)
659. Wang, Z., Haydon, P.G., Yeung, E.S.: Direct observation of calcium-independent intercellular ATP signaling in astrocytes. . Anal. Chem. **72**, 2001–2007 (2000)
660. Ward, M.J., Lee, J.: On the asymptotic and numerical-analyses of exponentially ill-conditioned singularly perturbed boundary value problems. Stud. Appl. Math. **94**, 271–326 (1995)
661. Watt, A.J.: Traveling waves in developing cerebellar cortex mediated by asymmetrical purkinje cell connectivity. Nat. Neurosci. **12**, 463–473 (2009)

662. Watts, D.J., Strogatz, S.H.: Collective dynamics of "small-world" networks. Nature **393**, 440–442 (1998)
663. Webber, M., Bressloff, P.C.: The effects of noise on binocular rivalry waves: a stochastic neural field model. J. Stat. Mech **3**, P03001 (2013)
664. Weinberger, H.F.: On spreading speeds and traveling waves for growth and migration in a periodic habitat. J. Math. Biol. **45**, 511–548 (2002)
665. Weiner, O.D., Marganski, W.A., Wu, L.F., Altschuler, S.J., Kirschner, M.W.: An actin-based wave generator organizes cell motility. PLoS Biol. **5**, 2053–2063 (2007)
666. Weissman, T.A., Riquelme, P.A., Ivic, L., Flint, A.C., Kriegstein, A.R.: Calcium waves propagate through radial glial cells and modulate proliferation in the developing neocortex. Neuron **43**, 647–661 (2004)
667. Werry, E.L., Liu, G.J., Bennett., M.R.: Glutamate-stimulated ATP release from spinal cord astrocytes is potentiated by substance P. J. Neurochem. **99**, 924–936 (2006)
668. Wetherington, J., Serranoa, G., Dingledine, R.: Astrocytes in the epileptic brain. Neuron **58**, 168–178 (2008)
669. White, J., Southgate, E., Thomson, J., Brenner, S.: The structure of the nervous system of the nematode Caenorhabditis elegans. Phil. Trans. R. Soc. Lond. B Biol. Sci. **314**, 1–340 (1986)
670. White, J.A., Rubinstein, J.T., Kay, A.R.: Channel noise in neurons. Trends. Neurosci. **23**, 131–137 (2000)
671. Wiley, D.A., Strogatz, S.H., Girvan, M.: The size of the sync basin. Chaos **16**, 015103 (2006)
672. Williams, G.S.B., Huertas, M.A., Sobie, E.A., Jafri, M.S., Smith, G.D.: A probability density approach to modeling local control of calcium-induced calcium release in cardiac myocytes. Biophys. J. **92**, 2311–2328 (2007)
673. Williams, G.S.B., Huertas, M.A., Sobie, E.A., Jafri, M.S., Smith, G.D.: Moment closure for local control models of calcium-induced calcium release in cardiac myocytes. Biophys. J. **95**, 1689–1703 (2008)
674. Wilson, H.R.: Computational evidence for a rivalry hierarchy in vision. Proc. Natl. Acad Sci. USA **100**, 14499–144503 (2003)
675. Wilson, H.R., Cowan, J.D.: Excitatory and inhibitory interactions in localized populations of model neurons. Biophys. J. **12**, 1–23 (1972)
676. Wilson, H.R., Cowan, J.D.: A mathematical theory of the functional dynamics of cortical and thalamic nervous tissue. Kybernetik **13**, 55–80 (1973)
677. Wilson, M.A., McNaughton, B.L.: Reactivation of hippocampal ensemble memories during sleep. Science **265**, 676–679 (1994)
678. Wilson, H.R., Blake, R., Lee, S.H.: Dynamics of traveling waves in visual perception. Nature **412**, 907–910 (2001)
679. Winfree, A.: The Geometry of Biological Time. Springer, New York (1980)
680. Wissner-Gross, Z.D., Scott, M.A., Steinmeyer, J.D., Yanik, M.F.: Synchronous symmetry breaking in neurons with different neurite counts. PLoS One **8 (2)**, e54905 (2013)
681. Wolszon, L.R., Rehder, V., Kater, S.B., Macagno, E.R.: Calcium wave fronts that cross gap junctions may signal neuronal death during development. J. Neurosci. **14**, 3437–3448 (1994)
682. Wong, R.O.L.: Retinal waves and visual development. Ann. Rev. Neurosci. **22**, 29–47 (1999)
683. Wu, J.: Propagating waves of activity in the neocortex: what they are, what they do. Neuroscientist **14**, 487–502 (2008)
684. Wu, J.Y., Guan, L., Tsau, Y.: Propagating activation during oscillations and evoked responses in neocortical slices. J. Neurosci. **19**, 5005–5015 (1999)
685. Wu, J., Guan, L., Bai, L., Yang, Q.: Spatiotemporal properties of an evoked population activity in rat sensory cortical slices. J. Neurophysiol. **86**, 2461–74 (2001)
686. Wylie, J.J., Miura, R.M.: Traveling waves in coupled reaction-diffusion models with degenerate sources. Phys. Rev. E **74**, 021909 (2006)
687. Xin, J.: Front propagation in heterogeneous media. SIAM Rev. **42**, 161–230 (2000)
688. Xu, W., Huang, X., Takagaki, K., Wu, J.Y.: Compression and reflection of visually evoked cortical waves. Neuron **55**, 119–129 (2007)
689. Yang, E., Schulman, H.: Structural examination of autoregulation of multifunctional calcium/calmodulin-dependent protein kinase II. J. Biol. Chem. **274**, 26199–26208 (1999)

690. Yao, Y., Choi, J., Parker, I.: Quantal puff of intracellular Ca^{2+} evoked by inositol triphosphate in Xenopus oocytes. J. Physiol. **482**, 533–553 (1995)
691. Yoshioka, T., Blasdel, G.G., Levitt, J.B., Lund, J.S.: Relation between patterns of intrinsic lateral connectivity, ocular dominance, and cytochrome oxidase–reactive regions in macaque monkey striate cortex. Cereb. Cortex **6**, 297–310 (1996)
692. Young, G.W.D., Keizer, J.: A single pool IP_3-receptor model for agonist stimulated Ca^{2+} oscillations. Proc. Nat. Acad. Sci. (USA) **89**, 9895–9899 (1992)
693. Yuste, R., Bonhoeffer, T.: Morphological changes in dendritic spines associated with LTP. Ann. Rev. Neurosci. **24**, 1071–1089 (2001)
694. Yuste, R., Denk, W.: Dendritic spines as a basic functional units of neuronal integration. Nature **375**, 682–684 (1995)
695. Zahradnikova, A., Zahradnik, I.: A minimal gating model for the cardiac Ca^{2+} release channel. Biophys. J. **71**, 2996–3012 (1996)
696. Zhang, L.: On the stability of traveling wave solutions in synaptically coupled neuronal networks. Diff. Int. Eq. **16**, 513–536 (2003)
697. Zimmermann, H.: Purinergic signaling in neural development. Sem. Cell Dev. Biol. **22**, 194–204 (2011)
698. Zinn-Justin, J.: Quantum Field Theory and Critical Phenomena, 4th edn. Oxford University Press, Oxford (2002)
699. Zinner, B.: Existence of traveling wavefront solutions for the discrete Nagumo equation. J. Diff. Eqns. **96**, 1–27 (1992)
700. Zucker, R.S.: Short term synaptic plasticity. Ann. Rev. Neurosci. **12**, 13–31 (1989)

Index

P.C. Bressloff, *Waves in Neural Media: From Single Neurons to Neural Fields*,
Lecture Notes on Mathematical Modelling in the Life Sciences,
DOI 10.1007/978-1-4614-8866-8, © Springer Science+Business Media New York 2014